Methods in Molecular Biology 1729

Springer Protocols

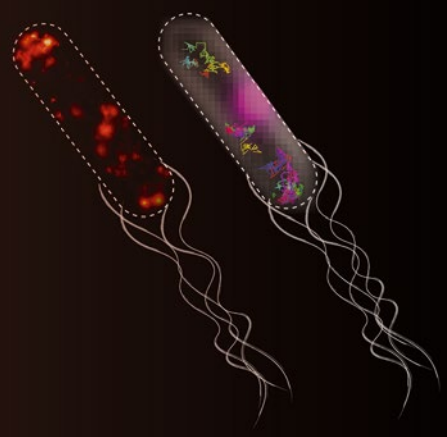

Michael D. Manson *Editor*

Bacterial Chemosensing

Methods and Protocols

Humana Press

METHODS IN MOLECULAR BIOLOGY

Series Editor
John M. Walker
School of Life and Medical Sciences
University of Hertfordshire
Hatfield, Hertfordshire, AL10 9AB, UK

For further volumes:
http://www.springer.com/series/7651

Bacterial Chemosensing

Methods and Protocols

Edited by

Michael D. Manson

Department of Biology, Texas A&M University , College Station, TX, USA

Humana Press

Editor
Michael D. Manson
Department of Biology
Texas A&M University
College Station, TX, USA

ISSN 1064-3745 ISSN 1940-6029 (electronic)
Methods in Molecular Biology
ISBN 978-1-4939-7576-1 ISBN 978-1-4939-7577-8 (eBook)
https://doi.org/10.1007/978-1-4939-7577-8

Library of Congress Control Number: 2017963360

Cover Illustration: Artist's impression of chemoreceptor distribution and mobility, based on data from photoactivation localization microscopy (PALM) and localized photoactivation single-particle tracking (LPA-SPT) in two *E. coli* cells (Chapter 18)

Printed on acid-free paper

This Humana Press imprint is published by Springer Nature
The registered company is Springer Science+Business Media, LLC
The registered company address is: 233 Spring Street, New York, NY 10013, U.S.A.

Preface

The chemosensory behavior of bacteria is the signal transduction system that is best understood at the molecular level. A good part of the reason for that status is the development of a large and diverse toolkit of both simple and sophisticated methods for the analysis of different aspects of the chemosensory signaling pathways. A large number of these methodologies have been developed using the traditional model systems of *Escherichia coli* and *Salmonella typhimurium*, but they are also generally applicable to a wide spectrum of other species. Interest is turning to other bacteria because of the diversity of chemoattractants and repellents that they recognize and because of the enormous range of ecological contexts in which chemotaxis is an important contributing factor to survival. This volume is designed to cover a wide range of up-to-date technologies that have been successfully applied to study the chemosensing behavior of the traditional model species. It is hoped that this extensive repertoire of approaches can be extended to understand chemotaxis, in particular, and chemosensing, in general, in the context of the enormously varied lifestyles adopted in the larger bacterial world.

College Station, TX, USA ***Michael D. Manson***

Contents

Contributors

Peter Ames • *Department of Biology, University of Utah, Salt Lake City, UT, USA*

Francois Anquez • *Laboratoire de Physique des Lasers, Atomes et Molécules, UMR CNRS 8523, Université Lille 1, Villeneuve d'Ascq, France*

Timofey D. Arapov • *Department of Biological Sciences, Virginia Tech, Blacksburg, VA, USA*

Howard C. Berg • *Departments of Molecular and Cellular Biology and of Physics, Harvard University, Cambridge, MA, USA; The Rowland Institute at Harvard, Cambridge, MA, USA*

Richard M. Berry • *Berry Group, Clarendon Laboratory, Department of Physics, University of Oxford, Oxford, UK*

Matthew S. Beyersdorf • *Department of Chemistry and Biochemistry, The University of North Carolina, Wilmington, NC, USA*

Robert B. Bourret • *Department of Microbiology and Immunology, University of North Carolina, Chapel Hill, NC, USA*

Ariane Briegel • *Department of Biology, Leiden University, Leiden, The Netherlands*

Abdelali Daddaoua • *Department of Environmental Protection, Estación Experimental del Zaidín, Consejo Superior de Investigaciones Científicas, Granada, Spain*

Christopher J. Day • *Institute for Glycomics, Griffith University, Southport, QLD, Australia*

Diana Di Paolo • *Cambridge Healthcare Research, St John's Innovation Centre, Cambridge, UK; Biological Physics Research Group, Clarendon Laboratory, Department of Physics, University of Oxford, Oxford, UK*

Jayna L. Ditty • *Department of Biology, College of Arts and Sciences, University of St. Thomas, St. Paul, MN, USA*

Roger R. Draheim • *School of Pharmacy and Biomedical Sciences, Institute of Biological and Biomedical Sciences, University of Portsmouth, Portsmouth, UK*

Maximilian K.G. Ehrhardt • *Department of Biochemistry, University of Otago, Dunedin, New Zealand*

Lucy V. Eke • *School of Pharmacy and Biomedical Sciences, Institute of Biological and Biomedical Sciences, University of Portsmouth, Portsmouth, UK*

Derek L. Englert • *Department of Chemical and Materials Engineering, University of Kentucky, Paducah, KY, USA*

Matilde Fernández • *Department of Environmental Protection, Estación Experimental del Zaidín, Consejo Superior de Investigaciones Científicas, Granada, Spain*

Vered Frank • *The Racah Institute of Physics, The Hebrew University, Jerusalem, Israel*

Monica L. Gerth • *Department of Biological Sciences, Victoria University of Wellington, Wellington, New Zealand*

Christopher J. Halkides • *Department of Chemistry and Biochemistry, The University of North Carolina, Wilmington, NC, USA*

Bo Hu • *Department of Microbiology and Molecular Biology, McGovern Medical School, The University of Texas, Houston, TX, USA*

Sneha Jani • *Molecular Foundry, Lawrence Livermore National Laboratory, Berkeley, CA, USA*
Arul Jayaraman • *Artie McFerrin Department of Chemical Engineering, Texas A&M University, College Station, TX, USA*
Mark S. Johnson • *Division of Microbiology and Molecular Genetics, Loma Linda University, Loma Linda, CA, USA*
Victoria Korolik • *Institute for Glycomics, Griffith University, Southport, QLD, Australia*
Tino Krell • *Department of Environmental Protection, Estación Experimental del Zaidín, Consejo Superior de Investigaciones Científicas, Granada, Spain*
Run-Zhi Lai • *Department of Biology, University of Utah, Salt Lake City, UT, USA*
Robert J. Lawrence • *School of Pharmacy and Biomedical Sciences, Institute of Biological and Biomedical Sciences, University of Portsmouth, Portsmouth, UK*
Pushkar P. Lele • *Artie McFerrin Department of Chemical Engineering, Texas A&M University, College Station, TX, USA*
Jun Liu • *Department of Microbial Pathogenesis and Microbial Sciences Institute, Yale School of Medicine, Advanced Biosciences Center, New Haven, CT, USA*
Daniel B. Lookadoo • *Department of Chemistry and Biochemistry, The University of North Carolina, Wilmington, NC, USA*
Michael D. Manson • *Department of Biology, Texas A&M University, College Station, TX, USA*
David Martín-Mora • *Department of Environmental Protection, Estación Experimental del Zaidín, Consejo Superior de Investigaciones Científicas, Granada, Spain*
Diego A. Massazza • *Instituto de Investigaciones en Ciencia y Tecnología de Materiales (INTEMA), Conicet-Universidad Nacional de Mar del Plata, Mar del Plata, Argentina*
Miguel A. Matilla • *Department of Environmental Protection, Estación Experimental del Zaidín, Consejo Superior de Investigaciones Científicas, Granada, Spain*
George W. Ordal • *Department of Medical Biochemistry, University of Illinois, Urbana, IL, USA*
Asuka A. Orr • *Artie McFerrin Department of Chemical Engineering, Texas A&M University, College Station, TX, USA*
Álvaro Ortega • *Department of Environmental Protection, Estación Experimental del Zaidín, Consejo Superior de Investigaciones Científicas, Granada, Spain*
Davi R. Ortega • *Division of Biology and Biological Engineering, California Institute of Technology, Pasadena, CA, USA*
Karen M. Ottemann • *Department of Microbiology and Environmental Toxicology, University of California Santa Cruz, Santa Cruz, CA, USA*
Rebecca E. Parales • *Department of Microbiology and Molecular Genetics, College of Biological Sciences, University of California, Davis, CA, USA*
John S. Parkinson • *Department of Biology, University of Utah, Salt Lake City, UT, USA*
Anja Paulick • *Max Planck Institute for Terrestrial Microbiology, Marburg, Germany; LOEWE Research Center for Synthetic Microbiology (SYNMIKRO), Marburg, Germany*
Daniel Penarete-Acosta • *Artie McFerrin Department of Chemical Engineering, Texas A&M University, College Station, TX, USA*
Zhuan Qin • *Department of Microbial Pathogenesis and Microbial Sciences Institute, Yale School of Medicine, Advanced Biosciences Center, New Haven, CT, USA*
Christopher V. Rao • *Department of Chemical and Biomolecular Engineering, University of Illinois at Urbana-Champaign, Urbana, IL, USA*

Miriam Rico-Jiménez • *Department of Environmental Protection, Estación Experimental del Zaidín, Consejo Superior de Investigaciones Científicas, Granada, Spain*
Birgit E. Scharf • *Department of Biological Sciences, Virginia Tech, Blacksburg, VA, USA*
Katharina M. Scherer • *Laser Analytics Group, Department of Chemical Engineering and Biotechnology, University of Cambridge, Cambridge, UK*
Andrew L. Seely • *Division of Math and Science, University of Arkansas Community College Batesville, Batesville, TX, USA*
Thomas S. Shimizu • *AMOLF Institute, Amsterdam, The Netherlands*
Ruth E. Silversmith • *Department of Microbiology and Immunology, University of North Carolina, Chapel Hill, NC, USA*
Jacopo Solari • *AMOLF Institute, Amsterdam, The Netherlands*
Victor Sourjik • *Max Planck Institute for Terrestrial Microbiology, Marburg, Germany; LOEWE Research Center for Synthetic Microbiology (SYNMIKRO), Marburg, Germany*
Claudia A. Studdert • *Instituto de Agrobiotecnología del Litoral (IAL), Conicet-Universidad Nacional del Litoral, CCT, Santa Fe, Argentina*
Nitesh Sule • *Artie McFerrin Department of Chemical Engineering, Texas A&M University, College Station, TX, USA*
Phanourios Tamamis • *Artie McFerrin Department of Chemical Engineering, Texas A&M University, College Station, TX, USA*
Linda Turner • *The Rowland Institute, Cambridge, MA, USA*
Ady Vaknin • *The Racah Institute of Physics, The Hebrew University, Jerusalem, Israel*
Hanna E. Walukiewicz • *Department of Chemical and Biomolecular Engineering, University of Illinois at Urbana-Champaign, Urbana, IL, USA*
Suzanne L. Warring • *Department of Biochemistry, University of Otago, Dunedin, New Zealand*
Kylie J. Watts • *Division of Microbiology and Molecular Genetics, Loma Linda University, Loma Linda, CA, USA*
Benjamin A. Webb • *Department of Biological Sciences, Virginia Tech, Blacksburg, VA, USA*
Wen Yang • *Department of Biology, Leiden University, Leiden, The Netherlands*
Rahmi Yusuf • *School of Pharmacy and Biomedical Sciences, Institute of Biological and Biomedical Sciences, University of Portsmouth, Portsmouth, UK*
Igor B. Zhulin • *Computer Science and Mathematics Division, Oak Ridge National Laboratory, Oak Ridge, TN, USA; Department of Microbiology, University of Tennessee, Knoxville, TN, USA*

Part I

Introduction

Chapter 1

The Diversity of Bacterial Chemosensing

Michael D. Manson

Abstract

Bacteria have a continuous and urgent need to inform themselves about the chemistry of their surroundings. They must rapidly adjust their patterns of gene expression, their metabolic and transport functions, and their behavior to cope with every challenge and opportunity with which they are presented. This volume collates the most recent methods developed to monitor and manipulate the processes by which bacteria sense and respond to their chemical environment.

Key words Signal transduction, Two-component systems, Chemoreceptors, Chemotaxis

1 Introduction

Bacteria are by far the most abundant cellular life on our planet, and they are nearly ubiquitous in every environment in which some form of liquid water is available. Some species tolerate an enormous range of extremes of temperature, pH, desiccation, radiation, pressure, nutrient limitation, host defense mechanisms, and other physical and chemical insults. They are uniformly small—although single cells of *Epulopiscium fishelsoni* [1] and *Thiomargarita nambiensis* [2] are visible to the naked human eye, and we are all familiar with the long threads of filamentous cyanobacteria [3] that clog almost any reasonably still body of water. As a consequence of their diminutive size, they are largely at the mercy of their immediate surroundings and, except in higher order structures like biofilms (more about them anon), largely at the mercy of their immediate surroundings. Thus, the paramount aspect of bacterial existence, possibly except growth and reproduction, is the ability to adapt rapidly and appropriately to the milieu in which they find themselves. And, they have been doing so for at least 3.5 billion years.

This volume focuses on the methods used to study one aspect of this adaptive behavior: the ability of bacteria to respond to the extraordinarily wide range of chemistry found in the varied

Michael D. Manson (ed.), *Bacterial Chemosensing: Methods and Protocols*, Methods in Molecular Biology, vol. 1729, https://doi.org/10.1007/978-1-4939-7577-8_1,

ecological niches they inhabit. The coverage obviously has to be limited because of the overwhelming breadth of the entire topic. My own familiarity is with the study of chemical sensing by the enteric bacteria that inhabit the mammalian gut, primarily *Escherichia coli* and *Salmonella enterica*. When several colleagues and I initiated the first BLAST (Bacterial Locomotion and Signal Transduction) Conference in 1991, the program was largely confined to those species, with a few outliers we lumped into a "funny bug" session. To my initial chagrin, the funny bugs now outnumber the two old standbys, although I proudly proclaim that we still have a lot to learn about them as well.

Thus, the history of the field reflects a bias toward protocols originally designed to study *E. coli* and *S. enterica*. However, these approaches can be, and in many instances have been, adapted to study a wide variety of other bacterial species, and even non-bacterial microorganisms, including Archaea and Protozoa. Also, new technologies have been developed especially to sample the extraordinary capabilities of some soil bacteria to sense a bewildering array of xenobiotic compounds that our industrial innovations have generated and, often unintentionally, released into the wider world.

Chemical sensing by bacteria can be roughly divided into three different categories. (We will not consider intracellular regulators that bind internalized molecules). The first, and usually simplest, consists of responses that control gene expression, usually at the level of transcription. These systems can be as simple as a single sensor, a single kinase under control of the sensor, and a transcriptional activator or repressor whose function is regulated by its state of phosphorylation. The sensor and the kinase are often distinct domains of a single polypeptide, typically, but not always, membrane bound, with an extracellular signal input domain that communicates with a cytoplasmic kinase. These systems are typically called two-component systems (TCS) and consist of an autophosphorylating histidine protein kinase (HPK) and a response regulator (RR) that is the substrate for phosphotransfer, and sometimes also dephosphorylation, by its cognate HPK. The definitive text, somewhat outdated but comprehensive and authoritative, is *Two-Component Signal Transduction*, edited by James Hoch and Thomas Silhavy [4].

The second is a control of already-existing physiological machinery. This second area is probably the least well understood because it is so often multifactorial. One of the common responses of both my biochemically oriented and my genetically based colleagues—they overlap—somewhat—is, "Oh, forget that, it's physiology, and physiology is just too complicated." Thus, although perhaps the most important in terms of rapid responses, chemical control of the activity of the transporters and other proteins that

maintain the homeostasis of the cell is generally also the least understood aspect of chemical sensing.

The final category is the one that fascinated me from the moment I first learned about it in 1972. Bacteria actually demonstrate purposeful behavior, a process called chemotaxis, although the way in which they do it is alien to most of what we understand about how animals behave. (They also demonstrate thermotaxis, phototaxis, magnetotaxis, and thigomotaxis—the last meaning that they have a sense of touch.) There are two sources that I recommend most highly for anyone interested in this amazing adaptation, which has some very non-intuitive aspects. The first is *Life at Low Reynolds Number* by Nobel laureate physicist Edward Purcell [5]. It lays out, in an understandable and entertaining fashion, the things that are different about how an organism interacts with the world if it is very small. It is a very different world indeed. Inertia means nothing and viscosity everything; how fast something is done does not affect the distance moved—only absolute displacement counts—and water is as thick as tar. Molecular bombardment makes it impossible to swim in a straight line for any length of time or distance, and the best way to get ahead is a biased random walk. Which leads to the second resource, a captivating look at the role of diffusion titled *Random Walks in Biology* by Howard Berg [6], a close colleague of Edward Purcell who took his PhD in physics into biology. It turns out that, at the size scale of bacteria, diffusion is really, really fast, far faster than a bacterium can swim. If you cannot outswim diffusion, why bother to swim at all? That is part of the story to be told in this volume. Parkinson et al. [7, 8] have written a recent (2015) update to their excellent 2008 review on bacterial chemoreceptors and their associated downstream signaling pathways.

The large majority of the chapters assembled here do, in fact, deal with different aspects of chemotaxis, from the behavior of bacterial populations to the movement of individual protein molecules. Another contemporaneous volume in this series deals specifically with bacterial motility. There will be some unavoidable overlap, but our collective intent is to have the two volumes complement one another. Many of the methods described will have general applicability outside of chemotaxis, and some chapters consider signal transduction systems not related to bacterial movement at all, so even if your bug does not swim or crawl, it is hoped that you will find something useful here.

The next, and much longer, introductory chapter will attempt to describe chemotaxis in sufficient depth to provide context for the detailed protocols that follow. The first of the actual methods sections will describe ways of studying the movement of cells or populations of cells. The second will cover genetic, biochemical, and optical methods for looking at signal transduction in living cells. The third section will describe techniques for capturing the

signal transduction process in frozen—in some cases literally—snapshots of the activities in living cells. The fourth section will describe techniques that can be used to follow the movement of individual proteins inside of living cells. The fifth section will introduce novel methods for screening the vast range of environmentally important chemicals that are detected by the wide spectrum of chemoreceptors that are found through the diversity of bacterial phylogeny. The sixth and final section introduces the latest and most sophisticated bioinformatic and molecular modeling approaches that advances in computer programming have brought to bear on the evolution and function of bacterial chemoreceptors. It is hoped that every reader will find substantial utility in a number of the protocols presented and that every method described will be of interest to a wide slice of the potential readership.

Acknowledgments

I first want to thank John Walker, the Series Editor, for giving me the opportunity to edit this volume, which has been a stimulating and eye-opening experience—and a lot of work. My wife, Lily Bartoszek, was of enormous assistance in helping me to bring the manuscripts, and especially their References, into a consistent format. Of course, I have to thank all the authors who took time out from their busy schedules to put the methods that they have perfected, and in many cases pioneered, into print in one convenient location. My own work has been supported by the National Science Foundation, the Bartoszek Fund for Basic Biological Science (yes, the same Bartoszek), and the generosity of the Department of Biology of Texas A&M University for allowing me to take time off from my ordinary duties to edit this volume.

References

1. Angert ER, Clements KD, Pace NR (1993) The largest bacterium. Nature 1362:239–241
2. Schulz HN, Schulz HD (2005) Large sulfur bacteria and the formation of phosphorite. Science 307:416–418
3. Golden JW, Yoon HS (2003) Heterocyst development in *Anabaena*. Curr Opin Microbiol 6:557–563
4. Hoch JA, Silhavy TJ (1995) Two-component signal transduction. ASM Press, Washington, DC
5. Purcell EM (1977) Life at low Reynolds number. Am J Phys 45:1–11
6. Berg HC (1993) Random walks in biology. Princeton University Press, Princeton, NJ
7. Hazelbauer GL, Falke JJ, Parkinson JS (2008) Bacterial chemoreceptors: high-performance signaling in networked arrays. Trends Biochem Sci 33:9–19
8. Parkinson JS, Hazelbauer GL, Falke JJ (2015) Signaling and sensory adaptation in *Escherichia coli* chemoreceptors: 2015 update. Trends Microbiol 23:257–266

Chapter 2

Transmembrane Signal Transduction in Bacterial Chemosensing

Michael D. Manson

Abstract

Like all living organisms, bacteria must communicate with the world around them. As they typically live as single cells, the communication with their environment must occur at the cell membrane, both in moving molecules in and out and in transmitting information about their surroundings to response elements within the cell. This volume is devoted primarily to methods used to study either the behavior of bacteria in response to their environment or methods used to study events that involve signaling pathways that are initiated by events at the cell membrane. The topics are arranged according to the scale of the events described: (1) Methods for studying bacterial chemotaxis at the population and whole-cell levels; (2) In vivo analysis of receptor function; (3) Cryo-EM methods for studying chemoreceptor structure; (4) Monitoring the intracellular movement of chemosensory proteins; (5) High-throughput methods for screening novel chemoeffectors; (6) Creating chemical tools for studying chemosensory signal transduction; (7) Computerized analysis of chemotaxis. Every effort has been made to get the most experienced and proficient practitioners of each of the methods described, and the editor is indebted to all who agreed to participate.

Key words Bacterial behavior, Chemoeffectors, Chemoreceptors, Tracking cells and molecules, Chemical tools, Bioinformatics, Molecular dynamics

1 Introduction

1.1 Overview

Many environmental factors affect the growth and metabolism of all organisms, including bacteria. Bacteria are everywhere: in the scorching Atacama and Sahara deserts, and in super-heated water in deep sea vents and hot springs. *Deinococcus radiodurans*, presumably adapted to survive desiccation in the desert, can tolerate enormous levels of gamma radiation—it was first isolated from nuclear reactor cooling tanks [1]. All of us have experienced how quickly bacterial contamination appears unbidden in the most inconvenient places, so much so that until Pasteur proved otherwise [2], the common notion was that microorganisms arose

Michael D. Manson (ed.), *Bacterial Chemosensing: Methods and Protocols*, Methods in Molecular Biology, vol. 1729, https://doi.org/10.1007/978-1-4939-7577-8_2,

through spontaneous generation. Nonetheless, many bacteria are extreme specialists, having very fastidious growth requirements [3] and living in highly subdivided ecological niches in the soil [4], in marine and freshwater environments [5], and on [6] and in [7, 8] host organisms. The majority of bacterial species have not yet been cultured and are known only through micrographs or DNA sequences.

The evolutionary adaptations, including chemosensory capabilities, of extremophiles and species with very narrow growth requirements are no doubt fascinating, but they are very difficult to study experimentally. We know much more about the more tractable generalists. For purposes of investigating signal transduction that is fortunate, because generalists have to respond to changing habitats, and they must therefore have diverse sensing mechanisms. With a few exceptions, the methods described in the chapters that follow have been worked out with model organisms: primarily *E. coli*, *S. enterica*, and, to a somewhat lesser extent, *Bacillus subtilis* and various Pseudomonads. However, most of the protocols that have been developed with model organisms can, with suitable modifications, be applied to a very wide range of culturable and more or less genetically tractable bacteria. Therefore, it is hoped that this volume will be valuable to anyone who is interested in how bacteria sense and respond to their chemical environments.

1.2 Two-Component Signal Transduction Systems that Regulate Gene Expression

As mentioned in the first chapter, the focus of this volume will be on signal transduction systems that are triggered by sensors located in the cell membrane. Many of these are under the control of histidine protein kinases [9]. In most cases, the signaling cascade is initiated by the binding of a ligand to an external substrate-binding domain. That binding generates a subtle conformation change that is transmitted through the membrane to a cytoplasmic domain that either has histidine protein kinase (HPK) activity itself or that regulates the activity of an HPK. In a few examples treated in this volume, the actual initiating event may be a perturbation of the membrane that initiates a conformational change in transmembrane receptor or the interaction of two cytoplasmic domains of a transmembrane receptor. In any case, the signal output is the change in the activity of an HPK. The affect can be either to increase or to decrease the activity of the kinase, or in some cases to increase or decrease the phosphatase activity also possessed by some kinases. The target of the phosphotransfer from the autophosphorylated HPK is the response regulator (RR), whose activity is controlled by its state of phosphorylation. If the HPK has a phosphatase activity, its target is the phosphorylated RR. The HPK and the RR together make up a two-component system (TCS) [10].

A relatively straightforward and illustrative example of the function of a TCS in gene regulation is the system that controls the induction of nitrate reductase and formate dehydrogenase and

the repression of nitrite reductase and fumarate reductase in *E. coli* [11]. Under conditions of oxygen limitation, *E. coli* is capable of carrying out anaerobic respiration, in which alternative terminal electron acceptors can replace molecular oxygen. Among these compounds are nitrate, nitrite, and fumarate. Expression of reductase enzymes that carry out the electron transfer is regulated by two factors: the absence of oxygen and the presence of the alternative acceptor. In the case of nitrate reductase, low levels of oxygen lead to the expression of a two-component system consisting of the NarX HPK and the NarL RR. When nitrate or nitrite binds to the extracellular (periplasmic) domain of NarX, it stimulates kinase activity, with the result that the levels of intracellular NarL-P increase. NarL-P, in turn, is a transcriptional activator for the *narGHI* operon that encodes nitrate reductase and the *fdnGHI* formate dehydrogenase operon and a transcriptional repressor of the *frdABCD* operon that encodes fumarate reductase and the *nirBCD* operon that encodes nitrite reductase. Furthermore, NarL-P activates transcription of *narXL* in a positive feedback loop and inhibits transcription of *dcuSR*, an operon that encodes a TCS that positively regulates expression of *frdABCD* in response to fumarate [12]. The overall regulatory scheme is shown in Fig. 1.

NarL is unusual among HPKs in that the conformational change that activates the kinase activity has been elucidated directly at the level of a structural change in its periplasmic, ligand-binding domain [13]. This motion seems to be an ~1 Å piston-like outward shift in the position of the second transmembrane helix of NarX. It is noteworthy that a NarX-Tar chemoreceptor chimera that contains the sensing domain of NarX is a repellent receptor for nitrate and nitrite [14, 15], an activity that depends upon stimulation of the receptor-associated CheA kinase (*see* below). Thus, some transmembrane signaling mechanisms are similar between HPKs and chemoreceptors, although many HPKs and many chemoreceptors do not function in such a straightforward way. An extensive literature summarizes what is known about TCSs [10], as TCSs are universal in both Eubacteria and Archaea [16] and regulate very diverse activities, including adaptation to a wide variety of environmental and host-derived signals.

1.3 Bacterial Chemotaxis Consists of a Biased Three-Dimensional Random Walk

An introduction to bacterial chemotaxis requires a brief explanation of the somewhat counter-intuitive way—at our size scale—that bacteria sense and move within their environment. As mentioned in the first chapter, bacteria do not have sufficient mass for momentum or inertia to play a significant role in their lives. They are also unable to move at instantaneous velocities that outrun diffusion, and bombardment by water molecules constantly reorients them so that they are unable to steer a predictable course [17]. Thus, their baseline behavior is to perform a three-dimensional

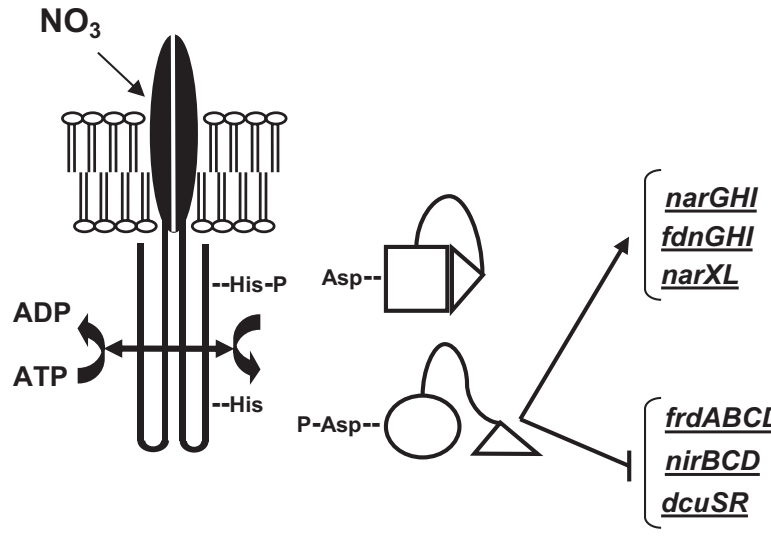

Fig. 1 Simplified diagram of the NarXL TCS regulon. NarXL are initially produced under anaerobic conditions. The NarX HPK binds NO_3 in its extracellular (periplasmic) domain. That binding initiates a transmembrane conformational change that activates the kinase activity of the NarX dimer, which autophosphorylates in trans on a highly conserved His residue. The phosphoryl group is then transferred to a conserved Asp residue on the regulatory domain (square) of the NarL RR. The resulting conformational change exposes the DNA-binding domain (triangle) so that it can interact with the promoters of the *narGHI, fdnGHI*, and *narXL* operons to stimulate their transcription and to the regulatory regions of the *frdABCD*, *nirBCD*, and *dcuSR* operons to repress their transcription. The diagram is schematic and is not intended to suggest any molecular mechanism

"random walk" that samples their environment over time. This is illustrated in Fig. 2 for a bacterium like *E. coli* that "runs" and "tumbles" by reversing the direction of flagellar rotation from counterclockwise (CCW) to clockwise (CW) and back again [18]. However, because bacteria cannot swim straight, the same effect can be achieved by cells reversing their direction of motion 180° or periodically slowing down or stopping to allow reorientation of their swimming direction. Several of the chapters in this volume will describe methods for tracking such motion and observing the movements of individual flagella in cells that are carrying out these random walks.

Bacteria are generally too small for there to be significant differences in the concentration of chemoeffector molecules from one end of the cell to the other, even in steep chemical gradients. Therefore, to detect gradients they must compare concentrations along their swimming paths. If concentrations increase with time they are swimming up the gradient, if they are decreasing they are swimming down the gradient. The same holds true for gradients of light, temperature, pH, etc. This situation provides a simple

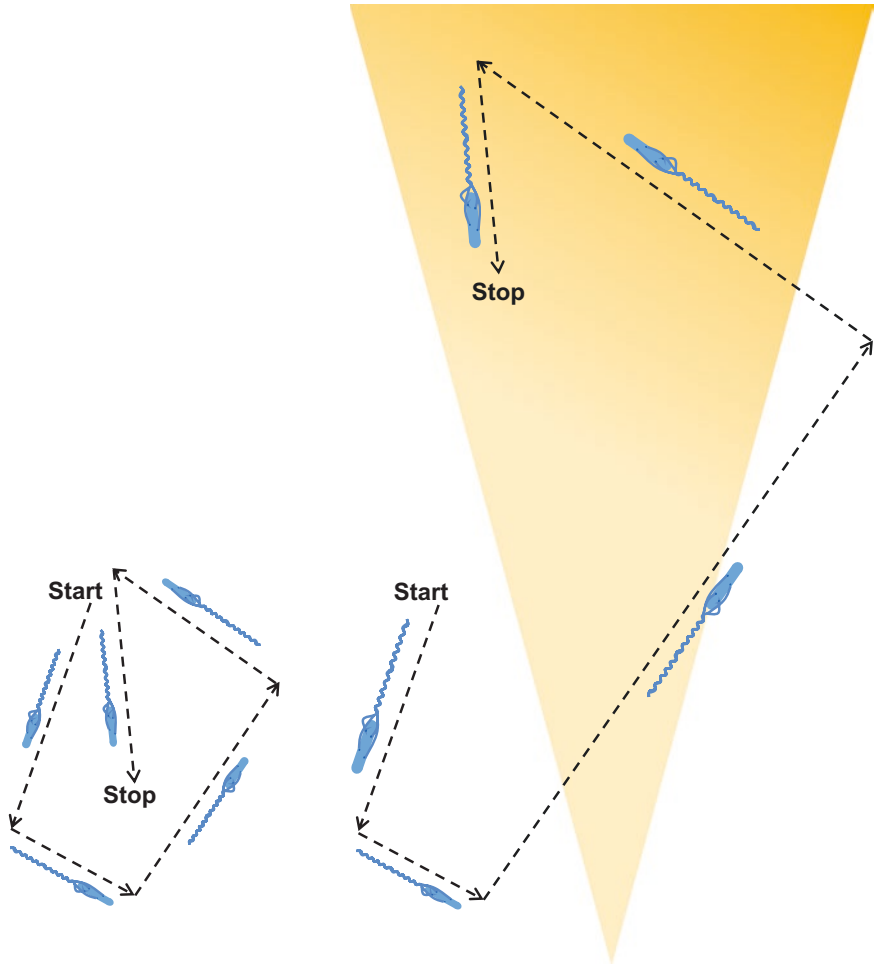

Fig. 2 Bacteria swim in a three-dimensional random walk. In the absence of a chemical gradient (left), a cell runs on a relatively straight course and then tumbles, as indicated by the shafts and the heads of the arrows, respectively, and it achieves no net displacement in any specific direction. In the presence of an attractant gradient, indicated by the inverted orange triangle, a cell lengthens its runs in the up-gradient direction, while its runs in the down-gradient direction remain of the same average length as in the absence of a gradient. That is, the cells respond primarily to conditions becoming more favorable. The result is a net displacement within the gradient toward a higher concentration of the attractant. In a repellent gradient, runs become longer in the down-gradient direction, and runs in the up-gradient direction remain of the same average length, resulting in a net migration toward a lower concentration of the repellent

solution to the problem of navigating in gradients. If the signal of an attractant stimulus is increasing, keep swimming without tumbling, reversing, stopping, etc. The same holds true for decreasing intensities of repellent stimuli [19]. Howard Berg has captured this idea by declaring bacteria to be optimists. If things are getting better, keep going. If things are getting worse or staying the same, try something else.

The end result of such an input/output system is a biased three-dimensional random walk (Fig. 2). If conditions improve, continue moving ahead for a longer period of time before abruptly changing direction. There is no point in moving ahead too long, however, because Brownian motion (molecular bombardment) prevents the cell from holding a straight course. Within a few seconds it will no longer be swimming on a favorable heading. Thus, the cell should randomly change orientation again with the chance that it will subsequently move in the right direction. If not, try, try again. The result is a random walk with the number of steps in a favorable direction being higher than the number of steps in a neutral or unfavorable direction. Although the efficiency is rather low, with the most rapid rate of migration in the favorable direction in a gradient being about one-tenth of the instantaneous swimming speed of the cell [19], it is the best performance their small size allows.

1.4 The Signal Transduction System Behind the Biased Random Walk

I will begin by describing the best known system, that of the enteric bacterium *E. coli*, which behaves in the manner outlined in Fig. 2. (The related enteric bacterium *Salmonella enterica* behaves in much the same way). The central players are the chemoreceptors, the chemotaxis (Che) proteins, and the CW/CCW switch at the flagellar motor. Many bacteria with complicated lifestyles have dozens of chemoreceptors [20, 21], but in *E. coli* there are only five. Four of these undergo covalent methylation and are thus collectively called methyl-accepting chemotaxis proteins (MCPs). The identities and properties of the *E. coli* chemoreceptors, Che proteins, and switch proteins are presented in Table 1.

Figure 3 shows a schematic view of the minimum unit of chemotaxis signaling, which contains two trimers of homodimeric receptor dimers connected by a CheA dimer and two CheW monomers. Different receptor dimers can combine to form functional trimers. Figure 4 provides an overview of the signal transduction system that underlies chemotaxis behavior in *E. coli*. The essence of the system is that the normal run-tumble behavior is driven by the steady-state activity of the CheA kinase. The activity of the CheA kinase is greatly stimulated when it is part of the CheA/CheW/receptor array. A cell that lacks the CheA kinase, the CheW scaffolding protein that couples CheA to the receptors, the CheY response regulator, or both of the high-abundance MCPs (Tsr and Tar) will always turn its flagella CCW and will always swim smoothly. A cell lacking the CheZ phosphatase will accumulate CheY-P and turn its flagella primarily CW, resulting in perpetual tumbling. Cells lacking the CheB methylesterase or the CheR methyltransferase will be unable to adapt: that is, they will not be able to return to normal run-tumble swimming after an attractant or a repellent stimulus. Receptors with a higher state of covalent modification (the amide group of glutamine or glutamyl methylesters)

Table 1
Chemotaxis signaling proteins in *Escherichia coli*

Chemoreceptors	Major functions
Tsr (high abundance MCP)	Attractant taxis toward serine[a], autoinducer-2[b,c] and DHMA[a,d], repellent taxis away from indole and leucine
Tar (high abundance MCP)	Taxis toward aspartate[a] and maltose[b], repellent taxis away from Ni^{2+}
Trg (low abundance MCP)	Taxis toward galactose[b], glucose[b] and ribose[b]
Tap (low abundance MCP)	Taxis toward dipeptides[b]
Aer (not an MCP)	Redox taxis[e]
Cytosolic chemotaxis proteins	
CheA	Receptor-associated histidine protein kinase
CheB	Receptor methylesterase and deamidase, activated by phosphorylation by CheA
CheR	Receptor methyltransferase, S-adenosylmethionine as the methyl group donor
CheW	Scaffolding protein associated with chemoreceptors
CheY	Response regulator, induces clockwise flagellar rotation (tumbling) when phosphorylated by CheA
CheZ	Phospho-CheY phosphatase

[a]Binds directly to receptor ligand-binding domain
[b]Binds to periplasmic binding protein, which then interacts with receptor periplasmic domain
[c]Autoinducer-2 is a quorum-sensing signal for many bacteria that binds to the periplasmic LsrB protein [22]
[d]DHMA is 3,4-dihydroxymandelic acid, a metabolite of norepinephrine [23]
[e]The activity of Aer is regulated by oxidation and reduction of its FAD moiety [24, 25]

are more effective in stimulating CheA activity than receptors with lower levels of covalent modification, and they require a higher concentration of attractant ligand to inhibit their kinase-stimulating activity [26].

The critical factor in determining the behavior of the flagellar motor is the intracellular concentration of CheY-P, because the CW ↔ CCW switch is controlled by the binding of CheY-P to FliM and FliN. The motor is in a very delicately balanced equilibrium, and small changes in the concentration of CheY-P can cause large changes in the probability that cells will turn their flagella CW or CCW; the Hill coefficient for CheY-P at the motor is around 11 [27]. The sensitivity of the system is further enhanced by the amplification of the signal that occurs within the receptor array. The binding of one kinase-inhibiting attractant ligand to a receptor can shut off up to 35 CheA kinase molecules [28]. The dissociation of a repellent ligand has the same effect, whereas binding of a repellent stimulates CheA kinase, and thus promotes tumbling.

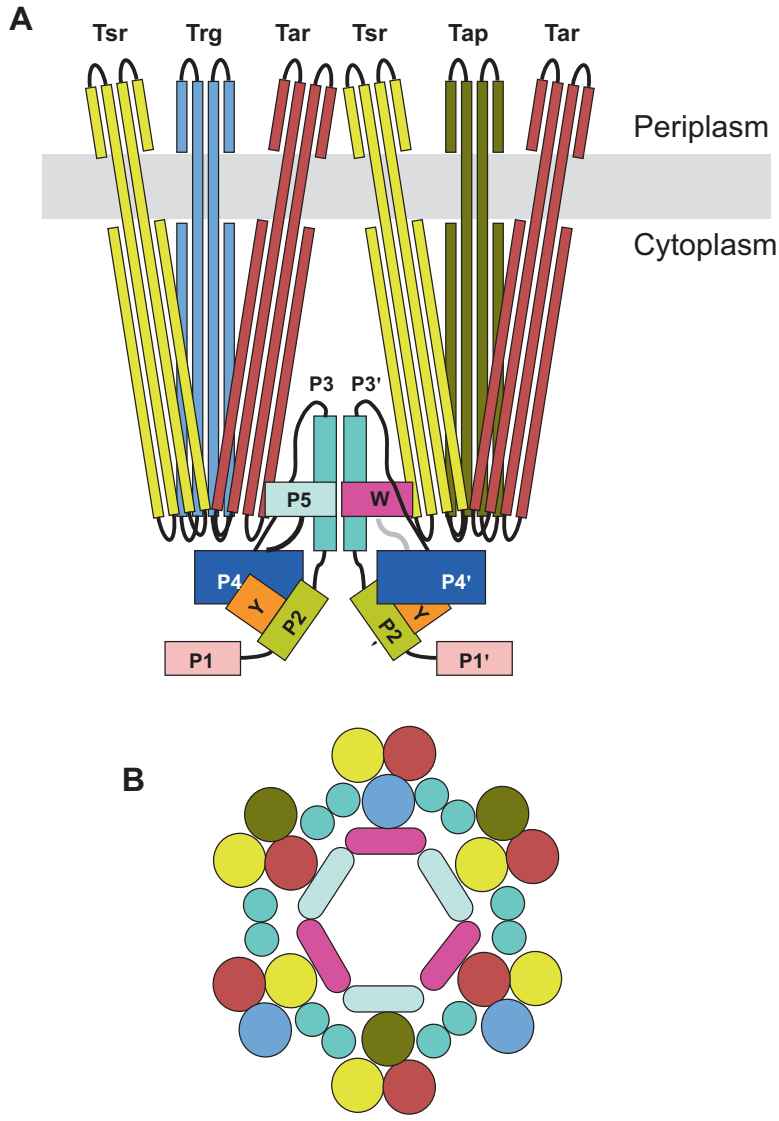

Fig. 3 (**a**) A schematic of a chemoreceptor signaling complex within the cell membrane (gray). The minimal signaling unit consists of a dimer of receptor trimers joined by a CheA dimer and two CheW monomers. Each receptor trimer may contain different combinations of receptor homodimers, as shown. Tsr and Tar are the high abundance chemoreceptors. CheA consists of five different domains. The P1 domain contains the His residue that is phosphorylated by the catalytic P4 domain, and the P2 domain binds CheY in position for phosphotransfer from P1. P3 is the dimerization domain, and P5, which bears strong structural similarity to CheW, is the domain that interacts with the receptor dimers and with CheW. (**b**) View of a receptor patch at the level where P5 and CheW interact with the distal tips of receptor dimers. P5 and CheW form a hexameric ring with alternating P5 and CheW components. Each ring contains three minimal signaling units. These units can be indefinitely extended through contacts with additional P5 and CheW subunits to form the hexagonal array of the receptor patch

Fig. 4 (continued) The cell will again tumble at the normal frequency until more receptors become bound to attractant. Iterations of this sequence of events lead to migration up an attractant gradient. Repellents stimulate CheA activity and decrease receptor methylation, and adaptation to a repellent is accomplished by methylation of receptors that have lost a repellent ligand. Thus, cells migrate down repellent gradients

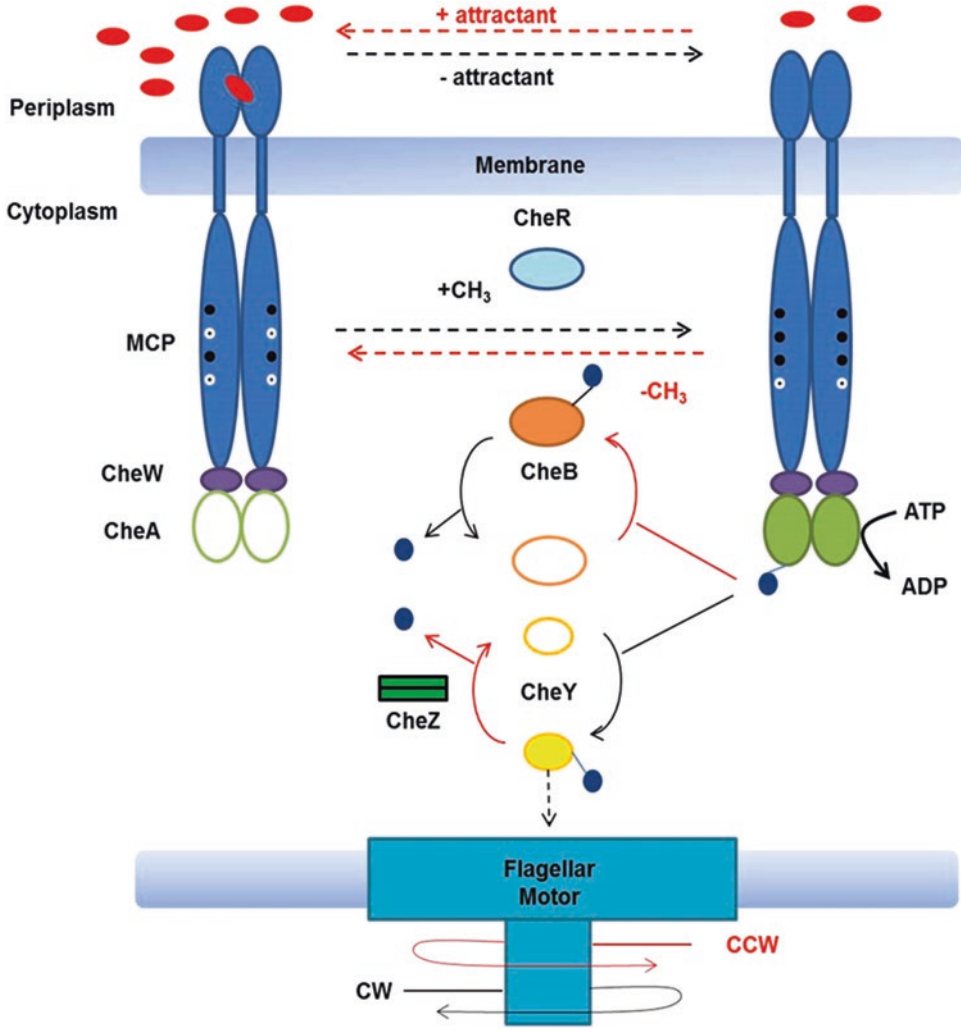

Fig. 4 Schematic of chemotaxis signal transduction in *E. coli*. The active forms of proteins are shown with solid symbols, and the inactive forms are shown with empty symbols. When a receptor dimer is not bound to attractant (right), it stimulates the autophosphorylation activity of CheA, which then transfers the phosphoryl group (blue circle) to CheY. Phosphorylated CheY (CheY-P) diffuses through the cell and binds to the switch complexes at the bases of the flagella to promote clockwise (CW) flagellar rotation, which leads to tumbling. Many CheY-P molecules can bind to a single switch complex. (There are at least 34 potential CheY-P binding sites per flagellar motor.) CheY-P is rapidly dephosphorylated by the CheZ phosphatase, and non-phosphorylated CheY cannot promote CW flagellar rotation. When an attractant molecule binds to a receptor dimer (left), it initially inhibits CheA activity. As a result, CheA does not autophosphorylate and transfer the phosphoryl group to CheY. Because of the CheZ phosphatase, the level of CheY-P within the cell falls rapidly (within <100 ms), and the flagellar motors turn counterclockwise (CCW), leading to longer runs. The antagonistic activities of CheR (a methyltransferase) and CheB (a methylesterase) are responsible for adaptation. CheR is constitutively active in methylating the receptors at specific glutamyl residues, using S-adenosylmethionine as the methyl donor. CheB, which is a substrate for phosphotransfer from CheA, removes the methyl groups when it is phosphorylated (CheB-P). Thus, an "empty" receptor contains a relatively small number of methyl groups. When CheA activity decreases, CheB-P levels fall, but more slowly than CheY-P levels. Thus, for a short time, a receptor bound to an attractant will not stimulate CheA activity. When CheB-P levels fall—CheB-P has a half-life of a few seconds—the activity of CheR leads to a higher level of receptor methylation, which restores the ability of the receptor to stimulate CheA.

The end result is an exquisitely sensitive ability to detect small temporal changes in the concentrations of chemoeffectors [28] and to convert those signals into significant increases in the length of runs in the favorable direction.

1.5 Detection of Gradients Requires a Chemical Memory

In order to determine whether the concentration of a chemoeffector is increasing or decreasing, two things are necessary. One is that the concentration must be quickly and accurately measured, an assessment based on the fraction of receptors that are bound to the molecule being sensed. The second requirement is that there be a memory of the situation from a few seconds earlier to provide a basis for comparison. In *E. coli*, this memory is provided, in the first instance, by the state of covalent modification of the receptors. (We are learning that other factors can be involved as well, even in *E. coli*, and the adaptation process that leads to memory can be very different in other bacteria, as will be seen in some of the chapters in this volume). However, the fact that MCPs are widely distributed in all different phyla of bacteria and of Archaea demonstrates that methylation and demethylation of receptors as a means of gradient sensing is a very ancient process, probably spread to the Archaea by lateral transfer from bacteria [29].

The adaptation process is shown schematically in Fig. 4. In *E. coli*, each dimeric receptor has four or five methylatable glutamyl residues per monomer, for a total of 8–10 in the dimer. In the absence of any stimulus, the receptors have an intermediate level methylation (an average of ~1 per monomer) that maintains an intermediate level of CheA-stimulating activity that keeps a nearly constant intracellular level of CheY-P. Binding of chemoeffector initiates a conformational change that is transmitted across the membrane and modified by the HAMP domain on the cytoplasmic side of the membrane into a conformational signal that is communicated to the output, membrane-distal end of the receptor that interacts with CheA. In the case of an attractant ligand, the signal is inhibitory. In the case of a repellent, the signal is excitatory.

With an attractant, the drop in CheA activity results in a decrease in the rate of Che-Y-P production. Because of the amplification phenomenon discussed above, and because there is a dedicated CheY-P phosphatase, CheZ, CheY-P levels drop rapidly and perceptibly, even in response to binding of small numbers of attractant ligands. The other consequence is that phosphorylation of CheB by CheA also decreases by some increment, but, although the half-life of CheB-P is only a matter of seconds, there is no phosphatase to accelerate the process. CheR meanwhile continues to add methyl groups to the glutamyl resides. In the first seconds this makes little difference in the level of receptor methylation, as CheB-P is still present and active. Soon, however, CheB-P levels fall, at least locally within the receptor patch, and the level of

methylation of the receptors increases. This methylation restores the CheA-stimulating activity of the receptor and also decreases the affinity of the receptor for the attractant ligand. Soon, the baseline activity of CheA is restored, CheY-P and CheB-P return to their pre-stimulus level, and the ligand-bound receptor retains a somewhat increased number of glutamyl methyl esters. The synopsis in the preceding paragraph fails to capture the highly dynamic aspect of this process, with ligands coming on and off the receptors and methylation probably occurring on all the receptors in an array neighborhood, whether they have bound ligand or not [30, 31]. However, only receptors that can bind a particular ligand remain with an elevated extent of methylation once the process of adaptation is complete [32]. Repellents generate essentially the reverse response, with receptor activity increasing upon ligand binding, levels of methylation decreasing, and cells tumbling. However, in shallow repellent gradients, the response is essentially identical to the attractant response, as receptors that lose their repellent ligands transiently inhibit CheA activity and increase their level of methylation. This is the basis for Howard Berg's assessment, noted above, that *E. coli* is an optimist.

One important aspect of MCP synthesis is that two of the glutamyl resides that are targets for methylation are translated as glutaminyl residues. This presumably prevents receptors newly incorporated in the receptor array from skewing the signal output of the receptor patch upon their introduction, as the properties of glutaminyl residues at these positions are very similar to those of glutamyl methyl esters. The CheB methylesterase also serves as a deamidase that converts the glutaminyl residue into methylatable/demethylable glutamyl residues [33]. The fortuitous consequence of this somewhat convoluted process is that in cells lacking both CheB and CheR, genetic engineering can be used to generate MCPs with any combination of stably modified or unmodified glutamyl residues, for the serine-receptor Tsr ranging from all EEEEE to all QQQQQ. Over this range, the activity of receptors in stimulating CheA and in affinity for ligand is regulated reciprocally over several orders of magnitude [34].

1.6 Chemoreceptors Are Arranged in Highly Ordered Arrays

One of the biggest surprises in the evolution of our understanding of bacterial chemotaxis was that chemoreceptors are not scattered randomly about the surface of the cell, as would be predicted if their placement were dictated by maximizing detection sensitivity for chemical ligands [35]. Instead, receptors are found in close-packed arrays, which in *E. coli* are located primarily near the old pole of the rod-shaped cell body [36]. Much exquisite work taking advantage of the latest sophistication in cryo electron microscopy has shown that the minimum signaling units shown in Fig. 3 are organized into extensive hexagonal close-packed arrays [37, 38]. This architecture is evident in all prokaryotic chemoreceptors, even

those that have a cytoplasmic rather than membrane-associated placement [39]. These elegant and ubiquitous structures enable the lateral spread of the conformational signals initiated by ligand binding to a constellation of different receptors to promote both signal integration and signal amplification [30, 31, 40]. Several of the chapters in this volume are devoted to methods for elucidating the detailed configuration of these remarkable molecular assemblies.

Acknowledgments

I especially want to thank John S. (Sandy) Parkinson for his contribution of two chapters, his encouragement, his organization of the annual ReceptorFest, and his co-authoring, with Gerald (Jerry) Hazelbauer and Joseph (Joe) Falke the two review articles that provide the best and most-comprehensive discussion of the signaling pathways associated with bacterial chemotaxis.

References

1. Krisko A, Radman M (2013) Biology of extreme radiation resistance: the way of *Deinococcus radiodurans*. Cold Spring Harb Perspect Biol 5:piia 012765
2. Dubos RJ (1960) Louis Pasteur: free lance of science. Charles Scribner's Sons, New York, NY
3. Singh S, Eldin C, Kowalczewska M, Raoult D (2013) Axenic culture of fastidious and intracellular bacteria. Trends Microbiol 21:92–99
4. Schloter M, Lebuhn M, Heulin T, Hartmann A (2000) Ecology and evolution of bacterial microdiversity. FEMS Microbiol Rev 24:647–660
5. Logares R, Bråte J, Bertilsson S, Clasen JL, Shalchian-Tabrizi K et al (2009) Infrequent marine-freshwater transitions in the microbial world. Trends Microbiol 17:414–422
6. Zeeuwen PL, Kleerebezem M, Timmerman HM, Schalkwijk J (2013) Microbiome and skin diseases. Curr Opin Allergy Clin Immunol 13:514–520
7. Cresci GA, Bawden E (2015) Gut microbiome: what we do and don't know. Nutr Clin Pract 30:734–746
8. Whiteside SA, Razvi H, Dave S, Reid G, Burton JP (2015) The microbiome of the urinary tract–a role beyond infection. Nat Rev Urol 12:81–90
9. Jung K, Fried L, Behr S, Heermann R (2012) Histidine kinases and response regulators in networks. Curr Opin Microbiol 15:118–124
10. Hoch JA, Silhavy TJ (1995) Two-component signal transduction. ASM Press, Washington, DC
11. Stewart V (1993) Nitrate regulation of anaerobic respiratory gene expression in *Escherichia coli*. Mol Microbiol 9:425–434
12. Zientz E, Bongaerts J, Unden G (1998) Fumarate regulation of gene expression in *Escherichia coli* by the DcuSR (*dcuSR* genes) two-component regulatory system. J Bacteriol 180:5421–5425
13. Cheung J, Hendrickson WA (2009) Structural analysis of ligand stimulation of the histidine kinase NarX. Structure 17:190–201
14. Ward SM, Delgado A, Gunsalus RP, Manson MD (2002) A NarX-Tar chimera mediates repellent chemotaxis to nitrate and nitrite. Mol Microbiol 44:709–719
15. Ward SM, Bormans AF, Manson MD (2006) Mutationally altered signal output in the Nart (NarX-Tar) hybrid chemoreceptor. J Bacteriol 188:3944–3951
16. Wuichet K, Cantwell BJ, Zhulin IB (2010) Evolution and phyletic distribution of two-component signal transduction systems. Curr Opin Microbiol 13:219–225
17. Purcell EM (1977) Life at low Reynolds number. Am J Phys 45:3–11
18. Larsen SH, Reader RW, Kort EN, Tso WW, Adler J (1974) Change in direction of flagellar rotation is the basis of the chemotactic response in *Escherichia coli*. Nature 249:74–77

19. Brown DA, Berg HC (1974) Temporal stimulation of chemotaxis in *Escherichia coli*. Proc Natl Acad Sci U S A 71:1388–1392
20. Miller LD, Russell MH, Alexandre G (2009) Diversity in bacterial chemotactic responses and niche adaptation. Adv Appl Microbiol 66:53–75
21. Krell T, Lacal J, Muñoz-Martínez F, Reyes-Darias JA, Cadirci BH et al (2011) Diversity at its best: bacterial taxis. Environ Microbiol 13:1115–1124
22. Hegde M, Englert DL, Schrock S, Cohn WB, Vogt C et al (2011) Chemotaxis to the quorum-sensing signal AI-2 requires the Tsr chemoreceptor and the periplasmic LsrB AI-2-binding protein. J Bacteriol 193:768–773
23. Pasupuleti S, Sule N, Cohn WB, MacKenzie DS, Jayaraman A et al (2014) Chemotaxis of *Escherichia coli* to norepinephrine (NE) requires conversion of NE to 3,4-dihydroxymandelic acid. J Bacteriol 196:3992–4000
24. Rebbapragada A, Johnson MS, Harding GP, Zuccarelli AJ, Fletcher HM et al (1997) The Aer protein and the serine chemoreceptor Tsr independently sense intracellular energy levels and transduce oxygen, redox, and energy signals for *Escherichia coli* behavior. Proc Natl Acad Sci U S A 94:10541–10546
25. Bibikov SI, Biran R, Rudd KE, Parkinson JS (1997) A signal transducer for aerotaxis in *Escherichia coli*. J Bacteriol 179:4075–4079
26. Li G, Weis RM (2000) Covalent modification regulates ligand binding to receptor complexes in the chemosensory system of *Escherichia coli*. Cell 100:357–365
27. Cluzel P, Surette M, Leibler S (2000) An ultrasensitive bacterial motor revealed by monitoring signaling proteins in single cells. Science 287:1652–1655
28. Tu Y (2013) Quantitative modeling of bacterial chemotaxis: signal amplification and accurate adaptation. Annu Rev Biophys 42:337–359
29. Briegel A, Ortega DR, Huang AN, Oikonomou CM, Gunsalus RP et al (2015) Structural conservation of chemotaxis machinery across Archaea and bacteria. Environ Microbiol Rep 7:414–419
30. Hazelbauer GL, Falke JJ, Parkinson JS (2008) Bacterial chemoreceptors: high-performance signaling in networked arrays. Trends Biochem Sci 33:9–19
31. Parkinson JS, Hazelbauer GL, Falke JJ (2015) Signaling and sensory adaptation in *Escherichia coli* chemoreceptors: 2015 update. Trends Microbiol 23:257–266
32. Sanders DA, Koshland DE Jr (1988) Receptor interactions through phosphorylation and methylation pathways in bacterial chemotaxis. Proc Natl Acad Sci U S A 85:8425–8429
33. Kehry MR, Bond MW, Hunkapiller MW, Dahlquist FW (1983) Enzymatic deamidation of methyl-accepting chemotaxis proteins in *Escherichia coli* catalyzed by the *cheB* gene product. Proc Natl Acad Sci U S A 80: 3599–3603
34. Lai RZ, Parkinson JS (2014) Functional suppression of HAMP domain signaling defects in the *E. coli* serine chemoreceptor. J Mol Biol 426:3642–3655
35. Berg HC, Purcell EM (1977) Physics of chemoreception. Biochem J 20:193–219
36. Maddock JR, Shapiro L (1993) Polar location of the chemoreceptor complex in the *Escherichia coli* cell. Science 259:1717–1723
37. Briegel A, Ortega DR, Tocheva EI, Wuichet K, Li Z et al (2009) Universal architecture of bacterial chemoreceptor arrays. Proc Natl Acad Sci U S A 106:17181–17186
38. Liu J, Hu B, Morado DR, Jani S, Manson MD et al (2012) Molecular architecture of chemoreceptor arrays revealed by cryoelectron tomography of *Escherichia coli* minicells. Proc Natl Acad Sci U S A 109:e1481–e1488
39. Briegel A, Ladinsky MS, Oikonomou C, Jones CW, Harris MJ et al (2014) Structure of bacterial cytoplasmic chemoreceptor arrays and implications for chemotactic signaling. elife 3:e02151
40. Shimizu TS, Aksenov SV, Bray D (2003) A spatially extended stochastic model of the bacterial chemotaxis signalling pathway. J Mol Biol 329:291–309

Part II

Methods for Studying Bacterial Chemotaxis at the Population and Whole-Cell Levels

Chapter 3

Two Spatial Chemotaxis Assays: The Nutrient-Depleted Chemotaxis Assay and the Agarose-Plug-Bridge Assay

Victoria Korolik and Karen M. Ottemann

Abstract

This chapter describes two spatial chemotaxis assays, the nutrient-depleted chemotaxis assay and agarose-plug-bridge assay, which enable the evaluation of putative chemoeffectors. These two assays have worked well with *Campylobacter jejuni* and *Helicobacter pylori*, and techniques for using these assays with these microbes are described.

Key words Chemotaxis, *Campylobacter jejuni*, *Helicobacter pylori*, Chemoeffector screening, Nutrient-depleted assay, Agarose-plug-bridge assay

1 Introduction

Microbes use chemotaxis to move in response to the presence of specific chemicals. These chemicals can be broadly divided into two classes: those that attract bacteria and those that repel them. Chemoeffectors attracting bacterial cells to a point of high effector concentration are considered attractants, and chemotaxis in the direction of increasing attractant concentrations is defined as "positive" chemotaxis [1]. In contrast, repellents cause bacteria to swim to points of lower chemoeffector concentrations and this is considered "negative" chemotaxis [1]. Chemotaxis is important in many settings, including mammalian infection [2–7]. A key step needed for understanding the role of chemotaxis in any setting, however, is to define the chemoattractants and chemorepellents.

There are a number of different methods in the literature that are used to measure chemotaxis in response to specific chemicals [2, 8, 9]. In some microbes, both qualitative and quantitative chemotaxis assays are difficult to perform in a consistent and reproducible manner [8, 10]. Furthermore, controls used by various research groups are not always appropriate for the assays performed [8, 10]. Several assays have been developed that work reliably with

Michael D. Manson (ed.), *Bacterial Chemosensing: Methods and Protocols*, Methods in Molecular Biology, vol. 1729, https://doi.org/10.1007/978-1-4939-7577-8_3,

C. jejuni and *H. pylori*. Both of these are so-called spatial assays, which rely on bacteria migrating in response to gradients of chemoeffectors. The first of these was developed for *C. jejuni* and is called the nutrient depleted chemotaxis assay [11, 12]. During this assay, bacteria are placed in a low concentration agarose solution and migrate toward or away from concentrated point sources consisting of agarose plugs of test ligands. The bacteria are then enumerated from the agarose plugs by plating. This assay is rapid and quantitative, but requires bacterial growth prior to enumeration, which can be slow. The second assay also monitors bacterial movement toward or away from chemicals in an agarose plug, but the bacteria are placed in liquid solutions, and the assay is monitored under the microscope [9, 13]. This assay is rapid but not quantitative, because the assay is scored simply as positive or negative based on appearance of a bacterial band.

2 Materials

Deionized water and analytical grade reagents were used for all solutions. Solutions were sterilized by autoclaving at 120 °C for 20 min. All solutions and agar were cooled to 55 °C prior to addition of supplements.

2.1 Materials Required for Growth of C. jejuni and H. pylori

1. Columbia Blood Agar (CHBA): 19.5 g Columbia Blood Agar base dissolved in 475 mL water. After sterilization, 25 mL (5%) defibrinated horse blood is added to cooled agar supplemented with 200 μL polymyxin B (1 mg/mL; 1250 IU), 200 μL vancomycin (25 mg/mL; 5 mg), 50 μL trimethoprim (50 mg/mL; 2.5 mg) and additional appropriate selection if required. Store at 4 °C.
2. Brucella Broth: 11 g Heart Infusion (HI) broth, 5 g tryptone, 1 g yeast extract dissolved in 500 mL water.
3. Fetal bovine serum, heat inactivated for 1 h at 55 °C.
4. Conditions of 5% O_2 and 10% CO_2 at 37 °C or 42 °C, achieved by either appropriate gas-controlling incubators or Campypaks (Oxoid) and sealable growth jars.

2.2 Materials for Nutrient-Depleted Chemotaxis Assay

1. 0.5% agar without nutritional supplements: 1.25 g Bacteriological Agar dissolved in 250 mL water. Autoclave and store at 4 °C.
2. 0.1% agar without nutritional supplements: 0.1 g Bacteriological Agar dissolved in 100 mL water. Autoclave and store at 65 °C until use (in order to keep 0.1% agar molten prior to solidifying at 37 °C; not more than 4 days).
3. 200 mM ligand: ligand dissolved in pre-sterilized water. Store at 4 °C.

4. 1% saline: 5 g NaCl dissolved in 500 mL water.
5. Stable bench top or table at 37 °C that has been checked using a spirit level.
6. Microcentrifuge.
7. Shaker.
8. Sterile disposable plastic transfer pipette.
9. Spectrophotometer.
10. Wet paper towels.
11. Large plastic container and smaller plastic container filled with water.

2.3 Materials for the Agarose-in-Plug Bridge Assay

1. 100 mM ligand solution, dissolved in pre-sterilized water.
2. Nusieve GTG Agarose (low melting temperature).
3. 10× PBS (10× PBS (per liter: 80 g NaCl, 2 g KCl, 11.5 g dibasic Na_2HPO_4-$7H_2O$, 2 g monobasic KH_2PO_4; pH 7.3 without any addition).
4. Fetal Bovine Serum (FBS), heat inactivated at 55 °C for 1 h prior to use.
5. Glass slides prepared by acetone washing (*see* **Note 1**).
6. Glass cover slips (*see* **Note 1**).
7. Liquid bacterial culture with bacteria at high motility (*see* **Note 2**).
8. Microscope with 2.5× brightfield objective and 40× phase objective.
9. Spectrophotometer.
10. Variable speed microcentrifuge.
11. Water bath (65 °C).

3 Methods

3.1 Nutrient-Depleted Chemotaxis Assay with C. jejuni

1. Culture *C. jejuni* strains on CHBA with appropriate selection under microaerobic conditions (5% O_2, 10% CO_2, 85% N_2) for 24 h at 42 °C.
2. Sub-culture *C. jejuni* strains in 10 mL Brucella Broth with appropriate selection in 25 cm^2 tissue culture flasks under microaerobic conditions at 42 °C for 18 h with shaking (50 rpm) (*see* **Note 2**).
3. Aliquot 0.1% agar into 50 mL tubes and temper/incubate at 37 °C overnight.
4. Prepare 0.5% agar plates by pouring 30–35 mL agar into petri dishes, to form a base of approximately 0.5 cm (*see* **Note 3**).

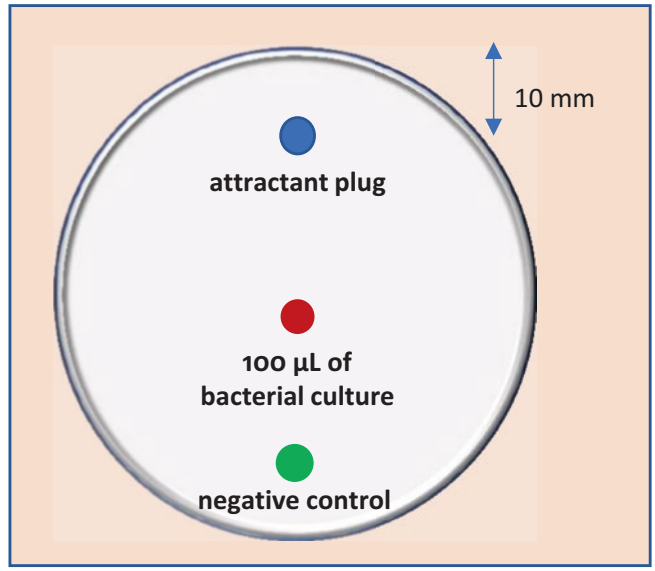

Fig. 1 Schematic diagram of the plate for the nutrient-depleted assay

5. Prepare solution of 0.5% agar containing 2 mM of selected ligand.
6. Using a marker pen, indicate the center of the agar plate, as this is the designated area for the placement of the bacterial suspension. The layout of the plate is shown in Fig. 1.
7. Remove one 6 mm diameter plug from the 0.5% agar petri dish. To remove the 6 mm diameter plugs, a sterile disposable plastic transfer pipette is cut at the 0.5 mL mark, and the transfer pipette is inserted into the 0.5% agar approximately 1 cm from the edge of the plate, squeezing the bulb prior to insertion. Using the suction created by the transfer pipette, the plug is removed by both releasing the bulb of the transfer pipette simultaneously with removing the transfer pipette from the 0.5% agar plate (*see* **Note 4**).
8. Once the plug is removed and discarded, use a marker pen to circle the well where the plug was removed and label with the ligand name (*see* **Note 5**).
9. Fill each well with 6–8 drops of 0.5% agar containing 2 mM of selected ligand (*see* **Note 6**).
10. Place the prepared 0.5% agar plates containing ligands at 37 °C on a stable bench top or table (*see* **Note 7**).
11. Overlay the prepared 0.5% agar plates (containing ligand wells) with 5 mL of tempered 0.1% agar, to create the prepared and overlaid agar plates. Leave these plates at 37 °C for 1–2 h to allow diffusion of the ligand in order to create a chemical gradient (*see* **Note 8**).

12. To create a humid environment for the chemotaxis assay, place a small container of water and stacks of wet paper towel around the plates on the bench/table and cover all components with a large container, being careful not to bump or move the bench/table or plates.
13. Collect the sub-cultured *C. jejuni* cells from **step 2** by centrifugation at 3000 × *g* for 5 min and discard the supernatant.
14. Wash the cell pellet by resuspending in 1 mL Brucella Broth, using gentle pipetting so as not to shear the flagella. **Do not vortex**! Centrifuge at 3000 × *g* for 5 min.
15. Resuspend the cells gently in 1% saline. Adjust the optical density using spectrophotometry to correspond to 1×10^9 cells/mL (~OD_{600nm} = 0.5 for *C. jejuni*).
16. Gently place a 100 μL drop of bacterial suspension (1×10^8 cfu) onto the center of the prepared and overlaid agar plates. Insert the pipette tip 1–2 mm into the 0.1% agar layer to gently expel the bacterial suspension (*see* **Note 9**).
17. Incubate the inoculated plates without disturbance for 4 h.
18. After 4 h, enumerate the bacteria associated with each ligand by removing a 5 mm area surrounding the ligand plug along with the plug itself. To remove the plug, cut a disposable plastic transfer pipette at the 1.5 mL mark and sterilize with UV for 20 min prior to use. The transfer pipette is inserted into the 0.5% agar squeezing the bulb prior to insertion. Using the suction created by the transfer pipette, the plug is removed by both releasing the bulb of the transfer pipette simultaneously with removing the transfer pipette from the 0.5% agar plate. Once the plug is removed, place into an Eppendorf tube containing 900 μL Brucella Broth.
19. Additionally, an equally sized center plug from where the bacterial suspension was placed is removed along with a plug from an area of the plate where no ligand is present in order to perform viability counts and ensure the chemotaxis assay has not been biased by bumping etc. (*see* **Note 10**).
20. A hole is punctured in the lid of the Eppendorf tubes containing removed plugs and incubated under microaerophilic conditions for 1 h at 37 °C to allow bacteria to dissociate from the plug into the media.
21. Perform bacterial enumeration using 1:10 serial dilutions and plating. For the test ligand and positive control dilutions, culture 10^{-3}–10^{-7} dilutions, and for the negative control culture 10^{-1} dilution onto 2% CBA and incubate at 42 °C for 48 h for viable counts.

22. For all chemotaxis assays a non-motile, non-chemotactic control *C. jejuni* strain (81116 *fla*A$^-$/*fla*B$^-$ mutant) is used to determine that no external bias has influenced movement of the bacteria during the assay. Additionally, plugs containing mucin (10 mg/mL stock) and plugs containing no ligand are included in all assays as controls. Mucin has been reported as a chemoattractant for *C. jejuni* [14], and movement toward mucin should occur with all strains tested. No movement should occur with plugs that do not contain ligands.

3.2 Agarose-in-Plug Bridge Assay with H. pylori

1. Culture *H. pylori* strains on CHBA with appropriate selection under microaerobic conditions (5% O_2, 10% CO_2, 85% N_2) for 24 h at 37 °C.
2. Sub-culture *H. pylori* strains in 8 mL Brucella Broth plus 10% FBS, with appropriate selection, in 50 mL flasks under microaerobic conditions at 37 °C for 18 h with shaking at 50 rpm (*see* **Note 2**).
3. Prepare agarose plugs with 10–80 mM final concentration of ligand. For example, for a 10 mM ligand plug, mix 50 μL 100 mM ligand, 0.01 g Nusieve agarose (2% final), 50 μL FBS extract, 50 μL 10× PBS, plus water to 500 μL. Heat at 70 °C until the agarose is melted. Cool to 4 °C for overnight storage or at 65 °C for immediate use.
4. Wash/prepare *H. pylori* cultures by measuring the OD_{600nm} (should be roughly 0.3–0.7), centrifuge at 2000 × *g*, for 5 min, resuspend in 1× PBS and repeat centrifugation, followed by resuspending in 1× PBS + 10% FBS to an OD_{600} of 1.0 (*see* **Note 11**). Confirm motility using microscopy. *H. pylori* can be kept under growth conditions for ~30 min.
5. Prepare chemotaxis chamber by melting ligand-agarose at 65 °C. Place two cover slips 1.5 cm apart on glass slide (Fig. 2A). Pipet 12 μl melted agarose between the slips. Place a glass cover slip on the top of the agarose, supported by the flanking cover slips. Incubate under microaerobic conditions for 5–10 min in order to equilibrate the plug to the ideal *H. pylori* conditions.
6. Critical controls are use of an *H. pylori* strain that lacks motility and chemotaxis, to confirm that the response requires chemotaxis. An additional control is to include plugs that lack ligand.
7. Pipet 100–120 μL of the washed *H. pylori* under the top glass cover slip.
8. Observe under 2.5× objective for areas adjacent to the Agarose plug (Fig. 2B) immediately and up to 15 min after initiating the assay (*see* **Note 12**) (Fig. 2).

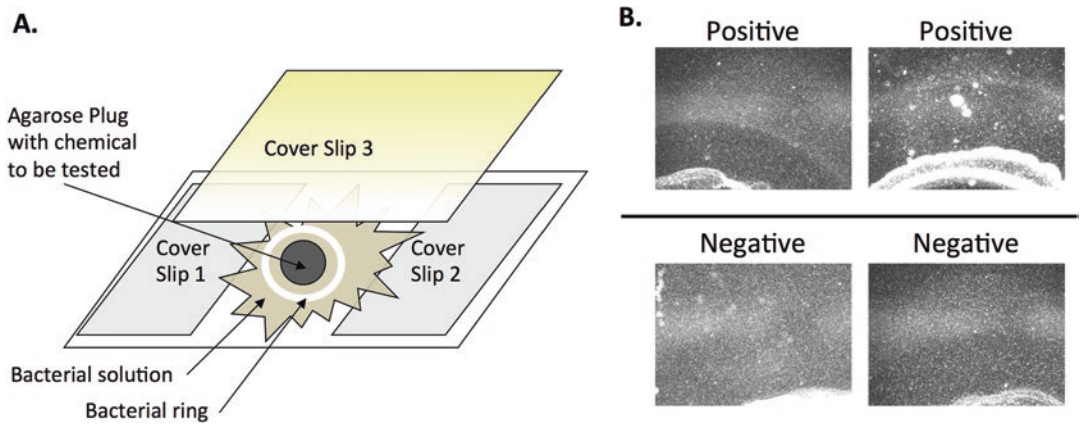

Fig. 2 The agarose-in-plug bridge assay. (**A**) Diagram of the assay set-up with three cover slips on a microscope slide. The agarose plus is in the center, surrounded by the bacterial solution. After time, the bacterial ring appears if there is a response. (**B**) Images of positive response (top) and no response (bottom)

4 Notes

1. To remove metals and other impurities that may be present in glass, rinse with acetone (three times) and then water (three times) and leave to dry overnight.
2. For *C. jejuni*, bacterial cells can be grown on solid agar plates or biphasically; no significant difference in subsequent motility has been observed between these methods of bacterial cell preparation for this assay. For *H. pylori*, growth in Brucella Broth + 10% serum to mid log phase produces reliable motility.
3. If the agar plate is too thin, the overlaid 0.1% agar tends to dry out, thereby reducing motility and viability of bacteria.
4. Ensure the transfer pipette is cut as straight as possible to allow for efficient suction and removal of the plug.
5. Ensure that the well where the plug was removed is labeled, as after the hole is refilled with 0.5% agar containing ligand to be tested, it is difficult to see where to remove the agar after the bacterial suspension has been added.
6. When replacing each well with 0.5% agar containing ligand, ensure that the agar fills the well so that it is flush with the surface of the agar; if too little is added the well becomes concave. 0.5% agar plates containing ligand can be stored for up to 12 h at 4 °C with no significant effect on chemotaxis assays.
7. Ensure that the bench top or table has been checked with a spirit level, as any slight slope can influence the movement of the bacterial suspension and bias the result. Let the plates sit

for 15 min or until they have reached 37 °C. If 0.5% agar plates are still below 37 °C when the 0.1% agar is overlaid, the plate will dry out, which will lower the viability of the bacterial suspension.

8. If the 37 °C area where the chemotaxis assay is to be performed does not retain high humidity, a humid atmosphere will need to be created. Otherwise, the 0.1% agar will dry out and decrease viability of the bacteria.
9. When inoculating plates with the bacterial suspension ensure that a very gentle expulsion technique is used; otherwise, the suspension can bead and run over the surface of the 0.1% agar instead of being placed in the center of the plate as a neat circle and can subsequently influence results.
10. Collect the plugs in the following order; ligand-associated bacteria (ligand plug), center (inoculum control) then random area (negative control).
11. *H. pylori* requires FBS for optimal motility [15]. This FBS can also be treated to remove small molecules as follows. Starting with heat-inactivated FBS, add 50 mM Na_2EDTA and boil for 30 min. Next, freeze the FBS at −20 °C, thaw, and centrifuge at 15,000 × *g* for 15 min. Next, filter through a 0.22 μm pore filter and dialyze for 15–20 h in 1× PBS with one buffer change.
12. Observe under 2.0–2.5× objective on phase I—the assay has the appearance of darkfield microscopy. Timing can vary; usually try immediately as well as ~15 min later. If incubating for 15 min, place the chambers in a sealable container containing a wet paper towel to prevent desiccation.

References

1. Wadhams GH, Armitage JP (2004) Making sense of it all: bacterial chemotaxis. Nat Rev Mol Cell Biol 5:1024–1037
2. Miller LD, Russell MH, Alexandre G (2009) Diversity in bacterial chemotactic responses and niche adaptation. Adv Appl Microbiol 66:53–75
3. Keilberg D, Ottemann KM (2016) How *Helicobacter pylori* senses, targets and interacts with the gastric epithelium. Environ Microbiol 18:791–806
4. Butler SM, Camilli A (2005) Going against the grain: chemotaxis and infection in *Vibrio cholerae*. Nat Rev Microbiol 3:611–620
5. Zautner AE, Tareen AM, Groß U, Lugert R (2012) Chemotaxis in *Campylobacter jejuni*. Eur J Microbiol Immunol (Bp) 2:24–31
6. Hendrixson DR, DiRita VJ (2004) Identification of campylobacter jejuni genes involved in commensal colonization of the chick gastrointestinal tract. Mol Microbiol 52:471–484
7. Lertsethtakarn P, Ottemann KM, Hendrixson DR (2011) Motility and chemotaxis in *Campylobacter* and *Helicobacter*. Annu Rev Microbiol 65:389–410
8. Li J, Go AC, Ward MJ, Ottemann KM (2010) The chemical-in-plug bacterial chemotaxis assay is prone to false positive responses. BMC Res Notes 3:77
9. HS Y, Alam M (1997) An agarose-in-plug bridge method to study chemotaxis in the Archaeon *Halobacterium salinarum*. FEMS Microbiol Lett 156:265–269
10. Kanungpean D, Kakuda T, Takai S (2011) False positive responses of *Campylobacter jejuni* when using the chemical-in-plug chemotaxis assay. J Vet Med Sci 73:389–391

11. Rahman H, King RM, Shewell LK, Semchenko EA, Hartley-Tassell LE et al (2014) Characterisation of a multi-ligand binding chemoreceptor CcmL (Tlp3) of *Campylobacter jejuni*. PLoS Pathog 10:e1003822
12. Hartley-Tassell LE, Shewell LK, Day CJ, Wilson JC, Sandhu R et al (2010) Identification and characterization of the aspartate chemosensory receptor of *Campylobacter jejuni*. Mol Microbiol 75:710–730
13. Collins KD, Andermann TM, Draper J, Sanders L, Williams SM et al (2016) The *Helicobacter pylori* CZB cytoplasmic chemoreceptor TlpD forms an autonomous polar chemotaxis signaling complex that mediates a tactic response to oxidative stress. J Bacteriol 198:1563–1575
14. Hugdahl MB, Beery JT, Doyle MP (1988) Chemotactic behavior of *Campylobacter jejuni*. Infect Immun 56:1560–1566
15. Sanders L, Andermann TM, Ottemann KM (2013) A supplemented soft agar chemotaxis assay demonstrates the *Helicobacter pylori* chemotactic response to zinc and nickel. Microbiology 159:46–57

Chapter 4

Quantification of Bacterial Chemotaxis Responses at the Mouths of Hydrogel Capillaries

Benjamin A. Webb, Timofey D. Arapov, and Birgit E. Scharf

Abstract

Many chemotaxis assays allow for the assessment of bacterial chemotaxis by determining the number of cells migrating toward a chemoattractant or away from a chemorepellent. Some of these assays use a capillary filled with a chemoeffector/agarose mixture to allow cells to accumulate at the mouth of the capillary. Subsequently, assumptions about the relative strengths of chemotaxis strength are based on visual comparisons. Here, we describe a modification of this assay that uses a hydrogel matrix to enable quantitative time-course measurements by analyzing image pixel intensities. This approach allows a high-throughput method when coupled with the aid of a motorized microscope stage.

Key words Hydrogel capillary, Alignment, ImageJ, Motorized stage, PEG-DA, Pixel intensity, Quantitative measurement

1 Introduction

The capillary assay for the detection of bacterial chemotaxis has evolved since its inception by Pfeffer in 1883 [1] to methods like the Adler capillary assay, the 96-well plate assay, the agarose capillary assay, video analysis methods, and many more [2–7]. The goal of each modification to the assay involved obtaining quantitative data, expanding data sets, making the assay easier to carry out, and expediting data processing. In the Adler assay, a capillary is filled with an attractant solution and its open end is placed into a bacterial suspension to allow the attractant to diffuse out. This results in the formation of a gradient of the attractant, which allows the cells to use chemotaxis to migrate into the capillary. The content of the capillary is serially diluted and plated, and colony forming units (CFUs) are enumerated to calculate the number of cells that entered the capillary [3]. This technique, although the gold standard for assessing chemotaxis in a quantitative manner, can be

Michael D. Manson (ed.), *Bacterial Chemosensing: Methods and Protocols*, Methods in Molecular Biology, vol. 1729, https://doi.org/10.1007/978-1-4939-7577-8_4,

cumbersome and relatively time consuming when compared to the agarose capillary assay. It also requires some manual dexterity.

The agarose capillary assay allows faster data generation because it does not rely on the calculation of CFUs. Instead, the cells are prevented from swimming into the capillary, and their accumulation at the capillary mouth is observed. Briefly, the attractant is mixed with molten agarose, and the mixture is pulled into the capillary where it solidifies. The mouth of the capillary is submerged into a chemotaxis chamber atop a microscope stage and observed under dark field at a magnification between 20× and 100×. A positive chemotactic response results in an accumulation of cells at the capillary mouth, and the light reflected by these cells is observed. Images are taken and visual comparisons are made between wild-type and mutant strains and different attractants [4]. A common problem with this method is that the agarose often protrudes from or withdraws into the capillary; in the latter case, the cells can enter the capillary. Both occurrences cause nonuniform cell accumulation that cannot readily be compared to the results from other capillaries. As a consequence, there is a loss of comparative data. Our newly developed assay is a modification of the agarose capillary assay that prevents matrix protrusion and recession. In addition, adaptations were incorporated to generate quantitative data and simplify the method of collecting larger data sets in shorter time. This technique is called the hydrogel capillary assay.

It is easy to form an agarose matrix in a capillary. However, the matrix is not anchored to the inner glass surface of the capillary, which allows it to slide along the glass surface. Polyethylene glycol diacrylate (PEG-DA) has been used extensively as a substrate for matrix formation from drug delivery devices to microfluidic chemotaxis chambers [8, 9]. Briefly, a PEG-DA solution is mixed with a photo-initiator molecule, such as Irgacure®. Upon photoactivation with ultraviolet light, the Irgacure® molecule forms a free radical that binds a PEG-DA oligomer to create a PEG-DA radical. This interaction initiates a chain reaction that binds together neighboring PEG-DA oligomers, in effect polymerizing the PEG-DA into a matrix filled with water; hence, the term “hydrogel.” To bind the matrix to a surface, the glass must be functionalized so that PEG-DA free radicals bind to it covalently and become fixed in place [10]. Here, we use a method of glass functionalization for permanently immobilizing a hydrogel to the inside of a capillary.

In the past, multiple chemotaxis chambers were positioned on a microscope stage and imaged over time. However, it is difficult to maintain a regular time interval because of the uncertainty of manually moving the stage, positioning the capillary, and taking a photograph at the appropriate time. To increase temporal precision and to improve the consistency of capillary

positioning in the image, we have taken advantage of a motorized microscope stage interfaced with computer software that allows the microscope stage to move to stored positions and acquire images at regular intervals.

Imaging the mouth of the capillary delivers information about an individual time point of the chemotaxis response. However, the ability to observe a temporal response in a quantitative manner can reveal other aspects of the response. These adaptations have been implemented mostly by Nikata et al. [6]. We took their assay one step further by developing a method to stitch snapshots together to generate a time course for the response. The images are analyzed with the computer program ImageJ, which visualizes cells in a two-dimensional plane as they move toward the capillary mouth. Results are presented as pixel intensities in a region of interest near the mouth of the capillary versus time. Taken together, we combined all these adaptations in the hydrogel capillary assay to create a modernized method to collect large data sets on a faster time scale.

In addition to the improvement of the hydrogel and the motorized stage, we are using an image alignment algorithm to assist in fast data processing. Because of small stage movements and differences between the placement angles of the capillaries, it can be difficult to analyze the same area around each capillary. For this reason, we used an image alignment algorithm implemented in MATLAB to rotate images so that the same region of interest can be consistently measured. These aligned images can then be rapidly analyzed in the ImageJ Time Series Analyzer plugin. By plotting the image pixel intensities versus time, the complete time course of chemotaxis at the capillary mouth can be documented. In conclusion, the hydrogel capillary assay builds upon past adaptations of the basic method to develop an assay that is relatively easy to perform, less time consuming, and capable of producing quantitative data.

2 Materials

2.1 Hydrogel Capillaries

1. 0.5 μL volume capillaries: Obtain 1 μL volume Drummond® microcaps. Cut the microcaps in half (16 mm each) using a scalpel (*see* **Note 1**).
2. 1% (vol/vol) solution of 3-(trichlorosilyl)propyl methacrylate (TPM) (Sigma-Aldrich): Dilute in sterile filtered paraffin oil.
3. 100% ethanol.
4. 10% (wt/vol) 2-Hydroxy-4′-(2-hydroxyethoxy)-2-methylpropiophenone (Irgacure®2959) (Sigma-Aldrich, 410896) dissolved in 70% ethanol.

5. Phosphate-buffered saline, pH 7.4 (PBS): Sterile filtered.
6. 10% (wt/vol) solution of polyethylene glycol-diacrylate (PEG-DA) with an average M_n of 10,000 (Sigma-Aldrich, 729094). Weigh out 0.1 g and dissolve in 1 mL of PBS, pH 7.4. To conserve resources, store the solution at −20 °C.
7. Forceps with a point fine enough to handle the capillaries but with good traction.
8. Vacuum desiccator. Place a small tube rack inside the desiccator.
9. Microfiber lens cleaning cloth.
10. Bunsen burner (oxidizing flame).
11. 10% (wt/vol) Irgacure®2959 (Sigma-Aldrich): Weigh out 0.1 g and dissolve in 1 mL of 70% ethanol. To conserve resources, store the solution at −20 °C indefinitely.
12. UV light source capable of producing a wavelength of 365 nm and 18 W cm^{-2}. We use the OmniCure S1000 UV light source (EXFO Photonic Solutions, Inc., Vanier, Quebec, Canada).
13. Antibiotics: 1:1000 dilutions of the following stocks, kanamycin (dissolved in water at 50 mg/mL), neomycin (dissolved in water at 120 mg/mL), ampicillin (dissolved in water at 100 mg/mL), and gentamycin (dissolved in water at 5 mg/mL).

2.2 Hydrogel Capillary Equilibration

1. Your chemotaxis medium of choice.
2. 2 mL microcentrifuge tube.
3. 0.5 mL microcentrifuge tube.
4. Attractants of choice.
5. Refrigerator set to 4 °C.

2.3 Chemotaxis Chambers

1. Microscope slide with dimensions 50 mm × 100 mm × 1 mm.
2. Cover slips with dimensions 18 mm × 18 mm × 0.2 mm.
3. Rubber O-rings from 1.5 mL Sarstedt screw cap tube. Cut O-rings in one position with scissors.
4. Machine grease. We use Apiezon M, Manchester, United Kingdom.
5. Forceps.
6. Hydrogel capillaries equilibrated with attractant.
7. Approximately 82 μL of motile cell culture: Any volume between 80 and 90 μL will fill up the chamber and prevent air bubbles from becoming trapped inside the chamber. Be consistent with volumes.

2.4 Microscopic Observation of Capillary Mouths

1. Inverted microscope. We use the Zeiss Axio Observer Z1.
2. Motorized scanning microscope stage, capable of moving in the *x*, *y*, and *z* directions.
3. Electronic coaxial drive for communication between the stage and the computer.
4. 2.5× objective. We use the Zeiss N-Achroplan 2.5×/0.07 objective.
5. A microscope stage incubator.
6. ZEN image acquisition software, capable of setting image tiles and positions.

2.5 Image Rotation

1. MATLAB version R2015a (MathWorks).
2. Enhanced Correlation Coefficient (ECC) algorithm: Obtained from the Image Alignment Toolbox (IAT) at iatool.net.

2.6 Image Analysis

1. ImageJ (Rasband).
2. Time Series Analyzer V3 plug in.
3. Rotated images.

3 Methods

3.1 Fabrication of Hydrogel Capillaries

1. Pipette 100 µL of 1% TPM solution into the bottom of a 2 mL tube and add 20–40 capillaries with the open mouth in the TPM solution. Capillary action will move the solution about 0.5 mm inside the capillaries. Incubate for 10 min.
2. Remove capillaries and place them into an empty 2 mL tube. Put them under vacuum in a desiccator for about 30 s to remove the TPM.
3. Place the capillaries into a 2 mL tube filled with 100% ethanol and gently vortex to remove excess TPM solution. Repeat this step by transferring the capillaries to a new tube with fresh 100% ethanol.
4. Transfer capillaries to a new tube filled with fresh 100% ethanol and put them under vacuum for 30 s.
5. Transfer capillaries to an empty tube and place under vacuum for about 2 min to remove the ethanol (*see* **Note 2**).
6. Use forceps to hold a capillary near the sealed end and wipe the surface of the capillary with microfiber lens cloth, then pass the capillary quickly through an oxidizing flame. Wipe the capillary one last time with the cloth. Repeat for all capillaries.
7. To create the hydrogel precursor solution, mix the Irgacure®2959 and PEG-DA solutions in a 1:20 ratio (5%

Irgacure® solution) (*see* **Note 3**). If you do not plan to use it immediately, freeze it as soon as possible. Add approximately 100 μL of the precursor solution to the bottom of a 2 mL tube and add the capillaries to the same tube with the open mouth in the solution. Place the tube in a vacuum pump and apply vacuum (200 mTorr) until air is evacuated from the capillaries. Once bubbles climb the wall of the tube, turn off the vacuum. Inspect capillaries to make sure that the precursor solution has completely filled the capillary.

8. Pipette about 30 μL of the precursor solution into the bottom of a 1.5 mL tube and place 6–9 capillaries into the tube with their mouths in the solution. Use forceps to evenly space the capillaries so that they are not touching each other.
9. Keeping the tube open, place the tube containing the capillaries in a tube rack holder and position the tube directly underneath the UV light source. Position the light source 12 cm away from the bottom of the tube.
10. Set the UV lamp to illuminate for 15 s and expose.
11. Once the exposure has finished, use forceps to remove the capillaries including the hydrogel mass attached at the capillary mouths and place into PBS with antibiotics.
12. Inspect hydrogel-containing capillaries under a dissecting scope: Using a microscope slide and silicon grease to create a slight enclosure, fill the area with distilled water, and place under the dissecting scope. Pull capillaries out of the PBS, submerge in water, and view the mouth of the capillary through the eyepiece. If you see excess hydrogel, remove the capillary and use a gloved hand to press the mouth of the capillary against a sopping wet Kim wipe. Gently twist and/or scrape the mouth against the Kim wipe. Re-inspect the capillary mouth under the dissecting scope. If the hydrogel is flush with the mouth, then store the hydrogel capillary in PBS with antibiotics at 4 °C for up to 4 months. If the hydrogel is not flush, then repeat the twist and scrape technique until flush.

3.2 Chemotaxis Chamber Preparation

1. Clean the microscope slide. Remove dust particles and avoid water stains.
2. Use forceps to pick up the cut O-rings and use a syringe to apply a circle of machine grease around one side of the O-ring, as well as to the cut ends of the O-ring. Use a *modest* amount of grease to avoid mixing with cell suspension.
3. Carefully set the O-ring down onto the microscope slide. Keep the cut section closed. Repeat for additional chambers.
4. Apply a *modest* amount of machine grease to the top side of the O-ring, as well as to the cut section of the O-ring. Repeat for additional chambers. The slide may be stored in a closed container to prevent contamination by dust.

3.3 Hydrogel Capillary Equilibration with Attractant

1. The day prior to an experiment, remove PBS and antibiotics from the tube containing the capillaries and wash the capillaries at least once with your chemotaxis buffer of choice. Add your chemotaxis buffer and incubate for at least 4 h at either 4 °C or room temperature (Equilibration 1).
2. Repeat **step 1** (Equilibration 2).
3. For each hydrogel capillary, pipette at least 50 μL of attractant solution (dissolved in chemotaxis buffer) into a 0.5 mL tube (100 μL for two capillaries 150 μL for three capillaries, etc.).
4. Remove hydrogel capillaries from the chemotaxis buffer and add them to the attractant solution. Cap the tube and incubate overnight at 4 °C (Equilibration 3) (*see* **Note 4**).

3.4 Image Optimization

Prior to an experiment, set up the experimental parameters for the microscope and camera using an image acquisition software, such as ZEN™. The following instructions are for optimal image acquisition on the Zeiss Axio Observer Z1. These parameters can be applied and optimized for other setups.

1. On the microscope stage, set up several chemotaxis chambers and fill them with cell suspensions at a range of optical densities (an OD_{600nm} of 0.12 is optimal for viewing for *S. meliloti* at an exposure of 1.3 ms at 4.8 V). Insert hydrogel capillaries equilibrated with chemotaxis buffer. Refer to Subheading 3.6 on how to insert a hydrogel capillary.
2. Set the lamp voltage within the range of 4.6–5.1 V. Use a 2.5× objective and camera attachment (AxioCam MR R3). Bring the mouth of the capillary into focus on the computer screen. Move the stage so that the mouth of the capillary protrudes into the field of view about one-fifth of the way from the edge of the image.
3. Set the exposure time to 1.3 ms.
4. Rotate the phase plate so that it rests between the phase rings and creates a pseudo dark field. On the Zeiss Axio Imager Z1, we find an optimal image when the plate is set between Ph2 and Ph3 at distances of 67 mm and 24 mm from Ph2 and Ph3, respectively. In the live image, you should see swimming cells, the edges of the capillary, and a dark background. Portions of the glass capillary will appear completely bright; however, the cell suspension should appear uniform and not too bright. Move the stage to view other chemotaxis chambers.
5. To find the range of optimal culture densities, take a photograph of each chamber and use any image analysis software to assess the image intensity of the suspension. Anything with a pixel intensity of >255 is overexposed. To reduce exposure, one can adjust several variables, such as cell suspension density, lamp voltage, and exposure time.

6. Once the optical density is optimized, repeat the steps above with a range of attractant concentrations. The attractant concentration should be optimized so that the response at the mouth of the capillary does not cause overexposure or an accumulation of cells behind the mouth of the capillary.

3.5 Microscope Experimental Parameters

1. Use the Zen software to create a program for image acquisition.
2. Set the light path to pass through the objective and reflect toward the camera.
3. Under the channels tab, check the box for TL Bright field.
4. Set the focus strategy to "Absolute fixed Z-position" and check the box for "Use Z position from tiles set up".
5. An exposure time of 1.3 ms is optimal for *S. meliloti*. Larger or smaller bacteria may need different exposure times.
6. Set the experiment length and image acquisition interval.

3.6 Capillary Assay

1. Add cell suspension to the chemotaxis chambers. Any volume between 80 and 90 μL will suffice, but stay consistent.
2. Use forceps to lay the capillary over the cut part of the O-ring and use your finger to gently press the capillary into the cell suspension. Immediately apply a generous amount of machine grease over the portion of the capillary that extends from the chamber (*see* **Note 5**).
3. Place a cover slip over the chamber by gently laying one edge of the cover slip down first and bringing the face of the cover slip down over the cell suspension and then release the cover slip. Haphazardly dropping of cover slips will likely result in trapping air bubbles in the chamber. Gently press down on the cover slip with the forceps to make the cover slip parallel with the microscope slide. Some cell suspension will be squeezed out of the chamber and adhere to the cover slip. Repeat for subsequent chambers (*see* **Note 6**).
4. Once all chambers are sealed, place the slide onto the stage in an appropriately sized slide holder. With a live view on the computer screen, move the stage so that the capillary of the first chamber is in focus. Make sure that the mouth of the capillary protrudes only about one-fifth of the way into the field of view. Save that position as position number one. Whichever distance you choose for the first capillary, remain consistent with the remaining capillaries. Repeat for the remaining chambers.
5. Once all positions are saved, start the program.

3.7 Image Exportation and Organization

Export images in a high resolution format, e.g., tiff (uncompressed). Select a destination folder for each individual scene. Repeat for remaining scenes. Be sure to maintain images at a high resolution.

3.8 Image Alignment

In these steps, the images will be rotated so that a perpendicular rectangular "Region Of Interest" (ROI) can be drawn in front of the mouth of capillary in the subsequent image analysis steps (Subheading 3.9). This solution was implemented in MATLAB using Image Alignment Toolbox (IAT). IAT can be found at the following URL (http://iatool.net/downloadiat/). An example alignment script can be found at "www.scharf.biol.vt.edu" It has been written to iterate through a folder and align all the images in this folder using an Enhanced Correlation Coefficient (ECC) algorithm employing only Euclidean transformations. The following instructions rely on MATLAB version R2015a and IAT and help guide a user through the steps needed to align a set of capillary images using the example script.

1. Copy and paste all the images for a particular scene into a new folder with a unique name, e.g., "scene 1."
2. For each set of images, create a template image by opening one image of a scene using an image editor, such as GNU Image Manipulation Program (GIMP) or Adobe Photoshop CS5. From the canvas edge, drag down a horizontal line and rotate the image using "free transformation" so that the mouth of the capillary is parallel to the horizontal dotted line. Save this rotated image in a new folder, which will contain all template images for each scene. (*See* Fig. 1 for an example of image rotation).
3. Open MATLAB and install the IAT tool box. Directions are available at (http://iatool.net/installation/). Additionally, add all files and folders that you wish to use with the path.
4. Run the alignment script. You will be prompted to select a template image. Navigate to select the appropriate template image for scene 1 from the collection of template images. Only the images that have been added to the MATLAB path will be available for selection.
5. Once selected, you will be prompted to select the folder with the images to be aligned. Navigate to select the folder containing images from scene 1. Once selected, the script will align the images and save them to the same folder containing the unaligned images. The aligned images open in their own window, which may cause a memory error to occur. If this happens, restart MATLAB before starting a new alignment. If this continues to occur, it is acceptable to close the windows as they open.

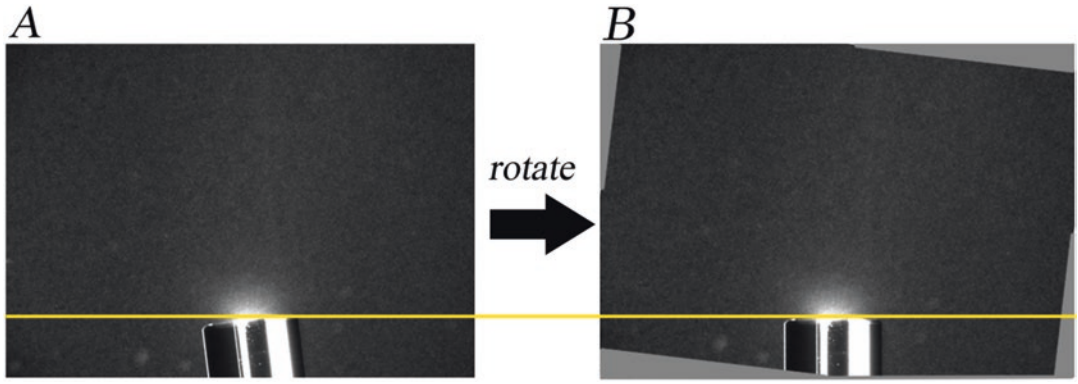

Fig. 1 Example of the image alignment step. (**a**) The capillary does not align with horizontal line. In an image editor software, a horizontal guide-line is placed near the capillary mouth and the image is rotated. (**b**) Once the image has been rotated, the edge of the capillary is parallel to the guide. This image serves as a template to rotate other images in a series. The gray areas are not analyzable and should be cropped prior to quantification

6. Put all rotated images into one folder and label them in a manner that keeps them in order, e.g., images from scene 1 could be given a prefix of "1-", images from scene 2 a prefix of "2-", and so forth.

3.9 Image Analysis

In the following steps you will measure integrated pixel intensities at the mouth of the capillary.

1. In ImageJ, select plugins and install the plugin called "Time Series Analyzer V3." Once finished downloading, open the plugin.
2. Open ImageJ, select "file, import," and select "image sequence." In the pop-up window, navigate to the file containing all the rotated images of the experiment and make note of the order in which they reside in the folder. Open the folder, double click the first image, and the images will automatically be imported as a sequence.
3. Draw a rectangular ROI with dimensions that encapsulate the chemotaxis response at the capillary mouth. An example of appropriate dimensions is 450 pixels long and 235 pixels high. Be sure not to include any part of the capillary.
4. In the ROI manager, select "add [t]" (or type the letter "t"), and this region of interest for this image will be added to the list in the ROI manager window. Repeat for all images. Reposition the ROI so that it rests in precisely the same spot as in the previous images and select "add [t]."
5. In the Time Series Analyzer V3 window, select "get total intensity." The program will determine the total pixel intensities for each image and report them in two pop-up windows, i.e., Time Trace Average and Time Trace(s).

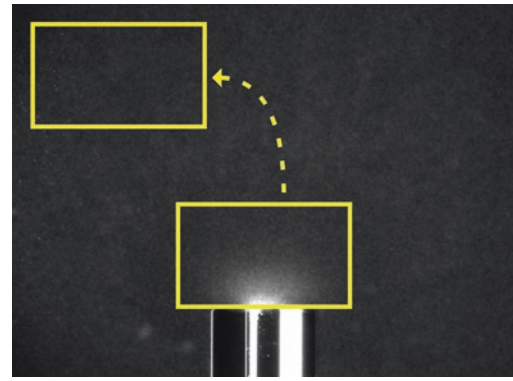

Fig. 2 Example of background ROI generation. The background ROI is moved away from the mouth of the capillary and does not encapsulate any part of the area of cell accumulation

6. In the Time Trace(s) window, values are reported as integrated pixel intensities. Make note of the image numbers, copy the integrated pixel intensities, and paste into a spreadsheet such as MS Excel.
7. Generate a background ROI by going back to the image sequence and move the ROI away from the area of cell accumulation in such a way that the pixel intensities within the ROI are not affected by the chemotactic response (*see* Fig. 2 for appropriate locations). Review the images throughout the image sequence to ensure that the ROI does not include an area of cell accumulation.
8. Repeat **steps 6** and 7 (*see* **Note** 7).

3.10 Data Processing and Plotting

1. Subtract the background values from the response values and plot against time. When plotting replicates, be sure to align the response and background values to an average time point for each value. For example, if the first value of S1 from repetition 1 was acquired at time 5:00 min, and the first value of S1 from repetition 2 was acquired at time 5:20 min, then align the values in two columns against an average time point of 5:10 min. You may need to omit values from the beginning and end of a repetition if there are no other repetitions that have values pertaining to a similarly close time point. For instance, if your time interval is 2 min and the first value of S1 from repetition 2 was acquired at 7:00 min, then the value should be aligned against the second value of S1 from repetition 1, which was acquired at 7:00 min.
2. To normalize the response values of a repetition, divide all values by the highest response value. Repeat for multiple repetitions.

4 Notes

1. When cutting microcaps in half, it helps to use a bright light source and a stationary magnifying lens. When sealing the cut end of the microcapillary, use an oxidizing flame from a Bunsen burner. If the capillary glass droops, too much heat was applied. When the glass barely turns red in the flame, then the capillary is sealed. A dissecting scope can be used to confirm the seal.
2. In Webb et al. [6], the inner glass surfaces of the capillaries were cleaned with a 3:1 solution of 17 M sulfuric acid, and a 30% hydrogen peroxide solution prior to being treated with a 1% (vol/vol) TPM solution. However, we found that this additional cleaning step is unnecessary.
3. Use aseptic technique when equilibrating the hydrogel capillaries.
4. It takes about 8 min for a steady and quick hand to set up the chambers prior to the first acquired image. Therefore, if you expect that certain strains are not going to have a chemotaxis response (or will have a slow response) insert the capillaries into these chambers first.
5. Use a running timer to note the time that the glass cover slip has been pressed down on the chemotaxis chamber with forceps.
6. PEG-DA with an average M_n of 10,000 is used here, but we have experimented with lower M_n PEG-DA (6000 and 2000) and found that the porosity of the material influences the chemotaxis response. In brief, PEG-DA with a higher M_n results in a faster response with a higher pixel intensity than PEG-DA with lower M_n. However, the chemotaxis responses observed while using PEG-DAs with higher M_n are short lived. These results are likely due to the variation in the steepness of the attractant gradient.
7. If the background ROI includes an area of cell accumulation, you will notice an upward trend in reported pixel intensities.

Acknowledgments

This study was supported by National Science Foundation grant MCB-1253234. We are indebted to Bahareh Behkam for sharing the Zeiss Axio Observer Research microscope and the Omnicure S1000 UV light source, and to Aziz Mahama Traore for training in hydrogel capillary fabrication.

References

1. Pfeffer W (1883) Locomotorische Richtungsbewegungen durch chemische Reize. Ber Deut Botan Ges 1:524–533
2. Bainer R, Park H, Cluzel P (2003) A high-throughput capillary assay for bacterial chemotaxis. J Microbiol Methods 55:315–319
3. Adler J (1973) A method for measuring chemotaxis and use of the method to determine optimum conditions for chemotaxis by *Escherichia coli*. J Gen Microbiol 74:77–91
4. Grimm AC, Harwood CS (1997) Chemotaxis of *Pseudomonas* spp. to the polyaromatic hydrocarbon naphthalene. Appl Environ Microbiol 64:4111–4115
5. Nikata T, Sumida K, Kato J, Ohtake H (1992) Rapid method for analyzing bacterial behavioral responses to chemical stimuli. Appl Environ Microbiol 58:2250–2254
6. Webb BA, Hildreth S, Helm RF, Scharf BE (2014) *Sinorhizobium meliloti* chemoreceptor McpU mediates chemotaxis toward host plant exudates through direct proline sensing. Appl Environ Microbiol 80:3404–3415
7. HS Y, Alam M (1997) An agarose-in-plug bridge method to study chemotaxis in the Archaeon *Halobacterium salinarum*. FEMS Microbiol Lett 156:265–269
8. Peppas NA, Bures P, Lepobandung W, Ichikawa H (2000) Hydrogels in pharmaceutical formulations. Eur J Pharm Biopharm 50:27–46
9. Cheng SY, Heilman S, Wasserman M, Archer S, Shuler ML et al (2007) A hydrogel-based microfluidic device for the studies of directed cell migration. Lab Chip 7:763–769
10. Revzin A, Russell RJ, Yadavalli VK, Koh WG, Deister C et al (2001) Fabrication of poly(ethylene glycol) hydrogel microstructures using photolithography. Langmuir 17:5440–5447

Chapter 5

A Static Microfluidic Device for Investigating the Chemotaxis Response to Stable, Non-linear Gradients

Nitesh Sule, Daniel Penarete-Acosta, Derek L. Englert, and Arul Jayaraman

Abstract

Microfluidic technology allows fast and precise measurement of chemotaxis responses to both attractant and repellent signals. One of the major drawbacks of current microfluidic chemotaxis assays is the presence of bacterial cells within the concentration gradient flow field, which has the potential for flow effects masking the chemotaxis response. This chapter describes a new microfluidic device for producing stable concentration gradients and measuring the response of cells to the gradient without exposing them to any flow. Unlike other methods described in the literature, this method is capable of producing gradients of any shape, almost instantaneously, allowing the measurement of time-dependent response of cells to a variety of signals.

Key words Chemotaxis, Behavioral assay, Microfluidic device

1 Introduction

Bacterial chemotaxis is the directed movement of bacteria in response to environmental stimuli such as nutrients, oxygen and pH, among others [1]. Chemotaxis enables bacteria to navigate through their environment in a purposeful manner and plays an important role in the survival and proliferation of the organisms. The study of chemotaxis also helps us understand a variety of biological phenomena at the molecular level, including molecular sensing, signal transduction, and molecular motors, and it has applications in areas ranging from medicine to the environment to nanorobotics.

Methods to study chemotaxis rely on observing the migration behavior of motile bacteria in the presence of a concentration gradient of a chemoeffector molecule. Several assays have been developed for investigating bacterial chemotaxis that vary in their complexity, ease of operation, and quantitative nature. A review of the different methods and their applications is found in Englert

Michael D. Manson (ed.), *Bacterial Chemosensing: Methods and Protocols*, Methods in Molecular Biology, vol. 1729, https://doi.org/10.1007/978-1-4939-7577-8_5,

et al. [2]. The first assay developed to study chemotaxis, the capillary assay [3], is perhaps still the most widely used method. It involves placing a chemoeffector-filled capillary in a bacterial suspension. After incubation, the number of cells migrating into the capillary is quantified by diluting and plating the liquid in the capillary and counting colonies. This assay is quantitative, robust, easy to perform and does not require specialized equipment. However, it is not particularly well suited to study repellent chemotaxis, and it relies on significant manual dexterity to avoid variability in the results. Moreover, it is time consuming, as it requires spreading bacterial suspensions on plates and counting colonies after overnight incubation.

A modification of this assay, the agarose capillary assay [4], or an improved version called the hydrogel capillary assay (*see* Chapter 4 of this volume), improves upon this by directly visualizing the bacteria under a microscope. Another technique, called the agarose-plug-bridge assay, which uses a similar approach but is even simpler and faster to set up, involves placing the agarose surrounded by the bacterial suspension [5] under a cover slip (*see* Chapter 3 of this volume). Although these alternative assays are easy, fast and very useful for high-throughput and qualitative investigation of bacterial chemotaxis, they do not provide accurate and precise quantitative data. Moreover, an important drawback of all the above assays is that the concentration gradient to which the bacteria are exposed to is not stable; because of diffusion, it changes with time. Therefore, these are end-point assays, they provide data that is integrated over the collection period rather than snapshots over time of chemotaxis migration.

Advances in microfabrication techniques have led to the development of different microfluidic devices for investigating chemotaxis that address some of the above-mentioned drawbacks. One of their primary advantages is their ability to generate stable and precise concentration gradients. Moreover, these techniques use very small volumes, allow high throughput, and enable quantitative analysis. A review of the application of microfluidic devices in studying bacterial chemotaxis can be found in [2, 6]. The first microfluidic chemotaxis assay was reported by Mao et al. [7]. The device in this assay produced a gradient by diffusion between two parallel streams of liquid in laminar flow. Upon entering the channel in the center, the bacteria encountered buffer and chemoeffector on either side and were exposed to a gradient formed by diffusion as they flowed through the device. This assay was modified by Englert et al. [2], who used a microfluidic gradient generator chip [8] to apply diffusive mixing and the splitting of streams in a network of serpentine microfluidic channels that generated a gradient. In this setup, the cells encountered a preformed gradient immediately upon entering the channel, and the gradient remained stable along the observation channel. Both these methods can generate linear concentration gradients, whereas another model,

reported by Pasupuleti et al. [9], utilized multiple input streams to change the strength of the gradient.

One of the limitations of the microfluidic assays described above is the presence of the bacteria within the fluid flow field, which results in the bacteria being exposed to the gradient for only ~20 s before exiting the device [10]. This limits the time available to observe a response and necessitates cells with high motility. The problems associated with observing chemotaxis using this design have been detailed by Wolfram et al. [11], who make a strong case for the need of a "static" microfluidic chemotaxis assay. Attempts to overcome the effect of fluid flow on migration have focused on separating the gradient flow from the bacteria by diffusion along a membrane [12] or a layer of hydrogel [13]. In these devices, the source of the chemoeffector and the sink are positioned parallel on either side of the cell chamber, which results in a linear concentration gradient between the source and sink. This limitation was overcome by Ahmed et al. [14] by varying the shape of the channel. However, all of the existing static devices require a long time (20–30 min) for the gradient to form and stabilize because of the relatively long distance (~1 mm) between the source and the sink.

Here, we describe a new "static" microfluidic assay for chemotaxis that addresses the limitations of the described above. We still utilize a microfluidic gradient generator to form stable concentration gradients of any desired shape (i.e., linear, exponential, etc.). Moreover, this assay allows bacteria to be exposed almost instantly to the concentration gradient without being exposed to fluid flow. The design involves using two layers separated by a porous membrane. The concentration gradient and the cells are in the two separate layers, and the membrane allows for diffusion of the gradient into the cell chamber without any flow. Thus, the bacteria have significantly more time to respond to the chemoeffector and are not exposed to any shear forces. Microscopic imaging of the bacteria in the cell chamber allows the quantitative measurement of bacteria migrating to precise and stable concentrations of chemoeffectors without the limitations of fluid flow. Since the gradient is stabilized within the bacterial channel within a few seconds, it is possible to observe the time-dependent chemotaxis response of the cells. We demonstrate the feasibility of this assay by determining the response of the well-characterized strain *Escherichia coli* RP437 to different gradients of the attractant serine.

2 Materials

2.1 Microfluidic Device

1. Photolithography mask (*see* **Note 1**).
2. Negative epoxy photoresist and developer (SU-8 2015, Microchem, Newton, MA).

3. Polydimethylsiloxane (PDMS) (Sylgard 184 silicone elastomer kit, Ellsworth Adhesives, Germantown, WI).
4. Silanes: halosilane, e.g., tridecafluoro tetrahydrooctyl trichlorosilane (Chlorosilane), aminosilane, e.g., bis[3-(trimethoxysilyl)propyl]amine (Bis-silyl amine).
5. Porous membranes: e.g., polyester track-etched (PETE) membranes, 0.1 μm pore-size.
6. Polished silicon wafer.
7. Punching devices: e.g., 0.5 mm biopsy punch or 20-G, Point #9 needle, Vita Needle Company, Needham, MA (*see* **Note 2**).
8. Tygon tubing: TD-100-80, 0.03″ ID × 0.09″ OD (*see* **Note 2**).
9. Tubing connectors: 24-G blunt-end needle hubs, port connectors (24 G stainless steel tubes ~0.4″ length), and port plugs (0.02″ OD stainless steel wire ~0.4″ length) (*see* **Note 2**).
10. Glass syringes: 1 mL, 500 μL (Hamilton, Reno, NV) (*see* **Note 3**).
11. Solvents: acetone, isopropyl alcohol (IPA), 70% ethanol.
12. Programmable spin coater (e.g., model WS-6505, Laurel Technologies Corp., North Wales, PA).
13. Mask aligner for contact lithography (e.g., model Q4000 MA, Neutronix-Quintel, Morgan Hill, CA).
14. Plasma cleaner (e.g., Model PDC-001, Harrick Plasma, Ithaca, NY), with vacuum pump and pure oxygen source.
15. Syringe pump: infusion pump with nanoliter flowrate and at least two syringe capacity (e.g., Model Fusion 200 with optional syringe rack, Chemyx, Stafford, TX).
16. Miscellaneous: Lidded glass container (e.g., 20 mL scintillation vial), hot plates, vacuum desiccator, dissecting microscope, polystyrene cups, glass Petri dishes, pipettes, pointed tweezers, wide flat-tip tweezers, scalpel, lint-free wipes.

2.2 Bacteria, Plasmids, Culture Media, and Buffers

1. *E. coli* strain RP437 [15].
2. Green Fluorescent Protein (GFP) expression plasmid: pCM18 [16].
3. Red Fluorescent Protein (RFP) expression plasmid: pDsRed-Express (Clontech, Palo Alto, CA).
4. Sterile tryptone broth (TB): 10 g/L tryptone, 8 g/L NaCl.
5. Phosphate-buffered saline (PBS): 8.71 g/L NaCl, 2.17 g/L $Na_2HPO_4{\cdot}7H_2O$, 0.26 g/L KH_2PO_4; dissolve in 800 mL H_2O, adjust pH to 7.4, and bring volume up to 1 L.
6. Sterile chemotaxis buffer (CB): 1× PBS, 0.1 mM EDTA, 0.01 mM L-methionine, and 10 mM DL-lactate.
7. Chemoeffector solutions (here, 10 mM L-serine diluted to appropriate concentrations in CB).

2.3 Microscopy and Image Analysis

1. Inverted fluorescence microscope with 10× objective and detector for image acquisition.
2. Image analysis software (e.g., ImageJ, available at https://imagej.nih.gov/ij/).

3 Methods

The microfluidic device described here consists of two layers. The bottom "observation" layer consists of four channels that form the cell chamber, and the top "gradient generator" layer consists of the laminar flow-based mixing network of channels that generate the concentration gradient. When the complete device is fabricated, these two layers are bonded together, with a porous membrane sandwiched in between. The membrane is bonded to the PDMS layers using a method modified from the protocols described in [17, 18]. The microfluidic device design and its overall assembled form is shown in Fig. 1.

3.1 Preparation of the Microfluidic Device Mold

1. Use a CAD file of the device design to obtain the photolithography masks from a high-resolution printer (*see* **Note 1**).
2. Prepare the silicon wafers by rinsing with acetone, followed by isopropanol. Dry the wafers gently using a dry air or nitrogen stream. Place the dried wafers for 15 min on a hot plate set to 65 °C.
3. Pour 1–2 mL of SU-8 2015 onto the silicon wafer. Coat the wafer with SU-8 using a spin coater set to 500 rpm for 10 s then 2250 rpm for 30 s (*see* **Note 4**).
4. Place the spin-coated wafer on the hot plate for "soft bake" at 65 °C, followed by 95 °C for 5 min (*see* **Note 4**).
5. Expose the spin-coated wafer to UV light through the photolithography mask using the mask aligner (*see* **Note 4**).

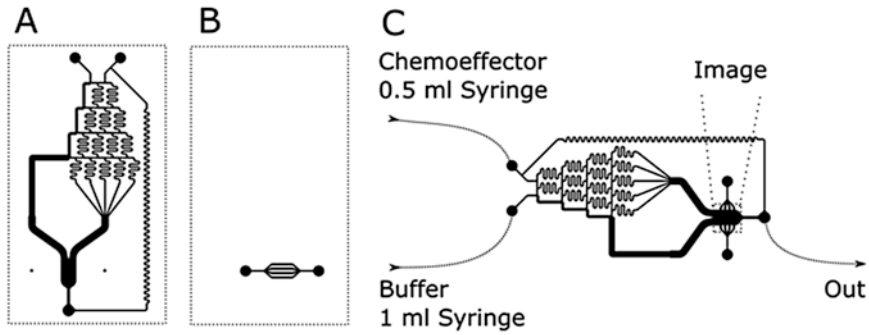

Fig. 1 Static microfluidic chemotaxis device design. (**a**) The top "gradient generator" layer, which produces a logarithmic gradient from two inputs. (**b**) The bottom "observation" layer, which consists of the cell chambers. (**c**) The complete device with the two layers overlaid, showing the appropriate connections

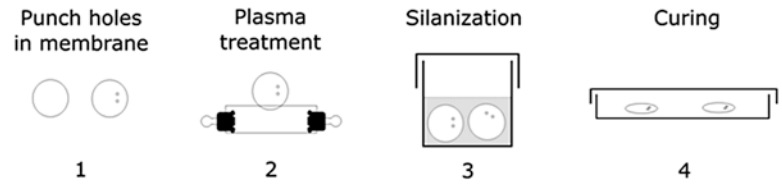

Fig. 2 Preparation of the membrane for bonding. (1) Two holes are punched in the PETE membrane held between protective sheets. (2) The membrane is held upright by sandwiching between two glass slides and exposed to oxygen plasma. (3) The plasma treated membrane is incubated in bis-silyl amine. (4) The silanized membrane is washed with isopropyl alcohol and dried

6. Place the spin-coated wafer on the hot plate for "hard bake" at 65 °C for 1 min followed by 95 °C for 10 min (*see* **Note 4**).
7. Develop the wafer by submerging it in SU-8 Developer. The development time is determined by the thickness of the SU-8 layer. Rinse wafer with isopropanol (*see* **Note 4**).
8. Place developed wafer on a hot plate at 120 °C for 30–60 min. The resulting finished wafer is the "master" mold.

3.2 Preparation of Membranes

The procedure for the preparation of membranes is shown in Fig. 2.

1. Prepare the bonding solution containing 2% Bis-silyl amine and 1% water in IPA in a tightly lidded glass container and heat to 80 °C.
2. Punch holes in the PETE membranes at the appropriate position.
3. Clamp the punched membranes on one side with glass slides held together by binder clips.
4. Treat the membranes with oxygen plasma for 2 min (*see* **Note 5**).
5. Using tweezers, transfer the membranes into the bonding solution, and heat at 80 °C for 20 min.
6. Transfer the membranes to a clean container and rinse thoroughly with IPA.
7. Place the membranes in a clean petri dish and allow to dry and cure at 80 °C for 20 min. If necessary, the membranes may now be stored at RT for bonding at a later time.

3.3 Device Fabrication

The overall scheme for fabricating the device is shown in Fig. 3.

1. Place each master mold in a flat petri dish.
2. Treat the master mold with chlorosilane (*see* **Note 6**).
3. Weigh out the appropriate amount of the silicone elastomer base in a polystyrene cup and add the curing agent in a 10:1

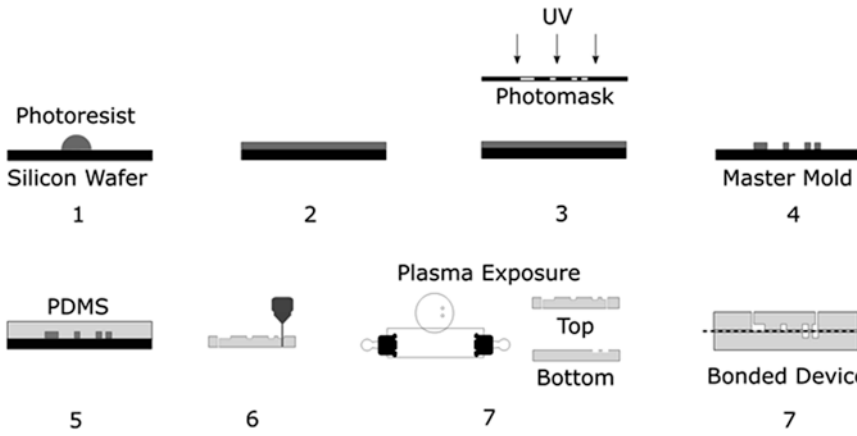

Fig. 3 Overview of steps 1–4 involved in making the device. Photolithography techniques are used to generate the silicon-wafer master molds with the desired pattern of the microfluidic channels. Using the master, PDMS molds containing the channels are prepared, with inlet and outlet holes (steps 5 and 6). The PDMS layers are bonded together with a membrane sandwiched in between (steps 7 and 8)

(base:curing agent) ratio to produce PDMS polymer (*see* **Note 7**). Mix thoroughly and degas the PDMS using a vacuum desiccator for 30–60 min until there are no more air bubbles.

4. Pour the PDMS onto the master molds and cure by incubating on hot plates at 150 °C for 20 min (*see* **Note 8**).
5. Gently, but firmly, cut out and remove the PDMS from the master mold. Cut and separate any multiple device patterns from the block of PDMS.
6. Punch holes at the inlets and outlets in the top PDMS layer using the punching tool.
7. Make sure the patterned surfaces are free of dust and debris (*see* **Note 9**).
8. Treat both PDMS layers as well as the previously treated membranes with oxygen plasma for 45 s (*see* **Note 5**).
9. Place the bottom layer onto a microscope stage and place the membrane on it so that the holes align with the pattern (*see* **Note 10**). Then align and place the top layer. Lightly tap on the top layer to ensure contact and to remove any air bubbles.
10. Complete the bonding by curing at 80 °C for 30 min.
11. Check the devices by eye and under a microscope to confirm proper bonding (*see* **Note 11**).

3.4 Growth and Preparation of Motile E. coli

1. Grow overnight cultures of *E. coli* RP437 in TB medium with the appropriate antibiotic at 32 °C, with shaking at 200 rpm (*see* **Note 12**).

2. Use the overnight culture to start a fresh culture in a 250 mL Erlenmeyer flask containing 20 mL of TB medium supplemented with the appropriate antibiotic (*see* **Note 13**). The starting optical density at 600 nm, OD_{600}, should be approximately 0.05. Grow the culture with shaking at 32 °C.
3. At an OD_{600} of ~0.5, harvest the cells by centrifuging 1–3 mL of culture at 400 × *g* for 10 min. Wash the cells gently with 15 mL of CB and resuspend the pellet in 1–2 mL of CB by gently rotating the tube (*see* **Note 14**).
4. Keep the cells at 32 °C and use within 30 min. For longer storage, keep the cells on ice and then warm before use.

3.5 Microfluidic Chemotaxis Assay

1. Cut the Tygon tubing to appropriate lengths.
2. Connect the tubing to the blunt needle hubs on one end and to the tubing connectors on the other end.
3. Using a pipette, add CB to the needle hubs and make sure there are no air bubbles.
4. Collect 1 mL CB in syringes and remove any air bubbles. Connect the syringes to the needle hubs without trapping any air.
5. Push the syringes until the CB comes out of the far end of the tubing.
6. Insert the tubing connectors into the ports punched in the top layer.
7. Connect the syringes to the syringe pump and run at 2–5 μL/min until all the channels in the device are filled with CB.
8. Fill a 0.5 mL syringe with the desired concentration of chemoeffector. Make sure there are no air bubbles. Connect this syringe to the hub connecting the tubing to the chemoeffector inlet port on the device, without trapping any air bubbles.
9. Gently fill a needle hub and a syringe with the resuspended cells prepared in Subheading 3.4.
10. Without introducing any air bubbles, connect the cell syringe to the needle hub and introduce the cells into the bacterial channel in the bottom layer.
11. Set the device on the microscope stage with the syringes connected to the syringe pump.
12. Run the pump at 10–20 μL/min for 5–10 min to purge the buffer in the tubing and fill with chemoeffector, then set the flow rate to 2 μL/min.
13. Gently push the cell suspension syringe to flush out existing cells from the cell chamber and introduce fresh cells. This also flushes out any existing gradient in the cell chamber and is

marked as time 0. At this point, the cell suspension tubing can be disconnected from the device and the ports can be plugged.

14. Image the cells at time 0 and again after appropriate intervals.

3.6 Data Analysis

1. Visualizing the gradient: The gradient formed in the "static" microfluidic device is shown in Fig. 4. The cell chamber was filled with buffer and the ports were plugged. The buffer and chemoeffector inlets were connected to a syringe containing CB and 200 μM fluorescein, respectively. After the tubing was purged with these solutions, flow was maintained at 2 μL/min and the device was imaged. The membrane allows the gradient, which is formed in the top "gradient generator" layer, to diffuse into the bottom "observation" layer. This gradient in the bottom layer is stable as long as the flow is maintained along the top layer. In this design, the diffusion distance is only 20 μm (the height of the cell chamber). Therefore the gradient generator acts as both source and sink for the cell chamber, and moreover, the gradient in the cell chamber is formed almost immediately. The gradient generator pattern shown in Fig. 1 is designed to produce a nonlinear (logarithmic) gradient, which can be seen in Fig. 4. Note that the fluorescence in the image is a combination of the fluorescence in the gradient generator and the cell chamber.
2. The chemotaxis response of *E. coli* RP437 to a nonlinear gradient of 0–100 μM serine in the device is shown in Fig. 5. Motile *E. coli* cells suspended in CB were introduced into the cell chamber. The chemoeffector inlet was connected to a syringe containing 100 μM serine. Flow was maintained at 2 μL/min,

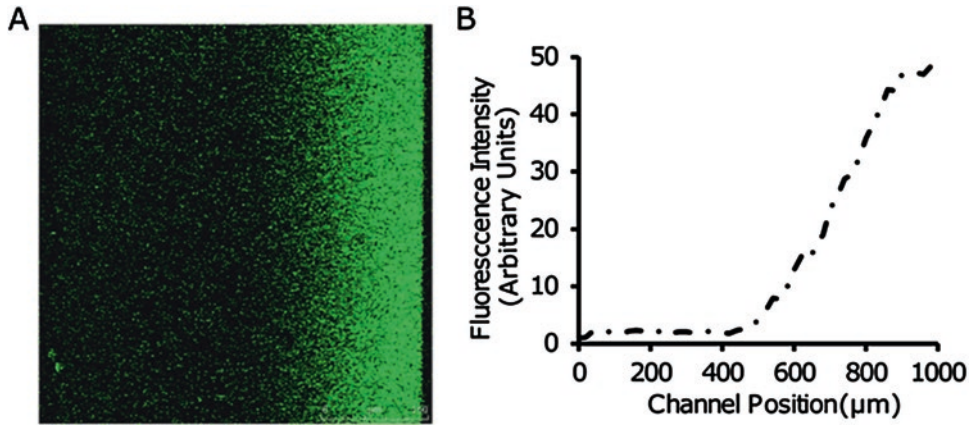

Fig. 4 Characterization of the concentration gradient formed in the device. CB and 200 μM fluorescein were flowed into the device, and the cell chamber region was imaged with an inverted fluorescence microscope. Fluorescence intensity was quantified using ImageJ. The plot of the intensity across the channel shows a logarithmic gradient

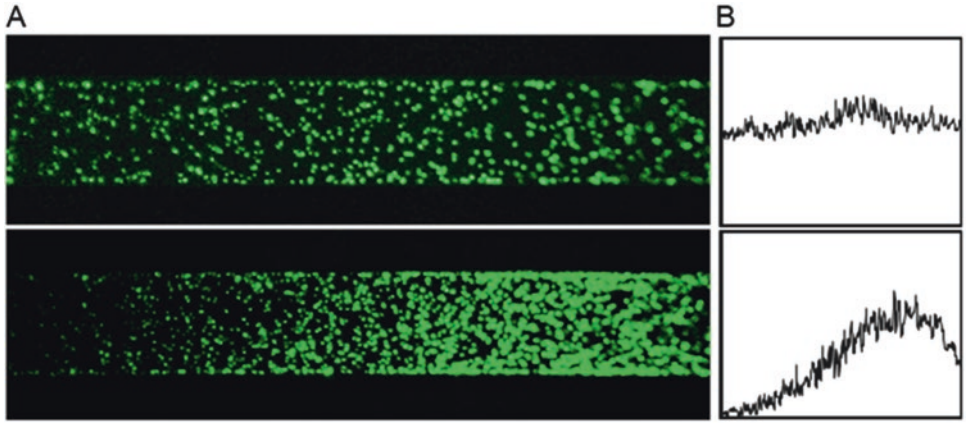

Fig. 5 Images of GFP-labeled *E. coli* RP437 in the microfluidic device. (**a**) Cells were imaged before (top) and after (bottom) exposure to a 0–100 μM L-serine gradient. (**b**) The fluorescence intensity across the channels indicates the change in distribution of cells as they migrate toward higher concentrations of serine

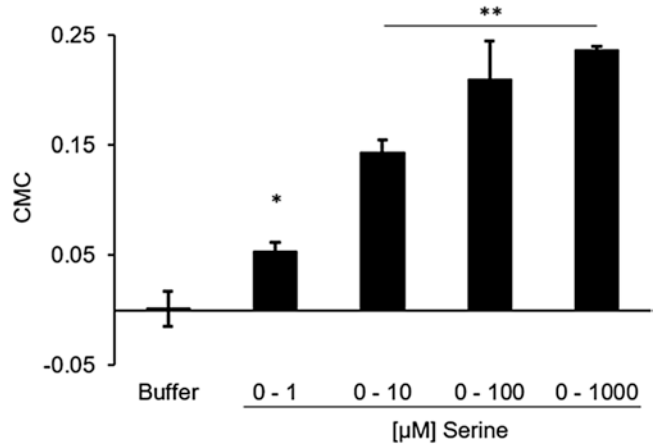

Fig. 6 Quantification of *E. coli* RP437 chemotaxis in the "static" microfluidic device. Cells were exposed to different gradients of serine. The CMC values were calculated by weighing the cells by their position in the channel with respect to the center, where the concentration gradient begins. * and ** indicate statistical significance at $p < 0.005$ and 0.0001 respectively, relative to the buffer control

and the cell chamber was imaged using an inverted fluorescence microscope at time 0 (Fig. 5a, Top) and after 10 min (Fig. 5a, Bottom) while maintaining the setup at 30 °C. The images were analyzed using ImageJ, and a plot of the fluorescence intensity across the channel is seen in Fig. 5b. The chemotaxis migration coefficient (CMC) values for response to different serine concentration gradients, ranging from 0–1 to 0–1000 μM of serine, were calculated as described in [2] and are shown in Fig. 6 (*see* **Note 15**).

4 Notes

1. High-resolution photomasks may be obtained from numerous commercial sources. The photomasks used in this protocol were obtained from CAD/Art services Inc., Brandon, OR (http://www.outputcity.com/index.html).
2. The punching device may be of any appropriate diameter or gauge. The diameter of the punching device used will determine the outer diameter of the port connectors and the port plugs. The inner diameter of the tubing will depend on the outer diameter of the port connectors. The outer diameter of the needle hubs will depend on the inner diameter of the tubing. The use of port connectors is optional, but makes it very convenient to connect the tubing to the device. In the absence of port connectors, the tubing may be direct inserted into the inlet and outlet holes using tweezers, while making sure that the membrane does not get damaged. If port connectors are not used, the outer diameter of the tubing will be determined by the diameter of the punching device.
3. The syringes for delivering the buffer and chemoeffector to the device are selected for the ratio of their inner diameter to obtain constant flow velocity in the device design described here. Any pair of syringes with 2:1 inner diameter ratio for buffer and chemoeffector respectively will work, but the pump rate may need to be adjusted accordingly.
4. The spin speeds and duration, and other parameters such as bake times, exposure time and developing time, are determined by the SU-8 being used and the thickness of the mold. The spin parameters described here will produce an SU-8 2015 mold 20 μm in height, and the bake and exposure parameters are appropriate for this mold thickness. More information on the different SU-8 photoresists and their appropriate use is available at the manufacturer's website (http://www.microchem.com/Prod-SU8_KMPR.html).
5. The plasma treatment used in this protocol was generated at 30 W RF power with an oxygen flow rate to the chamber between 5 and 10 mL/min.
6. The silicon-wafer master mold is made hydrophobic by treatment with a halosilane, so that the cured PDMS can be peeled off from it. The best way to treat the master mold may vary with the silane being used. Place two drops of the chlorosilane described here in a weighing dish. Place this dish along with the master molds in a vacuum desiccator and apply vacuum for 1 h to obtain a thin film of silane over the silicon-wafer master molds.

7. 30–35 g total weight of PDMS (10:1 base to curing agent ratio from Sylgard 184 kit) is sufficient to pour onto a master mold in a standard 100 mm petri dish.
8. The PDMS may be cured by incubating at lower temperatures for longer periods. The appropriate time depends on the thickness of the PDMS.
9. Dirt and debris from the PDMS surface can be removed using sticky tape. Examine the surface with a dissecting microscope to make sure the surface is clean.
10. Handle the membrane using wide, flat-tip tweezers. Upon aligning the membrane with the bottom layer, use a protective disc (from the membrane packaging) to gently push down and place the membrane, then lightly tap to remove any bubbles.
11. The presence of membrane wrinkles, or debris, between the layers of the device within the patterned area will result in pockets where fluid may accumulate. This will disrupt the flow and hence the concentration gradient in the device. Avoid using any devices that have such problems evident under a microscope. Careful placement of the membrane, and a clean dust-free environment, will ensure good devices.
12. The growth media and temperature are important for obtaining highly motile *E. coli*. Growth at higher temperature and in richer media will produce poorly motile cells. Other media and temperature may be appropriate for other bacterial strains.
13. For the binding protein components of certain chemoreceptors to be fully expressed, it may be necessary to grow the bacteria in the presence of the inducing chemoeffector, such as galactose, ribose, or maltose. In this case add 0.1% w/v of the sugar to the medium.
14. The cells must be handled very gently when washing and resuspending to avoid breaking the flagella and reducing motility. Avoid vigorous or excessive shaking. A tube rotator is recommended for convenient and gentle resuspension.
15. The trend and range of response measured with this device is similar to that observed with nonlinear serine gradients in the previously described microfluidic flow device. However, the CMC values calculated in this device cannot be directly compared to those calculated from the previously described microfluidic flow device due to the different initial distribution of cells in the observation channel in the current device. Whereas the cells are distributed in a narrow region in the center of the channel (and therefore the gradient) in the previous flow device, they are distributed all throughout the channel (and the gradient) in this device.

Acknowledgment

The authors would like to acknowledge partial support from the Ray B. Nesbitt Endowed Chair.

References

1. Wadhams GH, Armitage JP (2004) Making sense of it all: bacterial chemotaxis. Nat Rev Mol Cell Biol 5:1024–1037
2. Englert DL, Jayaraman A, Manson MD (2009) Microfluidic techniques for the analysis of bacterial chemotaxis. Methods Mol Biol 571: 1–23
3. Adler J (1973) A method for measuring chemotaxis and use of the method to determine optimum conditions for chemotaxis by *Escherichia coli*. J Gen Microbiol 74:77–91
4. Grimm AC, Harwood CS (1997) Chemotaxis of *Pseudomonas* spp. to the polyaromatic hydrocarbon naphthalene. Appl Environ Microbiol 63:4111–4115
5. HS Y, Alam M (1997) An agarose-in-plug bridge method to study chemotaxis in the Archaeon *Halobacterium salinarum*. FEMS Microbiol Lett 156:265–269
6. Ahmed T, Shimizu TS, Stocker R (2010) Microfluidics for bacterial chemotaxis. Integr Biol (Camb) 2:604–629
7. Mao H, Cremer PS, Manson MD (2003) A sensitive, versatile microfluidic assay for bacterial chemotaxis. Proc Natl Acad Sci U S A 100:5449–5454
8. Jeon NL, Dertinger SKW, Chiu DT, Choi IS, Stroock AD et al (2000) Generation of solution and surface gradients using microfluidic systems. Langmuir 16:8311–8316
9. Pasupuleti S, Sule N, Cohn WB, Mackenzie DS, Jayaraman A et al (2014) Chemotaxis of *Escherichia coli* to norepinephrine (NE) requires conversion of NE to 3,4-dihydroxymandelic acid. J Bacteriol 196:3992–4000
10. Englert DL, Manson MD, Jayaraman A (2009) Flow-based microfluidic device for quantifying bacterial chemotaxis in stable, competing gradients. Appl Environ Microbiol 75: 4557–4564
11. Wolfram CJ, Rubloff GW, Luo X (2016) Perspectives in flow-based microfluidic gradient generators for characterizing bacterial chemotaxis. Biomicrofluidics 10(6):061301
12. Diao J, Young L, Kim S, Fogarty EA, Heilman SM et al (2006) A three-channel microfluidic device for generating static linear gradients and its application to the quantitative analysis of bacterial chemotaxis. Lab Chip 6:381–388
13. Cheng S-Y, Heilman S, Wasserman M, Archer S, Shuler ML et al (2007) A hydrogel-based microfluidic device for the studies of directed cell migration. Lab Chip 7:763–769
14. Ahmed T, Shimizu TS, Stocker R (2010) Bacterial chemotaxis in linear and nonlinear steady microfluidic gradients. Nano Lett 10: 3379–3385
15. Parkinson JS, Houts SE (1982) Isolation and behavior of *Escherichia coli* deletion mutants lacking chemotaxis functions. J Bacteriol 151: 106–113
16. Hansen MC, Palmer RJ Jr, Udsen C, White DC, Molin S (2001) Assessment of GFP fluorescence in cells of *Streptococcus gordonii* under conditions of low pH and low oxygen concentration. Microbiology 147:1383–1391
17. Aran K, Sasso LA, Kamdar N et al (2010) Irreversible, direct bonding of nanoporous polymer membranes to PDMS or glass microdevices. Lab Chip 10:548–552
18. Sip CG, Folch A (2014) Stable chemical bonding of porous membranes and poly(dimethylsiloxane) devices for long-term cell culture. Biomicrofluidics 8(3):036504

Chapter 6

Visualizing Chemoattraction of Planktonic Cells to a Biofilm

Sneha Jani

Abstract

Bacterial chemotaxis in response to continuous chemical gradients has been extensively studied at the individual cell and population levels using a variety of well-established in vitro methods (Englert et al., Microfluidic techniques for the analysis of bacterial chemotaxis. Methods Mol Biol 571:1–23, 2009). In nature, bacteria are surrounded by heterogeneous chemical gradients; hence, it is essential to understand chemotaxis behavior under such conditions. Here, we describe a setup that allows visualization of the chemotaxis response of motile cells to the complex microenvironment of a biofilm maintained under static conditions. The biofilm is separated from the motile cells by a semi-permeable membrane. Cells swimming toward the biofilm are captured on the membrane and imaged using confocal laser scanning microscopy (CLSM). Chemotaxis toward specific molecules produced by the biofilm, such as autoinducer-2 (AI-2), can be studied using this setup. This system can be adapted to study chemotaxis toward poly-species biofilms, or even mammalian cells.

Key words Biofilm, Chemotaxis, Polycarbonate membrane, Insert-in-well, Autoinducer-2, Confocal laser scanning microscopy

1 Introduction

Bacteria rarely exist as individual cells in natural environments. They form complex communities called biofilms that are attached to surfaces encased in an extracellular matrix composed of polysaccharides, proteins, and nucleic acids. Biofilms are more tolerant to harsh environmental conditions, including dehydration and exposure to antimicrobial agents, than are individual planktonic cells. Furthermore, biofilms are more efficient at nutrient trapping, permit cross-feeding between species, and they allow cells to communicate with each other to regulate gene expression. It is, therefore, beneficial for bacteria to be part of a biofilm [1–4]. The microenvironment surrounding a biofilm is rich in molecules that can be sensed by free swimming bacteria, including bacterially generated signals such as autoinducer-2 (AI-2). In this chapter, a method is

Michael D. Manson (ed.), *Bacterial Chemosensing: Methods and Protocols*, Methods in Molecular Biology, vol. 1729, https://doi.org/10.1007/978-1-4939-7577-8_6,

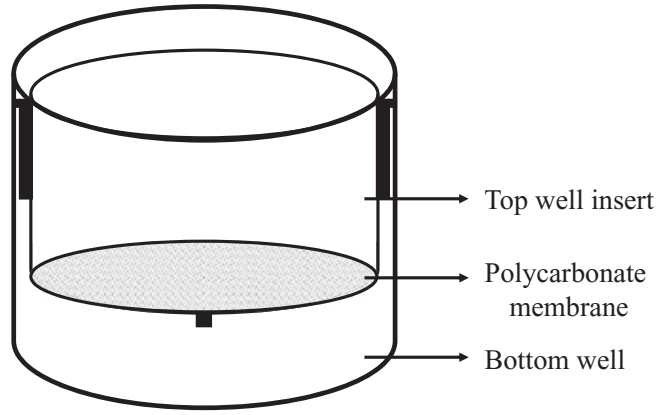

Fig. 1 Insert-in-well assembly. The top well insert with a polycarbonate membrane base is placed in a larger bottom well. The membrane and the bottom well are separated by a minimum distance of 0.9 mm

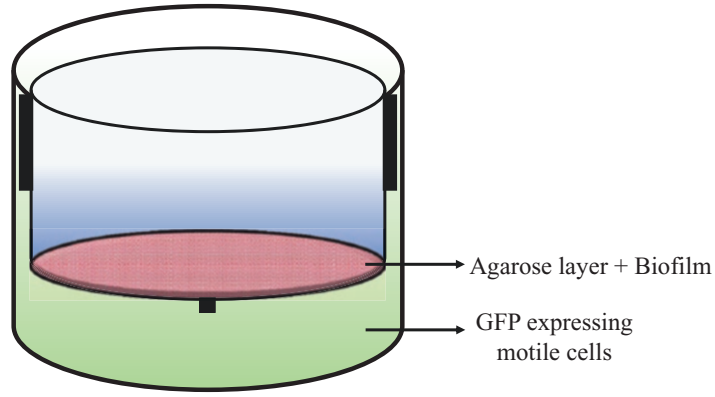

Fig. 2 Growth of biofilm and introduction of motile cells in the insert-in-well assembly. The RFP-expressing strain (red dots) is introduced into the insert and allowed to grow into a mature biofilm. The GFP-expressing motile cells are introduced into the bottom well at the appropriate time point, and the cells are allowed to respond to the molecules in the extracellular medium of the biofilm

described that was developed to study chemoattraction to the complex microenvironment of a biofilm.

The experimental setup, termed insert-in-well, consists of a cylindrical top well insert with a semi-permeable polycarbonate membrane base placed in a larger polystyrene bottom well (Fig. 1). The biofilm is first grown inside the insert under static conditions on top of a layer of agarose. At the appropriate time, the motile cells are introduced in the bottom well (Fig. 2). This results in the formation of gradients of several molecules from the biofilm into the bottom well. Motile cells respond to the gradients, and the cells that swim toward the biofilm get captured on the poly-L-lysine

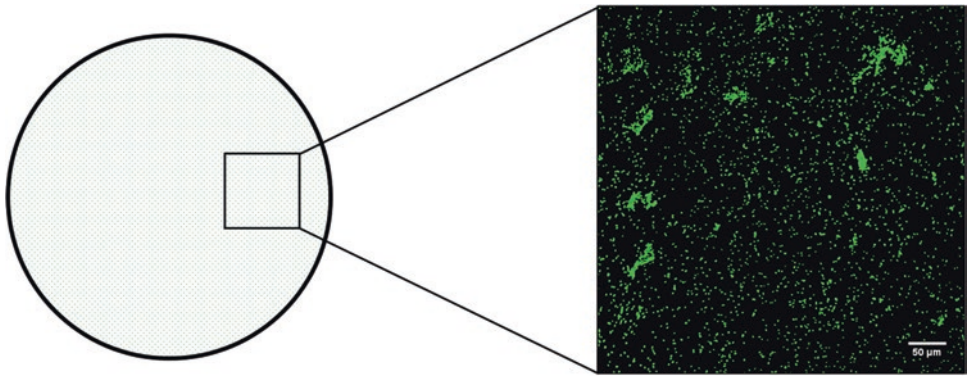

Fig. 3 Imaging the captured motile cells using CLSM. The GFP-expressing motile cells attached to the polycarbonate membrane of the insert in response to the biofilm microenvironment are imaged using an inverted confocal microscope. The independent images are acquired by moving to different locations on the membrane in a grid-like manner

coated membrane. At the end of the incubation period, the insert is removed from the well and the membrane is rinsed. Cells captured on the membrane are imaged using an inverted confocal laser scanning microscope by sampling several independent regions of the membrane (Fig. 3). The sum of pixel intensities for a defined number of images for each membrane is counted using ImageJ to determine the difference in membrane attachment between test and control samples and the relative data is plotted in the form of a histogram (Fig. 4).

2 Materials

2.1 Strains

1. *E. coli* MG1655 containing RFP expressing plasmid pDsRed-Express (Takara Bio USA, Inc., Catalog # 632412).
2. *E. coli* RP437 [5] containing GFP expressing plasmid pCM18 [6].

2.2 Media, Buffers, and Chemicals

1. LB medium is used for growing cells to saturation. Add 10 g tryptone, 5 g yeast extract, and 10 g NaCl to 1 L ultrapure water. Adjust pH to 7.0 with NaOH. Autoclave to sterilize. Add 1.5% agar for LB agar plates. Store the medium indefinitely at room temperature and plate at 4 °C.
2. Tryptone broth (TB) is used for growing highly motile cells. Add 10 g tryptone and 8 g sodium chloride to 1 L ultrapure water. Autoclave to sterilize. Store indefinitely at room temperature.
3. ABTCAA medium is used for growing biofilms. Dissolve 2 g $(NH_4)_2SO_4$, 6 g Na_2HPO_4, 3 g KH_2PO_4, 3 g NaCl, 2.5 g thiamine hydrochloride, and 5 g casamino acids (vitamin free) in 200 mL ultrapure water to make solution A. Dissolve 0.01 g

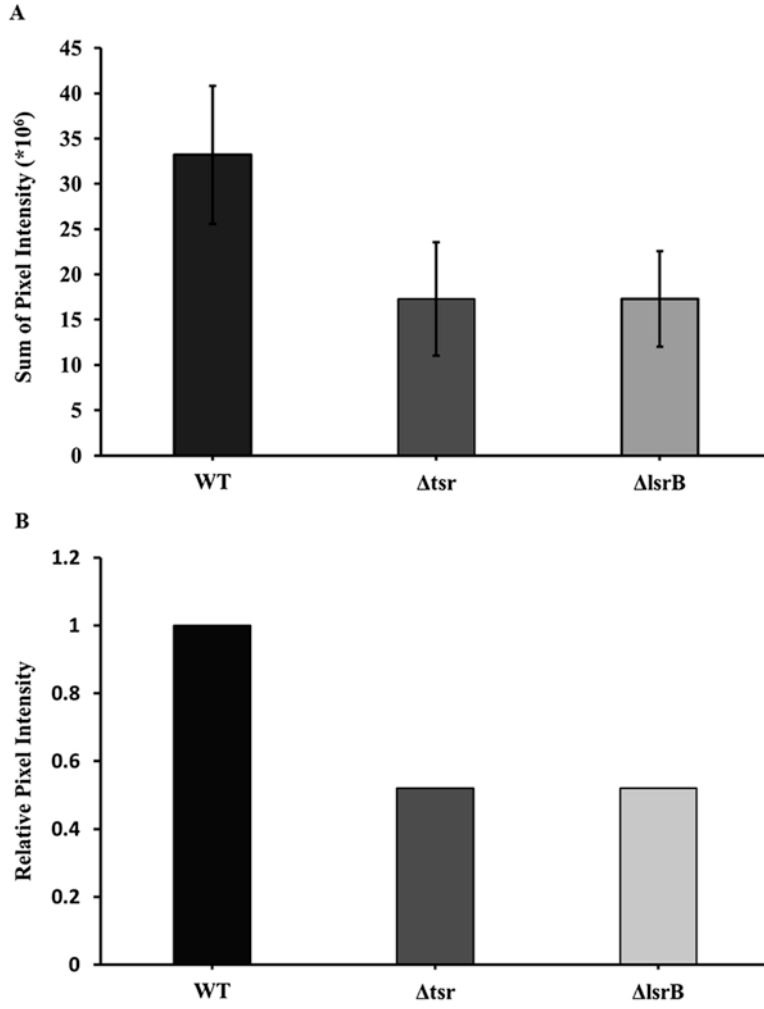

Fig. 4 Histograms depicting pixel intensity data obtained from ImageJ. The RFP-expressing *E.coli* MG1655 strain was grown for 24 h to form an AI-2 producing biofilm. The chemoreceptor Tsr and binding protein LsrB are required for chemotaxis toward AI-2. GFP-expressing motile WT (*E. coli* RP437) and isogenic Δ*tsr* and Δ*lsrB* mutant strains were introduced into independent wells and imaged. The sum of pixel intensities on the membranes for all strains was obtained using ImageJ. The data is plotted as histograms. (**a**) Raw data showing the sum of pixel intensities for each strain. The error bars represent standard error of the mean from three independent experiments. (**b**) WT normalized data depicting the pixel intensities relative to WT

$CaCl_2$, 0.2 g $MgCl_3$, and 0.0005 g $FeCl_3$ in 800 mL ultrapure water to make solution B. Mix solutions A and B and adjust the pH to 7.5 with 5 M KOH. Sterilize using a 0.22 μm pore size vacuum filter. Store the medium indefinitely at room temperature.

4. Phosphate-buffered saline (PBS). Dissolve 8 g NaCl, 0.2 g mM KCl, 1.44 g Na_2HPO_4, 0.24 g KH_2PO_4 in 1 L ultrapure water.

Adjust pH to 7.4 with HCl. Autoclave to sterilize. Store indefinitely at room temperature.

5. Poly-L-lysine hydrobromide (PLL) stock. Dissolve 5 mg of PLL (Sigma-Aldrich, Catalog # P6282) in 50 mL in ultrapure water. Store the sterile solution indefinitely at −20 °C.
6. Ampicillin stock solution. Dissolve 100 mg of ampicillin in 1 mL in ultrapure water. Store the sterile solution at −20 °C for up to 3 months.
7. Erythromycin stock solution. Dissolve 30 mg of erythromycin in 1 mL 200 proof ethanol. Store the sterile solution at 4 °C for up to 6 months.
8. Agarose, low-gelling temperature (Sigma-Aldrich, Catalog # A9414). 2.5% agarose in ABTCAA medium.

2.3 Insert-in-Well

1. Polycarbonate membrane inserts with carrier plate system (ThermoFisher Scientific, Catalog # 141078) (*see* **Note 1**).

2.4 Microscopy and Image Analysis

1. Leica TCS SP5 Resonant Scanner Confocal or equivalent fluorescent microscope.
2. ImageJ [7].

2.5 Miscellaneous

1. Tweezers.
2. Erlenmeyer flasks (for growing cells).
3. Tissue wipes.
4. 24 × 50 mm cover slips.
5. Digital dry bath.

3 Methods

Preparation of the inserts is carried out at room temperature in a biosafety cabinet (*see* **Note 2**).

3.1 Coating Insert Membrane

1. The polycarbonate membrane at the base of the insert is coated with PLL on the side facing the bottom well. This enhances attachment of motile cells to the membrane.
2. Open the inserts carrier system and carefully remove the inserts from the well using tweezers. Invert the inserts and place them on a clean bench.
3. Place 400 μL of PLL on the membrane. Allow it to cover the membrane surface for 30 min. Gently aspirate PLL from the edge of the membrane (*see* **Note 3**).
4. Place 400 μL of PBS on the membrane. Gently aspirate PBS and allow the membranes to air-dry for 30 min. When dry, place the inserts back in the carrier plate system at medium position (*see* **Note 4**).

3.2 Introduction of Agarose Layer

1. A layer of low-gelling agarose is introduced inside the insert 1 h before introducing the biofilm forming strain into the insert. It increases the barrier present between the biofilm and motile cells and also slows down the diffusion of molecules secreted by the biofilm into the bottom well.
2. Set the digital dry bath for heating microcentrifuge tubes to 75 °C. Weigh 15 mg of low-gelling agarose and add ABTCAA to 1 mL.
3. Resuspend well and incubate the tubes at 75 °C for 20 min (*see* **Note 5**).
4. Vortex the tube vigorously and add 250 μL of agarose into the insert to form a uniform layer over the membrane.
5. Allow the agarose to dry at room temperature for 30 min or at 4 °C for 15 min (*see* **Note 6**).

3.3 Growth of Biofilm Inside Insert

E.coli MG1655 forms robust biofilms in ABTCAA medium under static conditions [8]. The cells are first grown to saturation in rich LB medium, and then transferred to ABTCAA medium to induce biofilm formation. Growth and incubation conditions will have to be optimized based on the strain used.

1. Streak *E. coli* MG1655/pDsRed-Express on a LB agar plate containing 150 μg/mL ampicillin. Incubate the plate at 37 °C for 16 h.
2. Inoculate a single colony into 3 mL LB containing 150 μg/mL ampicillin in a 14 mL culture tube. Incubate for 16 h at 37 °C at 250 rpm.
3. Dilute the overnight culture to $O.D._{600nm} = 0.05$ in an ABTCAA medium.
4. Gently introduce 1 mL of the diluted culture into the insert, taking care not to accidentally stab the agarose layer or membrane. Place the carrier system in a sterilized zipper top plastic bag and incubate for 24 h at 37 °C in a well-humidified chamber (*see* **Note 7**).

3.4 Growth of Highly Motile Cells

1. Streak *E.coli* RP437/pCM18 (WT) and isogenic Δ*tsr* and Δ*lsrB* mutant strains on a LB agar plate containing 100 μg/mL erythromycin. Incubate the plate at 37 °C for 16 h.
2. Inoculate a single colony into 20 mL TB containing 100 μg/mL erythromycin in a 250 mL Erlenmeyer flask. Incubate with shaking at 30 °C at 250 rpm for 16 h.
3. Dilute the overnight culture to $O.D._{600nm} = 0.05$ in 20 mL TB in a 250 mL Erlenmeyer flask.
4. Incubate at 30 °C with shaking at 250 rpm until the cells reach mid-exponential phase ($O.D._{600nm} = 0.5$, *see* **Note 8**).

5. Spin 3 mL of the culture at 400 × *g* for 10 min.
6. Gently remove the supernatant and resuspend the cells in ABTCAA to $O.D._{600nm}$ = 0.05–0.1 (*see* **Note 9**).

3.5 Incubation of Motile Cells with Biofilm

1. Introduce 1.5 mL of the resuspended motile cells into the bottom well. Once all the wells have been filled, incubate the carrier system at 30 °C for 10 min (*see* **Note 10**).
2. Gently remove one insert at a time from the well using tweezers at the end of the incubation period.
3. Rinse the exposed membrane by dipping it in a petri dish containing PBS. Perform two rinses, using fresh PBS each time.
4. Tilt the insert slightly and blot excess liquid from the membrane by placing a tissue wipe along the wall of the insert.
5. Allow the membrane to dry for 15 min at room temperature (*see* **Note 11**).

3.6 Imaging Using CLSM

1. Place the insert on a 24 × 50 mm coverslip (*see* **Note 12**).
2. Place the coverslip on the microscope stage and image the membrane using the 10× objective. Use the bright field light to focus on the membrane. The pores of the membrane should be visible.
3. Use the Argon 488 nm laser to image the fluorescent GFP expressing bacteria captured on the membrane. Take 15–18 independent images covering the entire surface of the membrane.
4. Use ImageJ to obtain the Integrated Density of each image for each strain. It can be used to compare the response of different strains to a biofilm, or compare the response of one strain to biofilms grown under different conditions.
5. Set the measurements for analysis in ImageJ. Analyze→Set Measurements→ check Integrated density, then click OK.
6. Import the sequence of images to be analyzed by clicking on File→Import→Image Sequence. The Sequence Options dialog box opens up once you click on the first image in the sequence (*see* **Note 13**).
7. Determine the sum of pixel intensities (RawIntDen) for each image in the sequence. Analyze→Measure or Ctrl+M. The raw integrated density (RawIntDen) values appear in a separate Results dialog box. RawIntDen is the sum of the values of the pixels in the images.
8. Copy the data from the Results dialog box to Microsoft Excel. Add the RawIntDen values of all the images in the sequence to determine the sum of pixel intensities for the sequence of images.

9. The pixel intensities for all strains can be plotted as histograms or as relative pixel intensities normalized to WT (Fig. 4a, b, respectively). This allows comparison between the attraction of different strains to the biofilm.

4 Notes

1. The polycarbonate membrane has a pore diameter of 0.4 μm, which is small enough to prevent the motile cells from the bottom well entering the insert. Larger pore sizes are available and can be used if the assay needs to be modified.
2. Preparation of the inserts should preferably be done inside a biosafety cabinet to minimize contamination. If this is not possible, all the steps must be performed on a clean bench under sterile conditions. We recommend sterilizing the inserts by exposing to UV light for 20 min if any of the steps are carried out under non-sterile conditions.
3. PLL must be removed carefully by placing the pipette tip at a 45° angle at the edge of the base. Care must be taken to avoid touching the membrane with the pipette tip. Aspiration can be done using a micropipette or a vacuum aspirator.
4. The inserts can be placed at three different positions on the carrier system (low: 0.9 mm, medium: 3.3 mm, high: 6.3 mm). The position defines the distance between the membrane and the bottom of the well and can be optimized for the bacterial strain being used.
5. Agarose appears clear when it has melted completely. If the particles are visible after 20 min, continue heating until the particles dissolve.
6. The agarose solidifies quickly, and it is convenient to add it to two wells at a time and then place the tube back in the 75 °C dry bath to allow the agarose to reach the right temperature before using it again.
7. The lid of the carrier system sits loosely on the top of the plate, which leads to rapid evaporation along the edges. Placing the carrier system in a plastic bag reduces evaporation. If a humidified chamber is not available, a petri dish containing sterile water can be placed inside the plastic bag. Biofilm growth conditions for other strains can be optimized in a 24 well tissue culture plate.
8. *E. coli* RP437 is highly motile during mid-exponential phase, which is why we recommend using cells during this phase. The time point at which the motile cells are ready should coincide with the time point at which chemotaxis toward the biofilm is to be determined.

9. The resuspension density should be optimized for the strain used. A lower density of cells is preferred, as it prevents interference from random attachment on the membrane due to crowding.
10. Do not disturb the setup during the incubation period, as this disrupts the gradient.
11. The tissue wipe can be folded into a square, and one corner can be used to touch the polystyrene edge to remove excess liquid. Avoid touching the membrane.
12. The base of the insert has stubs that prevent the membrane from touching the glass. If the membrane is still wet, liquid from the membrane will contact the coverslip and interfere with imaging attached cells. The coverslip can be checked at this point to determine if it is wet. Allow it to dry for longer if this is the case.
13. If you have a mixed set of files and only want to include a particular set, enter the common part in "file name contains" and click OK.

References

1. Costerton JW (1995) Overview of microbial biofilms. J Ind Microbiol 15:137–140
2. Donlan RM (2002) Biofilms: microbial life on surfaces. Emerg Infect Dis 8:881–890
3. Davey ME, O'Toole GA (2000) Microbial biofilms: from ecology to molecular genetics. Microbiol Mol Biol Rev 64:847–867
4. Hall-Stoodley L, Costerton JW, Stoodley P (2004) Bacterial biofilms: from the natural environment to infectious diseases. Nat Rev Microbiol 2:95–108
5. Parkinson JS, Houts SE (1982) Isolation and behavior of *Escherichia coli* deletion mutants lacking chemotaxis functions. J Bacteriol 151:106–113
6. Hansen MC, Palmer RJ Jr, Udsen C, White DC, Molin S (2001) Assessment of GFP fluorescence in cells of *Streptococcus gordonii* under conditions of low pH and low oxygen concentration. Microbiology 147(Pt 5): 1383–1391
7. Schneider CA, Rasband WS, Eliceiri KW (2012) NIH image to imageJ: 25 years of image analysis. Nat Methods 9:671–675
8. Reisner A, Krogfelt KA, Klein BM, Zechner EL, Molin S (2006) In vitro biofilm formation of commensal and pathogenic *Escherichia coli* strains: impact of environmental and genetic factors. J Bacteriol 188: 3572–3581

Chapter 7

Labeling Bacterial Flagella with Fluorescent Dyes

Linda Turner and Howard C. Berg

Abstract

We describe labeling of bacteria with amino-specific or sulfhydryl-specific Alexa Fluor dyes, methods that allow visualization of flagellar filaments, even in swimming cells. Bacterial flagellar filaments are long (~10 μm), but of small diameter (~20 nm), and their rotation rates are high (>100 Hz), so visualization is difficult. Dark-field microscopy works well with isolated filaments, but visualization in situ is hampered by light scattered from cell bodies, which obscures short filaments or the proximal ends of long filaments. Differential interference contrast microscopy also works, but is technically difficult and suffers from a narrow depth of field and low image contrast; background subtraction and contrast enhancement are necessary. If filaments are fluorescent, they can be imaged in their entirety using standard fluorescence microscopes. For imaging in vivo, blurring can be prevented by strobing the light source or by using a camera with a fast shutter. The former method is preferred, since it minimizes bleaching.

Key words Bacteria, Flagellar staining, Motility

1 Introduction

A description of flagella and their role in bacterial behavior, together with a brief history of their study, is given in the introduction to our paper on real-time imaging of fluorescent flagellar filaments [1]. The labeling there was done with amino-specific Alexa Fluor carboxylic acid succinimidyl esters, from Molecular Probes, which required the use of sodium bicarbonate to raise the pH of the motility buffer, normally 7.0–7.8. For *Escherichia coli*, both cell bodies and filaments were labeled, the filaments more brightly, which was convenient, because one could see what both cells and filaments were doing. Our more recent work has been done with sulfhydryl-specific Alexa Fluor maleimide dyes, also from Molecular Probes, which work at pH 7. These dyes require that the flagellin outer-domain contain an accessible sulfhydryl group, which was accomplished by generating *fliC* cysteine substitutions, e.g., S353C or S219C. In either case, only flagellar filaments were labeled.

We have used amino-specific dyes with *E. coli* to visualize polymorphic transformations of filaments in swimming cells [1, 2] and

Michael D. Manson (ed.), *Bacterial Chemosensing: Methods and Protocols*, Methods in Molecular Biology, vol. 1729, https://doi.org/10.1007/978-1-4939-7577-8_7,

to visualize flagellar filaments manipulated by optical traps [3, 4]. We have used sulfhydryl-specific dyes to visualize flagella in swarms [5] and in tracked bacteria [6], and to study flagellar growth [7]—one can label filaments with a dye of one color, e.g., green, then grow the cells for a few more hours and label the filaments again with a dye of a different color, e.g., red, and obtain filaments that are green at their proximal ends and red at their distal ends. Amino-specific dyes have been used with other bacteria, for example, *Serratia marcescens* [8] and *Rhizobium lupini* [9]. Sulfhydryl-specific dyes also have been used with *Bacillus subtilis* [6, 10].

2 Materials

Materials are all standard but bacteria specific.

1. The motility buffer used to wash cells from growth medium should be free of amines or sulfhydryl groups.
2. Dyes from Molecular Probes are available from ThermoFisher Scientific, Waltham, MA. For labeling, 1 mg of dye is dissolved in 200 μL dimethylsulfoxide and kept frozen at −20 °C until use.

3 Methods

3.1 Washing Cells

1. This is the most critical step, because bacterial flagellar filaments break when dense cell suspensions are subjected to viscous shear. We wash cells free of growth medium and labeled cells free of excess dye by centrifugation in 15-mL round-bottom Corex tubes for 10 min at 1200 × *g*, followed by gentle resuspension of the pellet and addition of 10 mL of motility buffer. After centrifugation, the supernatant solution is poured out gently and time is given for the dregs to flow down the sides of the tube and reach the pellet. Then the tube is rocked slowly back and forth until the pellet is suspended, and finally the motility buffer is added (*see* **Note 1**).
2. Centrifugation is time-consuming. If a shorter handling-time is essential, the cells can be washed free of external medium by filtration [11]. Here, the washing takes place in less than 10 min. A filter flask equipped with a ground-glass support designed for 47 mm-diameter filters supports a Millipore HATF filter, pore size 0.45 μm (both from Millipore Corp.). A specially designed Delrin funnel with a flat base is placed a top the filter, 5 mL of log-phase motile cells are added, and suction is applied. Extreme care is taken to avoid pulling air through the filter—a small amount of fluid must remain to protect the cells from damage and filaments from breakage. To exchange the cell medium 4×, volumes as large as ~25 mL are pulled

through the filtering system. Then the funnel is removed and the filter is rolled up with a pair of tweezers and placed within the mouth of a centrifuge or culture tube. Motility medium is used to rinse the cells from the filter into the tube. The final volume for rinsing the cells from the filter need not be as large as the 7.5 mL used in [11]; 1 mL will suffice, but the cells are lost and the recovery is not as great as that obtained with the centrifugation method.

3.2 Labeling Cells

1. Grow cells to log-phase in 10 mL of growth medium and check the motility with a phase-contrast microscope.
2. Wash half of the culture into motility buffer by centrifugation or filtering, as described above. If centrifuging, repeat the washing procedure three more times to ensure that all growth medium is removed.
3. Compare the motility of the washed cells in buffer to that of the unwashed cells remaining in the culture flask (*see* **Note 2**).
4. Resuspend the final pellet in ~500 μL motility buffer.
5. For labeling *E. coli* genetically modified to contain a cysteine in flagellin and using the maleimide dyes, the labeling time can be as short as 15 min and the amount of dye as small as 4 μL per 500 μL of cells (*see* **Note 3**).
6. For labeling with the amino-specific Alexa Fluor carboxylic acid succinimidyl esters from Molecular Probes, add 25 μL of 1 M sodium bicarbonate per 500 μL of cell suspension to raise the pH to ≥7.8. Next add ~10 μL of dye per 500 μL of cells, and stir with gentle gyration on a shaker (100 rpm) for 45 min (*see* **Note 4**).
7. If using sulfhydryl-specific reactive Alexa Fluor fluorescent maleimide dyes add 10 μL of dye per 500 μL of cell suspension in motility buffer and stir with gentle gyration on a shaker (100 rpm) for 45 min.
8. Add 5–10 mL of motility buffer. Compare the motility of the labeled cells to the motility of the unused cells remaining in the culture flask by phase contrast microscopy (*see* **Note 5**).
9. Wash out the excess dye in the same manner used earlier to remove the growth medium and suspend the cells in motility buffer. The amount of background fluorescence remaining can be monitored in the fluorescence microscope (*see* **Note 6**).
10. If you can see fluorescent filaments but motility is lost, add growth medium to your buffer (1:1) and wait 5 min. If the cells were simply de-energized, motility will recover quickly, and you will see flagellar bundles form behind swimming cells.
11. If you see no flagella and no motility, then you do not know if you have broken off the flagella or simply interfered with motility. Add growth medium, as above. Give the cells 5 min

to recovery motility. This time window is long enough for recovery but short enough to avoid synthesis of new flagella (*see* **Note 7**).

3.3 Fluorescence Microscopy

1. The best way to visualize flagella is to use dilute cells in a thin preparation with a relatively small region of intense laser illumination through which the cells can swim at random, together with an oil-immersion objective of high numerical aperture [1]. The observer can test the effect of light by increasing the intensity of the illumination spot until the cells die and accumulate within it. From this point, decrease the intensity and go to a new region and observe the effect on the cells (*see* **Note 8**).
2. Fluorescent bleaching is a concern. If the desired viewing time is long, and the excitation light is bright, as with laser illumination, then strobing the beam is recommended (*see* **Note 9**).
3. A number of video clips of bacteria with fluorescent flagellar filaments are available on our web site (*see* **Note 10**).

4 Notes

1. If a small amount of mild detergent is added to the latter, say 0.0001% Tween-20, labeled filaments are less likely to stick to the walls of the centrifuge tube. Usually, the cells are washed four times. If one tries to speed up the process by flicking the bottom of a centrifuge tube containing a pellet with one's finger, or using a pipet to withdraw and expel the pellet, motility is notably degraded. After labeling, the effectiveness of washing can be monitored by fluorescent microscopy: the background needs to be dark, void of any dye.
2. The motility should be similar. If not, do not proceed until you figure out why cells are losing motility.
3. The amount of time and the amount of dye used for labeling can vary. Procedures should be optimized for the cell type under study.
4. For the amino-specific carboxylic acid succinimidyl esters in an aqueous medium at alkaline pH, there is a competing reaction of hydrolysis that destroys the dyes reactivity toward primary amines. We found that there was no advantage of increasing the labeling times for these dyes beyond 45 min and that times as short as 20 min proved effective for labeling.
5. At this point continue even if the motility of the labeled cells is diminished. The idea is to see whether the filaments have been labeled. The procedure can be modified later to optimize the motility of labeled cells.

6. It is important that the medium is dark in order to provide good contrast.
7. If you do not know whether flagella are there, you can check with conventional flagellar stains, *e.g.*, [12].
8. For *E. coli*, the photodynamic effect is evident in the behavior of the cells. At the highest intensity, the cells quickly die; at slightly lower intensity, the cells tumble and remain within the beam, then die and accumulate there; at even lower intensity the cells swim into the beam, immediately tumble, alter their trajectory, and leave the beam; and at even lower intensity, the correct intensity for recording cell behavior, the cells swim through the illumination spot with flagella bright enough to be seen. If a video recorder is used, many useful images will be obtained. However, if the cells stay in this region for any length of time, their filaments will bleach. Since the preparation is thin, most cells will swim with their flagellar bundles roughly normal to the microscope's optical axis, and thus optimally oriented for viewing. If motility is not important, motors can be stopped with 0.25% glutaraldehyde and filaments can be viewed at leisure, using a mercury arc [3]. If microscope slides have been treated with poly-L-lysine (0.01%), the glutaraldehyde will crosslink the filaments to the substratum.
9. In our early work, we used a slotted spinning wheel [1]. In our recent work, we used an acousto-optical modulator [6]. In either case, strobing can be synchronized with the video vertical sync pulse to give one exposure per video frame.
10. Go to http://www.rowland.harvard.edu/labs/bacteria/ and click on Movies.

Acknowledgment

This work was supported by grant AI016478 from the US National Institutes of Health, by a grant from the Physics of Living Systems program of the US National Science Foundation, and by the Rowland Institute at Harvard University.

References

1. Turner L, Ryu W, Berg HC (2000) Real-time imaging of fluorescent flagellar filaments. J Bacteriol 182:2793–2801
2. Darnton NC, Turner L, Rojevsky S, Berg HC (2007) On torque and tumbling in swimming *Escherichia coli*. J Bacteriol 189:1756–1764
3. Darnton NC, Berg HC (2007) Force-extension measurements on bacterial flagella: triggering polymorphic transformations. Biophys J 92:2230–2236
4. Darnton NC, Berg HC (2008) Bacterial flagella are firmly anchored. J Bacteriol 190:8223–8224

5. Turner L, Zhang R, Darnton NC, Berg HC (2010) Visualization of flagella during bacterial swarming. J Bacteriol 192:3259–3267
6. Turner L, Ping L, Neubauer M, Berg HC (2016) Visualizing flagella while tracking bacteria. Biophys J 111:1–10
7. Turner L, Stern AS, Berg HC (2012) Growth of flagellar filaments of *Escherichia coli* is independent of filament length. J Bacteriol 194:2437–2442
8. Darnton NC, Turner L, Breuer K, Berg HC (2004) Moving fluid with bacterial carpets. Biophys J 86:1863–1870
9. Scharf B (2002) Real-time imaging of fluorescent flagellar filaments of *Rhizobium lupin*i H13-3; flagellar rotation and pH-induced polymorphic transformations. J Bacteriol 184:5979–5986
10. Blair KM, Turner L, Winkelman JT, Berg HC, Kearns DB (2008) A molecular clutch disables flagella in the *Bacillis subtilis* biofilm. Science 320:1636–1638
11. Turner L, Berg HC (1990) Chemotaxis of bacteria in glass capillary arrays. Biophys J 58:919–930
12. Heimbrook ME, Wang WLL, Campbell G (1989) Staining bacterial flagella easily. J Clin Microbiol 27:2612–2615

Part III

In Vivo Analysis of Receptor Function

Chapter 8

All-Codon Mutagenesis for Structure-Function Studies of Chemotaxis Signaling Proteins

Peter Ames and John S. Parkinson

Abstract

The technique of all-codon mutagenesis can generate mutants that represent all possible amino acid replacements at any particular residue in a protein. It is thus a powerful tool to probe structure-function relationships in proteins of interest. In this chapter, we describe how we used all-codon mutagenesis to obtain mutants of the *Escherichia coli* serine receptor Tsr with amino acid replacements at residue F373, a functionally important site in this protein. We provide general protocols for mutagenesis of a target codon in a plasmid-borne gene and for the selection and screening of the resultant mutants. These techniques should be adaptable for the study of a variety of bacterial proteins.

Key words Chemoreceptor, Chemotaxis, Counter-selection, Polymerase chain reaction, Site-directed mutagenesis

1 Introduction

With modern molecular genetic tools we can readily identify genes of interest and obtain their nucleotide sequences. With a coding sequence in hand, we can infer the amino acid sequence of the protein product of a gene, which in turn may provide clues to its higher-order structures and its functional activities. However, to test mechanistic ideas about structure-function relationships in a protein, we must correlate structural changes in a gene product with their functional consequences. Classical forward genetic approaches (find a mutant with altered function, then characterize its mutational change) limit the potential power of structure-function analyses because the genetic code constrains the variety of amino acid changes that single base-pair-substitution mutations can produce. Conventional reverse genetic approaches (make a mutation, then characterize the functional changes it causes) also limit structure-function analyses, if only a subset of possible amino

Michael D. Manson (ed.), *Bacterial Chemosensing: Methods and Protocols*, Methods in Molecular Biology, vol. 1729, https://doi.org/10.1007/978-1-4939-7577-8_8,

acid replacements are chosen to characterize the effects of changes at a particular protein residue.

All-codon mutagenesis circumvents these limitations by yielding all possible amino acid replacements (missense mutants) at any residue of interest. The procedure is relatively simple and inexpensive. Characterizing and interpreting the functional alterations of the mutant proteins is more challenging, but beyond the scope of the protocol that follows. Here, we illustrate the all-codon method with a specific example: mutants of the *E. coli* serine chemoreceptor (Tsr) with single amino acid replacements at residue F373, an important contact site for trimer-of-dimer and signaling complex formation [1, 2]. The extension of the all-codon approach to any gene with an easily discernible function is straightforward.

2 Materials

2.1 PCR Mutagenesis

1. Plasmid template: pPA114 [2], derived from pACYC184 [3]: P15A origin of replication, confers resistance to chloramphenicol, wild-type *tsr* coding region whose expression is inducible with Na salicylate; purified using Qiagen miniprep kit with final DNA concentration of 100–200 ng/μl. Store at −20 °C (see **Note 1**).
2. Qiagen Spin Miniprep kit.
3. Oligonucleotide primers: These are typically 39-base pair complements with the targeted codon central in the sequence. Each of the three bases of the targeted codon is randomized in both primers, i.e., 25% A, 25% C, 25% G, 25% T.

   The primers used for Tsr-F373 mutagenesis were:

   nPA9:5′-GTAATTGACGGCATTGCCNNNCAGAC CAATATTCTGGCT-3′.

   nPA10:5′-AGCCAGAATATTGGTCTGNNNGGCAA TGCCGTCAATTAC-3.
4. dNTP mix: 10 mM each of dATP, dCTP, dGTP, dTTP in water. Aliquot and store at −20 °C.
5. Pfu Ultra High-Fidelity DNA Polymerase AD (2.5 U/μl, Agilent) with provided 10× reaction buffer.
6. Thermocycler.

2.2 Dpn1 Treatment

1. Qiagen PCR Purification Kit.
2. Restriction enzyme Dpn1 with provided buffer (e.g., from New England Biolabs).

2.3 Cell Transformation

1. Cells: In this example, we used *E. coli* strain UU1250 [2] [(*aer*)Δ1 *ygjG*::Gm (*tsr-hsdR*)Δ7028 (*tar-tap*)Δ5201 *zdb*::Tn5 (*trg*)Δ100] (*see* **Note 2**).

2. 0.1 M $CaCl_2$ and 0.1 M $CaCl_2$ in 2.05 M (15%) glycerol; both sterilized by autoclaving.
3. L-agar plates: 1% tryptone, 0.5% yeast extract, 0.5% NaCl, 1.5% agar containing selective antibiotic (e.g., chloramphenicol at 25 μg/ml).

2.4 Phenotypic Screen

1. T swim plates: 1% tryptone, 0.5% NaCl, 0.25% agar (*see* **Note 3**) containing antibiotic at one-half of the selective concentration used in hard plates and liquid medium (e.g., chloramphenicol at 12.5 μg/ml) and Tsr inducer, i.e., 0.6 μM Na salicylate for pPA114.
2. Sterile round—not flat—toothpicks.
3. L-broth: 1% tryptone, 0.5% yeast extract, and 0.5% NaCl; sterilized by autoclaving.

2.5 DNA Sequencing

1. DNA Sequencing Primers.

   We used three primers to sequence the entire *tsr* gene in pPA114:

   nPA13 (tsr1073-1099): ′-CGCAGAAAATCGCCGATATTAT CAGCG-3′.

   nPA14 (tsr1269-1243): 5′-GTCTTCAATCAGGCTTTTAAT TTCACG-3′.

   nRR45 (tsr630-604): 5′-GACGGCGAAGATGACCGCCAG TACGAC-3′.

3 Methods

3.1 PCR Reactions

This procedure is based on the "QuikChange" protocol originally described in the infstruction manual provided by Stratagene (now Agilent) for their PfuTurbo DNA polymerase

1. Combine in duplicate thin-walled plastic tubes on ice: 5 μl 10× reaction buffer, 150–200 ng of plasmid template pPA114, 1 μl (150 ng/μl) of both forward and reverse primers, 2 μl dNTP mix, deionized water to 50 μl.
2. Add 1 μl (2.5 U) PfuUltra High-Fidelity DNA Polymerase AD to 1 tube; the other is a control to later test the efficiency of template destruction by Dpn1.
3. Thermocycle the tubes using these parameters: initial denaturation for 1 min at 96 °C, then, for 18 cycles denature for 1 min at 95 °C, anneal primers for 1 min at 54 °C, extend for 12 min at 72 °C, incubate for another 5 min at 72 °C.

3.2 Dpn1 Treatment of PCR Products

After engineering and amplification of the mutant plasmids, the original template with its wild-type gene must be destroyed by treatment with the restriction enzyme Dpn1. This enzyme digests

DNA at the recognition sequence GATC, but only when the A residue has been methylated (as it should be in the template plasmid; *see* **Note 4**).

1. Transfer each PCR reaction to a fresh 1.5 ml Eppendorf tube.
2. Add 250 µl of solution PB (Qiagen's denaturing buffer), mix by pipetting, and transfer the mixture to DNA binding columns. Place the columns on a vacuum manifold and remove the PB by applying the vacuum.
3. Add 800 µl PE solution (Qiagen's elution buffer) and remove by again applying vacuum.
4. Transfer the DNA binding columns to fresh 1.5 ml Eppendorf tubes and centrifuge for 1 min at 10,000 rpm (~7500 RCF). This treatment removes the residual PE solution.
5. Transfer the DNA binding columns to fresh 1.5 ml Eppendorf tubes and apply 50 µl of EB (Qiagen's elution buffer) solution to the matrix in each column. Wait 1 min, then centrifuge as before. The eluate has a volume of 45 µl. Add 5 µl of 10× buffer for Dpn1 and 1 µl of Dpn1 to each eluted reaction. Incubate the tubes at 37 °C for at least 1 h before use in transformations.

3.3 Preparation of Competent Cells

1. Inoculate 2.5 ml of L-broth in a sterile tube from a single colony of UU1250 (or your strain to be transformed). Incubate overnight (16–18 h) with shaking at 37 °C.
2. Dilute the overnight culture 1/100 into 100 ml fresh L-broth in a sterile Ehrlenmeyer flask and shake at 37 °C until OD_{600} ~0.4. This typically takes 1.5–2 h with strain UU1250.
3. Centrifuge the cultures at 5000 rpm for 10 min at 4 °C. **From now on keep the cells on ice!** Pour off the supernatant, and resuspend the cell pellet by pipetting (**DO NOT VORTEX**) in 50 ml of 0.1 M ice-cold $CaCl_2$. Leave the resuspended cells on ice for 30 min.
4. Centrifuge as before and resuspend by pipetting (**DO NOT VORTEX**) in either: (a) 10 ml of ice-cold 0.1 M $CaCl_2$, if you intend to use the cells immediately, or (b) 10 ml of ice-cold 0.1 M $CaCl_2$ in 15% glycerol if you want to store the cells for future use. To store the cells, aliquot 1.0 ml into sterile eppendorf tubes, snap freeze on crushed dry ice and keep at −70 °C.

3.4 Transformation of Competent Cells

Reaction products from the mutagenic PCR are introduced into appropriate host cells made competent by treatment with 0.1 M $CaCl_2$, as described in Subheading 3.3.

1. Chill the Dpn1-digested PCR reactions on ice, mix in 200 µl of competent UU1250 cells, and leave on ice for 30 min.
2. Heat-shock the mixture at 42 °C for 2 min, then add 700 µl of L-broth and incubate at 37 °C for 1 h.

3. Spread 100 μl aliquots of the transformed cells onto selective L-agar plates and incubate the plates at 37 °C overnight (~16 h).

3.5 Phenotypic Screening of Transformants

Transformation of UU1250 with the Dpn1-treated PCR reactions should yield 300–400 colonies.

1. Inoculate transformant colonies with sterile round toothpicks into tryptone soft-agar plates containing 12.5 μg/ml chloramphenicol and 0.6 μM Na salicylate. With the same toothpick, also patch each colony onto solid-agar L-plates containing 25 μg/ml chloramphenicol.
2. Incubate the soft agar plates at 32.5 °C for about 6.5 h. Incubate the L master plates at 37 °C overnight (~16 h).
3. Score chemotaxis phenotypes on the soft agar plates (*see* **Note 5**). For all-codon mutagenesis of Tsr-F373, about 70% of the tested colonies exhibited less chemotactic spreading than did wild-type controls. These results suggest that most amino acid replacements at Tsr-F373 compromise wild-type function to some extent (Fig. 1).

3.6 Isolation of Mutant Plasmids

Inoculate desired mutants from the master plates to tubes with 4 ml of L-broth containing 25 μg/ml chloramphenicol. Incubate for 16–18 h at 37 °C and then purify plasmids from each clone with Qiagen's Spin Miniprep Kit (or comparable device).

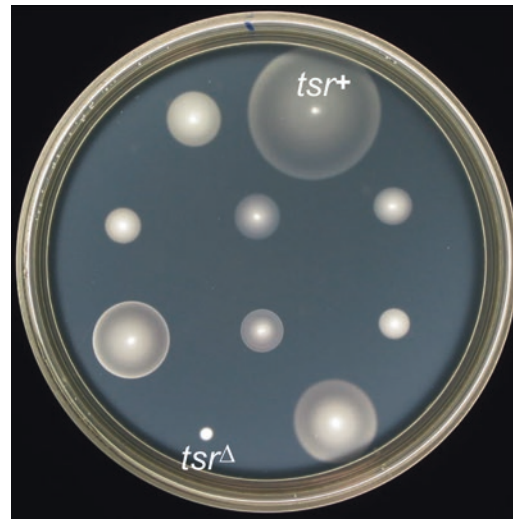

Fig. 1 Chemotaxis phenotypes of UU1250 colonies bearing mutant pPA114 plasmids created by all-codon mutagenesis. Transformants obtained from the mutant plasmid pool were incubated on tryptone soft-agar plates for 6.5 h at 32.5 °C. Eight mutant colonies are shown, along with pPA114 (*tsr*$^{+}$) and empty vector (*tsr*$^{\Delta}$) controls

3.7 DNA Sequencing

We purified plasmid DNA from a representative set of 36 transformant clones for sequencing by the DNA Core Facility at the University of Utah, using primer nPA14, which gives sequence coverage of the *tsr* region containing the F373 codon. Sequencing identified mutant codons for 15 different amino acid replacements at F373: A, G, H, I, K, L, M, N, P, Q, R, S, V, W, Y (*see* **Note 6**). Mutant plasmids chosen for further analyses were sequenced with additional primers to confirm that only codon 373 in the *tsr* gene contained mutational changes.

4 Notes

1. It is important that the plasmid DNA be isolated from a *dam*$^+$ host so that after PCR mutagenesis the template DNA can be counter-selected by Dpn1 digestion. A high proportion of dimeric plasmids will reduce the efficiency of the mutagenesis procedure. To reduce dimers in the plasmid prep, digest with a unique restriction enzyme that creates cohesive ends, recircularize by ligating at low DNA concentration, and transform a suitable host strain to prepare the plasmid template DNA.
2. Strain UU1250 carries a deletion that inactivates the *hsdR* gene, which encodes a component of the EcoK1 restriction system. DNA from the mutagenic PCR is potentially susceptible to destruction by HsdR because it will not be modified by adenine methylation at EcoK1 target sequences. If the PCR product DNA carries an EcoK1 recognition sequence (5′-AACNNNNNNGTGC-3′), as pPA114 does, in strain UU1250 it cannot be attacked by HsdR, and therefore yields a much higher efficiency of transformation.
3. The precise agar concentration needed for best swim plate performance must be determined empirically for each lot of agar. The optimal concentration will likely fall within 2.5–3.5 g/L.
4. Dpn1 treatment is most effective on PCR reactions that are first "cleaned up" using Qiagen's PCR Purification Kit.
5. Soft agar colony morphologies are most distinct immediately after removal from the incubator. They will be more difficult to assess after storage at 4 °C.
6. It is impractical to repeat the all-codon mutagenesis in hopes of fortuitously obtaining the few mutants not found in the first attempt. Rather, if additional substitutions are desired it is usually more efficient to create the desired remaining mutants by PCR mutagenesis with non-degenerate primers.

Acknowledgment

Our work is supported by research grant GM19559 from the National Institute of General Medical Sciences. DNA sequencing and primer synthesis were carried out by the Protein-DNA Core Facility at the University of Utah, which receives support from National Cancer Institute grant CA42014 to the Huntsman Cancer Institute.

References

1. Kim KK, Yokota H, Kim SH (1999) Four-helical-bundle structure of the cytoplasmic domain of a serine chemotaxis receptor. Nature 400:787–792
2. Ames P, Studdert CA, Reiser RH, Parkinson JS (2002) Collaborative signaling by mixed chemoreceptor teams in *Escherichia coli*. Proc Natl Acad Sci U S A 99:7060–7065
3. Chang ACY, Cohen SN (1978) Construction and characterization of amplifiable multicopy DNA cloning vehicles derived from the p15A cryptic miniplasmid. J Bacteriol 134:1141–1156

Chapter 9

Mutational Analysis of Binding Protein–Chemoreceptor Interactions

Andrew L. Seely

Abstract

Interactions between ligands and chemoreceptors in *Escherichia coli* and *Salmonella enterica* can be studied through genetic manipulation of the actors involved. Sequence analysis and modeling can reveal potential sites of interaction, and these sites can be deleted or mutated and the effects tested through various in vivo chemotaxis assays to ascertain their importance during interaction. Here, the approach for analysis of the interaction between a major *E. coli* chemoreceptor and its binding protein ligand is described.

Key words Site-directed mutagenesis, Alanine-scanning mutagenesis, Chemoreceptor, Binding protein, Polymerase chain reaction, Pfu Ultra, Chemotaxis, Transformation

1 Introduction

Investigation of the interaction between chemoreceptors and their ligands (either direct binding or indirect binding via a periplasmic protein) has played an integral role in characterizing bacterial chemotaxis. Some *E. coli* chemoeffectors, such as serine and aspartate, are sensed directly by their cognate membrane receptors, whereas others require the ligand to first associate with a periplasmic binding protein before recognition by the receptor occurs (Fig. 1; [1–4]). In either case, ligands are recognized by the periplasmic domain of the chemoreceptor, either at the interface of the receptor dimer (direct) or across its apex (binding proteins) [5–7].

The genes encoding the proteins of interest can be deleted through various means, then reintroduced after being cloned into a plasmid so that various mutant constructs can be analyzed. Once an area of interaction is tentatively identified, sequence analysis can reveal residues of interest to be mutated. A similar approach has been fruitful in previous studies, especially the analysis of the interaction between the *E. coli* aspartate chemoreceptor (Tar) and the maltose-binding protein [8, 9]. Figure 2 illustrates a hypothetical interaction between ligand-bound binding protein and chemorecep-

Michael D. Manson (ed.), *Bacterial Chemosensing: Methods and Protocols*, Methods in Molecular Biology, vol. 1729, https://doi.org/10.1007/978-1-4939-7577-8_9,

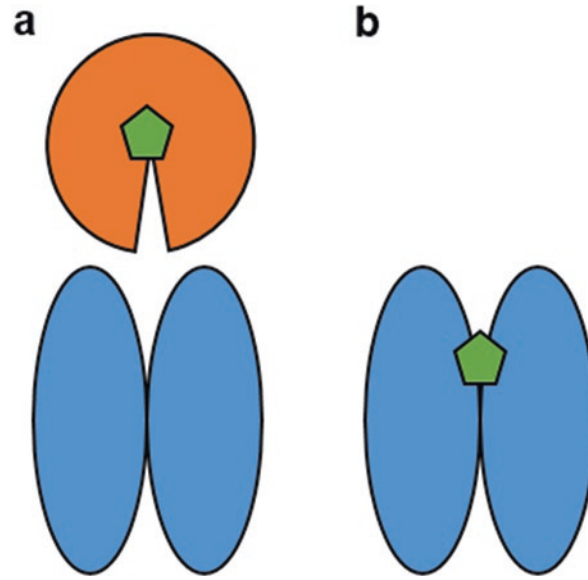

Fig. 1 Interaction of ligand with chemoreceptor. (**a**) Interaction with the chemoreceptor requires that the ligand (green pentagon) first bind to a periplasmic binding protein (orange circle). Once bound to ligand, the binding protein achieves a closed conformation and can interact with the chemoreceptor homodimer (blue ovals). (**b**) The ligand binds directly at the interface of the homodimeric periplasmic domain

tor, including the areas predicted to contain the residues most likely to be involved in the protein–protein interaction. Individual replacement of these residues in the plasmid-encoded genes can occur by first substituting alanine—a neutral residue—then changing those residues with potential to be involved in the interaction by other substitutions, e.g., charged residues can be replaced with those of the opposite charge, and hydrophobic residues can be replaced with hydrophilic ones, or vice versa. Quick Change mutagenesis kits can be used to easily replace selected residues, using high-fidelity polymerases and synthetic DNA primers in the polymerase chain reaction (PCR; [10]). This method allows for single residue replacements to be introduced and tested in strains in which the wild-type plasmid-encoded proteins support normal chemotaxis to specific ligands.

Differences in chemotaxis behavior are measured to quantify the differences in chemotaxis generated through these replacements, thereby identifying the importance—or lack thereof—of the residues being examined. The following protocols are followed after the gene of interest is cloned into an appropriate plasmid to be transformed into cells chromosomally deleted for that gene. Chemotaxis assays should be performed with wild-type and negative (typically non-polar deletion) controls to determine the effect of altering specific residues on the chemoreceptor–ligand interaction. Mutations that disrupt chemotaxis but do not alter expression or

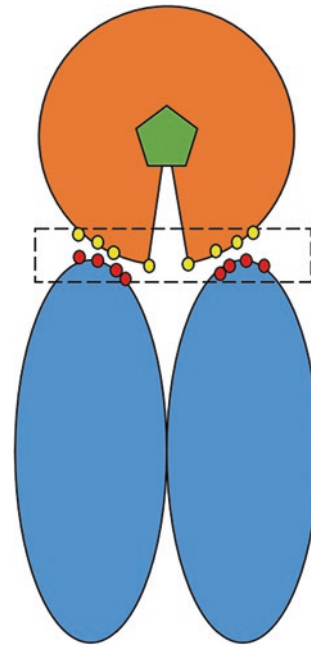

Fig. 2 Hypothetical interaction between a binding protein and a chemoreceptor. The image depicts a ligand-bound binding protein (orange circle with green pentagon) in close proximity with a chemoreceptor homodimer (blue ovals). The dashed box indicates the proposed area of interaction at interface of the two proteins, while red and yellow circles represent amino acids hypothesized to be important for interaction on both the chemoreceptor and binding proteins, respectively

normal function in other activities of the proteins of interest indicate residues that are important for specific protein–protein interactions that are required for chemotaxis.

2 Materials

Competent cells for transformation with plasmids should be stored at −80 °C and thawed on ice prior to transformation. All strains generated should be stored long term at −80 °C and streaked fresh before performing any chemotaxis assay. Synthetic primers and plasmids should be stored short term at −20 °C and thawed on ice prior to use. Prepare all solutions using ultrapure water, and store reagents according to manufacturer suggestions.

2.1 Primer Design

1. Obtain the nucleotide sequence of proteins of interest. In the study that served as the basis for this chapter, we looked at the interaction of the Tsr chemoreceptor and the LsrB autoinducer-2 (AI-2) periplasmic binding protein of *E. coli* ([11]; *see* Chapter 6 in this volume). Also, if available, obtain the crystal structures of the sensory domain of the chemoreceptor [12] and of the

ligand-bound binding protein [13] whose interaction you want to probe. A reasonably unsophisticated computer-based rigid docking of the two proteins can provide a good idea of the areas on the surface of the two proteins that are likely to interact. Extract the nucleotide sequences of the areas encoding potentially interacting regions (*see* **Note 1**) and design forward and reverse primers to replace residues of interest in plasmid-encoded protein (*see* **Note 2**). Forward primers should be designed directly from DNA sequence, substituting the appropriate nucleotides at the 5′ end and including 15–20 base pairs (bp) of downstream nucleotides (*see* **Note 3**). Reverse primers should be back-to-back with forward primers and complementary to the template DNA (*see* **Note 4**). Order these primers without modifications to their 5′ or 3′ ends.

2. Resuspend the primer stocks to a final concentration of 100 μM in ultrapure water and store at −20 °C.
3. Phosphorylate primers using phosphonucleotide kinase (PNK) at 37 °C prior to use.

2.2 Polymerase Chain Reaction (PCR)

1. Use *Pfu Ultra* high-fidelity DNA polymerase and the Stratagene Quik Change II Site Directed Mutagenesis kit (Stratagene, La Jolla, CA).
2. The thermal cycler program should include 20–30 cycles of denaturing, annealing and extension. The annealing temperature (T_A) should be approximately 5 °C lower than melting temperature of selected primers (*see* **Note 5**).

3 Methods

Thaw all previously frozen components on ice. Carry out procedures at room temperature unless specified otherwise.

3.1 Site-Directed Mutagenesis

1. In 0.5 mL PCR Eppendorf tubes, combine 2X *Pfu Ultra* High Fidelity Fusion Master Mix, forward and reverse primers for each specific mutation (10 μM each), template DNA (100 ng/μL), and sterile water to a final reaction volume of 50 μL.
2. Run PCR in thermal cycler using appropriate annealing temperature.
3. Digest PCR product with DpnI to remove wild-type DNA, then run digested product on 1% agarose gel with 10 kB DNA ladder for reference.
4. Excise amplified PCR product from agarose gel and extract DNA using desired Gel Extraction kit.
5. Ligate extracted DNA with desired DNA ligase enzyme or kit and store excess ligated plasmid product at –20 °C.

3.2 Heat Shock Transformation of Ligated Plasmid into Competent Cells

1. In a 1.5 mL Eppendorf tube, combine 60 μL of appropriate competent cells (deleted for the gene(s) of interest) with ligated plasmid bearing desired mutation.
2. Incubate on ice for 60 min without shaking.
3. Heat-shock cells at 42 °C for 2–5 min.
4. Allow cells to recover on ice for 5–10 min, then add 1 mL of growth media to tube and incubate with shaking at 37 °C for 60 min.
5. Spread varying dilutions of cells onto nutrient agar plates containing the antibiotic that selects for presence of the plasmid and incubate overnight at 37 °C.
6. Select single colonies (transformants) and grow in selective liquid media for plasmid isolation.

3.3 Confirming Presence of Mutation

1. Perform a plasmid mini-prep using desired kit to isolate the mutated plasmid (*see* **Note 6**).
2. Sequence the potentially mutated plasmid using primers designed to cover your entire gene of interest. Compare your whole-gene sequence with the known wild-type sequence to ensure that only the base pair changes that you introduced are present. Discard plasmids without your mutation of interest or those that contain additional base changes.
3. Repeat sequencing with other isolated transformants as needed until the desired mutation is procured.
4. Introduce plasmids containing the confirmed mutation into the appropriate competent cells for testing in chemotaxis assays (*see* **Note 7**). Compare results of chemotaxis involving the wild-type version of particular protein with results obtained from assays where the mutation was present. Flag for further investigation mutants that reduced chemotaxis.
5. Test the protein expression levels of target protein for each mutation that led to deficient chemotaxis (*see* **Note 8**). If applicable, check other functions of target protein, such as ability to bind ligand or perform alternative functions of the proteins to further ensure structural integrity is intact (*see* **Note 9**).
6. Refine your interaction model based on the chemotaxis assay results. Residues that reduce or eliminate chemotaxis to a ligand when altered likely serve an important role in that interaction and can be used to construct a docking model if the atomic structures of the binding protein and the chemoreceptor ligand-binding domain involved are known (*see* **Note 10**).

4 Notes

1. Ensure that you are obtaining the DNA sequence specific for your organism's protein. Some published protein sequences are for the same protein in related bacteria and have a few amino acid changes between closely related species. For instance, *E. coli* and *Salmonella* have similar LsrB AI-2-binding proteins that differ by just a few amino acids. We have used the structure of the *Salmonella enterica* LsrB protein (autoinducer-2-binding protein) and the *E. coli* Tsr protein to perform a preliminary computer generated docking model for the LsrB/Tsr interaction. Crucial residues are usually highly conserved, but this must be verified by sequence analysis.
2. When deciding the triplet codon of the amino acid replacement, a good rule of thumb is to choose a codon that is consistently used within the organism's DNA. For instance, if GCA is used to code for alanine throughout the genome, that codon should be chosen for alanine-scanning rather than GCG. Substituting with a codon not normally used in the genome may affect the expression of the protein.
3. Base pairs to be changed can also be placed in the center of the forward primer . Be sure to include 10–15 base pairs of wild-type DNA sequence on either side of the selected mutation. When calculating melting temperature (T_M) to be used in PCR reaction, do not include the three bases of the codon to be changed as they will not contribute to primer annealing.
4. Reverse primers should not overlap with forward primers to avoid duplications or additions to the replicated DNA. Start the 5′ end of the reverse primer at the codon for the residue immediately adjacent to the 5′ end of the first codon included in the forward primer. This ensures the primers will bind to both strands of the DNA during PCR to produce more copies of the altered gene of interest.
5. Annealing temperatures can be raised to increase the specificity of primer binding if non-specific binding during PCR becomes a problem.
6. The Sigma Mini-prep kit works well. Ideally, you will isolate between 100 and 200 ng/μL of plasmid. This concentration makes sequencing more efficient.
7. For two proteins that interact, we typically express the non-mutant protein from the chromosomal gene and the mutant protein from the plasmid. Expressing the two proteins from compatible plasmids is possible, if, for example, the interaction of two mutant proteins is to be tested, but in that case the expression level of both proteins must be carefully controlled (*see* **Note 8**).

8. Protein expression needs to be near that of the chromosomally encoded wild-type version to be relevant. This may require adjusting growth conditions or altering the level of induction of the plasmid-encoded gene to obtain the protein levels that support optimal chemotaxis.
9. If the mutant protein has other activities that are available to test, it is recommended to do so. For example, plasmids expressing mutations in the gene that encodes maltose-binding protein, *malE*, that interfere with maltose taxis can be tested for the ability to support the uptake of maltose with normal kinetics. Similarly, plasmids expressing mutations in the gene that encodes the aspartate/maltose chemoreceptor *tar* that interfere with maltose taxis can be tested for the ability to support aspartate taxis. Retention of alternative functions of these proteins demonstrates that the mutations obtained are specific for chemotaxis to the ligand being tested. We have recently used this approach to identify mutations in the *lsrB* gene, which encodes the binding protein for autoinducer-2, and the *tsr* gene, which encodes the serine chemoreceptor that specifically disrupt AI-2 chemotaxis (*see* Chapter 6 in this volume).
10. The computer-generated docking model can initially be done with rigid-body structures of the interacting proteins, but after a docking model has been validated by genetic analysis, a molecular-dynamic simulation of docking is a valuable extra step to assess the strength and specificity of the protein–protein interaction.

Acknowledgment

I would like to acknowledge the guidance of Dr. Michael Manson over the course of my research on bacterial chemotaxis. I would also like to acknowledge the student and postdoctoral members of the Manson Lab at Texas A&M University for their hard work and collaboration with these research endeavors.

References

1. Krikos A, Conley MP, Boyd A, Berg HC, Simon MI (1985) Chimeric chemosensory transducers of *Escherichia coli*. Proc Natl Acad Sci U S A 82:1326–1330
2. Mowbray SL, Koshland DE Jr (1990) Mutations in the aspartate receptor of *Escherichia coli* which affect aspartate binding. J Biol Chem 265:15638–15643
3. Hazelbauer GL, Engstrom P (1980) Parallel pathways for transduction of chemotactic signals in *Escherichia coli*. Nature 283:98–100
4. Englert DL, Adase CA, Jayaraman A, Manson MD (2010) Repellent taxis in response to nickel ion requires neither Ni^{2+} transport nor the periplasmic NikA binding protein. J Bacteriol 192:2633–2637
5. Bowie JU, Pakula AA, Simon MI (1995) The three-dimensional structure of the aspartate receptor from Escherichia Coli. Acta Crystallogr Sect D Biol Crystallogr 51:145–154
6. Milburn MV, Prive GG, Milligan DL, Scott WG, Yeh J et al (1991) Three-dimensional

structures of the ligand-binding domain of the bacterial aspartate receptor with and without a ligand. Science 254:1342–1347

7. Scott WG, Milligan DL, Milburn MV, Prive GG, Yeh J et al (1993) Refined structures of the ligand-binding domain of the aspartate receptor from salmonella typhimurium. J Mol Biol 232:555–573
8. Gardina P, Conway C, Kossman M, Manson M (1992) Aspartate and maltose-binding protein interact with adjacent sites in the tar chemotactic signal transducer of *Escherichia coli*. J Bacteriol 174:1528–1536
9. Zhang Y, Gardina PJ, Kuebler AS, Kang HS, Christopher JA et al (1999) Model of maltose-binding protein/chemoreceptor complex supports intrasubunit signaling mechanism. Proc Natl Acad Sci U S A 96:939–944
10. Carter P (1986) Site-directed mutagenesis. Biochem J 237:1–7
11. Hegde M, Englert DL, Schrock S, Cohn WB, Vogt C et al (2011) Chemotaxis to the quorum-sensing signal AI-2 requires the Tsr chemoreceptor and the periplasmic LsrB AI-2-binding protein. J Bacteriol 193:768–773
12. Tajima H, Imada K, Sakuma M, Hattori F, Nara T et al (2011) Ligand specificity determined by differentially arranged common ligand-binding residues in bacterial amino acid chemoreceptors Tsr and Tar. J Biol Chem 286:42200–42210
13. Miller ST, Xavier KB, Campagna SR, Taga ME, Semmelhack MF et al (2004) *Salmonella typhimurium* recognizes a chemically distinct form of the bacterial quorum-sensing signal AI-2. Mol Cell 15:677–687

Chapter 10

In Vitro Assay for Measuring Receptor-Kinase Activity in the *Bacillus subtilis* Chemotaxis Pathway

Hanna E. Walukiewicz, George W. Ordal, and Christopher V. Rao

Abstract

The sensing apparatus of the *Bacillus subtilis* chemotaxis pathway involves a complex consisting of chemoreceptors, the CheA histidine kinase, and the CheV and CheW adaptor proteins. Attractants and repellents alter the rate of CheA autophosphorylation, either by directly binding the receptors or by indirectly interacting with them through intermediate binding proteins. We describe an in vitro assay for measuring receptor-kinase activity in *B. subtilis*. This assay has been used to investigate the mechanism of signal transduction in *B. subtilis* chemotaxis and the disparate mechanisms employed by this bacterium for sensory adaptation and gradient sensing.

Key words Chemotaxis, *Bacillus subtilis*, Chemoreceptors, CheA, Kinase assay

1 Introduction

Chemotaxis refers to the directed migration of cells in response to external chemical gradients [1]. Bacteria use protein phosphorylation to transfer information from the chemoreceptors, which sense the ligands, to the motor proteins, which direct the motion of the cell. In the flagellated, Gram-positive bacterium *Bacillus subtilis* (reviewed in [2, 3]), this information flow involves a modified two-component system consisting of the CheA histidine kinase and the CheY response regulator. CheA forms a complex with the chemoreceptors and the CheW and CheV adaptor proteins. These complexes are associated with the membrane, as most of the chemoreceptors are transmembrane. Attractants and repellents alter the rate of CheA autophosphorylation, either by directly binding the receptors or by indirectly interacting with them through intermediate binding proteins [4]. CheA phosphorylates CheY by transferring the phosphoryl group from CheA to CheY [5]. Phosphorylated CheY (CheY-P) binds to the flagellar motors and induces counter-clockwise rotation of flagella, which causes the cells to move in a straight direction [6, 7]. The default mode,

Michael D. Manson (ed.), *Bacterial Chemosensing: Methods and Protocols*, Methods in Molecular Biology, vol. 1729, https://doi.org/10.1007/978-1-4939-7577-8_10,

clockwise rotation of the flagella, causes the cells to tumble randomly. By altering the frequency of runs and tumbles, *B. subtilis* is able to migrate up gradients of attractants (e.g., amino acids and sugars) and down gradients of repellents (e.g., toxins).

The core of the signal transduction pathway involved in chemotaxis can be reconstituted in vitro using purified membranes. Radiolabeled ATP can be used to monitor the rates of CheA autophosphorylation and subsequent transfer of the phosphoryl group to CheY [8]. This in vitro receptor-coupled kinase assay has been used extensively to investigate the mechanism of chemotaxis in *Escherichia coli* [9–14], in particular the role of chemoreceptor methylation [9–16]. Very briefly, *E. coli* tunes the activity and sensitivity of chemoreceptors to attractants/repellents by reversibly methylating conserved glutamate residues on the receptors [17]. Reversible chemoreceptor methylation enables the cells to adapt their response to attractants or repellents such that they respond not to the absolute concentration of attractants/repellents but rather to changes in concentration. This process is known as adaptation. Sensory adaptation enables these cells to sense chemical gradients [18]. The in vitro receptor-kinase assay was instrumental in elucidating the role of chemoreceptor methylation in sensory adaptation. By genetically substituting the conserved glutamyl residues with glutamines, which function as methylated glutamate mimics [16], researchers were able to determine how methylation tunes receptor-kinase activity.

More recently, the in vitro receptor-kinase assay has been used to investigate the mechanism of chemotaxis and sensory adaptation in *B. subtilis*. Unlike *E. coli*, *B. subtilis* employs three mechanisms for sensory adaptation [2]. The first involves reversible chemoreceptor methylation. The chemoreceptor methylation in *B. subtilis* is site specific, unlike the system in *E. coli*. In particular, the methylation of some conversed glutamyl residues activates the receptors, whereas the methylation of others inhibits the receptors [19–21]. In *E. coli*, receptor activity increases with the number of methylated glutamate residues.

In addition, *B. subtilis* employs two additional systems not present in *E. coli*. One involves CheV, which consists of an N-terminal CheW-like adaptor domain and a C-terminal response-regulator domain that can be phosphorylated by CheA. It is functionally redundant to CheW, as it can independently couple the chemoreceptors to CheA. CheV phosphorylation mediates adaptation by modulating CheA kinase activity through a negative feedback loop [21]. The third adaptation system involves CheC and CheD. CheD activates the chemoreceptors [21, 22]. CheC binds CheD and prevents it from activating the chemoreceptors [23, 24]. It is also a weak phosphatase for CheY-P [23]. CheY-P increases the affinity of CheC for CheD [25]. Thus, when CheY-P levels are high, more CheD is bound to CheC and less is bound to the

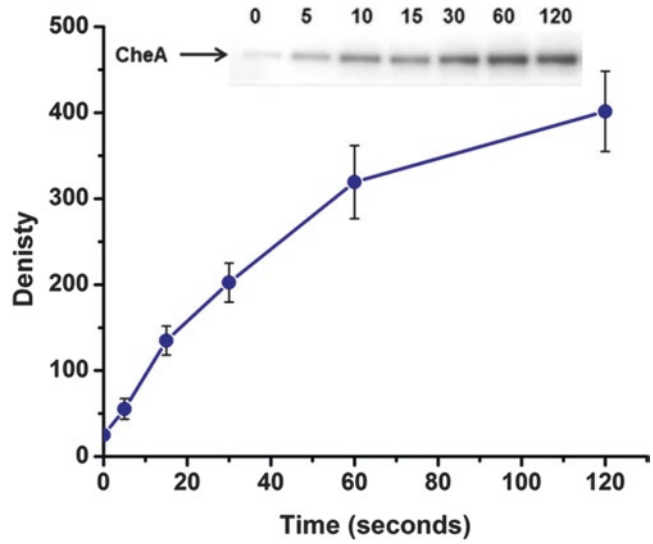

Fig. 1 Extended time course of CheA autophosphorylation. Purified CheA (2.4 μM final concentration) was incubated with 50 μM [γ-^{32}P]-ATP (4000–8000 cpm/pmol) in TKM buffer at room temperature in a volume of 0.2 mL. At indicated times, 10 μL aliquots were removed, added to 5 μL of 2X Laemmli sample buffer containing EDTA, and then run on a native 12% TBE gel. *B. subtilis* CheA autophosphorylation increases linearly for the first 20 s. For the in vitro kinase assay, we use 5 s

receptors. As a consequence, CheA kinase is inhibited when CheY-P levels are high. Although many questions still remain, our basic understanding of these three adaptation systems was obtained using the in vitro receptor-kinase assay [21].

This chapter discusses our protocol for measuring in vitro receptor-kinase activity in *B. subtilis*. The assay is analogous to the ones developed for *E. coli*, with a number of key exceptions. The first concerns the numerous extracellular proteases expressed by *B. subtilis* [26]. These proteases must be inactivated to prevent protein degradation. The second concerns the rate of CheA autophosphorylation: in *B. subtilis*, it is relatively slow compared to *E. coli*, at least in vitro (Figs. 1 and 2; [5, 27]). Therefore, unlike the *E. coli* assays, we are able to directly measure the rate of CheA autophosphorylation in *B. subtilis*. Finally, the chemoreceptors in *B. subtilis* do not form functional complexes unless they are expressed in the presence of CheA and CheW. CheA and CheW are then removed from the membrane preparations using high salt, high pH washes.

2 Materials

Prepare all the solutions using Millipore water and analytic grade regents. Prepare and store all reagents at room temperature.

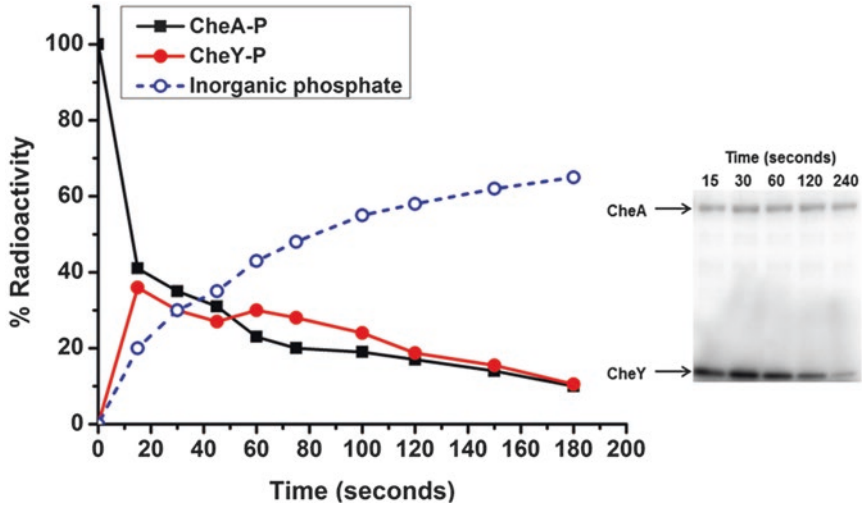

Fig. 2 Kinetics of phosphoryl group transfer from CheA to CheY. 50 μg of purified CheA was incubated with 0.1 mM [γ-^{32}P]-ATP (4000–8000 cpm/pmol) in a 0.2 mL total volume at room temperature. After 1 h, 50 μL aliquots were applied to ProbeQuant G-50 microcolumns that had been prespun at 735 × *g* for 1 min. Phosphorylated CheA was recovered from the column by centrifugation at 735 × *g* for 2 min. CheA concentration was measured using Pierce BCA protein assay kit. 5 pmol of purified CheAp was mixed with 500 pmol of purified CheY in TKM buffer at room temperature in a total volume of 50 μL. At indicated times, 5 μL aliquots were removed added to 2.5 μL of 2X Laemmli sample buffer containing EDTA and run on a native 12% TBE gel. This experiment illustrates that *B. subtilis* CheA autophorylation is a better alternative for kinase assays than CheY. *B. subtilis* phosphate transfer from CheA to CheY is not complete before spontaneous dephosphorylation of CheY begins. The rate of phosphotransfer from CheA-P to CheY is 3.76 μM^{-1} min^{-1}, and the rate for spontaneous CheY dephosphorylation is CheYp is 0.51 min^{-1}

2.1 Strains and Plasmids

1. Our base strain for the kinase assay is OI4507 (Δ*10mcp cheB cheR amyE::mcpB cheA cheW*), a derivative of the wild-type chemotactic strain OI1085 [28]. OI4507 expresses the asparagine receptor McpB as its sole chemoreceptor (*see* **Note 1**). This strain also lacks the CheR methyltransferase and CheB methylesterase. To increase the signal, McpB is expressed along with CheA and CheW from the T7 promoter obtained from the plasmid pST39 [29] using the *B. subtilis* integration vector pAIN750. T7 polymerase was expressed using the plasmid POLT7 [30, 31].

2.2 Membrane Preparation

1. Tryptose blood agar base (TBAB) plates: 33 g/L tryptose blood agar base and 3 g/L agar.
2. Tryptone broth (TBr): 10 g/L Bacto tryptone and 5 g/L NaCl.
3. Capillary assay minimal medium plus tryptone broth (CAMM+): 50 mM K_3PO_4 (pH 7.0), 1.2 mM $MgCl_2$, 0.14 mM $CaCl_2$, 1 mM $(NH_4)_2SO_4$, 0.01 mM $MnCl_2$, 20 mM sorbitol, and 0.2% (vol/vol) TBr.

4. Capillary assay minimal medium (CAMM): 50 mM K_3PO_4 (pH 7.0), 1.2 mM $MgCl_2$, 0.14 mM $CaCl_2$, 1 mM $(NH_4)_2SO_4$, 0.01 mM $MnCl_2$, and 20 mM sorbitol.
5. 1 M KCl.
6. Sonication buffer: 10 mM potassium phosphate buffer pH 7, 10 mM $MgCl_2$, 1 mM EDTA, 0.3 mM dithiothreitol, 20 mM KCl, 1 mM glutamate, 2 mM phenylmethanesulfonyl fluoride to inactivate proteases, and 20% glycerol.
7. MT buffer: 10 mM potassium phosphate buffer (pH 7), 1 mM $MgCl_2$, 0.1 mM EDTA, and 1 mM 2-mercaptoethanol.
8. MT+ buffer: 10 mM potassium phosphate buffer (pH 7), 1 mM $MgCl_2$, 0.1 mM EDTA, 1 mM 2-mercaptoethanol, and 0.1 mM Na_2CO_3.
9. High pH buffer: 0.18 M Na_2CO_3 (pH 11.3), 50 mM DTT, 1 mM $CaCl_2$, 1 mM $MgCl_2$, and 1 mM MnCl.
10. Micro Bio-Spin 6 Chromatography Columns (Bio-Rad).
11. Glass/Teflon homogenizer.
12. Pierce BCA protein assay kit.

2.3 In Vitro Assay for Receptor-Coupled Kinase Activity

1. TKM buffer: 50 mM Tris–HCl (pH 7.5), 50 mM KCl, and 5 mM $MgCl_2$.
2. [γ-^{32}P]-ATP (4000–8000 cpm/pmol).
3. 2X Laemmli sample buffer containing EDTA: 4% SDS, 20% glycerol, 10% 2-mercaptoethanol, 0.004% bromphenol blue, 0.125 M Tris–HCl (pH 6.8), and 25 mM EDTA.
4. 12% Tris/borate/EDTA (TBE) gel.
5. 1× TBE running buffer: 45 mM Tris borate (pH 8.0) and 1 mM EDTA.
6. Gel drier.
7. Phosphor screen.
8. Phosphoimager (Molecular Dynamics Storm).
9. LabWorks Imaging Software (UVP BioImaging Systems).

3 Methods

Carry out all the experiments at room temperature unless otherwise specified.

3.1 Preparation of Bacterial Membranes

1. Streak out the cells on TBAB plates and grow them overnight at 30 °C.
2. Scrape the cells from a plate into an Eppendorf tube and resuspend the cells in 1 mL TBr.

3. Measure the A_{600}.
4. Dilute the cells into 50 mL of TB to a starting A_{600nm} of 0.01.
5. Incubate the cells at 37 °C with continuous shaking (250 rpm) until they reach mid-exponential phase (approximately 6 h). Dilute the cells 1:10 (vol/vol) into 50 mL of fresh CAMM+ and incubate at 37 °C with continuous shaking (250 rpm) until they reach mid-exponential phase (approximately 6 h).
6. Dilute the cells in CAMM+ to an A_{600} of 0.01 and then incubate with continuous shaking (250 rpm) at 37 °C until they reach mid-exponential phase (approximately 10 h). Dilute the culture 1:10 (vol/vol) into 50 mL of fresh CAMM and incubate until the cultures reached an A_{600} of 0.6 (*see* **Note 2**).
7. Harvest the cells by centrifuging at 9900 × *g* for 15 min.
8. Wash three times in 1 M KCl to remove extracellular proteases by resuspending the pellet in 20 mL of 1 M KCl and centrifuging at 9900 × *g* for 15 min. Repeat this wash step three times.
9. Resuspend the cells in sonification buffer (3 mL of buffer per 1 g of wet cells; *see* **Note 3**).
10. Sonicate the cells using five rounds of 30 s pulses with a 1 min rest between each pulse.
11. Centrifuge sonicated cells at 17,600 × *g* for 15 min. Transfer the supernatant to a new tube.
12. Isolate the membrane by centrifuging supernatant at 120,000 × *g* for 2 h.
13. Resuspend the pellet in 1 mL of MT+ buffer.
14. Homogenize pellet using glass/Teflon homogenizer (25 up-down strokes).
15. Centrifuge homogenized pellet at 120,000 × *g* for 2 h.
16. Resuspend pellet in 1 mL of ice-cold high pH buffer.
17. Homogenize pellet using glass/Teflon homogenizer (25 up-down strokes).
18. Stir homogenized suspension for 1 h at 4 °C.
19. Desalt suspension using Micro Bio-Spin 6 chromotography column. Columns are first subjected to buffer exchange using MT+ buffer and then used to desalt the membrane sample according to the manufacturer's directions.
20. Centrifuge desalted suspension at 120,000 × *g* for 2 h to remove membrane-associated proteins.
21. Suspend membrane pellet in 1 mL of MT+ buffer.
22. Homogenize membranes using glass/Teflon homogenizer (25 up-down strokes).

23. Repeat **steps 20–22**.
24. Determine protein concentration in homogenized membranes using Pierce BCA protein assay kit.
25. Adjust protein concentration to an approximately 60 μM by adding the requisite amount of MT buffer.
26. Isolated membranes can be stored under these conditions by aliquoting them into single use aliquots and freezing at –80 °C.
27. If desired, perform immunoblots to ensure that the chemoreceptors are present and that the CheA, CheW, and CheV proteins have been stripped from the membranes.

3.2 In Vitro Assay for Receptor-Coupled Kinase Activity

1. Thaw aliquots of isolated membrane samples on ice.
2. Buffer-exchange membrane samples into TKM buffer using Micro Bio-Spin 6 chromotography columns. Columns are first subjected to buffer exchange using TKM buffer and then used to buffer-exchange the membrane sample according to the manufacturer's directions.
3. Quantify the chemoreceptor concentration within isolated membranes by running a quantitative immunoblot. Digitize the blot with a phosphorimager (Molecular Dynamics Storm PhosphorImager), and analyze the image density using LabWorks Imaging Software (UVP BioImaging Systems).
4. In an Eppendorf tube, mix isolated membrane containing approximately 6 μM of chemoreceptor (*see* **Note 4**) with 2 μM of purified CheA (*see* **Note 5**) in a total of 10 μL TMK buffer (*see* **Note 6**). Mix the sample well and incubate at room temperature for 10 min.
5. Next, add 3.2 μM of purified CheW (*see* **Note 7**). Up to 2 μM of purified CheD and 11.6 μM of purified CheV or CheVp can also be added if desired (*see* **Note 8**) to a total volume of 20 μL in TMK buffer (*see* **Note 9**).
6. Mix well and pre-incubate the reactions at room temperature for 40–60 min to permit formation of the receptor-protein complex.
7. Next add attractant to the Eppendorf tube, if called for in the experiment, and immediate thereafter initiate the reaction by adding [γ-^{32}P]-ATP (4000–8000 cpm/pmol) to a final concentration of 0.1 mM.
8. After 5 s, quench the reaction by adding of 15 μL of 2X Laemmli sample buffer containing 25 mM EDTA.
9. Immediately load entire sample volume onto a native 12% TBE gel and run for gel for 45 min at 200 V in 1X TBE buffer.
10. Wash finished gels 2 × 5 min in 1X TBE buffer to eliminate excess radioactivity and dry using a gel drier.

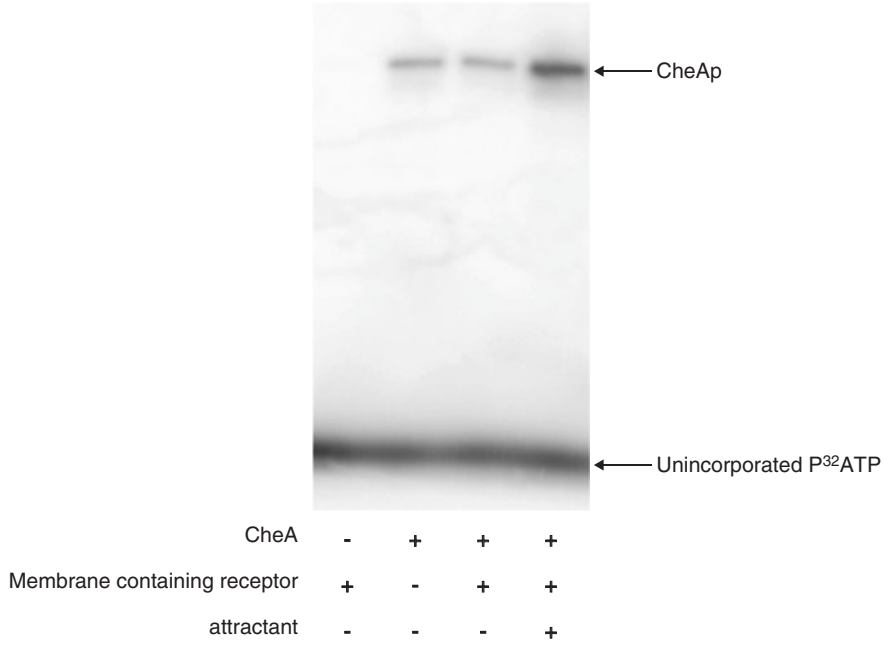

Fig. 3 Example of kinase assay results

11. Use dried gels to expose a phosphor screen overnight.
12. Digitize the gel image on the phosphor screen using a phosphorimager (Molecular Dynamics Storm PhosphorImager; Fig. 3).

4 Notes

1. We found that McpC, the sole chemoreceptor for proline, does not need to be overexpressed to obtain a strong signal for the kinase assay. Changes in CheA kinase activity can be observed using either strain OI1085 or OI4007 (*Δ10mcp amyE::mcpC*).
2. Multiple rounds of exponential growth are necessary to reduce variability [32]. The cells are initially grown in CAMM+ (CAMM containing tryptone) to generate higher biomass and then grown in CAMM to ensure robust expression of the chemotaxis genes.
3. The proteases of concern during membrane purification in *B. subtilis* are neutral metalloproteases and an alkaline serine protease (subtilisin). The neutral metalloproteases are sensitive to EDTA and subtilisin is sensitive to phenylmethylsulphonyl fluoride [26].
4. Sonicated membranes form spherical micelles. These micelles have two different receptor membrane architectures: micelles

in which the sensing domain of the receptor is oriented outward, and micelles in which the sensing domain of the receptor is oriented inward. Only the micelles in which the sensing domain of the receptor is oriented inward are likely to be accessible for kinase binding. For this reason, we use isolated membranes containing 6 μM of receptor, which is twice concentration seen in wild-type cells, with the assumption that only half will be accessible to kinase.

5. CheA protein can only be freeze-thawed once. Therefore, purified CheA kinase protein is aliquoted into single-use tubes and frozen at –80 °C. It is important to thaw CheA at room temperature to preserve full kinase activity.
6. CheA, CheW, and CheV were purified as follows [22]. Each protein was individually cloned into the glutathione S-transferase (GST) fusion expression plasmid pGEX-6P-2 and transformed into *E. coli* strain BL21. The cells were then grown in 2 L of LB [1% (wt/vol) tryptone, 0.5% (wt/vol) yeast extract, 0.5% (wt/vol) NaCl] with 100 μg/mL ampicillin at 37 °C and continuous shaking (250 rpm) to A_{600} of 0.8. Expression was then induced by adding 1 mM IPTG (isopropyl-β-D-thiogalactopyranoside). The cells were then grown at 25 °C with continuous shaking (250 rpm) for 12 h. For CheA, the cells were induced at 37 °C for 4 h. The cells were then centrifuged at 8000 × *g* for 8 min and resuspended in TBS (50 mM Tris, pH 7.5, 150 mM NaCl) buffer followed by sonication. The supernatants were clarified with two rounds of centrifugations (9000 × *g*, 15 min; 40,000 × *g*, 40 min) and then purified using GSTrap columns (5 mL; GE Healthcare) and an Akta Prime FPLC system (GE Healthcare). Supernatants were applied to 5 mL GSTrap columns pre-washed with 10 column volumes of TBS buffer. Protein-bound columns were washed with at least 15 column volumes of TBS buffer, and GST-tagged proteins were eluted with using 10 mL of glutathione elution buffer (GEB; 50 mM Tris, 5 mM glutathione, pH 8). To remove the GST tag, the purified proteins were cleaved using PreScission protease, as specified by the manufacture (Amersham Biosciences). The GSTrap column purification was then repeated. This time, the flow-through was collected and concentrated to ~ 5 mL using a cellulose ultrafiltration membrane (Millipore) in an Amicon ultrafiltration cell. Finally, the purified proteins were dialyzed in TKMD buffer [50 mM Tris, pH 8.0, 50 mM KCl, 5 mM $MgCl_2$, 0.1 mM dithiothreitol (DTT)] and aliquots are stored at –80 °C.
7. We found that when CheA and CheW are added simultaneously to chemoreceptor containing membranes that they preferentially form a CheA-CheW complex and do not bind the chemoreceptors. This can be avoided by adding CheA to receptor complexes first [33].

8. CheV is a two-domain protein with an N-terminal CheW-like domain and a C-terminal two-component receiver domain. In addition to coupling CheA to the receptor, CheV can also be phosphorylated on a conserved aspartate in the presence of phosphorylated CheA (CheAp). For this reason, it may be desirable to add either CheV or phosphorylated CheV (CheVp) to the membranes [34]. CheVp can be phosphorylated in vitro using acetyl phosphate [34].
9. Chemotaxis proteins are mixed with isolated membranes such that the chemotaxis protein to receptor ratios match the known in vivo concentrations in *B. subtilis* cells [32]. The total number of chemoreceptors per cell in *B. subtilis* is approximately 60,000. The cellular ratio of chemoreceptor dimers to CheA homodimers in *B. subtilis* is roughly 23 per CheA dimer [35].

Acknowledgment

This work was supported by National Institutes of Health Grant GM054365.

References

1. Adler J (1966) Chemotaxis in bacteria. Science 153:708–716
2. Rao CV, Glekas GD, Ordal GW (2008) The three adaptation systems of *Bacillus subtilis* chemotaxis. Trends Microbiol 16:480–487
3. Rao CV, Ordal GW (2009) The molecular basis of excitation and adaptation during chemotactic sensory transduction in bacteria. Contrib Microbiol 16:33–64
4. Glekas GD, Mulhern BJ, Kroc A, Duelfer KA, Lei V et al (2012) The *Bacillus subtilis* chemoreceptor McpC senses multiple ligands using two discrete mechanisms. J Biol Chem 287:39412–39418
5. Garrity LF, Ordal GW (1997) Activation of the CheA kinase by asparagine in *Bacillus subtilis* chemotaxis. Microbiology 143:2945–2951
6. Bischoff DS, Bourret RB, Kirsch ML, Ordal GW (1993) Purification and characterization of *Bacillus subtilis* CheY. Biochemistry 32:9256–9261
7. Bischoff DS, Ordal GW (1991) Sequence and characterization of *Bacillus subtilis* CheB, a homolog of *Escherichia coli* CheY, and its role in a different mechanism of chemotaxis. J Biol Chem 266:12301–12305
8. Borkovich KA, Kaplan N, Hess JF, Simon MI (1989) Transmembrane signal transduction in bacterial chemotaxis involves ligand-dependent activation of phosphate group transfer. Proc Natl Acad Sci U S A 86:1208–1212
9. Lai RZ, Manson JM, Bormans AF, Draheim RR, Nguyen NT et al (2005) Cooperative signaling among bacterial chemoreceptors. Biochemistry 44:14298–14307
10. Li M, Hazelbauer GL (2011) Core unit of chemotaxis signaling complexes. Proc Natl Acad Sci U S A 108:9390–9395
11. Swain KE, Gonzalez MA, Falke JJ (2009) Engineered socket study of signaling through a four-helix bundle: evidence for a yin-yang mechanism in the kinase control module of the aspartate receptor. Biochemistry 48:9266–9277
12. Bornhorst JA, Falke JJ (2000) Attractant regulation of the aspartate receptor-kinase complex: limited cooperative interactions between receptors and effects of the receptor modification state. Biochemistry 39:9486–9493
13. Borkovich KA, Simon MI (1990) The dynamics of protein phosphorylation in bacterial chemotaxis. Cell 63:1339–1348
14. Hazelbauer GL, Falke JJ, Parkinson JS (2008) Bacterial chemoreceptors: high-performance signaling in networked arrays. Trends Biochem Sci 33:9–19. https://doi.org/10.1016/j.tibs.2007.09.014

15. Borkovich KA, Alex LA, Simon MI (1992) Attenuation of sensory receptor signaling by covalent modification. Proc Natl Acad Sci U S A 89:6756–6760
16. Dunten P, Koshland DE Jr (1991) Tuning the responsiveness of a sensory receptor via covalent modification. J Biol Chem 266:1491–1496
17. Springer MS, Goy MF, Adler J (1977) Sensory transduction in *Escherichia coli*: a requirement for methionine in sensory adaptation. Proc Natl Acad Sci U S A 74:183–187
18. Sourjik V, Wingreen NS (2012) Responding to chemical gradients: bacterial chemotaxis. Curr Opin Cell Biol 24:262–268
19. Zimmer MA, Tiu J, Collins MA, Ordal GW (2000) Selective methylation changes on the *Bacillus subtilis* chemotaxis receptor McpB promote adaptation. J Biol Chem 275:24264–24272
20. Glekas GD, Cates JR, Cohen TM, Rao CV, Ordal GW (2011) Site-specific methylation in *Bacillus subtilis* chemotaxis: effect of covalent modifications to the chemotaxis receptor McpB. Microbiology 157:56–65
21. Walukiewicz HE, Tohidifar P, Ordal GW, Rao CV (2014) Interactions among the three adaptation systems of *Bacillus subtilis* chemotaxis as revealed by an in vitro receptor-kinase assay. Mol Microbiol 93:1104–1118
22. Glekas GD, Plutz MJ, Walukiewicz HE, Allen GM, Rao CV et al (2012) Elucidation of the multiple roles of CheD in *Bacillus subtilis* chemotaxis. Mol Microbiol 86:743–756
23. Muff TJ, Ordal GW (2007) The CheC phosphatase regulates chemotactic adaptation through CheD. J Biol Chem 282:34120–34128
24. Chao X, Muff TJ, Park SY, Zhang S, Pollard AM et al (2006) A receptor-modifying deamidase in complex with a signaling phosphatase reveals reciprocal regulation. Cell 124:561–571
25. Yuan W, Glekas GD, Allen GM, Walukiewicz HE, Rao CV et al (2012) The importance of the interaction of CheD with CheC and the chemoreceptors compared to its enzymatic activity during chemotaxis in *Bacillus subtilis*. PLoS One 7:e50689
26. Mantsala P, Zalkin H (1980) Extracellular and membrane-bound proteases from *Bacillus subtilis*. J Bacteriol 141:493–501
27. Tawa P, Stewart RC (1994) Kinetics of CheA autophosphorylation and dephosphorylation reactions. Biochemistry 33:7917–7924
28. Ullah AH, Ordal GW (1981) Purification and characterization of methyl-accepting chemotaxis protein methyltransferase I in *Bacillus subtilis*. Biochem J 199:795–805
29. Tan S (2001) A modular polycistronic expression system for overexpressing protein complexes in *Escherichia coli*. Protein Expr Purif 21:224–234
30. Rabkin SD, Richardson CC (1988) Initiation of DNA replication at cloned origins of bacteriophage T7. J Mol Biol 204:903–916
31. Conrad B, Savchenko RS, Breves R, Hofemeister J (1996) A T7 promoter-specific, inducible protein expression system for *Bacillus subtilis*. Mol Gen Genet 250:230–236
32. Cannistraro VJ, Glekas GD, Rao CV, Ordal GW (2011) Cellular stoichiometry of the chemotaxis proteins in *Bacillus subtilis*. J Bacteriol 193:3220–3227
33. Cardozo MJ, Massazza DA, Parkinson JS, Studdert CA (2010) Disruption of chemoreceptor signalling arrays by high levels of CheW, the receptor-kinase coupling protein. Mol Microbiol 75:1171–1181
34. Karatan E, Saulmon MM, Bunn MW, Ordal GW (2001) Phosphorylation of the response regulator CheV is required for adaptation to attractants during *Bacillus subtilis* chemotaxis. J Biol Chem 276:43618–43626
35. Li M, Hazelbauer GL (2004) Cellular stoichiometry of the components of the chemotaxis signaling complex. J Bacteriol 186:3687–3694

Chapter 11

FRET Analysis of the Chemotaxis Pathway Response

Anja Paulick and Victor Sourjik

Abstract

Most motile bacteria follow spatial gradients of chemical and physical stimuli in their environment. In *Escherichia coli* and other bacteria, the best characterized chemotaxis is in gradients of amino acids or sugars, but other physiological stimuli such as pH, osmolarity, redox potentials, and temperature are also known to elicit tactic responses. These multiple environmental stimuli are integrated and processed within a highly sophisticated chemotaxis network to generate coordinated chemotaxis behavior, which features high sensitivity, a wide dynamic range, and robustness against variations in background stimulation, protein levels, and temperature. Although early studies relied on behavioral analyses to characterize chemotactic responses in vivo, or on biochemical assays to study the pathway in vitro, we describe here a method to directly measure the intracellular pathway response using Förster resonance energy transfer (FRET). In *E. coli*, the most commonly used form of the FRET assay relies on the interaction between the phosphorylated response regulator CheY and its phosphatase CheZ to quantify activity of the histidine kinase CheA. We further describe a FRET assay for *Bacillus subtilis*, which employs CheY and the motor-associated phosphatase FliY as a FRET pair. In particular, we highlight the use of FRET to quantify pathway properties, including signal amplification, dynamic range, and kinetics of adaptation.

Key words FRET, CheA, Kinase activity, Real-time assay, Chemotaxis, *Escherichia coli*, *Bacillus subtilis*, Bacteria

1 Introduction

Peritrichously flagellated bacteria, such as *E. coli*, are propelled by several lateral flagella that are powered by their proton motive force [1]. Depending on the direction of flagellar rotation, counterclockwise (CCW) or clockwise (CW), swimming *E. coli* cells perform either a straight run, typically 2 s in duration, or a brief tumble to reorientate the cell body, respectively [2, 3]. The equilibrium between these two modes of swimming is controlled by the chemotaxis signaling network [4–6], which responds to temporal changes in environmental conditions. Sensing and processing of attractant and repellent stimuli are performed by sensory arrays that consist of five different types of chemoreceptors, an adaptor

Michael D. Manson (ed.), *Bacterial Chemosensing: Methods and Protocols*, Methods in Molecular Biology, vol. 1729, https://doi.org/10.1007/978-1-4939-7577-8_11,

protein CheW, and the histidine kinase CheA [7–11]. The chemotaxis network further contains the phosphatase CheZ and the methylation-dependent adaptation system that is composed of the methylesterase CheB and the methyltransferase CheR. The methylation system robustly maintains optimal levels of pathway activity independent of the background stimulation. It also provides the short-term memory that is required for temporal sampling of the environment by swimming cells. Attractant binding to the periplasmic domain of chemoreceptors inhibits the autophosphorylation activity of the kinase CheA, thus reducing the phosphorylation of the response regulator CheY. Conversely, repellent binding increases CheA activity and the amount of phosphorylated CheY (CheY~P), which in its phosphorylated state binds to the flagellar motor and changes the direction of rotation from CCW to CW to induce tumbles. CheY~P is subsequently dephosphorylated by CheZ to terminate the signal.

In the absence of external stimuli, CheA has an intermediate level of activity. In order to recover from an initial stimulation or to regain sensitivity in the presence of persistent stimuli, chemoreceptors undergo CheR-dependent methylation and CheB-dependent demethylation on four or five specific glutamyl residues. CheB preferentially acts on active chemoreceptors that activate CheA, whereas CheR preferentially methylates chemoreceptors whose ability to stimulate CheA activity is suppressed. Because methylation increases CheA kinase activity and decreases receptor sensitivity to attractants, the methylation system provides negative feedback that compensates, with an intrinsic delay, the chemoeffector-induced changes in the pathway activity.

In *E. coli* and other bacteria, sensory complexes are organized in large arrays within the inner membrane. These arrays are composed of hexagonally packed trimers of receptor dimers that are connected by CheA and CheW [7, 12]. *E. coli* possesses two types of chemoreceptors that differ in their levels of expression. The high abundance (or major) receptors Tar and Tsr sense, among other chemical compounds, aspartate and serine, respectively, as attractants, but they can also detect other stimuli, such as pH, temperature, and osmolarity. The low abundance (or minor) receptors, Trg, Tap, and Aer, mediate chemotaxis toward sugars, dipeptides, and redox potential, respectively [13–19], but they can also detect nucleotides or the quorum-sensing autoinducer-2 [20–22]. Apart from their different copy numbers, major and minor receptors differ in their mode of ligand binding, with Tar and Tsr binding their primary ligands directly and Trg and Tap binding their ligands indirectly through a periplasmic binding protein. In general, chemotaxis to indirectly binding ligands exhibits lower sensitivity and a narrower dynamic range of concentrations to which cells are responsive [23].

A number of studies have suggested that cooperative interactions between receptors in clusters lead to integration and amplification of the chemotactic signals perceived by different receptors, thus allowing response sensitivity to approach the physical limit of detection [24–33]. These cooperative interactions can be described using the Monod–Wyman–Changeux (MWC) model, which assumes that receptors within clusters operate in tightly coupled allosteric complexes (teams), with all receptors within one team switching synchronously between the active and inactive states [29, 31, 34]. At subsaturating levels of stimulation, the sign and the magnitude of the response of mixed receptor complexes are determined by the net change in stimulus strength [23, 35].

A striking feature of the chemotaxis system is the high precision of its adaptation over a wide range of ligand concentrations, which is achieved by the integral feedback that is provided by the adaptation system [36–38]. Precise adaptation fails at high ligand concentrations because of saturation of the methylation sites on the receptors [23, 36–41]. Notably, such imprecision might have a physiological relevance by preventing bacteria from swimming toward high toxic concentrations of amino acids that inhibit growth [40].

Whereas chemotaxis in gradients of chemical ligands is typically unidirectional, with cells swimming up an attractant gradient or down the repellent gradient, taxis toward temperature, osmolarity or pH is often bidirectional, with cells getting repelled by both extremes [42–45]. Mechanisms of bidirectional taxis are not well understood, but it is thought that the interplay between different chemoreceptors may provide a general mechanism of finding an optimal intermediate point within a gradient [43, 46–48].

Although both the core of the chemotaxis system, which consists of CheA, CheY, CheW, CheR, and CheB, as well as the overall strategy of chemotaxis, is conserved among bacteria, many chemotaxis systems are more complex than that of *E. coli*. The gram-positive bacterium *B. subtilis*, one of the best studied chemotaxis models besides *E. coli* [49], has not only transmembrane but also soluble chemoreceptors [50], and it possesses two phosphatases, FliY and CheC, with the former being associated with the flagellar motor [51, 52]. Furthermore, *B. subtilis* employs three adaptation systems: the methylation system containing CheR and CheB, the CheC-CheD-CheY system and the CheV system. The chemotactic response in *B. subtilis* is inverted compared to *E. coli*, with binding of an attractant activating CheA and increasing the level of CheY~P.

Whereas numerous studies of bacterial chemotaxis monitor bacterial swimming behavior [2, 53] or flagellar motor rotation [1, 54–56], an assay that allows direct quantification of the activity of the intracellular chemotaxis pathway has been developed recently [57, 58]. This assay uses Förster (fluorescence) resonance energy transfer (FRET). In *E. coli*, this assay relies on the phosphorylation-dependent interaction between CheY and CheZ fused to yellow and

cyan fluorescent proteins (CheY-YFP and CheZ-CFP, respectively). In *B. subtilis*, the assay instead utilizes the interaction between CheY and FliY [59]. In the following, we will describe how such stimulation-dependent FRET assay can be applied to quantify signal processing by the chemotaxis pathway.

In the last few decades, fusions of the proteins of interest to a fluorescent protein have been used extensively to visualize real-time protein behavior within cells, including their localization, mobility, and the dynamics of their interactions [60]. Among these applications, FRET, which detects the spatial proximity of two fluorescent proteins within the nanometer range [61], has become a popular technique to monitor protein interactions or large conformational changes in proteins within living cells in a nondestructive manner [61–63]. FRET relies on the nonradiative energy transfer from an excited donor to a nearby acceptor fluorophore through long-range dipole–dipole interactions, which require an overlap of the emission spectrum of the donor with the excitation spectrum of the acceptor (Fig. 1a). Energy transfer results in a decrease of the donor and an increase of the acceptor emission and also shortens the lifetime of the excited donor fluorophore. FRET efficiency varies as the inverse sixth power of the distance between the two fluorophores and can be quantified as

$$E_{\mathrm{FRET}} = \frac{r_0^6}{r^6 + r_0^6} \tag{1}$$

with r_0 the Förster radius describing the characteristic distance at which the energy transfer is half-maximal. The value of r_0 can be calculated based on the spectral overlap between the fluorophores, their relative orientation within the complex, and the optical properties of the surrounding media [64]. For the CFP/YFP pair with randomized orientation, r_0 is around 49 Å, which is similar to the size of GFP [57, 65]. Because of the very steep decline in E_{FRET} with distance, the energy transfer becomes negligible if fluorescent proteins are further apart than 100 Å, ensuring specificity of the detection. Although CFP and YFP remain the most commonly used fluorophores for FRET in bacteria, the increasing variety of engineered fluorescent proteins with improved optical properties has been developed in recent years to improve brightness, photostability, and spectral overlap for FRET [63, 66].

FRET can be detected using a number of different light microscopy techniques: (a) fluorescence lifetime imaging microscopy (FLIM), which is based on the measurement of the lifetime of the excited donor, which decreases in presence of energy transfer [67]; (b) acceptor photobleaching, which unquenches fluorescence of the donor [60, 68]; (c) ratio imaging of the acceptor to donor fluorescence, which relies on the fact that energy transfer enhances (sensitizes) the acceptor emission and quenches the donor emission [58, 61, 62].

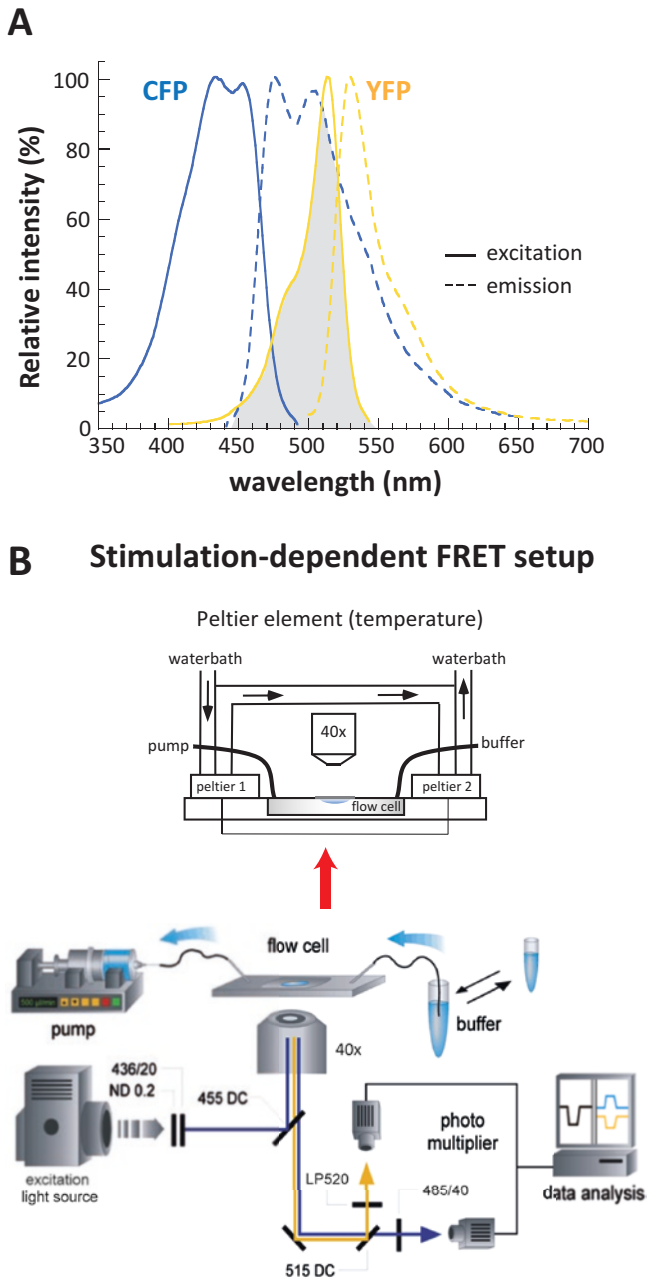

Fig. 1 Principle and experimental setup for FRET measurements. (**a**) Excitation and emission spectra of CFP and YFP. The excitation (solid line) and emission (dashed line) spectra of the donor CFP (blue) and the acceptor YFP (yellow) are shown. FRET relies on the nonradiative energy transfer through long-range dipole interactions from an excited donor to a nearby acceptor. In order for FRET to occur, the emission spectrum of the donor must overlap with the absorption spectra of the acceptor chromophore (area shaded in grey), meaning that the energy of the excited donor is suitable to excite the acceptor. Moreover, both fluorophores must be in close proximity (less than 100 Å), and their lifetime must be of sufficient duration. (**b**) Schematic representation of the microscopy setup used for stimulation-dependent FRET measurements, adapted from [60]. Details of the setup are indicated; see text for the explanation. Upper image: optional temperature control was performed by mounting the flow chamber into a custom-built thermocouple with Peltier elements connected to a water bath

For the *E. coli* chemotaxis pathway, ratio imaging has been used to quantify stimulus-induced changes in the activity of CheA kinase, using the phosphorylation-dependent interactions between CheZ-CFP and CheY-YFP as a readout [58]. Because the rate of CheY~P dephosphorylation is determined by the concentration of the CheZ/CheY~P complex, relative CheA kinase activity can be directly inferred from the relative concentration of this complex, assuming rapid equilibration of the CheY~P levels upon stimulation. Thus, changes in the kinase activity upon stepwise stimulation of *E. coli* cells that express the CheZ/CheY~P FRET pair can be followed as changes in the ratio of the YFP/CFP fluorescence (Figs. 1b and 2a–c). Such stimulation-dependent FRET measurement allows recording not only of the amplitude but also of the time-course of the pathway response, as well as the time course of the subsequent adaptation. In *B. subtilis*, the analogous experiment can be performed by following the concentration of the FliY/CheY~P complex (Fig. 2d). As noted above, whereas stimulation by attractant results in inhibition of the CheA activity, and therefore a lower YFP/CFP ratio in *E. coli* (Fig. 2b–c), the CheA activity and the YFP/CFP ratio in *B. subtilis* increase (Fig. 2e, f).

2 Materials

2.1 Strains

Escherichia coli K12 strains derived from RP437 [69] and deleted for native *cheY* and *cheZ* were routinely used for FRET experiments [57]. The FRET pair CheY-YFP and CheZ-CFP was expressed from a bicistronic construct under control of a P_{trc} promoter inducible by isopropyl-D-thiogalactopyranoside (IPTG) [70]. Chemoreceptors were expressed under control of a P_{nahG} promoter inducible by sodium salicylate [31, 58, 71]. The FRET reporter strain for *B. subtilis* 168 [72, 73] was constructed by genomic integration of the bicistronic construct *cfp-fliY-cheY-yfp*, inducible by IPTG, at the *amyE* locus [59].

2.2 Media and Buffers

1. For growth of *E. coli* and *B. subtilis* we used lysogeny broth (LB; 10 g/L Bacto tryptone, 5 g/L Bacto yeast extract, 5 g/L NaCl) or tryptone broth (TB; 10 g/L Bacto tryptone, 5 g/L NaCl) supplemented with antibiotic(s): 15 μg/mL chloramphenicol, 100 μg/mL ampicillin, 100 μg/mL spectinomycin) and inducer(s) (50 μM IPTG, 200 μM IPTG for *B. subtilis*, and 1 or 2 μM sodium salicylate).
2. Measurements were performed in tethering buffer (10 mM KPO_4, 0.1 mM EDTA, 1 μM methionine, 10 mM DL-lactate, pH 7).

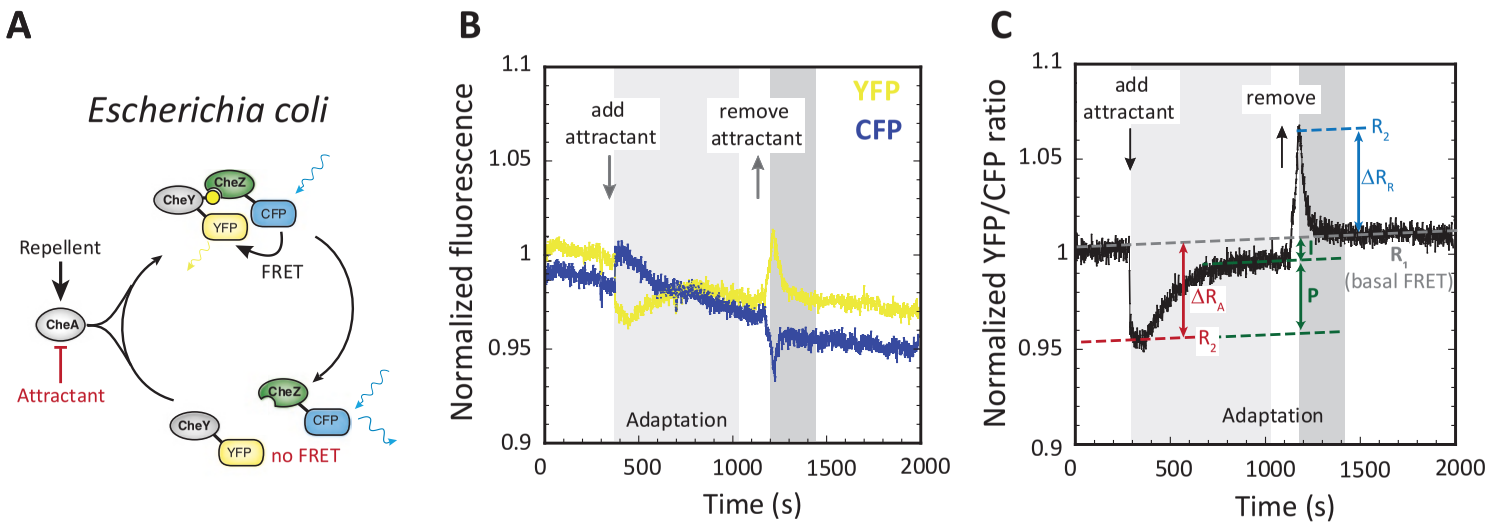

Fig. 2 FRET measurements of the pathway activity in *E. coli* and *B. subtilis*. (**a**–**c**) Stimulation-dependent FRET measurements of the kinase activity in *E. coli*. To monitor the relative CheA kinase activity, FRET measurements were performed for the CheZ-CFP/CheY-YFP pair (**a**). Addition of attractant reduces the CheA activity, and therefore the relative amount of CheZ/CheY~P complexes, leading to reduced energy transfer between CFP and YFP. As a result, the CFP intensity decreases and the YFP intensity increases (**b**). Changes in FRET can be best monitored using the YFP/CFP ratio (**c**), which is less noisy than the signals in individual channels (**b**). For clarity this ratio was normalized to its value at the beginning of the measurements. The initial stimulation is followed by methylation-dependent adaptation that returns the activity back to the steady state level. Removal of attractant upon adaptation (or addition of repellent) has an activating effect on receptors, followed again by adaptation that is mediated by receptor demethylation. (**d**–**f**) Stimulation-dependent FRET measurements of the kinase activity in *B. subtilis*. FRET measurements were performed for the CFP-FliY/CheY-YFP pair (**d**). In contrast to *E. coli*, the CheA activity in *B. subtilis* increases upon attractant stimulation, resulting in an increased concentration of FliY/CheY~P complexes and an increased FRET signal. Removal of an attractant after adaptation is complete results in a decreased FRET signal. As for *E. coli*, although the response is visible in individual channels (**e**), the normalized YFP/CFP ratio is less noisy and thus more convenient to use (**f**). The following values of the YFP/CFP ratio are relevant for calculation of the FRET value, and other response parameters are illustrated in (**c** and **f**): ratio in buffer-adapted cells (grey dashed line; R_1); response to attractant (red; R_A); response to repellent (blue; R_R); ratio after stimulation (R_2); basal ratio in absence of FRET (upon stimulation with saturating stimulus that inhibits kinase; R_0); as well as precision (P) and imprecision (I) of adaptation

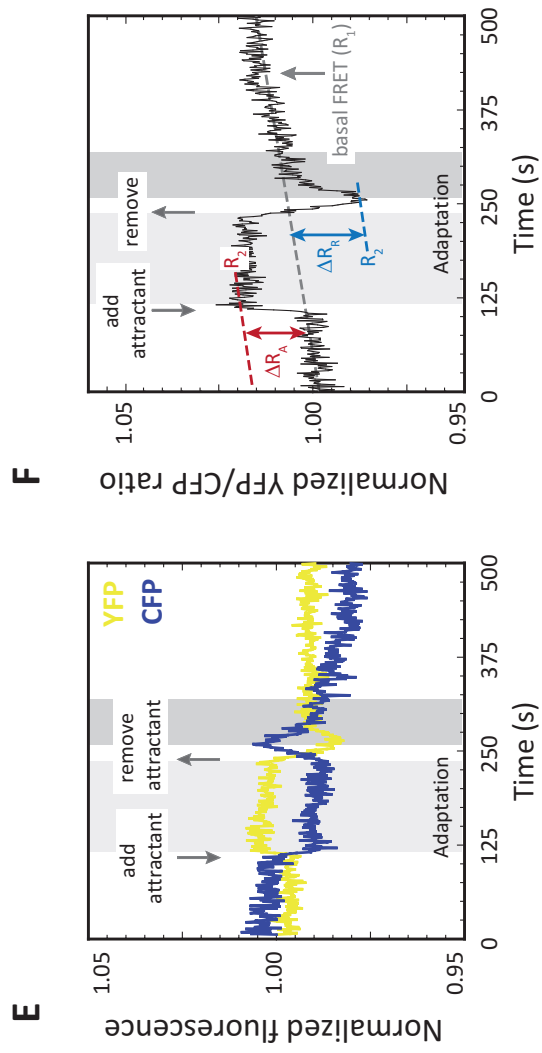

Fig. 2 (continued)

2.3 Instrumentation Setup for Stimulation-Dependent FRET Measurements

1. A schematic view of a typical microscope setup used for stimulation-dependent FRET is shown in Fig. 1b. It comprises a custom-modified fluorescence microscope (e.g., Axio Imager Z1 microscope, Zeiss) equipped with a 40×/0.75 EC Plan-Neofluar lens.
2. Samples were excited at 436/20 nm through a 455 nm dichroic mirror by a light source (120 W EXFO X-Cite® 120 lamp) attenuated with neutral density filters.
3. Fluorescence was continuously monitored in the yellow (e.g., 520 LP) and cyan (e.g., D485/40) channels using Peltier-cooled photon-counting photomultipliers (PMTs, H7421-40, Hamamatsu) with high quantum efficiency and low noise.
4. Photon counts were recorded by a PCI-6034 counting board, controlled by a custom written acquisition code (LabView7, National Instruments), with 0.2–1.0 s integration time, depending on the experiment.
5. Data were analyzed using KaleidaGraph (Synergy Software) or Excel (Microsoft).

3 Methods

Stimulation was performed by immobilizing cells in a flow chamber with 50 μL volume [74] that was kept under a constant flow of tethering buffer to ensure aeration and to add or remove attractants or repellents. The flow was maintained at a rate of 0.3 to 1 mL/min by a syringe pump (Harvard Apparatus 22). At the flow rate of 1 mL/min, the buffer in the chamber was replaced in about 6 s [58]. To mount the top and bottom coverslips (diameter 12 and 25 mm, respectively) to the flow chamber, we used Apiezon M and L Grease (or Apiezon T grease for temperature experiments). Temperature control in the flow chamber was achieved by a custom-built thermocouple/Peltier element connected to a water bath (Fig. 1b, upper panel).

3.1 Preparation of Cells and Stimulation-Dependent FRET Measurements

1. Strains were cultivated aerobically from a frozen stock at 30 °C in a shaking culture (275 rpm) overnight (~14 h) in TB (for *E. coli*) or LB (for *B. subtilis*) supplemented with the appropriate antibiotics. Cells were diluted 1:100 in 10 mL TB or LB supplemented with the appropriate antibiotics and inducer and grown aerobically at 34 °C in shaking conditions at 275 rpm. For expression of *cheY*-YFP and *cheZ*-CFP from pVS88 (pTrc99a; Amp^R) we added 50 μM IPTG, for chemoreceptor expression (pKG110 derivatives; Cam^R) we added salicylate in concentrations ranging from 0 to 10 μM [23, 31, 40, 57, 75–77]. To reduce variation in receptor ratios, cells were harvested

between OD_{600} 0.58 and 0.61, unless otherwise stated [43]. Expression of CFP-*fliY*-*cheY*-YFP in *B. subtilis* was induced with 200 μM IPTG, and the culture was grown to OD_{600} = 0.4 [59].

2. Cells were harvested by centrifugation (10 min at 5000 × *g*) and resuspended in 10 mL tethering buffer. *E. coli* cells could be kept for 30 min at 4 °C, but *B. subtilis* cells were used immediately after resuspension.
3. A coverslip (round, diameter 12 mm) was coated with poly-L-lysine and left for 20 min, then carefully washed with ddH_2O. For stimulus-dependent FRET, a dense monolayer of cells on the coverslip is optimal for measurements; thus cells were concentrated by centrifugation of 1.2 mL of cell suspension (6000 × *g*, 3 min) and resuspension of the pellet in 30–50 μL tethering buffer. This suspension was placed on the coated coverslip and incubated at room temperature (RT) for 20 min.
4. Before mounting the cell-coated coverslip, the flow chamber was flushed with buffer. To that end, the cover slips and/or the edges of the flow chamber were coated with grease and the upper and lower cover slips were mounted on the flow chamber. (*See* Chapter 18in this volume for a detailed description of mounting cover slips on the flow chamber.) The edges of the cover slip were sealed by carefully exerting pressure with tweezers. After rinsing the flow chamber with buffer at 0.5 mL/min flow rate for 1 min, the empty upper (small) cover slip was removed, and the edges of the flow chamber were again coated with grease. The cell-coated coverslip was mounted on the flow chamber that was filled with tethering buffer, and the flow was immediately started to remove unattached cells and provide cells with oxygen. The flow chamber was kept under constant flow of tethering buffer by a syringe pump, with the flow rate depending on the type of experiment. We routinely use 0.3 mL/min for temperature experiments, 0.5 mL/min for dose-response measurements, and 1.5 mL/min for response kinetics measurements; for more details ([23, 57, 58, 60, 77]; *see* **Note 1**). A field containing a monolayer of 300–500 cells was then visually selected in a phase-contrast or brightfield imaging mode. Prior to the experiments, cells were usually allowed to adapt to a constant flow of buffer for about 10 min.
5. Experiments were initiated by turning on the fluorescence illumination, PMTs, and the data acquisition code in LabVIEW7. To avoid saturation of the PMTs while at the same time achieving a high signal to noise ratio, fluorescence illumination needs to be adjusted by neutral density filters so that emission light

intensity at the field of view recorded by PMTs is around 5×10^5.

6. Fluorescence intensity signals are continuously recorded, and flow is maintained at all times except for briefly stoppage of the syringe pump to stimulate cells by transferring the inlet tubing to the ligand solution of interest (*see* **Note 1**). During transfer, the tubing was clamped to prevent air bubbles from entering the tube. Note that, depending on the tube length, the solution of interest takes several seconds to reach the flow chamber (*see* **Note 2**). Cells can be stimulated multiple times, and they remain responsive for at least up to 1 h ([78]; *see* **Note 3**).
7. Recorded fluorescence intensities of YFP and CFP were exported as text files from LabVIEW, and the FRET data were analyzed using KaleidaGraph (Synergy Software) or Excel (Microsoft), as described below.

3.2 Temperature Measurements

Cells were prepared and placed into the flow chamber as described above but were adapted to buffer and the starting temperature for at least 30 min before stimulation. The flow chamber was mounted onto a water-cooled Peltier element and temperature was set using a custom-written software controlling the Peltier element board [48]. Temperature is usually stabilized within several seconds, depending on the controller setting. Note that it is necessary to calibrate the actual temperature within the flow chamber with an electronic precision thermometer.

3.3 Analysis of FRET Data

Typical FRET experiments with stimulation by saturating amounts of attractant are shown in Fig. 2b, c for *E. coli* cells expressing CheY-YFP and CheZ-CFP and Fig. 2e, f for *B. subtilis* cells expressing CFP-FliY and CheY-YFP. As formation of both complexes is phosphorylation-dependent, FRET levels reflect cellular CheA activity. In *E. coli*, the addition of saturating amounts of attractant inhibits the kinase activity, resulting in a decreased energy transfer from CFP to YFP and thus lowering the ratio of YFP to CFP fluorescence intensity (Fig. 2b, c). The relative concentration of the CheZ/CheY~P enzyme–substrate complex is reflected by the FRET value [31, 57, 58].

The amplitude of the response calculated for a given stimulus is the difference between the YFP/CFP ratio before and after the stimulus, $R_1 - R_2$, where R_1 corresponds to the ratio at steady state (in buffer) and R_2 to the ratio after stimulation (*see* **Note 4**). The YFP/CFP ratio after stimulation with a saturating amount of attractant, i.e., the baseline in the absence of the kinase activity, is denoted as R_0. The maximum change in the YFP/CFP ratio after a saturating stimulation is $\Delta R_{max} = R_1 - R_0$. The constant $\alpha = [\Delta YFP/\Delta CFP]$ denotes the absolute value of the ratio between changes in fluorescence in YFP and CFP channels due to energy

transfer. This value is specific for a given microscopy setup and depends on the respective quantum yield of YFP and CFP and the efficiency of light detection in the YFP and CFP channels [23, 31, 57, 58, 77]. Because of a gradual loss of cells during measurement as well as faster bleaching of CFP compared to YFP, there will be a drift in the YFP/CFP ratio over time. Therefore, the baseline of the measurements must be interpolated before calculating ΔR (Fig. 2c, f, dashed lines). R_0 needs to be determined for each individual experiment, by adding saturating amounts of strain-specific attractants, e.g., a combination of 100 μM MeAsp and 30 μM serine for *E. coli* wild type, 100 μM MeAsp for the Tar-only strain, and 100 μM serine for the Tsr-only strain. The removal of attractant or the addition of repellent results in an opposite response, increasing the kinase activity and thus the YFP/CFP ratio in *E. coli* (Fig. 2c).

As is apparent in Fig. 2c, the initial response is followed by a gradual adaptation that is mediated by methylation or demethylation of receptors. Because the phosphorylation and dephosphorylation of CheY is much faster than methylation-dependent adaptation (and the measurement rate), the FRET value reflects the kinase activity during the adaptation phase, also. The stimulation-dependent FRET assay thus not only provides a direct readout of the response amplitude but allows the characterization of the adaptation kinetics. It is convenient to normalize the FRET value to its prestimulus level at the beginning of the measurement. Because the amplitude in the YFP/CFP ratio (ΔR) is relatively small compared to its basal level (R), the relative kinase activity (A), which corresponds to the *FRET* (Eq. 1), can be approximated by:

$$A = \frac{\left(\Delta R_{\max} - \Delta R\right)}{\Delta R_{\max}} \tag{2}$$

The FRET value and the relative kinase activity can be obtained similarly for *B. subtilis* (Fig. 2d–f), with the difference that attractant stimulation results in an increased YFP/CFP ratio that reflects an increase in the kinase activity. Consequently, the removal of attractant results in a decreased YFP/CFP ratio followed by adaptation. The main features of the pathway response that can be obtained with stimulation-dependent FRET are described in the following section, using *E. coli* as an example.

3.4 Dose-Response Measurements

The calculated relative kinase activity was used to obtain dose–response curves (Fig. 3) by measuring the pathway response to steps of increasing concentrations of stimulus. Here, changes in the kinase activity were always determined from defined background conditions to which the cells were adapted. Ligands are removed between each step, and the cells were allowed to adapt to this background. A dose–response curve can be used to obtain: (a) the EC_{50}, which is the level of stimulation that leads to a half-maximal

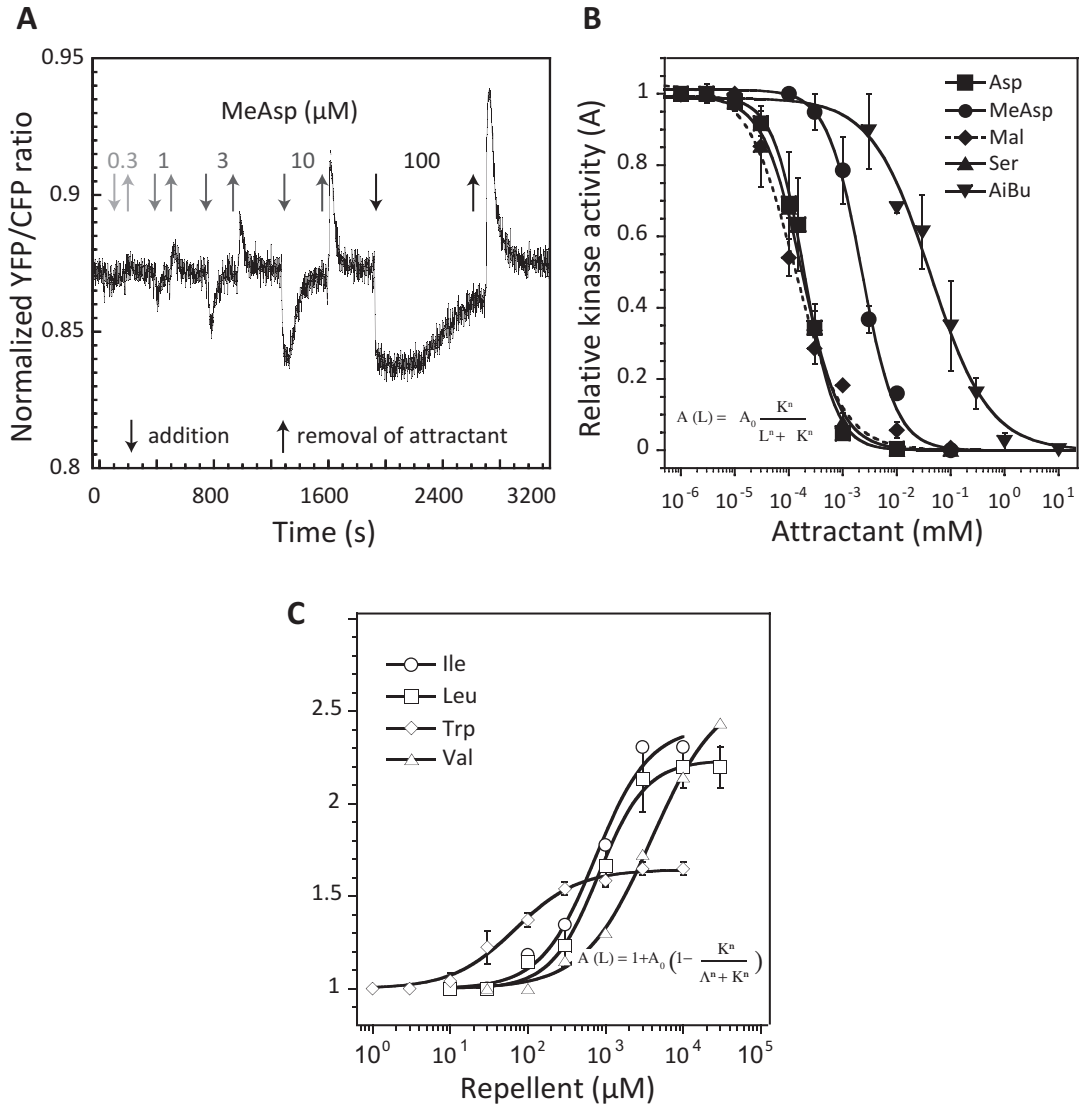

Fig. 3 Measurements of dose–response curves. (**a**) A typical dose-response measurement in which *E. coli* cells were stimulated by step-wise addition (downward pointing arrow) and subsequent removal (upward pointing arrow) of amino acid attractant (MeAsp) in a sequence of increasing concentrations up to a saturating stimulus. Cells were always allowed to equilibrate in buffer before the next stimulus. (**b**, **c**) To generate dose–response curves, the initial relative kinase activity upon stimulation with a given ligand concentration was fitted to a multisite Hill function, as depicted for attractant (**b**) or repellent (**c**) stimuli. Here L is ligand concentration; A_0 is the maximal amplitude of the response; n is the Hill coefficient, and K is EC_{50}, the stimulus concentration at the half maximal response. Data are adapted from [23, 59]

response; (b) the amplitude; and (c) the steepness (Hill coefficient) of the response. In a typical dose-response measurement, signals were recorded for 15 min in tethering buffer (or other condition) and cells were subsequently stimulated in a sequence of step-wise stimuli of increasing strength until saturation was reached, always changing back to buffer and allowing the cells to adapt before the

next stimulus (Fig. 3a). The relative kinase activity was calculated as described above, normalized to the saturating stimulus (fully inhibiting kinase activity, see above R_0). To generate dose–response curves, the relative kinase activity was fitted to a multisite Hill function, for attractants:

$$A(L) = A_0 \times \frac{K^n}{L^n + K^n} \tag{3}$$

for repellents:

$$A(L) = A_0 \times \left(1 - \frac{K^n}{L^n + K^n}\right) \tag{4}$$

where L is the ligand concentration A_0 is the maximal amplitude of the response; n is the Hill coefficient, which is a measure for the steepness of the curve; and K is EC_{50}, the stimulus concentration at the half-maximal response. Typical dose–response curves for different attractants and repellents are shown in Fig. 3b, c, respectively (adapted from [23, 59]). Differences between the EC_{50} values for individual ligands reflect different ligand specificities and copy numbers of receptors, as well as the extent of allosteric signal amplification by receptor clusters [23, 31, 58].

3.5 Adaptation Kinetics, Dynamic Range and Response Sensitivity

The FRET assay can also be applied to study the properties of methylation-dependent adaptation [39, 40, 75, 79]. In *E. coli*, CheR-mediated methylation of inactive receptors increases the activity of receptor-associated CheA, thus offsetting the initial inhibition of receptors by attractants. In FRET measurements, this is reflected by the recovery of the YFP/CFP ratio back to the baseline (Fig. 2b). The rate of this recovery (i.e., the adaptation rate) can be derived from the half-time of adaptation ($\tau_{1/2}$), which is the time needed for the kinase activity to recover to 50% of its adapted state after stimulation [75]. Another important feature is the precision of adaptation (P), describing how precise the recovery of the relative kinase activity is after stimulation to its prestimulus level (Fig. 2c). Conversely, the imprecision of adaptation (I) is the difference between the adapted activity in presence of stimulus and in buffer. Both values can be determined from the FRET measurements [39, 40, 75].

The dynamic range of the adaptive response describes the range of stimulus strength (e.g., ligand concentration) in which the cells can discriminate stimuli of varying strengths. To characterize the dynamic range of the adaptive response to chemical attractants, cells were stimulated by sequential addition of increasing ligand concentrations, raising the concentration approximately threefold each time (Fig. 4a, b). Before each subsequent stimulus, cells were allowed to adapt to the current ambient ligand concentration, in contrast to the dose-response measurements (Fig. 3a),

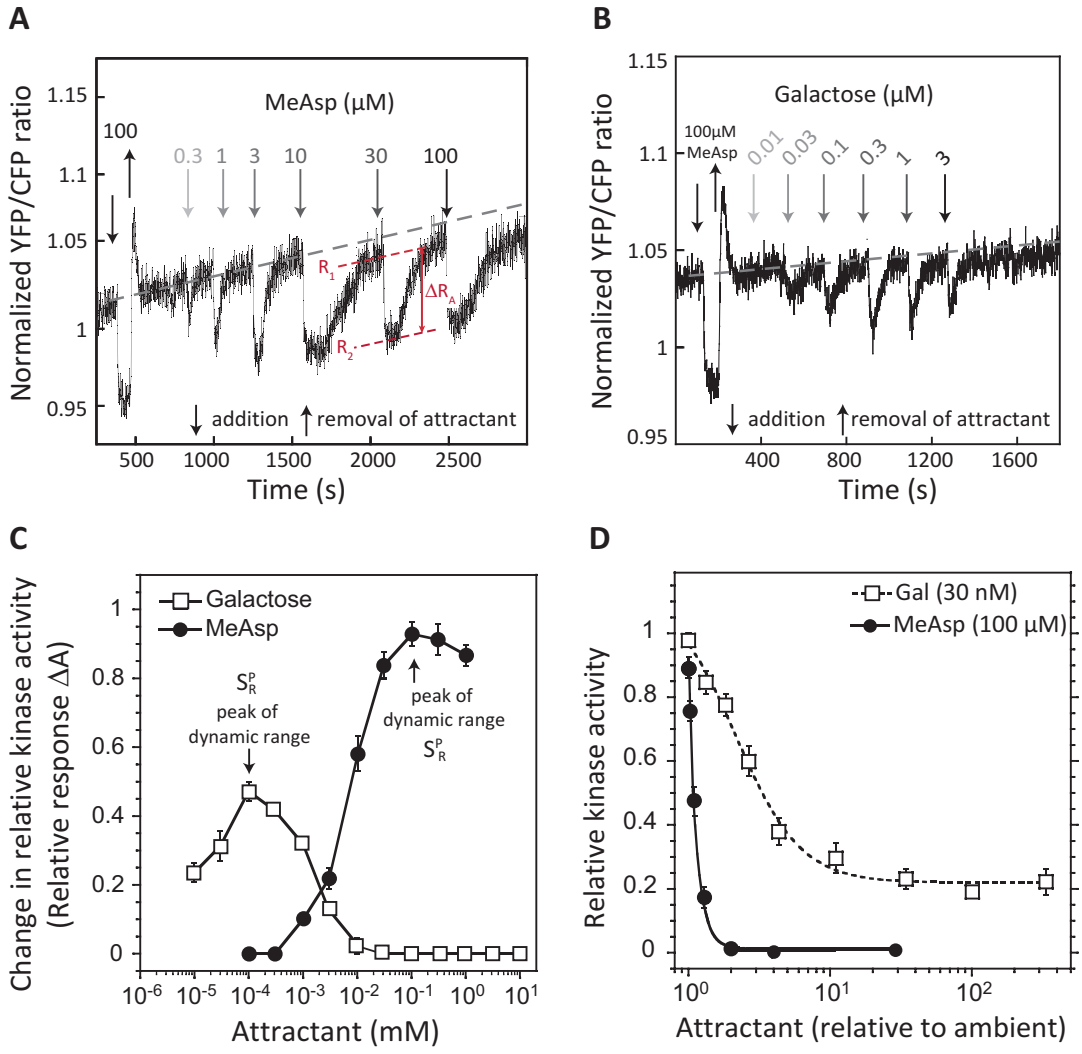

Fig. 4 Measurements of the dynamic range of the adaptive response. (**a**, **b**) Typical dynamic range measurements for attractants that bind receptors directly (**a**) or indirectly (**b**). Cells were stimulated by a sequential addition of the indicated concentrations of attractants, increasing approximately threefold between consecutive steps. Cells were always allowed to adapt to each current ambient ligand concentration before the next stimulus. The amplitude of the response (ΔR, highlighted in red) is calculated as the difference between the adapted YFP/CFP ratio at the given ambient concentration (R_1) and the ratio immediately after the stimulation (R_2). (**c**) Corresponding relative response amplitudes plotted as a function of the final ligand concentration after the stimulus. Arrows indicate the peak of the response, where the response sensitivity, the fractional change in the kinase activity divided by the fractional change in ligand concentration, is maximal. (**d**) Detailed measurement of the response sensitivity at the peak of the dynamic range (S_R^P) was performed by preadapting cells to the ligand concentration corresponding to the peak and measuring the dose–response curve (downward pointing arrow, addition of ligands; and upward pointing arrow, removal of ligands). The sensitivity is given by the initial slope of the activity plotted against the final ligand concentration. Data are adapted from [23]

in which cells are not adapted to buffer between consecutive stimuli. The relative response was then evaluated as before, except that R_1 corresponds to the current adapted activity and is plotted as a function of the current ligand concentration for each response (Fig. 4c). For ligands that bind directly to the sensory domains of receptors (e.g., amino acids), we generally observe a broad dynamic range, whereas ligands that bind indirectly via periplasmic binding proteins (e.g., some sugars), are sensed in a relatively narrow dynamic range [23].

In the dynamic range of the adaptive response, FRET measurements allow one to quantify the response sensitivity (S_R), which gives a measure of how sensitively relative changes in ligand concentrations can be detected (Fig. 4d). S_R is a measure of signal amplification, also known as the gain, and is defined as the ratio between the fractional change of kinase activity ($\Delta A/A$) and the fractional change in ligand concentration ($\Delta L/L$), where A and L are the prestimulus values of adapted activity and ambient ligand concentration, respectively [23]. The maximum value of S_R can be obtained at the peak of the dynamic range (S_R^P). Experimentally, cells are preadapted to a ligand concentration near the peak of the dynamic range (100 μM MeAsp or 30 nM galactose, as shown in Fig. 4c–d, and their dose–response curves above these ambient concentrations are determined. When the data are plotted against the final ligand concentration relative to the ambient concentration [23], the initial slope of the fit to the data gives S_R^P. Note that, for adaptation-deficient cells, the response sensitivity can be determined directly from the dose–response curve as the slope of the curve around EC_{50} [31, 76, 80]. In adaptation-deficient cells, the Hill coefficient n yields a measure of the apparent receptor cooperativity.

4 Notes

1. For rapidly metabolizable chemoeffectors, such as serine, the effects of ligand depletion at low ligand concentrations can be minimized by performing the measurements at a high flow rate (0.5 mL/min or even higher), which allows the liquid in the flow chamber to exchange within few seconds.
2. For preparation of the flow chamber, it is important to keep in mind that, besides the flow rate, the length of the tube determines the time until the chemicals reach the flow chamber. We recommend calibrating the time needed for the liquid to be exchanged using a fluorescent solution.
3. Cells usually remain responsive for 1 h or even longer in the flow chamber, but it is advisable to periodically control the amplitude of the response to a saturating stimulus to ensure that it remains unchanged.

4. Although changes in FRET can be observed in individual fluorescence channels (CFP or YFP), using the ratio (R) of the YFP to CFP signal greatly reduces measurement noise by eliminating noise sources that affect both channels (e.g., fluctuations in the illumination intensity). Nevertheless, when testing responses to general physical or chemical stimuli such as temperature, pH or osmolarity that may differentially affect individual fluorescent proteins and thus change the YFP/CFP ratio, it is important to inspect fluorescence intensity in individual channels in order to ensure that they exhibit opposite changes upon stimulation, as is expected for FRET. Moreover, a strain deleted for CheA provides a useful negative control in this case.

References

1. Berg HC (2003) The rotary motor of bacterial flagella. Annu Rev Biochem 72:19–54
2. Berg HC, Brown DA (1972) Chemotaxis in *Escherichia coli* analysed by three-dimensional tracking. Nature 239:500–504
3. Macnab RM, Koshland DE Jr (1972) The gradient-sensing mechanism in bacterial chemotaxis. Proc Natl Acad Sci U S A 69:2509–2512
4. Sourjik V (2004) Receptor clustering and signal processing in *E. coli* chemotaxis. Trends Microbiol 12:569–576
5. Sourjik V, Wingreen NS (2012) Responding to chemical gradients: bacterial chemotaxis. Curr Opin Cell Biol 24:262–268
6. Wadhams GH, Armitage JP (2004) Making sense of it all: bacterial chemotaxis. Nat Rev Mol Cell Biol 5:1024–1037
7. Briegel A, Li X, Bilwes AM, Hughes KT, Jensen GJ et al (2012) Bacterial chemoreceptor arrays are hexagonally packed trimers of receptor dimers networked by rings of kinase and coupling proteins. Proc Natl Acad Sci U S A 109:3766–3771
8. Liu J, Hu B, Morado DR, Jani S, Manson MD et al (2012) Molecular architecture of chemoreceptor arrays revealed by cryoelectron tomography of *Escherichia coli* minicells. Proc Natl Acad Sci U S A 109:E1481–E1488
9. Boldog T, Grimme S, Li M, Sligar SG, Hazelbauer GL (2006) Nanodiscs separate chemoreceptor oligomeric states and reveal their signaling properties. Proc Natl Acad Sci U S A 103:11509–11514
10. Shimizu TS, Le Novere N, Levin MD, Beavil AJ, Sutton BJ et al (2000) Molecular model of a lattice of signalling proteins involved in bacterial chemotaxis. Nat Cell Biol 2:792–796
11. Studdert CA, Parkinson JS (2007) *In vivo* crosslinking methods for analyzing the assembly and architecture of chemoreceptor arrays. Methods Enzymol 423:414–431
12. Gegner JA, Graham DR, Roth AF, Dahlquist FW (1992) Assembly of an MCP receptor, CheW, and kinase CheA complex in the bacterial chemotaxis signal transduction pathway. Cell 70:975–982
13. Adler J, Hazelbauer GL, Dahl MM (1973) Chemotaxis toward sugars in *Escherichia coli*. J Bacteriol 115:824–847
14. Kondoh H, Ball CB, Adler J (1979) Identification of a methyl-accepting chemotaxis protein for the ribose and galactose chemoreceptors of *Escherichia coli*. Proc Natl Acad Sci U S A 76:260–264
15. Mesibov R, Adler J (1972) Chemotaxis toward amino acids in *Escherichia coli*. J Bacteriol 112:315–326
16. Springer MS, Goy MF, Adler J (1979) Protein methylation in behavioural control mechanisms and in signal transduction. Nature 280:279–284
17. Hazelbauer GL, Engstrom P (1980) Parallel pathways for transduction of chemotactic signals in *Escherichia coli*. Nature 283:98–100
18. Manson MD, Blank V, Brade G, Higgins CF (1986) Peptide chemotaxis in *E. coli* involves the Tap signal transducer and the dipeptide permease. Nature 321:253–256
19. Rebbapragada A, Johnson MS, Harding GP, Zuccarelli AJ, Fletcher HM et al (1997) The Aer protein and the serine chemoreceptor Tsr independently sense intracellular energy levels and transduce oxygen, redox, and energy signals for *Escherichia coli* behavior. Proc Natl Acad Sci U S A 94:10541–10546

20. Hegde M, Englert DL, Schrock S, Cohn WB, Vogt C et al. (2011) Chemotaxis to the quorum-sensing signal AI-2 requires the Tsr chemoreceptor and the periplasmic LsrB AI-2-binding protein. J Bacteriol 193:768–773
21. Laganenka L, Colin R, Sourjik V (2016) Chemotaxis towards autoinducer 2 mediates autoaggregation in *Escherichia coli*. Nat Commun 7:12984
22. Liu X, Wood PL, Parales JV, Parales RE (2009) Chemotaxis to pyrimidines and identification of a cytosine chemoreceptor in Pseudomonas putida. J Bacteriol 191:2909–2916
23. Neumann S, Hansen CH, Wingreen NS, Sourjik V (2010) Differences in signalling by directly and indirectly binding ligands in bacterial chemotaxis. EMBO J 29:3484–3495
24. Bray D, Levin MD, Morton-Firth CJ (1998) Receptor clustering as a cellular mechanism to control sensitivity. Nature 393:85–88. https://doi.org/10.1038/30018
25. Ames P, Studdert CA, Reiser RH, Parkinson JS (2002) Collaborative signaling by mixed chemoreceptor teams in *Escherichia coli*. Proc Natl Acad Sci U S A 99:7060–7065
26. Briegel A, Ladinsky MS, Oikonomou C, Jones CW, Harris MJ et al (2014) Structure of bacterial cytoplasmic chemoreceptor arrays and implications for chemotactic signaling. elife 3:e02151
27. Maddock JR, Shapiro L (1993) Polar location of the chemoreceptor complex in the *Escherichia coli* cell. Science 259:1717–1723
28. Sourjik V, Berg HC (2000) Localization of components of the chemotaxis machinery of *Escherichia coli* using fluorescent protein fusions. Mol Microbiol 37:740–751
29. Mello BA, Tu Y (2005) An allosteric model for heterogeneous receptor complexes: understanding bacterial chemotaxis responses to multiple stimuli. Proc Natl Acad Sci U S A 102:17354–17359
30. Kalinin Y, Neumann S, Sourjik V, Wu M (2010) Responses of *Escherichia coli* bacteria to two opposing chemoattractant gradients depend on the chemoreceptor ratio. J Bacteriol 192:1796–1800
31. Sourjik V, Berg HC (2004) Functional interactions between receptors in bacterial chemotaxis. Nature 428:437–441
32. Berg HC, Purcell EM (1977) Physics of chemoreception. Biophys J 20:193–219
33. Bialek W, Setayeshgar S (2005) Physical limits to biochemical signaling. Proc Natl Acad Sci U S A 102:10040–10045
34. Monod J, Wyman J, Changeux JP (1965) On the nature of allosteric transitions - a plausible model. J Mol Biol 12:88–118
35. Adler J, Tso WW (1974) "Decision"-making in bacteria: chemotactic response of *Escherichia coli* to conflicting stimuli. Science 184:1292–1294
36. Alon U, Surette MG, Barkai N, Leibler S (1999) Robustness in bacterial chemotaxis. Nature 397:168–171
37. Barkai N, Leibler S (1997) Robustness in simple biochemical networks. Nature 387:913–917
38. Yi TM, Huang Y, Simon MI, Doyle J (2000) Robust perfect adaptation in bacterial chemotaxis through integral feedback control. Proc Natl Acad Sci U S A 97:4649–4653
39. Meir Y, Jakovljevic V, Oleksiuk O, Sourjik V, Wingreen NS (2010) Precision and kinetics of adaptation in bacterial chemotaxis. Biophys J 99:2766–2774. https://doi.org/10.1016/j.bpj.2010.08.051
40. Neumann S, Vladimirov N, Krembel AK, Wingreen NS, Sourjik V (2014) Imprecision of adaptation in *Escherichia coli* chemotaxis. PLoS One 9(1):e84904
41. Vladimirov N, Lovdok L, Lebiedz D, Sourjik V (2008) Dependence of bacterial chemotaxis on gradient shape and adaptation rate. PLoS Computl Biol 4(12):e1000242
42. Adler J, Li C, Boileau AJ, Qi Y, Kung C (1988) Osmotaxis in *Escherichia coli*. Cold Spring Harb Symp Quant Biol 53(Pt 1):19–22
43. Yang Y, Sourjik V (2012) Opposite responses by different chemoreceptors set a tunable reference point in *Escherichia coli* pH taxis. Mol Microbiol 86:1482–1489
44. Maeda K, Imae Y (1979) Thermosensory transduction in *Escherichia coli:* inhibition of the thermoresponse by L-serine. Proc Natl Acad Sci U S A 76:91–95
45. Maeda K, Imae Y, Shioi JI, Oosawa F (1976) Effect of temperature on motility and chemotaxis of *Escherichia coli*. J Bacteriol 127:1039–1046
46. Yoney A, Salman H (2015) Precision and variability in bacterial temperature sensing. Biophys J 108:2427–2436
47. Hu B, Tu Y (2013) Precision sensing by two opposing gradient sensors: how does *Escherichia coli* find its preferred pH level? Biophys J 105:276–285
48. Paulick A, Jakovljevic V, Zhang S, Erickstad M, Groisman A et al (2017) Mechanism of bidi-

rectional thermotaxis in *Escherichia coli*. eLife 6. https://doi.org/10.7554/eLife.26607.

49. Szurmant H, Ordal GW (2004) Diversity in chemotaxis mechanisms among the bacteria and archaea. Mirobiol Mol Biol Rev 68:301–319
50. Cannistraro VJ, Glekas GD, Rao CV, Ordal GW (2011) Cellular stoichiometry of the chemotaxis proteins in *Bacillus subtilis*. J Bacteriol 193(13):3220–3227
51. Szurmant H, Bunn MW, Cannistraro VJ, Ordal GW (2003) *Bacillus subtilis* hydrolyzes CheY-P at the location of its action, the flagellar switch. J Biol Chem 278:48611–48616
52. Szurmant H, Muff TJ, Ordal GW (2004) *Bacillus subtilis* CheC and FliY are members of a novel class of CheY-P-hydrolyzing proteins in the chemotactic signal transduction cascade. J Biol Chem 279:21787–21792
53. Larsen SH, Reader RW, Kort EN, Tso WW, Adler J (1974) Change in direction of flagellar rotation is the basis of the chemotactic response in *Escherichia coli*. Nature 249:74–77
54. Chen X, Berg HC (2000) Torque-speed relationship of the flagellar rotary motor of *Escherichia coli*. Biophys J 78:1036–1041
55. Silverman M, Simon M (1974) Flagellar rotation and the mechanism of bacterial motility. Nature 249:73–74
56. Sowa Y, Berry RM (2008) Bacterial flagellar motor. Q Rev Biophys 41:103–132
57. Sourjik V, Berg HC (2002) Binding of the *Escherichia coli* response regulator CheY to its target measured in vivo by fluorescence resonance energy transfer. Proc Natl Acad Sci U S A 99:12669–12674
58. Sourjik V, Berg HC (2002) Receptor sensitivity in bacterial chemotaxis. Proc Natl Acad Sci U S A 99:123–127
59. Yang Y, M Pollard A, Hofler C, Poschet G, Wirtz M et al (2015) Relation between chemotaxis and consumption of amino acids in bacteria. Mol Microbiol 96:1272–1282
60. Kentner D, Sourjik V (2009) Dynamic map of protein interactions in the *Escherichia coli* chemotaxis pathway. Mol Syst Biol 5:238
61. Wouters FS, Verveer PJ, Bastiaens PI (2001) Imaging biochemistry inside cells. Trends Cell Biol 11:203–211
62. Miyawaki A, Tsien RY (2000) Monitoring protein conformations and interactions by fluorescence resonance energy transfer between mutants of green fluorescent protein. Methods Enzymol 327:472–500
63. Lam AJ, St-Pierre F, Gong Y, Marshall JD, Cranfill PJ et al (2012) Improving FRET dynamic range with bright green and red fluorescent proteins. Nat Methods 9:1005–1012
64. Selvin PR (1995) Fluorescence resonance energy transfer. Methods Enzymol 246:300–334
65. Tsien RY (1998) The green fluorescent protein. Annu Rev Biochem 67:509–544
66. Hochreiter B, Garcia AP, Schmid JA (2015) Fluorescent proteins as genetically encoded FRET biosensors in life sciences. Sensors 15:26281–26341
67. Wallrabe H, Periasamy A (2005) Imaging protein molecules using FRET and FLIM microscopy. Curr Opin Biotechnol 16:19–27
68. Van Munster EB, Kremers GJ, Adjobo-Hermans MJ, Gadella TW Jr (2005) Fluorescence resonance energy transfer (FRET) measurement by gradual acceptor photobleaching. J Microsc 218(Pt 3):253–262
69. Parkinson JS, Houts SE (1982) Isolation and behavior of *Escherichia coli* deletion mutants lacking chemotaxis functions. J Bacteriol 151(1):106–113
70. Amann E, Ochs B, Abel KJ (1988) Tightly regulated *tac* promoter vectors useful for the expression of unfused and fused proteins in *Escherichia coli*. Gene 69:301–315
71. Yen KM (1991) Construction of cloning cartridges for development of expression vectors in gram-negative bacteria. J Bacteriol 173:5328–5335
72. Burkholder PR, Giles NH Jr (1947) Induced biochemical mutations in *Bacillus subtilis*. Am J Bot 34:345–348
73. Kunst F, Ogasawara N, Moszer I, Albertini AM, Alloni G et al (1997) The complete genome sequence of the gram-positive bacterium *Bacillus subtilis*. Nature 390:249–256
74. Berg HC, Block SM (1984) A miniature flow cell designed for rapid exchange of media under high-power microscope objectives. J Gen Microbiol 130:2915–2920
75. Krembel AK, Neumann S, Sourjik V (2015) Universal response-adaptation relation in bacterial chemotaxis. J Bacteriol 197:307–313
76. Oleksiuk O, Jakovljevic V, Vladimirov N, Carvalho R, Paster E et al (2011) Thermal robustness of signaling in bacterial chemotaxis. Cell 145:312–321
77. Sourjik V, Vaknin A, Shimizu TS, Berg HC (2007) *In vivo* measurement by FRET of pathway activity in bacterial chemotaxis. Methods Enzymol 423:365–391
78. Lan G, Sartori P, Neumann S, Sourjik V, Tu Y (2012) The energy-speed-accuracy tradeoff in sensory adaptation. Nat Phys 8:422–428

79. Lazova MD, Ahmed T, Bellomo D, Stocker R, Shimizu TS (2011) Response rescaling in bacterial chemotaxis. Proc Natl Acad Sci U S A 108:13870–13875

80. Endres RG, Oleksiuk O, Hansen CH, Meir Y, Sourjik V et al (2008) Variable sizes of *Escherichia coli* chemoreceptor signaling teams. Mol Syst Biol 4:211

Chapter 12

Monitoring Two-Component Sensor Kinases with a Chemotaxis Signal Readout

Run-Zhi Lai and John S. Parkinson

Abstract

Bacteria use two-component signal transduction systems to elicit adaptive responses to environmental changes. The simplest of these systems comprises a transmembrane sensor with histidine kinase activity and its cytoplasmic response regulator partner. Stimulus-response studies of two-component signaling systems typically employ expression reporters, such as β-galactosidase, that operate with relatively slow kinetics and low precision. In this chapter, we illustrate a new strategy for directly measuring the signaling activities of two-component sensor kinases in vivo. Our method exploits recent work that defines the recognition determinants for sensor-response regulator signaling transactions, which enabled us to couple histidine kinases to a FRET-based assay that uses signaling components of the *E. coli* chemotaxis system. We demonstrate the approach with NarX, a nitrate/nitrite sensor kinase, but the method should be applicable to other two-component sensor kinases.

Key words Förster resonance energy transfer (FRET), Histidine kinase, Response regulator, Protein interaction specificity, Crosstalk

1 Introduction

Bacteria sense, respond, and adapt to a wide range of environments, stressors, and growth conditions. Sensing and processing these signals accurately and quickly is critical to bacterial survival, proliferation and pathogenicity. Two-component signal transduction systems (TCSs) are the most prevalent systems used by eubacteria and archaea for these purposes [1]. Although they have diverse sensory domains, TCSs share a common biochemical signaling mechanism in which a histidine kinase (HK) donates phosphoryl groups to its cognate response regulator (RR) to produce an adaptive response, usually a change in gene expression. Studies from several groups have shown that the specificity of HK-RR interaction is determined by 4–5 highly conserved residues on the HK-RR interaction interface [2–6].

Michael D. Manson (ed.), *Bacterial Chemosensing: Methods and Protocols*, Methods in Molecular Biology, vol. 1729,
https://doi.org/10.1007/978-1-4939-7577-8_12,

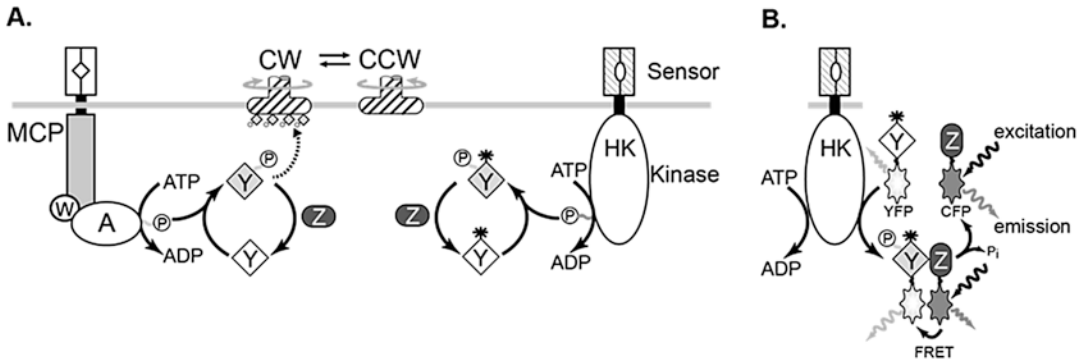

Fig. 1 (**a**) *E. coli* chemotaxis pathway and its application to TCS studies. CheW (W) couples the HK CheA (A) to chemoreceptor (MCP) control. CheY (Y) obtains phosphoryl groups from CheA; CheY-P is dephosphorylated by phosphatase CheZ (Z). CheY-P biases the flagellar rotation from counterclockwise (CCW) to clockwise (CW). CheY can be reconfigured (asterisk-Y) to be phosphorylated by other HKs. (**b**). Once a reconfigured CheY (asterisk-Y) is phosphorylated by a histidine kinase (HK), its phosphorylation-dependent interaction with CheZ is monitored by the FRET interaction between CFP and YFP. FRET signal changes are detected as intensity changes in the CFP and YFP emissions

Most RRs are transcription factors (e.g., 25 of 32 in *E. coli*) [7], so stimulus-response studies of two-component signaling systems have typically employed expression reporters, such as β-galactosidase, that operate with relatively slow kinetics and low precision. In contrast, an assay developed for in vivo studies of *E. coli* chemoreceptor signaling complexes, based on Förster resonance energy transfer (FRET), provides fast and accurate measures of CheA kinase activity, a type II histidine autokinase. The FRET assay reports on the ratio of phosphorylated to unphosphorylated forms of CheY, a well-characterized RR in the *E. coli* chemotaxis system [8, 9].

To adapt the chemotaxis FRET assay to the study of other histidine kinases, we reconfigured CheY into a signaling partner for a particular noncognate HK (Fig. 1). Here, we use NarX, a nitrate/nitrite sensor, to illustrate the approach. The basic strategy can easily be extended to study other TCS HKs.

2 Materials

2.1 Plasmids and Strains

1. Plasmids: pRZ48, a derivative of pACYC184 that confers chloramphenicol resistance and expresses NarX under the inducible control of sodium salicylate; pRZ55, a derivative of pVS88 [9] that confers ampicillin resistance and expresses fusion proteins CheY-YFP and CheZ-CFP under the inducible control of IPTG. The *cheY* coding region of pRZ55 carries mutations, introduced with a site-directed mutagenesis protocol as described in Chapters 8 and 14, that produce three amino acid replacements in CheY: T16M/M17L/I20G.

2. Strains: UU2980, a derivative of *E. coli* K12 strain RP437 [10], with relevant genotype: [(*narX-narL*)Δ4213 (*narP*)Δ4212 (*narQ*)Δ4563 (*cheA-cheZ*)Δ1214 (*tsr*)Δ5547 (*trg*)Δ4543 (*aer*)Δ1].

2.2 Instrumentation

1. A flow cell was fabricated to the specifications of Berg and Block [11], with the center opening changed from the original square design to a circular one (Fig. 2c).
2. FRET measurement instrumentation is essentially as described in Chapter 11 (Fig. 2a). Briefly, a Zeiss Axio Observer inverted microscope is fitted with a 75-W xenon source, a neutral density filter (1000-fold attenuation), an excitation bandpass filter (~460 nm), a dichroic mirror (458 nm cutoff), a second beam splitter (515 nm cutoff), and two photon-counting photomultipliers (PMTs), one behind a CFP emission bandpass filter, the other behind a YFP emission bandpass filter.

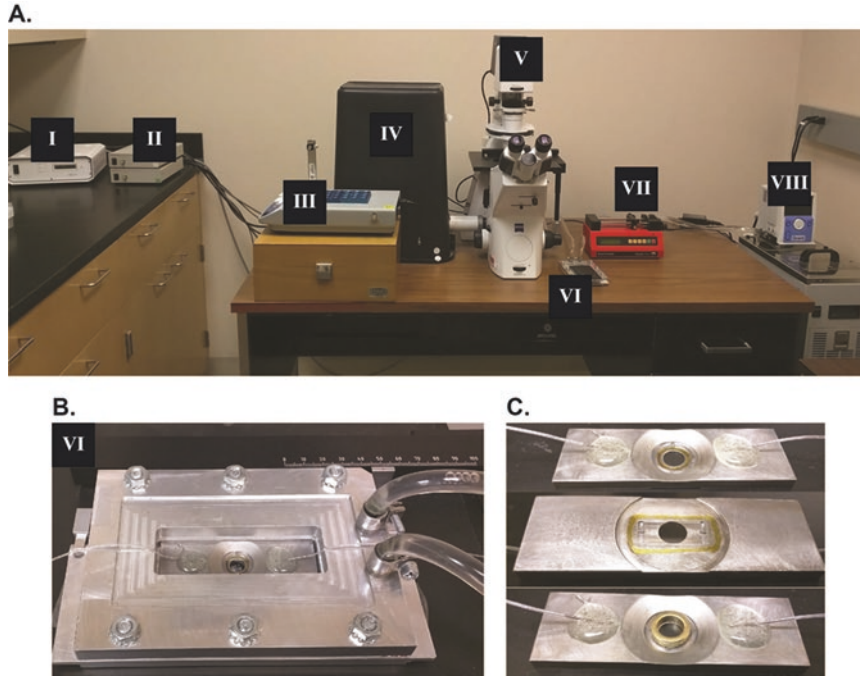

Fig. 2 (**a**) A FRET instrumentation setup. From left to right, instruments are: I—power supply for xenon lamp; II—power supplies for PMTs; III—heating block; IV—photon shield for PMTs (there are two PMTs inside); V—inverted Zeiss microscope; VI—temperature controlled chamber; VII—syringe pump; and VIII—circulating water bath. (**b**) A close-up view of the temperature-controlled chamber (IV). The chamber is mounted to the microscope (V) stage and connected to the circulating water bath (VIII) on the right-side via tubing. There is an assembled flow cell placed in the center of the chamber. (**c**) Three views of an assembled flow cell. From top to bottom, it shows a top view of a flow cell with a 12 mm top coverslip assembled with grease; a bottom view of a flow cell with a 25 mm bottom coverslip assembled with grease; and a top view of a flow cell with a 12 mm top coverslip assembled with a donut-shaped magnetic ring

The photomultipliers are connected to a data acquisition device and computer software (LabView—National Instruments) that records photon counts in 1-s bins (*see* **Note 1**).

3. A circulating water bath that can maintain a temperature at 30 °C.
4. An aluminum chamber with hollow center to maintain flow cell temperature is connected to the circulating water bath through flexible water-tight tubing (Fig. 2b).
5. A heating block for holding stimulant and buffer solutions at 30 °C.
6. A syringe pump with 50–100 mL capacity. (We use a Fusion 200 syringe pump from Chemyx Inc.).
7. A tabletop cell culture centrifuge for spinning down cells in 10 mL volume.
8. A tabletop high speed centrifuge for spinning down cells in 1.5 mL Eppendorf tubes.

2.3 Solutions and Reagents

1. Tryptone broth (T broth): 10 g/L tryptone, 5 g/L NaCl.
2. Antibiotics: ampicillin stock 100 mg/mL and chloramphenicol stock 25 mg/mL.
3. Tethering buffer: 10 mM potassium phosphate (pH 7.0), 0.1 mM K-EDTA, 10 mM sodium lactate (*see* **Note 2**).
4. Poly-L-lysine 0.1% (w/v).
5. Apiezon H grease (*see* **Note 3**).

3 Methods

3.1 Identifying Response Regulator Residues that Determine the Interaction Specificity Between a Histidine Kinase of Interest and Its Cognate Response Regulator

1. Align the CheY amino acid sequence with that of the target histidine kinase's cognate response regulator. In this example, we align the CheY sequence with the NarL and NarP sequences (Fig. 3a). This step can be performed with various multiple sequence alignment tools. We used Clustal Omega (http://www.ebi.ac.uk/Tools/msa/clustalo/).
2. Introduce amino acid replacements at CheY residues T16, M17, and I20, based on the sequence alignment, using a site-specific mutagenesis protocol for the *cheY* gene. In the case of NarX, the replacements in CheY were T16M/M17L/I20G (*see* **Note 4**).

3.2 Construct an E. coli Host Strain for the Assay

1. To reduce background noise from crosstalk, the entire *E. coli* chemotaxis system should be deleted from the strain background. In addition, if the target histidine kinase is encoded by *E. coli*, that histidine kinase gene and its cognate response regulator gene need to be deleted from the chromosome.

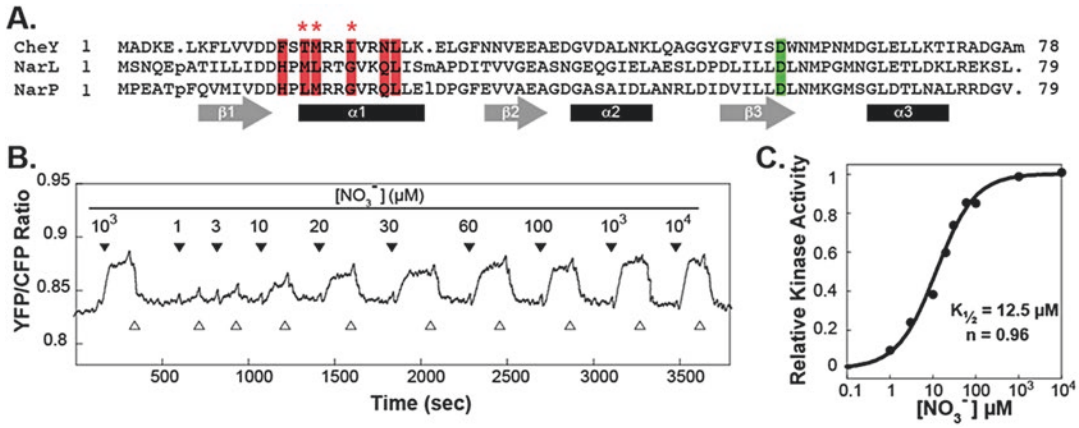

Fig. 3 (**a**) Sequence alignment of CheY with NarL and NarP, both of which are cognate RRs to NarX, a sensor HK. Important residues for HK-RR specificity are highlighted in red. Phospho-accepting residues are highlighted in green. Asterisk-labeled residues in CheY are the ones that determine HK-RR specificity and that were altered in CheY. (**b**) Reconfigured CheY was used to assess NarX in the FRET assay. NarX kinase activity increases, indicated by the increase in YFP/CFP ratio, with higher nitrate concentration. The addition and removal of nitrate stimuli are shown with black and white triangles, respectively. (**c**) Data from (**b**) fitted to a Hill equation, which yields the apparent affinity of NarX to nitrate (response $K_{½}$) and the Hill coefficient (n) of that dose response

We constructed a strain (UU2980) that has the chemotaxis genes and the two genes for nitrate/nitrite histidine kinases (*narX, narQ*) and response regulators (*narL, narP*) deleted. (*See* Subheading 2.1 for detailed genotype; *see* **Note 5**).

3.3 Prepare Poly-L-lysine-Coated Coverslips (See Note 6)

1. Clean 12 mm diameter round coverslips sequentially with distilled water, ethanol (75%), and then distilled water to wash off residual ethanol. Air-dry the coverslips before coating with poly-L-lysine.
2. Place 20 μL 0.1% (w/v) poly-L-lysine solution on the center of a cleaned coverslip, let sit for 20–30 min.
3. Remove the poly-L-lysine solution from the coverslip with a pipette.
4. Wash the coverslip three times with ~100 μL distilled water to remove excess poly-L-lysine.
5. Air-dry the coverslips.

3.4 Bacterial Culture and Sample Preparation

1. Transform a suitable host strain (e.g., UU2980) with both a histidine kinase-expressing plasmid (e.g., pRZ48) and a compatible plasmid expressing mutant CheY-YFP and wild-type CheZ-CFP (e.g., pRZ55).
2. Pick a few single colonies of the transformants to grow an overnight culture in T broth with 50 μg/mL ampicillin and 12.5 μg/mL chloramphenicol at 30 °C.

3. Dilute the overnight culture 1:100 to start a 10 mL T broth culture with 50 μg/mL ampicillin, 12.5 μg/mL chloramphenicol, and proper amount inducers (Here, we use 50 μM IPTG and 1.2 μM sodium salicylate).
4. Grow the culture at 30 °C with shaking for about 6 h to OD_{600} ~ 0.5.
5. While the cells are growing, turn on the water bath for the temperature controlled stage and the heating block for solutions.
6. Collect cells by centrifugation in a 10 mL sterile disposable culture tube using a tabletop centrifuge. Spin at ~1000 RCF for 5 min, wash cells with 5 mL tethering buffer twice, and then resuspend cells in the original volume of tethering buffer.
7. Keep cells on ice or in a refrigerator for 30–60 min to allow cell growth and protein synthesis to cease.
8. Spin down 1.5 mL cells in a 1.5 mL Eppendorf tube at 8000 rpm (~6000 RCF) for 3 min, decant the supernatant, and resuspend the pellet in 50 μL fresh tethering buffer (total volume is about 100 μL).
9. Place 50 μL of the cell suspension on the center of a poly-L-lysine-coated coverslip and let sit at room temp for 5–10 min.

3.5 Assemble Flow Chamber and Prepare Microscope for FRET Measurement

1. While cells are adhering to the coverslip, turn on the xenon lamp, the power supply for the PMTs (but do NOT turn on the PMTs), and the computer.
2. Use a 3-mL syringe and a blunt-end needle to place a ring of Apiezon H grease on the bottom of the flow cell, around the edge of the circular recess.
3. Place a clean 25 mm round coverslip to cover the bottom recess in the flow cell, gently tap the coverslip around the grease ring with forceps to secure the seal, then flip the flow cell over.
4. Apply a thin layer of grease to the lip of the circular recess in the center of the flow cell where the 12 mm cell-sample coverslip will sit. (*See* Chapter 18 in this volume for a detailed explanation.)
5. Put the feeding tube's silicon tube end into tethering buffer, and use a syringe with a 22-G blunt-end needle to draw tethering buffer through the tube.
6. Connect the other end (the thin end) of the feeding tube to one end of the flow cell, allow tethering buffer to fill the flow cell until a dome of buffer forms, clamp the feeding tube on the silicon tube part of the feeding tube. Connect the other end of the flow cell to a syringe pump with tubing.

7. Place the coverslip with cells onto the flow cell, let it sit on top of the dome of tethering buffer in the middle of the chamber with the cell-fixed side facing down, unclamp the feeding tube, start the pump, and adjust the flow rate as needed. We use 1 mL/min. While tethering buffer flows through the flow cell, align the top coverslip with the chamber and gently tap on the edge to seal. Ideally, the flow will suck down the coverslip to seal the flow chamber. Some gentle taps may be needed to make the seal tight (*see* **Note 7**).
8. Visually check that the flow cell is tightly sealed, then place it into the temperature controlled chamber, which should be placed on the microscope stage.

3.6 Assessing the Signaling Properties of the Histidine Kinase with FRET

1. Turn on the microscope, find a field of view with a single layer of cells (not too dense, but one that fills the entire field of view with a monolayer). Turn off the visible light source of the microscope. Place the lid cover onto the temperature controlled stage, with the inlet and outlet tubing carefully placed in the grooves on each side.
2. Turn off room illumination light, turn on the microscope excitation light source (xenon lamp), and turn on the PMTs.
3. Switch the light path in the microscope from eyepieces to the PMTs.
4. Start the assessment process by turning on the syringe pump and start LabView program to record.
5. Assess the signaling properties of the histidine kinases by flowing through various candidate effector chemicals, typically in a tenfold concentration difference series with a buffer wash in between additions of the potential effector (Fig. 3b).
6. After testing all concentrations, save data recorded in the LabView program.
7. Analyze the FRET data using a data analysis program. We use Kaleidagraph to analyze FRET data to provide values for the half-maximal response concentration ($K_{½}$) and Hill coefficient (n) (Fig. 3c).

4 Notes

1. For FRET measurements, the data acquisition device only needs counter functionality in two channels. National Instruments offers a good selection of multichannel counters.
2. Phosphate buffer might interfere with the signaling of some histidine kinases (e.g., PhoR). In that case, a 10 mM Tris–HCl buffer (pH 7.0) can be used instead of the phosphate buffer.

3. Apiezon H grease can be difficult to dispense. We use a dry bath or a small incubator to prewarm the grease to about 40 °C, which greatly improves its workability. At lower elevations than Salt Lake City, Apiezon L grease may work better.
4. There are a number of residues that contribute to HK-RR recognition specificity (highlighted in red in Fig. 3a). However, only four residues (T16, M17, I20, and L24) are critical for the specificity [1]. Residue L24 is identical in CheY, NarL, and NarP.
5. Although TCSs play important roles for bacterial proliferation, most TCSs can be deleted without affecting the host's growth in rich medium [12].
6. An alternative method for cleaning 12-mm coverslips uses boiling distilled water. Coverslips are secured in a coverslip cage and then dropped into boiling water for 0.5–1 h. After treatment in boiling water, coverslips are rinsed with distilled water and then 200-proof ethanol to avoid water marks.
7. Because our flow cell was fabricated with stainless steel, we can use a strong 12 mm magnetic ring (donut) as an alternative for sealing the top of the flow chamber without using grease. The advantage of using a magnetic ring, instead of grease, is that it minimizes smudging caused by grease.

Acknowledgment

Our work is supported by research grant GM19559 from the National Institute of General Medical Sciences. DNA sequencing and primer synthesis were carried out by the Protein-DNA Core Facility at the University of Utah, which receives support from National Cancer Institute grant CA42014 to the Huntsman Cancer Institute.

References

1. Laub MT, Goulian M (2007) Specificity in two-component signal transduction pathways. Annu Rev Genet 41:121–145
2. Capra EJ, Perchuk BS, Skerker JM, Laub MT (2012) Adaptive mutations that prevent crosstalk enable the expansion of paralogous signaling protein families. Cell 150: 222–232
3. Skerker JM, Perchuk BS, Siryaporn A, Lubin EA, Ashenberg O et al (2008) Rewiring the specificity of two-component signal transduction systems. Cell 133:1043–1054
4. Capra EJ, Laub MT (2012) Evolution of two-component signal transduction systems. Annu Rev Microbiol 66:325–347
5. Podgornaia AI, Casino P, Marina A, Laub MT (2013) Structural basis of a rationally rewired protein-protein interface critical to bacterial signaling. Structure 21:1636–1647
6. Haldimann A, Prahalad MK, Fisher SL, Kim SK, Walsh CT et al (1996) Altered recognition mutants of the response regulator PhoB: a new genetic strategy for studying protein-protein interactions. Proc Natl Acad Sci U S A 93:14361–14366

7. Mizuno T (1997) Compilation of all genes encoding two-component phosphotransfer signal transducers in the genome of *Escherichia coli*. DNA Res 4:161–168
8. Lai RZ, Parkinson JS (2014) Functional suppression of HAMP domain signaling defects in the *E. coli* serine chemoreceptor. J Mol Biol 426:3642–3655
9. Sourjik V, Vaknin A, Shimizu TS, Berg HC (2007) In vivo measurement by FRET of pathway activity in bacterial chemotaxis. Methods Enzymol 423:365–391
10. Parkinson JS, Houts SE (1982) Isolation and behavior of *Escherichia coli* deletion mutants lacking chemotaxis functions. J Bacteriol 151:106–113
11. Berg HC, Block SM (1984) A miniature flow cell designed for rapid exchange of media under high-power microscope objectives. J Gen Microbiol 130:2915–2920
12. Oshima T, Aiba H, Masuda Y, Kanaya S, Sugiura M et al (2002) Transcriptome analysis of all two-component regulatory system mutants of *Escherichia coli* K-12. Mol Microbiol 46:281–291

Chapter 13

Analyzing Protein Domain Interactions in Chemoreceptors by In Vivo PEGylation

Kylie J. Watts and Mark S. Johnson

Abstract

The instability of some proteins can hamper in vitro studies. This is true for the membrane-bound aerotaxis receptor, Aer, which exhibits significant proteolysis during the preparation of membrane vesicles. Permeabilized cells can closely mimic in vivo conditions, maintaining the intracellular milieu and geometry of interacting domains. Here, we describe an optimized method for determining solvent accessibility in permeabilized *Escherichia coli* cells. In this method, *E. coli* expressing Aer with a series of cysteine replacements are treated with toluene and ethanol, after which a large sulfhydryl reactive probe, PEG-mal, is added. PEGylated protein is separated from un-PEGylated protein by its apparent size difference on SDS-PAGE. The extent to which each cysteine residue becomes PEGylated is then used as a measure of solvent accessibility. When a library of single-Cys replacements is mapped, regions of low accessibility can suggest interacting protein surfaces. We successfully used this method to reveal inaccessible surfaces on both the Aer PAS and HAMP domains that were then shown by disulfide cross-linking to interact.

Key words PEG-maleimide, Solvent accessibility, Toluene–ethanol, Disulfide cross-linking, Chemoreceptor, Aer, Aerotaxis, PAS domain, HAMP domain

1 Introduction

Site-directed cysteine and disulfide chemistry are important experimental aids for uncovering protein structure and dynamics [1]. Rates of disulfide bond formation between engineered cysteines can reveal proximity, dynamics, and structure, while the reactivity of cysteines toward sulfhydryl-reactive probes can inform solvent accessibility and therefore local environment. Sulfhydryl-reactive probes can be purchased commercially and include iodoacetamides, maleimides, benzylic halides, and bromomethylketones. The adducts formed are typically identified by fluorescence, which requires that the target protein be present at sufficiently high concentration for visualization. For heterogeneous populations of proteins, the protein of interest must also be separable from the others so that it can be easily identified. Separation is typically

Michael D. Manson (ed.), *Bacterial Chemosensing: Methods and Protocols*, Methods in Molecular Biology, vol. 1729, https://doi.org/10.1007/978-1-4939-7577-8_13,

performed by SDS-PAGE, but comigrating Cys-containing proteins can confound results [2]. This problem can be circumvented by using a Western blot if the cysteine-adduct exhibits a detectable shift in mobility. For small probes, detectable shifts on SDS-PAGE may be evident with low molecular weight proteins [3], but for higher molecular weight proteins, larger probes are required. The sulfhydryl reactive probe methoxypolyethylene glycol maleimide (PEG-mal) is a larger probe that can be purchased in a variety of molecular weights from 2000 to 30,000 Da. We use PEG-mal with a molecular weight of 5000 Da (Fig. 1), which shifts the apparent mobility of the target protein ~10 kDa during SDS-PAGE (Fig. 2; [4, 5]). This allows the target protein to be identified in the presence of whole cell extract by Western blot [2, 4, 5].

In our studies on the aerotaxis receptor, Aer, from *E. coli*, we sought a way to introduce PEG-mal into permeabilized cells. The impetus for this effort stemmed from the instability of Aer, which is membrane-bound and easily proteolyzed in membrane vesicles [2]. Our goal was to assess Aer under conditions that maintained the intracelluar milieu and geometry of interacting domains. Techniques for whole cell permeabilization became available in the 1970s, with the preferred treatment being toluene [6]. The first

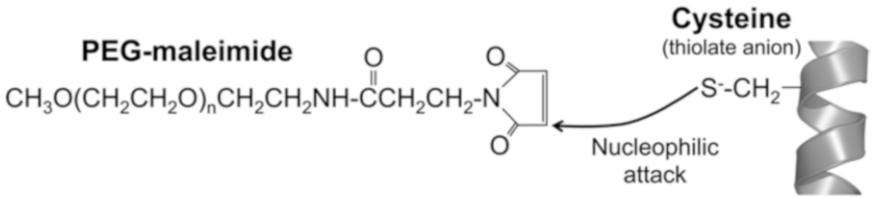

Fig. 1 The structure of the sulfhydryl reactive probe methoxypolyethylene glycol maleimide (PEG-maleimide or PEG-mal). PEG-mal undergoes nucleophilic attack from a thiolate anion to form a stable thioether bond, resulting in PEGylated protein

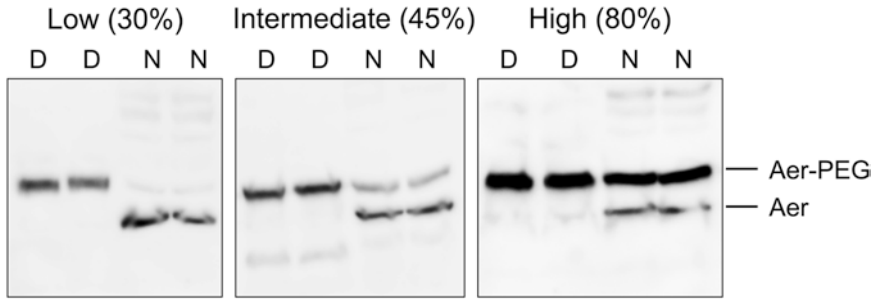

Fig. 2 Immunoblots of Aer-Cys proteins exemplifying low, intermediate and high PEGylation under native conditions (N lanes). PEGylation shifts the mobility of Aer (Aer-PEG), giving an apparent mass increase of ~10 kDa. Samples denatured without the inclusion of βME (D lanes) were PEGylated to apparent completion. *D* denatured, *N* native

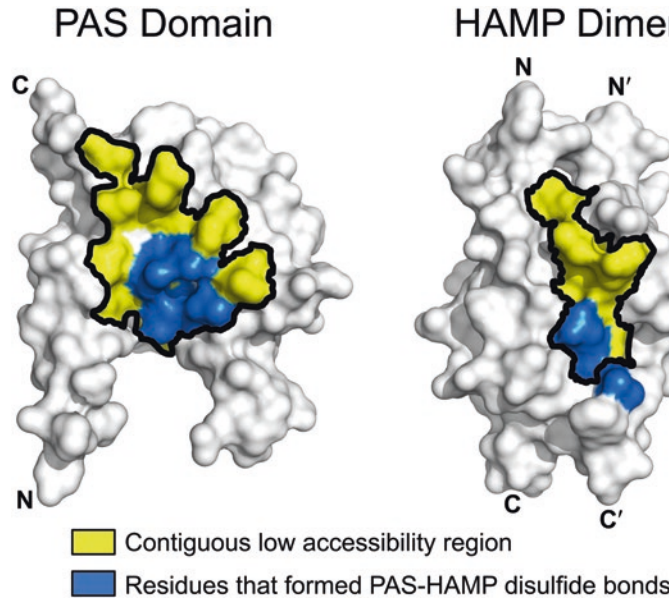

Fig. 3 Aer PAS monomer and HAMP dimer homology models showing contiguous regions of low PEGylation that indicate low solvent accessibility (yellow with black outlines). Cys residues that were substituted for the native residues shown in blue formed inter-subunit PAS-HAMP disulfide bonds, confirming that the low accessibility surfaces form a PAS-HAMP interface. Data from [4]

such studies involving chemotaxis proteins were reported in 1979, when *E. coli* and *Salmonella typhimurium* were pretreated with toluene to introduce *S*-adenosylmethionine into whole cells for methylation studies [7]. Combinations of toluene–ethanol treatment were later used for permeabilizing the fungus *Neurospora crassa* [8, 9]. The method that we optimized for Aer is a modification of an unpublished protocol developed by Claudia A. Studdert at the Universidad Nacional de Mar del Plata in Argentina. In this method, *E. coli* cells expressing Aer proteins with single Cys residues are permeabilized with toluene and ethanol and then incubated with PEG-mal [4]. PEGylated Aer is then separated from un-PEGylated protein by its apparent size difference during SDS-PAGE (Fig. 2). The extent to which each cysteine residue becomes PEGylated is used as a measure of solvent accessibility. When a library of Aer single-Cys replacements was mapped, regions of contiguous low accessibility emerged that suggested interacting protein surfaces (Fig. 3, [4]). When tested by in vivo disulfide cross-linking, these low accessibility surfaces were shown to interact (Fig. 3, [4]).

2 Materials

1. Tryptone broth (TB): Dissolve 10 g of Bacto™ tryptone powder and 5 g of NaCl in 800 mL of deionized water. Make up to 1 L with deionized water and autoclave (121 °C, 15 psi) for 30 min.
2. Wash buffer: 20 mM potassium phosphate, pH 7.0, 0.1 mM EDTA, and 0.1 mM $MgCl_2$. To make 200 mL of wash buffer, add 1.56 mL of 1 M monobasic potassium phosphate, 2.44 mL of 1 M dibasic potassium phosphate, 40 μL of 0.5 M EDTA, 20 μL of 1 M $MgCl_2$, and filter-sterilized water up to 200 mL. Store at room temperature.
3. Toluene–ethanol mixture: In a fume hood, add 12.5 mL of toluene and 50 mL of 100% ethanol. Mix thoroughly. Store in a glass-stoppered bottle at room temperature. Make up fresh every 2–3 months.
4. 50 mM PEG-mal (methoxypolyethylene glycol maleimide, 5000 MW): Aliquot PEG-mal into 0.1 g lots, gas each lot with argon or nitrogen, and store at −20 °C (*see* **Note 1**). Dissolve each aliquot as needed in 304 μL of filter-sterilized water. PEG-mal solutions can be stored at −20 °C between uses, although it should be used as quickly as feasible and with limited thawing.
5. 2× Sample buffer: 120 mM Tris, pH 6.8, 4% SDS, 30% glycerol, and 0.006% bromophenol blue. Dissolve 1.45 g of Tris base, 4 g of SDS, 30 g of glycerol, and 6 mg of bromophenol blue in 50 mL of deionized water. Adjust the pH to 6.8 with concentrated HCl. Adjust the volume to 100 mL with deionized water. Store at room temperature.

3 Methods

3.1 Creating a Library of Single-Cys Mutants

1. Clone the gene of interest into an appropriate bacterial expression plasmid. If no antibody is available to visualize the protein by Western blot, a tag may be incorporated on the N-terminus or C-terminus of the protein if it does not significantly impede function.
2. The protein of interest should not contain native Cys residues. Native Cys codons should be replaced with Ala or Ser codons by whole plasmid site-directed mutagenesis (e.g., using the QuikChange II® site-directed mutagenesis kit; Agilent Technologies, Santa Clara, CA). The stability and activity of the Cys-less protein should be assessed and compared with that of the wild-type protein. For cells expressing Aer, behavior is determined both from colony morphologies in succinate

minimal soft agar and by temporal assays in a microscope-based gas perfusion chamber [10].

3. Once a functional Cys-less mutant has been created, a library of single-Cys mutants can be created by plasmid-based site-directed mutagenesis. For the Aer HAMP and proximal signaling domains, a library of serial Cys replacements was created at each of 70 consecutive amino acids [4]. In contrast, an Aer-PAS homology model was used to guide the selection of 59 PAS domain residues for Cys replacement [4]. When protein structure or homology models are available, they can be used to guide residue selection and to make predictions about residue accessibility. For each mutation introduced, the entire gene should be sequenced. Protein stability and activity should be assessed before proceeding to PEGylation assays. Of the 129 single Cys replacements created in the Aer PAS, HAMP and proximal signaling domains, only four resulted in proteins that did not mediate aerotaxis [4].

3.2 Cell Permeabilization and PEGylation

1. Grow *E. coli* mutants with shaking for 12–16 h at 30 °C in 5 mL of tryptone broth (TB) with the appropriate antibiotic. A maximum of 12 Cys mutants can be tested at one time (12 mutants require four mini polyacrylamide gels). The Cys-less mutant should be included as a negative control.
2. Subculture 200 μL of each overnight culture into 4.5 mL of TB without antibiotic and shake at 30 °C until the OD_{600nm} is 0.4–0.45 (this usually takes ~3½ h).
3. Induce expression of the Cys-substituted proteins for 3 h with an appropriate inducer (*see* **Note 2**). For cells expressing Aer from the P_{tre} promoter, we use 50 μM IPTG.
4. For each mutant, label two 1.5 mL microcentrifuge tubes: one for the denatured (D) sample and one for the native (N) sample. For each culture, centrifuge 2 mL in each of the "D" and "N" tubes at 10,000 × *g* for 1 min (by performing two 1-mL spins and emptying the supernatant between spins). Pour out the supernatant.
5. To each tube, add 1 mL of wash buffer and vortex briefly to resuspend the cells (*see* **Note 3**).
6. Spin at 10,000 × *g* for 1 min and decant the supernatants.
7. Repeat the wash (**steps 5** and **6**).
8. To each tube, add 1 mL of wash buffer, vortex to resuspend, and then open the tubes.
9. To each tube, add 50 μL of 1:4 toluene–ethanol (1% final concentration of toluene and 4% ethanol) and shake for exactly 15 min in a microcentrifuge tube shaker.

10. Centrifuge each tube at 10,000 × *g* for 1 min and decant the supernatants into a separate glass beaker (*see* **Note 4**).
11. Tap each tube onto an absorbent towel to remove as much excess fluid as possible.
12. Resuspend each pellet with 50 μL of wash buffer by gently pipetting up and down.
13. Add 5 μL of 50 mM PEG-mal to each tube and, because PEG-mal is dense, resuspend by mixing with a pipette tip for several seconds. It takes ~3 min to add PEG-mal to 12 "N" tubes (4 tubes per min). Keep similar timing for each tube. Also add PEG-mal to the "D" tubes, although timing is not as critical as for the "N" tubes. Incubate all tubes open on the bench at room temperature. Incubate "N" tubes for exactly 15 min (*see* **Note 5**).
14. To each tube, add 100 μL of 2× sample buffer with (N) or without (D) β-mercaptoethanol (βME) (*see* **Note 6**). βME-containing sample buffer should contain 50 μL of βME per mL of 2× sample buffer. To keep the timing accurate, take the same amount of time to add sample buffer to the "N" tubes that it took to add the PEG-mal.
15. To perform a βME control, add 5 μL of βME to a control sample, mix, add 5 μL of PEG-mal, mix, and then add 100 μL of sample buffer without βME.
16. Boil tubes for 4 min and load 15 μL onto an SDS polyacrylamide gel (for Aer we use an 8% T, 3% C Tris–tricine gel). Load two "D" lanes, followed by two "N" lanes for each mutant (as shown in Fig. 2). Run the dye front off the gel in order to obtain optimal band separation. The presence of PEG-mal in the samples may cause the gel to run slightly unevenly.
17. Perform an immunoblot using an appropriate antibody.
18. Experiments should be repeated at least three times for each mutant so that the average extent of PEGylation can be obtained.

3.3 PEGylation Analysis

1. For most of the denatured "D" samples, you should consistently observe complete PEGylation, including PEGylation of any breakdown product. For Aer, PEGylated breakdown products are nearly the same size as the un-PEGylated Aer monomer (in Fig. 2 there are faint PEGylated breakdown product bands beneath the Aer monomers). For Aer, a mobility shift of ~10 kDa separates PEGylated Aer from non-PEGylated Aer (Fig. 2). No PEGylation should be observed for the Cys-less and βME controls.
2. Obtain a digital image of your immunoblot within the linear range of the detector. Determine the average densities of the

PEGylated and non-PEGylated bands. Calculate the percentage of PEGylation for "D" and "N" by dividing the PEGylated band density by the sum of the PEGylated + non-PEGylated band densities. The percentage of sample PEGylated in "D" is the maximum possible value for each sample. Thus, divide the percent PEGylation of N by the percent PEGylation of D to obtain the correct proportion of the protein that has been PEGylated. Average the PEGylation fractions from multiple experiments.

3. Categorize average PEGylation extents as low, intermediate or high accessibility. The boundaries of these categories should be determined for each protein domain. For the Aer PAS domain, we categorized 0–30% PEGylation as low accessibility, 31–50% PEGylation as intermediate accessibility, and >50% as high accessibility ([4]; *see* examples in Fig. 2). Interior-facing residues should have low accessibility, solvent-exposed residues should have high accessibility, and regions of considerable mobility or flexibility may show intermediate to high accessibility.
4. Protein surfaces that are predicted to be accessible to PEG-mal, but that are found to have low accessibility, are attractive sites for domain-domain interaction. To confirm interactions between neighboring domains of the same type, e.g., PAS-PAS interactions, the same single-Cys mutants that were created for the PEGylation assays can be used for disulfide cross-linking. To survey whether interactions between domains of different types are responsible for low solvent accessibility, one domain can be removed from the protein. PEGylation assays can then be repeated in both the presence and the absence of the domain, and the extents of PEGylation compared. For Aer, inaccessible HAMP domain residues became significantly more accessible when the PAS domain was removed from Aer [4] (*see* **Note 7**). To confirm PAS-HAMP interactions in Aer, PAS-HAMP di-Cys mutants were created and cross-linked in vivo using Cu(II)(1,10-phenanthroline)$_3$ [4]. Our method for in vivo cross-linking can be found in [10]. Residues on the inaccessible PAS and HAMP surfaces formed disulfide bonds, confirming that these surfaces collide and form a PAS-HAMP interaction face (Fig. 3, [4]).

4 Notes

1. PEG-mal is available from various suppliers, e.g., Laysan Bio (Arab, AL) or Sigma-Aldrich (St. Louis, MO). ≥90% substitution by NMR is preferable. In our experience, each new PEG-mal lot, even from the same company, can behave

differently, and some PEG-mal lots do not consistently produce 100% PEGylation in the denatured samples. Wherever possible, we recommend using PEG-mal from the same company and the same lot number to complete a series of experiments. PEG-mal is also available in molecular weights from 2000 to 30,000 Da. We have only used PEG-mal 5000 in the permeabilized cell assay.

2. Protein expression should be limited to levels equivalent to native cellular levels, but should be high enough to cause both a behavioral response and to generate a visible band on an immunoblot.
3. While optimizing the PEGylation protocol for Aer, we varied the concentrations of $MgCl_2$ and KPO_4 in the wash buffer. These concentrations, as well as the time and amount of toluene–ethanol treatment, may need to be optimized for different proteins, bacteria, or PEG-mal of different molecular weights.
4. Place the beaker containing waste toluene–ethanol into a fume hood to allow the toluene (~240 μL) to evaporate overnight.
5. The PEG-mal incubation time may need to be adjusted for different proteins. For Aer, the conditions described yielded an average chemical reactivity (relative to denatured protein) below 50%. Values should span a large dynamic range, and the reactions should not reach completion.
6. βME quenches the reaction by reacting with free maleimide. PEGylated protein adducts are stable to both boiling and βME.
7. Removing a protein domain may decrease protein stability and may not be feasible. Removing the complete PAS domain from Aer prevents protein maturation, but leaving nine C-terminal PAS residues in the sequence allows for maturation and a stable product.

Acknowledgment

We thank Claudia A. Studdert at the Universidad Nacional de Mar del Plata in Argentina for personally communicating her unpublished PEGylation protocol. The development and communication of the optimized method and the work described here was supported by the National Institute of General Medical Sciences of the National Institutes of Health under Award Numbers R01GM029481 to Barry L. Taylor, and R01GM108655 to Kylie J. Watts, respectively.

References

1. Bass RB, Butler SL, Chervitz SA, Gloor SL, Falke JJ (2007) Use of site-directed cysteine and disulfide chemistry to probe protein structure and dynamics: applications to soluble and transmembrane receptors of bacterial chemotaxis. Methods Enzymol 423:25–51
2. Amin DN, Taylor BL, Johnson MS (2006) Topology and boundaries of the aerotaxis receptor Aer in the membrane of *Escherichia coli*. J Bacteriol 188:894–901
3. Jones PC, Sivaprasadarao A, Wray D, Findlay JB (1996) A method for determining transmembrane protein structure. Mol Membr Biol 13:53–60
4. Garcia D, Watts KJ, Johnson MS, Taylor BL (2016) Delineating PAS-HAMP interaction surfaces and signalling-associated changes in the aerotaxis receptor Aer. Mol Microbiol 100:156–172
5. Lu J, Deutsch C (2001) Pegylation: a method for assessing topological accessibilities in Kv1.3. Biochemistry 40:13288–13301
6. Banfalvi G (2016) Permeability of biological membranes. Springer, Berlin
7. Paoni NF, Koshland DE Jr (1979) Permeabilization of cells for studies on the biochemistry of bacterial chemotaxis. Proc Natl Acad Sci U S A 76:3693–3697
8. Basabe JR, Lee CA, Weiss RL (1979) Enzyme assays using permeabilized cells of *Neurospora*. Anal Biochem 92:356–360
9. Quigley DR, Jabri E, Selitrennikoff CP (1987) Permeabilization of *Neurospora crassa* hyphae with toluene-ethanol and filipin. Curr Microbiol 14:269–274
10. Taylor BL, Watts KJ, Johnson MS (2007) Oxygen and redox sensing by two-component systems that regulate behavioral responses: behavioral assays and structural studies of Aer using in vivo disulfide cross-linking. Methods Enzymol 422:190–232

Chapter 14

Tuning Chemoreceptor Signaling by Positioning Aromatic Residues at the Lipid–Aqueous Interface

Rahmi Yusuf, Robert J. Lawrence, Lucy V. Eke, and Roger R. Draheim

Abstract

Aromatic tuning facilitates stimulus-independent modulation of receptor output. The methodology is based upon the affinity of amphipathic aromatic residues, namely Trp and Tyr, for the polar–hydrophobic interfaces found within biological membranes. Here, we describe the application of aromatic tuning within the aspartate chemoreceptor of *Escherichia coli* (Tar). We have also employed the method within other related proteins, such as sensor histidine kinases (SHKs), and therefore hope that other research groups find it useful to modulate signal output from their receptor of interest.

Key words Aromatic tuning, Stimulus-independent signaling, Signal output modulation, Signal pathway mapping, Polar–hydrophobic interfaces, Membrane–protein interactions

1 Introduction

Aromatic tuning, or repositioning the aromatic residues at the cytoplasmic end of the final transmembrane helix, has been shown to modulate the signal output of several bacterial receptors [1–4]. Two independent lines of inquiry have demonstrated the affinity of amphipathic aromatic residues, namely Trp and Tyr, for the polar–hydrophobic interfaces in biological membranes. The first monitored interaction between tryptophan-flanked or tyrosine-flanked alpha-helical peptides containing a repeating poly-Ala-Leu core, known as WALP and YALP peptides, respectively, was done with synthetic lipid bilayers of different thicknesses. When the distance between the Trp or Tyr residues and the hydrophobic–polar interfaces changed, the membrane was shown to adjust by shrinking, expanding, or undergoing phase inversion to position the Trp or Tyr at the interfacial regions [5–8]. The second line of research focused on the integration of a rationally designed transmembrane helix into a biological membrane. Moving the Trp and Tyr residues near the end of the TM helix resulted in a repositioning of the synthetic helix within the membrane [9–12]. Both sets of results

Michael D. Manson (ed.), *Bacterial Chemosensing: Methods and Protocols*, Methods in Molecular Biology, vol. 1729,
https://doi.org/10.1007/978-1-4939-7577-8_14,

strongly suggested that Trp and Tyr residues could be harnessed to reposition TM helices within a full-length membrane protein.

Initially, the aspartate chemoreceptor from *Escherichia coli* (Tar) was subjected to aromatic tuning because the mechanism of transmembrane communication was predicted to consist of an asymmetric displacement of the second transmembrane helix (TM2) [1, 13–18]. Within Tar, we moved the aromatic Trp-Tyr tandem about its original position at the cytoplasmic end of TM2, which resulted in an incremental tuning of signal output from the receptor. This effect was observed by monitoring the resultant changes in the extent of covalent modification of the receptor and of the direction of flagellar rotation in cells expressing these tuned receptors [1]. Subsequent studies demonstrated that the composition of this aromatic tandem was critical for the precise position of TM2 within the membrane and the resultant Tar signal output [12, 19–21]. We have since modulated signal output from other membrane-spanning receptors in *E. coli* and have developed a high-throughput assay that will be useful for other research groups desiring to tune output from their receptor of interest [2, 4].

2 Materials

All solutions should be prepared with autoclaved ultrapure water (prepared by purifying deionized water to attain a sensitivity of 18 MΩ cm at 25 °C) and analytical grade reagents. Prepare and store all reagents at room temperature unless stated otherwise.

2.1 Site-Directed Mutagenesis (SDM)

1. Quantified low copy-number plasmid (expressing the C-terminally tagged receptor of interest) eluted in water from a commercial plasmid DNA extraction kit (store at −20 °C) (*see* **Note 1**).
2. Resuspended lyophilized phopshorylated reverse primer (no mutations) in water at 100 pmol/μL (store at −20 °C; *see* **Note 2**).
3. Resuspended lyophilized unphosphorylated forward primers (with incremental mutations) in water at 100 pmol/μL (store at −20 °C).
4. Commercial recombinant *Pfu* polymerase (2.5 U/μL), 10× *Pfu* buffer containing 20 mM $MgSO_4$, dNTP mix (2 mM each), T4 DNA ligase, and *Dpn*I (10 U/μL) (store at −20 °C).
5. Autoclaved 0.2- and 1.5-mL tubes.
6. Programmable thermocycler, preferably with a gradient block to enhance the efficiency of thermal optimization.

7. TBE buffer (1×): 89 mM Tris-Cl, 89 mM boric acid, 0.2 mM ethylenediaminetetraacetic acid (EDTA).
8. DNA sample buffer (6×): 30% (v/v) glycerol, 0.2% (w/v) bromophenol blue, 0.1% (w/v) xylene cyanol.
9. Ethidium bromide (EtBr) (1 μg/mL) staining solution.
10. Chemically competent *E. coli* MC1061 cells (store at −80 °C; *see* **Note 3**).
11. Lysogeny broth (LB): 5 g/L yeast extract, 10 g/L NaCl, 10 g/L tryptone, 15 g/L agar (if solid medium required), antibiotic as required (store at +4 °C).

2.2 SDS–Acrylamide Gels

1. Mini PROTEAN® 3 System including casting stands, plates, combs, chambers, tanks, and a suitable power supply.
2. Separating gel buffer (1×): 0.5 M Tris-Cl, pH 6.8.
3. Stacking gel buffer (1×): 1.5 M Tris-Cl, pH 8.8.
4. 30% acrylamide–bis-acrylamide (37.5:1) solution (store at +4 °C).
5. Ammonium persulfate (APS): 20% (w/v) in water (*see* **Note 4**).
6. SDS: 10% (w/v) in water.
7. *N*,*N*,*N*′,*N*′-tetramethyl-ethylenediamine (TEMED) (store at +4 °C).
8. *n*-Butanol.
9. SDS-PAGE running buffer (1×): 2.5 mM Tris-Cl, 19.2 mM glycine, 0.01% (w/v) SDS.
10. Sample buffer (6×): 12.5% 0.5 M Tris-Cl (pH 6.8), 25% (v/v) glycerol, 2% (w/v) SDS, 0.1% (w/v) bromophenol blue, 5% (v/v) β-mercaptoethanol (store at −2 °C).
11. Appropriate commercial prestained protein ladder.

2.3 Immunoblotting and Visualization

1. Trans-Blot® SD Semi-Dry Transfer Cell and appropriate high-current power supply.
2. Nitrocellulose membrane.
3. Filter paper of appropriate thickness (*see* **Note 5**).
4. Semidry transfer buffer (1×): 2.5 mM Tris-Cl, 19.2 mM glycine, 20% (v/v) methanol (*see* **Note 6**).
5. TBS buffer (1×): 10 mM Tris-Cl, 150 mM NaCl, pH 7.5.
6. TBS-T buffer (1×): 1× TBS buffer with 0.05% (w/v) Tween 20.
7. Blocking solution (1×): 1× TBS buffer with 2% (w/v) semidry milk powder.

8. Chemiluminescent component A (1×): 1 M Tris-Cl, 250 mM luminol, 90 mM *p*-coumaric acid, pH 8.5 (store at +4 °C in dark).
9. Chemiluminescent component B (1×): 1 M Tris-Cl, 30% (v/v) H_2O_2, pH 8.5 (store at +4 °C in dark).

2.4 Monitoring Rotation of Individual Flagella

1. Waring bender with a 20-mL cup (*see* **Note 7**).
2. Tryptone broth (TB): 10 g/L tryptone, 5 g/L NaCl.
3. Tethering buffer (1×): 10 mM potassium phosphate, 100 mM NaCl, 10 μM EDTA, 20 μM L-methionine, 20 mM sodium DL-lactate, 20 μg/mL chloramphenicol, pH 7.0.
4. Anti-flagellar filament antibody (gift of J.S. Parkinson; *see* **Note 8**).
5. Circular 12-mm coverslip.
6. Apiezon-L grease.
7. Flow chamber. Built as described in ref. 22.
8. Microscope capable of viewing bacteria at 1000× magnification.

2.5 In Vivo Methylation Analysis

1. Tryptone broth (TB) as described above.
2. Sterilized 10 mL vials.
3. 100% (w/v) trichloroacetic acid (TCA): Add 227 mL of water to 500 g of TCA.
4. Long (ca. 30 cm) SDS-PAGE electrophoretic equipment: tank, glass plates, spacers, binder clips, combs and an appropriate power supply.
5. Solutions required for immunoblotting and visualization, as described above.

3 Methods

3.1 Identifying the Aromatic Residues to Be Repositioned

1. Predict the residue composition of the TM helices by submitting the primary sequence of the receptor to both TMHMM [23] and DGpred [11] (*see* **Note 9**).
2. Select appropriate aromatic residues at the C-terminus of the final TM helix to reposition. In the case of *E. coli* Tar, this was the Trp-209/Tyr-210 tandem [1] (Fig. 1; *see* **Note 10**).
3. Design a family of tuned receptor variants where the aromatic residues are repositioned three residue steps in either direction about their original position. When moving the residues into the membrane, usually referred to as the minus-series of receptors, the displaced residues should simply be placed on

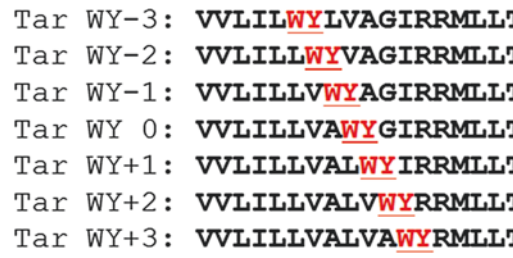

Fig. 1 Incremental tuning of signal output from the aspartate chemoreceptor of *E. coli* (Tar). At the C-terminal end of Tar TM2, a Trp-Tyr (red) tandem was moved about its original position at the cytoplasmic polar–hydrophobic interface (reproduced from ref. 3 with permission from BioMedCentral)

the other side of the aromatic residues. Moving the aromatic residues out of the membrane, usually known as the plus-series of receptors, should result in an extension of the aliphatic core in tetra-residue repeats (Fig. 1; *see* **Note 10**).

3.2 Creation of Aromatically Tuned Receptors

1. Use commercially synthesized forward and reverse primers to reposition the aromatic residues as described in Subheading 2 and accompanying notes.
2. Perform one polymerase chain reaction (PCR) for each aromatically tuned variant to be created. In a sterile 0.2 mL tube, mix the following: 5 μL 10× *Pfu* buffer with 20 mM $MgSO_4$, 5 μL dNTPs (2 mM each), 0.5 μL forward primer (100 pmol/μL), 0.5 μL reverse primer (100 pmol/μL), 1 μL plasmid DNA (≈50 ng/μL), 1 μL *Pfu* DNA polymerase (2.5 U/μL), and autoclaved ultrapure water to 50 μL. Initially, employ the following reaction conditions (*see* **Note 11**): one initial denaturation cycle (95 °C, 3 min), 16 amplification cycles (95 °C, 30 s; 55 °C, 30 s; 72 °C, 15 min) and one final extension cycle (72 °C, 5 min). Ensure that the reaction has cooled to room temperature and add 1 μL *Dpn*I (10 U/μL) and incubate at 37 °C for 1 h.
3. Run the entire 50-μL reaction through a single well in a medium-sized (15 cm) 1% agarose gel in 1× TBE at 120 V for 1 h. Incubate the gel in 1 μg/mL EtBr for 20 min and image with a low-intensity 290 nm light source. Subsequently, extract the single DNA band representing the linearized plasmid band, employ a commercially available gel extraction kit and elute in 30 μL autoclaved ultrapure water.
4. Ligate the eluted linearized plasmid in a single reaction containing: 5 μL 10× T4 DNA ligase buffer, 30 μL eluted plasmid, 1 μL T4 DNA ligase and autoclaved ultrapure water to 50 μL at 37 °C for 1 h.

5. Transform the ligated PCR product by mixing 20 μL of the ligated product with 80 μL competent *E. coli* MC1061 cells in a sterile 1.5-mL tube. Incubate on ice for 1 h, then heat shock at 42 °C for 45 s and return to ice for 2 min. Add 500 μL room temperature LB broth without antibiotics and incubate at 37 °C for 1 h. Centrifuge at 14,000 × *g* in a tabletop centrifuge, decant 900 μL of supernatant, resuspend the cells in the remaining solution and plate them onto an appropriately selective LB plate.
6. Resultant colonies should be used to start overnight cultures in LB broth containing the selective antibiotic. Plasmid DNA purification and sequencing should be performed to confirm the presence of the repositioned aromatic residues.

3.3 Expression Testing

1. Transform the sequence-confirmed plasmids into the bacterial strains of interest as described above. When aromatically tuning signal output from Tar, plasmid pRD200 [13], which expresses a C-terminal V5-tagged variant, was transformed into the chemoreceptor-deficient *E. coli* strain VB13 [24].
2. Grow the transformed cells in an appropriate medium and include the appropriate inducer (*see* **Note 12**). Continue growing until the desired OD_{600nm} is reached. For analysis of VB13/pRD200, cells were harvested in a tabletop centrifuge at an OD_{600nm} of 0.6 ± 0.1.
3. Resuspend cell pellet in 50 μL 6× SDS sample buffer, transfer to a sterile 1.5-mL tube, incubate at 95 °C for 10 min, and freeze at −20 °C for 10 min. Repeat the boil–freeze cycle two more times with a final incubation at 95 °C for 10 min. Vortex the sample and lightly centrifuge to ensure all condensation is at the bottom of the 1.5-mL tube.
4. For every two gels to be poured, mix 6.1 mL autoclaved ultrapure water, 5 mL acrylamide mixture, 3.75 mL 1× separating gel buffer, 150 μL 10% SDS, 37.5 μL 20% SDS, and 7.5 μL TEMED in a 50 mL conical tube. Immediately pour mixture into two sets of glass plates in the casting chamber and cover with a thin layer of *n*-butanol. After 30 min, decant the butanol, wash the surface of the separating gel with water and dry with a paper towel. For every two stacking gels to be poured, mix 5.3 mL of autoclaved ultrapure water, 2.5 mL of 1× stacking gel buffer, 1.3 mL of acrylamide solution, 100 μL of 10% (w/v) SDS, 25 μL of 20% (w/v) APS, and 10 μL TEMED in a 50 mL conical tube. Fill the remaining space in between the glass plates held in the casting chamber and insert the appropriate combs. The gels should polymerize and be ready for use within an hour.
5. Load 10 μL of desired sample into the SDS–acrylamide gels. Ensure that an appropriate volume of prestained protein ladder

is also loaded. Electrophorese initially at 70 V for 20 min to ensure that the samples completely enter the SDS–acrylamide gel then increase to 120 V until the dye front migrates out of the bottom of the gel.

6. Following electrophoresis, pry the gels plates open with a spatula, remove the SDS–acrylamide gel and soak it in 1× transfer buffer for 30 min (*see* **Note 13**). Cut filter paper and nitrocellulose for each SDS–acrylamide gel run and soak them in 1× transfer buffer for 30 min.
7. Perform semidry electrophoretic transfer by layering, from the anode to the cathode: filter paper, nitrocellulose membrane, the SDS–acrylamide gel and finally, the other filter paper. Run at 25 V for 30 min. Place the nitrocellulose in 50-mL conical tubes with 10 mL 1× TBS and rotate for 5 min. Decant and replace with 10 mL 1× TBS. Decant again and replace with 10 mL of 1× blocking buffer for 1 h. Wash twice with 10 mL TBS-T for 5 min. Finally, incubate overnight at +4 °C in 10 mL 1× blocking buffer containing an appropriate dilution of primary antibody (*see* **Note 14**). Wash twice with 10 mL 1× TBS-T for 10 min and then add 10 mL 1× TBS-T with secondary antibody conjugated to horse radish peroxidase (HRP) and incubate for 6 h at +4 °C. Finally, wash twice with 10 mL TBS-T and once with 10 mL TBS.
8. Image the immunoblots by mixing equal volumes of component A and component B of the chemiluminescent agent and place 1 mL on top of the blot for 5 min. Subsequently, decant and image with a camera capable of detecting chemilumiscence and an appropriate imaging software package.
9. Ensure that all aromatically tuned variants are expressed at similar levels and that no degradation is observed. Select viable aromatically tuned variants for subsequent signal output analysis. Two methods for analyzing Tar signal output are provided below. However, we have also developed a new fluorescent-based system that could be adapted for use with other receptors [2, 4, 12, 25].

3.4 Signal Output Analysis: Flagellar Rotation

1. Grow VB13/pRD200 cells in 1× TB medium at 32 °C until OD_{600nm} reaches 0.6 ± 0.1 and add chloramphenicol to a final concentration of 30 μg/mL. Pellet cells in a tabletop centrifuge and resuspend in 25 mL 1× tethering buffer.
2. Shear the flagellar filaments from the VB13/pRD200 cells by exposing cells to six 10-s intervals of agitation at high speed in a 20-mL stainless steel cup on a Waring blender. Interspersed between bouts of agitation are 15-s intervals to facilitate cooling of the sample. Cells are the pelleted by centrifugation in a

tabletop centrifuge and resuspended in 5 mL of 1× tethering buffer and kept on ice.

3. For analysis, 20 μL of these cells are added to 20 μL of a 200-fold dilution of anti-flagellar filament antibody and loaded onto a 12-mm diameter coverslip with a peripheral ring of Apiezon-L grease. (*See* Chapter 18 of this volume for a detailed description of this process.) Incubate the coverslip for 20 min at room temperature and attach to a flow chamber and pass 1× tethering buffer through to remove nonattached cells.
4. Observe cells at 1000× magnification and record several fields of view. Play these fields of view back and assign cells to one of five categories: cells that turned their flagella only CCW, cells that possessed flagella that rotated mostly CCW, cells that rapid exhibit rapid CCW/CW switching, cells that possess flagella that rotate mostly CW and, finally, those that rotate only CW. An example of such categorization is described in detail within ref. 1.
5. Perform experimentation with the wild-type (untuned) and the aromatically tuned variants in order to determine which receptors are activated or squelched compared to wild-type receptor. In addition, assays involving responses to cognate stimulus facilitated by the tuned variants can be performed as previously described [1].

3.5 Signal Output Analysis: Covalent Modification

1. Grow cells expressing one of the aromatically tuned or wild-type receptors at 32 °C in 1× TB containing the appropriate antibiotic to an OD_{600nm} of 0.6. In the case of Tar, VB13/pRD200 cells were employed. Harvest cells by centrifugation and wash thrice in 10 mL of 10 mM potassium phosphate, 0.1 mM EDTA (pH 7.0) and finally resuspend in 5 mL 1× methylation buffer. Transfer 1-mL aliquots to small 10-mL vials and incubate at 32 °C for 10 min. Add L-methionine to 2 μM and incubate at 32 °C for 30 min.
2. Add desired chemoeffectors to cells and incubate at 32 °C for an additional 20 min. For VB13/pRD200 cells, 100 μL of 100 mM aspartate or 10 mM $NiSO_4$ were employed. Add an equal volume of 1× methylation buffer to one of the aliquots as a control. Terminate the reactions by adding 100 μL of ice-cold 100% (w/v) TCA and incubate on ice for 15 min. Centrifuge samples at 13,000 × *g* for 10 min and wash twice with 10% (w/v) TCA and finally with 100% (v/v) acetone. After the final centrifugation at 13,000 × *g*, resuspend pellets in 200 μL of 6× SDS sample buffer.
3. As above, run samples on a medium-format (ca. 30-cm long) SDS–acrylamide gel. Transfer to nitrocellulose, subject to antibodies, develop and image as above.

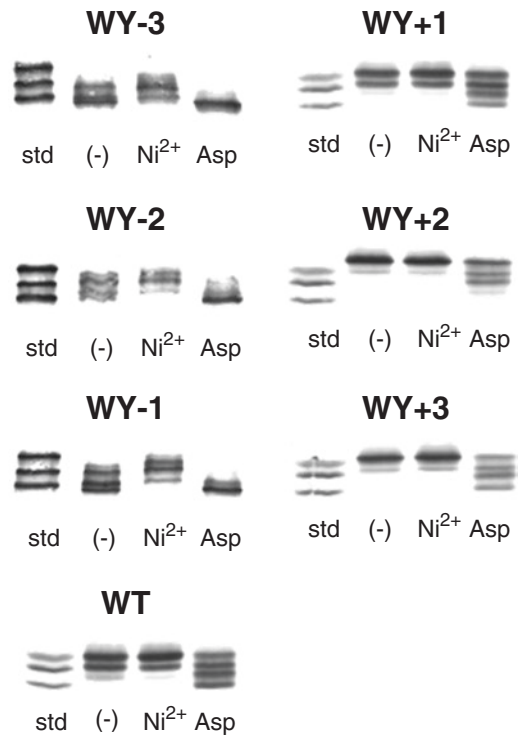

Fig. 2 Extent of methylation of the aromatically tuned variants of Tar in vivo. Transducer-depleted VB13 cells expressing the wild-type or tuned Tar proteins from the plasmid pRD200 were exposed to 100 mM aspartate or 10 mM Ni^{2+}. The level of methylation affects the migration rate during SDS-PAGE, with the more highly methylated forms moving faster. As migration standards, the EEEE, QEQE and QQQQ forms of the wild-type Tar were loaded in the leftmost lane. The QEQE and QQQQ forms of Tar migrate like the doubly methylated and quadruply methylated Tar respectively (adapted with permission from [1]. Copyright 2006 American Chemical Society

4. Enhanced or reduced methylation due to aromatic tuning and/or alterations due to stimulus perception will be seen as increased or decreased migration respectively (Fig. 2).

4 Notes

1. Traditionally, we have employed standard molecular cloning methods. However, the rapidly decreasing cost of gene synthesis has ushered in the potential for significant fiscal and temporal savings compared to traditional methods. In addition, it remains important to select an epitope tag carefully as the alteration of the C-terminal tail of a chemoreceptor may have functional implications [26].

2. We found it challenging to determine whether all reverse primer present was phosphorylated when the reaction was performed within our lab. We observed significantly greater success, measured as percent SDM reactions initially successful, when primers were phosphorylated by the manufacturer as an additional step during synthesis. In addition, the manufacturer suggested resuspension and subsequent dilution in 1X TE buffer (10 mM Tris-Cl, 1 mM EDTA, pH 8.0); however, we attained greater SDM success when autoclaved ultrapure water was employed.
3. Different strains of competent *E. coli* cells can be purchased from various manufacturers. However, we attained similar success with the classical method involving glycerol and $CaCl_2$ [27].
4. We have found that the best mechanism to ensure that the 20% (w/v) APS remains reactive is to make it fresh every workday in which SDS–acrylamide gels are being made.
5. Filter paper is available in different thicknesses. We have found it imperative to stack enough filter paper on either side of the gel–nitrocellulose tandem to ensure that the semidry transfer chamber firmly clicks shut. Otherwise, a smeared transfer that makes subsequent densitometry challenging may occur.
6. We have found that making the transfer buffer fresh for every transfer enhances reproducibility, which is essential for densitometry. Evaporation of methanol has been isolated as the source of the problem.
7. When shearing flagella, cover the blender cup in Parafilm. Ensure that the temperature of the steel cup does not become too warm by interspersing pauses between the blending events.
8. It is also possible to tether cells by means of the "sticky" filament FliC protein described in [28].
9. The *T*rans*m*embrane *H*elix—*M*arkov *M*odel (TMHMM) server version 2.0 can be found at http://www.cbs.dtu.dk/services/TMHMM/, while ΔG prediction (DGpred) server version 1.0 can be found at http://dgpred.cbr.su.se/. The results from these servers will be slightly different as each software package employs different parameters for prediction of TM helices.
10. The majority of TM helices share a common motif of positively charged residues that bracket amphipathic aromatic residues, which flank a mostly aliphatic core [29]. The appropriate residues for aromatic tuning reside at the cytoplasmic end of the C-terminal TM helix. In addition, a Trp-Tyr-Ala triplet was shown to sufficient in the place of a Trp-Leu-Phe triplet when aromatically tuning signal output from *E. coli* EnvZ [2] sug-

gesting that employing the native residues is not essential for aromatic tuning to be successful.

11. These are the conditions that we used, but they may have to be adjusted for different applications.
12. In the case of VB13/pRD200 cells, LB and TB medium were employed and no inducer was required, as the native *tar* promoter governed expression of the receptor.
13. After completion of SDS-PAGE, the gels should reside in 1× transfer buffer for exactly 30 min. Less time often results in bubbles during transfer due to failure to remove SDS for the gels, whereas longer time can result in more-diffuse bands due to diffusion within the gel while residing in the transfer buffer.
14. For our expression system, we found that a 1:10,000 dilution of the anti-V5 primary antibody and a 1:80,000 dilution of the secondary goat anti-mouse HRP antibody gave the best results. For each different antibody, an optimization process involving dot-blotting should be employed.

Acknowledgment

R.Y. was generously supported by the Indonesia Endowment Fund for Education, Ministry of Finance (S-4833/LPDP.3/2015). R.J.L. and L.V.E. received support from the University of Portsmouth. R.R.D. was supported with start-up funding from the Faculty of Science and from the Institute of Biological and Biomolecular Science (IBBS) at the University of Portsmouth.

References

1. Draheim RR, Bormans AF, Lai RZ, Manson MD (2006) Tuning a bacterial chemoreceptor with protein-membrane interactions. Biochemistry 45(49):14655–14664
2. Norholm MH, von Heijne G, Draheim RR (2015) Forcing the issue: aromatic tuning facilitates stimulus-independent modulation of a two-component signaling circuit. ACS Synth Biol 4:474–481
3. Yusuf R, Draheim RR (2015) Employing aromatic tuning to modulate output from two-component signaling circuits. J Biol Eng 9:7
4. Lehning CE, Heidelberger JB, Reinhard J, Norholm MH et al (2017) A modular high-throughput in vivo screening platform based on chimeric bacterial receptors. ACS Synth Biol 6(7):1315–1326
5. Killian JA, Salemink I, de Planque MR, Lindblom G, Koeppe RE II et al (1996) Induction of nonbilayer structures in diacylphosphatidylcholine model membranes by transmembrane alpha-helical peptides: importance of hydrophobic mismatch and proposed role of tryptophans. Biochemistry 35: 1037–1045
6. de Planque MR, Greathouse DV, Koeppe RE II, Schafer H, Marsh D et al (1998) Influence of lipid/peptide hydrophobic mismatch on the thickness of diacylphosphatidylcholine bilayers. A 2H NMR and ESR study using designed transmembrane alpha-helical peptides and gramicidin A. Biochemistry 37:9333–9345
7. de Planque MR, Boots JW, Rijkers DT, Liskamp RM, Greathouse DV et al (2002) The

effects of hydrophobic mismatch between phosphatidylcholine bilayers and transmembrane alpha-helical peptides depend on the nature of interfacially exposed aromatic and charged residues. Biochemistry 41:8396–8404

8. de Planque MR, Bonev BB, Demmers JA, Greathouse DV, Koeppe RE II et al (2003) Interfacial anchor properties of tryptophan residues in transmembrane peptides can dominate over hydrophobic matching effects in peptide-lipid interactions. Biochemistry 42:5341–5348
9. Nilsson I, Saaf A, Whitley P, Gafvelin G, Waller C et al (1998) Proline-induced disruption of a transmembrane alpha-helix in its natural environment. J Mol Biol 284:1165–1175
10. Braun P, von Heijne G (1999) The aromatic residues Trp and Phe have different effects on the positioning of a transmembrane helix in the microsomal membrane. Biochemistry 38:9778–9782
11. Hessa T, Meindl-Beinker NM, Bernsel A, Kim H, Sato Y et al (2007) Molecular code for transmembrane-helix recognition by the Sec61 translocon. Nature 450(7172):1026–1030
12. Botelho SC, Enquist K, von Heijne G, Draheim RR (2015) Differential repositioning of the second transmembrane helices from *E. coli* Tar and EnvZ upon moving the flanking aromatic residues. Biochim Biophys Acta 1848:615–621
13. Draheim RR, Bormans AF, Lai RZ, Manson MD (2005) Tryptophan residues flanking the second transmembrane helix (TM2) set the signaling state of the Tar chemoreceptor. Biochemistry 44:1268–1277
14. Falke JJ, Hazelbauer GL (2001) Transmembrane signaling in bacterial chemoreceptors. Trends Biochem Sci 26:257–265
15. Falke JJ, Erbse AH (2009) The piston rises again. Structure 17:1149–1151
16. Miller AS, Falke JJ (2004) Side chains at the membrane-water interface modulate the signaling state of a transmembrane receptor. Biochemistry 43:1763–1770
17. Isaac B, Gallagher GJ, Balazs YS, Thompson LK (2002) Site-directed rotational resonance solid-state NMR distance measurements probe structure and mechanism in the transmembrane domain of the serine bacterial chemoreceptor. Biochemistry 41:3025–3036
18. Hall BA, Armitage JP, Sansom MS (2011) Transmembrane helix dynamics of bacterial chemoreceptors supports a piston model of signalling. PLoS Comput Biol 7:e1002204
19. Wright GA, Crowder RL, Draheim RR, Manson MD (2011) Mutational analysis of the transmembrane helix 2-HAMP domain connection in the *Escherichia coli* aspartate chemoreceptor Tar. J Bacteriol 193:82–90
20. Adase CA, Draheim RR, Manson MD (2012) The residue composition of the aromatic anchor of the second transmembrane helix determines the signaling properties of the aspartate/maltose chemoreceptor Tar of *Escherichia coli*. Biochemistry 51:1925–1932
21. Adase CA, Draheim RR, Rueda G, Desai R, Manson MD (2013) Residues at the cytoplasmic end of transmembrane helix 2 determine the signal output of the Tar_{Ec} chemoreceptor. Biochemistry 52:2729–2738
22. Berg HC, Block SM (1984) A miniature flow cell designed for rapid exchange of media under high-power microscope objectives. J Gen Microbiol 130:2915–2920
23. Krogh A, Larsson B, von Heijne G, Sonnhammer EL (2001) Predicting transmembrane protein topology with a hidden Markov model: application to complete genomes. J Mol Biol 305:567–580
24. Ward SM, Delgado A, Gunsalus RP, Manson MD (2002) A NarX-Tar chimera mediates repellent chemotaxis to nitrate and nitrite. Mol Microbiol 44:709–719
25. Heininger A, Yusuf R, Lawrence R, Draheim RR (2016) Identification of transmembrane helix 1 (TM1) surfaces important for EnvZ signalling and dimerisation. Biochim Biophys Acta 1858:1868–1875
26. Lai RZ, Bormans AF, Draheim RR, Wright GA, Manson MD (2008) The region preceding the C-terminal NWETF pentapeptide modulates baseline activity and aspartate inhibition of Escherichia coli Tar. Biochemistry 47:13287–13295
27. Cohen SN, Chang AC, Hsu L (1972) Nonchromosomal antibiotic resistance in bacteria: genetic transformation of *Escherichia coli* by R-factor DNA. Proc Natl Acad Sci U S A 69:2110–2114
28. Kuwajima G (1988) Construction of a minimum-size functional flagellin of *Escherichia coli*. J Bacteriol 170:3305–3309
29. Nyholm TK, Ozdirekcan S, Killian JA (2007) How protein transmembrane segments sense the lipid environment. Biochemistry 46: 1457–1465

Chapter 15

Analyzing Chemoreceptor Interactions In Vivo with the Trifunctional Cross-Linker TMEA

Claudia A. Studdert and Diego A. Massazza

Abstract

Chemoreceptors are dimeric proteins that contain a periplasmic or extracellular domain for ligand binding and an extremely well-conserved cytoplasmic domain for output response control. This latter domain consists in a long α-helical hairpin that forms a four-helix coiled-coil bundle in the dimer. Dimers associate into trimers of dimers in the crystal structure obtained for the cytoplasmic domain of the *Escherichia coli* serine chemoreceptor, Tsr. Further studies confirmed that this crystal structure reflects the basic unit within the in vivo organization of chemoreceptors. The trimers of dimers form large and stable chemoreceptor clusters in all the prokaryotes that have been studied. Here, we describe the use of TMEA, a trifunctional cross-linker that reacts with sulfhydryl groups, as a tool to study the geometry and dynamics of the interaction between receptors of the same or different types in living cells.

Key words TMEA, Trifunctional cross-linker, In vivo cross-linking, Chemoreceptor interactions, Trimer of dimers, Cysteine reporter

1 Introduction

In vivo cross-linking is one of the experimental approaches available for exploring the structure of receptor signaling complexes in their native context. The use of bifunctional cross-linkers, as well as the introduction of cysteine residues that can form disulfide bridges, provides important information about protein interactions in whole cells [1, 2]. However, the homodimeric nature of chemoreceptors, and their organization in trimers of dimers that can be formed by different homodimers, makes it difficult to interpret the results of bifunctional cross-linking. For examples, it is unclear whether the cross-linked subunits belong to the same dimer, to different dimers within the same trimer, or even between dimers located in different trimers.

TMEA [Tris-(1-maleimidoethyl-amide)], a trifunctional maleimide-based cross-linker with a spacing between maleimide groups of 10.3 Å (Fig. 1a), provides a tool to trap the internal

Michael D. Manson (ed.), *Bacterial Chemosensing: Methods and Protocols*, Methods in Molecular Biology, vol. 1729, https://doi.org/10.1007/978-1-4939-7577-8_15,

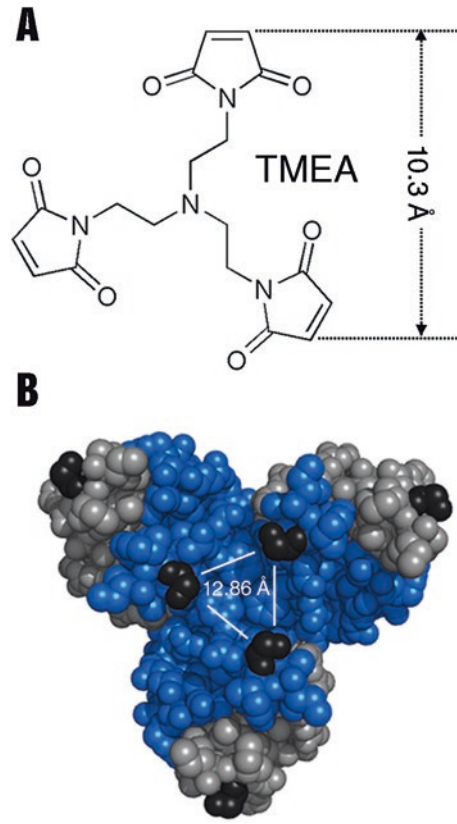

Fig. 1 Introduction of cysteine residues to be targeted by TMEA. (**a**) Structure of TMEA. (**b**) Cross-sectional view of the cytoplasmic portion of a trimer of dimers of Tsr (seen from the membrane) containing residues 364–410 (S366 highlighted in black). The inner subunit of each dimer is colored blue, whereas the external one is colored gray

subunits of a trimer of dimers, thereby greatly simplifying the interpretation of the results. This reagent was used to answer a variety of questions concerning the higher-order arrangement and dynamics of chemoreceptors in *E. coli* living cells. Because of the high conservation of the cytoplasmic domain of chemoreceptors, both in amino acid sequence [3] and in chemoreceptor array organization as determined by cryo-electron tomography [4], this method can be applied to chemoreceptors from a wide variety of microorganisms in order to evaluate their in vivo organization.

2 Materials

1. Tryptone broth: 1% tryptone, 0.5% NaCl. Sterilize.
2. KEP Buffer: 10 mM potassium phosphate (pH 7), 0.1 mM EDTA. Sterilize and store at room temperature.

3. TMEA [tris (2-maleimidoethyl) amine]: Cross-linking reagent purchased from Pierce (now Thermo Fisher Pierce). Prepare a 25 mM stock and a 2.5 mM working solution in DMSO and store at −20 °C.
4. NEM (*N*-ethylmaleimide): Reagent used to quench the unreacted thiol groups before denaturing the samples. Prepare a 1 M stock solution in DMSO and store at −20 °C.
5. Denaturing gel electrophoresis (SDS-PAGE): Cross-linking products are electrophoresed in conventional polyacrylamide gels [5] with modifications that have been suggested to improve the resolution of differently methylated species of chemoreceptors [6]. Essentially, the separation gel has a low percentage of bisacrylamide (typically, 10% acrylamide–0.05% bisacrylamide) and a pH of 8.2 (*see* **Note 1**). In these gels, proteins smaller than 50 kDa run with the front dye.
6. Immunoblotting: Cross-linking products are visualized by standard immunoblotting procedures using a specific anti-Tsr antiserum directed against the highly conserved portion of its signaling domain. This antiserum recognizes both Tsr and Tar chemoreceptors, and also the other chemoreceptors of *E. coli* and many chemoreceptors of other microorganisms. As secondary antibody we use either Cy5-labeled (Amersham) or alkaline phosphatase-conjugated (Sigma) goat anti-rabbit immunoglobulin G. Cy5-labeled antibodies can be detected with a fluorimager (Storm 840, Typhoon, Amersham), whereas alkaline phosphatase-conjugated antibodies are developed with nitro blue tetrazolium and 5-bromo-4-chloro-3-indolyl phosphate (both from Sigma). Images are converted to grayscale with a digital scanner and analyzed by ImageQuant software (Amersham).

3 Methods

In this section we describe in detail the use of TMEA to study chemoreceptor array organization and dynamics. First, we describe how to choose the cysteine reporter residues. Then we go through the cross-linking assay and describe examples of how it can be used to learn different aspects of chemoreceptor organization in living cells.

3.1 Introduction of Cysteine Reporter Residues

1. Before starting, it is important to analyze whether the primary sequence of the protein of interest has any native cysteine residue. If this is the case, it is advisable to replace the native Cys codons by alanine or serine codons, as long as the replacement does not cause an alteration in chemotactic function (*see* **Note 2**).

For the particular case of the *E. coli* Tsr and Tar receptors, there are no cysteine residues in their native sequence.

2. Model the cytoplasmic domain of the chemoreceptor under study using the crystal structure of Tsr (1QU7, [7]) as a template. Using a protein visualization interface (SWISS MODEL, RASMOL, PyMOL, etc.), evaluate the predicted distance between different residues in the subunits facing the trimer axis, as these are potential targets of the cross-linker when replaced by Cys. The maleimide groups in TMEA groups lie 10.3 Å apart (Fig. 1a). These groups react with the cysteine thiol and, if the Cys residues are correctly spaced, can cross-link all three axial subunits of a chemoreceptor trimer. The original Cys replacements in Tsr were introduced at positions 369 or 366. The corresponding distances between the α-carbons from these residues in the axial subunits of the trimer are 14.7 and 12.86 Å, respectively. TMEA treatment of cells carrying these Cys-substituted Tsr molecules generated 2- and 3-subunit cross-linking products, indicating that in both cases the thiol groups have an appropriate trigonal geometry (Fig. 1a). However, because only the Tsr S366C derivative was able to support serine chemotaxis as well as wild-type Tsr, as assessed in soft agar plates, this was the replacement of choice for subsequent experiments [8, 9].

   Inspection of the crystal structure of Tsr makes it evident that the 3-subunit products are formed by the covalent trapping of the three internal subunits of the trimer, as the cysteine residues in the external ones are very far from each other (Fig. 1b). In later experiments Cys replacements at positions that displayed the proper trigonal symmetry but were expected to be located at greater distances from each other, based on the crystal structure, also gave rise to 2- and 3-subunit cross-linking products upon TMEA treatment, but with significantly decreased efficiency, as expected [10].

3. Make the Cys replacement at the selected codon in the chemoreceptor-coding plasmid by site-directed mutagenesis [e.g., by using the QuikChange (Stratagene) mutagenesis kit]. Verify the presence of the residue change(s) causing the Cys replacement as the only mutation by sequencing the entire chemoreceptor gene coding region (*see* **Note 3**).
4. Assess the ability of the Cys-substituted chemoreceptor to drive chemotaxis (*see* **Note 4**).

3.2 Direct Cross-Linking Assay in E. coli

Here, conditions that worked with *E. coli* are described. Some steps might have to be modified for other organisms.

1. Grow an overnight culture of *E. coli* cells carrying the chemoreceptor-encoding expression plasmid at 37 °C in TB with the appropriate antibiotic.

2. Subculture 100 μL of each overnight culture into 5 mL of TB plus antibiotic and incubate with shaking at 30 °C for 1.5 h.
3. Induce the expression of the chemoreceptor at the desired level for 3 h or until they reach mid-exponential phase. In general, induction conditions that produce the normal cellular complement of the receptor being studied are best.
4. Harvest the cells by centrifugation at 6000 × *g*, wash twice with KEP buffer, and resuspend in KEP buffer to OD_{600nm} = 2.
5. For each mutant protein tested, label two 1.5 mL microcentrifuge tubes: one for the cells treated with TMEA (+) and one for the cells without treatment (−). Place 0.5 mL of the cell suspensions into the tubes and incubate for 5 min at 30 °C.
6. Add 10 μL of 2.5 mM TMEA solution (50 μM final concentration, +) or 10 μL of DMSO (−), vortex, and incubate for 20 s at 30 °C (*see* **Note 5**). Quench the reactions by addition of 5 μL of 1 M NEM (10 mM final concentration).
7. Harvest the cells by centrifugation at 6000 × *g* and resuspend them in 50 μL of Laemmli sample buffer.
8. Boil for 5 min to lyse the cells. Vortex. Run the protein samples in a low-bisacrylamide polyacrylamide gel (*see* **Note 1**).
9. Visualize the chemoreceptors by immunoblotting (*see* **Note 6**).

3.3 Analysis and Interpretation of Cross-Linking Assays

1. In cells that express only one chemoreceptor carrying a properly positioned cysteine residue, TMEA treatment of the cells will generate both 2- and 3-subunit cross-linking products, which represent the ability of the reagent to trap two or three of the internal subunits of the trimer of dimers (Fig. 2a). For the S366C replacement in Tsr (or its equivalent S364C replacement in Tar), which is targeted by TMEA with high efficiency, virtually all the trimers can be targeted by the reagent, as is deduced from quantification of the resulting bands. About half of the amount of Tsr (or Tar) protein that can be visualized in nontreated cells (Fig. 2, lanes 1 and 5) is shifted into 2- or 3-subunit cross-linked species upon treatment with TMEA (Fig. 2, lanes 6 and 10). This represents the maximal possible cross-linking products for this particular reporter residue, considering that the external subunit of each dimer is not covalently attached to any other subunit by TMEA (*see* **Note 7**).
2. In cells that express two chemoreceptors displaying different mobilities, each carrying a Cys reporter, the occurrence of cross-linked products of intermediate mobility will indicate the ability of these two chemoreceptors to form mixed trimers of dimers. An example for cells expressing Tsr S366C and Tar S364C is shown in Fig. 2b, lanes 7–9. In the 2-subunit region of the gel, the extra band corresponds to a Tsr-Tar cross-linking

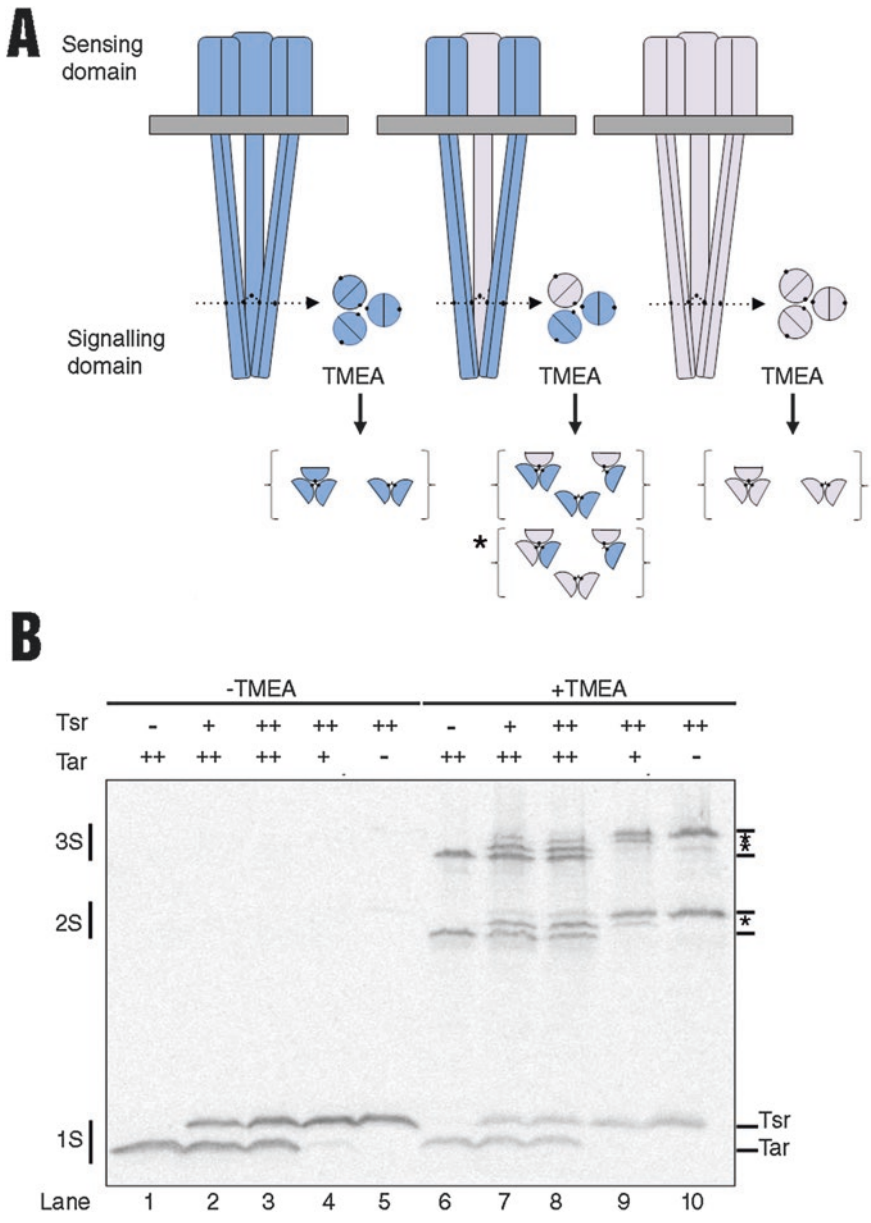

Fig. 2 Basic cross-linking assay. (**a**) Schematic representation of the assay. Pure (left and right) or mixed (center) trimers of dimers are shown from the side and in cross-sectional view at the level of the Cys substitution (black dot). After TMEA treatment and denaturation of the cell extract, different kinds of cross-linked products are obtained. (**b**) Example gel. Cells expressing only Tar-C (lanes 1 and 6), only Tsr-C (lanes 5 and 10), or different relative amounts of both Cys-substituted receptors (lanes 2–4 and 7–9) were treated (lanes 6–10) or not (lanes 1–5) with TMEA and analyzed by immunoblotting with an anti-Tsr antiserum. On the left, regions corresponding to the monomers (1S) or to the cross-linked products of two (2S) or three (3S) subunits are indicated. On the right, the position of each cross-linked product is indicated. Lines point out pure products and asterisks mixed ones

product. In the 3-subunit region of the gel, two extra bands can be detected: they represent TMEA-cross-linked products from mixed trimers of dimers containing different numbers of Tsr and Tar subunits (*see* **Note 8**).

3.4 Cross-Linking Exchange Assay

The TMEA cross-linking assay described in Subheading 3.2 provides a snapshot of chemoreceptor trimers in the cell that reflects the instantaneous composition of the receptor population. In the polar chemoreceptor clusters, trimers of dimers are inter-connected through contacts with the coupling protein CheW and the kinase CheA, forming very large arrays [12]. To explore how dimers exchange among different trimers within the array under different conditions, we devised an exchange assay [8]. The principal idea of the assay is to follow the fate of established trimers made by one chemoreceptor type following strong induction of a second chemoreceptor type. The particular example described uses the Tsr and Tar receptors, but it can easily be extended to any other chemoreceptor pair that will cross-link upon the appropriate Cys substitution.

1. Grow a strain carrying a constitutively, (preferably) chromosomally, expressed Tar-C reporter and an inducible Tsr-C plasmid to midlog phase.
2. Add a concentration of the inducer that will allow expression of Tsr-C to the desired level.
3. At different times following induction, harvest cells from a portion of the culture, resuspend them in KEP buffer, and treat them with TMEA as described in Subheading 3.2.
4. Analyze the pattern of cross-linked products for each of the time points, as described below.
5. Two possible exchange patterns can be observed after short times of induction. If Tar-C trimers are highly dynamic the composition of trimers after Tsr-C induction will depend entirely on the relative cellular levels of the two types of receptors as the induction proceeds. At short induction times, the newly made Tsr-C molecules will be found in mixed trimers as depicted in Fig. 3a (exchange alternative). An example of this situation is shown in Fig. 3b: in the absence of CheA and CheW, almost all Tsr-C molecules are found in mixed cross-linked products, indicating that they are being incorporated into mixed trimers (Fig. 3b, lane 5). Only after a long induction time, when there is a higher total level of Tsr-C than of Tar-C, can pure Tsr-C trimers be found (Fig. 3b, lane 6).

   In contrast, if Tar-C trimers are less dynamic, forming part of a very stable array in the presence of CheA and CheW, the recently made Tsr-C molecules will be found only in pure

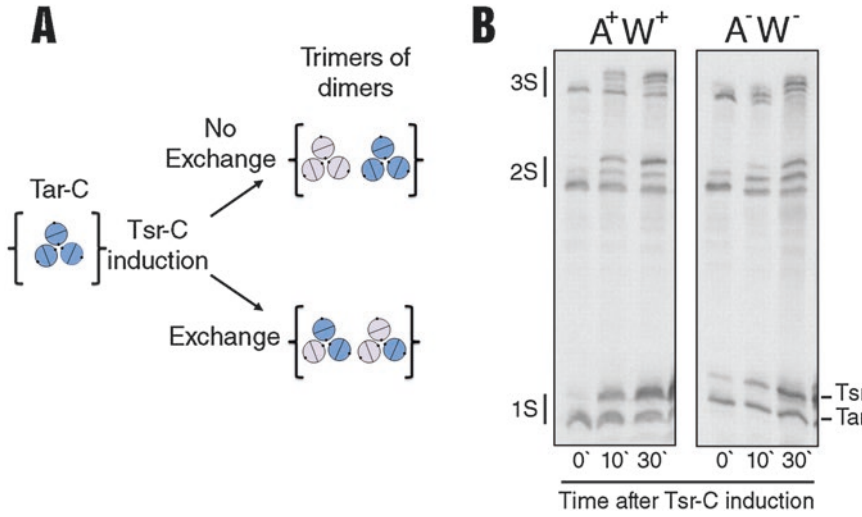

Fig. 3 Exchange assay to assess trimer dynamics. (**a**) Schematic representation of the assay. The strain that contains chromosomally encoded Tar-C makes only Tar-C trimers (left). Upon a brief induction of Tsr-C, newly synthesized Tsr-C dimers can freely incorporate into mixed trimers of dimers with preexisting Tar-C dimers (right, exchange condition) or segregate to form pure Tsr-C trimers (right, no-exchange condition) if the preexisting Tar-C dimers are not readily available for exchange. (**b**) Example gel. The exchange experiment was done in cells containing (left) or lacking (right) CheA and CheW. In the presence of CheA/W, more pure than mixed cross-linking products are detected at 10 and 30 min after induction (lanes 2 and 3), indicating that the exchange is severely compromised. In contrast, in the absence of CheA/W, almost all the newly synthesized Tsr-C molecules form part of mixed cross-linking products after 10 min of induction (lane 5), and only when Tsr-C reaches a higher intracellular concentration are the pure Tsr-C products detectable (lane 6)

cross-linked products, and mixed products will be restricted to the trimers formed by newly synthesized Tsr-C molecules together with newly synthesized Tar-C molecules (Fig. 3a, no exchange alternative). An example of this situation is shown in Fig. 3b. The limited exchange is easily visualized by the "sandwich" appearance of the cross-linking products, both in the 2- and 3-subunit regions, in which pure Tar-C and pure Tsr-C are much more abundant than the corresponding mixed products (Fig. 3b, lanes 2 and 3).

6. The rate of exchange can be calculated at short times after induction, i.e., at low levels of the induced receptor, by quantifying the fractional abundance of both receptors in TMEA-untreated samples and the cross-linked products in the 2-subunit region of the gel (*see* **Note 8**). At a maximal exchange rate, the abundance of the 2-subunit mixed product will reflect the relative abundance of the two receptors, whereas this number will deviate from the expected one if the exchange is severely restricted.
7. Using this technique, we determined that the presence of both CheA and CheW is required to form a stable chemoreceptor

array. We also found that a CheA derivative containing only the P3 dimerization domain and the P5/CheW-interaction domain can provide all the contacts needed for the assembly of a stable array [8].

3.5 Cross-Linking Competition Assay

The trimer-based interpretation of the TMEA cross-linking results predicts that high relative levels of a receptor with no Cys reporter should decrease the number of cross-linked products seen with a receptor having a TMEA reporter site (Fig. 4a, trimer-proficient chemoreceptor). In contrast, if the chemoreceptor in excess is not able to form mixed trimers with the receptor containing the reporter site, then its overexpression should not affect the amount of cross-linking products (Fig. 4a, trimer-deficient chemoreceptor). To carry out competition experiments, we built a strain with a chromosomally encoded Tar-S364C (Tar-C) reporter and no other receptors [8, 13]. In this strain, the competitiveness of any other unmarked receptor can be assessed. This approach is useful in order to identify receptors with defects in the ability to form trimers.

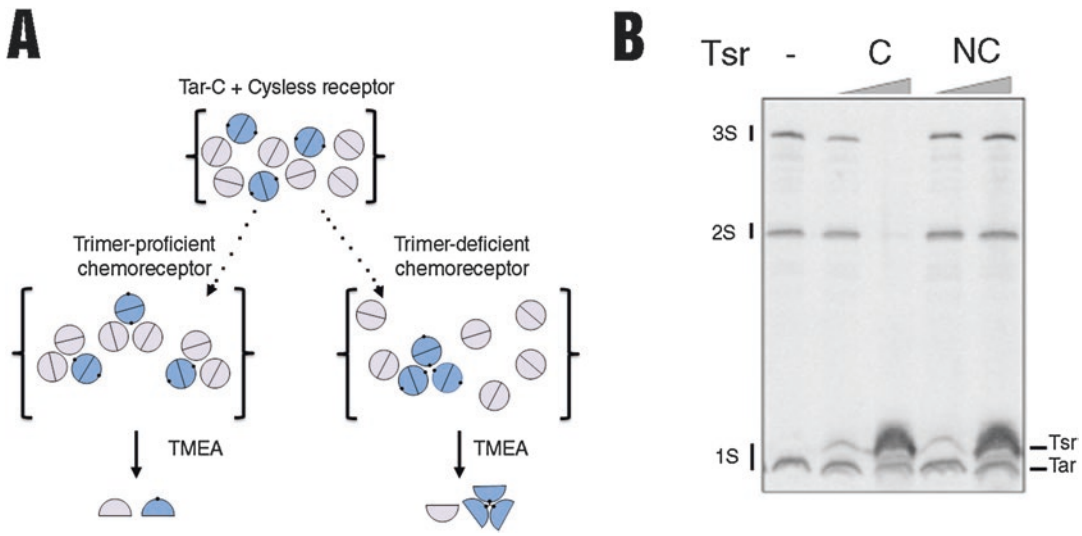

Fig. 4 Competition assay to assess the ability of unmarked chemoreceptors to form trimers. (**a**) Schematic representation of the assay. High levels of unmarked receptors (light gray) are expressed in a strain that contains only one type of Cys-substituted receptor (dark gray). Individual dimers in such a strain (top) can assemble into mixed trimers of dimers in which the Cys-containing receptor will be in the minority and thus not generate cross-linked products after treatment with TMEA (bottom left, competitor), or pure Cys-containing trimers that will yield cross-linked products if the second receptor is unable to incorporate into mixed trimers (bottom right, noncompetitor). (**b**) Example gel. Cells expressing only Tar-C (lane 1), or Tar-C plus a competitor Tsr (C, lanes 2 and 3), or Tar-C plus a noncompetitor Tsr mutant (NC, lanes 4 and 5) were treated with TMEA and analyzed by immunoblotting with an anti-Tsr antiserum. As the level of wild type Tsr increases, the Tar-C cross-linking products almost disappear (lane 3), whereas this does not happen when the noncompetitor Tsr mutant is overexpressed (lane 5)

The example in Fig. 4b shows the TMEA cross-linking pattern of Tar-C in the absence of any other receptor or in the presence of different levels of Tsr lacking the Cys reporter. Wild-type Tsr or variants thereof that are able to join mixed trimers of dimers behave as competitors and completely suppressed Tar-C cross-linked products when overexpressed (Fig. 4b, lane 3), In contrast, Tsr mutants with defects in interreceptor interactions (e.g., Tsr I377P) do not interfere with the formation of Tar-C cross-linked products, even when expressed at a very high level (Fig. 4b, lane 5). Using this assay, we have been able to identify Tsr mutants that display trimer-forming defects (*see* **Note 9**). We have also been able to evaluate the ability of chemoreceptors from different organisms to interact with *E. coli* receptors. In this way, we determined that a chemoreceptor from *Rhodobacter sphaeroides*, whose cytoplasmic hairpin is one heptad (seven residues in each arm) shorter than the *E. coli* receptors, can still form mixed trimers with Tar [14]. However, PctApp, an amino acid chemoreceptor from *Pseudomonas putida* that has a cytoplasmic domain two-heptads longer than that of the *E. coli* receptors, is unable to form mixed trimers with Tar [15]. On the other hand, the inability of a two-heptad longer Tsr functional derivative to compete, although it could still form pure trimers, demonstrates that receptors of different lengths in the same cell can assemble and signal independently [16].

4 Notes

1. In our experience, the resolution of the cross-linked products is somehow tricky, especially in the 3-subunit region. The resolution is usually improved by using freshly prepared and filtered acrylamide solution stock (40% acrylamide–0.2% bisacrylamide), ultrapure water, and high quality reagents (Tris, SDS, even the glycine in the electrophoresis buffer). The resolution of the mixed cross-linked products of 2 and 3 subunits can be improved by increasing the length of the gels or decreasing the final acrylamide-bisacrylamide concentration to 8%:0.04%. Sometimes, it also helps to lower the current to slow down the band migration.
2. If it is impossible to generate a functional Cys-less functional chemoreceptor, care has to be taken with the interpretation of results, as the cross-linking reagent will react both with the native and the reporter cysteine residues. Control experiments with the native protein (that is, without any introduced Cys residue) should be performed.
3. Before sequencing, the presence of the introduced Cys residue can easily be screened by PEGylation using maleimide-PEG (basic protocol in Chapter 13).

4. In *E. coli*, we test function in soft agar tryptone plates using a receptorless strain transformed with the corresponding chemoreceptor-encoding plasmid. Both Tsr S366C and the equivalent Tar S364C are comparable to the wild-type receptors in this assay.
5. The extents and patterns of cross-linking do not change with TMEA treatments between 5 s and 2 h. This is probably due to rapid reaction of TMEA with all the available subunits, followed by quenching of the nonreacting maleimide groups by intracellular thiols. Higher TMEA concentrations do not enhance the yield of cross-linking products.
6. Low-bisacrylamide gels are very soft and elastic. Care should be taken while detaching gels from glass or aluminum plates in order to set up the transfer to PVDF or nitrocellulose membranes. It is advisable to soak the gel in transfer buffer before taking it off the plates, and to remove the gel very gently.
7. Using this assay, we have also demonstrated that the presence of high levels of CheW disrupt the trimers of dimers, presumably by competing for the interaction with the tip of the receptor that is also involved in dimer-to-dimer interactions [11].
8. A careful quantification of the cross-linked products with respect to the relative amount of each chemoreceptor species detected in the absence of any TMEA treatment allows assessment of whether there is a bias to form pure (composed by only one type of receptor) versus mixed trimers of dimers. For simplicity, and considering that a good resolution of bands in the 3-subunit region of the gels is not easily achieved, it is advisable to quantify the 2-subunit products, which has provided reliable results in experiments in which the relative concentrations of receptors was varied. Two receptors that are able to form pure and mixed trimers with the same probability will generate 2-subunit mixed products with a frequency of 2pq (with p and q being the fractional abundance of each receptor).
9. A mutant receptor that is characterized as noncompetitor in a competition assay is hypothetically unable to form mixed trimers, and it is probably also defective in pure trimer formation. However, we have found noncompetitor mutants that are still able to form 3-subunit pure (and even mixed) products when they are tested by direct cross-linking. This result could reflect the instability of the trimers, so that they become cross-linked if they contain the Cys reporter but fail to compete with Tar for inclusion in a mixed trimer. We recommend that the results of the competition assay should be complemented by direct cross-linking assays to strengthen any conclusions about trimer formation ability.

Acknowledgment

We thank Andrea Pedetta (University of Mar del Plata) for comments on the manuscript.

References

1. Chelsky D, Dahlquist FW (1980) Chemotaxis in *Escherichia coli*: associations of protein components. Biochemistry 19:4633–4639
2. Ames P, Studdert CA, Reiser RH, Parkinson JS (2002) Collaborative signaling by mixed chemoreceptor teams in *Escherichia coli*. Proc Natl Acad Sci U S A 99:7060–7065
3. Alexander RP, Zhulin IB (2007) Evolutionary genomics reveals conserved structural determinants of signaling and adaptation in microbial chemoreceptors. Proc Natl Acad Sci U S A 104:2885–2890
4. Briegel A, Ortega DR, Tocheva EI, Wuichet K, Li Z et al (2009) Universal architecture of bacterial chemoreceptor arrays. Proc Natl Acad Sci U S A 106:17181–17186
5. Laemmli UK (1970) Cleavage of structural proteins during the assembly of the head of bacteriophage T4. Nature 227:680–685
6. Kehry MR, Engstrom P, Dahlquist FW, Hazelbauer GL (1983) Multiple covalent modifications of Trg, a sensory transducer of *Escherichia coli*. J Biol Chem 258: 5050–5055
7. Kim KK, Yokota H, Kim SH (1999) Four-helical-bundle structure of the cytoplasmic domain of a serine chemotaxis receptor. Nature 400:787–792
8. Studdert CA, Parkinson JS (2005) Insights into the organization and dynamics of bacterial chemoreceptor clusters through in vivo crosslinking studies. Proc Natl Acad Sci U S A 102:15623–15628
9. Studdert CA, Parkinson JS (2004) Crosslinking snapshots of bacterial chemoreceptor squads. Proc Natl Acad Sci U S A 101:2117–2122
10. Massazza DA, Parkinson JS, Studdert CA (2011) Cross-linking evidence for motional constraints within chemoreceptor trimers of dimers. Biochemistry 50:820–827
11. Cardozo MJ, Massazza DA, Parkinson JS, Studdert CA (2010) Disruption of chemoreceptor signalling arrays by high levels of CheW, the receptor-kinase coupling protein. Mol Microbiol 75:1171–1181
12. Liu J, Hu B, Morado DR, Jani S, Manson MD et al (2012) Molecular architecture of chemoreceptor arrays revealed by cryoelectron tomography of Escherichia coli minicells. Proc Natl Acad Sci U S A 109:E1481–E1488
13. Parkinson JS, Ames P, Studdert CA (2005) Collaborative signaling by bacterial chemoreceptors. Curr Opin Microbiol 8:116–121
14. Massazza DA, Izzo SA, Gasperotti AF, Herrera Seitz MK, Studdert CA (2012) Functional and structural effects of seven-residue deletions on the coiled-coil cytoplasmic domain of a chemoreceptor. Mol Microbiol 83:224–239
15. Herrera Seitz MK, Soto D, Studdert CA (2012) A chemoreceptor from Pseudomonas putida forms active signalling complexes in *Escherichia coli*. Microbiology 158(Pt 9):2283–2292
16. Herrera Seitz MK, Frank V, Massazza DA, Vaknin A, Studdert CA (2014) Bacterial chemoreceptors of different length classes signal independently. Mol Microbiol 93:814–822

Part IV

Cryo-EM Methods for Studying Chemoreceptor Structure

Chapter 16

Use of Cryo-EM to Study the Structure of Chemoreceptor Arrays In Vivo

Wen Yang and Ariane Briegel

Abstract

Cryo-electron microscopy (cryo-EM) allows the imaging of intact macromolecular complexes in the context of whole cells. The biological samples for cryo-EM are kept in a near-native state by flash freezing, without the need for any additional sample preparation or fixation steps. Since transmission electron microscopy only generates 2D projections of the samples, the specimen has to be tilted in order to recover its 3D structural information. This is done by collecting images of the sample with various tilt angles in respect to the electron beam. The acquired tilt series can then be computationally back-projected. This technique is called electron cryotomography (ECT), and has been instrumental in unraveling the architecture of chemoreceptor arrays. Here we describe the method of visualizing in vivo bacterial chemoreceptor arrays in three main steps: immobilization of bacterial cells on EM grids by plunge-freezing; 2D image acquisition in tilt series; and 3D tomogram reconstruction.

Key words Cryo-EM, Cryotomography, Plunge freezing, Chemoreceptor arrays

1 Introduction

Electron cyrotomography (ECT) is a new technique that has recently been used to gain insight into structure and function of macromolecular complexes inside intact cells, such as bacteria, archaea, and even small eukaryotic cells [1, 2]. Rapid progress in the development of both hardware and software involved in ECT in the past decade has provided the technological basis necessary for the understanding of structure and function of bacterial chemoreceptor arrays. The arrays were first identified as cytosolic plate-like structures at cell poles. They lie parallel to the membrane and have perpendicular pillar-like densities of the chemoreceptors spanning into the periplasmic space [3]. The plate like density is called the base plate; it is comprised of the histidine kinase CheA and the linking protein CheW. Subsequent improvement in resolution revealed the hexagonal packing of chemoreceptors above the CheA/CheW base plate with a center-to-center spacing of 12 nm [4].

Michael D. Manson (ed.), *Bacterial Chemosensing: Methods and Protocols*, Methods in Molecular Biology, vol. 1729, https://doi.org/10.1007/978-1-4939-7577-8_16,

Further improvement was achieved by implementing image correction procedures such as contrast transfer function (CTF) correction and subvolume averaging. These advances finally revealed the native architecture of the chemoreceptor arrays: they consist of a hexagonally packed lattice of the trimers of receptor dimers networked by rings formed by CheW and the P5 domain of CheA. Neighboring CheA/CheW rings are structurally connected via the dimerization domain P3 of CheA [5, 6]. In addition to the abundant structural information, ECT has also provided important insights in understanding the molecular mechanism of receptor signaling and CheA kinase functioning [7, 8].

ECT allows the study of chemoreceptor arrays in the context of whole cells in a near-native state. In order to withstand the high vacuum of the cryogenic electron microscope, the cells have to be embedded in a thin layer of vitreous ice. The most commonly used method to generate thin, vitrified samples is called plunge-freezing (Fig. 1) [1]. A few microliters of sample (e.g., cell culture) is spread out over an EM grid. Excess water is blotted away either manually or automatically with filter paper, and the grid is then plunged into liquid ethane or ethane–propane mixture that is cooled by liquid nitrogen. This allows freezing of the sample at an extremely high cooling rate (>10,000 K/s) and prevents water from crystallizing, instead forming vitreous ice. Thus, cellular structures are preserved in a near-native state [10]. Vitrified specimens on EM grids must be transferred and stored below 120 K (−153 °C) to maintain the "frozen-hydrated" state [11].

In order to gain 3D information of the biological specimen, a series of 2D projection images is collected while the sample is incrementally tilted along the axis perpendicular to the electron beam (Fig. 2) [14]. However, this typically requires the acquisition of ~100 or more individual 2D images of the sample. Since the

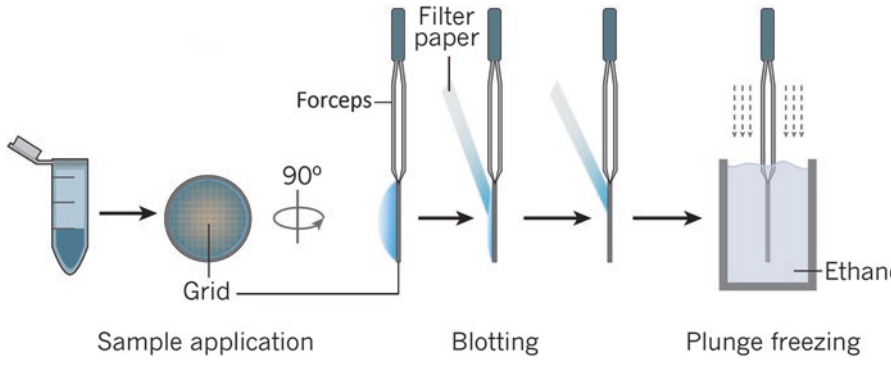

Fig. 1 Sample preparation procedure for cyro-EM. A few microliters of bacterial cells suspension mixed with gold nanoparticles is applied to an EM-grid held by forceps. During blotting, filter paper wicks off the excessive liquid and leaves a thin aqueous layer. Plunge freezing fixes this aqueous layer into vitreous ice, and bacterial cells are preserved at their near-native state. *Reproduced with permission from* [9]

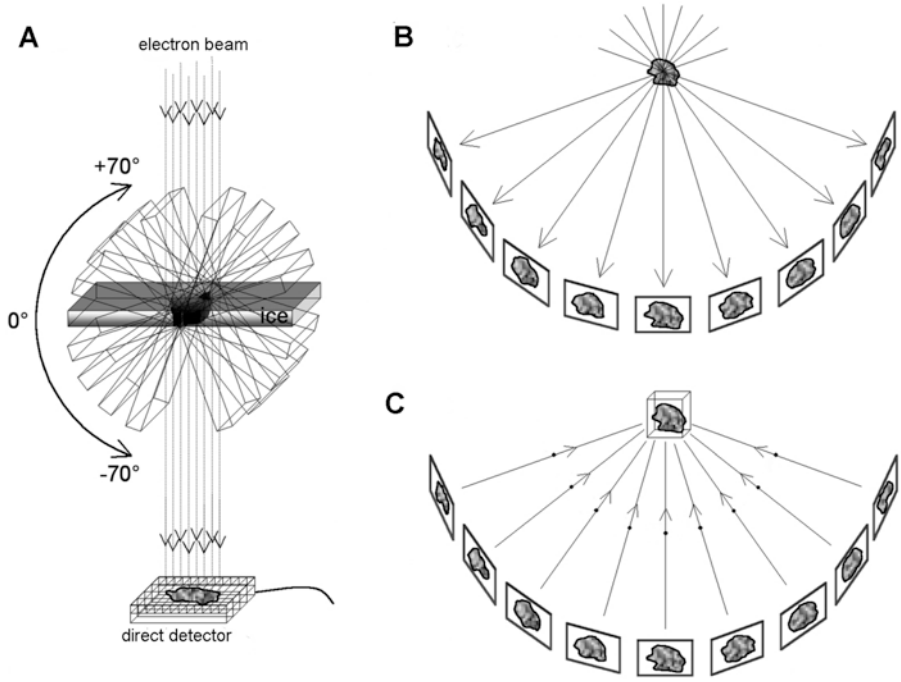

Fig. 2 Basic principle of cryotomography. (**a**) The specimen holder tilts according to the preset tilting scheme around a tilting axis perpendicular to the electron beam, and projection images of the same illumination area on the specimen are recorded on the detector. (**b**) The 2D images captured in a tilt-series correspond to a set of projections of the 3D sample with different tilt angles in respect to the electron beam. (**c**) After precise alignment, the successive projection images are merged computationally into one density map (referred to as tomogram) correspond to the specimen volume for example by weighted back-projection [12]. *Reproduced with permission from* [13]

vitrified samples are very electron-dose sensitive, the most critical factor is to limit the total electron dosage in order to allow complete tilt-series acquisition before structures are irreversibly destroyed by radiation damage [15]. Based on the type of sample, total electron dose, magnification, defocus value, tilting range, and angular increment, all must be selected carefully for data collection [16, 17].

Once a tilt series of a biological sample is collected, the tomogram (the 3D density map) can be computationally calculated by back-projection of the 2D images into the sample volume. A successful 3D reconstruction relies on precise alignment of the 2D images of the tilt series. Alignment of the 2D images prior to 3D reconstruction is therefore essential. Instead of cross-correlation methods, an alignment based on gold fiducial particles is commonly used, especially in the case of thicker samples such as intact bacterial cells. Here, gold colloidal particles, typically 5–15 nm in diameter, are mixed together with the biological sample. These highly electron dense particles are easily visible in the individual 2D images of a tilt series and can be used to align the individual 2D

projections [18]. Several software packages are available for tomogram reconstruction, either fully automatic or interactive through a graphic user interface. Several different reconstruction schemes are available, such as weighted back-projection [12], SIRT [19] or SART [20]. In-depth information on these computational methods can be found in the respective publications. Additional data-processing steps such as contrast transfer function (CTF) correction [21, 22] and subvolume averaging [23, 24] can also be applied to obtain higher signal-to-noise ratios in the cryo-EM maps to study the structure of chemoreceptor arrays.

Although ECT is an important tool for structural studies of molecular machines, the high cost of the required specialized equipment and in-depth expertise of the operators prevents many laboratories from utilizing this technique. Therefore, this chapter provides methods that focus primarily on cryo-EM sample preparation and evaluation that is essential to generate adequate samples for ECT. The method description below is based on the particular instrument in our laboratory; adjustment of parameters and condition may be required for alternative instrument setups. Unless your laboratory is a dedicated cryo-EM facility, access to high-end equipment is available at one of several open-access EM facilities worldwide (*see* **Note 1**). Although this chapter provides suggestions for data collection parameters for imaging chemoreceptor arrays, the on-site expert staff of a cryo-EM facility should provide the necessary in-depth advice on proper data acquisition and processing.

2 Materials

2.1 Consumables

1. Quantifoil grids (Cu 200 mesh R2/2; Quantifoil Micro Tools GmbH, Germany).
2. Colloidal gold solution (10 nm) (Sigma, St. Louis, MO, USA).
3. Bovine Serum Albumin solution (5%) (Sigma, St. Louis, MO, USA).
4. Bacterial culture.
5. Ethane.
6. Liquid nitrogen.

2.2 Equipment

1. Sputter coater (e.g., Quorum Technologies, UK).
2. Leica EM GP immersion freezer (Leica Microsystems, Vienna, Austria) or similar (*see* **Note 2**).
3. Tecnai Talos G2 (FEI Company, Hillsboro, OR, USA) or similar (*see* **Note 3**).

4. Cryo-transfer holders (Gatan Inc., Pleasanton, CA, USA).
5. Titan Krios (FEI Company, Hillsboro, OR, USA) (*see* **Note 3**).

2.3 Software

1. FEI Tomography (FEI Company, Hillsboro, OR, USA) (*see* **Note 4**).
2. IMOD [25, 26] (*see* **Note 5**).

3 Methods

3.1 Plunge Freezing Bacterial Cells on EM Grids

1. Grow bacteria culture to mid-exponential phase at an OD_{600} of 0.5 (*see* **Note 6**).
2. Place EM grids Quantifoil side up, glow discharge under 10^{-2} Mbar pressure, at 25 mA current for 45 s (*see* **Note 7**).
3. For the blotting chamber on the Leica freezer, set the temperature to room temperature; set the humidity to 95%; set the temperature of cryogen container to −183 °C.
4. Fill the liquid nitrogen tank, let the cryogen container cool down to the target temperature; and then fill up cryogen container carefully with ethane (*see* **Note 8**).
5. Wait until all parameters set up for the blotting chamber have been reached, secure an EM grid with the forceps provided with the plunge freezer and load it into the blotting chamber.
6. Mix 100 μL colloid gold solution with 25 μL 5% BSA solution and vortex briefly; spin down the BSA treated gold nanoparticles at 18,400 × *g* for 10 min; discard the supernatant and keep the pellets of colloidal gold for next step.
7. Mix 20 μL of bacteria culture with the colloidal gold prepared in **step 6** briefly on a vortex mixer.
8. Apply 3 μL cell culture mixture onto the carbon film coated side of the grid.
9. Set blotting time to 1 s and activate auto-plunge; blotting is done on the carbon film side followed by automatic plunging (*see* **Note 9**).
10. Transfer the frozen grid from liquid ethane swiftly to a labeled grid box in liquid nitrogen (*see* **Note 10**).
11. Screw the lid on the grid box tight and quickly transfer the grid box to a 50 mL conical tube in a nitrogen Dewar.
12. Check the quality of the ice on the grid with the cryogenic microscope operating at 120 kV to evaluate the success of the plunge-freezing (Fig. 3; *see* **Note 11**).

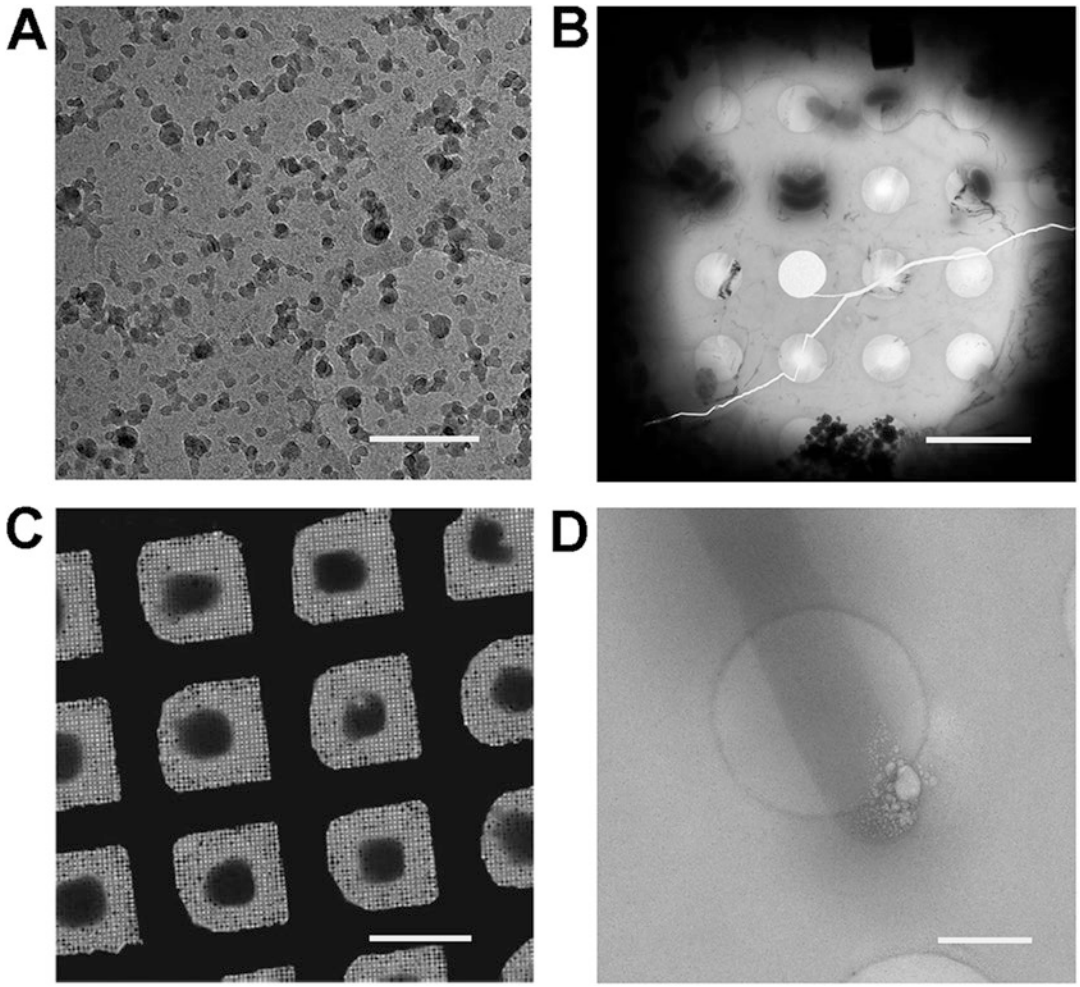

Fig. 3 Common problems found on cryo-EM grids due to contamination, mishandling, glow discharge failure, or radiation damage. (**a**) The dark blobs are usually the result of contaminants in the liquid ethane. *Adapted and reproduced with permission from* [27]. Scale bar is 250 nm. (**b**) A mesh square shows a big crack of the carbon film, extensive crystalline ice as indicated by the irregular dark marks and chucks of ice contamination at the bottom of the image. Scale bar is 5 μm. (**c**) Failure in proper glow discharging results insufficient hydrophilicity on the grid, which leads to thick ice core in each grid square center. *Reproduced with permission from* [28]. Scale bar is 100 μm. (**d**) The "bubbling" of cellular structures, here at an *E. coli* cell pole, is the typical result of radiation damage. Scale bar is 1 μm

3.2 Single Tilt-Series 2D Image Acquisition

Although different data acquisition software have various tilt series setup schemes, certain parameters are common for visualizing the chemoreceptor arrays. The general process of acquiring a tilt-series projection is outlined as follows.

1. Examine the loaded grid at low magnification with a low electron dose to find an area with optimal ice thinness; then localize the region of interest. For imaging bacterial chemoreceptors, it is preferred to target cell poles fixed in a hole of the carbon membrane where the sample thickness is minimized (Fig. 4) (*see* **Note 12**).

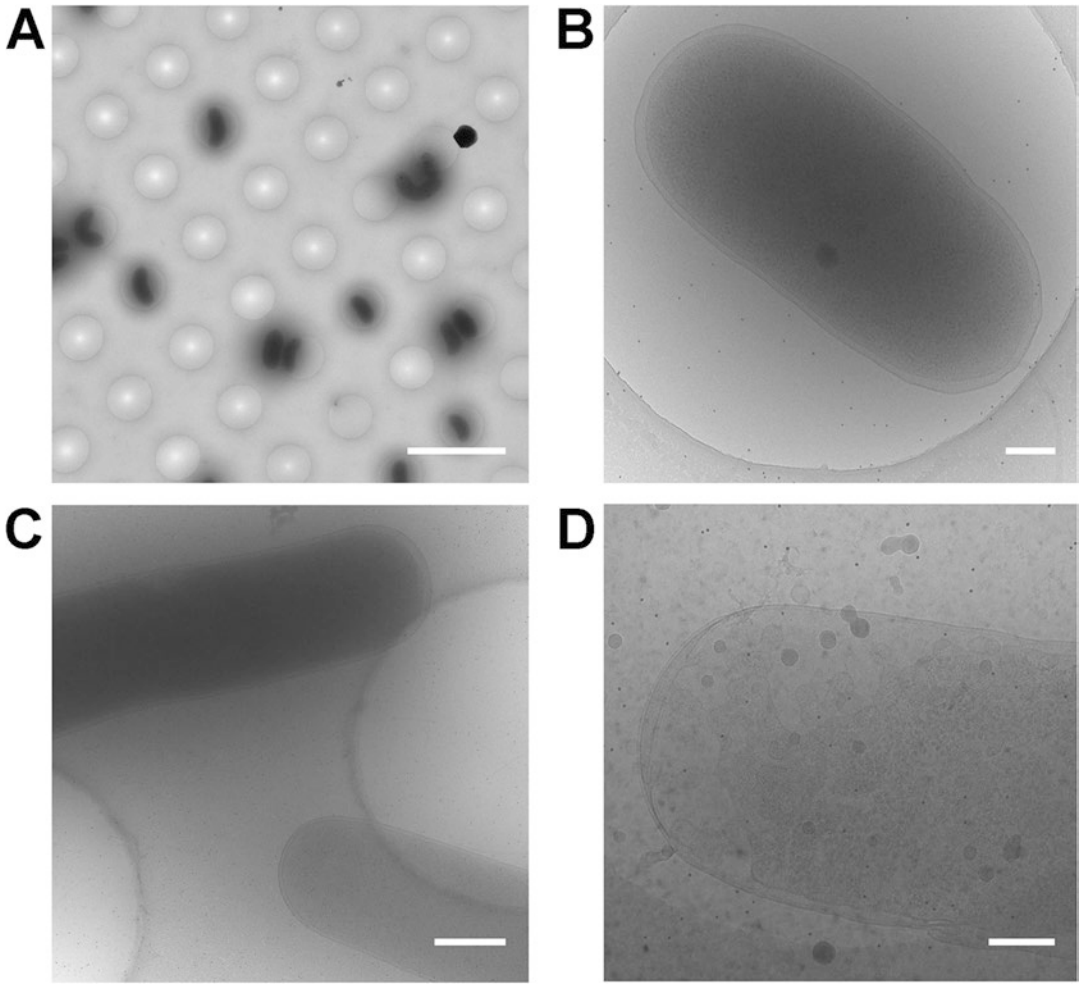

Fig. 4 Good cryo-EM specimens for bacteria chemoreceptor arrays study. (**a**) An ideal ice thickness with abundant *Vibrio cholerae* cells embedded. Scale bar is 5 μm. (**b**) For small cells (<2 μm in length), it is easy to find whole cells located in the holes of the carbon film. The vitreous ice appears as transparent, and the well-distributed black dots are gold nanoparticles serving as fiducials for images alignment. Scale bar is 200 nm. (**c**) For large cells, gentle lysis can effectively help to reduce the sample thickness without structurally disturbing the chemoreceptor array. Intact *E. coli* cell on the left appears much darker compared to the lysed cell on the right. Scale bar represents 500 nm. (**d**) A gently lysed *E. coli* cell in the hole is considerably thinner compared to intact cells, and the ordered pattern of the chemoreceptors can be identified at high magnification. Scale bar is 200 nm

2. Set the total electron dosage for single tilt series as 120 electrons/Å^2 (*see* **Note 13**).
3. Set up the increment, range and imaging scheme for tilting. For chemoreceptor arrays in the context of a native cell, we usually record over an angular range of ±60° with 1° or 2° increments. We typically use a tilting scheme where imaging starts at 0° and continues tilting to one extreme angle, then returns to zero tilt before tilting through the other side.

4. Set the defocus to −10 μm.
5. The magnification suitable for imaging chemoreceptor arrays roughly corresponds to a 3.5 Å pixel size (*see* **Note 14**).
6. Most software for ECT supports fully automated tracking and focusing for each tilt angle. For some software, it is important to select an area for tracking and autofocusing along the tilt axis close to the field of view but without overlapping to avoid damaging the data collection area. Depending on the software, camera hardware, and the data collection parameters used, it typically takes 20–60 min to collect the data for one single-tilt series (*see* **Note 15**).

3.3 Building Tomogram and Visualizing Chemoreceptor Arrays

1. IMOD is the data processing software package used in our lab. As a widely distributed, well-maintained and user-friendly software package, it offers informative description of each program on its website (http://bio3d.colorado.edu/imod/). A detailed description on cryo-tilt series data processing is also provided (http://bio3d.colorado.edu/imod/betaDoc/cryoExample.html). This open-source software package allows for CTF correction and provides the option for either SIRT or weighted back-projection to generate the tomographic reconstruction. For subvolume averaging, the PEET software package has been developed by the same research group as IMOD and provides the means to align and average subvolumes extracted from tomograms (http://bio3d.colorado.edu/PEET/). Please note that there are multiple options for tomogram reconstruction and further data processing available (*see* **Note 5**).
2. The tomographic image directly shows the native location and assembly forms of chemoreceptor arrays, and higher resolution cryo EM maps (20–35 Å) can also be obtained with additional data processing (Fig. 5).

4 Notes

1. Unless your laboratory is a dedicated cryo-EM facility, access to high-end equipment, such as a TITAN Krios Instrument (FEI Company, Hillsboro, OR, USA), is available at one of several multiuser EM facilities worldwide (Table 1) [31].
2. Other popular choices for commercial automatic plunge freezer include Cryoplunge (Gatan, Inc., Pleasanton, CA, USA) and Vitrobot (FEI Company, Hillsboro, OR, USA). Detailed protocol on how to use the Vitrobot has been described previously [32, 33].

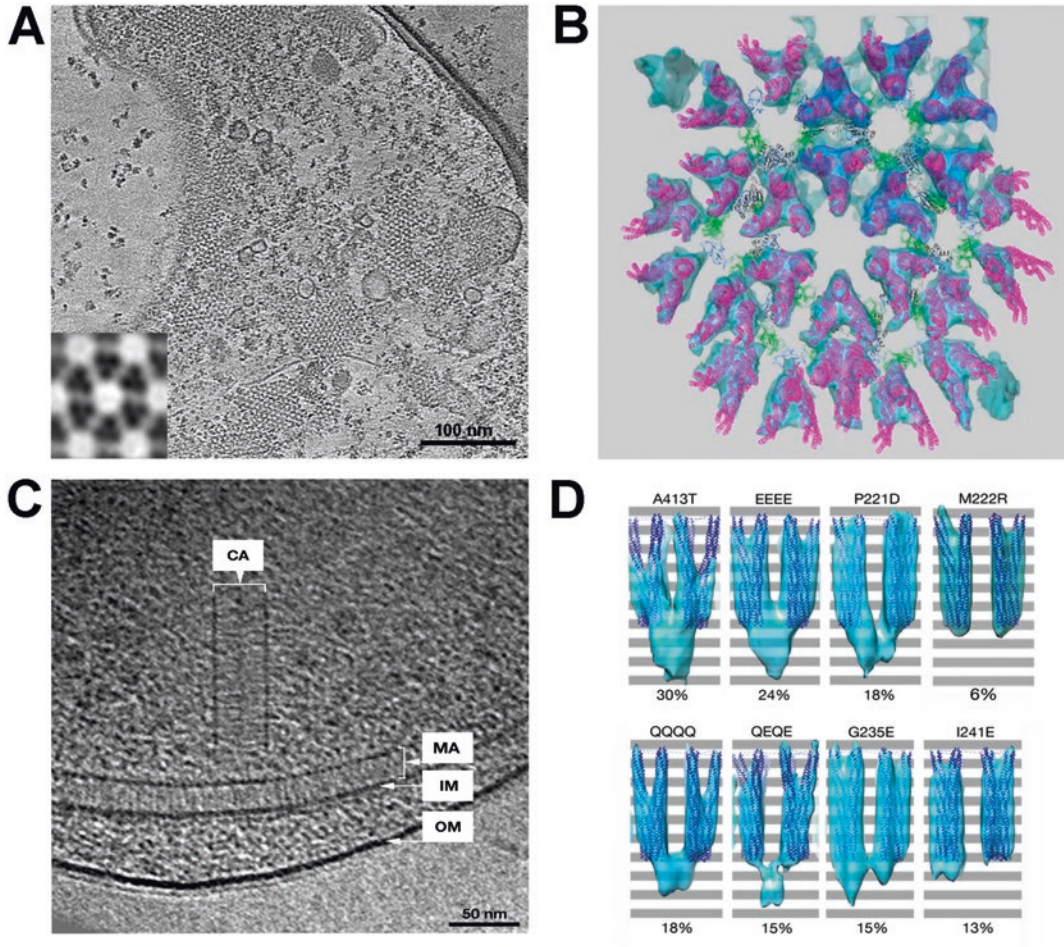

Fig. 5 Images generated from cryo-tomography data for chemoreceptor arrays studies. (**a**) On the left panel, the top view of chemoreceptor arrays is shown in a slice through a tomographic reconstruction of an *E. coli* cell overproducing chemotaxis proteins. Inset shows the hexagonal packing of receptor trimers. *Reproduced with permission from* [29]. (**b**) The cryo-EM map after subvolume averaging allows the docking of the crystal structures of receptors (magenta). The receptors are networked by rings of CheW and CheA (CheW (green), CheA domains P3 (gray), P4 (black), and P5 (blue)). *Reproduced with permission from* [5]. (**c**) The side view of chemoreceptor arrays can be easily identified in tomograms because of the high electron density "base plate" structure formed by CheA and CheW. A membrane-bound chemoreceptor array (MA) is parallel to the inner membrane (IM), whereas a cytoplasmic chemoreceptor array (CA) appears as a "sandwich" structure in *Vibrio cholerae*, with two baseplates visible on either side. *OM* outer membrane. *Reproduced with permission from* [30]. (**d**) Subvolume averaging of the tomographic reconstruction of chemoreceptor arrays locked in specific activation states reveals that the electron density of the ternary signaling complexes varies in different functioning states. Crystal structures (purple) have been fitted into the EM density map (blue). *Reproduced with permission from* [7]

Table 1
The cryo-EM facilities currently in operation allowing multiuser access

Country	City	Location
China	Beijing	Tsinghua University, National Center for Protein Sciences (Beijing)
	Beijing	Institute of Biophysics, Chinese Academy of Science (CAS) Core Facility of Protein Research
	Shanghai	National center for Protein Sciences (Shanghai)
England	Oxford	Diamond Light Source Ltd., Electron Bio-Imaging Centre (eBIC)
Netherlands	Leiden	Leiden University, Institute of Biology Leiden (IBL), Netherlands Centre for Nanoscopy (NeCEN)
USA	Houston	Baylor College of Medicine, National Center for Molecular Imaging (NCMI)
	New York	New York Structural Biology Center, National Resource for Automated Molecular Microscopy (NRAMM)
	Washington, DC	HHMI Janelia Research Campus

Table is reproduced with permission from [33]

3. A cryo-EM operating at 120 keV and a cryo holder are the basic requirement for assessing the sample quality and visualizing chemoreceptors in vivo.
4. Automated tilt-series data acquisition schemes for cryo-EM samples have been under rapid development, providing the user a wide variety of software packages to choose from. SerialEM [34], TOM [35], UCSF tomography [36], or commercial packages like FEI Tomography (FEI Company, Hillsboro, OR, USA) are a few of the most widely used choices.
5. There are numerous software packages available for tomogram reconstruction besides of IMOD, such as SPIDER [37], TOM [35], Bsoft [38], Protomo [39], UCSF tomography [30] and Xplore3D (FEI Company, Hillsboro, OR, USA). A complete list of software packages applicable for ECT data collecting and data reconstructing can be found on the website (https://en.wikibooks.org/wiki/Software_Tools_For_Molecular_Microscopy).
6. One fundamental limitation of this technique is the sample thickness. The vitrified sample has to be thin enough to allow

the electrons to pass through the sample. Therefore, samples optimally are less than 500 nm when imaged with 300 keV instrument. Some of the model organisms that are used to study bacterial chemotaxis exceed an ideal cell diameter. Therefore, multiple methods have been developed to effectively reduce the bacterial cells thickness and facilitate the visualization of chemoreceptor arrays. Both antibiotic and lysozyme treatment can lead to cytoplasmic content release with the native structure of arrays preserved [5, 7, 40]. Similarly, a phage gene has been engineered into *E. coli*, allowing for controlled inducible lysis to flatten the cells [41]. In addition, small and DNA free "minicells" of model organisms are the result of strains with disrupted localization of the cell division machinery. Such cells are ideal candidates for ECT, and were previously used for describing the chemoreceptor array structure [5, 6].

7. The carbon side of EM grids normally remains hydrophilic within 2 h after being glow discharged; if grids are not used in time, repeat the glow discharge process shortly before use.
8. Wear safety glasses or face shield when using ethane.
9. Three microliters of cell mixture with 1 s blotting time usually yields a vitreous ice layer thin enough for imaging; if the volume of the cell mixture is increased, extend the blotting time accordingly. In addition, sample-specific features like viscosity should be taken into account before choosing the optimal blotting time to achieve ideal ice thickness.
10. Mishandling of the sample by warming it above 120 K (−153 °C) will cause crystallization of the ice film, which irreversibly damages the specimen; also, exposing the grid to atmospheric moisture results in ice contamination on the surface of the grids.
11. Examination is essential for new specimen; this step is optional for samples where the blotting conditions have been previously determined.
12. Small bacteria, such as *Vibrio cholerae*, can be found lying entirely inside the holes of the carbon film, which is ideal for data collection. Other bacteria can span several holes as well as the carbon film in between due to an extended cell length of several microns or more. Because the chemoreceptor arrays localize mainly at the cell poles, choose cell poles that are trapped in one of the holes for imaging.
13. The total dosage depends both on the specimen as well as the desired resolution. Some intact bacterial cell specimens have been shown to tolerate accumulative dosage up to 200 electrons/Å^2. A more moderate dose of 160 electrons/Å^2 has been widely used and is a good starting point for initial dose testing.

However, these dose values are very high and will impact the finer structural details in your sample. Therefore, when aiming for higher resolution in lysed cell samples, it is suggested to keep the dosage well below 100 electrons/Å^2.

14. The choice of magnification also depends on the specific detector that is used for data collection.
15. Most software packages support automatic batch tomography for collecting data sets from multiple positions on one grid. In this case, the process of individual tilt-series acquisition remains the same as described previously. In addition, an "atlas" of the whole gird can be recorded at a relatively low magnification for picking target positions for data collection. Batch tomography also requires an additional calibration steps for accurate localization of the targets.

Acknowledgment

We thank Dr. Christoph Diebolder from NeCEN for helpful comments to improve the manuscript.

References

1. Gan L, Jensen GJ (2013) Electron tomography of cells. Q Rev Biophys 45:27–56
2. Koning RI, Koster AJ (2009) Cryo-electron tomography in biology and medicine. Ann Anat 191:427–445
3. Zhang P, Khursigara CM, Hartnell LM, Subramaniam S (2007) Direct visualization of *Escherichia coli* chemotaxis receptor arrays using cryo-electron microscopy. Proc Natl Acad Sci U S A 104:3777–3781
4. Briegel A, Ding HJ, Li Z, Werner J, Gitai Z, Dias DP et al (2008) Location and architecture of the *Caulobacter crescentus* chemoreceptor array. Mol Microbiol 69:30–41
5. Briegel A, Li X, Bilwes AM, Hughes KT, Jensen GJ et al (2012) Bacterial chemoreceptor arrays are hexagonally packed trimers of receptor dimers networked by rings of kinase and coupling proteins. Proc Natl Acad Sci U S A 109:3766–3771
6. Liu J, Hu B, Morado DR, Jani S, Manson MD et al (2012) Molecular architecture of chemoreceptor arrays revealed by cryoelectron tomography of *Escherichia coli* minicells. Proc Natl Acad Science U S A 109:e1481–e1488
7. Briegel A, Ames P, Gumbart JC, Oikonomou CM, Parkinson JS et al (2013) The mobility of two kinase domains in the *Escherichia coli* chemoreceptor array varies with signalling state. Mol Microbiol 89:831–841
8. Cassidy CK, Himes BA, Alvarez FJ, Ma J, Zhao G, Perilla JR et al (2015) CryoEM and computer simulations reveal a novel kinase conformational switch in bacterial chemotaxis signaling. Elife 4:e08419
9. Fernandez-Leiro R, Scheres SHW (2016) Unravelling biological macromolecules with cryo-electron microscopy. Nature 537: 339–346
10. Dubochet J, Adrian M, Chang J-J, Homo J-C, Lepault J et al (1988) Cryo-electron microscopy of vitrified specimens. Q Rev Biophys 21:129–228
11. Tocheva EI, Li Z, Jensen GJ (2010) Electron cryotomography. Cold Spring Harb Perspect Biol 2:a003442
12. Radermacher M, Wagenknecht T, Verschoor A, Frank J (1986) A new 3-D reconstruction scheme applied to the 50S ribosomal subunit of *E. coli*. J Microsc 141:RP1–RP2
13. Grunewald K, Medalia O, Gross A, Steven AC, Baumeister W (2003) Prospects of electron cryotomography to visualize macromolecular complexes inside cellular compartments: implications of crowding. Biophys Chem 100: 577–591

14. Frank J (ed) (2006) Electron tomography. methods for three-dimensional visualization of structures in the cell, 2nd edn. Springer, New York, NY
15. Comolli LR, Downing KH (2005) Dose tolerance at helium and nitrogen temperatures for whole cell electron tomography. J Struct Biol 152:149–516
16. Koster AJ, Grimm R, Typke D, Hegerl R, Stoschek A et al (1997) Perspectives of molecular and cellular electron tomography. J Struct Biol 120:276–308
17. Diebolder CA, Koster AJ, Koning RI (2012) Pushing the resolution limits in cryo electron tomography of biological structures. J Microsc 248:1–5
18. Lawrence MC (1992) Least-squares method of alignment using markers. In: Frank J (ed) Electron tomography: three-dimensional imaging with the transmission electron microscope. Springer, New York, NY, pp 197–204
19. Penczek P, Radermacher M, Frank J (1992) Three-dimensional reconstruction of single particles embedded in ice. Ultramicroscopy 40:33–53
20. Andersen AH, Kak AC (1984) Simultaneous algebraic reconstruction technique (SART): a superior implementation of the art algorithm. Ultrason Imaging 6:81–94
21. Fernandez JJ, Li S, Crowther RA (2006) CTF determination and correction in electron cryotomography. Ultramicroscopy 106:587–596
22. Xiong Q, Morphew MK, Schwartz CL, Hoenger AH, Mastronarde DN (2009) CTF determination and correction for low dose tomographic tilt series. J Struct Biol 168:378–387
23. Walz J, Typke D, Nitsch M, Koster AJ, Hegerl R et al (1997) Electron tomography of single ice-embedded macromolecules: three-dimensional alignment and classification. J Struct Biol 120:387–395
24. Nicastro D, Schwartz C, Pierson J, Gaudette R, Porter ME et al (2006) The molecular architecture of axonemes revealed by cryoelectron tomography. Science 313:944–948
25. Kremer JR, Mastronarde DN, McIntosh JR (1996) Computer visualization of three-dimensional image data using IMOD. J Struct Biol 116:71–76
26. Mastronarde DN (2008) Correction for non-perpendicularity of beam and tilt axis in tomographic reconstructions with the IMOD package. J Microsc 230:212–217
27. Grassucci RA, Taylor DJ, Frank J (2007) Preparation of macromolecular complexes for cryo-electron microscopy. Nat Protoc 2: 3239–3246
28. Dobro MJ, Melanson LA, Jensen GJ, McDowall AW (2010) Three-plunge freezing for electron cryomicroscopy. Methods Enzymol 481:63–82
29. Briegel A, Wong mL, Hodges HL, Oikonomou CM, Piasta KN et al (2014) New insights into bacterial chemoreceptor array structure and assembly from electron cryotomography. Biochemistry 53:1575–1585
30. Briegel A, Ladinsky MS, Oikonomou C, Jones CW, Harris MJ et al (2014) Structure of bacterial cytoplasmic chemoreceptor arrays and implications for chemotactic signaling. Elife 3:e02151
31. Glaeser RM (2016) How good can cryo-EM become? Nat Methods 13:28–32
32. Iancu CV, Tivol WF, Schooler JB, Dias DP, Henderson GP et al (2006) Electron cryotomography sample preparation using the Vitrobot. Nat Protoc 1:2813–2819
33. Chen S, McDowall A, Dobro MJ, Briegel A, Ladinsky M et al (2010) Electron cryotomography of bacterial cells. J Vis Exp 39. pii:1943
34. Mastronarde DN (2005) Automated electron microscope tomography using robust prediction of specimen movements. J Struct Biol 152:36–51
35. Nickell S, Forster F, Linaroudis A, Net WD, Beck F et al (2005) TOM software toolbox: acquisition and analysis for electron tomography. J Struct Biol 149:227–234
36. Zheng SQ, Keszthelyi B, Branlund E, Lyle JM, Braunfeld MB et al (2007) UCSF tomography: an integrated software suite for real-time electron microscopic tomographic data collection, alignment, and reconstruction. J Struct Biol 157:138–147
37. Frank J, Radermacher M, Penczek P, Zhu J, Li Y et al (1996) SPIDER and WEB: processing and visualization of images in 3D electron microscopy and related fields. J Struct Biol 116:190–199
38. Heymann JB, Cardone G, Winkler DC, Steven AC (2008) Computational resources for cryo-electron tomography in Bsoft. J Struct Biol 161:232–242
39. Winkler H (2007) 3D reconstruction and processing of volumetric data in cryo-electron tomography. J Struct Biol 157:126–137
40. Briegel A, Ortega DR, Tocheva EI, Wuichet K, Li Z et al (2009) Universal architecture of bacterial chemoreceptor arrays. Proc Natl Acad Sci U S A 106:17181–17186
41. Fu X, Himes BA, Ke D, Rice WJ, Ning J et al (2014) Controlled bacterial lysis for electron tomography of native cell membranes. Structure 22:1875–1882

Chapter 17

Visualizing Chemoreceptor Arrays in Bacterial Minicells by Cryo-Electron Tomography and Subtomogram Analysis

Zhuan Qin, Bo Hu, and Jun Liu

Abstract

Bacterial chemoreceptors form a highly ordered array in concert with the CheA kinase and the CheW coupling protein. The precise architecture of the array is responsible for high sensitivity, high dynamic range, and strong amplification of chemotaxis signaling. Cryo-electron tomography (cryo-ET) has emerged as a unique tool to visualize bacterial chemotaxis arrays at molecular level. Here we describe a detailed cryo-ET and subtomogram averaging procedure to determine in situ structure of the chemoreceptor arrays in *Salmonella* minicells. The procedure should be readily applicable to visualize other large macromolecular assemblies in their cellular context.

Key words Cryo-electron tomography, Chemoreceptor array, Core signaling complex, Subtomogram averaging, Minicell, Macromolecular assembly

1 Introduction

Cryo-electron tomography (cryo-ET) is the method of choice for imaging three-dimensional (3D) cellular structures at molecular level. The technique involves collecting a series of 2D images of frozen-hydrated specimen at different angles at high magnification by using a transmission electron microscope. The 2D images are then aligned and reconstructed to generate a 3D tomographic reconstruction by a computer powered by sophisticated algorithms. A typical tomogram from a frozen-hydrated cellular structure contains massive amounts of information, but the usefulness of that information is limited by poor contrast and low resolution. To obtain the in situ structures at higher resolution, subtomogram averaging is becoming an increasingly powerful tool that is applicable to a broad range of biological applications [1, 2].

Cryo-ET combined with subtomogram averaging has been used to study structural organization of bacterial chemoreceptor arrays. The arrays are assembled by the chemoreceptors, the CheA kinase, and the CheW coupling protein. The overall architecture of

Michael D. Manson (ed.), *Bacterial Chemosensing: Methods and Protocols*, Methods in Molecular Biology, vol. 1729, https://doi.org/10.1007/978-1-4939-7577-8_17,

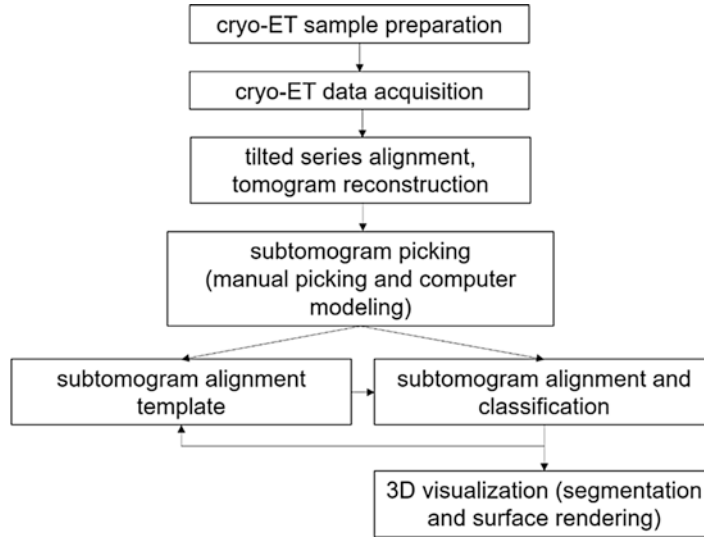

Fig. 1 Flowchart for in situ structural analysis of bacterial chemoreceptor arrays using cryo-electron tomography and subtomogram analysis

the array and its core complex has been extensively visualized in bacteria [3–6] and in vitro array [7] by cryo-ET. In particular, structures from subtomogram averaging suggested that one CheA dimer and two CheW monomers connect two trimers of receptor dimers at the cytoplasmic portion of the arrays [4, 5], consistent with the stoichiometry estimated by the purified core complex in nanodiscs [8]. The models of the chemoreceptor array have been built by fitting crystal structures of key components into the electron density determined by cryo-ET [4, 5, 7]. Here we describe a detailed pipeline that can be used to extract thousands of subtomograms from bacterial minicells and to align them in order to determine the in situ structure of the chemoreceptor array (Fig. 1).

2 Materials

2.1 Strains and Reagents

1. Bacterial strain: *Salmonella enterica* serovar Typhimurium minicell (TH16943, a wild-type strain except that the *araBAD* coding sequences were replaced with *ftsZ*).
2. Culture medium: Lysogeny broth (LB), a nutritionally rich medium.
3. Dilution buffer: Sterile Phosphate-buffered saline (PBS).
4. Fiducial markers: 10 nm colloidal gold particles (AURION, www.emsdiasum.com).
5. Cryogen: Compressed ethane gas and liquid nitrogen.

2.2 Equipment and Software

1. 300 kV cryo-electron microscope equipped with field emission gun (Polara, FEI Company).
2. Electron counting direct detection camera (K2 Summit, Gatan).
3. PELCO easiGlow discharger (https://www.tedpella.com/).
4. EM Grids (QUANTIFOIL, R2/2, Cu 200 mesh, www.quantifoil.com).
5. EM tweezers (EMS 78328-26, www.emsdiasum.com).
6. Cartridges for loading EM grids (special design for FEI Polara).
7. Air Bath shaker (www.bionexus.net).
8. Beckman Ultracentrifuge (www.beckman.com).
9. Plunge freezer.
10. Whatman qualitative filter paper (grade 1, www.sigmaaldrich.com).
11. Pipettors and pipette tips (www.fishersci.com).
12. SerialEM software (bio3d.colorado.edu/SerialEM).
13. IMOD program (bio3d.colorado.edu/IMOD).
14. i3 packages (www.electrontomography.org).
15. Matlab (www.mathworks.com/products/matlab).
16. SPARX (sparx-em.org/sparxwiki/SparxWiki).
17. UCSF Chimera (www.cgl.ucsf.edu/chimera).

3 Methods

3.1 Bacterial Minicell Preparation

1. To recover bacteria from −80 °C glycerol stock, use a sterile loop or pipette tip to scrape off some of the frozen bacteria and drop into 5 mL LB broth.
2. Incubate the bacterial culture at 37 °C overnight in a shaking incubator.
3. A 100 mL fresh culture is inoculated by a 1:100 dilution of the overnight culture and then cultured at 37 °C for 4 h to late log phase.
4. Centrifuge the 100 mL bacterial culture at 10,000 × *g* for 5 min to remove most large cells.
5. The supernatant is transferred to a new centrifuge tube and centrifuged at 41,000 × *g* for 15 min to spin down the minicells.
6. The pellet of minicells from **step 5** is suspended in 100 μL PBS.

3.2 Cryo-EM Sample Preparation

1. Use EM tweezers to pick the carbon-coated EM grids and put them on a microscope glass slide so that the carbon surface faces upward.
2. Place the grids with the glass slide inside the glow discharger and glow discharge the grids for 20 s, using the auto-discharging program.
3. Add fresh liquid nitrogen into the plastic chamber of the plunge freezer.
4. Wait till the boiling of the liquid nitrogen subsides, then add ethane gas at a moderate flow speed into the precooled cup in the plunge freezer. Wait till the ethane becomes liquid and solid mixture, which is liquid in the center of the cup and solid starts to form on the edge.
5. Grab a glow-discharged grid using an EM tweezers. Load the grid into the plunge freezer.
6. The minicell culture is mixed with 10 nm colloidal fiducial gold particles and deposited onto the freshly glow-discharged grid.
7. After 1 min, blot the grid for 3 s using a piece of filter paper so that only a thin layer of sample is left on the grid. Immediately after the blotting, drop the grid into the liquid ethane in the central cup of the plunger.
8. Wait for 5 s, then transfer the grid from the liquid ethane to liquid nitrogen as quickly as possible.
9. Transfer the grids into a precooled grid storage box. Store the grid box at liquid nitrogen temperature before transferring to the electron microscope (*see* **Note 1**).

3.3 Transfer of the Cryo-ET Grid into the Electron Microscope

1. Cool down the cryo-transfer holder. Add liquid nitrogen into the cartridge-loading chamber with the cryo-transfer holder inserted. Add liquid nitrogen to the cryo-transfer holder Dewar. Wait for about 20 min to allow boiling of the liquid nitrogen to subside.
2. Transfer the grid from the storage box into the cryo-transfer holder under liquid nitrogen and insert the holder into the electron microscope (*see* **Note 2**).

3.4 Configure the Dose on the Electron Microscope

1. Turn on the low dose mode of the *SerialEM* [9] and configure four areas with independent magnification, spot size and beam intensity.
2. Configure the "Record" area with a magnification of 15,400×.
3. Configure the "View" area with magnification of 2,300×. Set a defocus offset of −60 μm.
4. Configure the "Focus" area with the same magnification, spot size and intensity as the "Record" area. The focus area should

be 3 μm away from the record area but on the same tilt axis. Put the "Track" area at the same setting as the "Focus" area.

5. Align the center of the "View" area with the center of the "Record" area.

3.5 Cryo-ET Data Acquisition

1. Use the "View" area to screen the grid.
2. Open a new navigator window using the "Navigator" menu of *SerialEM*. Click "Add Stage Position" for each area.
3. Set up a new montage. Use the "File" menu in *SerialEM* to configure the montage as 8 × 8 pieces in X and Y.
4. Toggle the "Acquire" checkbox in the navigator window for all the stage positions.
5. Run "Acquire at Points" in the "Navigator" menu in *SerialEM*, then select "Rough eucentricity" to generate a low-magnification montage for each stage position.
6. Click "Load Map" in the navigator window to view the montage as shown in Fig. 2a.
7. Add regions of interest to collect tomograms in each montage. Click "Add Points" in the navigator window and select the minicells for tomographic data collection. The ideal minicells should be embedded in thin vitreous ice (Fig. 2).
8. Repeat **step 7** until every minicell in thin ice is selected.
9. Return to **step 6** to process another montage.
10. Toggle the "Tilt Series" checkbox in the navigator window for the first region selected. Set the tilt angle range as −60° to +60°, with a fixed increment of 3° in the Tilt Series Setup Dialog. Set the starting angle to be 0° at ~4 μm defocus. Apply the setting to all regions of interests by toggle the "Tilt Series" checkbox.
11. Set the parameters under the "Camera" menu in *SerialEM*. Set the Record parameters to collect images to dose-fractionation mode and to save the subframes. Set the folder for the subframes to be the same as the tilt series. The typical exposure time at each tilt is 1 s. The total cumulative dose of the tilt series should be ~50 $e^-/Å^2$.
12. Run "Acquire at Points" in the "Navigator" menu in *SerialEM* and select "Rough Eucentric", "Realign to Item", "Autofocus" and then select "Acquire Tilt Series" as the primary task.

3.6 Tomographic Data Processing

1. Use "Motioncorr" [10] to do drift correction of the frames in the tilt series and then stack them as one tilt series [11].
2. Perform fiducial-based alignment using either *tomoauto* [12] for automatic alignment or *etomo* to do alignment step by step [13].
3. Generate tomograms using *tomo3d* [14] from the aligned tile series.

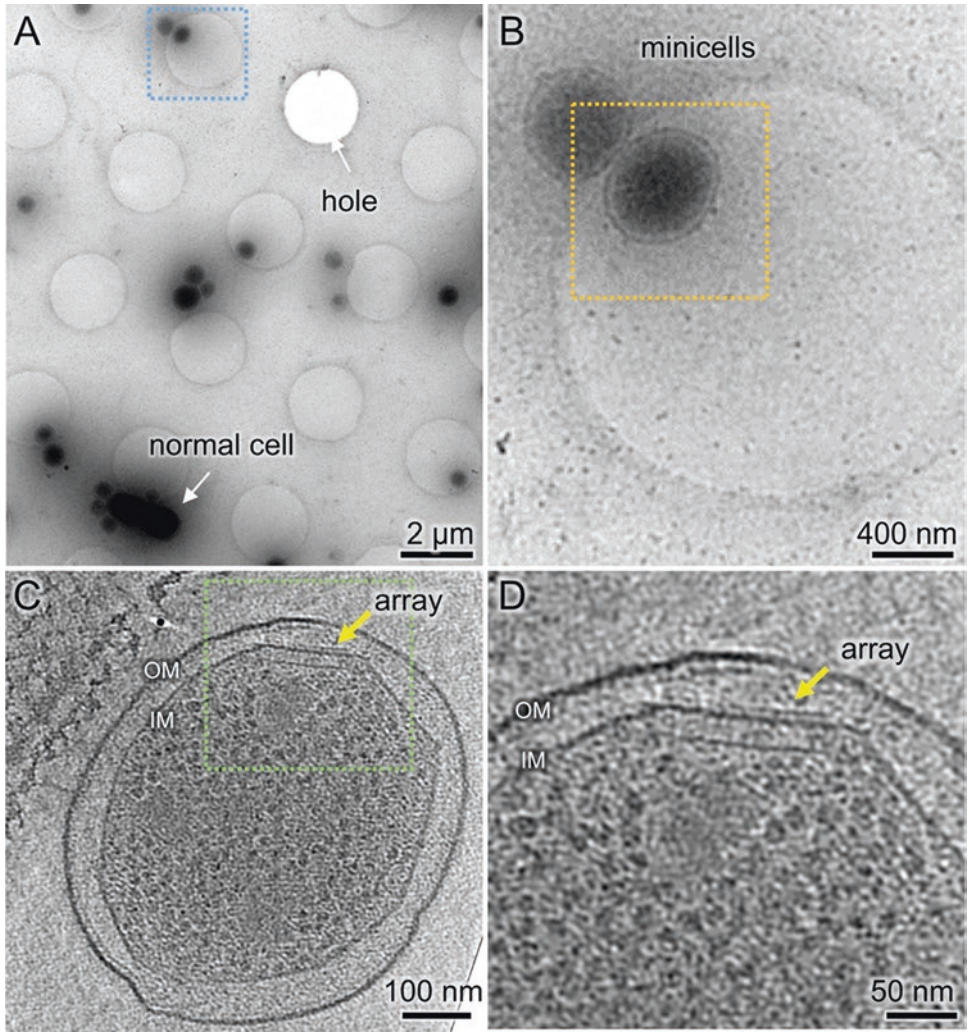

Fig. 2 Cryo-electron tomography of bacterial minicells and chemoreceptor arrays in situ. (**A**) A montage of cryo-EM images at low magnification shows normal cell, minicells and an empty hole without ice. The montage picture was obtained at 2300× magnification with a ~68 μm defocus. (**B**) A zoom-in view of two minicells in the blue frame in (**A**). (**C**) A tomogram was reconstructed from one minicell embedded in thin vitreous ice. (**D**) A zoom-in view shows the chemoreceptor array

3.7 Subtomogram Analysis: Data Extraction

1. Select the minicell tomograms that contain large visible chemoreceptor arrays (Figs. 2c, d and 3a–c; *see* **Note 3**).
2. Use the *i3display* from *i3* [2, 15] to open a 4 × 4 × 4 binned tomogram (e.g. to open a tomogram called *map_name*, use the command: *i3display map_name*).
3. Select positions using *shift* + *left mouse* to manually mark 3-D positions of the arrays beneath the inner membrane (*see* Fig. 3a–d). Repeat this step until most of the visible arrays in the tomogram are selected.

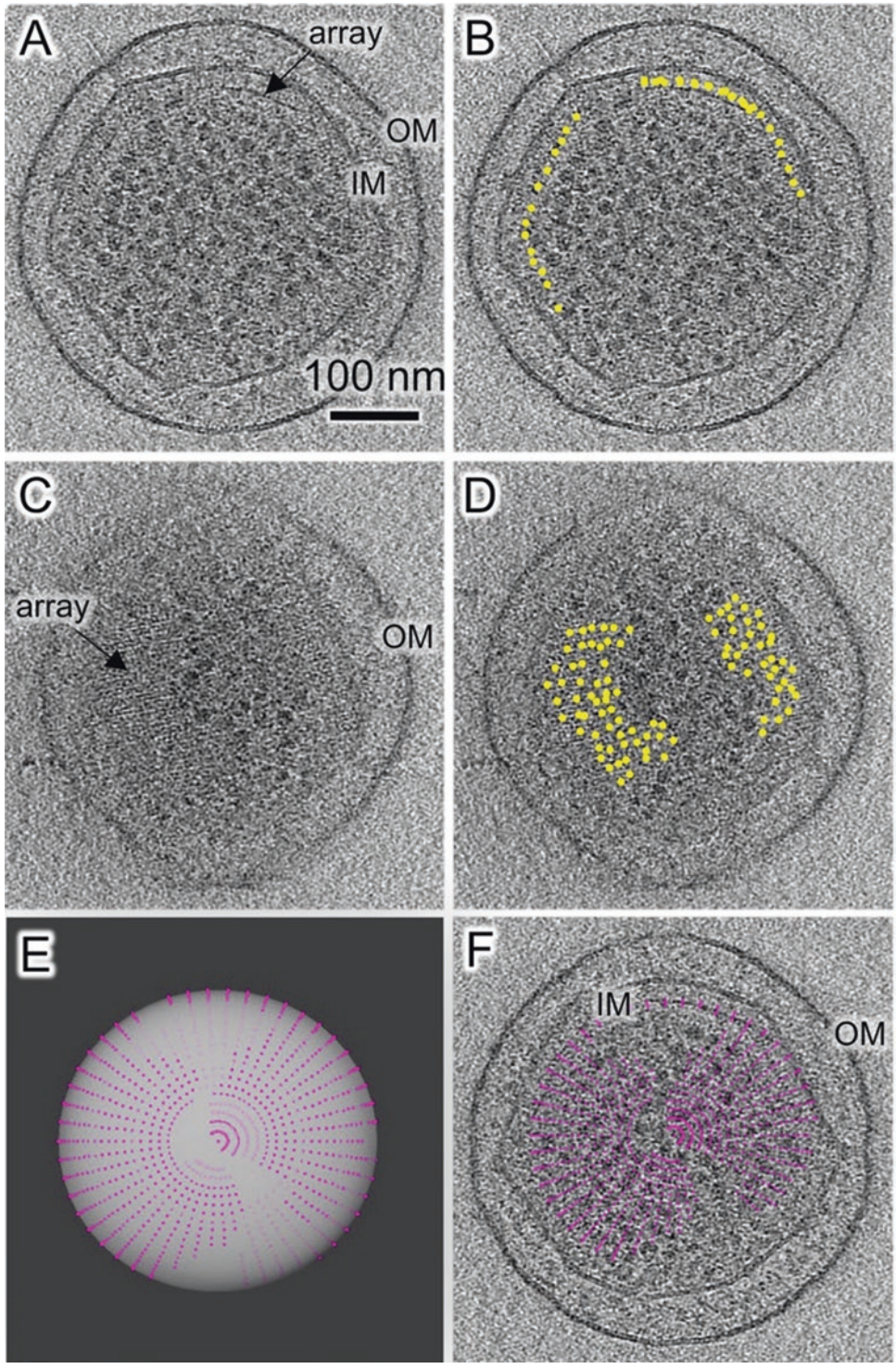

Fig. 3 Localization of chemoreceptor arrays in a minicell. (**a**) A slice of the minicell tomogram shows chemoreceptor arrays around the inner membrane (IM). (**b**) The chemotaxis arrays in (**a**) are selected manually. (**c**) A slice of the same minicell tomogram shows the chemotaxis array at the top of the cell. (**d**) The arrays in (**c**) are selected manually. (**e**) An ellipsoid surface model is built based on the coordinates selected manually, and new coordinates (colored in magenta) are generated from the model. (**f**) A slice of the tomogram is superimposed with new coordinates

4. Close i3display and then save their coordinates (x, y, z) into a *.pos* file (e.g., *file_name.pos*; *see* **Note 4**).
5. If the current saved points are inadequate to build an ellipsoid model, reopen the tomogram with the *.pos* file using command: *i3display -pos file_name.pos map_name*. Select more positions manually using *shift + left mouse* along the inner membrane (*see* **Note 5**).
6. Close i3display again and save the coordinates as another *.pos* file (*file_name_cell.pos*).
7. Based on the second *.pos* file (*file_name_cell.pos*), an ellipsoid model can then be built using Matlab. A uniformly distributed mesh on the ellipsoid surface is generated, and each point on the mesh should have a coordinate and normal vector (or surface normal; *see* **Note 6**).
8. Select the points from the mesh that has a nearby coordinates from the first *.pos* file (*file_name.pos*; *see* **Notes 6** and **7**). Those points (3D coordinates) are then used to extract initial subtomograms for alignment.
9. Compute the Euler angles for the selected points using the normal vector. Compute the rotation matrix by the command *i3euler*. Save the 3D coordinates and the rotation matrix in *.trf* (*see* **Note 4**).
10. Repeat **steps 2–9** till all tomograms with visible arrays are processed.

3.8 Subtomogram Analysis: Alignment and Averaging

1. First, build the initial reference for subtomogram alignment. Manually select about 30–50 subtomograms that have clear hexagonal lattices in a top view (Fig. 3c).
2. Align the manually selected subtomograms to generate the average map. Apply sixfold symmetry using the command *i3sym* from i3. Place a mask that covers 24 triangular prisms at the center using the command *i3mask* from i3. A top view of the initial reference was shown in Fig. 4a.
3. Align subtomograms from all ellipsoid models (stored in *.trf* from Subheading 3.7, **step 1**) iteratively to the initial reference by transitional and rotational alignment.
4. After aligning the subtomograms, classify them over the bottom layer including the CheA-P5/CheW plane and CheA-P4 domain. An example of the classification result is shown in Fig. 4b.
5. Select the subtomograms from the classes with triangular prisms at the edge of the top view (outside of the 24 triangular prisms at the center of the reference), and also with the known CheA-P4 pattern (Fig. 4b). This step is used to discard subtomograms without chemoreceptor arrays (*see* **Note 8**).

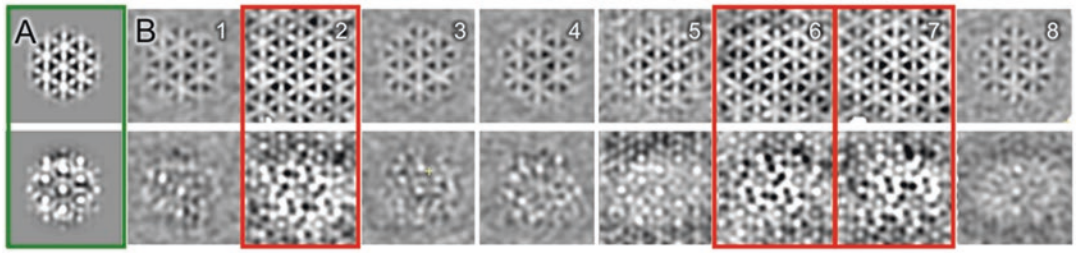

Fig. 4 Subtomogram analysis of the chemoreceptor arrays. (**a**) Two different slides of the initial reference derived from chemoreceptor arrays. (**b**) Eight class averages show well-organized chemoreceptor arrays. The top panel shows the slices at the level of the receptor. The bottom panels show the slices at the level of CheA P4. Based on this classification, classes 2, 6, and 7 were selected for further alignment

6. Shift the center of the subtomograms so that they have the same pattern at CheA-P4 layer in one class average. Here (*see* Figs. 4b and 5b) Class 2 is selected, and subtomograms in Class 6 and 7 are shifted.
7. Align the subtomograms iteratively toward their global average by transitional and rotational alignments. Update the alignment reference in each iteration.
8. Compute the distance between the centers of any two subtomograms from the same cell, then discard the duplicate subtomograms with lower quality based on correlation coefficient comparing with the global average.
9. Refine the geometry parameters (coordinates and Euler angles) of subtomograms using 2 × 2 × 2 binned tomograms through multiple iterations (Fig. 5a–c). Update the alignment template in each iteration. Discard low quality subtomograms (correlation coefficient comparing with global average < Mean − 2SD). Also discard duplicated subtomograms.
10. Determine the resolution of the chemoreceptor array using the Fourier Shell Correlation (FSC) between two independent reconstructions. This allows the resolution of the receptor array structure to be estimated.

3.9 Subtomogram Analysis:Segmentation and Visualization

1. Before opening the global average in *Chimera* [15], the file from *i3* needs to be modified. First, convert the file from *.img* format into *.mrc* format using the command: *i3cut -fmt mrc input output*, where input is the file name of the *.img* map and output is the file name of the *.mrc* map (*see* **Note 9**). Second, inverse the contrast of the image using the command: *i3compute output * -1* (*see* **Note 10**). Then open the output map using this command: *chimera output*.
2. In *Volume Viewer* window, adjust the threshold of the densities (*see* **Note 11**), then select *Tools*, and click *Segment* Map [16].

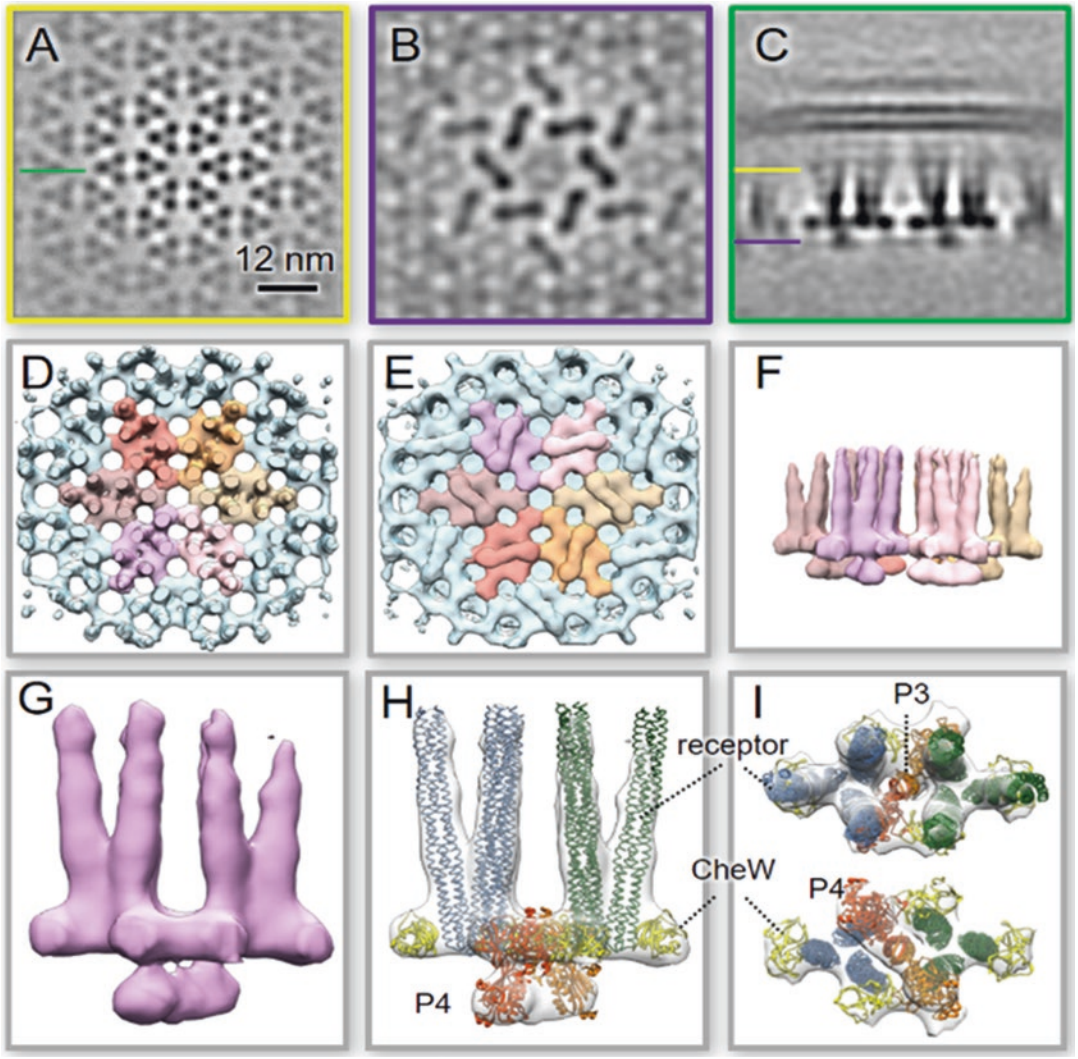

Fig. 5 The structures of the chemoreceptor array derived from subtomogram averaging and atomic structure fitting. The global average of the receptor array is shown in three different slices: a top view (**a**), a bottom view (**b**), and a side view (**c**). The location of the slices is shown by the colored lines. (**a**) A slice from the middle of the receptor trimers. (**b**) A slice from the CheA-P4 domains. (**c**) A slice perpendicular to the slices in **a** and **b**. (**d**–**f**) Six core complexes at the center of the array are segmented and displayed corresponding to the views in **a**, **b**, and **c**, respectively. (**g**) The surface rendering of one core complex in side view. The atomic model (modified from PDB:3ja6) is fitted into the electron density as shown in a side view (**h**), a top view (the top panel in **i**) and a bottom view (the bottom panel in **i**)

3. In *Segment Map* window, the segment map should be the name of the target map. Click *Segment* at the bottom of the window, then click *Ungroup* multiple times till all different molecules in the map are separated into different volumes, or the map cannot be segmented further (*see* **Note 12**).

4. Turn off the view of map. Go to *Chimera* main window and click *Tools*, *General Controls* and then *Model Panel*. In the *Model Panel* window, unselect *S* for the map to turned the view off.
5. Manually join multiple regions if they belong to the same protein. Use *left mouse* + *Ctrl* to select the first region, use *left mouse* + *Ctrl* + *Shift* to add additional regions. To join multiple regions together, click Group in *Segment Map* window. Repeat this step until all molecules are processed (*see* **Note 13**).
6. Join the regions of proteins together if they belong to the same core complex. The operation is similar to **step 4**.
7. After finishing segmentation, click *File* in the *Segment Map* menu and save segmentation result as a .seg file by clicking *Save segmentation as*.
8. Cut out the electron density from the map using segmented regions as a mask. Select a region to cut using *left mouse* + *Ctrl*. Click *Regions* in the *Segment Map* menu, and click *invert selection* to remove all regions except those that are wanted regions. Then click *Subtract selected from map*, and a new map will show up in the *Volume Viewer* window (*see* **Note 14**).
9. Repeat **step 7** till all regions are selected. Save those maps in the *Volume Viewer* window.
10. Color the maps and adjust threshold in the *Volume Viewer* window (*see* Fig. 5d–f).
11. Select one core complex map and fit the atomic model into the density using rigid body fitting (Fig. 5g–i).
12. First, download the core complex atomic model (PDB:3ja6). Click *File* in the main *Chimera* Window, select *Fetch by ID*, and put 3ja6 after selecting PDB, then click *Fetch* (*see* **Note 15**).
13. Second, change the coordinates of the map. Click *Features* in *Volume Viewer* window, click *Coordinates*, and put the pixel size 5.21 after the *Voxel size* in *Volume Viewer* window.
14. Third, click *Tools* in the *Volume Viewer*, click *Fit in Map*, and select the atomic model and the map for the fitting before clicking *Fit* (*see* **Note 16**).

4 Notes

1. EM grids should be kept in liquid nitrogen after plunge freezing.
2. The grid transferring system is quite variable for different microscopes. Follow the specific instruction for each system.
3. Chemoreceptor arrays should be visible and relatively large in size.

4. The *.pos* and *.trf* files can be viewed and edited by Linux text editor such as *vi*, *emacs* and *nedit*.
5. If there are sufficient points to build an ellipsoid model in the first *.pos* file, copy *file_name.pos* to *file_name_cell.pos*.
6. This part is coded in custom script by using MATLAB.
7. The distance between the coordinates could be 10–50 pixels.
8. Because of reference bias, the average of random cellular background may give a similar structure as the reference, but it will not give structural detail beyond the reference.
9. The original files used in *i3* cannot be recognized by *Chimera*. They have to be converted to files in MRC format.
10. In original density map, chemoreceptor array densities are black. To display them in *Chimera*, the contrast of the map must be reversed.
11. The surface rendering of the map can vary considerably at different thresholds of the densities.
12. The segmentation is based on watershed method. For more information, see the Segger documentation (http://ncmi.bcm.edu/ncmi/software/segger/docs).
13. The edge of the segmentation may not be accurate, as the signal to noise ratio is low in some regions of the map.
14. An alternative method is to select the wanted region and to go to *Regions* and click *Subtract selected from map*. Yet this procedure may produce artifacts from the mask and thus is not recommended.
15. If the map or the atomic model is not visible, go to *Favorites* in the main window, click *Side View*, and click *View All* in the *Viewing* window, which resets the view in *Chimera*.
16. If the atomic model is far from the density map and clicking *Fit* does not generate a reasonable fitting, move the atomic model manually and try the rigid body fitting again. To move the atomic model or the map manually, go to *Favorites* in the main window, select *Model Panel*, and unselect *A* in front of the target. Then use the mouse to move the target in the main window.

Acknowledgment

This work was supported in part by grants R01AI087946 from the NIAID, R01GM110243 from the NIGMS, and AU-1714 from the Welch Foundation. The direct electron detector was funded by NIH award S10OD016279.

References

1. Briggs JA (2013) Structural biology in situ—the potential of subtomogram averaging. Curr Opin Struct Biol 23:261–267
2. Winkler H, Zhu P, Liu J, Ye F, Roux KH et al (2009) Tomographic subvolume alignment and subvolume classification applied to myosin V and SIV envelope spikes. J Struct Biol 165:64–77
3. Briegel A, Ortega DR, Tocheva EI, Wuichet K, Li Z et al (2009) Universal architecture of bacterial chemoreceptor arrays. Proc Natl Acad Sci U S A 106:17181–17186
4. Briegel A, Li X, Bilwes AM, Hughes KT, Jensen GJ et al (2012) Bacterial chemoreceptor arrays are hexagonally packed trimers of receptor dimers networked by rings of kinase and coupling proteins. Proc Natl Acad Sci U S A 109:3766–3771
5. Liu J, Hu B, Morado DR, Jani S, Manson MD et al (2012) Molecular architecture of chemoreceptor arrays revealed by cryoelectron tomography of *Escherichia coli* minicells. Proc Natl Acad Sci U S A 109:E1481–E1488
6. Zhang J, Xu Y, Shen J, Luo X, Chen J et al (2005) Dynamic mechanism for the autophosphorylation of CheA histidine kinase: molecular dynamics simulations. J Am Chem Soc 127:11709–11719
7. Cassidy CK, Himes BA, Alvarez FJ, Ma J, Zhao G et al (2015) CryoEM and computer simulations reveal a novel kinase conformational switch in bacterial chemotaxis signaling. Elife 4:pii:e08419
8. Li M, Hazelbauer GL (2011) Core unit of chemotaxis signaling complexes. Proc Natl Acad Sci U S A 108:9390–9395
9. Mastronarde DN (2005) Automated electron microscope tomography using robust prediction of specimen movements. J Struct Biol 152:36–51
10. Li X, Mooney P, Zheng S, Booth CR, Braunfeld MB et al (2013) Electron counting and beam-induced motion correction enable near-atomic-resolution single-particle cryo-EM. Nat Methods 10:584–590
11. Pettersen EF, Goddard TD, Huang CC, Couch GS, Greenblatt DM et al (2004) UCSF Chimera—a visualization system for exploratory research and analysis. J Comput Chem 25:1605–1612
12. Morado DR, Hu B, Liu J (2016) Using Tomoauto: a protocol for high-throughput automated cryo-electron tomography. J Vis Exp 107:e53608
13. Kremer JR, Mastronarde DN, McIntosh JR (1996) Computer visualization of three-dimensional image data using IMOD. J Struct Biol 116:71–76
14. Agulleiro JI, Fernandez JJ (2015) Tomo3D 2.0—exploitation of advanced vector extensions (AVX) for 3D reconstruction. J Struct Biol 189:147–152
15. Winkler H (2007) 3D reconstruction and processing of volumetric data in cryo-electron tomography. J Struct Biol 157:126–137
16. Goddard TD, Huang CC, Ferrin TE (2007) Visualizing density maps with UCSF Chimera. J Struct Biol 157:281–287

Part V

Monitoring the Intracellular Movement of Chemosensory Proteins

Chapter 18

Bacterial Chemoreceptor Imaging at High Spatiotemporal Resolution Using Photoconvertible Fluorescent Proteins

Jacopo Solari, Francois Anquez, Katharina M. Scherer, and Thomas S. Shimizu

Abstract

We describe two methods for high-resolution fluorescence imaging of the positioning and mobility of *E. coli* chemoreceptors fused to photoconvertible fluorescent proteins. Chemoreceptors such as Tar and Tsr are transmembrane proteins expressed at high levels (thousands of copies per cell). Together with their cognate cytosolic signaling proteins, they form clusters on the plasma membrane. Theoretical models imply that the size of these clusters is an important parameter for signaling, and recent PALM imaging has revealed a broad distribution of cluster sizes. We describe experimental setups and protocols for PALM imaging in fixed cells with ~10 nm spatial precision, which allows analysis of cluster-size distributions, and localized-photoactivation single-particle tracking (LPA-SPT) in live cells at ~10 ms temporal resolution, which allows for analysis of cluster mobility.

Key words Bacterial chemotaxis, Superresolution microscopy, Photoactivation localization microscopy (PALM), Single-particle tracking, Receptor clustering, Membrane protein mobility

1 Introduction

The use of fluorescent proteins such as GFP allows for in vivo labeling of native proteins at high specificity to achieve high-contrast imaging of their spatial organization within a cellular context. Yet information attainable by traditional fluorescence microscopy is fundamentally limited by the so-called diffraction limit of spatial resolution—even with microscope objectives of highest performance, one can only achieve resolution of roughly half the wavelength of light (~250 nm for green fluorescence). This means that molecules separated by less than this distance cannot be distinguished from one another, placing strong constraints on practical applications that are particularly relevant for the bacterial cell (which measures only several-fold larger than this diffraction-limited length scale). There are at least two ways in which the diffraction limit can hinder practical applications. For situations in which the *spatial*

Michael D. Manson (ed.), *Bacterial Chemosensing: Methods and Protocols*, Methods in Molecular Biology, vol. 1729, https://doi.org/10.1007/978-1-4939-7577-8_18,

arrangement of molecules is of interest, the diffraction limit effectively blurs the image of the arrangement, thereby obscuring relevant details regarding shape and/or size of cellular structures. For situations in which the *spatial dynamics* of molecules are of interest, the diffraction limit hinders reliable tracking of movement, as the blurred image of molecules or molecular assemblies often overlap with one another.

Here, we describe two imaging methods that utilize photo convertible fluorescent proteins to overcome each of these difficulties, and our experimental protocols for applying them to bacterial chemoreceptors. Photoactivation localization microscopy (PALM [1]) allows one to image chemoreceptors with increased spatial resolution within fixed samples. Localized photoactivation single-particle tracking (LPA-SPT) allows one to study the movement of individual clusters of receptors within the crowded environment of live cells. In both techniques, the photoactivatable protein probe is initially dark and can be converted into a fluorescent state using near-UV (405 nm) light, as schematized in Fig. 1, to separate a small subset of the proteins of interest from the bulk of the population. If the spatial extent of this subset is smaller than the diffraction limit, its microscopic image is a spot of a size determined by the diffraction limit, also known as the point-spread function (PSF) of the imaging system. As illustrated in Fig. 1, the width s of a fitted bell-shaped function to this spot cannot be smaller than the diffraction-limited width of the PSF of the microscope (typically ~100 nm). However, its position can be estimated at a precision that increases with the number (N) of collected photons as $s/N^{1/2}$ and readily reaches near-nanometer precision for typical fluorophores, from which $>10^3$ photons can be collected [2].

The amount of information one can extract from fluorescence measurements is fundamentally limited by the number of photons that fluorophores emit before they bleach, commonly referred to as the "photon budget" of the experiment. The two techniques described in this chapter make use of this finite photon budget in contrasting manners. Whereas PALM expends the entire photon budget of each fluorophore in a single image frame to maximize the localization precision of single molecules in fixed cells (where protein mobility is negligible), LPA-SPT distributes the photon budget over multiple frames, to obtain information about the mobility of protein clusters in live cells. Figure 2 provides an overview of the workflow for the two methods.

1.1 PALM Imaging and Cluster-Size Analysis of Bacterial Chemoreceptors

In recent years, a number of fluorescence imaging techniques have emerged that allow one to overcome the aforementioned diffraction limit of spatial resolution in optical microscopy [3–5]. PALM belongs to this family of so-called super-resolution (SR) imaging techniques. This technology depends on the capability to image single molecules and takes advantage of the simple principle that, if

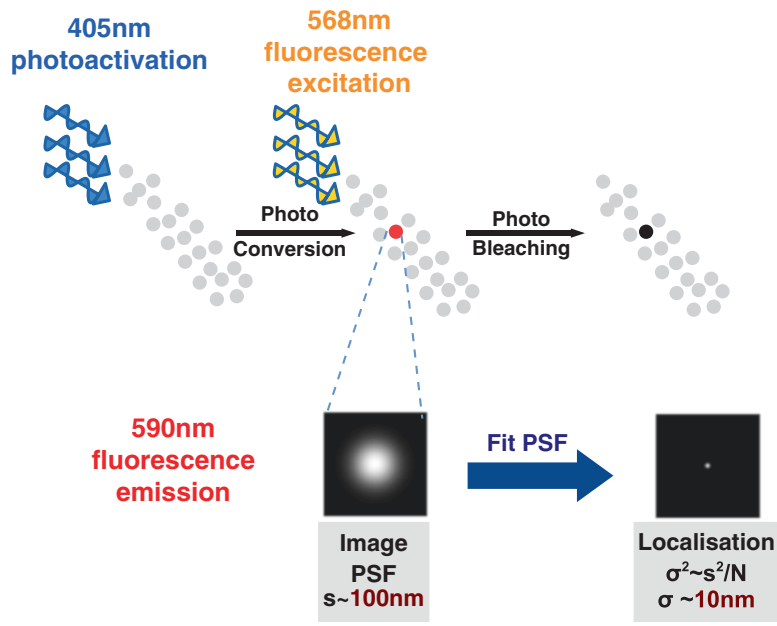

Fig. 1 Photoactivation and precise localization of photoconvertible fluorophores. The two techniques described here, PALM and LPA-SPT, both take advantage of photoconvertible fluorophores to enable precise localization of the labeled protein, even in "crowded" samples in which such molecules (gray) are present at high density. The labels can be converted from a dark (inactive) state to a bright (active) state by irradiation with 405 nm light. Subsequent exposure to light of the excitation wavelength (568 nm in our experiments) leads to emission that is imaged as a diffraction-limited point-spread function (PSF). Fits to a bell-shaped (usually Gaussian) function allows the position of objects to be estimated at ~10 nm precision if ~10^3 photons can be counted from each fluorophore before irreversible bleaching

the density of light emitters is low enough, their diffraction-limited images do not overlap in space. Thus, the position of each emitter can be localized at a much higher precision than the width of the diffraction-limited spot [2, 6]. PALM allows the application of this principle to samples with a high spatial density of labeled molecules. It does so by utilizing photoactivatable (or photoswitchable) fluorescent proteins to limit the number of actively emitting labels at any moment in time to a small fraction of total population [1]. The imaging experiment proceeds in an iterative fashion, with a small subset of the total fluorophore population being photoactivated, imaged and bleached. The process is repeated until unbleached labels in the sample are exhausted. In short, PALM allows one to work around the diffraction limit by separating, in time, the appearance of individual fluorophores, which would be indistinguishable as independent emitters if imaged simultaneously. From the sequence of acquired images (typically 10^3–10^5 in

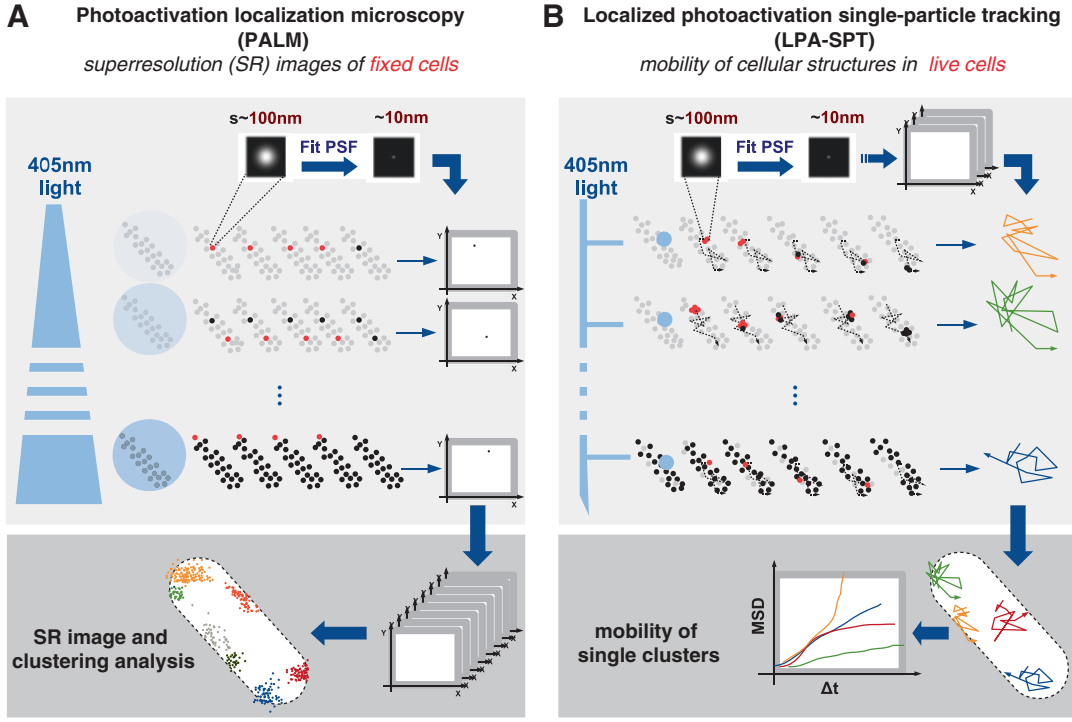

Fig. 2 Comparison of workflow between PALM and LPA-SPT. Because of their limited photostability, each fluorescent label provides only a finite photon budget for measurements. A compromise must be found between the localization precision and the number of frames over which a particle can be followed. The two methods presented in this chapter make contrasting use of the photon budget. (**a**) For PALM imaging, one expends the full photon budget on localization precision, by imaging each individual fluorophore within a single image frame. Light of the photoactivation wavelength (405 nm) homogeneously illuminates the sample, and fluorophores stochastically switch to their bright state. The activation power is kept sufficiently low to ensure that two fluorescently active molecules will be, on average, separated by more than the microscope resolution. Fluorescent labels are progressively photobleached over the course of the experiment, thus depleting the pool of photoactivatable labels in the sample. The intensity of the photoactivation light is thus progressively increased to maintain a nearly constant activation rate. All single molecules positions, estimated with ~10 nm precision, are then assembled to form a super-resolution image. (**b**) For LPA-SPT, the photon budget is distributed across multiple image frames, thereby obtaining information about mobility at the cost of decreased precision of localization. The choice of imaging parameters must strike a balance between length (longer is better), density (lower is better) and localization precision (the higher the better) of tracks. Localized photoactivation relieves the fundamental trade-off between track length and localization precision (which benefits from stronger photoactivation) and track density (which benefits from weaker photoactivation) by providing strong photoactivation within a small fraction of the sample volume. Photoactivation light is delivered in pulses. Particles are then localized in subsequent image frames and tracked to obtain trajectories. This photoactivation/acquisition sequence is iterated to obtain data for several trajectories per cell, which are tracked and analyzed to build up statistics for individual tracks, single cells, as well as the entire ensemble of tracks

number, depending on the sample), a single SR image is constructed by superposition of the probability density functions for the positions of all detected emitters (Fig. 2). Given that one can usually collect 10^2–10^3 photons from a single fluorescent protein before bleaching, it can be localized at a precision of ~200 nm/sqrt(10^2–10^3) = 5–20 nm, an order-of-magnitude improvement over conventional wide-field or confocal imaging.

Our protocol for PALM imaging of labeled chemoreceptors (in this case Tar-mEos2) in fixed bacteria is detailed in Subheading 3.1. PALM imaging of bacterial chemoreceptors was pioneered by Greenfield et al. [7], and our protocol closely follows their approach. Our protocol additionally includes modifications for exploring chemoreceptor organization under ligand stimulation (in this case α-methyl-D/L-aspartate, hereafter referred to as MeAsp). A feature of primary biological interest in the nanoscale spatial organization is the size distribution of chemoreceptor arrays, which we quantify using a simple clustering algorithm applied to the localized PALM coordinates.

1.2 LPA-SPT Analysis of Chemoreceptor Mobility

Single-particle tracking is a powerful method for characterizing the mobility of molecules and subcellular structures within cells, but its utility is usually limited to samples with low object densities because frequent collisions and near encounters preclude reliable tracking. The latter problem is particularly severe in bacteria, given their small size (cell dimensions of 2–4 × 1 μm), only an order of magnitude greater than the PSF for a typical fluorescence microscope (~0.2 μm). Thus, only objects with a very low copy number per cell are typically trackable. PALM tracking (also known as "spt-PALM") overcomes this limitation [8] by using photoactivatable fluorophores, which can be switched on and tracked one at a time. PALM tracking has been successfully applied by many investigators [9–11], but the track lengths are limited by the relatively low photostability of photoactivatable proteins. In practical applications, individual photoactivated proteins tend to bleach within <10 frames, on average.

In Subheading 3.2, we describe a modified PALM tracking technique that allows tracking over a greater number of frames, under conditions in which the tracked particles contain multiple fluorophore labels. As in PALM tracking, this method utilizes photoactivatable fluorophores to enable tracking within a high density of labeled particles. However, instead of activating one fluorophore at a time using uniform illumination, it concentrates the photoactivation beam onto diffraction-limited spots to enhance the probability activating multiple fluorophores for particles that happen to lie within these photoactivation "hot spots." We have found this localized photoactivation single-particle tracking (LPA-SPT) method to be particularly useful for tracking bacterial chemoreceptors, which form a dense arrangement of arrays on the plasma

membrane. However, the technique is, in principle, applicable to any oligomeric protein complex in which each subunit is fluorescently labeled, or even to single molecules if they are engineered to contain multiple fluorophore labels.

2 Materials

2.1 Strains and Plasmids

1. Strains and plasmids used in this study are listed in Table 1. For both methods introduced in Subheading 1, any photoswitchable or photoactivatable protein can be employed as a fluorescent fusion to the protein of interest. Experiments described here utilized Tar-mEos2 (except in Fig. 5, where CheA-mEos3.2 was used). Plasmid pSJAB4 expresses Tar-mEos2 from an IPTG inducible promoter, a C-terminal fusion of mEos2 fused to the coding region of the *tar* gene with a six amino-acid (GSGGGG) linker. Strain UU1250, a gift from J.S. Parkinson, is a derivative of the chemotaxis wild-type strain RP437 with all chemoreceptors deleted [Δ*aer*-1 Δ*tsr*-7028 Δ(*tar-tap*)5201 Δ*trg*-100]. The induction level of fusion proteins (Tar-mEos2 or CheA-mEos3.2) was chosen to be the level that maximizes the rate of chemotactic ring expansion on soft agar motility plates ([12]) prepared with tryptone broth (TB). The functionality of the Tar-mEos2 fusion protein was tested via CheY-CheZ FRET assays [13].
2. Cell culturing: Strains TSS902, TSS1020, and TSS1836 were inoculated from a glycerol stock into tryptone broth (TB) and grown overnight until saturation at 30 °C in the presence of 100 μg/ml ampicillin for TSS902 and TSS1020 and

Table 1
Plasmids (A) and strains (B) used in this study

A	Gene	Backbone	Resistance	Source
pSJAB4	*tar-mEos2*	pTrc99A [20]	Ampicillin	This study
pSJAB93	*hns-mEos3.2*	pBAD33 [21]	Chloramphenicol	This study
pGP53	*cheA-mEos3.2*, *cheW*	pKG116 [22]	Chloramphenicol	J.S. Parkinson

B	Parent strain	Parent strain genotype	Plasmid
TSS902	UU1250 [23]	Δ*tsr*,Δ*tartap, Δtrg,Δaer*	pSJAB4
TSS1020	VH1 [24]	*Δtsr,Δtartap, Δtrg,Δaer*, Δ*cheRBYZ*	pSJAB4
TSS1836	UU1607 [25]	Δ*cheAW*	pGP53
TSS1893	HS1 [26]	Δ*hns*	pSJAB93

34 μg/ml chloramphenicol for TSS1836. The next morning, the saturated culture was inoculated 1:100 into fresh H1 minimal medium (100 μl in 10 ml) supplemented with 0.5% glycerol, 20 μM IPTG for TSS1020 and TSS902, and 0.6 μM NaSal for TSS1836 containing the following amino acids at 1 mM concentration: proline, methionine, lysine, and threonine. The medium was supplemented with 100 μg/ml of ampicillin for TSS902 and TSS1020 and 34 μg/ml chloramphenicol for TSS1836. After 6 h and 15 min growth at 33.5 °C to OD_{600nm} = 0.2, cells were harvested by centrifugation at for 5 min. The supernatant was discarded, and the cells were resuspended and washed with motility medium (*see* Subheading 2.3). The centrifugation and washing step was repeated twice. About 30 min after the washing was completed, cells were considered ready for microscopy.

2.2 Growth Media

1. Tryptone broth (TB): 1% Bacto tryptone, 0.5% NaCl.
2. H1 minimal salts medium: 50 mM KPO_4, 7.6 mM $(NH_4)SO_4$, 0.5 mM $MgSO_4$, 1.25 μM $Fe_2(SO_4)$, Thiamine 1%, NaCl 67 mM (supplemented with 0.5% glycerol and 1 mM of the following *L*-amino acids: threonine, methionine, proline, and leucine). All chemicals used in growth media preparation were purchased from Sigma-Aldrich.

2.3 Buffer Solutions

All imaging experiments, including those involving chemical fixation and ligand stimulation, were conducted in motility buffer medium, with which cells were washed and resuspended after growth. All chemicals used for preparation of buffers were purchased from Sigma-Aldrich.

1. Motility medium: 10 mM KPO, 0.1 mM EDTA, 10 mM lactic acid, 1 μM methionine, pH 7.
2. 1 mM MeAsp motility medium: Dissolve final amount of MeAsp acid in half the final volume of motility medium, which results in a turbid white solution. Add saturated NaOH until the solution clears, and then add motility medium to the final volume. Add saturated NaOH until pH 7 is reached (*see* **Note 1**).
3. 4% w/v paraformaldehyde motility medium: Dissolve 4 g of paraformaldehyde powder in 80 ml of motility medium and put it on a magnetic shaker hot plate at 80 °C. Add saturated NaOH (around 200 μl) until the solution clears. Add 37% HCl until pH 7.

2.4 Coverslip Cleaning

Extremely clean coverslips are essential both for PALM and LPA-SPT. In fact, every scattering particle coming from "dirt" that is smaller than ~250 nm in diameter will produce a PSF that can be challenging for the analysis software to distinguish

from an emitting fluorescent protein, thereby giving rise to false positive artifacts. Our protocol for coverslip cleaning requires the following:

1. Deionized milli-Q water.
2. Hydrogen peroxide, 50% w/v.
3. 100% ethanol.
4. 100% acetone.
5. Hellmanex detergent.
6. A sonicator.
7. Filtered pressurized nitrogen.

The protocol steps are:

1. Place the coverslip in a coverslip holder that fits in a beaker.
2. Rinse the coverslip with an abundance of milli-Q water.
3. Leave the coverslip in 1% Hellmanex dissolved in milli-Q water for >5 h (overnight is best).
4. Rinse thoroughly with milli-Q water.
5. Fill the beaker with 100% acetone. Submerge coverslips and sonicate for 15 min.
6. Rinse thoroughly with milli-Q water.
7. Fill the beaker with 100% ethanol. Submerge coverslips and sonicate for 15 min.
8. Rinse thoroughly with milli-Q water.
9. Fill the beaker with 50% hydrogen peroxide. Submerge coverslips and incubate at 80 °C overnight.
10. Safely dispose of the hydrogen peroxide and rinse thoroughly with milli-Q water.
11. Dry the coverslips with filtered pressurized nitrogen.
12. Coverslips can be kept in air for about 2 weeks, provided that the beaker containing them is properly sealed with Parafilm or aluminum foil.

2.5 Cell Attachment and Drift Correction

To correct for sample drift, which can occur during the long acquisition time of PALM, we employ 100 nm-wide gold-coated silica beads as fiducial markers within the imaging field of view. We use poly-L-lysine to attach both gold-coated beads and fixed cells to cleaned glass coverslips.

For LPA-SPT, we employ anti-flagellar antibodies for attaching cells to the coverslip. (Anti-FliC antibodies bind specifically to bacterial flagellar filaments and non-specifically to the glass surface.) We utilize:

1. Poly-L-lysine solution 0.1% w/v (Sigma-Aldrich).

2. Gold-coated polystyrene beads (diameter < 200 nm, Sigma-Aldrich).
3. Anti-FliC antibodies (rabbit polyclonal, a gift of H.C. Berg).

2.6 Preparation of PALM Imaging Chamber

1. 25 × 75 mm² glass slides.
2. Rubber spacer (1 mm thick, silicon isolator, Press-to-Seal series, Sigma).
3. 25 × 75 mm²; 200 μm thick coverslips.

2.7 LPA-SPT Consumables for Flow Cell

1. Round coverslips (no. 1, 12 mm diameter; no. 2, 22 mm diameter).
2. Vacuum grease (Apiezon L).

2.8 General Microscopy

PALM and LPA-SPT equipment requirements mostly overlap, and an optical path for localized photoactivation can be easily added to an existing PALM setup. We list here all the components needed to build a PALM setup and the additional optics required for building a localized photoactivation path for LPA-SPT. We provide a sketch of our setup in PALM mode in Fig. 3, and in LPA-SPT mode in Fig. 9. We note that, by simply removing the microlens array, it is possible to switch between the two modes.

1. Nikon Ti-E inverted microscope with Perfect Focus System (PFS).
2. Automated XY stage (Mad City Labs).
3. Halogen lamp for bright field imaging.
4. High numerical aperture (1.49 NA) 100X TIRF objective lens (Nikon).
5. Filter cubes, used for mEos2 green-state and red-state imaging (for green state: EX R405/491/561/635 multi-edge, EM FF01-525/45-25. For red state: EX R405/491/561/635 multi-edge, EM NF02 405S-25/NF03 561E-25/FF01-607/70-25).
6. Optical table.
7. Temperature/humidity controlled room.
8. Solid-state lasers for fluorophore excitation and photoactivation: 405 nm (Coherent CUBE 100 mW), 491 nm (Cobolt Calypso 200 mW), 515 nm (Cobolt Fandango 150 mW), 568 nm (Coherent Sapphire 200 mW).
9. Acousto-optic tunable filter (AOTF, AA, France) for shutter ing/pulsing excitation lasers (*see* **Note 2**).
10. Signal generator for analog control.
11. Back-thinned, electron-multiplying CCD (EMCCD) camera (Princeton Instruments ProEM and Andor iXon 897).
12. General optomechanics and accessories (Thorlabs and Radiant Dyes).

13. Computer interface hardware (National Instruments).
14. Data acquisition PC.

2.9 Additional Component for PALM

1. Neutral density filter wheel (Thorlabs).

2.10 Additional Components for LPA-SPT

1. Microlens array (Flexible Optical B.V., APO-GB-P1500-R13.9, BK-7 glass, $F \approx 25$ mm, pitch = 1500 μm, 36 lenses, 10×10 mm^2).
2. Mechanical shutter (Uniblitz) with automated control for 405 nm laser.

2.11 Fluidics

1. Gold-plated flow cell [14].
2. Fluidic pump (Harvard Apparatus, PHD-2000).
3. Polyethylene fluidic tubing (PORTEX fine bore polyethylene tubing, 0.58 mm ID, 0.96 mm OD).
4. Fluidic switch (Hamilton HVM 3-2).

3 Methods

3.1 PALM Imaging of Bacterial Chemoreceptors

Cells are first cultured as described above and then left in neutral buffer for ~45 min prior to fixation with 4% paraformaldehyde, coverslip attachment, and incubation in PALM imaging chamber. For experiments in which a ligand stimulus is applied, the buffer suspension is aliquoted into two or more parts and subjected to ligand stimuli of different concentration and/or duration (but always leaving one part as unstimulated control) prior to fixation, and a separate PALM imaging chamber is prepared for each aliquot. PALM image analysis and filtering of localizations are achieved by either custom-written Matlab code or by means of open-source GUI-based software. The resulting PALM localizations are then grouped into clusters by means of a simple distance-based clustering algorithm. These analyses yield the number of localizations falling within each cluster, as well as an estimate of the area occupied by each cluster.

3.2 PALM Setup Summary

Requirements and typical microscopy setups for PALM imaging have been discussed extensively in the literature [1]. Here we provide a brief description of our PALM imaging setup, which is also used for LPA-SPT with slight modifications. Our setup is built around the Nikon Ti-E inverted microscope (*see* Fig. 3 for a detailed scheme).

1. Excitation path: 491 nm and 568 nm lasers for exciting the green and red states, respectively, of mEos2/mEos3.2 are passed through an acousto-optic tunable filter (AOTF), which

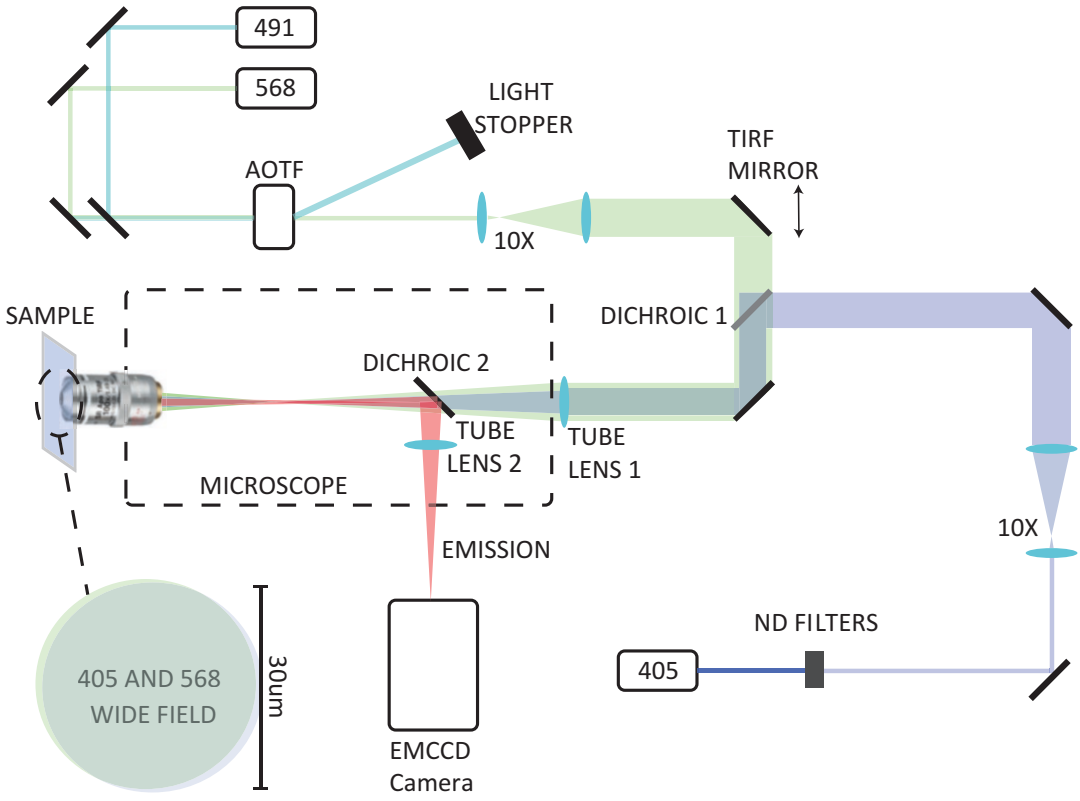

Fig. 3 Optical setup for PALM imaging. Excitation and activation paths are shown in green and blue, respectively. An AOTF placed in the excitation path allows laser exposure times to be controlled separately from the camera's frame interval (e.g., for stroboscopic illumination). The excitation (561 nm) beam is expanded by a 10× telescope and focused on the back focal plane of the objective to achieve EPI illumination with a flat profile across the camera field of view. Translation of one of two mirrors ("TIRF mirror") placed between the telescope and tube lens is used to achieve highly inclined illumination to minimize reflections of the excitation beam. A 488 nm laser is also coupled to the same excitation path for green-state wide-field imaging of mEos2 and mEos3.2. The activation (405 nm) beam is also expanded 10× and combined with the excitation path through a dichroic mirror (Dichroic1) to achieve EPI illumination. The activation intensity is modulated via both a neutral density filter wheel and analog computer control of the power of the 405 nm laser. Light emitted from the sample (red) is collected through the objective, reflected by a second dichroic mirror (Dichroic2) and imaged by an EMCCD camera

is used as a shutter to convert the continuous laser illumination into excitation light pulses of desired timing. The excitation light is then magnified 10× via a telescope. The collimated expanded beam is focused on the objective back focal plane via a tube lens (focal length of 300 mm for our setup) placed immediately in front of the rear aperture of the microscope, yielding (after the microscope objective) a nearly parallel beam that passes through the sample plane with a size of approximately 60 μm (full width at half maximum). The 568 nm power is set to 50 mW at the laser module, of which 25 mW is transmitted to the sample plane in our setup.

2. Photoactivation path: The photoactivation 405 nm beam illuminates the sample continuously at low power in a typical PALM experiment. In our setup, a dichroic mirror combines the photoactivation (405 nm) laser with the excitation (568 nm) laser. The 405 nm beam is also focused onto the back focal plane of the objective, creating a photoactivation beam that passes through the sample plane with approximately the same dimensions as the excitation beam. Neutral density (ND) filters placed in a filter wheel in front of the 405 nm laser, as well as analog control of laser power, are used to modulate the intensity of the photoactivation beam over the course of the experiment in order to keep the number of activated fluorophores per image frame approximately constant.
3. Imaging path: The emitted light is collected via the 100× 1.49NA Nikon TIRF objective and passed through a series of emission filters to block both the 405 and 568 nm light (405 and 561 notch filters in series, Semrock) and to band-pass the emission of the red state of mEos2. The filtered emission is then passed through 1.5× magnifier built into the microscope and imaged on the EMCCD sensor via the microscope tube lens. The total magnification is thus 150×, and the effective pixel size is 106.7 nm.
4. Sample positioning: We use a standard sample holder for regular microscopy slides to position our imaging chamber for imaging. The imaging chamber consists of a rubber spacer sandwiched by a rectangular coverslip and a standard glass microscope slide (Fig. 4). The holder is coupled to a motorized stage that allows for computer-controlled movement of the sample.
5. Acquisition software: We employ custom-written software to control our microscopy and data-acquisition hardware. The program allows precise control of laser and camera timings and other experimental parameters. For PALM experiments, we use continuous 405 nm illumination with analog control of the power level, and 568 nm excitation with an exposure time of 60-100 ms per camera frame.

3.3 Chamber Preparation

Rectangular coverslips are cleaned as described in Subheading 2.4. The coverslip has to be chemically treated to firmly attach fixed bacteria on its glass surface, and the following steps describe such a treatment employing poly-L-lysine, which we employ for fixed-cell attachment to glass surfaces. To prepare the coverslip for attachment we follow the steps below.

1. Deposit 40 μl of poly-L-lysine (PLL) at the center of the coverslip by pipetting (*see* **Note 3**) and let sit for ~20 min.
2. Thoroughly rinse with milli-Q water by pipetting to remove excess PLL from the glass surface.

3. Deposit 5 μl of 1% v/v solution of gold-coated silica beads, which are sonicated for 5 min previous to deposition on the PLL-coated region and let sit for 15 min.
4. Rinse twice with motility medium by pipetting.
5. Incubate bacterial suspension on the area covered with PLL for 15 min.
6. Rinse three times with motility medium.

3.4 Bacterial Cell Preparation

Cells are cultured as described in Subheading 2.1 (*see* **Note 4**), harvested by centrifugation (4165 × *g*, 5 min washing twice with 50 ml of motility medium), and finally resuspended in 1 ml motility medium. Incubate at room temperature for 45 min prior to fixation and PALM imaging. For experiments with ligand stimulation, the suspension is aliquoted into three parts prior to fixation.

1. Unstimulated cells: Cells are held in neutral motility medium before fixation.
2. Cells shortly after stimulation: Cells are exposed to 1 mM MeAsp for a duration of ~10 min prior to fixation.
3. Cells under prolonged stimulation: Cells are exposed to 1 mM MeAsp for a duration much longer than the chemotactic adaptation time, usually 1 h.
4. Each sample is chemically fixed with 4% paraformaldehyde (PFA) as described below prior to attachment to the coverslip.
5. Fixation: Because PALM depends on iteratively accumulating many images of fluorophore subpopulations, the acquisition sequence for a single PALM image can extend over long times (often >1 h). PALM images will thus reflect cellular structures accurately only if the labeled structures are stationary over the course of the acquisition. Chemical fixation is thus desirable for most PALM experiments, to ensure that movement of cellular structures is negligible. For this purpose, PAF powder is dissolved in motility medium to a final concentration of 4% w/v, as described in Subheading 2. We find that paraformaldehyde solution should be prepared fresh on the day of the PALM experiment to minimize false positives in the sample. Just before the fixation step, cells suspended in motility medium (with or without ligand stimulation) are centrifuged (4165 × *g*, 5 min), and the supernatant is decanted to achieve an OD of about 2. We add 40 ml of the fixative solution to the cell pellet. Fixation proceeds by incubation at room temperature for 10 min (*see* **Note 5**). For best imaging results, perform the fixation of each sample just prior to PALM imaging. We find that this procedure minimizes false positive localizations and maximizes quantitative reproducibility of the PALM experiment. If multiple samples (e.g., different stimulation

conditions) are to be imaged on the same day, it is advisable to fix the different samples at different times.

6. Imaging chamber: We perform PALM imaging in a sealed chamber filled with motility medium, assembled on a conventional microscope slide by means of a square piece of 1 mm-thick microscopy rubber, out of which a circular hole 2 cm in diameter has been carved, as illustrated in Fig. 4. The multiuse rubber spacer is first cleaned in H_2O_2 at ~100 °C for 15 min, then rinsed with milli-Q water and acetone to maximize adhesion to glass. It is then placed on the microscopy slide so as to create an open circular chamber. The chamber is filled with 170 μl of motility medium and sealed with the treated coverslip on which bacteria were immobilized (*see* **Note 6**).

3.5 PALM Imaging Protocol

After positioning the sample and focusing with the objective, a suitable field of view (FOV) is chosen in brightfield (*see* **Note 7**). The criteria for choosing a good FOV are as follows.

1. Presence of at least one (bright) fiducial marker.
2. Good cell attachment (cells are not wobbling and lie parallel to the glass surface).
3. Cells in the FOV are non-overlapping and well separated.
4. After choosing the FOV, we record a brightfield image and switch the microscope to fluorescence mode. A typical chemoreceptor imaging experiment under our conditions involves the acquisition of about 80,000 frames. In our PALM imaging

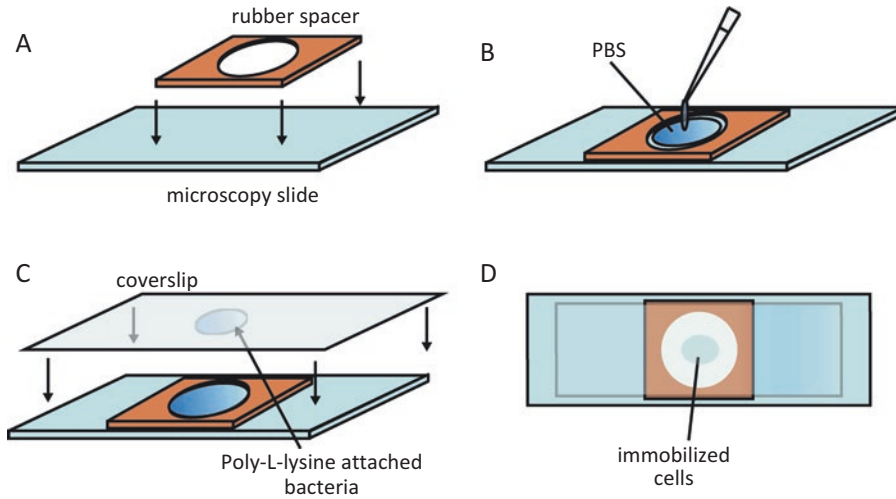

Fig. 4 Preparation of the PALM imaging chamber. (**a**) A rubber spacer with a circular hole is placed on a clean microscopy slide. (**b**) The circular chamber is filled with PBS buffer. (**c**) The chamber is sealed with a coverslip on which fixed bacteria are immobilized using poly-L-lysine. (**d**) The chamber is ready for imaging

protocol, both the photoactivation and the excitation illumination are continuous. Care should be taken to limit the 405 nm intensity to avoid overactivation. When the photoactivation rate is too high, the chances of switching on two fluorophores within the DL area become significant and lead to complications and/or artifacts in the PSF fitting procedure. We control the photoactivation rate by both analog control of the 405 nm laser power and by a double filter wheel equipped with neutral density filters of optical density (OD) ranging from 0.1 to 0.8 on the first wheel and from 1.0 to 4.0 in the second wheel. Because the number of activatable fluorophores will decay exponentially over time if the photoactivation beam intensity is constant, we increase its intensity over time accordingly to maintain an approximately constant activation rate. 405 nm power is ramped up exponentially by analog control over 20,000 frames, at which point the neutral density filter is switched to one of a lower OD, and the process is repeated. Depending on the power losses occurring in the optical paths, which can vary for different microscopy setups, these parameters might need to be adjusted accordingly. Our imaging protocol is summarized in Table 2.

5. Excitation is carried out at high power to minimize the occurrence of activated fluorophores that continue to emit across more than one frame. In practice, some emission across frames is unavoidable, but minimizing this fraction facilitates analysis, especially when PALM is used not only to localize molecules, but also to count them.

Table 2
Experimental parameters for PALM imaging

	0–20k frames	20–40k frames	40–60k frames	60–80k frames
Frame duration	100 ms	100 ms	100 ms	100 ms
Frame rate	10 fps	10 fps	10 fps	10 fps
Excitation power (568 nm)	50 mW	50 mW	50 mW	50 mW
Activation power (405 nm)[a]	$V_0 \times \exp(1.6 \times n/n_{max})$	$V_0 \times \exp(1.6 \times n/n_{max})$	$V_0 \times \exp(1.6 \times n/n_{max})$	$V_0 \times \exp(1.6 \times n/n_{max})$
Neutral density filter O.D.	3.8	3.1	2.4	1.7

[a]In each 20k-frame segment, n ranges from 0 to n_{max}, where n_{max} = 20,000 and V_0 = 20 mW

3.6 PALM Data Analysis

1. Image reconstruction: Our PALM image analysis procedure makes use of the freely available software ThunderStorm developed and described in [15]. This program is implemented in Fiji (imageJ) as a plugin which can be downloaded at https://github.com/zitmen/thunderstorm/wiki/Installation. The software takes as its input the set of raw images from the PALM experiment in the form of an "image stack". As in any other standard PALM analysis protocols, ThunderStorm first finds the positions of the maxima corresponding to the emitter PSFs in each image and uses those positions as initial-guess parameters for fitting a two-dimensional Gaussian function to each PSF to localize the fluorophore. After this procedure is repeated for each frame, an SR image is constructed by superimposing all localizations from all frames. We also make use of the "drift correction" function in ThunderStorm in the mode "fiducial markers" to compute the sample drift over time by means of the localizations corresponding to the gold-coated silica beads deposited on the coverslip.
2. Drift correction: We employ immobilized 100 nm diameter gold-coated silica beads as described in 3.3 Chamber preparation to correct for the sample drift in the x–y directions. The position of the beads is recorded at each frame, and the position of all the other localizations in that frame is translated by the difference vector between the initial position of the fiducial marker and the position of that marker at that frame. Given the long acquisition time of our experiments (around 100–150 min), correcting for sample drift is essential (Fig. 5).
3. Additional postprocessing: In our protocol we consistently apply two additional postprocessing routines to the raw list of localizations. First, remove duplicate localizations (localizations that converged to the same position). Second, eliminate all localizations belonging to the same molecule in consecutive frames, or molecules that are blinking instead of bleaching. This last phenomenon (fluorophore blinking) is one of the main causes of artifacts in PALM images, as it can produce "clusters" of localizations that are actually coming from multiple localizations of the same protein. Such localizations can be combined into one single localization based on a specified distance within which molecules are merged together in the subsequent frames, and accounting for an allowed number of frames in which the molecule can disappear. Routines for both corrections are implemented in ThunderStorm. A representative PALM image of receptor clusters is shown in Fig. 6.

3.7 Cluster Analysis

Once the raw list of localizations has been generated, we can proceed with cluster identification. For our purposes, the following simple algorithm yields satisfactory results.

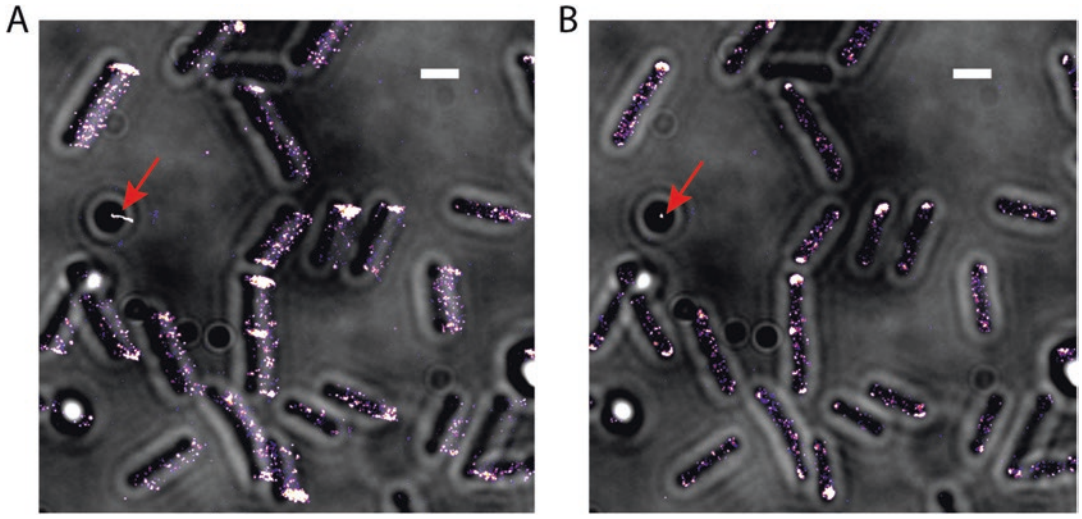

Fig. 5 Drift correction by use of fiducial markers. (**A**) Uncorrected PALM image (prior to drift correction) overlaid with brightfield image of cells acquired at the start of the experiment. Considerable sample drift over the duration of PALM acquisition (150 min) is clearly visible, both in the trace of the fiducial marker (indicated by red arrow) and by the large number of PALM localizations outside of the initial cell positions in the brightfield image. (**B**) PALM image after drift correction. The trace of the fiducial marker is reduced to a point and the features of the sample (CheA clusters in this case) are recovered. Scale bar: 1 μm. Strain used: TSS1836. Genotype: Δ*cheAW* cells (UU1607) expressing CheW and CheA::mEos3.2 from plasmid (pGP53) at 0.6uM NaSal induction. *See* Table 2 for imaging conditions

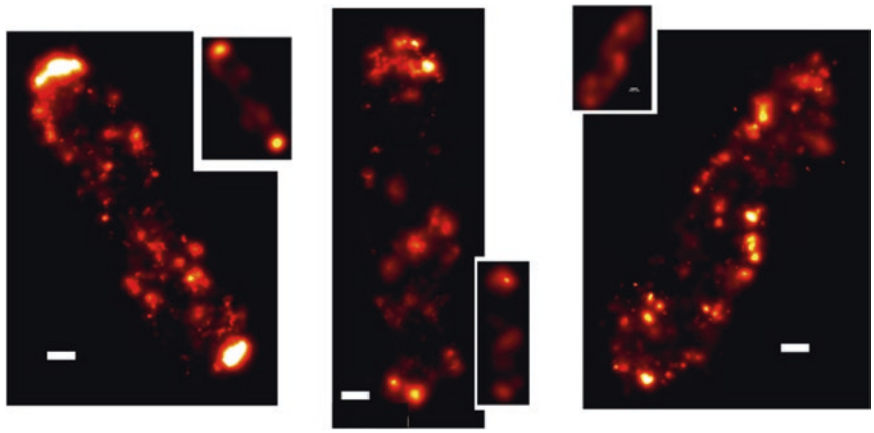

Fig. 6 Representative PALM images of a strain expressing Tar-mEos2. There is considerable diversity in the nanoscale organization of chemoreceptors, as exemplified by these three cells. The insets show simulated diffraction-limited images constructed by convolving each PALM image (main panels) with a Gaussian function of the same width as the PSF of our microscope. Scale bar: 200 nm. Strain used: TSS902 (*see* Table 1 for details)

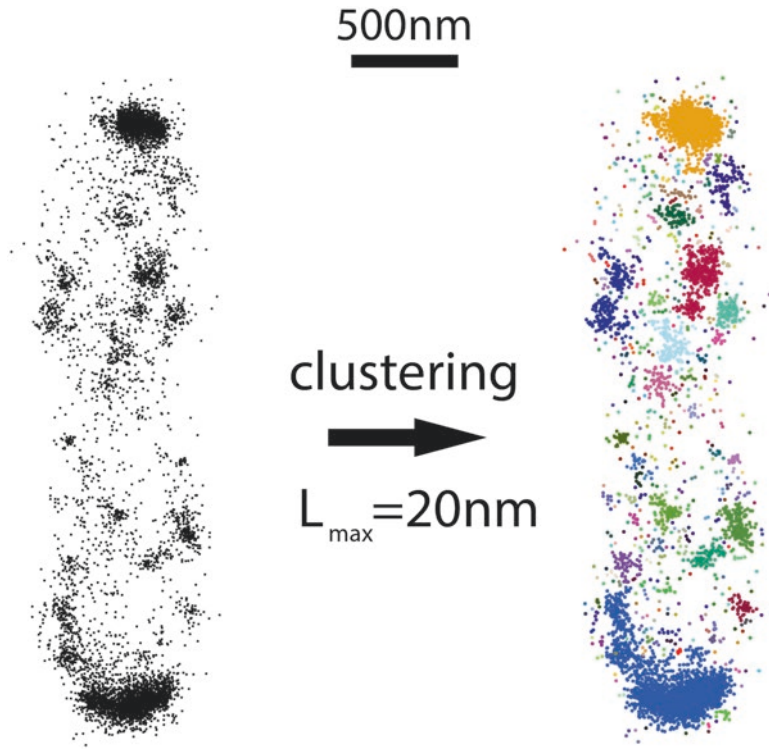

Fig. 7 Example input and output of clustering algorithm. The full set of single-molecule PALM localizations within a cell (left, black points) are partitioned into clusters (right, colored points) by a simple criterion: localizations separated by a distance less than a threshold L_{max} (here set to 20 nm) are assigned to the same cluster. Each identified cluster is represented in a different color. Scale bar: 500 nm. Strain used: TSS902 (*see* Table 1 for details)

1. Compute all the pairwise distances between localizations in a cell.
2. Assign two localizations to the same cluster if their distance is <20 nm.

A sample output of our code is presented in Fig. 7. We also tried to implement more sophisticated algorithms such as DBSCAN [16], but a comparable cluster identification efficiency was obtained.

Each cluster identified by our algorithm is depicted in a different color in Fig. 7. After the localizations are grouped into clusters, we can count the number of localizations for each cluster in the cell and repeat the procedure for each cell in the PALM image. Upon collecting enough statistics, we can build a cluster size distribution for each sample (Fig. 8). In agreement with [7], we find that the distribution of cluster size, N, is extremely broad, ranging from single localizations to >2000 localizations. Large clusters ($N > 100$) make up only a few per cent of the cluster population (Fig. 8,

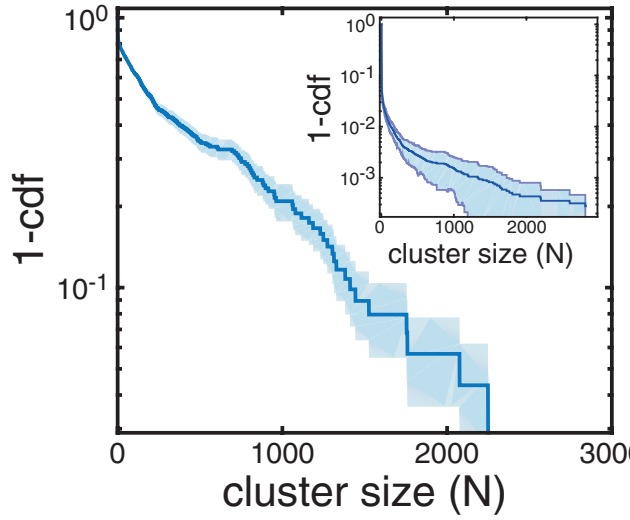

Fig. 8 PALM cluster-size statistics for a strain expressing Tar-mEos2. The main panel shows the complementary cumulative distribution function (1-cdf) for the probability that a localized receptor is found in a cluster of size *N* (or equivalently, the fraction of receptors found in clusters of size smaller than or equal to *N*). Inset: Complementary cumulative distribution function (1-cdf) for the probability that a cluster is of size *N* (or equivalently, the fraction of clusters with size smaller than or equal to *N*)

inset), but contain more than half of the receptor population (Fig. 8, main panel).

3.8 Localized Photoactivation Single-Particle Tracking (LPA-SPT) of Chemoreceptors

Cells expressing labeled chemoreceptors are cultured according to standard procedures (*see* Subheading 2.1), immobilized on a round coverslip, and incubated in a flow cell [14] under buffer flow. By use of a micro-lens array, we generate a squared grid of twenty-five diffraction-limited (DL) foci of the 405 nm laser at the sample plane that switch mEos2 fluorophores from the green-emitting (inactive) to red-emitting (active) state in the vicinity of the DL photoactivation spots. Upon translating the sample to a new field of view (FOV), the X–Y position of the stage is fine-tuned manually to ensure a good overlap of the photoactivation spots with immobilized bacteria. We then deliver a short 405 nm laser pulse and image the red state of mEos2 by means of a 568 nm laser until all activated fluorophores are bleached. Before the pulse, no mEos2 fluorophores are visible in the red channel. After the pulse, a few Tar-mEos2 clusters appear in the FOV as mEos2 labels that happen to lie near the DL photoactivation foci are switched to the red-emitting state as a result of 405 nm irradiation. Because the 405 nm photoactivation pulse is focused to a diffraction-limited spot, one can obtain a low enough spatial density of activated clusters

for reliable tracking. In addition, by tuning the energy of this photoactivation pulse, one can photoactivate, on average, more than one fluorophore per cluster. By adjusting the intensity of the 568 nm excitation, the number of image frames over which Tar-mEos2 clusters can be tracked before photobleaching can be increased.

3.9 Localized Photoactivation Path

The optical path for localized photoactivation is implemented on the same PALM setup described earlier. A microlens array is placed in the 405 nm laser path to create a telescope with the tube lens at the aperture of the microscope (Fig. 9; *see* **Note 8**). This creates a bundle of parallel beams organized in an array that converges at, and overfills, the back focal plane of the microscope objective. The beams are focused on the sample by the microscope objective, creating an

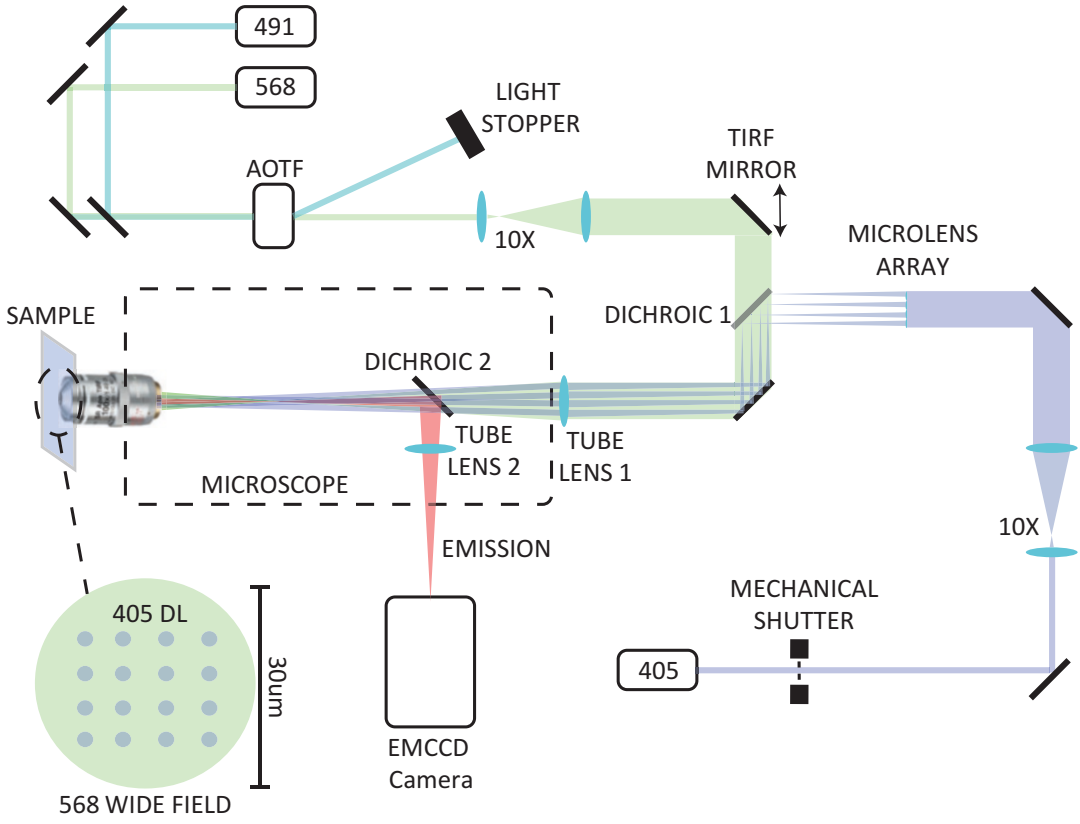

Fig. 9 Optical setup for Localized PhotoActivation Single-Particle Tracking (LPA-SPT). The excitation path is identical to that described in Fig. 3 for PALM imaging. The activation path is also unchanged except that in this localized activation mode, the 405 nm activation beam is not attenuated and passes through a mechanical shutter to generate millisecond pulses and is converted into a beamlet bundle by a micro-lens array that forms a telescope with the tube lens. Each expanded beamlet leaving the micro-lens tube-lens telescope overfills the back focal plane of the objective with a different angle of incidence to yield an array of diffraction-limited (DL) activation spots on the sample plane

array of diffraction limited spots for localized photoactivation. By inserting/removing the microlens array, one can switch between the PALM and LPA-SPT configurations.

3.10 LPA-SPT Sample Preparation

1. Coverslip treatment and preparation: Round coverslips (no. 1, 12 mm) are cleaned as described in Subheading 2.4. For sealing purposes, a ring-like pattern of vacuum grease must be deposited at the rim of the round coverslip. To achieve this, we use a short cylindrical hollow metal tube, which has the same diameter as the round coverslip and a wall thickness of about 1 mm. One end of the tube is dipped into a thin film of vacuum grease prepared by sandwiching the grease between two microscope slides and rubbing. The grease spreads homogeneously on the circular face of the tube, which is then applied to the coverslip by placing the greased face of the tube onto the coverslip and gently rotating several times before removal. For LPA-SPT experiments we usually use anti-FliC antibodies to attach the cells, as we have found that use of PLL often leads to less reproducible results with live cells, possibly because of perturbations of cell physiology [17]. Anti-FliC antibodies bind non-specifically to the glass surface of the coverslip and very specifically to bacteria's flagella.
2. Cells are concentrated via centrifugation to a final OD ~ 2 in motility medium.
3. Fifteen microliter of concentrated cells is deposited on the round coverslip on the side with the deposited vacuum grease, and 1.5 μl of antibody solution (2 ng/ml) are immediately added.
4. After 20 min incubation at room temperature, the coverslip is ready to be mounted on the flow cell.

3.11 Cleaning of Flow Cell

Prior to mounting the treated coverslip, the flow cell has to be cleaned to remove impurities (dirt and unwanted particles or chemicals coming from previous experiments). For cleaning, we connect a syringe to polyethylene tubing and flow solvents through the inlet and the outlet of the flow cell to clean and also purge air bubbles that tend to form in the vicinity of the inlet and outlet. Our flow cell cleaning protocol consist of the following steps.

1. Ethanol 100% is flushed into the flow cell by means of a syringe on either side successively.
2. Acetone is flushed into the flow cell by means of a syringe on either side successively.
3. Ethanol 100% is flushed into the flow cell by means of a syringe on either side successively.
4. Check if any air bubbles are in the vicinity of the inlets (*see* **Note 9**). If so, repeat **step 3**.

5. Connect the flow cell to the fluidic pump and seal with an empty greased coverslip.
6. Flow Milli-Q-water for 5 min at 400 μl/min.
7. Flow buffer for 5 min at 400 μl/min.

3.12 Coverslip Mounting

The flow cell is sealed with the coverslip on which bacteria are attached. To seal the flow cell without air bubbles, it is essential that some liquid is present in the chamber. After the last step of the cleaning protocol, flow is stopped and the empty coverslip removed. The buffer-air interface at the now open top window of the flow cell is allowed to bulge and form a convex dome-like droplet by gradually raising the buffer reservoir at the end of the feed tube above the height of the flow cell to apply a gentle gravity flow. The coverslip with attached bacteria is then gently laid on the droplet, the side with the cell suspension face down, and flow is switched on immediately by applying negative pressure at the flow cell outlet connected to a syringe pump. As liquid is sucked away, the bulge on which the coverslip rests recedes. The coverslip is assisted to its seat at the top face of the flow cell by a gentle push with a wooden toothpick, to achieve sealing of the flow cell just before the bulge disappears. The flow cell is now ready for imaging.

3.13 Fluidic Switch Valve

Use of a fluidic switch valve allows for media exchange in the flow cell. For tracking receptor clusters in the presence or absence of stimulation, we feed buffer through one inlet of the switch and buffer with stimulus (e.g., 1 mM MeAsp) through the other. The switch is operated manually to perform tracking experiments in the presence and absence of stimulus.

The syringe pump is operated in suction mode, and thus using a 50 ml syringe and a flow rate of 400 μl/min, measurements can proceed uninterrupted for up to 2 h. For experiments of longer duration, one can stop the flow and empty the syringe, being careful not to create air bubbles in the chamber or to compromise the grease seal of the coverslip by perturbing pressure in the flow cell.

3.14 LPA-SPT Imaging Protocol

Cells are continuously perfused with fresh motility medium (at 400 μl/min) in the flow cell assembled as described above. Focal drift in the z-direction is minimized by closed-loop feedback (Perfect Focus System, Nikon). A joystick is used to control the X–Y positioning of the motorized stage for fine adjustments of the field-of-view (FOV) to enhance overlay of the DL 405 nm photoactivation spots with the immobilized bacteria. In our standard protocol, image acquisition in each FOV consists of four repeats of the following sequence: one photoactivation frame, in which a 405 nm pulse is delivered to the sample for localized photoactivation, followed by 249 tracking frames, during which time a 568 nm pulse is delivered for widefield excitation and imaging of fluorescence emission via the

camera. Unless otherwise stated, the data described here use a frame rate of 15 fps (frame duration = 65 ms), excitation laser pulse of 30 ms, and an activation pulse of 5 ms. Thus, the number of image frames per FOV is 1000, and the acquisition lasts 65 s. With these settings, we find an average number of tracks per FOV of N_{tracks} = 604 ± 144 (mean ± stdev.) and an average track length of L = 10 ± 9 (mean ± stdev.).

These parameters were chosen empirically for our experiments, but they can be adjusted for each type of sample to achieve a good balance between track length, throughput (i.e., number of tracks per unit of acquisition time), and precision of localization (*see* **Note 10**). The key parameter is the duration of the 405 nm pulse, which determines the density of activated clusters after each localized activation pulse. If this duration is too long, the frequency of collisions/near-encounters becomes too high for reliable tracking. If the duration is too short, trajectories will be fewer in number and shorter in length, limiting the quality and quantity of data.

The LPA-SPT imaging sequence described above is repeated for many FOVs across the field of coverslip-attached cells. Using a motorized stage, we sample the coverslip in an approximately periodic 2-D grid across the square window of the flow cell, using a motorized stage to initialize the positioning of FOVs in a periodic array (with pitch 500 μm). We use manual fine-tuning of FOV position to maximize coincidence between the DL 405 nm photoactivation spots and attached bacteria. By systematically sampling FOVs in a well-spaced grid, we avoid imaging the same cells twice. This grid-like sampling of FOVs with sufficient spacing was found to be important for reproducible results, as tracking results were found to depend on the number of imaging cycles a cell has undergone (presumably due to the relatively strong 405 nm irradiation, which can perturb cell physiology). Combined with sufficient care to keep acquisitions within each field of view reasonably short (*see* above), we found that reproducible results are achievable in LPA-SPT.

The 405 nm intensity at the DL photoactivation spots is ~100 times higher than that for the area outside the spots, so the efficiency of activation is concomitantly high at, and very close to, each photoactivation spot. However, the entire FOV is exposed to a finite intensity of 405 nm irradiation, with a non-uniform intensity profile in the region between spots that is determined by the square-grid arrangement of microlenses in the array (*see* high-contrast and low-contrast images of the microlens-generated spots provided in Fig. 10a). Given that the total FOV area is much greater than that of all spots combined, there is also a considerable fraction of "off-spot" activation events (*see* Fig. 10b). In our typical analyses, we also include tracks originating in off-spot photoactivation to increase tracking statistics.

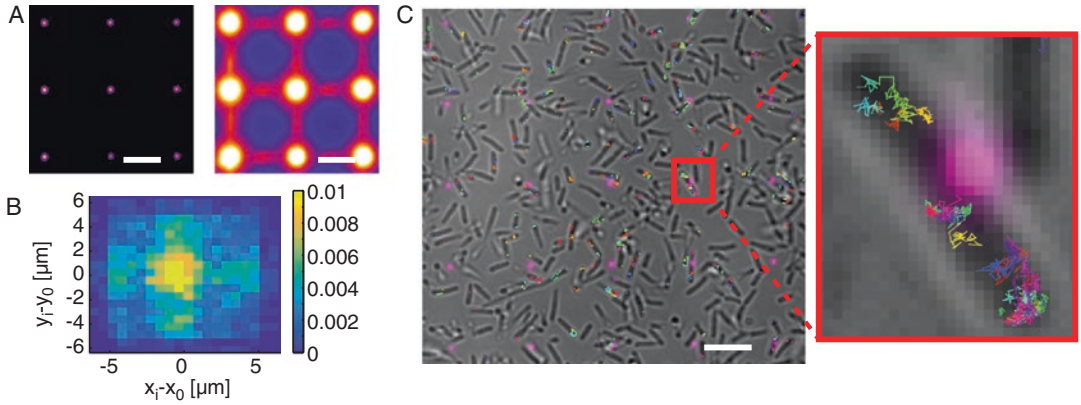

Fig. 10 Localized photoactivation and sample trajectories. (**a**) Low-contrast and high-contrast images of the micro-lens-generated array of photoactivation spots at the sample plane (left and right image, respectively). The high-contrast image reveals the presence of a pattern of low-intensity 405 nm light between the diffraction-limited foci that form photoactivation hot spots. (**b**) Two-dimensional histogram (probability mass function) for the initial position of tracks $[x_i,y_i]$ relative to the nearest photoactivation hot spot $[x_0,y_0]$. Photoactivation density is clearly peaked at the hot spots ($[x_i - x_0,y_i-y_0] = [0,0]$), but a considerable fraction of localizations also occur outside of this central peak, with a pattern that closely resembles the unit cell of the repeating pattern in the high-contrast image of panel A. Data from 25 FOVs, number of tracks ~30,000, strain used: TSS1020. (**c**) Typical field of view (left) with image of photoactivation hot spots (violet) and receptor-cluster trajectories overlaid. Zoomed view of a cell lying near a photoactivation hot spot (right) reveals the diversity of trajectories, which vary with respect to their length, mobility, and cellular location. Scale bar: 5 μm. Localized-activation pulse: 5 ms. 405 nm Power: 100 mW. *N* tracks = 631. Only tracks lasting for five or more frames were retained. Strain used: TSS1020 (*see* Table 1)

3.15 LPA-SPT Data Analysis

Tracks are obtained from LPA-SPT image sequences using the u-track package [18], integrated into custom MATLAB scripts to automate data handling. The tracking algorithm performs very well on LPA-SPT data, which consist of low-background images of point emitters with well-separated trajectories. An example FOV (Fig. 10c) demonstrates the efficiency of tracking under our standard conditions for Tar-mEos2 imaging (~500 tracks of length >5 frames per FOV, in which 1000 frames are acquired). Track length is also enhanced in LPA-SPT, relative to PALM tracking, as shown in Fig. 11a.

The brightfield image of each FOV is segmented to extract masks for cellular position analyses of tracks. For each track we identify the bacterium to which it belongs, as well as its location along the long axis of the cell. Positional information about individual tracks is useful, for example, in looking at differences between the mobility of chemoreceptor clusters residing at the cell poles ("polar clusters") and those residing elsewhere ("lateral clusters"). These two cluster types have been found, through diffraction-limited imaging, to have contrasting mobilities, with polar clusters moving more rapidly than lateral ones [19]. With LPA-SPT, we

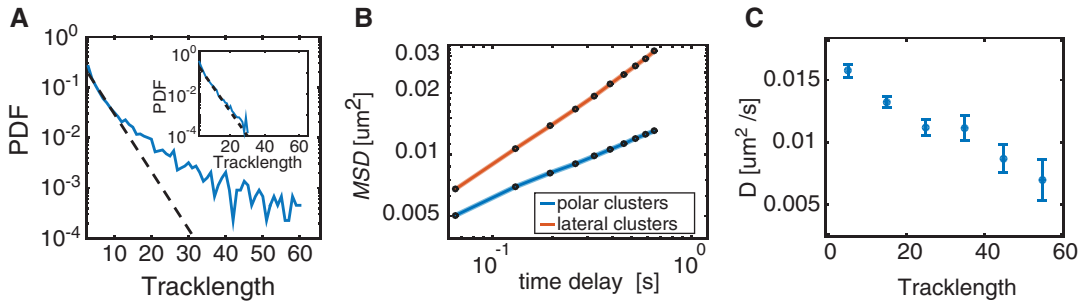

Fig. 11 Example tracking statistics from LPA-SPT experiments. (**a**) Comparison of track-length distributions from a typical LPA-SPT experiment (main panel) and PALM tracking (inset). LPA-SPT tracks are significantly enriched for long trajectories that give the distribution a broad tail. Dashed lines are fits of the initial decay by an exponential $a \times e^{-bn}$, where n is the number of frames and $b = 0.26$ for the main panel, and $b = 0.25$ for the inset. For the main panel, the mean, standard deviation and maximum track length were 8, 9, and 61, respectively, and the number of tracks was ~4400, collected from ~600 cells in ten FOVs. For the inset, the mean, standard deviation and maximum track-length were 4, 3, and 31, respectively, and the number of tracks was ~6000. (**b**) Mobility of clusters in different cellular locations. The mean-squared displacement (MSD) grew sublinearly with time. Fitting a linear function to the first three points of the MSD versus time curve yielded an apparent diffusivity $D_{lin} = (6.0 \pm 0.8) \times 10^{-3}$ μm²/s for polar clusters and $D_{lin} = (13.5 \pm 0.8) \times 10^{-3}$ μm²/s for lateral clusters. Errors on D_{lin} were obtained from the covariance matrix of the linear fitting parameters. Fitting with a power law (MSD ~ $D_{PL}t^{\alpha}$) yielded $\alpha = 0.4 \pm 0.01$ and $D_{PL} = (21.7 \pm 0.4) \times 10^{-3}$ μm²/s$^{\alpha}$ for polar clusters, $\alpha = 0.69 \pm 0.02$ and $D_{PL} = (42.3 \pm 0.7) \times 10^{-3}$ um²/s$^{\alpha}$ for lateral clusters. Polar clusters were defined as those spending 80% or more of their time in regions within 15% of the cell length from the cell pole. Lateral clusters were defined as those spending 80% or more of their time beyond 15% of the cell length from the cell pole. (**c**) Relationship between mobility and length of tracks. The negative correlation is consistent with the expectation that, on average, tracks for larger clusters are longer (because they will have more photoactivated fluorophores), and larger clusters diffuse less rapidly. The number of tracks was ~ 5000, collected from ~1100 cells in nine FOVs. Strain used: TSS1020, except for panel (**a**) inset, which used strain TSS1893. *See* Table 1 for strain information, and Table 3 for imaging conditions

Table 3
Experimental parameters for single-particle tracking

	Excitation power, mW	Excitation duration, ms	Frame duration	Activation pulse, ms	Activation power, mW	Activation frequency	Number of frames
LPA-SPT	60	30	65 ms (15 fps)	1	100	1/250 frames	10^3
PALM-SPT	100	5	65 ms (15 fps)	N.A.	0.01	Continuous	10^4

also find a strong difference between mobility of polar and lateral Tar-mEos2 clusters (Fig. 11b), but with the signs reversed (i.e., polar clusters move more slowly than lateral ones). The reason for this apparent discrepancy merits further study, but it likely reflects the depth of sampling. The diffraction-limited imaging employed

in [19] resolves only the largest clusters in the cell, whereas LPA-SPT enables tracking across the full range of cluster sizes, from single receptor dimers to the largest clusters in the cell.

LPA-SPT can photoactivate multiple fluorophore labels per tracked cluster, and the expected number of activated labels increases with cluster size. Combined with the expectation that larger clusters will tend to move slower (because of increased viscous drag), we expect a negative correlation between mobility and track length. Such a trend is indeed observed in our SPT data (Fig. 11c). Thus, the length distribution of tracks from LPA-SPT carries information about the size of clusters.

4 Notes

1. Care should be taken when pH-ing the MeAsp solution as the pH curve of MeAsp is extremely steep around pH 7. If pH 7 is exceeded and HCl has to be added to lower the pH, salts will form and this should be avoided. Use very small NaOH volume increments or increase the temperature to ~80 °C to facilitate dissolution.
2. The use of an AOTF in the excitation path is optional in both PALM and LPA-SPT—it is possible to localize single or clustered emitters also with continuous illumination. Use of the AOTF provides more flexibility in the design of the single-particle tracking protocol in LPA-SPT experiments, by enabling stroboscopic illumination (i.e., excitation times shorter than the camera exposure).
3. In preparing PALM coverslips, care should be taken in obtaining a round droplet on the coverslip. The poly-L-lysine tends to slip away from very clean glass, so a perfectly flat surface is recommended.
4. An experimental variable that strongly affects the frequency of false-positive detections is growth medium. We successfully perform PALM imaging of cells grown in a well-defined medium (H1 for our experiments). However, our attempts to image cells grown in less controlled culture media failed. Indeed control cells expressing no fluorescent protein exhibited a large number of false-positive detections when cells are grown in TB. By contrast, the false-positive rate was negligible when the same cells are grown in H1 minimal medium. Extensive washing with buffer of cells prior to imaging does not eradicate such false positives. Growth on minimal salts medium is thus recommended for PALM imaging.
5. For PALM imaging, optimal values for fixation time and temperature may vary considerably between different organisms/strains/growth conditions. We find that room temperature

and fixation for 10 min in 4% PFA is a suitable protocol for chemoreceptor imaging. Temperature does not affect the efficiency of fixation while longer fixation time gives rise to increased false-positive localizations in our hands.

6. In constructing the PALM imaging chamber, the sealing step requires some practice. In particular, care should be taken to avoid wetting the top surface of the rubber spacer, as this can impair the integrity of the seal between the spacer and treated coverslip. Poor sealing in turn leads to increased sample drift and, in extreme cases, to leakage. To minimize wetting of the spacer, sealing should be executed with care and as rapidly as possible. In the event of accidental wetting, the seal may yet be rescued if the amount of liquid wetting the surface is small, by carefully drying it from the sides of the chamber with absorbent paper.
7. False-positive PALM localizations can result from many variables that are not under control of the experimenter, e.g., impurities in the sample, autofluorescence of cellular components, products of fixation. Our experience is that cleaning every component (including the rubber spacer and the glass slides) of the PALM chamber with H_2O_2 at ~100 °C helps reduce the number of false positives. We performed tests in cells that do not express labeled proteins and we nevertheless find false positives even under the most careful cleaning conditions. In Fig. 12, we present cumulative distribution functions of the number of localizations per cell for two experiments, one in which the number of false positives is much smaller than the labeled proteins (leading to saturation of the cumulative distribution curve), and another in which a high incidence of false positives leads to continued increase of the cumulative emitter count over ~10^5 frames (and severely corrupts data to preclude reliable analyses, e.g., cluster size estimation).
8. The specifications for the LPA-SPT micro-lens array (focal length at 405 nm $F \approx 25$ mm, pitch = 1500 μm, array of $6 \times 6 = 36$ microlenses) must be chosen to match those for the objective lens and other components of the imaging system. In our setup, the tube lens in the excitation/photoactivation path has a focal length of 300 mm ("Tube Lens 1" in Figs. 3 and 9). To fill the back aperture of the 100X NA1.49 objective (diameter ≈ 17 mm), we had to expand about 12× each 1500-μm beamlet from the micro-lens array, leading to the requirement $F \approx 300/12 = 25$ mm. The pitch was chosen such that the distance between activation spots at the sample plane was about 10 μm. Using 150X magnification for imaging, this pitch gives $5 \times 5 = 25$ photoactivation spots within the FOV of our EMCCD camera (chip size = 8192×8192 μm^2).

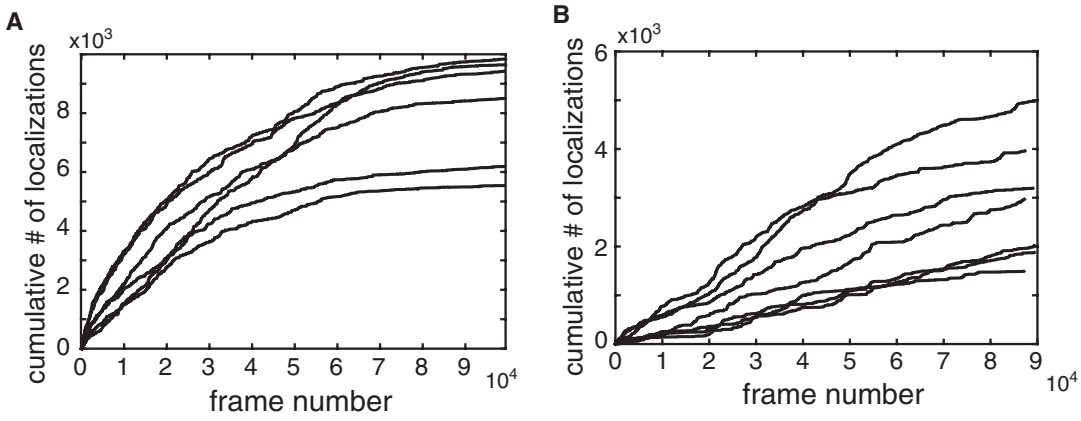

Fig. 12 Cumulative counts of PALM localizations over the course of an experiment. (**a**) An example of an experiment with a low incidence of false-positive localization, in which saturation is clearly visible in the cumulative localization count for each cell. Strain used: TSS1836 (*see* Table 1). Data from TSS1836, *see* Table 1 for imaging conditions. (**b**) An example of an experiment with a high incidence of false-positive localizations, which prevents the cumulative localization count in each cell from reaching saturation. Such high false-positive rates are highly problematic for cluster size estimation

9. Removing air bubbles is particularly important, as they can drastically perturb cell attachment, flow profile, the imaging quality and integrity of the vacuum-grease seal; an air bubble reaching the imaging chamber often forces one to terminate the experiment prematurely.
10. For reliable tracking in LPA-SPT, it is essential to limit the photoactivation pulse energy so as to avoid excessive emitter crowding, which can cause problematic collisions and near encounters between tracked objects. Conversely, insufficient photoactivation energy leads to a lower throughput and shorter track lengths. The optimal imaging parameters thus depend not only on the properties of the fluorophore labels and mobility of tracked particles, but also on the density of the tracked particles/clusters and the number of fluorophore labels per particle/cluster. For optimizing imaging conditions, it is thus advisable to test a number of acquisition parameter sets, not only for each strain/labeled-protein combination, but also whenever expression levels or protein labeling is modified significantly.

Acknowledgments

We thank J.S. Parkinson and G. Pinas for strains, plasmids, and helpful discussions; A.S.N. Seshasayee for strain HS1; and H.C. Berg and K.A. Fahrner for the gift of anti-FliC antibody. This work was supported by NWO/FOM and the Paul G. Allen Family Foundation.

References

1. Betzig E et al (2006) Imaging intracellular fluorescent proteins at nanometer resolution. Science 313:1642–1645
2. Thompson RE, Larson DR, Webb WW (2002) Precise nanometer localization analysis for individual fluorescent probes. Biophys J 82: 2775–2783
3. Betzig E (2015) Single molecules, cells, and super-resolution optics (nobel lecture). Angew Chem Int Ed Engl 54:8034–8053
4. Hell SW (2007) Far-field optical nanoscopy. Science 316:246–249
5. Huang B, Bates M, Zhuang X (2009) Super-resolution fluorescence microscopy. Annu Rev Biochem 78:993–1016
6. Betzig E (1995) Proposed method for molecular optical imaging. Opt Lett 20:237–239
7. Greenfield D et al (2009) Self-organization of the Escherichia coli chemotaxis network imaged with super-resolution light microscopy. PLoS Biol 7:1–12
8. Manley S et al (2008) High-density mapping of single-molecule trajectories with photoactivated localization microscopy. Nat Methods 5:155–157
9. English BP, English BP, Hauryliuk V, Sanamrad A, Tankov S et al (2011) Single-molecule investigations of the stringent response machinery in living bacterial cells. Proc Natl Acad Sci U S A 108:E365–E373
10. Niu L, Yu J (2008) Investigating intracellular dynamics of FtsZ cytoskeleton with photoactivation single-molecule tracking. Biophys J 95: 2009–2016
11. Stracy M, Lesterlin C, Garza de Leon F, Uphoff S, Zawadzki P et al (2015) Live-cell superresolution microscopy reveals the organization of RNA polymerase in the bacterial nucleoid. Proc Natl Acad Sci U S A 112:E4390–E4399
12. Adler J (1966) Chemotaxis in bacteria. Science 153:708–716
13. Sourjik V, Vaknin A, Shimizu TS, Berg HC (2007) In vivo measurement by FRET of pathway activity in bacterial chemotaxis. Methods Enzymol 423:365–391
14. Berg HC, Block SM (1984) A miniature flow cell designed for rapid exchange of media under high-power microscope objectives. J Gen Microbiol 130:2915–2920
15. Ovesny M, Krizek P, Borkovec J, Svindrych Z, Hagen GM (2014) ThunderSTORM: a comprehensive ImageJ plug-in for PALM and STORM data analysis and super-resolution imaging. Bioinformatics 30:2389–2390
16. Daszykowski M, Walczak B (2009) Density-based clustering methods. In: Reedijk J (ed) Reference module in chemistry, molecular sciences and chemical engineering, vol 2.29. Elsevier, Waltham, MA, pp 635–654
17. Colville K, Tompkins N, Rutenberg AD, Jericho MH (2010) Effects of poly(L-lysine) substrates on attached *Escherichia coli* bacteria. Langmuir 26:2639–2644
18. Jaqaman K, Loerke D, Mettlen M, Kuwata H, Grinstein S (2008) l Robust single-particle tracking in live-cell time-lapse sequences. Nat Methods 5:695–702
19. Thiem S, Kentner D, Sourjik V (2007) Positioning of chemosensory clusters in *E. coli* and its relation to cell division. EMBO J 26: 1615–1623
20. Amann E, Ochs B, Abel KJ (1988) Tightly regulated tac promoter vectors useful for the expression of unfused and fused proteins in *Escherichia coli*. Gene 69:301–315
21. Guzman LM, Belin D, Carson MJ, Beckwith JJ (1995) Tight regulation, modulation, and high-level expression by vectors containing the arabinose PBAD promoter. J Bacteriol 177: 4121–4130
22. Guarente L (1983) Yeast promoters and *lacZ* fusions designed to study expression of cloned genes in yeast. Methods Enzymol 101: 181–191
23. Ames P, Studdert CA, Reiser RH, Parkinson JS (2002) Collaborative signaling by mixed chemoreceptor teams in *Escherichia coli*. Proc Natl Acad Sci U S A 99:7060–7065
24. Endres RG, Oleksiuk O, Hansen CH, Meir Y, Sourjik V et al (2008) Variable sizes of *Escherichia coli* chemoreceptor signaling teams. Mol Syst Biol 4:211
25. Frank V, Piñas GE, Cohen H, Parkinson JS, Vaknin A (2016) Networked chemoreceptors benefit bacterial chemotaxis performance. MBio 7:1–9
26. Srinivasan R, Scolari VF, Lagomarsino MC, Seshasayee AS (2015) The genome-scale interplay amongst xenogene silencing, stress response and chromosome architecture in *Escherichia coli*. Nucleic Acids Res 43: 295–308

Chapter 19

Imaging of Single Dye-Labeled Chemotaxis Proteins in Live Bacteria Using Electroporation

Diana Di Paolo and Richard M. Berry

Abstract

For the last 2 decades, the use of genetically fused fluorescent proteins (FPs) has greatly contributed to the study of chemotactic signaling in *E. coli*, including the activation of the response regulator protein CheY and its interaction with the flagellar motor. However, this approach suffers from a number of limitations, both biological and biophysical. For example, not all fusions are fully functional when fused to a bulky FP, which can have a similar molecular weight to its fused counterpart. FPs may interfere with the native interactions of the protein, and their chromophores have low brightness and photostability, and fast photobleaching rates. Electroporation allows for internalization of purified CheY proteins labeled with organic dyes into *E. coli* cells in controllable concentrations. Using fluorescence video microscopy, it is possible to observe single CheY molecules diffusing within cells and interacting with the sensory clusters and the flagellar motors in real time.

Key words Electroporation, Single-molecule fluorescence microscopy, Chemotaxis, Bacterial motility

1 Introduction

Chemotaxis is the biasing of movement toward regions that contain higher concentrations of beneficial, or lower concentrations of toxic, chemicals. It is one of the best understood bacterial sensory pathways. In *E. coli*, chemotactic signaling is mediated by the phosphorylation of the response regulator protein CheY. CheY~P transduces changes of environmental chemical gradients, detected by specific transmembrane chemoreceptors, to the flagellar motors by binding to the C-ring of the motor and inducing a cascade of conformational changes that modulate the direction of rotation.

To perform an accurate study of the interactions between chemotaxis proteins and the bacterial flagellar motor, is essential to investigate their behavior in vivo. Most current research relies on the use of fluorescent proteins (FPs) [1, 2]. The fluorescent protein technique avoids the problem of purifying, labeling and introducing

Michael D. Manson (ed.), *Bacterial Chemosensing: Methods and Protocols*, Methods in Molecular Biology, vol. 1729, https://doi.org/10.1007/978-1-4939-7577-8_19,

proteins into cells, and the task of producing specific antibodies to surface or internal antigens. These fluorescent fusions have allowed studies of the copy number, diffusion patterns and intracellular localization of proteins involved in processes such as gene expression or membrane transport [3, 4]. However, this method has limitations. (1) Being genetically encoded, all target proteins are labeled, which can be an advantage for some applications, such as estimation of cytoplasmic concentrations, but is less good for tracking single molecules. (2) FPs are much less bright (sixfold for GFP) [5, 6] and photo-stable (100-fold for GFP) [7] than commercially available small organic dyes and are, therefore, far from ideal for single-molecule tracking purposes. (3) Because the FPs are relatively large, not all fusions are fully functional, limiting the interpretation of the data and the proteins available for study.

Organic dyes remain the prime choice for in vitro experiments due to their greater photostability, small size (up to 100-fold smaller than FPs) and ease of intramolecular labeling (mainly through the use of cysteine residues). All these factors are particularly important for single-molecule fluorescence imaging and tracking. However, as these are not compatible with genetic fusion, a means for reintroducing externally dye-labeled proteins into cells is required for in vivo studies. Electroporation exploits the phenomenon that application of an external electrical field to a low ionic strength cell suspension creates transient pores in the membrane, allowing the uptake of DNA or other macromolecules. Combined with cysteine-maleimide dye labeling and single-molecule fluorescence microscopy, this is an extremely powerful tool to investigate protein intracellular behavior and interactions for a wide variety of moieties in an even wider range of bacterial species [7]. In this chapter, we showcase the applicability of this technique to the chemotaxis signaling pathway by imaging and tracking in real time single CheY molecules that travel between the chemoreceptor clusters and the flagellar motors.

2 Materials

2.1 Cell Growth

1. Lysogeny Broth (LB): Yeast extract 5 g, Tryptone 10 g, NaCl 5 g—Make up to 1 L with Milli-Q H_2O. Adjust to pH 7.0 and autoclave.
2. 2× TY: Yeast extract 10 g, Bacto Tryptone 16 g, NaCl 5 g. Make up to 1 L with Milli-Q. Adjust to pH 7.0 and autoclave.
3. LB-Agar: Agar 16 g, Yeast extract 5 g, Bacto Tryptone 10 g, NaCl 5 g. Make up to 1 L with Milli-Q. Adjust to pH 7.0 and autoclave.

4. Tryptone Broth (TB): Bacto Tryptone 10 g, NaCl 10 g. Make up to 1 L with Milli-Q. Adjust to pH 7.0 and autoclave.

2.2 Protein Purification and Labeling

Filter through a 0.22 μm pore filter and degas.

1. Lysis buffer: 10% glycerol, 50 mM Tris–HCl, 150 mM NaCl, 25 mM imidazole, pH 8.
2. Elution Buffer: 10% glycerol, 50 mM Tris–HCl, 150 mM NaCl, 500 mM imidazole, pH 8.
3. Labeling Buffer: 50 mM Tris–HCl, 150 mM NaCl, 0.1 mM TCEP, pH = 6.8 (*see* **Note 1**).

2.3 Electro-competent Cells

Prepare all media below and place on ice until used.

1. 500 mL sterile Milli-Q H_2O.
2. 300 mL of 10% glycerol solution.
3. GYT medium (10 mL) [8]: 10% (v/v) glycerol, 0.125% (w/v) yeast extract, 0.25% (w/v) tryptone. Filter-sterilize through a prerinsed 0.22 μm pore filter. Store in 1 mL aliquots at 4 °C.

2.4 Electroporation, Recovery and Visualization

Filter through a 0.22 μm pore filter and degas.

1. Electroporation Buffer (EP buffer): Tris–HCl 50 mM, NaCl 25 mM, TCEP 0.1 mM, pH = 7.5.
2. Super Optimal Broth with Catabolite Repression (SOC).
3. Motility Buffer (MB): 6.2 mM K_2HPO_4, 3.8 mM KH_2PO_4, 50 μM EDTA, pH = 7.0.
4. 0.1 cm electroporation cuvettes.
5. Thin gel-loading tip.
6. Burnt coverslips: 25 × 60 mm No. 1.5 (0.16–0.19 mm thick) Thermo Scientific (*see* **Note 2**).
7. Double-sided tape (3 M).
8. Microscope slides 75 × 25 mm.
9. Coverslips 22 × 22 mm, No. 1.5.

2.5 Strains Used for Imaging

The JPA802 *E. coli* strain, shown in Fig. 3, is a derivative of RP437 with a sticky filament phenotype [9] (various regions in the *fliC* gene were truncated so that the hydrophobic regions of the flagellin protein are exposed; the resulting protein is known as $FliC^{st}$.) This strain is wild type for motility and chemotaxis. The JPA1814 *E. coli* strain shown in Figs. 4 and 5 was a derivative of JPA802 containing a FliM-YPet fusion constructed as described in [10].

3 Methods

We report below expression and purification methods for *E. coli* CheY, but readers should apply procedures suitable to their own proteins of interest. Considerations about the concentration of protein to be labeled and the buffer to use apply generally.

3.1 Cloning of the cheY Gene

A *cheY* gene containing a 5′ insertion of a Cys residue before the wild-type sequence, *(cys)cheY*, was cloned using Gibson Assembly into the enterobacterial expression vector pFloat [11, 12], which is derived from pET30a (Novagen) and engineered to include in frame of its 5′ region a 6×His (His6) sequence, a small ubiquitin-like modifier (SUMO) solubility tag, and a human rhinovirus 3C protease cleavage sequence (LEVLFQ/GP). Formation of the correct construct was confirmed by DNA by sequencing. Both the His6- and SUMO tags were removed after protein purification using PreScission Protease, a genetically engineered fusion protein consisting of human rhinovirus 3C protease and GST (glutathione S-transferase), which specifically cleaves between the Gln and Gly residues of the recognition sequence LeuGluValLeuPheGln/GlyPro. The plasmid encoding *(cys)cheY* was transformed into the *E. coli* strain BL21(DE3) (Novagen), and cells were grown in LB medium supplemented with kanamycin to OD_{600nm} = 0.6 with shaking at 225 rpm at 37 °C.

3.2 CheY Expression and Purification

1. Induce (Cys)CheY expression at OD_{600nm} = 0.6 by adding isopropyl-β-D-1-thiogalactopyranoside (IPTG) to a final concentration of 0.5 mM at 18 °C overnight with shaking at 225 rpm.
2. Harvest cells at 7000 × *g* for 20 min at 4 °C.
3. Resuspend pellet in Lysis Buffer (*see* Subheading 2) in the presence of 1 mM dithiothreitol (DTT, disulfide bond reducing agent), one tablet of SIGMAFAST™ Protease Inhibitor Cocktail (EDTA-Free), and 1 μL of Benzonase nuclease (Sigma-Aldrich).
4. Lyse cells by sonication while chilled on ice.
5. Clear the resulting cell lysate by centrifugation at 35,000 × *g* for 45 min at 4 °C and then by filtration through a 0.45 μM pore filter.
6. Set up a nickel affinity chromatography column by pouring 1.5 mL Ni-NTA Agarose slurry (Bio-Rad) into a chromatography drip column, allowing to settle for 10 min and then equilibrating with 30 mL of Lysis Buffer.
7. Apply the filtered lysate to the column and allow protein to bind.
8. Wash the column with at least 50 mL of Lysis Buffer.

9. Elute with 10 mL of Elution Buffer in the presence of 1 mM tris(2-carboxyethyl)phosphine (TCEP, s disulfide bond-reducing agent stronger than DTT).
10. Store fractions at 4 °C.
11. Assess protein purity via SDS-PAGE.
12. If necessary, perform further purification by size exclusion chromatography, equilibrating the column with Labeling Buffer.
13. Following protein purification, assess its purity again by SDS-PAGE and concentrate relevant fractions down to a final concentration of 100–200 μM.
14. Divide into 100 μL aliquots, flash-freeze, and store at −80 °C.

3.3 CheY Labeling

1. Taking advantage of the Cys residue, label the purified protein with a maleimide modification of a suitable organic dye (Atto647 was used in this case; *see* **Note 3**).
2. Add a 2–10× molar excess of dye to the purified protein in a reaction volume of 100–300 μL (*see* **Note 4**)
3. Allow the labeling reaction to proceed in the dark overnight at 4 °C (*see* **Note 5**).
4. Remove the residual unreacted dye by size-exclusion chromatography using EP buffer or a similar low-salinity buffer. If possible, monitor both protein absorption at 280 nm and dye absorption at the right wavelength (647 nm in this case; *see* **Note 6**).
5. Assess peak fractions on a SDS-PAGE gel using a transparent loading dye (*see* Subheading 2) and scan *first* for fluorescence using a UV-Vis device and *then* for protein presence with Coomassie staining.
6. Combine all relevant fractions that show both fluorescence and protein stain and concentrate to 10–40 μM (*see* **Note 7**).
7. Add 50% glycerol to the solution and store at −20 °C wrapped in foil. Alternatively, aliquot the protein in small volumes (2–5 μL), and flash-freeze in liquid nitrogen. Store at −80 °C in the dark.

3.4 Protein Internalization

Electrocompetent cells are made using a modified version of the protocol reported in [13] with the intention of preserving cell motility. Cell motility before and after the washing steps is checked by microscopic examination.

1. Grow an overnight culture for the strain of interest by inoculating 5 mL of TB at 30 °C (*see* **Note 8**). Add antibiotic as needed.
2. Inoculate 500 mL of TB medium in a 2 L flask with ~4 mL of the bacterial culture. Culture at 30 °C with shaking at 225 rpm. Monitor the OD_{600nm} (*see* **Note 9**).

3. When OD_{600nm} reaches 0.4, cool the flask down on ice for 15–30 min. Swirl the culture occasionally to make sure the cooling occurs evenly. Place centrifuge bottles on ice for the next steps. Cool down the rotor and centrifuge (*see* **Note 10**).
4. Transfer the culture to ice-cold centrifuge bottles. Harvest the cells by centrifugation at 1000 × *g* for 15 min at 4 °C. Discard the supernatant and resuspend the cell pellet in 500 mL of ice-cold sterile Milli-Q H_2O (*see* **Note 11**).
5. Harvest the cells by centrifugation at 1000 × *g* for 20 min at 4 °C. Discard the supernatant and resuspend the cell pellet in 250 mL of ice-cold 10% glycerol.
6. Harvest the cells by centrifugation at 1000 × *g* for 20 min at 4 °C. Discard the supernatant and resuspend the cell pellet in 10 mL of ice-cold 10% glycerol (*see* **Note 12**).
7. Harvest the cells by centrifugation at 1000 × *g* for 20 min at 4 °C. Discard the supernatant and resuspend the cell pellet in 1 mL of ice-cold GYT medium (*see* **Note 13**).
8. Divide into 40 μL aliquots, flash-freeze in liquid nitrogen, and store at −80 °C.

3.5 Electroporation

A MicroPulserTM Electroporator (Bio-Rad) or other similar device is used to apply an electric field of chosen intensity to allow for internalization of the dye-labeled proteins of interest. Minimizing any damage to cells is key. Figure 1 shows a visual summary of a typical experiment.

1. Thaw on ice one 40 μL aliquot of electrocompetent cells for 10–20 min.
2. Also put on ice one 0.1 cm electroporation cuvette and one 1.7 mL sterile tube labeled NEP (Nonelectroporated Positive Control).

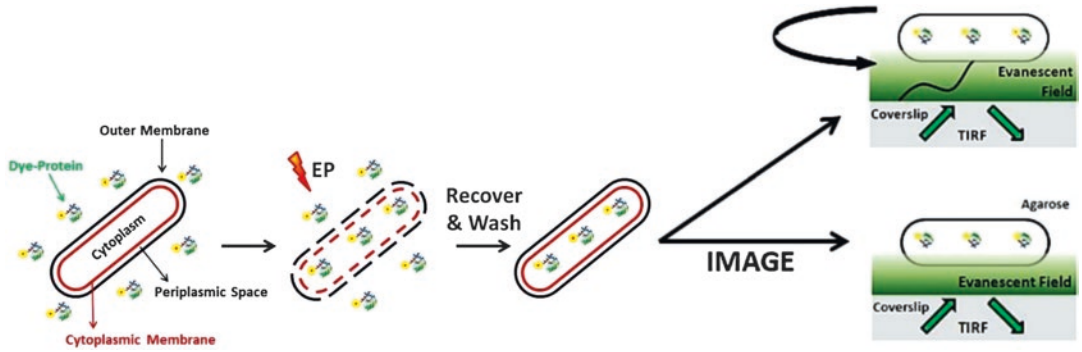

Fig. 1 Steps of a typical electroporation experiment. Electrocompetent cells are incubated with the fluorescent molecules of interest prior to electroporation. After internalization, they are recovered in rich medium, extensively washed and imaged

3. Line up in a rack at room temperature two more sterile tubes labeled Negative Control and EP (Electroporated) samples.
4. Prepare the Negative Control sample by adding 1 μL of cells from the aliquot to 9 μL of MB.
5. Transfer half volume of the starting aliquot of cells (i.e., 20 μL) into the chilled NEP tube.
6. Add the chosen quantity of fluorescently labeled protein to both EP and NEP samples and incubate on ice for 5–10 min.
7. Using a thin gel-loading tip, transfer the EP sample into the chilled electroporation cuvette and incubate on ice for 1–2 min (*see* **Note 14**).
8. Wipe off the cuvette electrodes thoroughly to remove as much water as possible.
9. Apply an electric field of the chosen strength to the cell suspension (*see* **Note 15**).
10. Immediately add 500 μL of SOC medium to both the EP and NEP samples.
11. Transfer the EP cells to the clean tube previously prepared at room temperature.
12. Agitate both the EP and NEP samples at 30 °C, 450 rpm in a Thermomixer (Eppendorf) for a suitable amount of time (*see* **Note 16**).
13. Pellet both the EP and NEP samples for 1 min at 4700 × *g* in a bench-top centrifuge.
14. Remove noninternalized proteins by resuspending EP and NEP cells in 500 μL of MB, then centrifuging again for 1 min at 4700 × *g*; repeat this step at least four times.
15. After the last wash, resuspend the cell pellets in 90–150 μL of MB and prepare for imaging.

3.6 Cell Sample Preparation

Depending on the experiment, samples for imaging can be prepared in two ways: using agarose pads (if the aim is to perform single molecule imaging and tracking) or tunnel slides (if the aim is to monitor cell motility as well as fluorescence behavior). Other visualization methods can be used where deemed suitable.

1. For 1% agarose pads, resuspend 0.1 g of agarose (BD/DIFCO) in 10 mL of MB.
2. Microwave until completely melted.
3. Create pads by pipetting a droplet (~300 μL) of 1% agarose on the center of a burnt coverslip and leave it to spread until naturally set. The pad should be raised about 0.5–1 mm from the glass.
4. Leave the pad to dry for 10–15 min.

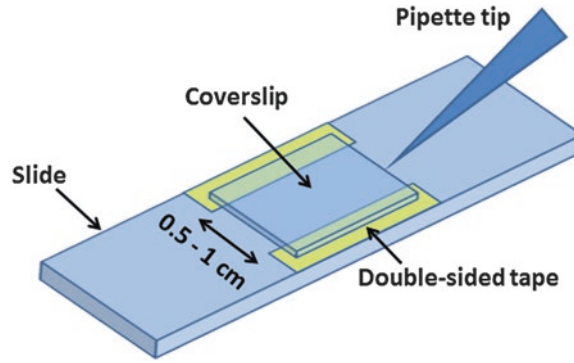

Fig. 2 Schematic of a tunnel slide. The central chamber has a volume of 25–50 μL

5. Pipette 5 μL of cells onto it in little droplets and add a burnt coverslip on top.
6. If using an inverted microscope objective, flip the sample before imaging.
7. For tunnel slides (*see* **Note 17**), attach two strips of double-sided tape (3 M) to the longer sides of a rectangular microscopy slide and place a glass coverslip on top (Fig. 2).
8. Flush 30 μL of cells in the tunnel through the small air space between the slide and the coverslip.
9. Incubate in a dark humidity chamber (containing a piece of wet tissue paper) upside down for 10 min.
10. Remove nonstuck cells by washing the slide with 100 μL of MB three times, adsorbing liquid from the opposite side with a piece of tissue paper.
11. Seal the open ends of the tunnel with transparent nail varnish to prevent evaporation.

3.7 Cell Imaging Results

Imaging is ideally performed both in bright-field and with fluorescence alternatively, using dye-matching laser lines. In our experiments, cells were visualized on a customized inverted Olympus IX-71 microscope equipped with a 637 nm "red" diode laser (Vortran Stradus; Vortran Laser Technology, Sacramento, CA, USA) and a 532 nm "green" Nd:YAG laserDPSS laser (Samba; Cobolt AB, Solna, SwedenMGL-III-532 nm-100 mW, CNI). Near-TIRF (nTIRF) and TIRF (Total Internal Reflection Fluorescence) techniques were used. Movies and images were recorded using an EMCCD camera (iXon+, BI-887, Andor, Belfast, UK) and manufacturer's software (Andor). All measurements were carried out in continuous wave (CW) mode for both green and red lasers. Illumination intensities used ranged between 400 nW/μm^2 for the green laser and 0.1–1 μW/μm^2 for the red laser.

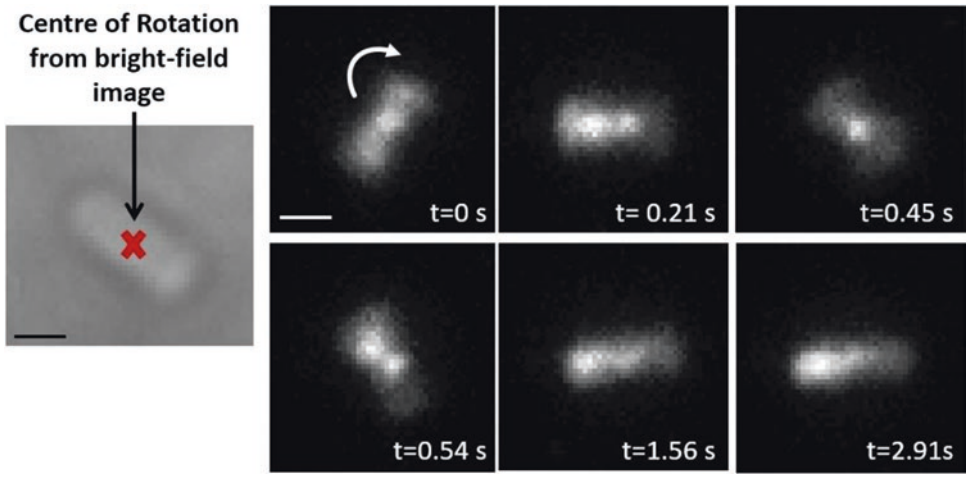

Fig. 3 Frames from video fluorescence microscopy performed over 3 s showing single molecules diffusing/binding inside a tethered, rotating, electrocompetent *E. coli* JPA802 cell electroporated with 1.25 μM (25 pmol) of CheY(Cys)-Cy3B. At times during the movie (for example at $t = 0$ s, $t = 0.21$ s and $t = 0.45$ s), it is possible to see a bright spot on top of the center of rotation, indicating a possible interaction of CheY with the motor. At other times (for example at $t = 1.56$ s and $t = 2.91$ s), the bright spot localizes at one pole of the cell, perhaps associated with a chemoreceptor array. Finally, in some frames (for example at $t = 0.21$ s and $t = 0.54$ s), it is possible to observe two bright spots in the cell, one of which is always at the center of rotation and the other of which seems to be located at, or travelling to, the cell pole. Thus, it appears that at least two labeled CheY molecules are present in this cell. Exposure time was 30 ms. The intensity used for Cy3B was 400 nW/μm^2. The intensity used for Atto647 was 0.86 μW/μm^2. Scale bar = 1 μm (*Image reproduced with permission from* [15])

Figures 3, 4, and 5, taken from [14], show examples of video microscopy images obtained with the described technique. Movies are also available to download as Electronic Supporting Material of reference [14].

Figure 3 shows TIRF images of a tethered electrocompetent *E. coli* cell electroporated with 1.25 μM (25 pmol) of CheY labeled at the C-terminus with the organic dye Cy3B. This cell, imaged in a tunnel slide, is rotating clockwise at 4 Hz, a speed comparable with the typical speed of tethered wild-type cells (3–10 Hz), proving that motility recovery after heavy protein loading during electroporation is possible.

Having established that uptake of fluorescent molecules does not affect the electroporated cells more than the application of the electric pulse alone, the interaction of single labeled CheY molecules with motors (and with other possible loci) in real time in a rotating tethered cell was investigated. To carry out single-molecule experiments without the loss of resolution caused by overlapping spots, the cellular uptake of labeled proteins upon electroporation was first characterized and calibrated to yield internalization of very few molecules per cell (ideally less than five). The final labeled protein concentration of 20 nM for the electroporation was found to suit this criterion in most experiments.

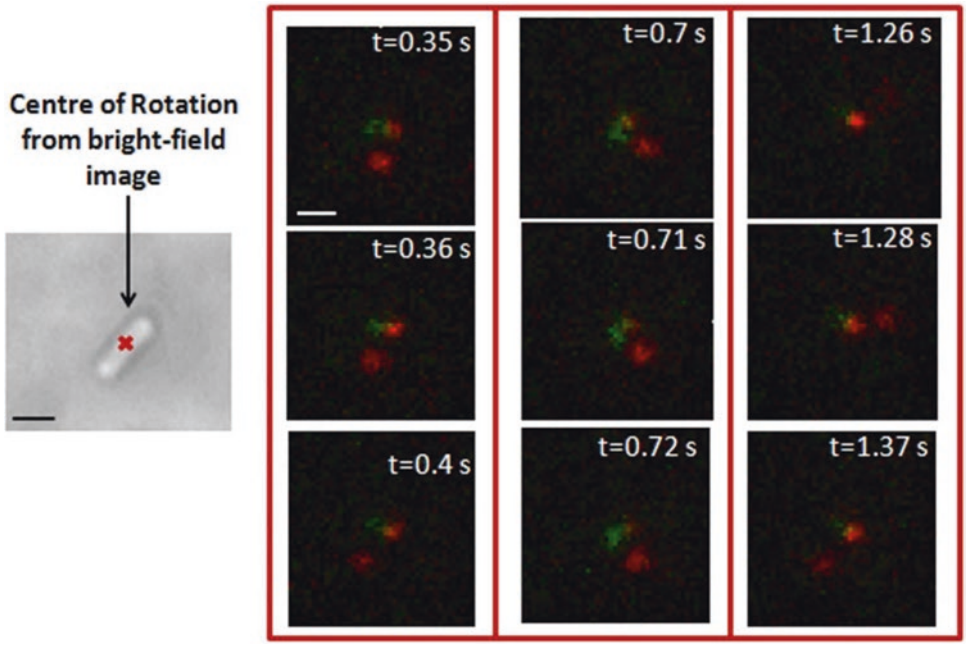

Fig. 4 Frames from two-color fluorescence video microscopy performed over 3 s (substack) showing single molecules diffusing/binding inside a tethered, rotating *E. coli* JPA1814 electrocompetent cell electroporated with 20 nM (0.4 pmol) Atto647-(Cys)CheY. For most of the movie, it is possible to see a bright red spot on top of the center of rotation (green), suggesting a possible interaction of CheY with the motor. At other times (for example at $t = 0.35$ s and $t = 0.71$ s), it is possible to see a second bright spot that localizes at one pole of the cell. As in Fig. 3, it appears that at least two labeled CheY molecules are present in this cell. Exposure time 10 ms. Intensity used for YPet: 400 nW/μm^2. Intensity used for Atto647: 1 μW/μm^2. Scale bar in the brightfield image (in black) = 1 μm. The scale bar in the fluorescence image (in white) = 500 nm (*Image reproduced with permission from* [15])

Figure 4 shows a tethered cell electroporated with Atto647-(Cys)CheY imaged both in brightfield (left) and in fluorescence (TIRF, right): the convention is red for internalized proteins and green for motor spots, labeled through FliM-YPet. Throughout the movie, from which the frames in Fig. 5 are extracted, a persistent red spot can be seen overlapping the green one at the center of rotation, and another, dimmer red spot appears at one cell pole.

In Fig. 5, frames from two-color video microscopy show single molecules of Atto647-(Cys)CheY diffusing/binding inside *E. coli* JPA1814 electrocompetent cells deposited on a 1% agarose pad. As in Fig. 4, motor fluorescence is shown in green and CheY in red.

3.8 Conclusion

The electroporation approach described in this chapter offers the exciting possibility of a new generation of single-molecule in vivo fluorescence experiments in live bacteria. We have demonstrated its potential in the chemotaxis field in *E. coli* and in *Rhodobacter sphaeroides* (data not shown), but this very powerful technique, combined with cysteine-maleimide dye labeling and single-

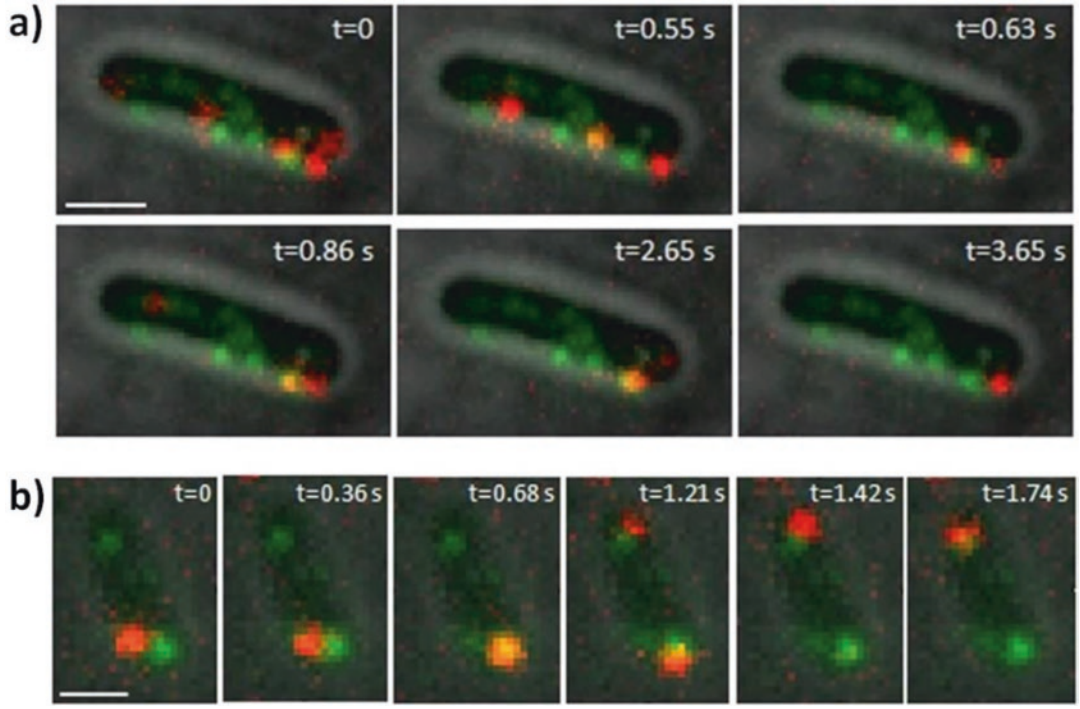

Fig. 5 Frames from two-color video microscopy showing single molecules diffusing/binding inside *E. coli* RP437 JPA1814 electrocompetent cells electroporated with 20 nM Atto647-(Cys)CheY. (**a**) In this acquisition, performed over 20 s, CheY mostly localizes with the green motor spots in the cell; it also dwells at some other unlabeled loci, which could well correspond to polar or lateral chemoreceptor clusters, especially visible in the last frame shown ($t = 3.65$ s). Scale bar = 1 μm. (**b**) In this acquisition, performed over 40 sec, at $t = 0$ CheY is located next to a motor at the bottom of the cell, it travels to the motor after ~550 ms and dwells there for ~220 ms. At $t = 1$ s, another CheY molecule co-localizes with the same motor, dwelling there for 230 ms. At $t = 0.9$ s, yet another CheY molecule localizes with the top cell pole, for ~800 ms. Finally, a fourth CheY molecule appears at the top motor at $t = 1.74$ s, but it disappears after only 20 ms. Scale bar = 500 nm. For both acquisitions, the exposure time was 10 ms. The intensity used for YPet was 400 nW/μm^2. The intensity used for Atto647 was 1 μW/μm^2 (*Image reproduced with permission from* [15])

molecule fluorescence microscopy, could be easily applied to a wide range of targets in an even wider range of bacterial species.

4 Notes

1. The optimal pH for cysteine-maleimide reactions is 7.4. As the labeling reaction was carried out overnight at 4 °C, and because the pH of Tris buffer is temperature dependent, the labeling buffer was prepared at pH 6.8 at room temperature, which corresponds to pH 7.4 at 4 °C.
2. The procedure for burning coverslips is as follows. Ramp up the heat in a furnace at 90 °C/h until reaching 500 °C; burn at 500 °C for 1 h; cool at 150 °C/h until room temperature is reached.

3. The dye was resuspended in dimethyl sulfoxide (DMSO). For compounds with low aqueous solubility, like most fluorescent maleimide dyes, use of an organic cosolvent, such as DMSO, is essential. DMSO in the labeling reaction needs to be kept <3% vol/vol. The dye should be selected according to the laser wavelengths available on the imaging set-up.
4. Try to keep the protein concentration during the labeling reaction between 50 and 100 μM.
5. Most conventional choices for the duration and temperature of the labeling reaction are: at room temperature for 1 h or overnight at 4 °C. The authors found that the second procedure yielded a better labeling efficiency. However, readers are encouraged to try both conditions and to optimize this part of the protocol for their protein of interest. Whichever condition is chosen, it is essential to carry out the labeling reaction in the dark to avoid bleaching.
6. Unlabeled and labeled proteins may elute at the same time from the size exclusion column, as 1 kDa molecular weight difference due to the presence of the dye may not be enough to separate the two. This does not constitute an issue, as the unlabeled protein will not be visible when imaging. Moreover, for single-molecule imaging purposes, unless a mutant lacking the protein of interest is used for electroporation, there will always be a much more numerous background of endogenous wild-type proteins in the electroporated cells.
7. If such a concentration is not achieved, do not add any glycerol and proceed in one of the following two ways. (a) Aliquot by small volumes (i.e., 2–5 μL) and flash-freeze in liquid nitrogen. The protein can then be stored at −80 °C for up to 2 years. (b) Store the labeled protein at 4 °C wrapped in foil. In the latter case, use within a month if the protein is stable at such temperature, or sooner if it is not.
8. TB was chosen as the conventional growth medium to enhance *E. coli* motility. Other growth media can be used for other bacterial species.
9. Optimum results (>10^9 transformants/μg) are obtained with standard strains of *E. coli* when the OD_{600nm} of the culture is 0.35–0.4. For efficient transformation, it is essential that the number of viable cells does not exceed 10^8 cells/mL, i.e., OD~0.4.
10. For maximum efficiency of transformation, it is crucial that the temperature does not rise above 4 °C at any stage.
11. When resuspending cells, first add 1 mL of ice-cold sterile Milli-Q H_2O, pipette up and down, and then add the rest.

12. Take care when decanting the supernatant because the bacterial pellets loosen in 10% glycerol.
13. Best done by gentle swirling rather than pipetting or vortexing. Electrocompetence can be tested by incubating cells with 1 μL of a plasmid carrying an antibiotic resistance gene, performing electroporation, then plating cells on LB-Agar + antibiotic and incubating overnight at 37 °C. Appearance of numerous colonies will indicate that the cells were electrocompetent.
14. Take the next steps as quickly as possible to avoid the temperature rising above 4 °C.
15. The recommended voltage for efficient DNA delivery inside *E. coli*, which yields 10^9–10^{10} transformants/μg of DNA, is reported in the literature to be 1.80 kV for 0.1 cm cuvettes, corresponding to a field strength of 18 kV/cm [13]. In order to return electroporated cells to a motile state as soon as possible after application of the electric pulse, we lowered the voltage in our experiments to limit cell/motor damage and increase the cell survival rate and chance of recovering motility. A voltage of 1.2 kV, corresponding to a field strength of 12 kV/cm for 0.1 cm cuvettes, was found to be a good tradeoff between internalization efficiency and optimal transformation conditions for *E. coli*.
16. Cells can be recovered for a varying amount of time according to the aim of the experiment being carried out (from minutes to hours). If, for instance, one is only interested in characterizing the amount of fluorescent molecules internalized subsequently a defined electroporation protocol (assuming the voltage or the amount of labeled protein to incubate the cells with needs optimization), a recovery of 5 min will be enough. If, instead, one is interested in studying dynamics of the internalized protein in viable cells, or some other property that requires cells to have recovered a fully healthy phenotype (like motility, as shown in Figs. 3 and 4), longer recovery protocols at suitable temperatures, growth media and volumes of the latter, are possible following electroporation. Recovery time in this case can range from several minutes to hours, the final bottleneck being that those among the original electroporated cells which survive electroporation and start dividing again will progressively dilute the amount of initially internalized labeled proteins to their daughter cells, and therefore a tradeoff between recovery and fluorescence conservation is needed.
17. Deposition in tunnel slides is ideal to monitor bacterial motility and internalized fluorescence at the same time.

Acknowledgments

We thank Prof. Achillefs N. Kapanidis for use of the Total Internal Reflection Fluorescence microscope. D.D.P. was supported by a UK EPSRC DTC studentship. BBSRC is thanked for continuous funding of the work in the Berry laboratory.

References

1. Prasher DC, Eckenrode VK, Ward WW, Prendergast FG, Cormier MJ (1992) Primary structure of the *Aequorea victoria* green-fluorescent protein. Gene 111:229–233
2. Day RN, Davidson MW (2009) The fluorescent protein palette: tools for cellular imaging. Chem Soc Rev 38:2887–2921
3. Leake MC, Chandler JH, Wadhams GH, Bai F, Berry RM et al (2006) Stoichiometry and turnover in single, functioning membrane protein complexes. Nature 443:355–358
4. Miesenbock G, De Angelis DA, Rothman JE (1998) Visualizing secretion and synaptic transmission with pH-sensitive green fluorescent proteins. Nature 394:192–195
5. Dempsey GT, Vaughan JC, Chen KH, Bates M, Zhuang X (2011) Evaluation of fluorophores for optimal performance in localization-based super-resolution imaging. Nat Methods 8:1027–1036
6. Shaner NC, Steinbach PA, Tsien RY (2005) A guide to choosing fluorescent proteins. Nat Methods 2:905–909
7. Crawford R, Torella JP, Aigrain L, Plochowietz A, Gryte K et al (2013) Long-lived intracellular single-molecule fluorescence using electroporated molecules. Biophys J 105:2439–2450
8. Tung WL, Chow KC (1995) A modified medium for efficient electrotransformation of *E. coli*. Trends Genet 11:128–129
9. Kuwajima G (1988) Construction of a minimum-size functional flagellin of *Escherichia coli*. J Bacteriol 170:3305–3309
10. Delalez NJ, Wadhams GH, Rosser G, Xue Q, Brown MT et al (2010) Signal-dependent turnover of the bacterial flagellar switch protein FliM. Proc Natl Acad Sci U S A 107: 11347–11351
11. Gibson DG, Young L, Chuang RY, Venter JC, Hutchison CA III et al (2009) Enzymatic assembly of DNA molecules up to several hundred kilobases. Nat Methods 6:343–345
12. Rogala KB, Dynes NJ, Hatzopoulos GN, Yan J, Pong Sheng K et al (2015) The *Caenorhabditis elegans* protein SAS-5 forms large oligomeric assemblies critical for centriole formation. Elife 4:e07410
13. Sambrook J, Russell DW (2001) Molecular cloning: a laboratory manual, 3rd edn. Cold Spring Harbor Laboratory Press, Cold Spring Harbor, NY
14. Dower WJ, Miller JF, Ragsdale CW (1988) High efficiency transformation of *E. coli* by high voltage electroporation. Nucleic Acids Res 16:6127–6145
15. Di Paolo D, Afanzar O, Armitage JP, Berry RM (2016) Single-molecule imaging of electroporated dye-labelled CheY in live *Escherichia coli*. Philos Trans R Soc Lond B Biol Sci 371:(1707) pii:0150492

Chapter 20

Fluorescence Anisotropy to Detect In Vivo Stimulus-Induced Changes in Chemoreceptor Packing

Vered Frank and Ady Vaknin

Abstract

The anisotropy of the fluorescence emitted from fluorescent proteins, such as yellow fluorescent protein (YFP), is sensitive to Homo-FRET between the proteins. This effect can be used to detect in vivo ligand-induced changes in packing or conformation of tagged chemoreceptors. Such measurements of clustered or dispersed core-signaling units revealed quantitative dose-dependent responses of these sensors.

Key words Fluorescence anisotropy, Homo-FRET, Chemoreceptors

1 Introduction

When randomly oriented fluorophores are continuously excited with polarized light, the steady-state anisotropy of the emitted light is generally affected by two principal processes: the rate of rotational diffusion and the efficiency of energy transfer between fluorophores (Homo-FRET) [1]. Rotation diffusion is the dominant mechanism for depolarization in case of small fluorophores, such as fluorescein [2]. However, the rotational diffusion is much slower in the case of large proteins. In particular, in fluorescent proteins, such as yellow fluorescent protein (YFP), the internal fluorophore domain is rigidly anchored to the outer beta-barrel structure, thus leading to relatively high fluorescence anisotropy, even when these proteins are freely diffusing in solution [3]. Therefore, since the effect of rotational diffusion is generally small, the fluorescence anisotropy of these proteins is sensitive to depolarization by Homo-FRET. This property of fluorescent proteins can be used to monitor in vivo and in real time changes in the packing of tagged proteins [4] (*see* **Note 1**).

We have used fluorescence anisotropy to detect the direct response of chemoreceptors to external stimuli [5–7]. To monitor fluorescence anisotropy from live bacterial cells expressing

Michael D. Manson (ed.), *Bacterial Chemosensing: Methods and Protocols*, Methods in Molecular Biology, vol. 1729, https://doi.org/10.1007/978-1-4939-7577-8_20,

tagged chemoreceptors, we implemented the basic anisotropy-measurement scheme into a microscope system, monitoring monolayers of bacterial cultures immobilized on a cover glass and located in a flow chamber, which allows the application and removal of stimuli (*see* **Note 2**).

2 Materials

2.1 Buffers and Media

1. Tryptone broth (TB): dissolve 10 g of Bacto Tryptone and 5 g of NaCl in 1 L of double-distilled water (DDW). Autoclave.
2. Potassium phosphate buffer (Kpi; 1 M): mix 26.2 g of H_2KO_4P in 0.5 L of DDW. Add HK_2O_4P until the pH is 7 (around 57.5 g of HK_2O_4P). Run through a 0.45 μm pore size filter.
3. Motility buffer: 10 mM Kpi, 0.1 mM EDTA, 1 μM methionine and 10 mM DL-lactate, pH 7. Run through a 0.45 μm pore size filter.

2.2 Flow Chamber

1. Gold-plated flow chamber built as described by Berg and Block [8].
2. Bacterial cells are attached by poly-L-lysine (0.1%, Sigma) to a round 12 mm diameter and 0.17 mm thick round cover glass (Glaswarenfabrik Karl Hecht).
3. Apiezon M grease, for measurements below 30 °C, or Apiezon H grease, for measurements above 30 °C.

3 Methods

3.1 Optical System Setup

We used an upright fixed-stage Nikon FN1 microscope equipped with a 40× Plan-Fluor objective, NA 0.75 (Fig. 1). Fluorescence excitation was done using a 150 W xenon lamp (Hamamatsu, Bridgewater NJ) coupled to the microscope via fiber optics and UV filter. Figure 1a shows the optical system setup. The excitation beam passed through linear glass polarizer (Edmund Optics, Barrington NJ), an ET508/6× excitation filter (Chroma Technology, Brattleboro VT), and was reflected by an FF520Di01 dichroic mirror (Semrock, Rochester NY). The fluorescence emitted from the YFP fluorophores was collected using an FF01-542/27 emission filter (Semrock) and split into its parallel (I_{par}) and perpendicular (I_{per}) polarizations using a polarizing beam-splitter cube (Newport, Irvine CA). The two polarizations were monitored using photon counters (H7422P; Hamamatsu). The photon counters were connected to a PCI NI 6602 data-acquisition card controlled by LABVIEW (National Instruments). The steady-state anisotropy of the emitted fluorescence (r) is defined as

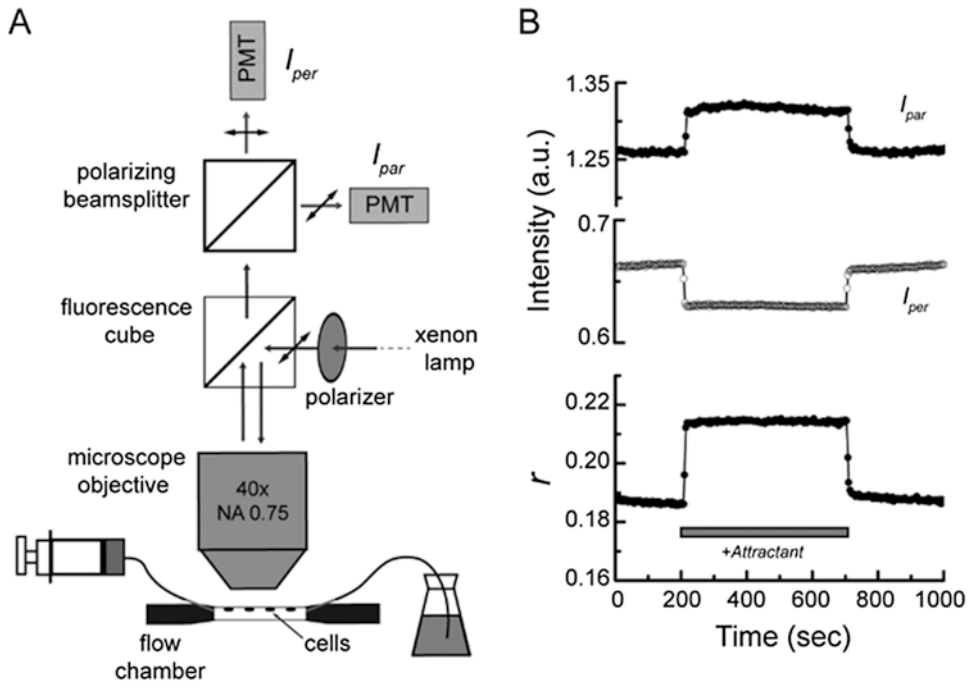

Fig. 1 Anisotropy measurement of population of cells attached to a cover glass and placed in a flow chamber. (**A**) The light path in the optical system. (**B**) Upper panel – fluorescence intensity in the parallel (filled circles) or perpendicular (open circles) channel measured from *E. coli* cells deleted for the chemoreceptors and *che* genes and expressing Tar-mYFP. Lower panel – The corresponding anisotropy. Attractant (α-methyl-aspartate, 1 mM) was added to the flow at the time indicated by the bar

$$r = \frac{I_{\text{par}} - g \cdot I_{\text{per}}}{I_{\text{par}} + 2g \cdot I_{\text{per}}}$$

where the g factor g is used to correct I_{per} for imperfections in the optical system. This factor was determined by adjusting the anisotropy recorded from freely diffusing fluorescein in solution to zero. This calibration yielded anisotropy of 0.32 for purified YFP, which is close to the value found previously in studies using spectrofluorometers [3].

The cells were immobilized on a cover glass and placed in the flow chamber. To flow medium through the chamber, we used a syringe pump (Harvard Apparatus) at flow rates between 600 and 2000 μL/min (*see* **Note 3**). To control the temperature of the cells, we used an in-house system made from an aluminum stage-fitting platform, a temperature controller, two Peltier elements, and a water-cooled copper block. To adjust the temperature of the inflow to the temperature of the chamber, the inlet pipe was threaded through a second copper-block heat exchanger connected to the stage. We used a T-type thermocouple to measure the temperature in the flow chamber.

3.2 Bacterial Growth

1. Grow cells overnight at 30 °C in 1 mL of TB with appropriate antibiotics.
2. Dilute the cells 100 fold in 10 mL of TB supplemented with the appropriate antibiotics and inducers, and grow at 33.5 °C with agitation of 285 RPM to an OD_{600nm} of approximately 0.45.
3. Wash the cells by centrifuging for 10 min at 1000 × *g* and resuspend in an equal volume of motility buffer. Repeat this step twice. The cells at this stage can be kept at 4–8 °C before applying them to the cover glass.

3.3 Sample Preparation

1. Clean the cover glasses with ethanol, apply approximately 50 μL of poly-L-lysine to each cover glass, and allow adhering (without drying) between 15 and 45 min for flagellated or non-flagellated cells respectively.
2. Wash the excess poly-L-lysine several times with water and finally with motility buffer. Finally, remove the excess buffer by absorption with a Kim wipe.
3. Concentrate the cells fivefold by centrifugation for 5 min at 1000 × *g* and resuspension in 2 mL motility buffer.
4. Apply approximately 0.1 mL of cells suspension to the cover glass and let it adhere to the glass at room temperature for 15–30 min. Make sure that the suspension is not drying out.

3.4 Flow-Chamber Preparation

1. Clean the flow chamber gently with heptane. Let it dry.
2. Apply a thin layer of grease to the surface of the flow chamber rim and attach new cover glass. (*See* Chapter 18 for a detailed description.)
3. Flow ethanol through the tubing and chamber.
4. Remove bubbles from the flow chamber and from the tubes by pressing gently the syringe.
5. While pressing the syringe, move the tube to flask with DDW and let DDW flow through for a few minutes.
6. Let motility buffer flow through for a few minutes.

3.5 Fluorescence Measurement

1. Place the cell holding cover glass in the flow chamber. Apply gentle suction using the pump at low flow rates (200–300 μL/min) until the cover-glass is in place and the flow chamber is sealed.
2. Set the flow to the rate needed for the experiment and flow through motility buffer for a few minutes to wash away the unattached cells.
3. Search for a field with well-packed monolayer of cells (*see* **Note 4**).

4. Record anisotropy baseline for a few minutes (*see* **Note 5**).
5. Attractants or repellents dissolved in motility buffer can then applied to the cells with continuous flow while continuously monitoring the resulting changes in anisotropy (*see* **Note 6**).

4 Notes

1. When attaching the mYFP tag to the protein, one should be aware that, although rotational diffusion of the tag is not an efficient mechanism of depolarization, it can make some contribution. The anisotropy value of mYFP in dilute solutions is approximately 0.32 and not 0.4, which would be expected for a fixed and randomly oriented fluorophores. In the case of the chemoreceptors, to allow mYFP nearly free rotational diffusion independent of that of the receptor, we linked the mYFP tag to the native C-terminal flexible domain of the receptor via additional glycine-based flexible linker. Similar results were obtained with or without the C-terminal flexible linker.
2. To avoid protein self-associations derived by the fluorescence tag, we selected mYFP as the tag of choice (EYFP with A206K mutation) [9]. This protein is known to remain monomeric, with no measurable self-aggregation.
3. The mixing time in the flow chamber can be estimated by using a flow of sodium-fluorescein. We usually use flow rate of 600–800 μL/min. At this flow rate, the mixing time of the flow chamber is 20–30 s [7].
4. Measuring a monolayer of immobilized cells helps to reduce scattering.
5. In contrast to spectral-shift FRET, a single type of fluorophore is used in anisotropy measurements, making the baseline anisotropy level informative and less sensitive to variations in expression levels or other variations in fluorescence intensity.
6. To avoid seeing a response of the chemoreceptors to changes in osmolality [5], we generally keep the attractant concentration lower than 10 mM.

Acknowledgment

The use of fluorescence anisotropy for detecting chemoreceptor responses was pioneered in the lab of Howard C. Berg [5]. This work was funded by Israel Science Foundation.

References

1. Lakowicz JR (2006) Principles of fluorescence spectroscopy, 3rd edn. Springer, New York
2. Clayton AH, Hanley QS, Arndt-Jovin DJ, Subramaniam V, Jovin TM (2002) Dynamic fluorescence anisotropy imaging microscopy in the frequency domain (rFLIM). Biophys J 83: 1631–1649
3. Lidke DS, Nagy P, Barisas BG, Heintzmann R, Post JN et al (2003) Imaging molecular interactions in cells by dynamic and static fluorescence anisotropy (rFLIM and emFRET). Biochem Soc Trans 31(Pt 5): 1020–1027
4. Sharma P, Heo Y, Jang BK, Liu YY, Li JY et al (2004) Nanoscale organization of multiple GPI-anchored proteins in living cell membranes. Cell 116:577–589
5. Vaknin A, Berg HC (2006) Osmotic stress mechanically perturbs chemoreceptors in *Escherichia coli*. Proc Natl Acad Sci U S A 103:592–596
6. Vaknin A, Berg HC (2007) Physical responses of bacterial chemoreceptors. J Mol Biol 366: 1416–1423
7. Frank V, Vaknin A (2013) Prolonged stimuli alter the bacterial chemosensory clusters. Mol Microbiol 88:634–644
8. Berg HC, Block SM (1984) A miniature flow cell designed for rapid exchange of media under high-power microscope objectives. J Gen Microbiol 130:2915–2920
9. Zacharias DA, Violin JD, Newton AC, Tsien RY et al (2002) Partitioning of lipid-modified monomeric GFPs into membrane microdomains of live cells. Science 296:913–916

Part VI

High-Throughput Methods for Screening Novel Chemoeffectors

Chapter 21

Chemotaxis to Atypical Chemoattractants by Soil Bacteria

Rebecca E. Parales and Jayna L. Ditty

Abstract

Although the mechanism of bacterial chemotaxis has been extensively studied in enteric bacteria, the hunt for novel and atypical chemoeffectors (in enterics and distantly-related species alike) has necessitated the modification of classic chemotaxis assays to deal with recalcitrant and potentially toxic chemicals. Here, we describe detailed protocols for the quantitative and qualitative assessment of chemotaxis responses that are categorized into short-term direct population response assays and long-term metabolism-based assays that can be used to identify novel chemoeffector molecules and the specific chemoreceptors involved. We emphasize the importance of behavior-based assays to verify the biochemical and physiological relevance of newly identified chemoeffector-receptor pairs.

Key words Chemotaxis, Energy taxis, Signal transduction, Chemoreceptor, Attractant, Chemoeffector, Methyl-accepting chemotaxis protein

1 Introduction

Over the past 60 years, chemotaxis has been studied primarily in the enteric *Escherichia coli* and *Salmonella* model systems. Investigations of microbial chemotaxis systems outside the *E. coli* and *Salmonella* paradigm have revealed that, although the general two-component signal transduction mechanism is conserved, the types and numbers of chemoeffectors detected by different bacteria vary widely [1–3]. For example, in addition to the MCP-like energy taxis receptor (Aer), the four known *E. coli* methyl-accepting chemotaxis proteins (MCPs) Tsr, Tar, Trg, and Tap primarily detect sugars and amino acids. Soil bacteria, which are known for their broad catabolic abilities, tend to have significantly more chemoreceptors encoded in their genomes; for example, *P. putida* F1 (a model strain for bioremediation [4]) encodes 27 MCP-like proteins [5], and numerous studies have shown that *P. putida* F1 and other soil bacteria respond to a wide variety of attractants, including aromatic acids, hydrocarbons, and pollutants [6–12]. As such, there is significant interest in identifying novel chemoreceptors for

Michael D. Manson (ed.), *Bacterial Chemosensing: Methods and Protocols*, Methods in Molecular Biology, vol. 1729, https://doi.org/10.1007/978-1-4939-7577-8_21,

assessing the bacterial chemotaxis responses to these atypical, often toxic, and sometimes volatile, chemoattractants.

The other chapters in this section describe current and effective methods for the identification of novel chemoreceptor-ligand pairs. Although these in vitro biochemical methods are extremely helpful in identifying chemoeffector-receptor interactions, it remains imperative to verify that these in vitro interactions have in vivo physiological relevance, especially since not all chemicals that bind to specific chemoreceptors necessarily function as attractants in vivo [13, 14]. Therefore, classic chemotaxis assays that have been appropriately modified to deal with recalcitrant and toxic chemoeffectors should be used to assess the responses of chemoreceptor mutants and their complemented variants. Such in vivo evaluations are essential to demonstrate the physiological and genetic links between specific chemoreceptors and their cognate ligands.

The type of assay used to properly assess any chemotactic response depends on different key variables known to affect swimming behavior. Some observed chemotaxis responses might be metabolism-dependent, which can occur when the cell detects an intermediate in the degradation of the test chemical [15]. When metabolism of a potential chemoeffector is involved, assays should be conducted with appropriate metabolic mutants to identify the actual chemoeffector. In addition, it is becoming increasingly clear that many chemotactic responses to nontraditional chemoeffectors are inducible [9, 10, 16–20]. Therefore, assays of cells that are grown under various metabolic conditions may be required. For example, the use of wild-type cells that have been induced for the ability to degrade a particular chemical vs. uninduced cells should be compared. In addition, the analysis of regulatory mutants that are defective in expressing genes encoding the catabolism of a particular attractant may be informative. Some chemotactic signal transduction pathways may not directly detect a chemoeffector molecule but may instead alter behavior via various modes of energy taxis [21], requiring the use of energy taxis (e.g., *aer*) mutant strains [8, 22].

The chemotaxis protocols described in this chapter focus on classic chemotaxis assays that are relatively simple, do not require expensive or complex equipment, and are modified to take into account the properties of non-traditional and potentially toxic chemical attractants. The protocols are organized into short-term, direct population (Subheading 3.1), and long-term growth requiring (Subheading 3.2) assays that are also loosely grouped based on the amount of time required (minutes to hours, respectively) to characterize the chemotaxis response. We describe the fundamental theory behind each type of assay, the advantages and limitations of each, and highlight representative results and appropriate controls for these assays in the corresponding figures.

2 Materials

2.1 Materials Used in All the Various Chemotaxis Assays

1. Bacterial culture grown to either mid-exponential growth phase for short-term assays (*see* **Note 1**) or overnight cultures for long-term assays (*see* **Note 2**).
2. Stock attractant chemical(s); sterile (*see* **Note 3**).
3. Chemotaxis buffer: (CB; 50 mM potassium phosphate buffer [pH 7.0], 0.05% glycerol, 10 μM EDTA) aerated; sterile (*see* **Note 4**).
4. Glass culture tubes (150 × 16 mm); sterile.
5. Glass screw capped test tubes (16 × 100 mm); sterile.
6. Side-arm flasks (125 mL); sterile.
7. Petri dishes (90 × 15 mm or 33 × 10 mm depending on assay); sterile.
8. Microfuge tubes (1.5 mL); sterile.
9. P1000, P200, and/or P20 micropipettes and tips; sterile.
10. Razor blades and ruler (mm scale).
11. Forceps, glass rods, and scissor; sterile.
12. Table-top centrifuge.
13. Spectrophotometer.
14. Incubator.
15. Water bath.
16. Block heater.
17. Autoclave.
18. Phase-contrast microscope (40× objective, 10× ocular objective).
19. Bucket-of-light (*see* **Note 5**) for assays described in Subheadings 3.1, 3.2, 3.6, and 3.7.
20. Digital camera (*see* **Note 6**) for assays described in Subheadings 3.1–3.3, 3.6, and 3.7.

2.2 Materials Specific to Short-Term Population Assays

1. 2% low-melting temperature agarose (NuSieve GTG Agarose, *see* **Note 7**) suspended in CB (1.0 mL aliquots).
2. Stock of 100 mM glycerol; sterile.
3. Coomassie blue (a few crystals).
4. Plastic cover slips (24× 24 mm) cut into four equal strips.
5. Glass microscope slides (25 × 75 mm).
6. Glass coverslips (24 × 24 mm).
7. Concentrated (2×) chemotaxis buffer (CB; 50 mM potassium phosphate buffer [pH 7.0], 0.05% glycerol, 10 μM EDTA) in 16 × 150 mm glass test tubes (10 mL aliquots), sterile (*see* **Note 4**).

8. 4.0% Noble agar in 16 × 150 mm glass test tubes (10 mL aliquots), sterile (*see* **Note 8**).
9. 0.5% Noble agar in CB (2.5 mL aliquots); sterile.

2.3 Materials Specific to the Qualitative Capillary Assay

1. 2% agarose in CB (5.0 mL); sterile.
2. Drummond Microcaps® 1-μL microcapillary tubes.
3. Glass scintillation vials; sterile.
4. Chemotaxis chambers: 25 × 75 mm glass microscope slide, a 22 × 22 mm glass cover slip, and a glass U-tube (*see* **Note 9**); sterile.
5. Phase-contrast microscope with 4× or 5× objective and capability for negative contrast pseudo dark-field or oblique dark-field settings (*see* **Note 10**) equipped for use with a digital camera.

2.4 Materials Specific to the Quantitative Capillary Assay

1. CB in an autoclavable squirt bottle; sterile.
2. Lysogeny broth (LB) agar plates [23], or other appropriate growth medium agar plates.
3. Glass test tubes (13 × 150 mm; sterile) containing 1 mL CB for a tenfold dilution series.
4. Drummond Microcaps® 1-μL microcapillary tubes and bulb dispenser.
5. Glass scintillation vials; sterile.
6. Chemotaxis chambers: 90 × 15 mm Petri dishes each containing a 25 × 75 mm glass microscope slide, a 22 × 22 mm glass cover slip, and a glass U-tube (*see* **Note 9**); sterile.

2.5 Materials Specific to the Quantitative Swim Plate Assay

1. Concentrated (2×) minimal salts broth (MSB, [24]) with 0.1% Hutner's mineral base [25] (100 mL; *see* **Note 11**).
2. MSB medium; sterile.
3. 0.5% Noble agar in distilled water; sterile (100 mL; *see* **Note 8**).

2.6 Materials Specific to the Gradient Plate Assay

1. Minimal salts broth (MSB, [24]) with 0.1% Hutner's mineral base [25] in 100 mL distilled water (*see* **Note 11**), sterile.
2. Concentrated (2×) minimal salts broth (MSB, [24]) with 0.1% Hutner's mineral base [25] in 100 mL distilled water (*see* **Note 11**), sterile.
3. 2× CB in 16 × 150 mm glass test tube (one 10 mL aliquot); sterile.
4. 0.5% Noble agar (50 mL) in distilled water; sterile (*see* **Note 8**).
5. 4.0% Noble agar in 150 × 16 mm glass test tube (one 10 mL aliquot); sterile.

3 Methods

The methods described here are grouped based on whether: (1) the response of the original population of cells is observed/quantified (short-term assays) or; (2) growth is required during the assay (long-term assays). For example, in the agarose plug and chemical-in-plug assays, the attractant diffuses from a semisolid agar plug into a relatively dense suspension of cells in buffer or semisolid agar, respectively. The cells sense and move up the gradient of attractant and accumulate at the optimal attractant concentration; the response can therefore be seen within a relatively short time and does not require either growth of the cells or metabolism of the attractant during the assay. Therefore, responses of cells in a specific physiological state, such as those that are induced for catabolism of a particular chemical, can be evaluated and compared to responses of uninduced cells. In addition, because metabolism is not required, chemicals that do not serve as growth substrates can be tested as attractants. This means that responses of catabolic mutants can be tested, which may help identify whether a particular chemical is directly sensed or if a downstream metabolite is the actual attractant. It may also help differentiate chemotaxis (direct binding of a chemical to a receptor) from energy taxis (sensing oxygen, redox, etc. [21]) responses. Similarly, in capillary-based assays, the chemical diffuses from a microcapillary, metabolism of the chemical is not required, and cells in their current physiological state respond within a short time.

In contrast, in soft agar swim plate assays, catabolism of the attractant by the bacterial cells is responsible for generating the concentration gradient to which the bacteria respond. In this assay, the attractant serves as the sole carbon and energy source and, consequently, only attractants that serve as growth substrates for the strain under study can be tested. As a result, responses of mutants with catabolic defects cannot be evaluated in soft agar swim plate assays, but comparisons of wild type and chemoreceptor mutants can easily be quantified. However, an alternative growth-based plug assay, the gradient plate assay, combines the ease and simplicity of the swim plate assay with a source of diffusing attractant. In this assay, the cells grow on an alternative carbon source and respond to an attractant diffusing from a central agar plug into the soft agar medium. Therefore, metabolism is not required to generate the gradient or for growth, so catabolic mutants and nonmetabolizable attractants can be evaluated using this assay.

3.1 Agarose Plug Assay

The agarose plug assay [26] is a quick qualitative assay that can be used to monitor both positive and negative chemotaxis. Responses can generally be seen within a few minutes. Since the assay is fast and easy, it can be used to test for responses to a variety of potential

attractant or repellent chemicals or to rapidly screen the responses of many bacterial isolates or mutant strains. This assay is particularly useful for testing responses to volatile chemicals, because the experimental chamber used limits volatilization. In this assay, a small volume of molten agarose containing the potential attractant chemical of interest is solidified between a microscope slide and a coverslip (Fig. 1a). A suspension of motile cells in buffer is pipetted into the chamber surrounding the agarose plug, and a response can be observed as a dense ring of cells accumulating around the edge of the agarose plug. The location of the ring of cells relative to the agarose plug depends on the concentration and solubility of the chemical, whether it is sensed as an attractant or repellent, and the sensitivity of the cells to that particular chemical. As both positive and negative responses can be observed with this assay, it is important to determine whether the chemical is being sensed as an attractant or repellent using an alternative assay.

Another advantage of this assay is that it can be used to examine whether a chemotactic response is inducible by pre-growing the cells in the appropriate medium and comparing the response to that of the same strain grown in uninduced conditions. In addi-

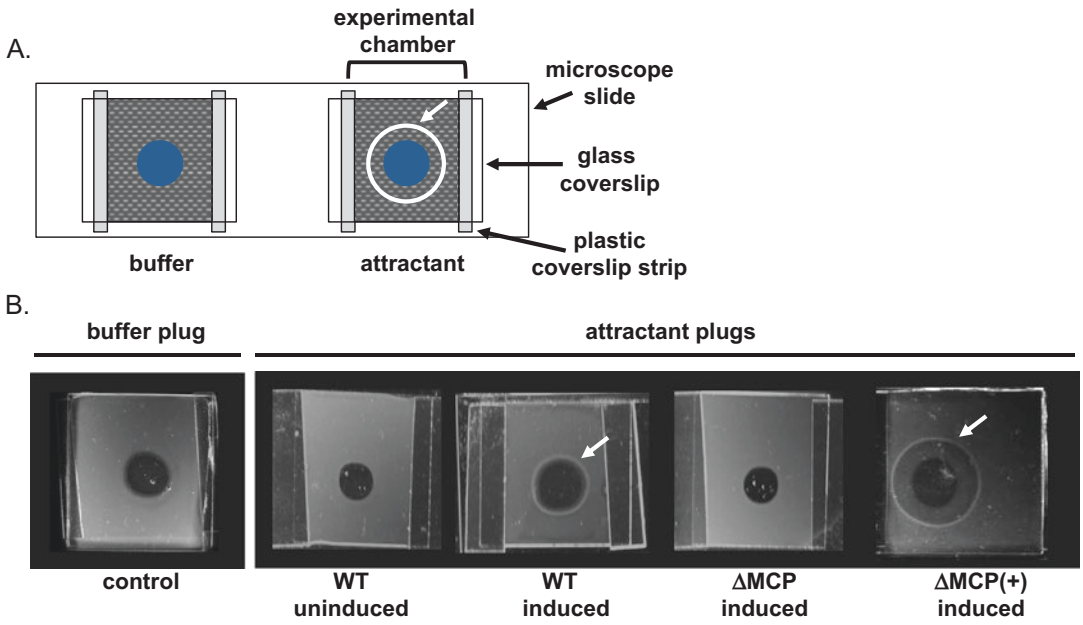

Fig. 1 Agarose plug assay. (**a**) Diagrammatic representation of an agarose plug assay. (**b**) Representative qualitative chemotactic response of wild-type cells to a buffer control (no response; left panel), wild-type cells grown in uninduced (WT uninduced) and induced (WT induced) conditions, and a chemoreceptor mutant (ΔMCP) and complemented chemoreceptor mutant (ΔMCP(+)) grown in induced conditions (right panel; *see* **Note 42**). The white arrows indicate a positive chemotaxis response, which is visualized as a white ring of cells accumulating at the optimum attractant concentration that diffused away from the center plug. Responses do not require growth of the cells and are generally seen within 1–5 min

tion, responses can be seen without magnification and easily documented using a digital camera and backlighting [42] (*see* **Note 5**). A major disadvantage is that some batches and/or brands of low-melting temperature agarose contain contaminating chemicals that may be sensed as chemoeffectors by some bacteria (*see* **Note 7**). Therefore, it is critical to carry out control assays using plugs that contain buffer only and compare the response to control plugs with responses toward plugs containing a known attractant. In addition, the best results are obtained with cultures that are highly motile. Therefore, it is essential to start with cultures that have been enriched for motile cells (*see* **Note 12**) and to handle the cultures very gently during harvesting and resuspension so that the flagella remain intact and undamaged (*see* **Note 13**). It is important to check the cultures for motility prior to and after harvesting. If the majority of the cell population is not motile, you will not get clear results from the assay.

1. Inoculate culture(s) in appropriate medium and grow for 18–24 h prior to the experiment. 3 mL cultures are generally sufficient.
2. Transfer an aliquot of the overnight culture(s) to 10 mL of an appropriate medium in side-arm flasks and grow the cells to mid-exponential growth phase (OD_{600nm} between 0.3 and 0.7) (*see* **Note 14**).
3. Prepare 10× stock solutions of control and test attractants and/or repellents (*see* **Note 15**). (These can be prepared in advance, if desired).
4. Set up the agarose plug chambers. First, score plastic cover slips into four equal sections using a razor blade and then split them. On a glass microscope slide, set two plastic strips approximately 16 mm apart. Place a glass coverslip on top of the two plastic strips for each experimental chamber. Make sure that the edges of the glass cover slip cover half of each plastic strip. Two experimental chambers can be set up on each slide such that a control plug is placed next to the test plug for easy comparison (Fig. 1a).
5. Melt 1.0 mL aliquots of 2% low-melting temperature agarose in a block heater set at 65 °C. If desired, dissolve a few crystals of Coomassie blue in the agarose to provide contrast for the plug (*see* **Note 16**). Maintain the agarose in a molten state until used in the assay.
6. When the culture reaches exponential phase, check the cells for motility using a phase-contrast microscope (*see* **Note 17**). If a large percentage of the cells are not motile, **STOP HERE** and do not proceed with the experiment.

7. Harvest cells in sterile centrifuge tubes for 3 min at 4500 rpm (*see* **Note 13**). You will need to collect enough cell material to obtain ~3.0 mL of cells with a final optical density of 0.7 (*see* **Note 18**).
8. Remove the supernatant and wash the cell pellet gently to resuspend the cells in sterile, aerated CB (*see* **Notes 4** and **13**).
9. Collect the cell pellet by spinning in a centrifuge for 3 min at 4500 rpm.
10. Gently resuspend the pellet in sterile aerated CB.
11. Transfer each resuspended culture into sterile 16 × 100 mm glass test tubes and adjust the OD_{600nm} to 0.7 with sterile aerated CB.
12. Verify that the cells are still motile by microscopy (*see* **Note 17**). If a large percentage of the cell population is not motile, **STOP HERE** and do not proceed with the experiment.
13. To prepare the chemoeffector-containing agarose plugs, transfer 18 μL of the molten 2% low-melting temperature agarose to a microfuge tube and add 2.0 μL of the 10× stock attractant or repellent solution and mix.
14. Remove the glass coverslip from a plug chamber. Quickly pipette 12 μL of the agarose plug mixture (buffer only or containing chemoeffector) onto the microscope slide between the two plastic strips. Wait ~30 s to allow the plug to cool slightly and then cover with the glass coverslip. Gently press down on the cover slip to make good contact between the agarose and the cover slip. Allow the agarose to solidify between the slide and cover slip for ~4 min before initiating the assay (*see* **Note 19**).
15. To start the assay, introduce ~230 μL of the motile cell suspension into the chamber and record the time. Make sure to fill the chamber completely (*see* **Note 20**).
16. Observe the area around the agarose plug for the presence or absence of a white ring of accumulated cells, which typically takes 2–10 min to form, and compare the response to the buffer-only plug (*see* **Note 21**).
17. Document the results of each assay using a digital camera with backlighting (*see* **Note 5**).
18. After the assays are complete, verify that the cells in the chambers are still motile using phase contrast microscopy (*see* **Note 22**).

3.2 Chemical-in-Plug Assay

Originally, the chemical-in-plug assay was designed to detect repellent responses by *E. coli* [27]; however, the assay also allows for the detection of positive chemotactic responses [8, 28]. The chemotaxis response is observed as the accumulation of a dense white ring of cells around or near the agar plug (Fig. 2). As with the agarose plug assay, a second type of assay should be carried out to

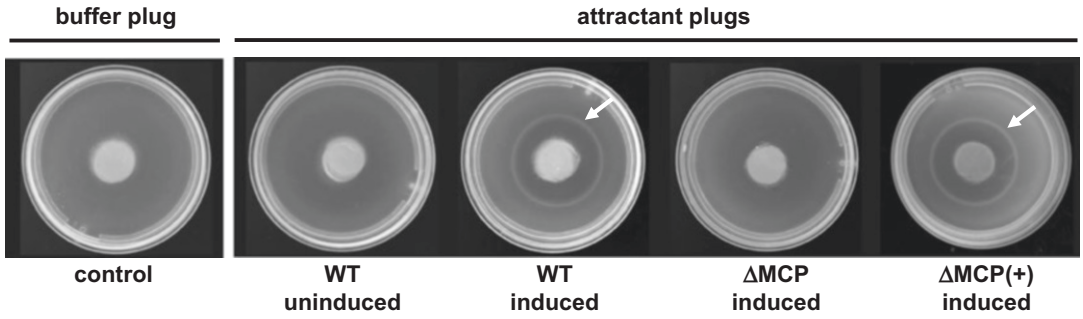

Fig. 2 Chemical-in-plug assay. Representative qualitative chemotaxis responses of wild-type cells to a buffer control (no response; left panel), wild-type cells grown in uninduced (WT uninduced) and induced (WT induced) conditions, and a chemoreceptor mutant (ΔMCP) and complemented chemoreceptor mutant (ΔMCP(+)) grown in induced conditions (right panel; *see* **Note 42**). The white arrows indicate a positive chemotactic response, which is seen as a white ring of cells that accumulate at the optimum attractant concentration that diffused away from the center plug. Responses do not require cell growth and are generally seen within 30–60 min

distinguish between positive and negative chemotaxis. Like the agarose-plug assay, the chemical-in-plug assay does not require growth of the test organism during the assay, and a response can generally be seen in less than an hour. Therefore, this assay can be used to test if a response is inducible by pre-growing cultures under different conditions. Previous studies have demonstrated that false positive responses occur using this method, so non-motile and/or non-chemotactic mutant strains should be used as negative controls [29]. We describe here a protocol to test responses to single attractants in small diameter (33 × 10 mm) Petri dishes.

1. Grow cultures as outlined in **steps 1** and **2** in Subheading 3.1.
2. Autoclave 10 mL of 4.0% Noble agar in sterile screw-capped 16 × 150 mm glass test tubes and keep the agar molten in a 55 °C water bath. You will need one tube for each attractant to be tested and one for the buffer control plugs.
3. Add 10 mL of sterile 2× CB to 10 mL of 4.0% Noble agar and mix by inverting the tube. Return tubes to the 40 °C water bath. You will need one tube for each attractant to be tested and one for the buffer control plugs.
4. Add the appropriate amount of attractant, repellent or CB to obtain the desired final concentration into a sterile 90 × 15 mm Petri dish. Pour 20 mL of the 2% Noble agar in CB solution into the Petri dish (to a depth of ~5.0 mm) and swirl the plate gently to mix the attractant with the agar (*see* **Note 23**).
5. Prepare 2.5 mL aliquots of molten 0.5% Noble agar and keep them in a 40 °C water bath. You will need one 2.5 mL aliquot for each assay.

6. Once the cultures are grown, check the cells for motility (*see* **Note 17**). If a large percentage of the cells are not motile, **STOP HERE** and do not proceed with the experiment.
7. Harvest ~2.5 mL of the culture by centrifugation at 4500 rpm for 5 min (*see* **Note 13**).
8. Remove the spent medium with a sterile pipette or by decanting, and gently resuspend the pellet in 2.5 mL of 2× sterile, aerated CB by inverting the tube (*see* **Note 13**).
9. Check the cells for motility (*see* **Note 17**). If a large percentage of the cell population is not motile, **STOP HERE** and do not proceed with the experiment.
10. Mix the cell suspension with 2.5 mL of molten 0.5% Noble agar by gently inverting the tube, and pour the suspension into a 33 × 10 mm Petri plate.
11. Cut off the tip of a sterile P1000 micropipette tip using a sterile razor blade. Using the wider, uncut sterile end, remove a plug of 2% agarose containing the attractant. Using a sterile glass rod, gently push the agar plug out of the micropipette tip and into the center of the Petri dish containing the cells in soft agar.
12. Incubate the plates at room temperature for 30–60 min (*see* **Note 24**) and then examine the area around the agarose plug for the presence or absence of a bright ring of accumulated cells.
13. Document the results of each assay using a digital camera and backlighting (*see* **Note 5**).

3.3 Qualitative Capillary Assay

In this assay, the cells are attracted to a gradient of attractant diffusing from the mouth of a microcapillary tube (Fig. 3a, b). The attractant is suspended in agarose, or it can be present in crystal or power form, so that the cells accumulate at the tip of the capillary [5, 17]. When viewed under dark field microscopy at low magnification (*see* **Note 10**), the responding cells appear as a bright white cloud that accumulates in 1–30 min (Fig. 3b). As it is relatively quick and easy, this assay is useful for screening the responses to several attractants by a single strain, or the responses of different bacterial isolates or a series of mutants. Like the agarose plug and chemical-in-plug assays described above, pre-growing cells under appropriate conditions for the qualitative capillary assay can be used to evaluate whether a chemotactic response is inducible. Responses can be documented over time by taking multiple images at various time points, or the results of this qualitative assay can be quantified by counting the number of bacterial cells accumulating near the tip of a capillary [30, 31]. The qualitative capillary assay is particularly useful for testing responses to chemicals with low solubility in water [17, 32].

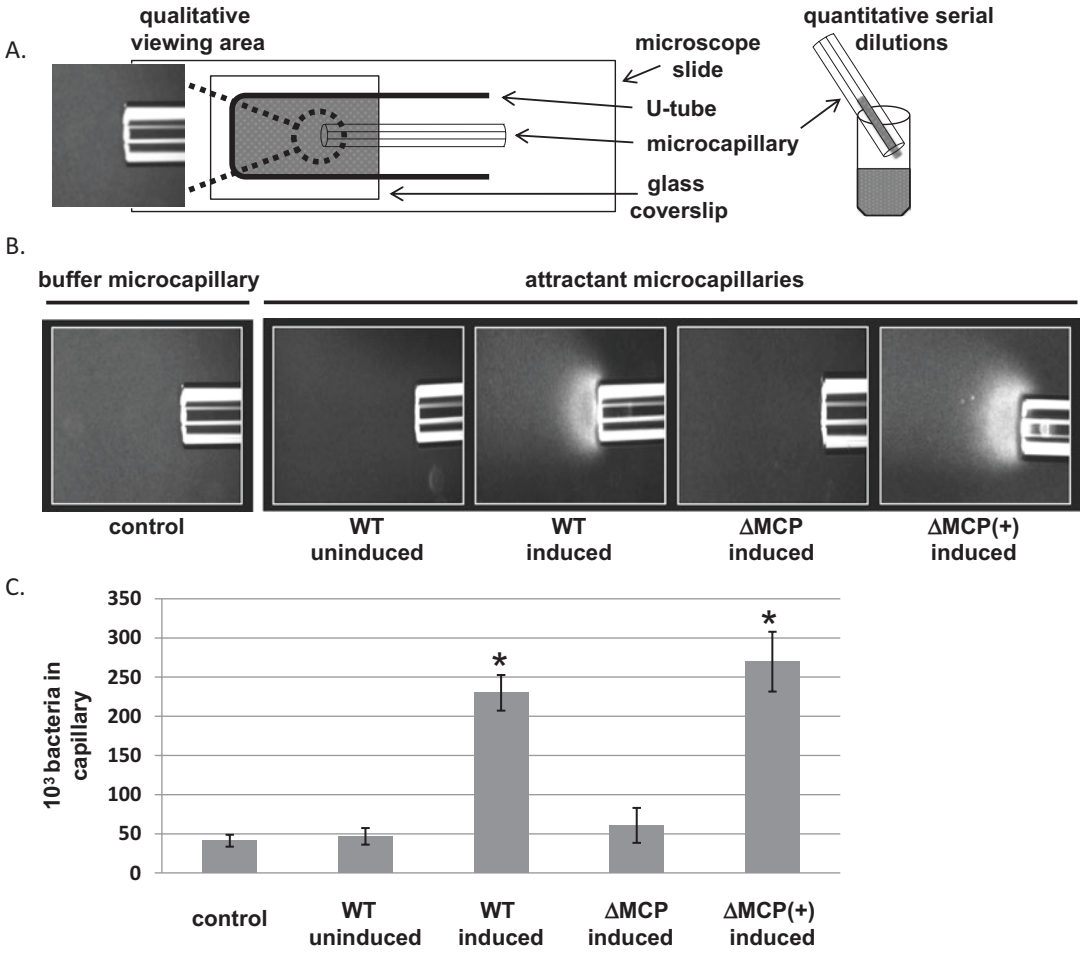

Fig. 3 Capillary-based assays. (**a**) Diagrammatic representation of qualitative and quantitative capillary assay setups. In qualitative assays (left), the microcapillary is filled with attractant in a solid form (either solid chemical powder or crystal or chemical embedded in agarose) and the accumulation of cells responding to the attractant diffusing from the capillary is visualized by dark field microscopy in the viewing area. In quantitative assays, the microcapillary is filled with an attractant dissolved in buffer, and the number of bacteria that migrate into the microcapillaries is calculated by carrying out serial dilutions of the capillary contents and plating (right). (**b**) Representative responses of cells in qualitative capillary assays under dark field microscopy to an attractant (right panel) relative to a buffer control (left panel). The accumulation of cells at the tip of the microcapillary (white cloud of cells in the viewing area) indicates a positive chemotaxis response to the attractant. Responses of wild-type cells to a buffer control (no response; left panel) and to attractant by wild-type cells grown in uninduced (WT uninduced) and induced (WT induced) conditions, and chemoreceptor mutant (ΔMCP) and complemented chemoreceptor mutant (ΔMCP(+)) strains grown under inducing conditions (right panel) are shown (*see* **Note 42**). Responses do not require growth of the cells, and in some cases can be seen within 5–10 min. However, responses may take much longer (30–60 min), depending on the solubility of the attractant and the sensitivity of the cells to the attractant. (**c**) Representative response of wild-type, mutant, and complemented cells in quantitative capillary assays. Capillary assays were performed with microcapillary tubes containing the optimum concentration of attractant or buffer control over 30 min. The quantified responses of wild-type cells to a buffer control (control), wild-type cells grown in uninduced (WT uninduced) and induced (WT induced) conditions, and chemoreceptor mutant (ΔMCP) and complemented chemoreceptor mutant (ΔMCP(+)) grown under inducing conditions (right panel) are shown (*see* **Note 42**). Asterisks indicate significant differences from the control ($p < 0.05$)

1. Grow cultures as outlined in **steps 1** and **2** in Subheading 3.1.
2. Fill 1.0 μL microcapillary tubes with attractant or buffer (*see* **Note 25**).
3. Melt 5 mL of 2% agarose in CB and place in a sterile glass scintillation vial.
4. Add the appropriate amount of sterile attractant or buffer control to the molten agarose and gently swirl to mix.
5. While the agarose is still molten, use sterile forceps to pick up a sterile 1 μL microcapillary tube and melt one end in a Bunsen burner flame to seal it.
6. Swipe the microcapillary through the flame twice to heat it, and drop its open end down into the scintillation vial containing the attractant or control compound of interest (*see* **Note 26**). Repeat until you have filled a sufficient number of capillaries for all of the planned samples and allow the agarose to solidify. Include controls plus a few extra of each.
7. Set up the needed number of chemotaxis chambers, each consisting of a glass U-tube sandwiched between a glass microscope slide and a glass coverslip (*see* **Note 27**).
8. When the cultures are ready, check motility using a phase contrast microscope (*see* **Note 17**). If a large percentage of the cells are not motile, **STOP HERE** and do not proceed with the experiment.
9. Harvest 10 mL of each bacterial culture in sterile centrifuge tubes by centrifugation at 4500 rpm for 5 min (*see* **Note 13**).
10. Remove the spent medium with a sterile pipette or by decanting and gently resuspend the pellet in 5 mL of sterile, aerated CB by inverting the tube (*see* **Note 13**).
11. Collect the cell pellet by centrifugation at 4500 rpm for 5 min and gently resuspend the cell pellet in sterile, aerated CB.
12. Transfer each culture into sterile 16 × 100 mm glass test tubes and adjust the optical density at OD_{600nm} to 0.3 with sterile, aerated CB.
13. Verify that the cells are still motile by microscopy (*see* **Note 17**). If a large percentage of the cells are not motile, **STOP HERE** and do not proceed with the experiment.
14. Fill a chemotaxis chamber with the motile cell suspension.
15. Place the microscope slide under the 4× objective of a phase-contrast microscope equipped with a digital camera (*see* **Note 28**). Focus the image on the center of the cell suspension using a dark-field setting (*see* **Note 10**).
16. Remove one capillary from the solidified attractant and insert it into the cell suspension (*see* **Note 29**). Quickly adjust the

stage so that the tip of the microcapillary is in the center of the field of view and adjust the fine focus as necessary (*see* **Note 30**).

17. To document the development of a chemotaxis response over time, obtain the first digital image as quickly as possible and record the time. Allow the cells to respond for up to 60 min, obtaining additional digital images as needed (*see* **Note 24**).
18. At the end of the assay, verify that the cells are still motile using a higher magnification (*see* **Note 22**).

3.4 Quantitative Capillary Assay

The quantitative capillary assay [33] provides a direct measure of the response of a bacterial population to a gradient of attractant. In this assay, a microcapillary tube containing attractant solution is inserted into a suspension of motile bacteria in buffer (*see* **Note 27** and Fig. 3a). Cells sense the gradient of attractant that develops as the attractant diffuses from the microcapillary and respond by swimming up the concentration gradient and entering the microcapillary tube. After an incubation period (generally 30–60 min), the microcapillary tube is removed and the chemotactic response is quantified by determining the number of cells that accumulated within each attractant-containing capillary compared to the number present in a control capillary containing buffer only. The assay can also be used to evaluate responses to repellents, although with less quantitative accuracy, in which case fewer cells accumulate relative to the buffer-only capillary.

By pre-growing cells under the appropriate conditions, this assay can be used to test whether the response to a particular attractant is inducible [34], and it can be used to determine the minimum attractant concentration detected as well as the peak concentration for the response [34]. Unfortunately, the assay is quite time consuming, and there are many steps where errors can be introduced. Therefore, several biological and technical replicates and appropriate statistical analyses must be conducted to obtain convincing results. The cells must be very motile to obtain reproducible results. Therefore, starting with a highly motile population of cells (*see* **Note 12**), and checking the motility of the cells at harvest and following resuspension for the assay, is essential (*see* **Note 17**). Because the cells that accumulate in capillaries must be enumerated by plate counting, it is important to avoid the introduction of contaminating microorganisms during the assay.

1. Grow cultures as outlined in **steps 1** and **2** in Subheading 3.1.
2. Add 5 mL of sterile CB or attractant in CB to sterile glass scintillation vials and fill the microcapillaries as outlined in **steps 5** and **6** in Subheading 3.3.

3. Set up the appropriate number of chemotaxis chambers for the planned experiments and harvest motile cells as outlined in **steps 7–14** in Subheading 3.3.
4. Fill a chemotaxis chamber with the motile cell suspension and introduce a capillary containing either buffer or attractant into the cell suspension (*see* **Note 29**) and replace the lid of the Petri dish. Record the start time and incubate for 30 min at 30 °C (or another time and temperature appropriate for your strain).
5. Carry out triplicate assays for each condition.
6. After incubation, remove the microcapillary from the chamber using sterile forceps and rinse any cells off of the outside of the capillary with sterile CB.
7. Using a second pair of sterile forceps, break off the sealed end of the microcapillary and expel the contents into the first of a series of tenfold serial dilution tubes (*see* **Note 31**).
8. Verify that the cells remained motile during the assay by placing the chemotaxis chamber under the phase contrast microscope.
9. Complete the series of tenfold dilutions and plate aliquots onto duplicate LB plates.
10. Incubate the plates at a temperature and time appropriate for your strain and count colonies from plates that have between 30 and 300 colonies. Calculate the number of cells that entered each capillary in CFUs/mL by taking into account the dilution factor.
11. Average results from at least three independent experiments and apply appropriate statistical analyses.

3.5 Competition Capillary Assay

In many cases, multiple attractants are detected by the same receptor [1, 9, 13, 35]. It is possible to determine whether two different attractants are detected by the same or different chemoreceptors using competition assays [36]. Such assays can be carried out as qualitative or quantitative assays. In competition assays, one attractant (the test attractant) is present only in the capillary, and the second attractant (the competing attractant) is present in both the capillary and the cell suspension. If both the attractants are detected by different receptors, the presence of the competing attractant will have no effect on the response to the test attractant. If, however, they are detected by the same chemoreceptor, the response to the test attractant will be decreased or eliminated. Additional assays with the test and competing attractants switched can verify the results.

3.6 Quantitative Soft-Agar Swim Plate Assay

Because the cells grow during these assays, it is not necessary to handle the cells as gently to maintain motile cultures. However, care must be taken to avoid contamination.

Julius Adler originally developed soft agar swim plate assays for studies of *E. coli* chemotaxis [37]. The assay is based on the ability of bacteria to swim through a soft agar matrix as they detect and respond to attractants that serve as carbon and energy sources. In the original qualitative version of the assay, a bacterial colony is stabbed with a toothpick into the center of a Petri dish containing a low concentration of attractant embedded in soft agar. Bacterial cells catabolize the attractant, creating a concentration gradient and swim through the soft agar following the gradient. The chemotaxis response can be observed as a distinct ring of growth that forms as the bacteria grow and move away from the site of inoculation (Fig. 4). Swim plates are useful for enriching for highly motile populations of cells by sequentially transferring cells from the outer edge of the ring of growth (*see* **Note 12**). They have also been used to enrich for non-motile and generally non-chemotactic mutants by sequentially transferring cells that do not move away from the point of inoculation. In either case, after several transfers, single colonies of motile or non-motile/non-chemotactic cells should be isolated on an appropriate medium, and they can be stored as frozen stocks for future use.

We describe here a quantitative version of the swim plate assay, although for screening purposes the qualitative assay using toothpick inoculation remains useful. Consistent responses can be obtained in swim plate assays by carefully controlling the number of cells inoculated. Results are quantified by measuring the final diameter of the growth ring (Fig. 4, right panel) or the rate of ring formation for replicate plates from at least three independent assays. Statistical tests should be used (Fig. 4, right panel) to determine significant differences in responses when comparing different strains (e.g., wild-type and chemoreceptor mutants). Because the attractant also serves as the sole carbon and energy source in this assay, colony size depends on both the growth rate of the strain on the chemical being tested and its chemotaxis response to the chemical. Therefore, it is important to inoculate equal numbers of cells and independently assay the growth rates of any strains being compared before concluding that the observed differences are due solely to chemotaxis defects. If the growth rates of the strains on the test compound differ in liquid medium, an alternative chemotaxis assay that does not require growth should be used. When comparing multiple strains, we have found that the best results are obtained when the responses of various strains are tested on the same plate; therefore, the use of large diameter Petri plates (140×20 mm) is helpful (*see* **Note 32**).

An obvious limitation of this assay is that only compounds that can be metabolized by the strain(s) of interest can be tested as

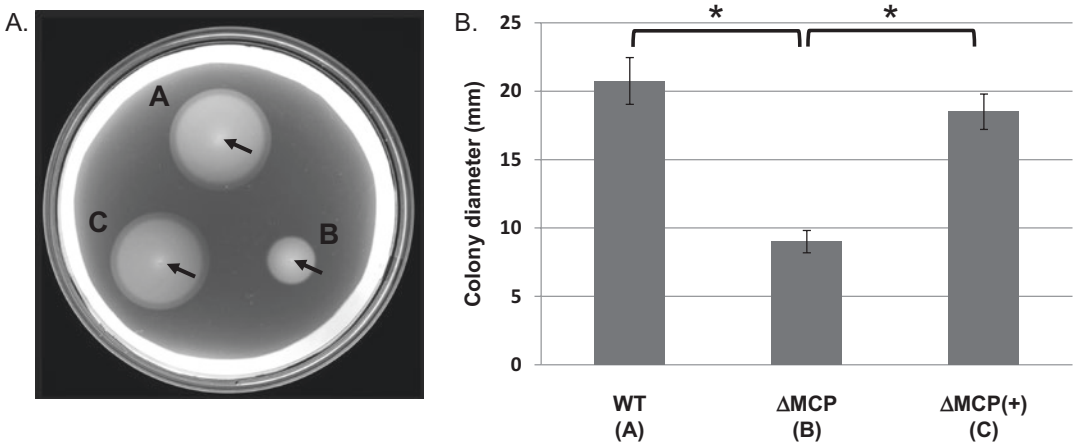

Fig. 4 Soft-agar swim plate assay. The chemotaxis response is visualized as a sharp ring of growth that forms as the bacteria move outward from the original point of inoculation (center of the ring of growth, indicated by black arrows) as the cells multiply in number and swim through the agar, following the gradient of attractant created as they metabolize the attractant compound. (**a**) Representative image of equal numbers of wild-type (WT (A)), chemoreceptor mutant (ΔMCP (B)), and complemented chemoreceptor mutant (ΔMCP(+) (C)) strains in soft agar (0.3%) containing a growth substrate that also serves as the attractant (*see* **Note 42**). (**b**) Quantified responses. The colony diameters were measured and averaged from at least triplicate experiments. Error bars indicate standard deviations. Bars between strains indicate the comparison, and asterisks indicate significant differences ($p < 0.05$)

attractants. Also, responses to volatile attractants can be difficult to evaluate with this assay because losses of the chemical to evaporation affect the formation of the gradient. Finally, studies have shown that energy-taxis responses can mask chemotaxis responses in swim plates [5, 38]. It may therefore be necessary to evaluate the phenotypes of chemoreceptor mutants in an energy taxis mutant (e.g., Δ*aer*) background.

1. Inoculate culture(s) in appropriate medium and grow for 18–24 h prior to the experiment. 3 mL cultures are generally sufficient.
2. Autoclave 100 mL 2× minimal salts broth (MSB; 40 mM phosphate, pH 7.3; 0.1% ammonium sulfate; 0.1% Hutner's mineral base [25]), and 100 mL of 0.5% Noble agar in water in separate Erlenmeyer flasks (*see* **Note 33**). Cool both the flasks in a ~45 °C water bath after autoclaving.
3. Add the sterile stock carbon source/attractant solution to the MSB salts solution to the appropriate final concentration (0.5–2.0 mM; *see* **Note 34**). Add the MSB salts solution to the Noble agar solution and gently swirl to mix.
4. Immediately pour equal amounts (~66 mL) into each of three sterile 140 × 20 mm Petri dishes (*see* **Note 35**).

5. Allow the medium to solidify at room temperature. Note that the medium is only semi-solid. Handle the plates very carefully to avoid disturbing the agar and do not invert!
6. Harvest overnight cultures at 4500 rpm for 5 min using sterile centrifuge tubes (*see* **Note 13**).
7. Decant or aseptically remove the spent medium with a pipet.
8. Add 5.0 mL of MSB medium and gently resuspend the cells by inverting the tube (*see* **Note 13**).
9. Transfer 3 mL of each culture into sterile 16 × 100 mm glass test tubes and adjust the OD_{600nm} to 0.40 ± 0.02 using sterile MSB medium (*see* **Note 36**).
10. Inoculate the swim plates with 2 μL of each culture using a micropipettor and sterile tips (*see* **Note 37**).
11. Carefully move the swim plates to a 30 °C incubator, right side up (*see* **Note 38**), and incubate for 16–24 h (*see* **Note 39**).
12. Examine the swim plates for the presence of large, circular colonies that migrate from the original point of inoculation (*see* **Note 40**). Incubate longer if the colonies are still small.
13. Record digital images of each plate using backlighting (*see* **Note 5**).
14. Measure the diameter of each colony swim ring (again using backlighting) from at least triplicate experiments.
15. Average the results and perform appropriate statistical analyses.

3.7 Gradient Soft-Agar Swim Plate Assay

This assay also requires growth of the culture, but in this case the attractant does not serve as the carbon and energy source [39]. Therefore, one can test responses to compounds that do not serve as carbon and energy sources. For example, unlike the soft agar swim plate assay, catabolic mutants that are unable to grow on the attractant can be evaluated for a response, which may reveal whether the test chemical is directly detected by the wild-type strain or if the test chemical is metabolized by the bacterium to form the actual attractant that is detected. The gradient plate assay is a variation of the soft agar swim plate assay, but in this case the source of the attractant is an agar plug that is placed on the surface of a soft-agar plate, similar to the chemical-in-plug assay. A carbon and energy source (preferably a weak or non-attractant for the bacteria) is present in the soft agar to allow growth of the bacteria. Cultures are inoculated a set distance away from the plug containing the test chemical. We have found that ~2 cm generally works well, but the optimal distance may need to be determined for each bacterial strain and chemical. If the chemical diffusing from the plug is sensed as an attractant, a response is generally seen within 24 h; the time will vary depending on the test chemical, the strain,

and the growth substrate. A positive response is observed when the cells move and grow preferentially toward the plug (Fig. 5), forming an oblong colony. Responses can be quantified (Fig. 5) by calculating the response index (RI), in which the distance from the point of inoculation to the edge of the colony closest to the agar plug (D1) is divided by the sum of D1 plus the distance from the point of inoculation to the edge of the colony farthest from the agar plug (D2). RI values >0.52 correspond to attractant responses, those <0.48 correspond to repellent responses, and intermediate values represent no response [39].

1. Grow cultures and prepare swim plates using 90 × 15 mm Petri dishes as outlined in **steps 1–5** in Subheading 3.6.
2. Prepare agar plugs as outlined in **steps 2–4** and **11** in Subheading 3.2.
3. Harvest and prepare the cells as outlined in **steps 6–9** in Subheading 3.6.
4. Using a micropipette and sterile tips, inoculate the gradient plates by pipetting 2 μL of the cell suspension 2.0 cm away from the center of the agar plug (*see* **Note 41**).
5. Incubate, examine, and record results as outlined in **steps 11–15** in Subheading 3.6.
6. Calculate the RI as shown in Fig. 5.

4 Notes

1. Choose an appropriate medium for your organism and consider whether multiple growth conditions are necessary to test whether the chemotactic response is inducible.
2. For some assays, a complex growth medium can be used for the growth of overnight cultures. Any residual carbon source or cellular waste products are removed by a series of washes before experimentation.
3. We have found that 50–100× stock concentrations of attractants work well for the described assays. For volatile and insoluble compounds, we use research-grade (>98%) stocks without dilution (if liquid) or in some cases directly add crystals (if solid). You will need to optimize the attractant concentration for your organism. Note that some toxic compounds may serve as both attractants and repellents, depending on the concentration tested.
4. Chemotaxis buffer (CB) is a buffer that supports cellular motility. In general, CB is a phosphate-based solution that contains a chelating agent to remove heavy metal ions that can inhibit motility [40] and an energy source to prolong motility [32].

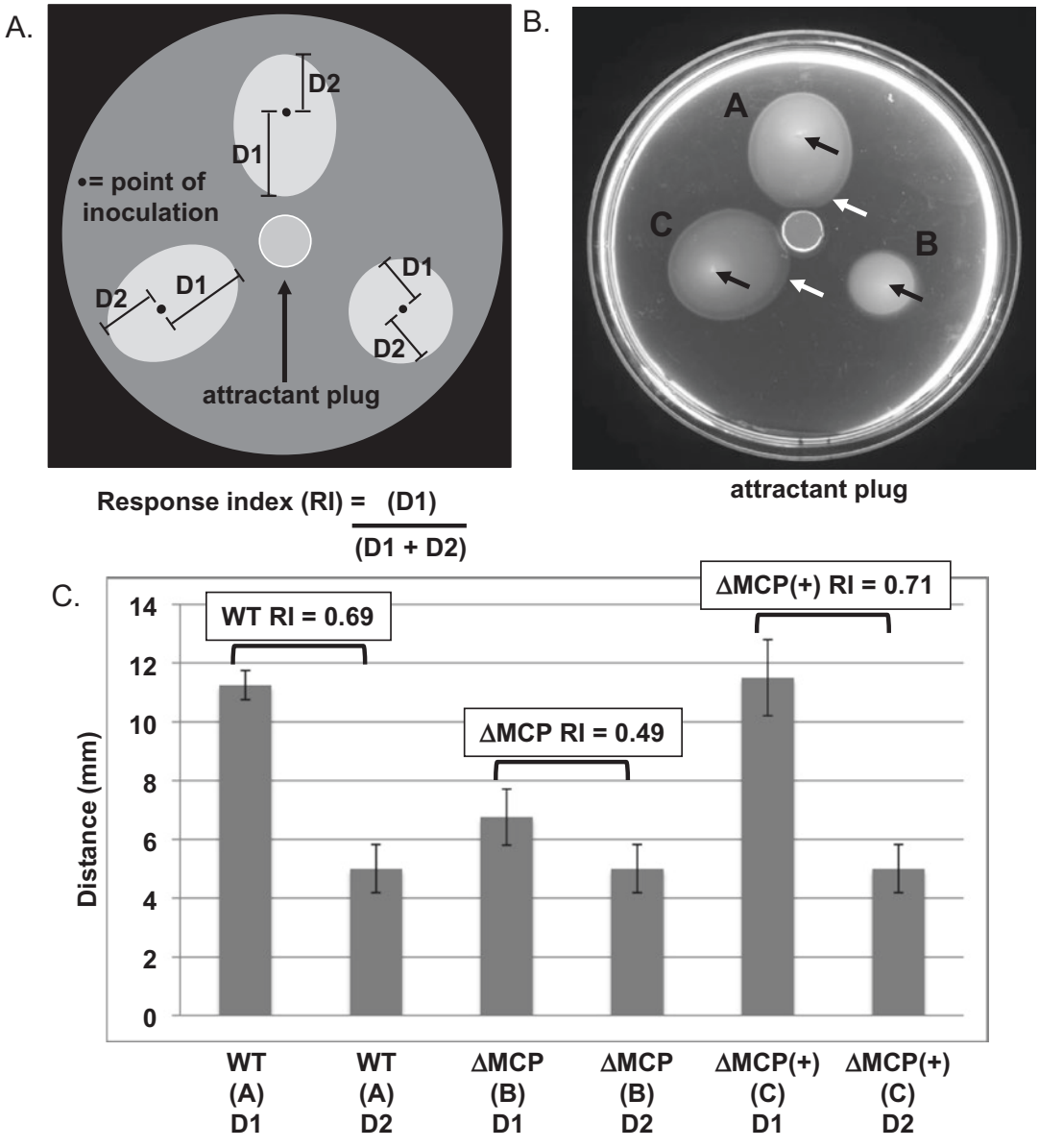

Fig. 5 Gradient plate assay. (**a**) Diagrammatic representation of the measurements taken for quantitative gradient plate assays. D1 and D2 represent the radius from the point of inoculation relative to growth toward or away from the attractant plug, respectively. (**b**) Representative gradient swim plate of wild type (WT (A)), chemoreceptor mutant (ΔMCP (B)), and complemented chemoreceptor mutant (ΔMCP(+) (C)) toward an attractant-containing plug (*see* **Note 42**). Black arrows indicate the point of inoculation, and white arrows indicate the oblong growth of the colony toward the attractant plug. (**c**) Quantitative analysis of gradient plate assays. The D1 and D2 distances were averaged from at least triplicate experiments and used to calculate the response index (RI) for the wild type (WT (A)), chemoreceptor mutant (ΔMCP (B)), and complemented chemoreceptor mutant (ΔMCP(+) (C); *see* **Note 42**). Error bars indicate standard deviations

When used for resuspending obligate aerobes, the CB should be aerated by vigorous shaking to suspend oxygen in the solution. The recipe provided here has been used extensively for assays with *Pseudomonas*. It is, however, important to adjust the buffer for strain-specific motility requirements [41].

5. The "bucket-of-light" is an apparatus that provides indirect illumination via backlighting [42]. It is inexpensive and easy to build with basic hardware.
6. For better contrast in publication quality images, it is best to set the digital camera to the black-and-white setting.
7. The use of contaminant-free low-melting-temperature agarose in attractant plugs is imperative. Some low-melting-temperature agarose brands contain contaminating compounds that serve as chemoattractants for different bacterial species; therefore, the use of buffer-only control agarose plugs is absolutely essential. It is also suggested that agarose plug aliquots be melted only once to avoid degradation of the agarose matrix. Therefore, only the needed amount of buffer-agarose and attractant-agarose should be prepared for each day's experiment.
8. When conducting chemotaxis assays in a defined medium, it is important to use a purified form of agar. We have found Noble agar (Difco, Becton, Dickinson and Co, Franklin Lakes, NJ) to be the best choice of agar for chemotaxis applications.
9. Glass U-tubes are made by flame-sealing the ends of 100 μL volume glass capillary tubes. Hold both the ends of each capillary tube with forceps and heat the center of the glass until it is bendable. Bend the ends of the capillary toward each other until a "U" shape has been formed. The U tube must be in the same plane to lay flat on the surface of the microscope slide. ([Editor's note] One can also use appropriately sized plastic O-rings that have a section cut out of them to allow introduction of cells suspensions and the capillary tubes. This avoids the somewhat delicate issue of bending the U tubes in a flat plane).
10. It is best to visualize the cells using negative contrast pseudo dark-field or oblique dark-field settings on your phase contrast microscope. Visualization and imaging (using black-and-white settings on the digital camera; *see* **Note 6**) of illuminated white cells on a dark background can be achieved by setting the condenser to a different phase setting than what is appropriate for the chosen lens. ([Editor's note] One can also use a reverse-phase-contrast microscope).
11. A defined medium that best suits the growth of your bacterial strain should be chosen for these assays, and attractants to be tested are added to the growth medium. We have found that

lowering the concentration of base minerals aids in the chemotactic response.

12. Transferring cultures through successive swim plates, by inoculating cells from the outside edge of a growth ring and inoculating them at the center of a fresh swim plate and repeating the process 2–3 times, can result in a population with an increased percentage of motile cells. Once a motile population is selected, single colonies isolated from the outer ring of the final swim plate should be stored as a frozen stock in complex growth medium known to support robust growth of your bacterial strain. ([Editor's note] It should be kept in mind that by selecting for more-highly motile cells that unanticipated mutations may be introduced into the population). It is therefore best to use this motile culture as the parental strain when generating chemoreceptor or catabolic mutants to examine in chemotaxis assays to ensure that all strains are otherwise isogenic.
13. It is imperative to harvest cultures under gentle centrifugation conditions that do not exceed a centrifugal force of ~2,400 × *g* to preserve the flagellar structure. Typically, bacterial flagella will remain intact during longer centrifugation times at slower speeds. It is also important to gently resuspend the cells from the resulting pellets to preserve flagellar integrity. Either gently invert centrifuge tubes to resuspend the pellet in CB or use a large-bore micropipette tip and resuspend very slowly with repeat pipetting.
14. Different bacterial strains may be more or less motile at different stages of growth; therefore, optical density of the culture may need to be adjusted for your strain of interest.
15. CB alone should always be used as a negative control, as some bacteria are attracted to contaminants present in some batches of low-melting temperature agar. If low-level chemotaxis responses are detected in the negative control, the response should be confirmed with an alternative assay. Known attractants should also be used as positive controls to verify that the culture was motile and generally chemotactic.
16. Coomassie blue can be added to the agarose for contrast in photographic images such that the agarose plug is visualized as a black plug (Fig. 1b) that can be easily discriminated from the surrounding cell suspension.
17. Only proceed with the assay if the majority of the cells in the population appear to be motile when examined by phase-contrast microscopy.
18. Optimize this optical density for your strain of interest. The goal is to obtain a density that results in good contrast between the background cell culture and the white ring of responding cells in photographic images.

19. The agarose plug must be completely solidified such that it will not mix with the cell suspension when it is added to the experimental chamber.
20. The average volume of the experimental chamber space is 230 μL. Place the tip of a cell suspension-filled 1000 μL micropipette tip onto the slide of the experimental chamber near one of the plastic side strips and slowly pipet the cell solution into the experimental chamber, flooding the space between the slide and cover slip and surrounding the agarose plug.
21. The incubation time may need to be adjusted depending on the bacterial strain; however, if the incubation time is longer than 15 min, oxygen may become limiting and affect cell motility and/or result in an aerotaxis response, during which the cells move toward the sides of the experimental chamber that are exposed to the air.
22. Verification that the majority of the cell population is still motile at this point in the assay should be attained to confirm that the absence of a response was not simply because the cells were no longer motile.
23. We have found that final concentrations of 1.0–10 mM are optimal for chemotactic responses in this assay. You may need to optimize the attractant concentration for your strain.
24. If incubation times longer than 1 h are required to see a response, it is difficult to determine whether the response is to the attractant or could be a response to a metabolic intermediate. If a particular response is inducible, longer incubation times may result in the induction of cells that were not pregrown in the presence of the attractant.
25. Prepare the microcapillaries just before the assay, especially for volatile compounds. Fresh stocks of volatile compounds that have been shaken to increase saturation of the compound should be used.
26. Following this process will pull solution into the capillary via capillary action. Alternatively, capillaries can be filled under vacuum [43].
27. The chemotaxis chamber consists of a sterile U-shaped glass capillary tube (*see* **Note 8**) between a sterile glass microscope slide and a sterile glass cover slip, housed in a sterile Petri dish to maintain aseptic conditions (Fig. 3a).
28. Optimal camera settings include black and white image, no flash, with macro setting engaged.
29. Remove residual attractant from the outside of the capillary by rolling the microcapillary against the inside of the sterile Petri dish. Before inserting the capillary into the cell suspension, verify that an air bubble was not introduced at the tip of the

microcapillary. Air bubbles keep the attractant from properly diffusing into the cell suspension. In addition, an air bubble could elicit an aerotaxis response.

30. Set the microscope stage in the correct focus plane using a mock chemotaxis chamber setup so that you can easily remove and insert experimental slides onto the stage with minimal fine adjustments relative to the strength of the response. Focus in the plane that corresponds to the middle of the capillary such that the crisp edges lining the capillary can be visualized (Fig. 3b).
31. Use the bulb dispenser that comes with the purchase of the microcapillaries to expel cells into a diluent. Because a small volume (less than 1 μL) is expelled, dispense the contents directly on the side of the glass test tube holding the diluent so that surface tension will draw the cell suspension from the microcapillary. An alternative protocol is to break off the heat-closed microcapillary end (after rinsing the capillary), place it into a sterile microfuge tube, and centrifuge under high speed for 30 s to expel contents via centrifugal force.
32. Quantitative swim plate assays can be carried out in standard 90 × 15 mm Petri dishes, but colony size differences are often more obvious when allowed to grow and expand over larger distances in 140 × 20 mm Petri plates.
33. A total 200 mL volume will generate approximately three 140 × 20 mm swim plates.
34. Optimizing the attractant concentration for your specific strain is important. We have found that 1 mM is a good starting concentration for aromatic acids. Volatile hydrocarbons should be added immediately to cooled molten agar to minimize loss to evaporation.
35. Pouring thick swim plates is important to minimize desiccation, and swim plates should be used within a day or two of pouring to avoid desiccation and additional solidification that will inhibit cell migration.
36. Because colony diameter depends on the inoculum, it is critical to ensure that equal numbers of cells are being used for each strain.
37. Dispense the cells midway into the agar to ensure the cells will induce swimming behavior. Do not dispense the cells onto the bottom of the Petri plate, as swarming behavior could be induced on the bottom plate surface [44].
38. Do not invert the plates for incubation, as the agar solution is not solid enough to withstand inversion.
39. Optimize incubation time, temperature, and the type and amount of carbon source for your particular bacterial strain.

Cultures can be incubated in plastic containers or zip-lock plastic bags containing a damp paper towel to decrease the drying of the soft agar at increased temperatures or during longer incubations.

40. A cone-shaped double ring is often seen in swim plates. Cells near the bottom of the plate may be oxygen-limited and most likely form the outermost ring due to energy taxis, during which the oxidation and reduction of FAD is recognized in response to metabolic changes in energy state and affecting swimming behavior [21]. The inner ring represents the chemotaxis response to the chemical attractant. Conducting chemotaxis assays in an *aer2* mutant background is helpful to differentiate energy taxis vs. chemotaxis. This can be especially important because energy taxis has been demonstrated to mask chemotaxis defects in the swim plate assay [5, 38].
41. Adjust the optimum distance between the plug and the point of inoculation depending on attractant solubility. It is helpful to set up a paper template marked with the center plug and equidistant representative points of inoculation for reproducible inoculations.
42. In some cases, the amount of a specific MCP protein produced in the cell can affect the chemotaxis response, so it may be necessary to optimize the expression of cloned MCP genes in complementation experiments. We have found that using a medium-copy plasmid with a tunable promoter [45] can be useful in such cases [5].

Acknowledgment

Chemotaxis research in the authors' laboratories has been supported by a grant from the National Science Foundation (MCB 0919930). Any opinions, findings, and conclusions or recommendations expressed in this material are those of the authors and do not necessarily reflect the views of the National Science Foundation.

References

1. Matilla MA, Krell T (2017) Chemoreceptor-based signal sensing. Curr Opin Biotechnol 45:8–14
2. Krell T, Lacal J, Munoz-Martinez F, Reyes-Darias JA, Cadirci BH et al (2011) Diversity at its best: bacterial taxis. Environ Microbiol 13:1115–1124
3. Wuichet K, Zhulin IB (2010) Origins and diversification of a complex signal transduction system in prokaryotes. Sci Signal 3:ra50
4. Gibson DT, Koch JR, Kallio RE (1968) Oxidative degradation of aromatic hydrocarbons by microorganisms I. Enzymatic formation of catechol from benzene. Biochemistry 7:2653–2661

5. Parales RE, Luu RA, Chen GY, Liu X, Wu V et al (2013) *Pseudomonas putida* F1 has multiple chemoreceptors with overlapping specificity for organic acids. Microbiology 159: 1086–1096
6. Gordillo F, Chávez FP, Jerez CA (2007) Motility and chemotaxis of *Pseudomonas* sp. B4 towards polychlorobiphenyls and chlorobenzoates. FEMS Microbiol Ecol 60:322–328
7. Grimm AC, Harwood CS (1997) Chemotaxis of *Pseudomonas* spp. to the polyaromatic hydrocarbon naphthalene. Appl Environ Microbiol 63:4111–4115
8. Luu RA, Schneider BJ, Ho CC, Nesteryuk V, Ngwesse SE et al (2013) Taxis of *Pseudomonas putida* F1 toward phenylacetic acid is mediated by the energy taxis receptor Aer2. Appl Environ Microbiol 79:2416–2423
9. Luu RA, Kootstra JD, Nesteryuk V, Brunton C, Parales JV et al (2015) Integration of chemotaxis, transport and catabolism in *Pseudomonas putida* and identification of the aromatic acid chemoreceptor PcaY. Mol Microbiol 96:134–147
10. Parales RE, Ditty JL, Harwood CS (2000) Toluene-degrading bacteria are chemotactic to the environmental pollutants benzene, toluene, and trichloroethylene. Appl Environ Microbiol 66:4098–4104
11. Lacal J, Reyes-Darias JA, Garcia-Fontana C, Ramos JL, Krell T (2013) Tactic responses to pollutants and their potential to increase biodegradation efficiency. J Appl Microbiol 114: 923–933
12. Paul D, Singh R, Jain RK (2006) Chemotaxis of *Ralstonia* sp. SJ98 towards *p*-nitrophenol in soil. Environ Microbiol 8:1797–1804
13. Lacal J, Alfonso C, Liu X, Parales RE, Morel B et al (2010) Identification of a chemoreceptor for tricarboxylic acid cycle intermediates: differential chemotactic response towards receptor ligands. J Biol Chem 285:23126–23136
14. Bi S, Yu D, Si G, Luo C, Li T et al (2013) Discovery of novel chemoeffectors and rational design of *Escherichia coli* chemoreceptor specificity. Proc Natl Acad Sci U S A 110: 16814–16819
15. Ni B, Huang Z, Fan Z, Jiang CY, Liu SJ (2013) *Comamonas testosteroni* uses a chemoreceptor for tricarboxylic acid cycle intermediates to trigger chemotactic responses towards aromatic compounds. Mol Microbiol 90:813–823
16. Rabinovitch-Deere CA, Parales RE (2012) Three types of taxis used in the response of *Acidovorax* sp. strain JS42 to 2-nitrotoluene. Appl Environ Microbiol 78:2308–2315
17. Grimm AC, Harwood CS (1999) NahY, a catabolic plasmid-encoded receptor required for chemotaxis of *Pseudomonas putida* to the aromatic hydrocarbon naphthalene. J Bacteriol 181:3310–3316
18. Hawkins AC, Harwood CS (2002) Chemotaxis of *Ralstonia eutropha* JMP134(pJP4) to the herbicide 2,4-dichlorophenoxyacetate. Appl Environ Microbiol 68:968–972
19. Vangnai AS, Takeuchi K, Oku S, Kataoka N, Nitisakulkan T et al (2013) Identification of CtpL as a chromosomally encoded chemoreceptor for 4-chloroaniline and catechol in *Pseudomonas aeruginosa* PAO1. Appl Environ Microbiol 79:7241–7248
20. López-Farfán D, Reyes-Darias JA, Krell T (2016) The expression of many chemoreceptor genes depends on the cognate chemoeffector as well as on the growth medium and phase. Curr Genet 63:457–470
21. Alexandre G (2010) Coupling metabolism and chemotaxis-dependent behaviours by energy taxis receptors. Microbiology 156:2283–2293
22. Sarand I, Osterberg S, Holmqvist S, Holmfeldt P, Skarfstad E et al (2008) Metabolism-dependent taxis towards (methyl)phenols is coupled through the most abundant of three polar localized Aer-like proteins of *Pseudomonas putida*. Environ Microbiol 10:1320–1334
23. Sambrook J, Fritch EF, Maniatis T (1989) Molecular cloning: a laboratory manual, 2nd edn. Cold Spring Harbor Laboratory, Cold Spring Harbor, NY
24. Stanier RY, Palleroni NJ, Doudoroff M (1966) The aerobic pseudomonads: a taxonomic study. J Gen Microbiol 43:159–271
25. Gerhardt P, Murray RGE, Wood WA, Krieg NR (eds) (1994) Methods for general and molecular bacteriology. American Society for Microbiology, Washington, D.C.
26. HS Y, Alam M (1997) An agarose-in-plug bridge method to study chemotaxis in the archaeon *Halobacterium salinarum*. FEMS Microbiol Lett 156:265–269
27. Tso W-W, Adler J (1974) Negative chemotaxis in *Escherichia coli*. J Bacteriol 118:560–576
28. Storch KF, Rudolph J, Oesterhelt D (1999) Car: a cytoplasmic sensor responsible for arginine chemotaxis in the archaeon *Halobacterium salinarum*. EMBO J 18:1146–1158
29. Li J, Go AC, Ward MJ, Ottemann KM (2010) The chemical-in-plug bacterial chemotaxis assay is prone to false positive responses. BMC Res Notes 3:77
30. Nikata T, Sumida K, Kato J, Ohtake H (1992) Rapid method for analyzing bacteria behavioral

responses to chemical stimuli. Appl Environ Microbiol 58:2250–2254

31. Kato J, Ito A, Nikata T, Ohtake H (1992) Phosphate taxis in *Pseudomonas aeruginosa*. J Bacteriol 174:5149–5151
32. Lacal J, Muñoz-Martínez F, Reyes-Darías JA, Duque E, Matilla M et al (2011) Bacterial chemotaxis towards aromatic hydrocarbons in *Pseudomonas*. Environ Microbiol 13: 1733–1744
33. Adler J (1973) A method for measuring chemotaxis and use of the method to determine optimum conditions for chemotaxis by *Escherichia coli*. J Gen Microbiol 74:77–91
34. Harwood CS, Rivelli M, Ornston LN (1984) Aromatic acids are chemoattractants for *Pseudomonas putida*. J Bacteriol 160:622–628
35. Webb BA, Compton KK, Castañeda Saldaña R, Arapov TD, Ray KW et al (2017) *Sinorhizobium meliloti* chemotaxis to quaternary ammonium compounds is mediated by the chemoreceptor McpX. Mol Microbiol 103:333–346
36. Mesibov R, Adler J (1972) Chemotaxis toward amino acids in *Escherichia coli*. J Bacteriol 112:315–326
37. Adler J (1966) Chemotaxis in bacteria. Science 153:708–716
38. Alvarez-Ortega C, Harwood CS (2007) Identification of a malate chemoreceptor in *Pseudomonas aeruginosa* by screening for chemotaxis defects in an energy taxis-deficient mutant. Appl Environ Microbiol 73:7793–7795
39. Pham HT, Parkinson JS (2011) Phenol sensing by *Escherichia coli* chemoreceptors: a nonclassical mechanism. J Bacteriol 193:6597–6604
40. Moulton RC, Montie TC (1979) Chemotaxis by *Pseudomonas aeruginosa*. J Bacteriol 137:274–280
41. Moench TT, Konetzka WA (1978) Chemotaxis in *Pseudomonas aeruginosa*. J Bacteriol 133:427–429
42. Parkinson JS (2007) A "bucket of light" for viewing bacterial colonies in soft agar. Methods Enzymol 423:432–435
43. Meyer G, Schneider-Merck T, Böhme S, Sand W (2002) A simple method for investigations on the chemotaxis of *Acidithiobacillis ferrooxidans* and *Desulfovibrio vulgaris*. Acta Biotechnol 22:391–399
44. Kearns DB (2010) A field guide to bacterial swarming motility. Nat Rev Microbiol 8: 634–644
45. Khan S, Gaines J, Roop RM, Farrand SK (2008) Broad-host-range expression vectors with tightly regulated promoters and their use to examine the influence of TraR and TraM expression on Ti plasmid quorum sensing. Appl Environ Microbiol 74:5053–5062

Chapter 22

Screening Chemoreceptor–Ligand Interactions by High-Throughput Thermal-Shift Assays

Maximilian K.G. Ehrhardt, Suzanne L. Warring, and Monica L. Gerth

Abstract

Identifying the ligands sensed by chemoreceptors remains challenging, in part because current screening methods are low-throughput, costly, and/or time-consuming. In contrast, fluorescence thermal shift (FTS) assays provide a fast and inexpensive approach to chemoreceptor–ligand screening. In FTS assays, the temperature at which a protein denatures is measured by monitoring the fluorescence of a dye with affinity for hydrophobic regions of the protein, which are exposed as the protein unfolds. A detectable increase (or "shift") in the melting temperature (T_m) of the protein in the presence of a potential ligand indicates binding. Here, we present our protocol for using FTS assays for the screening of chemoreceptor ligands in a high-throughput, 96-well plate format. We have also included details on the use of Biolog Phenotype Microarray plates as a convenient ligand library, although the methods described should be generally applicable to other library formats as well.

Key words Ligand, Signal molecule, Screening, Binding, Differential scanning fluorometry, Fluorescence thermal shift assay, Chemoreceptor, Ligand binding domain, High-throughput

1 Introduction

Chemoreceptors are the sensing proteins of bacterial chemotaxis systems [1] that enable bacteria to detect chemical gradients in the environment and bias their swimming behavior in order to navigate toward favorable conditions (for reviews on chemotaxis, *see* [2, 3]). Chemoreceptors bind chemical signals (i.e., ligands) and signal the downstream chemotaxis machinery to modulate rotation of the flagellar motor. These proteins typically have three structurally and functionally discrete domains: a ligand binding domain (LBD), a linker domain, and a signaling domain. The LBD determines the specificity of the chemotactic response, and therefore these sensor domains play a central role in chemotaxis.

A current challenge in chemotaxis research is the identification of chemical signals detected by a given chemoreceptor. Several in vivo and in vitro approaches have been developed to identify the

Michael D. Manson (ed.), *Bacterial Chemosensing: Methods and Protocols*, Methods in Molecular Biology, vol. 1729, https://doi.org/10.1007/978-1-4939-7577-8_22,

ligands of chemoreceptors [4–7]. Functional redundancy and masking by other behaviors (such as aerotaxis) can hamper attempts to link individual chemoreceptor proteins to their cognate ligands using in vivo assays, particularly for bacteria with large numbers of chemoreceptors. Furthermore, although in vitro approaches, such as isothermal titration calorimetry [6] and fluorescence resonance energy transfer (FRET)-based assays [7], have been successfully used to identify chemoreceptor ligands, these techniques are low-throughput and require specialized equipment, precluding wider application of these methods.

Fluorescence-based thermal shift (FTS) assays (also sometimes referred to as differential scanning fluorimetry or ThermoFluor assays) offer advantages over these techniques because they are rapid and inexpensive, and they use thermal-cycling instrumentation common in molecular biology laboratories. Indeed, FTS assays are widely used in screens to identify ligands that bind to and stabilize purified proteins [8]. In FTS assays, the temperature at which a protein unfolds is monitored by changes in the fluorescence of a dye with affinity for hydrophobic regions of the protein (e.g., SYPRO Orange), which are exposed as the protein is denatured. In general, most ligands stabilize proteins upon binding and therefore result in a detectable increase (or "shift") in the melting temperature (T_m) of the protein [9, 10]. The difference in the T_m of the protein in the presence and absence of ligand can be easily calculated, and it is related to the binding affinity of the protein and the concentration of ligand. FTS assays have low volume requirements for samples, are easy to set up, and easy to scale to a high-throughput format. Each assay takes only a few hours to run and analyze.

One potential drawback of FTS assays for the study of chemotaxis systems is that chemoreceptors are multi-domain, typically membrane-bound proteins. In FTS assays, multi-domain proteins or proteins with exposed hydrophobic patches can produce high background fluorescence and/or non-ideal, multi-phasic melt curves. However, the LBDs of chemoreceptors can often be expressed as soluble recombinant proteins, without the other domains or transmembrane regions, and therefore are amenable to FTS assays.

For LBD–ligand screening, we have combined FTS assays with Biolog Phenotype Microarray (PM) plates [11, 12]. PM plates contain potential metabolic substrates (e.g., amino acids, organic acids, sugars), originally designed for performing microbial growth tests [13]. In our screen, the substrates are used as potential ligands. These commercially available 96-well plates are inexpensive, and each plate provides enough material for multiple FTS assays. By combining FTS assays with Biolog PM plates, hundreds of potential ligands can be screened in a single day.

Several excellent protocols for FTS assays have been published previously [9, 14, 15]. Here, we present our development of a high-throughput FTS assay for identifying the ligands of chemoreceptor LBDs using PM plates. This method, which should be generally applicable to other types of ligand binding proteins and other types of ligand libraries, offers a useful tool to advance our understanding of signal molecule–receptor interactions.

2 Materials

2.1 Equipment

1. Real-time PCR instrument (e.g., Roche LightCycler 480).
2. Multichannel pipette capable of handling 1–50 μL volumes.
3. Swinging-bucket centrifuge with multiwell plate rotor (e.g., Eppendorf 5804 with an A-2-DWP rotor).

2.2 Materials

1. White 96-well PCR plates (e.g., LightCycler 480 Multiwell Plate 96, White).
2. Optically clear 96-well plate sealing films (e.g., LightCycler 480 Sealing Foils).
3. SYPRO Orange dye (5000× concentrate in DMSO, Life Technologies).
4. Biolog Phenotype Microarray (PM) plates 1–4 (*see* **Note 1**).
5. Adhesive 96-well plate sealing films (e.g.,VWR Aluminum Foils).
6. Multichannel pipette reservoir trough (e.g., Eppendorf Autoclavable Reagent Reservoirs).
7. Purified LBD or binding protein of interest (*see* **Notes 2** and **3**) in a suitable storage buffer such as 50 mM potassium phosphate, 200 mM sodium chloride, pH 7.0 (*see* **Note 4**).
8. Protein dilution buffer: 50 mM potassium phosphate, 200 mM sodium chloride, pH 7.0 (*see* **Notes 4** and **5**).

3 Methods

3.1 Preparation of Biolog PM Ligand Library Plates

1. Prepare the Biolog PM ligand library plate of interest by adding 50 μL of sterile deionized water to each well using a multichannel pipette (*see* **Note 6**).
2. Pipette up and down repeatedly until the compounds are fully dissolved.
3. When not in use, seal the plate with an aluminum sealing film to prevent evaporation and cross-contamination (*see* **Note 7**).

3.2 Assay Plate Preparation

1. Prepare a master mix of protein and dye by adding each reagent in the order listed below into a 2 mL tube (*see* **Note 8**). We routinely use final concentrations of ~10 μM protein and 5× SYPRO Orange. It is critical to note that the protein and dye concentrations may need to be optimized for each LBD or binding protein studied (*see* **Note 9**). Adjust the volumes and concentrations as needed (Table 1).
2. Aliquot 18 μL of the master mix into each well of the white 96-well assay plate.
3. Using a multichannel pipette, aliquot 2 μL from each well of the resuspended Biolog plate into the corresponding assay plate wells. Mix gently by pipetting and avoid introducing air bubbles if possible. The final volume used in our standard assay is 20 μL.
4. Centrifuge the plate at 1000 × *g* for 2 min to collect the solutions at the bottom of the wells and to remove any bubbles.
5. Seal the assay plate with optically clear sealing film (*see* **Note 10**).

3.3 Data Acquisition

1. Open the real-time PCR instrument software and place the assay plate into the instrument. Set up the instrument for a standard protein melt curve experiment. Ensure the instrument filters are set for SYPRO Orange (*see* **Note 11**) and that the reaction volume is set to 20 μL. Run the temperature scan from 20 °C to 90 °C at ~1 °C per min. We use the program shown in Table 2 on the Roche Lightcycler 480.

3.4 Data Analysis and Interpretation

1. Review the melt curves. In FTS experiments, the fluorescence intensity is plotted as a function of temperature. An ideal melt curve will have a sigmoidal shape, with low pre-transition fluorescence and a sharp transition upon unfolding (Fig. 1a). The fluorescence signal should be high, but without saturating the detector at the maximum fluorescence response. A decrease in signal after the maximum fluorescence (and deviation from a true sigmoidal curve) is normal; this is due to protein precipitation and aggregation. (For troubleshooting non-ideal curves, *see* **Notes 9** and **12**).
2. Calculate the T_m of each curve. The simplest way to do this is to determine the first derivative of the melting curve; this feature is included in most RT-PCR software packages (*see* **Note 13**). In the Roche LightCycler 480 software, the negative of the first derivative ($-\mathrm{d}F/\mathrm{d}T$) is plotted versus temperature. In this analysis, the T_m is represented by the peak minimum of the derivative curve (Fig. 1b).
3. Export the data in a generic format, such as a comma-separated value (csv), that can be opened in your data analysis software of choice (e.g., Excel, GraphPad Prism, Origin). Calculate

Table 1
Reagents for assay plate preparation

Reagent	Volume (μL)
Dilution buffer (*see* **Note 5**)	1798
5000× SYPRO Orange	2
Purified protein (100 μM)	200
Total	2000

Table 2
Program for temperature scan

Target (°C)	Acquisition mode	Hold (hh:mm:ss)	Ramp Rate (°C/s)
20	None	00:02:00	4.4
90	Continuous		0.02
20	None	00:02:00	2.2

the change in melting temperature (ΔT_m) of each compound by subtracting the T_m value obtained for the protein alone ("no ligand" control) from the T_m value obtained in the presence of each compound. Plot this data as a histogram showing the ΔT_m for each potential ligand (Fig. 1c).

4. Criteria for hit selection: False positives and negatives are a concern with any high-throughput approach. Potential hits (especially from Biolog plates, where the concentrations of ligands are unknown) should always be followed up by performing FTS assays with known concentrations of pure ligands. Although there is no absolute cutoff for identifying hits in FTS assays, in our experience, a ΔT_m value ≥2 °C is a strong indication of ligand binding (*see* **Note 14**). We consider a compound that results in an average ΔT_m of <1 °C to represent a non-binding compound under our standard assay conditions. We rescreen any potential ligands that show a ΔT_m value of >1 °C with increasing concentrations of the compound of interest, using pure chemicals at known concentrations (typically 0, 1, 2, 5 and 10 mM of ligand). Ligand binding usually results in concentration-dependent stabilization, and therefore increasing the ligand concentration can result in larger, more easily detected changes in T_m. All potential hits from the FTS assays should be validated using complementary techniques, such as isothermal titration calorimetry (ITC) and/or in vivo chemotaxis assays.

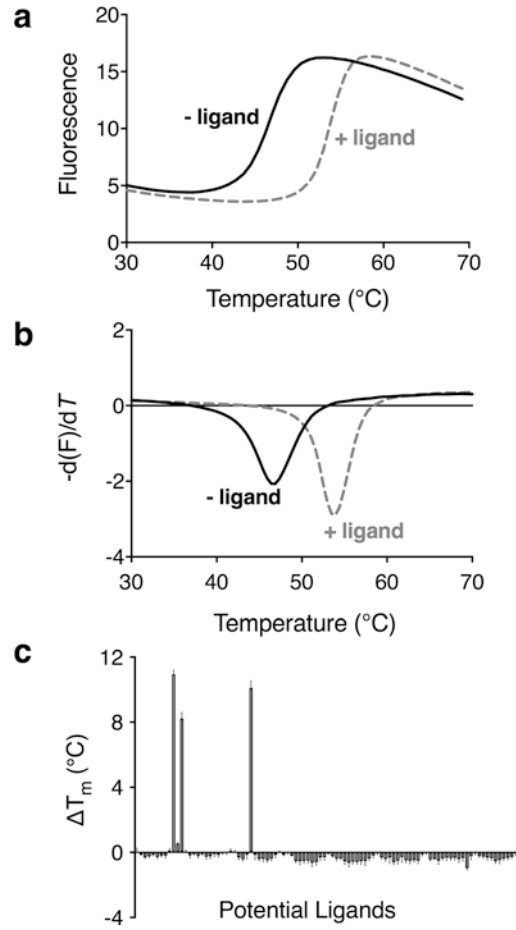

Fig. 1 Typical FTS assay data and analysis. The data shown is for PscA-LBD from *Pseudomonas syringae* pv. *actinidiae*. (**a**) Fluorescence intensity versus temperature for the unfolding of the recombinant LBD in the absence (solid black line) and presence (dashed gray line) of a ligand, in this case, L-glutamate. (**b**) The first derivatives (d*F*/d*T*) of the melt curves shown in panel (**a**) are plotted versus temperature. The peak in the first derivative of the fluorescence (i.e., the lowest part of the curve) represents the melting temperature, or T_m, that occurs at the midpoint of the unfolding transition. (**c**). The change in melting temperature (ΔT_m, calculated as the T_m in the presence of ligand, minus the T_m in the absence of ligand) of the LBD for each ligand tested is shown. In this example, 95 potential ligands from Biolog plate PM3 were screened. Figure adapted from [11]

4 Notes

1. Biolog PM plates 1–4 contain various potential sources of carbon, nitrogen, phosphorus, and sulfur for bacteria, which are also likely chemoattractants and therefore potential ligands of chemoreceptors. Each plate contains 95 compounds (dried

onto the bottom of the wells) and an empty well (at position A1), which, for the purposes of ligand screening, serves as the "protein only" reference well. The full plate maps are available on the Biolog website: http://www.biolog.com/pdf/pm_lit/PM1-PM10.pdf. We routinely use these plates as our initial ligand screen; however, other PM plates and/or ligand libraries of interest may also be utilized. As a starting point, we recommend preparing ligand-library stocks at 20 mM in sterile, deionized water, and performing the FTS screen at ~2 mM final ligand concentrations.

2. To identify the soluble, periplasmic LBD within the full-length chemoreceptor, we use a combination of TOPCONS [16] (which predicts transmembrane regions) and CD-search [17] (which searches for any identifiable protein domains within the sequence). As an example, if TOPCONS predicted transmembrane regions of residues 20–40 and 320–345 in the amino acid sequence of a putative chemoreceptor, then the soluble LBD portion of the chemoreceptor would be predicted to be residues 41–319. We typically clone the corresponding nucleotide sequence of the LBD of interest into a pET28 plasmid for expression with a His6-tag at the N-terminus, which facilitates purification by immobilized metal affinity chromatography.
3. Under our standard assay conditions, approximately 0.5 μg of protein in total is needed per 96-well plate assayed (e.g., 200 μL of a 100 μM protein that has an estimated molecular mass of 30 kDa). We recommend starting with a ~100 μM protein stock, if possible.
4. Other buffers can be used, but avoid buffers containing compounds that may cause high background fluorescence, or effect the stability of the protein. If possible, also avoid buffers such as Tris that exhibit a strong dependence of pH on temperature. Another suitable, commonly used buffer for FTS assays is 100 mM HEPES, 150 mM NaCl, pH 7.5.
5. Prechill the protein dilution buffer to 4 °C. Keep the protein at 4 °C and/or on ice until ready to use.
6. The exact concentrations of individual compounds in the Biolog PM plate wells are proprietary and not released by the manufacturer. For plates PM 1–3, preparation in this manner should result in stock solutions of approximately 10–20 mM. Plate PM4, which contains phosphorus and sulfur compounds, is designed to be used at lower concentrations (mimicking physiological ranges). Therefore, we suspend this plate in a smaller volume (~20 μL). Even then, in our experience any shifts in melting temperature (i.e., potential hits) from plate PM4 tend to be smaller (often in the range of

1–2 °C). It is important to examine the shifts from plate PM4 carefully and to follow up any potential hits with additional assays.

7. We have found the resuspended PM plate compounds to be generally stable for up to 1 week when kept sealed and stored at 4°C in the dark.
8. Do not add the undiluted 5000× dye directly to the protein, as it may lead to damage caused by contact with high concentrations of DMSO present in the dye solution.
9. The protein and dye concentrations may need to be optimized for each LBD or binding protein studied, as the protein size and hydrophobicity can impact both the total fluorescence and the overall shape of the protein melt curve. Protein concentrations used for FTS assays typically range from 0.5 μM to 20 μM, while SYPRO Orange dye concentrations typically range from 0.5× to 10×. If 10 μM protein and 5× SYPRO Orange produce unsuitable melt curves, running a matrix of various protein and dye concentrations to find the optimal concentrations may improve the results (Table 3).

   It is important to note that, if the protein is already misfolded at 20 °C (as indicated in the melt curve by a high initial fluorescence, with no clear sign of an unfolding event) optimization of the protein and/or dye concentrations is unlikely to improve the situation. In this case, using FTS assays to screen various buffer conditions may help to identify a more suitable purification and/or storage buffer, in which the protein is folded and stable. There are many FTS-based buffer screens described in the literature; we routinely use the buffer screen developed by Seabrook and Newman [18].
10. It is best to run the prepared plate immediately, as some proteins may be unstable when diluted.
11. SYPRO Orange has an excitation maximum (ex) of 492 nm and an emission maximum (em) of 575 nm. When setting up

Table 3
Example matrix for optimization of protein and dye concentration

0.5 μM protein 0.5× dye	0.5 μM protein 1× dye	0.5 μM protein 5× dye	0.5 μM protein 10× dye
5 μM protein 0.5× dye	5 μM protein 1× dye	5 μM protein 5× dye	5 μM protein 10× dye
10 μM protein 0.5× dye	10 μM protein 1× dye	10 μM protein 5× dye	10 μM protein 10× dye
20 μM protein 0.5× dye	20 μM protein 1× dye	20 μM protein 5× dye	20 μM protein 10× dye

a run, select the closest ex/em filters available in your particular instrument. For the Roche Lightcycler 480 System I, we use the excitation 483 nm and emission 568 nm filter combination.

12. Curves with high initial fluorescence and no clear indication of an unfolding event suggest that the protein is already unfolded or aggregated at room temperature (*see* **Note 9**). Curves with high initial fluorescence intensity and a visible transition to the unfolded state may be due to the dye binding to a ligand (sometimes LBDs co-purify with their physiological ligand already bound), and/or binding to exposed hydrophobic domains that are exposed in the native state; this often does not affect the calculated T_m. Bi-phasic melt curves may be observed when a mixture of bound and unbound proteins exists. In this scenario, increasing the ligand concentration may resolve the peaks. Multi-phasic curves can also be observed with multi-domain proteins, where each domain unfolds at a different temperature. In this scenario, each transition may be analyzed separately (either by using the first derivative to identify both T_ms, or by fitting the data to a double Boltzmann model).
13. Alternatively, the T_ms can also be calculated by nonlinear fitting of the melt curves to the Boltzmann equation (assuming a sigmoidal shape to the unfolding curve) using software such as GraphPad Prism or Origin.
14. For the identification of potential ligands from FTS assays, we recommend performing at least two biological replicates (using independently purified batches of protein) and analyzing the means and standard errors of these replicates.

Acknowledgment

The authors gratefully acknowledge financial support from a Marsden Fast Start grant administered by the Royal Society of New Zealand. MKGE is supported by a University of Otago Doctoral Scholarship.

References

1. Adler J (1969) Chemoreceptors in bacteria. Science 166:1588–1597
2. Wadhams GH, Armitage JP (2004) Making sense of it all: bacterial chemotaxis. Nat Rev Mol Cell Biol 5:1024–1037
3. Hazelbauer GL, Falke JJ, Parkinson JS (2008) Bacterial chemoreceptors: high-performance signaling in networked arrays. Trends Biochem Sci 33:9–19
4. Adler J (1973) A method for measuring chemotaxis and use of the method to determine optimum conditions for chemotaxis by *Escherichia coli*. J Gen Microbiol 74:77–91

5. Ames P, Parkinson JS (2007) Phenotypic suppression methods for analyzing intra- and intermolecular signaling interactions of chemoreceptors. Methods Enzymol 423: 436–457
6. Lacal J, Alfonso C, Liu X, Parales RE, Morel B et al (2010) Identification of a chemoreceptor for tricarboxylic acid cycle intermediates: differential chemotactic response towards receptor ligands. J Biol Chem 285:23126–23136
7. Sourjik V, Vaknin A, Shimizu TS, Berg HC (2007) In vivo measurement by FRET of pathway activity in bacterial chemotaxis. Methods Enzymol 423:365–391
8. Pantoliano MW, Petrella EC, Kwasnoski JD, Lobanov VS, Myslik J et al (2001) High-density miniaturized thermal shift assays as a general strategy for drug discovery. J Biomol Screen 6:429–440
9. Niesen FH, Berglund H, Vedadi M (2007) The use of differential scanning fluorimetry to detect ligand interactions that promote protein stability. Nat Protoc 2:2212–2221
10. Cimmperman P, Baranauskiene L, Jachimoviciute S, Jachno J, Torresan J et al (2008) A quantitative model of thermal stabilization and destabilization of proteins by ligands. Biophys J 95:3222–3231
11. McKellar JLO, Minnell JJ, Gerth ML (2015) A high-throughput screen for ligand binding reveals the specificities of three amino acid chemoreceptors from *Pseudomonas syringae* pv. *actinidiae*. Mol Microbiol 96:694–707
12. Brewster JL, McKellar JLO, Finn TJ, Newman J, Peat TS et al (2016) Structural basis for ligand recognition by a cache chemosensory domain that mediates carboxylate sensing in *Pseudomonas syringae*. Sci Rep 6:35198
13. Bochner BR, Gadzinski P, Panomitros E (2001) Phenotype microarrays for high-throughput phenotypic testing and assay of gene function. Genome Res 11:1246–1255
14. Vivoli M, Novak HR, Littlechild JA, Harmer NJ (2014) Determination of protein-ligand interactions using differential scanning fluorimetry. J Vis Exp 91:51809
15. Huynh K, Partch CL (2015) Analysis of protein stability and ligand interactions by thermal shift assay. Curr Protoc Protein Sci 79:28.9.1–28.9.14
16. Tsirigos KD, Peters C, Shu N, Kall L, Elofsson A (2015) The TOPCONS web server for consensus prediction of membrane protein topology and signal peptides. Nucleic Acids Res 43(W1):W401–W407
17. Marchler-Bauer A, Bryant SH (2004) CD-search: protein domain annotations on the fly. Nucleic Acids Res 32(W1):W327–W331
18. Seabrook SA, Newman J (2013) High-throughput thermal scanning for protein stability: making a good technique more robust. ACS Comb Sci 15:387–392

Chapter 23

High-Throughput Screening to Identify Chemoreceptor Ligands

Matilde Fernández, Álvaro Ortega, Miriam Rico-Jiménez, David Martín-Mora, Abdelali Daddaoua, Miguel A. Matilla, and Tino Krell

Abstract

The majority of bacterial chemoreceptors remain functionally un-annotated. The knowledge of chemoreceptor function, however, is indispensable to understanding the evolution of the chemotaxis system in bacteria with different lifestyles. Significant progress in the annotation of chemoreceptor function has been made using experimental strategies that are based on the individual, genetically engineered ligand binding domain (LBD) of chemoreceptors. There is now evidence that all major classes of LBDs can be produced as individual domains that retain their ligand binding activity. Here, we provide a protocol for the combined use of high-throughput ligand screening using Differential Scanning Fluorimetry followed by Isothermal Titration Calorimetry to identify and characterize ligands that bind to recombinant chemoreceptor LBDs. This approach has been shown to be very efficient for determining the function of novel chemoreceptors.

Key words Chemoreceptor, Ligand binding domain, Thermal-shift assays, Isothermal titration calorimetry, Differential scanning fluorimetry

1 Introduction

Chemosensory signaling cascades represent a major mechanism in bacterial signal transduction. Signaling is initiated by stimulus perception by the chemoreceptor that triggers a signaling cascade that ultimately determines the level of CheY phosphorylation. Typically, the signaling molecule binds directly, or in a complex with a ligand binding protein, to the chemoreceptor ligand binding domain (LBD). Chemosensory pathways mediate either chemotaxis, alternative cellular processes, or type IV pili-mediated motility [1].

Escherichia coli is the traditional model organism used to study chemotaxis and chemoreceptors [2]. It has four chemoreceptors, whose ligand profiles have been determined. It also possesses an aerotaxis receptor. However, genome analyses reveal that many

Michael D. Manson (ed.), *Bacterial Chemosensing: Methods and Protocols*, Methods in Molecular Biology, vol. 1729, https://doi.org/10.1007/978-1-4939-7577-8_23,

other bacteria have a much higher number of chemoreceptors, in some cases more than 80 [3, 4]. The large majority of chemoreceptors are of unknown function, but such information is indispensable for identifying the environmental forces that direct the evolution of different bacteria.

Chemotaxis assays using single chemoreceptor mutants is a typical approach for finding receptor ligands. However, disadvantages of this approach are the possibilities that there may be multiple chemoreceptors that respond to the same ligand [5] and the fact that energy taxis evoked by a metabolizable compound may mask specific responses [6].

Over the last few years, significant progress in chemoreceptor annotation has been made using an approach that is initiated by in vitro experimentation. This approach is based on the fact that the individual LBDs of all major LBD classes, namely the 4-helix bundle (4HB) [7, 8], the sCACHE [9, 10], dCACHE [11, 12], and helical bimodular (HBM) domain [13, 14], can all be produced as soluble proteins that retain binding affinity for their cognate ligands. Initially, these recombinant domains were submitted to isothermal titration calorimetry (ITC) ligand screening [15]. Although very useful, this approach is very labor-intensive. A ligand screen using Differential Scanning Fluorimetry (DSF) of commercially available ligand collections has been reported to accelerate the screening process [16]. (*See* also Chapter 22 in this volume.) In a DSF analysis, a fluorescent dye is added to the protein, and a temperature gradient is applied to the resulting mixture. During protein unfolding, hydrophobic regions of the proteins are exposed, leading to binding of additional dye and resulting in changes in fluorescence that can be monitored (Fig. 1a) [17]. The resulting data permit the calculation of the midpoint of the protein unfolding transition, or Tm. In general, ligand binding to a protein alters the Tm of unfolding, and this approach can be used in a high-throughput format to screen ligand collections. As a representative example, Fig. 1b shows T_m changes of the recombinant LBD of the McpH chemoreceptor that were induced by each of the 95 compounds present in a collection of bacterial nitrogen sources. Ligands that induce Tm shifts of more than 2 °C are considered significant. Although this technique provides rapid information on potential ligands, it does not represent definite proof of binding, as false positive hits are observed with some frequency. Therefore, additional binding experiments are required to confirm the DSF data [18]. In our laboratory, we have been using ITC, and a schematic drawing of an adiabatic microcalorimeter is shown in Fig. 2a. This technique involves the injection of aliquots of ligand solutions into a sample of purified chemoreceptor LBD and the measurement of the resulting heat changes. Figure 2b shows the titration of McpH-LBD with xanthine, which was shown in Fig. 1b to increase the Tm of McpH-LBD by 3.7 °C. The upper panel shows the raw titration data, and the downward-directed peaks

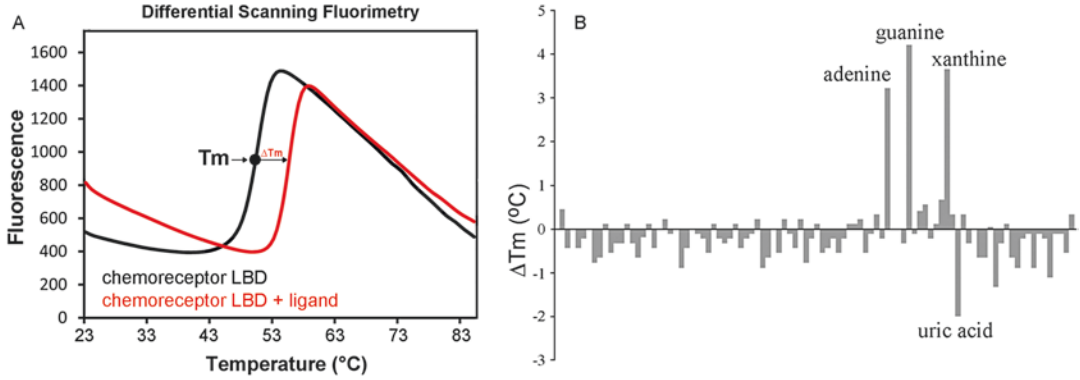

Fig. 1 Differential scanning fluorimetry based high-throughput screens to identify chemoreceptor ligands. (**a**) Representative DSF data of a chemoreceptor LBD in the absence and presence of bound ligand. (**b**) T_m variations observed for the screen of McpH-LBD with compounds form the Biolog plate PM3 containing different bacterial nitrogen sources. Modified versions of Figures published in [19, 23]

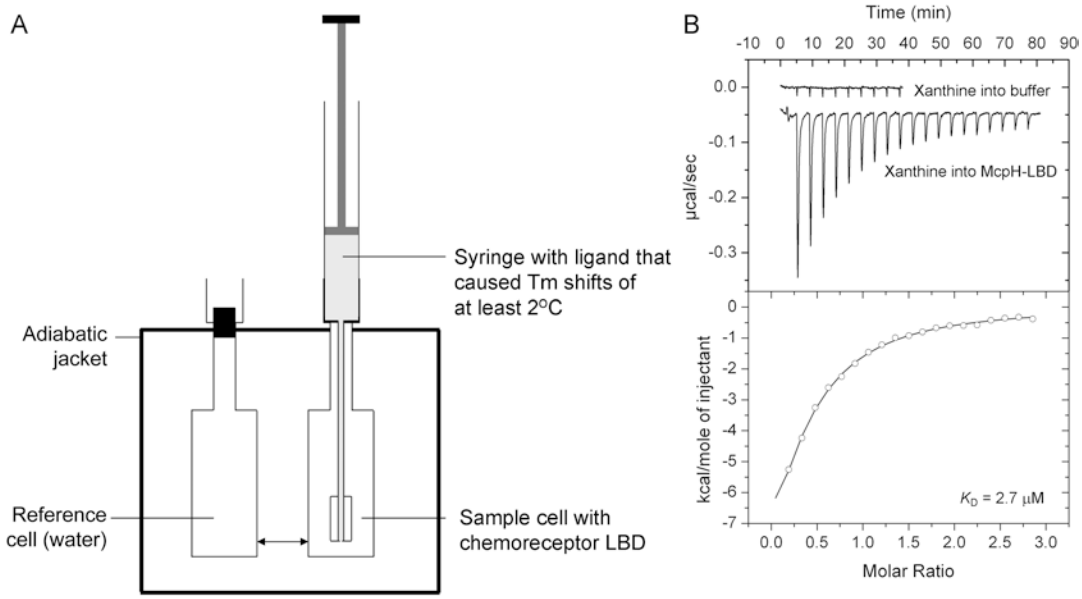

Fig. 2 The use of Isothermal Titration Calorimetry (ITC) to verify hits from DSF-based ligand screens. (**a**) Schematic drawing of an adiabatic microcalorimeter. Modified version of Figure from [24] (**b**) Titration of 10.4 µM McpH-LBD with 4.8 µL aliquots of 439 µM xanthine. Upper panel: Raw titration data. Lower panel: Dilution heat-corrected and concentration-normalized integrated peak areas of raw data. The continuous line shows the best fit with the "One binding site" model of the MicroCal version of ORIGIN

indicate exothermic heat changes that diminish as the protein becomes saturated with ligands. A curve fit of the corrected and integrated peak areas (lower panel in Fig. 2b) was used to determine a K_D of 2.7 µM. Microcalorimetric data provide definite proof of binding, and subsequent microbiological studies have shown that the McpH chemoreceptor indeed mediates attractant chemotaxis to the four purines labeled in Fig. 1b.

The detailed experimental protocol for this combined DSF-ITC approach is reported here. This approach was found to be very useful for the identification of novel chemoreceptor types, such as receptors that are specific to metabolizable purines [19], different polyamines [20], or α-ketoglutarate [21].

2 Materials

2.1 High-Throughput Thermal Shift Assay

1. Purified recombinant protein (*see* **Note 1**).
2. Compound collection to be screened (for example form BioLog Inc. or InterBioScreen Ltd.).
3. 96-well PCR plates (4titude Ltd.).
4. LightCycler 480 Sealing Foil (Roche Life Science).
5. SYPRO orange (Thermo Fisher Scientific).
6. Real-Time PCR instrument (BioRad).
7. Multi-channel and single-channel micropipettes.
8. Centrifuge Allegra X-22R (Beckman Coulter) or similar equipped with Rotor S2096, with swinging-bucket rotor for microtiter plates).

2.2 Isothermal Titration Calorimetry

1. Microcalorimeter.
2. Apparatus for sample degassing.
3. 2 mL loading syringe with 20 cm-long needle.
4. Two 10 mL plastic syringes and sterile filter units.
5. Sample cell ligand (2 mL): Purified recombinant LBD, dialyzed into a physiological buffer, as for its oligomeric state please (*see* **Note 1**).
6. Syringe ligand (0.5 mL): Ligand identified in thermal-shift assays, dissolved in protein dialysis buffer.
7. Buffer for protein dialysis (50 mL).

3 Methods

3.1 Preparation of the Screen Plate and Recording of Unfolding Curves for the High-Throughput Thermal-Shift Assay

1. Dissolve the compounds to be screened in Milli-Q water to a final concentration of 10–20 mM. In the case of the Biolog plates, this can be done by transferring water with a multichannel pipette to the wells of the plate (*see* **Note 2**).
2. To help compound dissolution, place the plate on an orbital shaker for 20 min.

3. Take a new 96-well PCR plate (screen plate) and add 2.5 µL aliquots of compound solutions to the individual wells. To one well (control, no ligand) add the same amount of water instead.
4. Dilute 3 µL of SYPRO orange (5000×) into 237 µL of Milli-Q water and mix (*see* **Note 3**).
5. Add 2 µL of diluted SYPRO and 20.5 µL of purified protein (15–100 µM, according to its oligomeric state; *see* **Note 1**) to each well of the screen plate.
6. Cover the plate with LightCycler 480 Sealing Foil. Make sure that the foil seals each of the wells.
7. Introduce plates into a centrifuge equipped with a swinging-bucket rotor for microtiter plates and centrifuge for 10 s at 1000 × *g*.
8. Introduce the plate into a Real-Time PCR instrument.
9. Open the corresponding software and set up the program for the determination of a "melting curve" (*see* **Note 4**).
10. For program setup using the Bio-Rad iQ5 software, do the following:
    (a) Open software and click on "Protocol", then on "Create new."
    (b) In the lower part of the screen, click on "insert," introduce "1" into "cycle" and "repeats."
    (c) Define "Step 1": specify "3 min" as dwell time and "23 °C" as setpoint.
    (d) In the line below, put "2" into "cycle," then define "Step 1": specify "11 s" as dwell time and "23 °C" as set point, then select "Melt Curve" on the same line, introduce "0.5 °C" into "temperature change" and "95 °C" into "end temperature."
    (e) Click on "Save and Exit Protocol Editing."
    (f) In the main menu click on "Plate," then on "Create New" in the "Select Plate Setup" window.
    (g) Click on "Unkn" and select all wells by clicking on the upper-left square of the grid and dragging the cursor across the grid.
    (h) Make sure that the correct fluorophore (for example "SYBR") is selected in the window "Probe/Primer."
    (i) Select: "25" in window "Sample volume," then "Film" in the window "Seal type" and "Plates" in the window "Vessel type."
    (j) Click on "Save and Exit Plate Editing."
    (k) Click on "Run" to start.

3.2 Data Analysis for Thermal-Shift Assay

1. Open the resulting data file (file.opd) and click on "analyze." "Melt Curve Charts" are shown on the left, and "Melt Peak Charts" are on the right. Inspect the melt curves and look for displaced melt peaks (*see* **Note 5**).
2. Click on "display wells," deselect the grid by clicking on the blue square at the upper-left corner of the grid, then select (by clicking) the well that did not contain ligand (control) and the wells you wish to analyze (those with displaced melt peaks).
3. Click "Apply," then "OK." The program now displays the results of the selected wells.
4. Examine the graphic results and derive the Tm, which is the temperature that corresponds to the minimal d(RFU)/dT in the data display.
5. The numerical data sheet is displayed on the lower part of the screen. Click on the square at the left corner of the table to select it. Click on "Export to Excel" for further analyses, if required.

3.3 Sample Preparation for Isothermal Titration Calorimetry

1. Ligands are selected that caused Tm changes of more than 2 °C in the thermal-shift assays. To minimize dilution heats in an ITC experiment, the protein and the ligand must be in the same buffer. The most straightforward way is to dialyze the protein into a physiological buffer and to use the dialysis buffer to make up the ligand solution. For pH and solubility issues (*see* **Notes 6** and **7**).
2. Prior to the experiment, the protein and ligand samples are filtered using 0.22 μm cut-off filters and degassed for around 5 min. For volatile and hydrophobic compounds (*see* **Note 8**).
3. The protein concentration is determined precisely using either colorimetric or spectroscopic assays.

3.4 Determining the Ligand-into-Buffer Dilution Control

1. Switch on the instrument 1 h before use and set the analysis temperature.
2. Make sure that ligands are at a temperature slightly below the analysis temperature. Using the loading syringe, fill the sample cell with buffer, close, and equilibrate for 10 min. Avoid the introduction of air bubbles during filling of the sample cell.
3. Fill the injector syringe with ligand. Close the loading port of the syringe, briefly dry the outside of the injector syringe needle with a paper towel, and insert the injector syringe into the instrument. Equilibrate for 5 min.
4. In the meantime, set the following parameters in the VPviewer software (for Microcal instruments): reference power, 10 μcal/s; initial delay, 60 s (time from the beginning of the experiment to the first injection); stirring speed of injector,

300 rpm; feedback mode/gain, "high"; ITC equilibration options, activate "No check temperature" and "Fast equilibration"; injection parameters, define volume of injections, 3–15 μL; set speed of injection, 0.5 μL/s; time between injections, 240 s; filter period, 2 s (a data point is recorded every 2 s).

5. Start the titration and assess the data. If the peaks observed are small (below 0.1 μcal/s, ideally around 0.01–0.02 μcal/s) proceed. In the case peaks are large and not uniform, dilute the ligand in the syringe and repeat the control experiment. In the case that the signal measured is noisy, it is recommended to clean the instrument (*see* **Note 9**), after which another ligand-into-buffer control experiment is performed.

3.5 The Protein-Ligand Titration Experiment

1. Use the loading syringe to rinse the sample cell thoroughly with buffer. Make sure that there is no buffer left in the sample cell.
2. Load the protein into the sample cell with the loading syringe, close the instrument, and equilibrate for 10 min.
3. Fill the injector syringe with ligand. Close the loading port of the syringe, briefly dry the outside of the injector syringe with a paper towel, and insert the injector syringe into the instrument. Equilibrate for 5 min.
4. Start the experiment using the same experimental settings as for the ligand dilution control.

3.6 Analysis of the ITC Data

Using the MicroCal version of ORIGIN proceed with the data analysis. The detailed steps of data analysis are provided in the manual. Briefly, data analysis consists of the following steps.

1. Open the raw data for the control and the actual titration experiments and create two individual project files.
2. Normalize the data by the introduction of the exact concentrations for both ligands.
3. Manually optimize the automatically created baseline to assure optimal peak integration.
4. Correct the titration data by subtracting control data.
5. Curve fit to generate thermodynamic parameters.

3.7 Trouble-Shooting an ITC Experiment

1. Problem: sample cell ligand not saturated at the end of the titration: To obtain high-quality data, the sample cell ligand needs to be saturated during an experiment. The saturation of a macromolecule with a ligand is determined by their affinity and the protein sample concentration. If protein saturation has not been achieved, the experiment should be repeated with a higher syringe ligand concentration.

2. Problem: no, or very weak, heat signals. The magnitude of heats observed is a function of the analysis temperature. At a certain analysis temperature, exothermic and endothermic contributions cancel each other out, resulting in no net heat changes. Therefore, to conclude that a ligand does not bind, the experiment has to be repeated at a second analysis temperature. Only in the case that no heat changes are measured in experiments conducted at two different analysis temperatures can it be concluded that there is no binding. In general, an increase in the analysis temperature favors exothermic signals, whereas a reduction in the analysis temperature favors endothermic signals. If the heat signals are weak, the experiment should also be repeated at a different temperature to increase the signal.
3. Problem: optimizing the signal-to-noise ratio. In an optimal ITC experiment, there is a balance between signal magnitude and the number of peaks. In general, some 20 data points are sufficient to determine binding parameters precisely. Suboptimal data are characterized by a large number of small peaks, which when integrated generate a significant error, or by a small number of large peaks, which will result in an increased error during the curve fitting process. The size and number of peaks depends, among other factors, on the concentrations of ligands as well as the injection volumes. To optimize an ITC experiment, the experiment can be repeated with different ligand concentrations and/or injection volumes.

4 Notes

1. The 4-helix bundle and the HBM domain need to be dimeric for ligand recognition. This is because their ligand binding sites are at the dimer interface such that amino acids from both monomers of the dimer make contacts with the ligand. If the protein to be analyzed is of this domain type, experiments need to be conducted (analytical ultracentrifugation, gel filtration) to verify that at least a fraction of the protein is present as dimer. This issue was central in the study of the CtpH (4HB) [14] and McpS/McpQ (HBM) chemoreceptors [22]. If the protein is monomeric the sample should be concentrated, which will shift the equilibrium to the dimeric state.
2. For Biolog Phenotype Microarray plates, compounds were dissolved in 50 μL of Milli-Q water, which, according to the manufacturer, results in compound concentrations between 10 and 20 mM. After the transfer of 2.5 μL ligand aliquots to the screen plate, the Biolog plates can be sealed with Sealing Foil and stored at −20 °C for further use.

3. Diluted SYPRO Orange cannot be stored for more than 1 day.
4. Typically, a linear temperature gradient is applied ranging from 23 to 85–95 °C, with a step size of 0.5 °C.
5. In some cases the recombinant LBDs do not fold or are unstable. Unfolded proteins can be easily identified by inspecting melt curves; there is no unfolding transition and the initial fluorescence readings at the onset of the experiment are unusually high (fluorescent dye is already bound to the unfolded protein). Such proteins cannot be used for screening and, in our hands, changing the solvent to stabilize the protein structure was unsuccessful.
6. If the ligand is pH active, when it dissolves in buffer it will alter the pH. As a consequence, the pH of the protein solution and the ligand sample differ, and in an ITC titration the resulting heats from buffer protonation/deprotonation mask binding heats. Therefore, the pH of the ligand solution has to be adjusted to that of the protein by the addition of either concentrated acid or base.
7. If the ligand has low solubility, a ligand stock solution in DMSO can be prepared, which is then diluted tenfold in dialysis buffer. It is important to add 10% (v/v) of DMSO to the protein to be titrated. In general, buffer systems containing 10% DMSO cause some alterations in protein stability and binding parameters but still permit the analysis of compounds that are poorly soluble in water.
8. Some compounds, particularly hydrocarbons, are volatile and tend to stick to plastic surfaces. To control their concentration, the filter and degas steps are omitted from the sample preparation. To prevent sticking to plastic surfaces, the samples are made up in glass vessels.
9. The reason for noisy data is in 99% of the instances because of insufficient cleaning of the instrument. The frequency at which the instrument should be cleaned depends, among other factors, on the propensity of ligands to precipitate or to attach to surfaces. However, it is recommended to clean the instrument at least once a week, following the manufacturer's instructions. The sample compartments need to be rinsed extensively with water following cleaning. The best way to determine the state of cleanliness of an instrument is to perform a titration of water with water.

Acknowledgment

We acknowledge financial support from FEDER funds and Fondo Social Europeo through grants from the Junta de Andalucía (grant

CVI-7335) and the Spanish Ministry for Economy and Competitiveness (grants BIO2013-42297 and BIO2016-76779-P).

References

1. Wuichet K, Zhulin IB (2010) Origins and diversification of a complex signal transduction system in prokaryotes. Sci Signal 3:ra50
2. Parkinson JS, Hazelbauer GL, Falke JJ (2015) Signaling and sensory adaptation in *Escherichia coli* chemoreceptors: 2015 update. Trends Microbiol 23:257–266
3. Lacal J, Garcia-Fontana C, Munoz-Martinez F, Ramos JL, Krell T (2010) Sensing of environmental signals: classification of chemoreceptors according to the size of their ligand binding regions. Environ Microbiol 12:2873–2884
4. Kaneko T, Minamisawa K, Isawa T, Nakatsukasa H, Mitsui H et al (2010) Complete genomic structure of the cultivated rice endophyte *Azospirillum* sp. B510. DNA Res 17:37–50
5. Parales RE, Luu RA, Chen GY, Liu X, Wu V et al (2013) *Pseudomonas putida* F1 has multiple chemoreceptors with overlapping specificity for organic acids. Microbiology 159:1086–1096
6. Alvarez-Ortega C, Harwood CS (2007) Identification of a malate chemoreceptor in *Pseudomonas aeruginosa* by screening for chemotaxis defects in an energy taxis-deficient mutant. Appl Environ Microbiol 73:7793–7795
7. Milligan DL, Koshland DE Jr (1993) Purification and characterization of the periplasmic domain of the aspartate chemoreceptor. J Biol Chem 268:19991–19997
8. Ni B, Huang Z, Wu YF, W, Fan Z, Jiang CY et al (2015) A novel chemoreceptor MCP2983 from *Comamonas testosteroni* specifically binds to cis-aconitate and triggers chemotaxis towards diverse organic compounds. Appl Microbiol Biotechnol 99:2773–2781
9. Garcia V, Reyes-Darias JA, Martin-Mora D, Morel B, Matilla MA et al (2015) Identification of a chemoreceptor for C2 and C3 carboxylic acids. Appl Environ Microbiol 81:5449–5457
10. Goers Sweeney E, Henderson JN, Goers J, Wreden C, Hicks KG et al (2012) Structure and proposed mechanism for the pH-sensing *Helicobacter pylori* chemoreceptor TlpB. Structure 20:1177–1188
11. Glekas GD, Mulhern BJ, Kroc A, Duelfer KA, Lei V et al (2012) The *Bacillus subtilis* chemoreceptor McpC senses multiple ligands using two discrete mechanisms. J Biol Chem 287:39412–39418
12. Nishiyama S, Takahashi Y, Yamamoto K, Suzuki D, Itoh Y et al (2016) Identification of a *Vibrio cholerae* chemoreceptor that senses taurine and amino acids as attractants. Sci Rep 6:20866
13. Lacal J, Alfonso C, Liu X, Parales R, Morel B et al (2010) Identification of a chemoreceptor for tricarboxylic acid cycle intermediates: differential chemotactic response towards receptor ligands. J Biol Chem 285:23126–23136
14. Rico-Jimenez M, Reyes-Darias JA, Ortega A, Diez Pena AI, Morel B et al (2016) Two different mechanisms mediate chemotaxis to inorganic phosphate in *Pseudomonas aeruginosa*. Sci Rep 6:28967
15. Krell T (2008) Microcalorimetry: a response to challenges in modern biotechnology. Microb Biotechnol 1:126–136
16. McKellar JL, Minnell JJ, Gerth ML (2015) A high-throughput screen for ligand binding reveals the specificities of three amino acid chemoreceptors from *Pseudomonas syringae* pv. actinidiae. Mol Microbiol 96:694–707
17. Niesen FH, Berglund H, Vedadi M (2007) The use of differential scanning fluorimetry to detect ligand interactions that promote protein stability. Nat Protoc 2:2212–2221
18. Krell T (2015) Tackling the bottleneck in bacterial signal transduction research: high-throughput identification of signal molecules. Mol Microbiol 96:685–688
19. Fernandez M, Morel B, Corral-Lugo A, Krell T (2016) Identification of a chemoreceptor that specifically mediates chemotaxis toward metabolizable purine derivatives. Mol Microbiol 99:34–42
20. Corral-Lugo A, de la Torre J, Matilla MA, Fernandez M, Morel B et al (2016) Assessment of the contribution of chemoreceptor-based signaling to biofilm formation. Environ Microbiol 18:3355–3372
21. Martín-Mora D, Ortega A, Reyes-Darias JA, García V, López-Farfán D et al (2016) Identification of a chemoreceptor in *Pseudomonas aeruginosa* that specifically mediates chemotaxis towards alpha-ketoglutarate. Front Microbiol 7:1937

22. Martin-Mora D, Reyes-Darias JA, Ortega A, Corral-Lugo A, Matilla MA et al (2016) McpQ is a specific citrate chemoreceptor that responds preferentially to citrate/metal ion complexes. Environ Microbiol 18:3284–3295
23. Fernández M, Morel B, Corral-Lugo A, Rico-Jiménez M, Martín-Mora D et al (2016) Identification of ligands for bacterial sensor proteins. Curr Genet 62:143–147
24. Krell T, Lacal J, Garcia-Fontana C, Silva-Jimenez H, Rico-Jimenez M et al (2014) Characterization of molecular interactions using isothermal titration calorimetry. Methods Mol Biol 1149:193–203

Chapter 24

Identification of Specific Ligands for Sensory Receptors by Small-Molecule Ligand Arrays and Surface Plasmon Resonance

Christopher J. Day and Victoria Korolik

Abstract

Ligand–receptor interactions triggering signal transduction components of many sensory pathways, remain elusive due to paucity of high-throughput screening methods. Here we describe our use of small molecule microarrays comprising of small glycans, amino and organic acids, salts, and other known chemoeffectors, for screening of ligands specific to various sensory receptors, followed by surface plasmon resonance to verify the veracity and to determine the affinity constants of the interactions. This methodology allows for rapid and identification of the direct ligand binding between the sensory receptors and their specific ligands.

Key words Amino acids, Salts of organic acids, High-throughput screening, Methyl-accepting chemotaxis proteins, Transducer-like proteins

1 Introduction

For many motile organisms, the chemotaxis effectors are commonly identified by hard plug assays (HAP) or capillary chemotaxis assays, following targeted mutants or of transposon mutant libraries or by selecting mutants that showed no taxis in the presence of specific ligands [1–4], while affinity measurements of interactions were traditionally done using radiometric methodologies [5].

Recent developments of a variety of array platforms allow for production of protein and glycan arrays through the use of chemically reactive substrates including amine, epoxide, NHS, hydroxyl, gold, and avidin. Using epoxide functionalized slides we first used amino acids as an array format with the primary amine groups being reactive with the epoxide surface [6]. We have used this methodology to identify the aspartate receptor of *Campylobacter jejuni*, CcaA [6]. With this as a proven technology, extra chemotactic chemicals were added, as epoxide will react from amine groups through to hydroxyl groups. This enabled sugars

Michael D. Manson (ed.), *Bacterial Chemosensing: Methods and Protocols*, Methods in Molecular Biology, vol. 1729, https://doi.org/10.1007/978-1-4939-7577-8_24,

and salts of organic acids to be added to the array, leading to the discovery of the multiple ligands of CcmL, the multiligand receptor of *C. jejuni* [7] and the first know glycan binding dCache_1 receptor domain specific for galactose, CcrG [8].

The array data was verified by the use of surface plasmon resonance (SPR) which allows measurements of the affinity of an interaction between proteins and a ligand as small as 100 Da.

This chapter describes in detail the protocols to screen chemotaxis receptors with high-throughput technologies and verify the interactions with SPR.

2 Materials

All solutions are prepared using deionized water and analytical grade reagents followed by filtration using a 0.22 μm bottle top or syringe filter. All buffers for SPR analysis are also degassed prior to use. The materials are stored at room temperature unless otherwise stated.

2.1 Buffers, Solutions and Reagents for Array Analysis

1. Assay buffer: Phosphate buffered saline pH 7.4; 8 g NaCl, 0.2 g KCl, 1.44 g Na_2HPO_4, and 0.24 g KH_2PO_4 dissolved in 1 L of Milli-Q water and the pH adjusted to 7.4 with HCl.
2. Wash buffer: Phosphate buffered saline pH 7.4 with 0.05% Tween 20.
3. Blocking buffer: Phosphate buffered saline pH 7.4 with 1% bovine serum albumin.
4. Amino acids: *See* Table 1 for full list and source. Prepared as 100 mM stocks in either PBS or Milli-Q water. 10 M NaOH or 10 M HCl may be added in incremental steps to improve solubility as indicated.
5. Salts of organic acids: *See* Table 1 for full list and source. Prepared as 100 mM stocks in either PBS or Milli-Q water. 10 M NaOH or 10 M HCl may be added in incremental steps to improve solubility as indicated in Table 1. (Simple and complex glycan compounds can also be printed, as described in ref. 9.)
6. Monosaccharides: *See* Table 1 for full list and source. Prepared as 100 mM stocks in either PBS or Milli-Q water. All monosaccharides are soluble without pH adjustment.
7. Arrayit Superepoxy III glass substrates.
8. Arrayit Spotbot Extreme Printing Robot.
9. 0.22 μm filtered deionized water.
10. 50 mL centrifuge tubes (sterile).
11. 1.5 mL centrifuge tubes (autoclaved).

Table 1
Printed chemotaxis ligands

Compounds for printing	Soluble Water/PBS	Company and Cat#
Alanine	Yes	Sigma-Aldrich A7469
Arginine	No - Add NaOH	Sigma-Aldrich A8094
Asparagine	No - Add NaOH	Sigma-Aldrich A4159
Aspartic acid	No - Add NaOH	Sigma-Aldrich A7219
Aspartic acid potassium salt	Yes	Sigma-Aldrich 11230
Aspartic acid sodium salt	Yes	Sigma-Aldrich 11195
Cysteine	No - Add HCl	Sigma-Aldrich C7352
Cysteine-HCl	Yes	Sigma-Aldrich C6852
Fucose	Yes	Sigma-Aldrich F2252
Fumaric acid	No - Add NaOH	Sigma-Aldrich F8509
Sodium Fumarate	Yes	Sigma-Aldrich F1506
Galactose	Yes	Sigma-Aldrich G5388
Glucosamine	Yes	Sigma-Aldrich G1514
Glucose	Yes	Sigma-Aldrich G7021
Glutamic acid	No - Add NaOH	Sigma-Aldrich G1251
Sodium glutamate	Yes	Sigma-Aldrich 49621
Glutamine	No - Add NaOH	Sigma-Aldrich G3126
Glycine	Yes	Sigma-Aldrich G7126
Histidine	Yes	Sigma-Aldrich H6034
Isoleucine	No - Add NaOH	Sigma-Aldrich I2752
Leucine	No - Add NaOH	Sigma-Aldrich 61819
Lysine	Yes	Sigma-Aldrich 62840
Malic acid	No - Add NaOH	Sigma-Aldrich M7397
Sodium malate	Yes	Sigma-Aldrich M1125
Methionine	Yes	Sigma-Aldrich M5308
Phenylalanine	No - Add NaOH	Sigma-Aldrich P2126
Proline	No - Add NaOH	Sigma-Aldrich 81709
Purine	Yes	Sigma-Aldrich P55805
Ribose	Yes	Sigma-Aldrich R9629
Serine	Yes	Sigma-Aldrich 84959

(continued)

Table 1
(continued)

Compounds for printing	Soluble Water/PBS	Company and Cat#
Succinic acid	No - Add NaOH	Sigma-Aldrich S9512
Sodium succinate	Yes	Sigma-Aldrich 224731
Thiamine	Yes	Sigma-Aldrich T4625
Threonine	No - Add NaOH	Sigma-Aldrich T8625
Tryptophan	No - Add NaOH	Sigma-Aldrich T0254
Tyrosine	No - Add NaOH	Sigma-Aldrich 93829
Valine	No - Add NaOH	Sigma-Aldrich 94619
α-Ketoglutaric acid	No - Add NaOH	Sigma-Aldrich K1128
α-Ketoglutaric acid (sodium salt)	Yes	Sigma-Aldrich K2010

12. Thermo Scientific 65 µL gene frames (AB-0577).
13. A slide scanner capable of scanning to at least 10 µM resolution and preferentially at least three channels of color including 488, 555, and 647 nm lasers. For the assays below an Innopsys InoScan 1100AL was used.

2.2 SPR Using Nickel Affinity (NTA) Sensor Chips

1. Series S NTA sensor chip for Biacore T100/T200/S200.
2. Assay Buffer: Phosphate buffered saline pH 7.4; 8 g NaCl, 0.2 g KCl, 1.44 g Na_2HPO_4, and 0.24 g KH_2PO_4 dissolved in 1 L of Milli-Q water and the pH adjusted to 7.4 with HCl.
3. 100 mM nickel chloride.
4. 100 mM nickel sulfate.
5. 50 mM NaOH.
6. EDTA regeneration buffer: 1× HBS-EP (1:10 dilution in Milli-Q water of 10× HBS-EP purchased from GE) with addition of 300 mM EDTA.
7. Purified His-Tagged MCP/Tlp protein at 100 µg/mL minimum concentration.
8. A control His-tagged protein that does not interact with the compounds to be tested at 100 µg/mL minimum concentration (*see* **Note 1**).
9. 1.5 mL, 650 µL tubes, 96-well plates and plate seals.
10. Biacore T100/T200/S200.

2.3 SPR Using Amine Coupling (CM5) Sensor Chips

1. Series S CM5 sensor chip for Biacore T100/T200/S200.
2. 10 mM sodium acetate solutions pH ranging from 3.0 to 5.5 in 0.5 pH increments.
3. Assay Buffer: Phosphate buffered saline pH 7.4; 8 g NaCl, 0.2 g KCl, 1.44 g Na_2HPO_4, and 0.24 g KH_2PO_4 dissolved in 1 L of MilliQ water and the pH adjusted to 7.4 with HCl. The supplied 1× Hepes buffered saline with 0.1% Tween 20 (1× HBS EP+, GE) can also be utilized as an assay buffer and can be better to test amino acids that have divergent pH due to solubility issues.
4. 50 mM NaOH.
5. Amine coupling kit (e.g., GE Biacore) containing EDC/NHS and ethanolamine.
6. Purified chemotaxis protein at 200 μg/mL minimum concentration.
7. 1.5 mL, 650 μL tubes, 96 well plates and plate seals.
8. Biacore T100/T200/S200.

3 Methods

3.1 Array Printing

Set up the printing method within the Spocle Generator program (array method generating software from ArrayIt):

1. Set the settings for a single 384 well plate (*see* **Note 2**).
2. Set the settings for the use of capillary metal pins 6 (946MP6; *see* **Note 3**) from ArrayIt in a 3 column-by-2 row format.
3. Set number of slides to be printed.
4. Enter a setting for 10 preprint spots with a contact time of 0 s.
5. Between 4 and 10 printed spots with a contact time of 0.5 s.
6. Set up each pin grid as a 16 × 16 or 20 × 20 grid depending on print spots per sample.
7. Set a spot-to-spot distance to 300 μm in each direction.
8. Set array printer to reload pins from source plate after every 50 spots.
9. Use default wash parameters.
10. Use Spocle Generator program to generate three subarray prints spaced as follows:

    Subarray 1: First spot at 6 mm from top of slide 6 mm from side of slide

    Subarray 2: First spot at 30 mm from top of slide 6 mm from side of slide.

Subarray 3: First spot at 54 mm from top of slide 6 mm from side of slide.

11. Save files you have generated, ensuring you have selected all files to be saved, including check boxes to ensure map files are saved.
12. Generate a .gal file using Gal-file generator program by browsing and selecting files from your array folder and load the methods file, plate file and map file into the boxes available.
13. Ensure environment in the printer is between 40% and 60% relative humidity and chilled to at least 10 °C.
14. Lay substrates out as per methodology design with one slide for preprint spots (as described above).
15. Insert printing pins, capillary metal pins 6 (946MP6) from ArrayIt (as described above).
16. Insert the source plate.
17. Run the print program within SpotApp.
18. Allow the slides to dry on the printer for at least 2 h after the print run has finished and allow the slides to sit at 4 °C overnight to complete the sample–substrate chemical interaction.
19. Scan the slide with 488 nm/555 nm/647 nm at 10 μm resolution after overnight at 4 °C to ascertain if all spots printed. Check with generated .gal file.
20. Neutralize the slide by immersing in cold Blocking buffer for 2 h at 4 °C.
21. Rinse in 1× PBS and dry in a 50 mL tube spun at 500 × *g*.
22. Rescan the slide with 488 nm/555 nm/647 nm at 10 μm resolution to check if all spots have ceased to autofluoresce (*see* **Note 4**).
23. Store slides at 4 °C for a maximum of 3 months.

3.2 Array Assay of a Purified Protein (see Note 5)

1. Add 1–2 μg of purified, His, Gs or similarly tagged protein, at maximum volume of 30 μL, to a 1.5 mL centrifuge tube.
2. Add equal molar concentration of anti-tag antibody (*see* **Notes 6** and **7**).
3. Signal amplification can be used to identify binding in the arrays. In that case, use of a labeled secondary and tertiary antibody is recommended with fluorophores such as Alexa488, 555 or 647 (such as Alexa Fluor® 488 Signal-Amplification Kit for Mouse Antibodies A-11054 from Thermo Fisher Scientific). Secondary antibody is added at ½ the concentration (mg/mL) of primary antibody, and tertiary antibody (mg/mL) is added at ½ the concentration of secondary antibody. For example, if 6 μg of primary antibody is added, than

3 μg of secondary and 1.5 μg of tertiary are added. Make up to a final volume to 70 μL with Assay buffer. Incubate the tube at room temperature in the dark for 15 min.

4. Apply gene frames to the slide, starting with the first gene frame on the top left hand corner (right top hand corner of slide is notched). Second gene frame lines up (blue to blue) with the bottom of the first gene frame on the very left hand side of the slide. The bottom gene frame lines up on the very left hand edge and with the bottom of the second gene frame (blue to blue; s*ee* **Note 8**).
5. If the antibodies have not previously been used on an array of this type, an antibody-only control will have to be performed. Set up a second tube containing only assay buffer and the antibodies at the same concentrations used in the described experiment.
6. Prepare three of the gene frame coverslips and put to one side.
7. Add 70 μL of the protein–antibody mix to one gene frame area of the slide at a time. Pipette the 70 μL of protein–antibody mix into the bottom corner and quickly put on the coverslip. Use the coverslip to move the solution across the gene frame area and try to avoid bubbles. A small amount of liquid should come out of the gene frame area.
8. Repeat the above until all three areas on the slide are filled with protein–antibody mix under a coverslip and incubate in the dark at room temperature for 15 min.
9. Remove coverslips and gene frames in a pipette box lid under 0.5 cm of Assay buffer to ensure the slide does not dry out.
10. Prepare four 50 mL centrifuge tubes containing either 45 mL of Wash buffer (three tubes) or 45 mL of Assay buffer (one tube).
11. Transfer array from pipette box lid to the first tube of wash buffer and wash for 2 min with slow inversion of the tube.
12. Repeat the washing step of the array with remaining two tubes of wash buffer (total wash time, 6 min).
13. Rinse in tube containing assay buffer and transfer to empty 50 mL centrifuge tube. Dry by centrifuging at 500 × *g* for 5 min.
14. Scan slide at the emission wavelength of the fluorescent labels on the antibodies used with the scanner set at 10 μm resolution.
15. Analyze using scanner array analysis software or freeware software available from internet and load the .gal file over image. For example, the Mapix acquisition and analysis software pack-

age (Innopsys), ScanArray software from PerkinElmer, or freeware Spotfinder program from TIGR.

16. Positive interaction is identified as a visible group of spots that is significantly more fluorescent than the slide background and was not autofluorescent on the postneutralization scan or did not come up with antibody only control (Fig. 1).

3.3 SPR Using a His-Tagged Protein on an NTA Chip

1. Ensure that the NTA chip is at room temperature and dry before inserting into Biacore.
2. Methodology setup for SPR using Biacore T100/T200/S200:
3. Buffer A is Assay Buffer (1× PBS).
4. Temperature is set to 25 °C.
5. Set concentration of analytes to μM.
6. Use multichannel detection rather than single or dual detection setting from the drop down menu.
7. Set for 10 Hz recording rather than 1 Hz.
8. Set up one cycle with the sample and link it to cycle_1.
9. Cycle_1 contains the following steps:

   Regeneration: Regeneration buffer (EDTA buffer), contact time 30 s, flow rate 30 μL/min. Check extra wash box and use H_2O and check stabilization box with a time of 60 s.

   Enhancement: Nickel solution (1:1 mix of $NiCl_2$ and $NiSO_4$; *see* **Note 9**). Contact time 30 s, flow rate 30 μL/min.

   Capture 1: Flow cell 1 only captures nonbinding tagged protein. Contact time 180 s, flow rate 10 μL/min.

   Capture 2: Flow cell 2 only captures tagged Tlp protein. Contact time 180 s, flow rate 10 μL/min.

   Capture 3: Flow cell 3 can be used to capture a second protein, or to do another capture on the original protein, if only one is being tested. Contact time 180 s, flow rate 10 μL/min.

   Capture 4: Flow cell 4 only can capture a third tagged protein, be used for a second capture of the second protein, or be used for a third capture if there is only one protein being tested. Contact time 180 s, flow rate 10 μL/min. (If only capturing 1 protein, make Capture 3 to flow cells 3 and 4 and skip Capture 4).

   Sample: Single cycle kinetics, flow rate of 30 μL/min. Contact time of 60 s and disassociation time of 600 s.

   Regeneration 2: Regeneration buffer (EDTA buffer), contact time 30 s, flow rate 30 μL/min.

Regeneration 3: 50 mM NaOH, contact time 30 s, flow rate 30 μL/min. Check extra wash box and use H_2O and check stabilization box with a time of 60 s.

10. Set up each analyte with two rows in the spreadsheet table display.

    Row 1: 5 times the zero concentration, as nonbinding control. These tubes should only contain the Assay buffer.

    Row 2: Dilution series. On first run set up a 1:5 dilution series 0.8 μM, 4 μM, 20 μM, 100 μM and 500 μM. Once a concentration range is known, then subsequent runs can use a 1:2 dilution series around the saturation point.

    A total of 9 analytes can be tested in Biacore tubes or 16 analytes can be tested using a 96-well plate.

11. Set up the tubes and/or plates for analytes and samples using the rack positions obtained from the method. Ensure that the same Assay buffer is used to prepare dilutions that are being used as the running buffer in buffer line A of the Biacore machine.

12. Ensure that the amino acids or salts that require HCl or NaOH to dissolve are adjusted to pH 7.4 when they are diluted into the Assay buffer. Highly basic or acidic solutions may damage your protein or remove it from the chip surface. If suitable pH cannot be achieved in PBS, use HBS EP+ buffer.

13. Analyze using the Biacore evaluation software.

3.4 SPR Using a Purified Protein Immobilized on a CM5 Sensor Chip

1. Ensure that the CM5 chip is at room temperature and dry before inserting into Biacore.

2. Methodology for Immobilization of protein to Biacore sensor chips using Biacore T100/T200/S200 is as follows:

    Set up pH scout of protein. To get the protein to react with the chip surface, it first has to make contact through a charge-based interaction. The pH scout allows you to identify the optimal pH for this to occur.

    Calculate the isoelectric point (pI) of your protein (*see* **Note 10**).

    Use the pH scout Wizard template.

    For proteins with pI ranges above pH 6.0, test the pH scout at pH 5.5, 5.0, 4.5, 4.0. For pI below 6.0 adjust the pH range to start at the pI and go down, ensuring that the pH scout does not drop below pH 2.5.

    Prepare a solution of your protein with at least a 1:2 dilution into 10 mM sodium acetate at the pHs to be tested so that the protein is at a final concentration of 100 μg/mL.

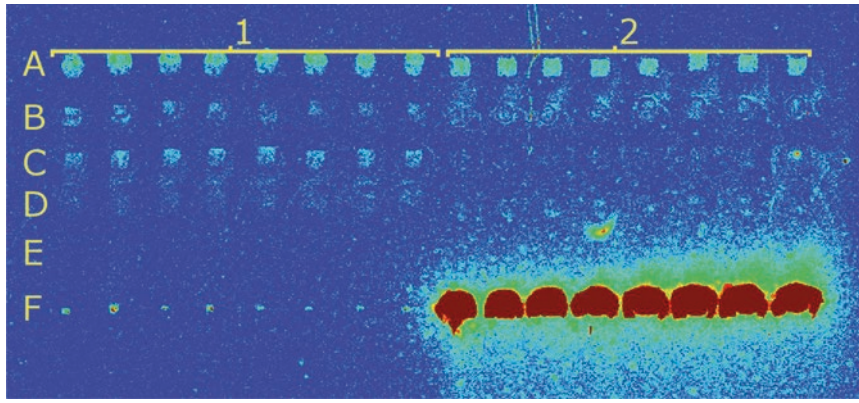

Fig. 1 Chemotaxis Array result. A–F represent the rows of the print with spots present, 1–2 represent the columns with each ligand being printed in eight replicate spots. F2 are printed control spots and do not indicate binding. A1 and A2 represents clear positive binding, whereas B1, B2 C1 and F1 represent less clear-cut binding that would have to be subjected to statistical analysis against the average background

The higher the concentration of the protein, the better for getting reliable pH scout results, because the dilution into sodium acetate will approach the stated pH.

Follow the Wizard template for setup.

The best pH to use is the highest pH that provides a strong interaction between the chip surface and the protein.

3. Immobilization of protein to CM5 chip.

   Select amine coupling from the list of coupling options.

   Check blank immobilization for flow cell 1.

   For test protein, check the box for the flow cell to be used, and select time based immobilization. Immobilize for 600 s at a flow rate of 10 μL/min. This should capture between 3000 and 10,000 RU of protein.

   Set up the protein exactly as determined in the pH scout with the optimal pH used.

   Follow the wizard setup.

4. Set up a Biacore run to screen for interactions as follows

   Select buffer line A as your Assay Buffer (1X PBS).

   Set temperature to 25 °C.

   Set concentration of analytes to μM.

   Use dual channel detection if analyzing one protein or multi-channel detection if testing more than one protein.

   Set for 10 Hz recording rather than 1 Hz.

Set up one cycle with the purpose to be sample and link it to cycle_1. Cycle_1 contains the following steps:

Sample: Single cycle kinetics, flow rate of 30 μL/min. Contact time of 60 s and disassociation time of 600 s.

Regeneration 1: Use a regeneration buffer that will cause minimum damage to your protein, such as the NaAc buffer used for immobilization. Contact time 120 s, flow rate 30 μL/min.

5. Set up each analyte with two rows in the table.

   Row 1: 5× zero concentration, as nonbinding control. This is just Assay buffer.

   Row 2: Dilution series. On first run set up a 1:5 dilution series 0.8 μM, 4 μM, 20 μM, 100 μM and 500 μM. Once a concentration range is known, then subsequent runs can use a 1:2 dilution around the saturation point.

   A total of 9 analytes can be tested in Biacore tubes or 16 analytes using a 96-well plate.

6. Set up using the rack positions obtained from the method. Ensure that the same Assay buffer is used to make up dilutions that are being used to run the machine.
7. Ensure that the amino acids and salts that required addition of HCl or NaOH for solubility are readjusted to pH 7.4 where possible when diluted to a 1 mM stock concentration in Assay buffer for Biacore analysis. Highly basic or acidic solutions may damage your protein or remove it from the chip surface. If suitable pH cannot be achieved in PBS, use HBS EP+ buffer.
8. Analyze using the Biacore evaluation software.

3.5 SPR Analysis Using the Biacore S200 ABA Function for Determining Competitive or Independent Binding Sites for Different Ligands

The ABA inject function is only available on the Biacore S200 model. This method can be used to determine competitive or independent binding of a protein that binds more than one ligand. We have recently identified proteins capable of binding multiple ligands (chemosensory proteins). The following methodology has been developed to compare multiple binding events.

1. Preparation of the chip is the same as for the CM5 assay above.
2. Analysis is performed using the specific ABA injection function. This is located within the methodology menu: Binding Assays; Fragment/LMW; Competition analysis using ABA inject and follow the Wizard set up steps.
3. The analysis requires running buffer (e.g., 1X PBS), and ligands A and B in running buffer at a concentration sufficient for saturation (*see* **Note 11**).

4. There are three injections in each assay: A followed by (A)B, followed by A again. The combinations below are required for testing:

   Running buffer alone in all three injections.

   Running buffer in first and third injection with ligand A in the middle injection.

   Running buffer in first and third injection with ligand B in the middle injection.

   Ligand A in all three injections.

   Ligand B in all three injections.

   Ligand A in first and third injection with ligand A and ligand B in the middle injection.

   Ligand B in first and third injection with ligand A and ligand B in the middle injection.

   Injections of Ligand A or B followed by ligand B or A respectively alone followed by ligand A or B again can also be performed once it has been determined that there is a direct competition between the ligands.

5. Analysis is done with the ABA injection analysis tool in the S200 Evaluation software package (for explanation of the outcomes, *see* **Note 12** and Table 2). This can be done with or without adjustment for molecular weight.

4 Notes

1. Typically, the best control for an NTA chip is a heat or chemically denatured version of the same His-tagged protein. However, denatured protein (we used Tlp proteins of *Campylobacter jejuni*) in all cases tested so far is not suitable as a control for Biacore because it loses solubility in assay buffers when it is denatured. Use of denatured protein will result in blockage of the flow cells and the need to replace the IFC within the Biacore.
2. Use either ArrayIt brand or Griener branded conical/V-bottom polypropylene 384-well plates.
3. 946MP6 pins were chosen, as these provide a 200 μm spot diameter, which is the preferred size when using a low density print. If you wish to increase print density, e.g., by printing more than 2400 spots per subarray then 946MP4 pins would be the preferred choice.
4. If the slide still contains high levels of autofluorescence, block for an additional hour in Blocking buffer and an hour in 1X PBS at 4 °C.

5. This protocol can be applied to glycan arrays with some modifications, as per Day et al., 2009 [10]. Glycan arrays can be obtained from several sources, including academic sources such as the Institute for Glycomics Glycan Array or the Mammalian Glycan Array for the Consortium for Functional Glycomics from The SCRIPPS Research Institute or commercially through several companies including RayBiotech, Chemily, MoBiTech, or Dextra Laboratories.
6. Antibody used for His-tagged proteins is the Cell Signaling Technology His-Tag (27E8) Mouse mAb. For GST-tagged protein, the GST (26H1) Mouse mAb is used.
7. IgG antibodies are 150 kDa, whereas *Campylobacter* Tlp proteins range from 25 to 40 kDa, including the tag. Equal molar antibody therefore requires addition of between 3.75 and 6 μg of antibody. Antibody concentrations range from 1 to 10 mg/mL. The above His-tag is typically sold at 10 mg/mL, but check each batch with the manufacturer for concentration.
8. The gene frames come between two pieces of plastic. One side has a hole. The side with the hole in it is the plastic piece you will need to remove to place the gene frame on the slide. You will need to trim the plastic covering to the blue edge before applying to the slide. The frame is wider than it is tall. Ensure that the longest edge is resting across the slide rather than along the slide.
9. In our hands, a 1:1 mix of 100 mM $NiCl_2$ and 100 mM $NiSO_4$ is most effective for activation of the NTA chip surface for the capture of proteins. This 1:1 mix allows for greater protein capture levels and, for some proteins, more stable capture than either solution used separately. This is not the recommended solution supplied by the manufacturer.
10. The pI of a protein is most easily calculated using one of several on-line isoelectric point calculators. The full sequence of your protein, including tags, is required for the calculation. This will provide an idea of where to set your pH scale for the pH scout. Normally, it is best to use a sodium acetate solution 0.5 pH units below your calculated pI as a starting point and then go lower, as the solution that the protein is in usually is a buffer and will not reach the pH of the solution used for scouting or immobilization.
11. ABA injection tests can only be made with ligands that have previously been tested with SPR and where the K_D is known and the concentration and time to saturation is known. The time to saturation is the time it takes for the curve to flatten at a concentration at least twice the K_D.

12. The explanation below explains the information gained from each run, with theoretical examples.

Running buffer alone in all three injections: This sets the baseline for the experiment.

Running buffer in first and third injections with ligand A in the middle injection: This sets the response units maximum (Rmax) for ligand A. For the sake of this example, set this value to an Rmax = 10.

Running buffer in first and third injection with ligand B in the middle injection: This sets the response units maximum (Rmax) for ligand B. For the sake of this example, set this value to an Rmax = 20.

Ligand A in all three injections: If the assay is working well, this should give a response of ~10 from baseline with the first injection, with little or no change with the second and third injections. There should be a relatively straight line once the protein is saturated.

Ligand B in all three injections: If the assay is working well, this should give a response of ~20 from baseline with the first injection with little or no change with the second and third injections. There should be a relatively straight line once the protein is saturated.

Table 2
Explanation of outcomes of the ABA injection outcomes

Step No.	Injection A1	Injection B	Injection A2	Outcome
4.1	Rmax = 0	Rmax = 0	Rmax = 0	Buffer blank.
4.2	Rmax = 0	Rmax = 10	Rmax = 0	Setting Rmax of ligand A
4.3	Rmax = 0	Rmax = 20	Rmax = 0	Setting Rmax of ligand B
4.4	Rmax = 10	Rmax = 10	Rmax = 10	Ensuring the system is injecting without missing and that injection is long enough to saturate protein.
4.5	Rmax = 20	Rmax = 20	Rmax = 20	Ensuring the system is injecting without missing and that injection is long enough to saturate protein.
4.6	Rmax = 10 Rmax = 10 Rmax = 10	Rmax~10 Rmax~30 Rmax~20	Rmax = 10 Rmax > 10 Rmax > 10	A outcompetes B A and B have independent binding sites B outcompetes A
4.7	Rmax = 20 Rmax = 20 Rmax = 20	Rmax~20 Rmax~30 Rmax < 20	Rmax = 20 Rmax > 20 Rmax > 10	B outcompetes A A and B have independent binding sites A outcompetes B

Ligand A in first and third injection with ligand A and ligand B in the middle injection or *Ligand B in first and third injection with ligand A and ligand B in the middle injection:* This is the step in which the assay determines whether the binding is competitive or independent. The outcomes are shown in Table 2.

References

1. Melton T, Hartman PE, Stratis JP, Lee TL, Davis AT (1978) Chemotaxis of *Salmonella typhimurium* to amino acids and some sugars. J Bacteriol 133:708–716
2. Mesibov R, Adler J (1972) Chemotaxis toward amino acids in *Escherichia coli*. J Bacteriol 112:315–326
3. Schmidt J, Müsken M, Becker T, Magnowska Z, Bertinetti D et al (2011) The *Pseudomonas aeruginosa* chemotaxis methyltransferase CheR1 impacts on bacterial surface sampling. PLoS One 6:e18184
4. Tareen AM, Dasti JI, Zautner AE, Gross U, Lugert R (2010) *Campylobacter jejuni* proteins Cj0952c and Cj0951c affect chemotactic behaviour towards formic acid and are important for invasion of host cells. Microbiology 156(Pt 10):3123–3135
5. Mowbray SL, Koshland DE Jr (1987) Additive and independent responses in a single receptor: aspartate and maltose stimuli on the Tar protein. Cell 50:171–180
6. Hartley-Tassell LE, Shewell LK, Day CJ, Wilson JC, Sandhu R et al (2010) Identification and characterization of the aspartate chemosensory receptor of *Campylobacter jejuni*. Mol Microbiol 75:710–730
7. Rahman H, King RM, Shewell LK, Semchenko EA, Hartley-Tassell LE et al (2014) Characterisation of a multi-ligand binding chemoreceptor CcmL (Tlp3) of *Campylobacter jejuni*. PLoS Pathog 10:e1003822
8. Day CJ, King RM, Shewell LK, Tram G, Najnin T et al (2016) A direct-sensing galactose chemoreceptor recently evolved in invasive strains of *Campylobacter jejuni*. Nat Commun 7:13206
9. Waespy M, Gbem TT, Elenschneider L, Jeck AP, Day CJ (2015) Carbohydrate recognition specificity of trans-sialidase lectin domain from *Trypanosoma congolense*. PLoS Negl Trop Dis 9:e0004120. Erratum in: PLos Negl Trop Dis 9:e0004344
10. Day CJ, Tiralongo J, Hartnell RD, Logue CA, Wilson JC et al (2009) Differential carbohydrate recognition by *Campylobacter jejuni* strain 11168: influences of temperature and growth conditions. PLoS One 4:e4927

Part VII

Creating Chemical Tools for Studying Chemosensory Signal Transduction

Chapter 25

Fluorescence Measurement of Kinetics of CheY Autophosphorylation with Small Molecule Phosphodonors

Ruth E. Silversmith and Robert B. Bourret

Abstract

The *Escherichia coli* chemotaxis protein CheY is a model receiver domain containing a native tryptophan residue that serves as a fluorescent probe for CheY autophosphorylation with small molecule phosphodonors. Here we describe fluorescence measurement of apparent bimolecular rate constants for reaction of wild type and mutant CheY with phosphodonors acetyl phosphate, phosphoramidate, or monophosphoimidazole. Step-by-step protocols to synthesize phosphoramidate (K^+ salt) and monophosphoimidazole (Na^+ salt), which are not commercially available, are provided. Key factors to consider in developing autophosphorylation assays for other response regulators are also discussed.

Key words CheY, Tryptophan fluorescence, Stop-flow kinetics, Acetyl phosphate, Phosphoramidate, Monophosphoimidazole, Autophosphorylation, Receiver domain, Response regulator

1 Introduction

Bacterial chemotaxis is one of a large family of signaling systems called two-component systems (TCSs) [1, 2]. A hallmark of TCSs is His → Asp phosphotransfer, whereby a phosphoryl group is transferred from a conserved His residue on a histidine kinase (HK) to a conserved Asp residue located on the receiver domain of a response regulator (RR). Unlike most RRs that contain both a receiver domain and an output domain, the chemotaxis RR CheY consists only of a receiver domain. Historically speaking, CheY from *Escherichia coli* (and its 98% identical cousin from *Salmonella enterica* serovar Typhimurium) have been the subject of multiple transformative experiments that have elucidated fundamental features of receiver domain function. For example, studies involving CheY were used to characterize the binding of divalent cation to the receiver domain active site [3–5], demonstrate roles for conserved residues in catalyzing phosphotransfer [6–8], demonstrate the requirement of divalent cation for catalysis of receiver domain phosphorylation and dephosphorylation [3, 9], as well as establish

Michael D. Manson (ed.), *Bacterial Chemosensing: Methods and Protocols*, Methods in Molecular Biology, vol. 1729, https://doi.org/10.1007/978-1-4939-7577-8_25,

the detailed mechanisms of the phosphorylation-induced conformational change conserved amongst receiver domains [6, 10–13].

Notably, the discovery of the ability of receiver domains to catalyze their own phosphorylation via reaction with small molecule phosphodonors also involved CheY [14]. The reactivity of CheY with small molecule phosphodonors established that the essential catalytic machinery for phosphotransfer from the HK to RR resides in the RR receiver domain. Likewise, the recently discovered ability of phosphorylated receiver domains to catalyze reaction of the phosphoaspartate with imidazole as a model of the Asp → His phosphotransfer seen in phosphorelays [15] was established including CheY as a model system [16].

A fortuitous feature of *E. coli* CheY that helps make it an attractive model system for receiver domain functional studies is the presence in the active site of a native Trp residue that acts as a fluorescence probe. The intrinsic fluorescence intensity of CheY Trp 58 (Asp57 is the site of phosphorylation) is sensitive to binding of the catalytically essential Mg^{2+} [3] as well as to the phosphorylation state of CheY, with the phosphorylated state quenched by 30–50% relative to the unphosphorylated state [14]. Therefore fluorescence spectroscopy can be used as a tool for rigorous quantitative studies of metal binding affinities [3, 4] and kinetic analysis of both autophosphorylation [14, 17–22] and autodephosphorylation [18–20].

An ongoing goal of our laboratory is to understand the structural determinants that vary amongst receiver domains and modulate the rates at which they catalyze their own phosphorylation. Toward this end, we use *E. coli* CheY (and its built-in Trp probe) as a model receiver domain. We change variable residues on CheY to mimic those that naturally occur in other response regulators and measure the effects on CheY autophosphorylation kinetics using Trp fluorescence [18, 19, 22].

We describe below the methodology to execute and analyze kinetic measurement of autophosphorylation rate constants for reaction of wild type and mutant CheY proteins with small molecule phosphodonors. We typically use three different phosphodonors for these studies. Acetyl phosphate ($CH_3CO_2PO_3^{2-}$) is a high energy phosphoanhydride metabolite that is physiologically relevant [23] and is commercially available. Some RRs do not utilize acetyl phosphate as a phosphodonor, including *E. coli* CheB [14] and *Bacillus subtilis* PhoP [24] and Spo0F [25]. Thus, we also test phosphoramidate (PAM; $^{+}H_3NPO_3^{2-}$), which is the simplest compound that contains the P-N linkage present in the physiological HK phosphodonor. PAM is not commercially available and the synthesis, based on a published protocol [26], is described in detail below. Third, we use monophosphoimidazole (MPI), which is virtually identical to the HK phosphohistidine side chain. MPI is

also not commercially available and the synthesis, based on the published protocol [27], is described below.

The Trp fluorescence approach described here for CheY can be used to measure autophosphorylation of some other response regulators. Like CheY, about 4% of receiver domains have a Trp one residue C-terminal to the Asp (D) site of phosphorylation (termed position D+1). For example, fluorescence of the Trp at D+1 in *E. coli* PhoB responds to both metal ion and phosphoryl groups [28]. Quantitative characterization reveals a different dependence of PhoB autophosphorylation rate on phosphodonor concentration than observed with CheY, because PhoB forms dimers whereas CheY does not [29]. About 0.8% of response regulators contain a Trp at position D+2. Fluorescence of the D+2 Trp in *Brucellus abortis* NtrX changes in response to phosphorylation [30]. About 0.9% of receiver domains contain a Trp three residues to the N-terminal side of the conserved Lys (K). Fluorescence of the K-3 Trp residues in *Rhodobacter sphaeroides* CheY3, CheY4, and CheY5 is quenched by phosphorylation [31]. Phosphorylation also reduces fluorescence of naturally occurring Trp residues in *Salmonella enterica* PhoP [32] and Phe residues in *Helicobacter pylori* CheV2 [33]. Changes in Trp fluorescence were used to monitor metal ion binding in *Caulobacter crescentus* DivK [34]; the effect of phosphorylation on fluorescence was not reported, although it seems likely to occur. Modification of a response regulator to introduce a fluorophore near the active site is another option, but requires additional characterization to assess whether the modification alters the properties of the protein. A Trp residue introduced into *Bacillus subtilis* Spo0F two residues to the C-terminal side of the conserved Asp residues (DD) involved in metal ion binding exhibits fluorescence quenching upon metal binding [35]; again, the effect of phosphorylation was not described. A Badan fluorophore coupled to a Cys residue introduced into *E. coli* CheY at DD+4 was a sensitive reporter of both phosphorylation and binding to the CheA histidine kinase [36]. An advantage of an artificial fluorophore such as Badan is optical properties that are easily distinguished from those of naturally occurring amino acids.

Although fluorescence provides a convenient means to measure the fraction of the CheY population that is phosphorylated as a function of time, 95% of response regulators do not contain a Trp residue near the active site, so other methods must be used to measure autophosphorylation kinetics. Phos-tag gels can separate phosphorylated from unphosphorylated response regulators and so would appear to be a universally applicable method [37, 38]. However, attempts in our laboratory to use Phos-tag technology have not been successful for all RRs tested. Another option is to use radiolabeled phosphodonors, which are not commercially

available. Methods for synthesis of [^{32}P]phosphoramidate [39] and [^{32}P]acetyl phosphate [40, 41] have been reported.

Regardless of the assay method employed, several factors are known to influence response regulator autophosphorylation kinetics and should be considered in experimental design: (1) A divalent cation is essential for the reaction, and metal binding affinity varies substantially between response regulators [3, 4, 34, 42–44]. (2) Receiver domains exist in equilibrium between active and inactive conformations, and autophosphorylation can be orders of magnitude faster under conditions that favor the active conformation [45, 46]. (3) Output domains can inhibit autophosphorylation to varying degrees in different response regulators [47]. (4) Ionic strength affects autophosphorylation of *E. coli/Salmonella* CheY [17, 20, 22] and so may be presumed to affect other response regulators.

2 Materials

2.1 Chemical Synthesis of the Potassium Salt of Phosphoramidate (KPAM)

1. Fume hood—it is essential that this procedure be carried out in a fume hood.
2. Phosphorus(V) oxychloride ($POCl_3$) (*see* **Note 1**).
3. Concentrated ammonium hydroxide (NH_4OH). NH_4OH is a solution of NH_3 in water (other monikers include "ammonia water" and "aqueous ammonia"). Concentrated NH_4OH is 28–30% (w/w) NH_3.
4. Acetone.
5. 95% (v/v) ethanol.
6. Diethyl ether (*see* **Note 2**).
7. 50% (w/v) KOH: weigh out 50 g of KOH into a 250 mL graduated cylinder and bring up to 100 mL with distilled water and mix. Wear gloves and eye protection.
8. 1.0 L separatory funnel with stand.
9. Large stir/hot plate.
10. Plastic tub.
11. Thermometer.
12. Vacuum filtration setup: e.g., Buchner funnel with qualitative filter paper (55 mm diameter Whatman #5) /1 L filter flask connected via filter trap to house vacuum.

2.2 Chemical Synthesis of the Sodium Salt of Monophosphoimidazole (Na_2MPI)

1. Fume hood.
2. Potassium salt of phosphoramidate (KPAM) (synthesis described here).
3. Imidazole.

4. $CaCl_2 \cdot 2H_2O$.
5. Vacuum filtration setup as described in Subheading 2.1, **item 12** for phosphoramidate synthesis.
6. Mortar and pestle.
7. 95% (v/v) ethanol.
8. Diethyl ether (*see* **Note 2**).
9. Chelex® 100, Na^+ form.
10. Arsenazo III Ca^{2+} indicator: 20× reagent is 1 mM Arsenazo III in 20 mM Hepes, pH 7.0.
11. Ammonium molybdate: Phosphate assay Reagent A is 0.42% (w/v) ammonium molybdate in 0.5 N H_2SO_4. To prepare, mix 0.42 g ammonium molybdate tetrahydrate with 2.78 mL concentrated H_2SO_4 and bring up to 100 mL with water.
12. Ascorbic acid: Phosphate assay Reagent B is 10% (w/v) aqueous ascorbic acid made immediately before use.
13. Lyophilizer.

2.3 Measurement of Autophosphorylation Kinetics for Wild-Type and Mutant CheY

1. The required instrumentation is a fluorescence spectrometer with thermostatting and rapid kinetics capabilities. This could be a standard fluorescence spectrometer equipped with an external rapid mixing accessory. For example, we routinely use a Perkin Elmer LS-50B spectrometer interfaced with an Applied Photophysics RX-2000 Rapid Kinetics Accessory. An external thermostatted water bath circulates water through the rapid kinetics accessory and the cuvette chamber. This set-up allows us to measure rate constants up to ~1.5 s^{-1}. Alternatively, one could use a true stop flow spectrofluorometer (e.g., Jobin Yvon Fluorolog 322 spectrofluorometer equipped with an F-3009 μFlow stopped-flow apparatus). We use this instrument to measure rate constants greater than ~1.5 s^{-1}.
2. Computer equipped with graphing software that can perform data manipulation and curve fits. We use Microsoft Excel for data manipulation and GraphPad Prism for curve fitting.

3 Methods

3.1 Chemical Synthesis of the Potassium Salt of Phosphoramidate (KPAM) (Based on [26])

1. Wear gloves, lab coat, and eye protection for the entire procedure.
2. In a fume hood, place a 2.0 L Erlenmeyer flask in a plastic tub. Add about 2 in. of crushed ice to the tub and a thin layer of ice under the flask. Place the tub/flask on a stir plate and place a magnetic stir bar in the flask.

3. Measure out 200 mL water and 100 mL concentrated NH_4OH and add to the flask (final concentration will be ~10% NH_3) and stir gently (*see* **Note 3**). Suspend a thermometer from a clamp into the liquid and monitor temperature until it reaches 4 °C.
4. Placing the hood door as low as possible as to allow comfortable movement, use a 25 mL glass pipette to gradually add 18.3 mL of $POCl_3$ to the stirring aqueous NH_4OH (*see* **Note 4**). Add the $POCl_3$ over a 5–7 min time span. There will be fuming. After addition of the $POCl_3$, allow the reaction to continue mixing for about 15 min, at which point the fuming will have stopped and the solution should be clear.
5. Add 800 mL acetone to the solution and mix briefly. Pour the solution into a 1 L separatory funnel placed on a ring stand. Collect the bottom aqueous layer into a 500 mL Erlenmeyer flask. Dispose of the top organic layer (*see* **Note 5**).
6. Using a pH meter, adjust the pH of the sample to 6.0 with concentrated acetic acid (it should take about 8 mL of acetic acid). You can leave the fume hood for this step. Crystallization of the ammonium salt of phosphoramidate (NH_4PAM) will be evident as the pH approaches 6.0. Cool the solution on ice and allow to sit for 3–4 h at 4 °C. Add an equal volume of 95% (v/v) ethanol and let sit on ice for another 30 min.
7. In the fume hood, collect the crystals with the Buchner funnel vacuum filtration apparatus. Wash the crystals with 95% (v/v) ethanol and then with diethyl ether. Allow the crystals to dry for 2 h or overnight in the fume hood. Yield of the NH_4PAM is 6–8 g.
8. To convert the ammonium salt of phosphoramidate (NH_4PAM) into the potassium salt of phosphoramidate (KPAM), place the NH_4PAM into a 100 mL beaker. While working in the fume hood (*see* **Note 6**), add 1.75 mL of 50% (w/v) KOH for each gram of NH_4PAM (e.g., add 12.6 mL of 50% (w/v) KOH for 7.2 g of product). Heat gently in the hood with slow stir until temperature reaches 50–55 °C. Then, allow to stir gently keeping temperature between 50 and 55 °C for 10 min, by which time the vast majority of the NH_3(g) should be driven off.
9. Cool the sample on ice until the temperature is <10 °C. Using a pH meter, adjust the pH to 6.0 with concentrated acetic acid to bring about crystallization of the KPAM. Pour the slurry into 500 mL 95% (v/v) ethanol to complete the crystallization. Filter the crystals in the hood using the vacuum filtration apparatus. Wash the crystals with 95% (v/v) ethanol, and then diethyl ether. Air dry crystals in the fume hood for 2 h or overnight. The KPAM yield is usually about the same number of grams of NH_4PAM that were converted.

10. Store NH_4PAM and KPAM desiccated at −20 °C. Under these conditions, the PAM is stable for at least 10 years.
11. The KPAM is typically >95% pure with the rest of the phosphorus present as inorganic phosphate (P_i) as measured by ^{31}P NMR (the ^{31}P chemical shift of PAM is −1.24 ppm relative to P_i at pH 8.0 [21]).

3.2 Chemical Synthesis of the Sodium Salt of Monophosphoimidazole (Na_2MPI) (Based on [27])

1. Mix 4.0 g KPAM, 1.06 g imidazole, and 40 mL water in a 100 mL beaker. Adjust the pH to 7.2 with concentrated HCl (*see* **Note 7**). Let the reaction incubate overnight at room temperature with no stirring.
2. The reaction now contains a mixture of products and reactants. The desired MPI product is obtained by selective precipitation and crystallization. Dissolve 4.56 g $CaCl_2 \cdot 2H_2O$ in 3–5 mL of water. Add the entire $CaCl_2$ solution to the reaction with slow stirring. An immediate copious white precipitate is formed. Filter the suspension using the vacuum filtration apparatus and collect the filtrate. Dispose of the solid, which contains calcium salts of inorganic phosphate and PAM.
3. To the filtrate, add 2 × 1 mL of 95% (v/v) ethanol. Each addition results in immediate localized precipitate that eventually dissolves. Remove 0.5 mL filtrate and add to 0.5 mL 95% (v/v) ethanol and grind with mortar and pestle. Add the ground crystals back to the sample. Repeat with 1.0 mL each of filtrate and 95% ethanol. This usually induces crystallization throughout the reaction sample. If crystallization does not occur, repeat the mortar and pestle process with 1.0 mL each of filtrate and 95% (v/v) ethanol. Crystallization is allowed to proceed for 15 min at room temperature. These crystals are primarily the calcium salt of diphosphoimidazole (DPI). Vacuum filter and save the filtrate.
4. Measure the volume of the filtrate in a graduated cylinder. Transfer to an Erlenmeyer flask and add two volumes of 95% (v/v) ethanol to the filtrate. This will bring the ethanol from about 10–15% (v/v) to about 70% (v/v) and will crystallize out the monophosphoimidazole as a calcium salt (CaMPI). Let the sample sit on ice for 15 min. Filter the crystals, wash them with 95% ethanol and then diethyl ether, and allow the crystals to dry in the fume hood for 2 h or overnight. The yield is typically 0.8–1.2 g of CaMPI.
5. To convert CaMPI to Na_2MPI, add 20 mL water to 0.40 g of CaMPI in a 50 mL conical tube and vortex vigorously. If there is visible insoluble matter, crush with spatula to disperse.
6. Dispense the suspension into ten 2 mL centrifuge tubes and centrifuge 10 min at 16,000 × *g* in a benchtop centrifuge.

Decant the supernatants, pool, and place on ice. Dispose of the pellets, which are mainly calcium phosphate.

7. Suspend about 15 mL Chelex® 100, Na^+ form resin in water and pour into a small chromatography column. Wash the resin with about 75 mL of water.
8. Load the pooled supernatants from **step 6** onto the column and collect the eluate in 5 mL fractions. After the sample has loaded, apply water to the top of the column to elute the entire sample.
9. Assay the fractions for both Ca^{2+} and acid-hydrolysable phosphate as follows: For Ca^{2+} detection, mix 95 μL of the fraction and 5 μL 20× Arsenazo III reagent (*see* Subheading 2.2, **item 10**) in a microtiter plate. Blue indicates the presence of Ca^{2+} (>50 μM) and pink indicates the absence of Ca^{2+} (<50 μM). For detection of MPI, make reagent C from a mixture of 6 parts Reagent A to 1 part Reagent B (Subheading 2.2). In a microtiter plate, mix 30 μL fraction plus 70 μL reagent C. The formation of a blue color within several minutes indicates the presence of MPI.
10. Pool all fractions that lack Ca^{2+} but contain MPI and flash freeze in an ethanol/dry ice bath. In our experience, all of the fractions that contain MPI also lack Ca^{2+}.
11. Lyophilize frozen sample until all ice is gone. Weigh the product (typical yield is 200 mg) and store desiccated at −20 °C. Under these conditions, the Na_2MPI is stable for up to 1 year.
12. Analysis of Na_2MPI preparations can be carried out using ^{31}P NMR, where the chemical shifts for MPI and DPI (diphosphoimidazole) relative to P_i at pH 8.0 are −6.9 ppm and −7.1 ppm, respectively [21]. A typical preparation gave 79 mol% MPI, 17 mol% DPI, 4 mol% P_i.

3.3 Fluorescence Measurement of CheY Autophosphorylation Kinetics

A rapid mixing or stop flow apparatus contains two syringes, each of which is loaded with a different reactant. For CheY autophosphorylation measurements, one syringe is loaded with a solution containing CheY in reaction buffer. The other syringe is loaded with a solution containing the phosphodonor (the concentration varies) in reaction buffer and KCl so that the ionic strength due to phosphodonor plus KCl is kept constant. Balancing the ionic strength is essential because increasing ionic strength at a constant phosphodonor concentration slows the reaction [20, 22]. Time courses for four different phosphodonor concentrations are measured for each CheY/phosphodonor pair. The protocol below is applicable to a rapid mixing accessory that injects equal volumes of the two reactants to initiate a reaction.

1. Set up the fluorescence spectrometer to continuously monitor fluorescence emission at 346 nm with excitation at 295 nm. Program the instrument to take data points at time intervals appropriate to the kinetics of the reaction (this will take some adjustment as knowledge of the kinetics of the reaction is acquired). Adjust the sensitivity of the instrument so that 5 μM CheY gives an appreciable fluorescence signal when present in the cuvette attached to the rapid mixing accessory. Set thermostatting at 25 °C.
2. Make 8.0 mL of CheY reactant solution containing wild-type or mutant CheY (10 μM) in 1× reaction buffer (100 mM Hepes, pH 7.0, 10 mM $MgCl_2$) (*see* **Notes 8** and **9**). Note that the final concentration of CheY in the reaction will be 5 μM.
3. Make 2.0 mL of each of four phosphodonor reactant solutions with different concentrations of a given phosphodonor. Each phosphodonor solution contains 1× reaction buffer and phosphodonor supplemented with KCl so that the sum of the ionic strength contributed by the phosphodonor and KCl is 200 mM. When deducing ionic strength contributions, one needs to consider the nature of the salt. KPAM and KCl are 1:1 salts (an equimolar combination of one +1 cation and one −1 anion) and the ionic strength contribution is equal to the salt concentration (e.g., 50 mM KPAM or KCl contributes 50 mM ionic strength). However, the commercially available LiK acetyl phosphate and Na_2MPI (synthesis described above) are 2:1 salts (two +1 cations and one −2 anion) whereby the contribution to ionic strength is equal to three times the phosphodonor concentration (*see* **Note 10**); Thus, a 50 mM acetyl phosphate solution contributes 150 mM to the ionic strength and should be supplemented with 50 mM KCl to get a total ionic strength of 200 mM. A typical set of phosphodonor reactant solutions for wild type CheY would be 20 mM acetyl phosphate (140 mM KCl), 30 mM acetyl phosphate (110 mM KCl), 40 mM acetyl phosphate (80 mM KCl) and 60 mM acetyl phosphate (20 mM KCl), all containing 1× reaction buffer. This would give final reaction concentrations of 10, 15, 20, and 30 mM acetyl phosphate as the reactants are diluted twofold in the final reaction.
4. Load syringe 1 with 2 mL of the CheY reactant solution and syringe 2 with entire 2 mL of the first phosphodonor solution. Allow 3 min to come to temperature equilibration.
5. While actively measuring fluorescence, inject reactants into cuvette using the rapid mixing apparatus. After the dead volume of the rapid mixer has been filled, valid phosphorylation time courses will be recorded. After each time course has come to completion, inject another shot of reactants so that you have a series of replicate time courses (Fig. 1a).

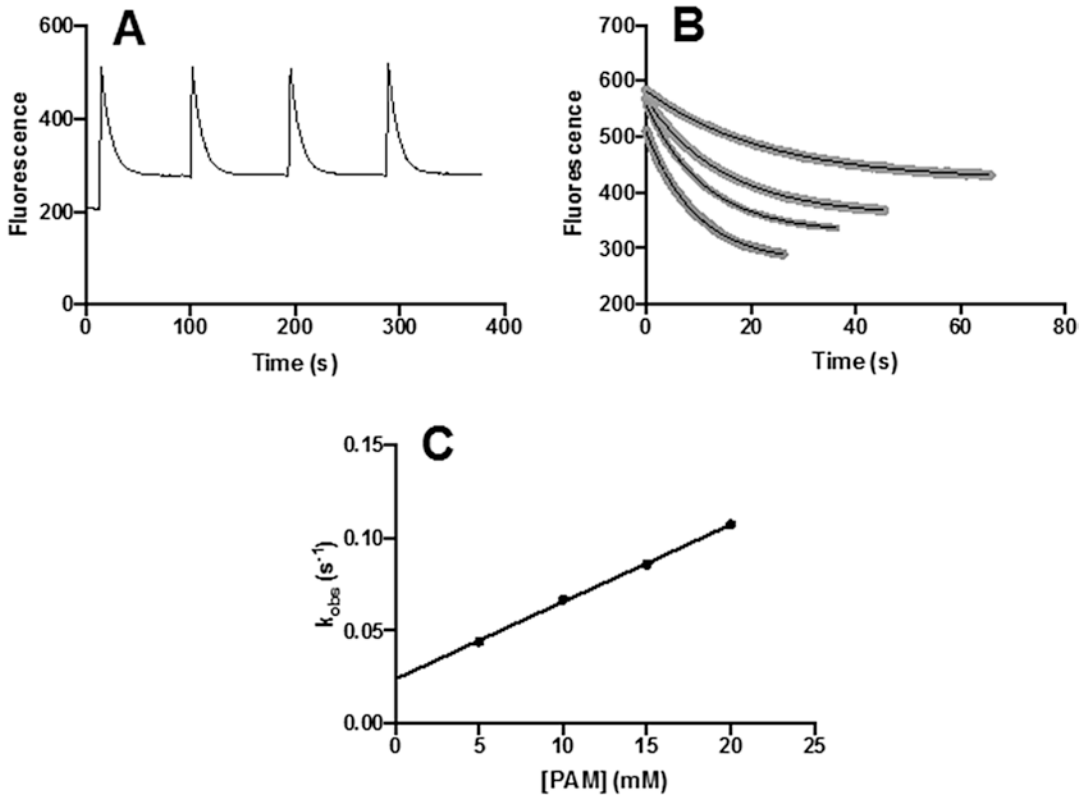

Fig. 1 Sample data for reaction of CheY E89S with KPAM. (**a**) Fluorescence time course for repetitive shots of the rapid mixer, each of which shows the reaction of CheY E89S (10 μM in reaction buffer) with KPAM (40 mM in reaction buffer supplemented with 160 mM KCl). The final reaction contains 5 μM CheY and 20 mM KPAM. The reaction buffer is 100 mM Hepes, pH 7.0, 10 mM $MgCl_2$. (**b**) Representative trimmed time courses from reactions containing 5 μM CheY and 5, 10, 15, or 20 mM PAM. The gray curve shows the recorded data, and the black line is the best fit curve to an exponential decay. Intervals between data points are 0.100 s for the 5 and 10 mM PAM time courses and 0.050 s for the 15 and 20 mM PAM time courses. (**c**) k_{obs} values derived from best fit curves are plotted versus the PAM concentration in the reaction. The slope (4.2 M^{-1} s^{-1}) is the apparent bimolecular rate constant for autophosphorylation and corresponds to k_{phos}/K_S. The y-intercept (0.024 s^{-1}) gives the autodephosphorylation rate constant (k_{dephos}) for this CheY mutant

6. Repeat **steps 4** and **5** for the three remaining phosphodonor solutions.
7. Obtain the data from the fluorescence spectrometer software as time versus fluorescence and transfer to a spreadsheet program such as Excel.
8. Each time course starts with an initial intensity (I_{max}, the highest fluorescence value following mixing) and decays to a constant value ($I_{plateau}$). Trim the time courses as follows for data analysis: Use I_{max} as your zero time point. For the final time point, use the point at which the change in fluorescence inten-

sity has reached a value that is equal to 95% ($I_{max}-I_{plateau}$). Taking 95% of the time course allows analysis of four half-lives while avoiding consideration of the plateau in the curve fitting. The plateau itself is not included in analysis because essentially constant experimental values can distort the fit to a theoretical exponential decay.

9. Move the trimmed time versus intensity data into GraphPad Prism. Graph the time courses and fit the curves to a single exponential decay (Fig. 1b). This will reveal the k_{obs}, the apparent first order rate constant for autophosphorylation at a given phosphodonor concentration.
10. Graph the k_{obs} values versus the phosphodonor concentration (Fig. 1c). This step of the data analysis is based on the idea that the k_{obs} depends on the affinity of CheY for the phosphodonor and the first order rate constants for the phosphorylation and dephosphorylation reactions, leading to the equation:

$$k_{obs} = \left(k_{phos} / K_S\right)[PD] + k_{dephos}$$

where PD is phosphodonor, K_S is the dissociation equilibrium constant for noncovalent binding of phosphodonor to CheY, k_{phos} is the first order rate constant for the chemical reaction to form CheYp, and k_{dephos} is the autodephosphorylation rate constant.

The slope of the best fit line for the relationship between [PD] and k_{obs} is k_{phos}/K_S, the ratio of the first order rate constant for phosphorylation to the dissociation binding constant of phosphodonor to CheY. k_{phos}/K_S represents the apparent bimolecular rate constant for the reaction (*see* **Notes 11–13**).

4 Notes

1. $POCl_3$ is a liquid that is packaged in a sealed container. Once open, use within 6 months. $POCl_3$ has multiple potentially dangerous properties. It is highly toxic, corrosive, and reacts violently with water. Read the safety information from the manufacturer, wear appropriate personal protective equipment, and handle with care.
2. Store diethyl ether for a maximum of 1 year after opening. The ether can oxidize over time to form peroxides, which are explosive.
3. Be sure to add the water first, followed by the strong base.
4. In the reaction of NH_4OH with $POCl_3$, use caution when adding the $POCl_3$. The liquid has a tendency to "percolate" in the pipette and may dribble out even without expulsion.

5. In the reaction of NH_4OH with $POCl_3$, undesired products $NH_4PO_2(NH_2)_2$ and $PO(NH_2)_3$ are formed along with the desired $NH_4HPO_3NH_2$ (the ammonium salt of PAM, NH_4PAM). During the acetone extraction, the undesired products partition into the acetone layer and the desired product is in the aqueous layer.
6. NH_3 gas will start to be released immediately upon addition of the 50% (w/v) KOH to the NH_4PAM. Thus, it is essential to carry out this step (and the remainder of the steps for conversion of NH_4PAM to KPAM) in the fume hood.
7. Careful adjustment of the pH to 7.2 is critical for the reaction of KPAM with imidazole. A pH of 7.2 allows sufficient imidazole (pKa ~7) to be unprotonated and sufficient PAM (pKa ~8) to be protonated, allowing the imidazole to act as a nucleophile toward the PAM phosphorous with NH_3 as the leaving group.
8. The standard buffer for the autophosphorylation reaction is 100 mM Hepes, pH 7.0. The pH of 7.0 (and not higher) is critical for the reaction of PAM and MPI with CheY. While the reaction with acetyl phosphate is largely pH-independent, reaction with PAM and MPI requires protonation of the nitrogen atom on the leaving group and slows dramatically at pH values above 7.0 [21].
9. The standard concentration of divalent cation for wild-type CheY autophosphorylation reactions is 10 mM Mg^{2+}. The K_d for binding Mg^{2+} to wild type CheY is 0.5–1 mM [3, 4], so 10 mM essentially saturates the metal binding sites. However, affinities of other response regulators for Mg^{2+} vary over two orders of magnitude [3, 4, 34, 42–44], so it is important that a sufficient concentration of Mg^{2+} is used. If high concentrations of Mg^{2+} lead to phosphodonor precipitation, then it may be possible to use Mn^{2+} instead, which tends to bind with higher affinity [3, 4] yet still supports autophosphorylation [29]. If subsaturating concentrations of metal ion are used, then the observed rate constant will reflect the fraction of the population bound to Mg^{2+}, which can substantially affect the results.
10. The ionic strength (I) of a solution can be calculated from the molar concentrations and charges of the ions in solutions, according to the following relationship:

$$I = \frac{1}{2}\sum_{i=1}^{n} c_i z_i^2$$

where c_i is the molar concentration of the ion i, z_i is the charge of the ion i, and the sum is taken over all of the ions (n) in the solution. For example, 50 mM of the LiK salt of acetyl phosphate (LiKAcOP) contains 50 mM K^+, 50 mM Li^+, and 50 mM

$AcOP^{2-}$, and the ionic strength contribution would be calculated as,

$$I = 0.5\left[(50)\left(1^2\right) + 50\left(1^2\right) + 50(-2)^2\right] = 150\,\text{mM}$$

11. Accurate measurement of k_{phos}/K_S depends on accurate knowledge of the phosphodonor concentration. The purity of acetyl phosphate, KPAM and Na_2MPI can be determined using ^{31}P NMR.
12. For CheY, k_{obs} values and consequently, k_{phos}/K_S values, are independent of protein concentration. In other words, it is not necessary to measure protein concentration accurately when doing assays, and variations in specific activity between different protein preparations do not affect k_{obs}. In contrast, PhoB autophosphorylation involves dimer formation, and measurements are affected by protein concentration [29].
13. For CheY, only the initial linear portion of the familiar Michaelis–Menten curve is seen, and saturation of the reaction rate with increasing phosphodonor concentration is not observed at constant ionic strength. This appears to be a consequence of weak phosphodonor binding [17], such that saturating phosphodonor concentrations are not experimentally accessible.

Acknowledgments

This work was supported by National Institute of General Medical Sciences of the National Institutes of Health under award number R01GM050860. The content is solely the responsibility of the authors and does not necessarily represent the official views of the National Institutes of Health.

References

1. Bourret RB, Silversmith RE (2010) Two-component signal transduction. Curr Opin Microbiol 13:113–115
2. Zschiedrich CP, Keidel V, Szurmant H (2016) Molecular mechanisms of two-component signal transduction. J Mol Biol 428:3752–3775
3. Lukat GS, Stock AM, Stock JB (1990) Divalent metal ion binding to the CheY protein and its significance to phosphotransfer in bacterial chemotaxis. Biochemistry 29:5436–5442
4. Needham JV, Chen TY, Falke JJ (1993) Novel ion specificity of a carboxylate cluster Mg(II) binding site: strong charge selectivity and weak size selectivity. Biochemistry 32:3363–3367
5. Stock AM, Martinez-Hackert E, Rasmussen BF et al (1993) Structure of the Mg(2+)-bound form of CheY and mechanism of phosphoryl transfer in bacterial chemotaxis. Biochemistry 32:13375–13380
6. Appleby JL, Bourret RB (1998) Proposed signal transduction role for conserved CheY residue Thr87, a member of the response regulator active site quintet. J Bacteriol 180:3563–3569
7. Lukat GS, Lee BH, Mottonen JM et al (1991) Roles of the highly conserved aspartate and lysine residues in the response regulator of bacterial chemotaxis. J Biol Chem 266: 8348–8354

8. Bourret RB, Hess JF, Simon MI (1990) Conserved aspartate residues and phosphorylation in signal transduction by the chemotaxis protein CheY. Proc Natl Acad Sci U S A 87: 41–45
9. Hess JF, Bourret RB, Oosawa K et al (1988) Protein phosphorylation and bacterial chemotaxis. Cold Spring Harb Symp Quant Biol 53:41–48
10. Cho HS, Lee SY, Yan D et al (2000) NMR structure of activated CheY. J Mol Biol 297: 543–551
11. Formaneck MS, Ma L, Cui Q (2006) Reconciling the "old" and "new" views of protein allostery: a molecular simulation study of the chemotaxis Y protein (CheY). Proteins 63:846–867
12. Lee SY, Cho HS, Pelton JG et al (2001) Crystal structure of activated CheY. Comparison with other activated receiver domains. J Biol Chem 276:16425–16431
13. McDonald LR, Boyer JA, Lee AL (2012) Segmental motions, not a two-state concerted switch, underly allostery in CheY. Structure 20:1363–1373
14. Lukat GS, McCleary WR, Stock AM et al (1992) Phosphorylation of bacterial response regulator proteins by low molecular weight phospho-donors. Proc Natl Acad Sci U S A 89:718–722
15. Goulian M (2010) Two-component signaling circuit structure and properties. Curr Opin Microbiol 13:184–189
16. Page SC, Silversmith RE, Collins EJ et al (2015) Imidazole as a small molecule analogue in two-component signal transduction. Biochemistry 54:7248–7260
17. Da Re SS, Deville-Bond D, Tolstykh T et al (1999) Kinetics of CheY phosphorylation by small molecule phosphodonors. FEBS Lett 457:323–326
18. Immormino RM, Silversmith RE, Bourret RB (2016) A variable active site residue influences the kinetics of response regulator phosphorylation and dephosphorylation. Biochemistry 55:5595–5609
19. Immormino RM, Starbird CA, Silversmith RE et al (2015) Probing mechanistic similarities between response regulator signaling proteins and haloacid dehalogenase phosphatases. Biochemistry 54:3514–3527
20. Mayover TL, Halkides CJ, Steward RC (1999) Kinetic characterization of CheY phosphorylation reactions: comparison of P-CheA and small-molecule phosphonors. Biochemistry 38: 2259–2271
21. Silversmith RE, Appleby JL, Bourret RB (1997) Catalytic mechanism of phosphorylation and dephosphorylation of CheY: kinetic characterization of imidazole phosphates as phosphodonors and the role of acid catalysis. Biochemistry 36:14965–14974
22. Thomas SA, Immormino RM, Bourret RB et al (2013) Nonconserved active site residues modulate CheY autophosphorylation kinetics and phosphodonor preference. Biochemistry 52:2262–2273
23. Wolfe AJ (2010) Physiologically relevant small phosphodonors link metabolism to signal transduction. Curr Opin Microbiol 13: 204–209
24. Liu W, Hulett FM (1997) *Bacillus subtilis* PhoP binds to the *phoB* tandem promoter excusively within the phosphate starvation-inducible promoter. J Bacteriol 179: 6302–6310
25. Zapf JW, Hoch JA, Whiteley JM (1996) A phosphotransferase activity of the *Bacillus subtilis* sporulation protein Spo0F that employs phosphoramidate substrates. Biochemistry 35: 2926–2933
26. Sheridan RC, McCullough JF, Wakefield ZT (1972) Phosphoramidic acid and its salts. Inorg Synth 13:23–26
27. Rathlev T, Rosenberg T (1956) Non-enzymic formation and rupture of phosphorus to nitrogen linkages in phosphoramido derivatives. Arch Biochem Biophys 65:319–339
28. McCleary WR (1996) The activation of PhoB by acetyl phosphate. Mol Microbiol 20:1155–1163
29. Creager-Allen RL, Silversmith RE, Bourret RB (2013) A link between dimerization and autophosphorylation of the response regulator PhoB. J Biol Chem 288:21755–21769
30. Fernandez I, Otero LH, Klinke S et al (2015) Snapshots of conformational changes shed light into the NtrX receiver domain signal transduction mechanism. J Mol Biol 427: 3258–3272
31. Ferre A, De La Mora J, Ballado T et al (2004) Biochemical study of multiple CheY response regulators of the chemotactic pathway of *Rhodobacter sphaeroides*. J Bacteriol 186: 5172–5177
32. Perron-Savard P, De Crescenzo G, Le Moual H (2005) Dimerization and DNA binding of the *Salmonella enterica* PhoP response regulator are phosphorylation independent. Microbiology 151:3979–3987
33. Pittman MS, Goodwin M, Kelly DJ (2001) Chemotaxis in the human gastric pathogen

Helicobacter pylori: different roles for CheW and the three CheV paralogues, and evidence for CheV2 phosphorylation. Microbiology 147:2493–2504

34. Guillet V, Ohta N, Cabantous S et al (2002) Crystallographic and biochemical studies of DivK reveal novel features of an essential response regulator in *Caulobacter crescentus*. J Biol Chem 277:42003–42010
35. Madhusudan M, Zapf J, Hoch JA et al (1997) A response regulatory protein with the site of phosphorylation blocked by an arginine interaction: crystal structure of Spo0F from *Bacillus subtilis*. Biochemistry 36:12739–12745
36. Stewart RC, VanBruggen R (2004) Phosphorylation and binding interactions of CheY studied by use of Badan-labeled protein. Biochemistry 43:8766–8777
37. Barbieri CM, Stock AM (2008) Universally applicable methods for monitoring response regulator aspartate phosphorylation both in vitro and in vivo using Phos-tag-based reagents. Anal Biochem 376:73–82
38. Barbieri CM, Wu T, Stock AM (2013) Comprehensive analysis of OmpR phosphorylation, dimerization, and DNA binding supports a canonical model for activation. J Mol Biol 425:1612–1626
39. Buckler DR, Stock AM (2000) Synthesis of [(32)P]phosphoramidate for use as a low molecular weight phosphodonor reagent. Anal Biochem 283:222–227
40. Jagadeesan S, Mann P, Schink CW et al (2009) A novel "four-component" signal transduction mechanism regulates developmental progression in *Myxococcos xanthus*. J Biol Chem 284:21435–21445
41. Stadtman ER (1957) Preparation and assay of acetyl phosphate. Methods Enzymol 3:228–231
42. Feher VA, Zapf JW, Hoch JA et al (1995) ^{1}H, ^{15}N, and ^{13}C backbone chemical shift assignments, secondary structure, and magnesium-binding characteristics of the *Bacillus subtilis* response regulator, Spo0F, determined by heteronuclear high-resolution NMR. Protein Sci 4:1801–1814
43. Sheftic SR, Garcia PP, White E et al (2012) Nuclear magnetic resonance structure and dynamics of the response regulator Sma0114 from *Sinorhizobium meliloti*. Biochemistry 51:6932–6941
44. Zundel CJ, Capener DC, McCleary WR (1998) Analysis of the conserved acidic residues in the regulatory domain of PhoB. FEBS Lett 441:242–246
45. Ames SK, Frankema N, Kenney LJ (1999) C-terminal DNA binding stimulates N-terminal phosphorylation of the outer membrane protein regulator OmpR from *Escherichia coli*. Proc Natl Acad Sci U S A 96:11792–11797
46. Schuster M, Silversmith RE, Bourret RB (2001) Conformational coupling in the chemotaxis response regulator CheY. Proc Natl Acad Sci U S A 98:6003–6008
47. Barbieri CM, Mack TR, Robinson VL et al (2010) Regulation of response regulator autophosphorylation through interdomain contacts. J Biol Chem 285:32325–32335

Chapter 26

Synthesis of a Stable Analog of the Phosphorylated Form of CheY: Phosphono-CheY

Daniel B. Lookadoo, Matthew S. Beyersdorf, and Christopher J. Halkides

Abstract

CheY is a response regulator of bacterial chemotaxis that is activated by phosphorylation of a conserved aspartate residue. However, studies of CheY-phosphate have proven challenging due to rapid hydrolysis of the aspartyl-phosphate in vitro. To combat this issue, we have designed a stable analog suitable for structural and functional studies. Herein, we describe a method for the chemical modification of *Thermotoga maritima* CheY to produce a phospho-analog designated as phosphono-CheY. Our modification produces a stable analog in the constitutively active form that enables the study of signal transfer to the downstream target.

Key words Phosphonomethyl trifluoromethanesulfonate, Two-component system, Cysteine modification, Phosphate analog, Chemical modification, Response regulator, Chemotaxis, Phosphono-CheY

1 Introduction

Chemotaxis is an extensively studied and highly conserved signal transduction system. Following phosphorylation by CheA, the response regulator protein CheY binds the switch protein FliM at the base of the flagellar motor, changing the direction of flagellar rotation [1]. However, the precise mechanism of flagellar motor switching, particularly events subsequent to the initial binding of CheY-phosphate (CheY-P) to FliM, remains a point of debate within the scientific literature [2–4]. Ultimately, a better understanding of how interactions between each of the switch proteins (FliG, FliM and FliN) are modulated by CheY-P binding is desired.

This study is complicated by the rapid hydrolysis of CheY-P in vitro [5], a problem that is circumvented by rendering the signal transduction protein permanently stable through chemical modification (Fig. 1). Covalent modification of proteins is routine for applications such as the development of irreversible inhibitors, activity-based protein profiling, and complex structural studies [6]. Reproducing natural modifications in a highly efficient and

Michael D. Manson (ed.), *Bacterial Chemosensing: Methods and Protocols*, Methods in Molecular Biology, vol. 1729,
https://doi.org/10.1007/978-1-4939-7577-8_26,

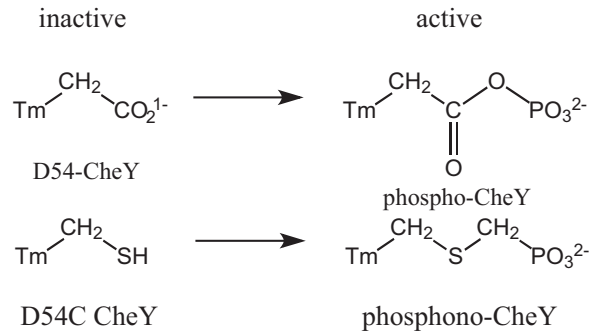

Fig. 1 Comparison between CheY-phosphate and phosphono-CheY. Phosphono-CheY is synthesized by introducing a cysteine residue in place of the active-site aspartate (D54C). The phosphonomethyl-group is then introduced by reaction with PMT. This produces a constitutively active-state analog with high similarity to true CheY-phosphate

controlled manner is an invaluable tool for interrogating biological systems, both in vitro and in vivo [7]. The methodology described herein implements a chemical modification, allowing access to a stable CheY-P analog.

Common molecular biology and biochemical techniques are employed so that this approach can be successfully undertaken in any laboratory. Similar methodology has been readily applied to study chemotaxis in both *E. coli* and *T. maritima* over the past two decades [8–12]. Phosphono-CheY is advantageous over other recognized CheY-phosphate analogs due to its increased stability and potential in vivo applications and should provide a more vivid description of chemotaxis and signal transduction.

2 Materials

All solvents and chemicals are of the highest grade commercially available and used without further purification.

2.1 Determination of Protein Concentration and Free Thiol

1. All absorbance measurements are performed on an Agilent Technologies Cary series 100 UV-Vis spectrophotometer.
2. 5,5-Dithiobis(2-nitrobenzoic acid) (DTNB) 20 mM stock reagent: 79.2 mg DNTB in 10 mL of Milli-Q water.
3. DTNB buffer: 100 mM potassium phosphate buffer pH 7.25.

2.2 Phosphono-methylation of D54C/C81A CheY from T. maritima

1. The stable analogue, phosphono-CheY, is prepared following the procedure previously described with minor modifications [13]. All phosphonomethylation reactions are carried-out using a D54C/C81A CheY mutant and phosphonomethyltriflate (PMT; *see* **Note 1**).

2. PMT is synthesized as previously described, with one modification ([8]; *see* **Note 2**).
3. Alkylation buffer: 500 mM Bis-Tris at pH 7.0 (*see* **Note 3**).
4. Calcium chloride 2 M stock: 2.2196 g in 10 mL of Milli-Q water.
5. Dithiothreitol (DTT) 250 mM stock solution: 385.6 mg in 10 mL of Milli-Q water.
6. Ethylenediaminetetraacetic acid disodium salt (EDTA) 500 mM stock solution at pH 8.0: 1.86 g in 10 mL of Milli-Q water.

2.3 Purification via Cation-Exchange HPLC

1. All Cation-Exchange High Performance Liquid Chromatography (CEX-HPLC) experiments are performed on an Agilent Technologies 1260 Infinity quaternary liquid chromatography system equipped with a variable wavelength detector (VWD) and 500 µL manual injection loop.
2. A PolyCAT A™, 200 × 9.4 mm, 5 µm, 300 Å column (supplied by PolyLC Inc.) is utilized for the CEX-HPLC purification of phosphonomethylation mixtures. Cation-exchange mobile phase A: 20 mM ammonium acetate at pH 6.40 with 10% (v/v) acetonitrile. Cation-exchange mobile phase B: 75 mM ammonium acetate at pH 6.40 with 10% (v/v) acetonitrile.

2.4 Characterization via Reversed-Phase HPLC

Routine Reversed-Phase High Performance Liquid Chromatography (RP-HPLC) experiments are performed on an Agilent Technologies 1260 Infinity binary liquid chromatography system with a diode array detector (DAD), evaporative light scattering detector (ELSD), standard autosampler (ALS) and thermostatted column compartment. An Agilent Technologies Poroshell 120 (C18, 150 × 2.1 mm, 120 Å) is utilized for RP-HPLC analysis of phosphonomethylation reactions. Reversed-phase mobile phase A: Milli-Q water with 0.10% (v/v) trifluoroacetic acid. Reversed-phase mobile phase B: acetonitrile with 0.10% (v/v) trifluoroacetic acid.

3 Methods

3.1 Determination of Protein Concentration and Free Thiol

1. 10 µL of the 250 mM DTT stock is added to a 1.0 mL protein aliquot containing 10 mg of CheY and allowed to incubate for 45 min at 25 °C.
2. The protein sample is buffer exchanged using Sephadex G-25 Penefsky spin-columns into the alkylation buffer [14].
3. The protein concentration is determined by an A_{280} assay using a molar absorptivity of 2980 M^{-1} cm^{-1} for CheY.
4. A DTNB assay is conducted to determine the percentage of free thiol present, before undergoing alkylation [15]. Free thiol concentration is calculated based on the change in absorbance at 410 nm over 50 min (*see* **Note 4**).

3.2 Phosphono-methylation of D54C/C81A CheY from T. maritima

1. 7.3 mg of PMT (30 mM) and 18.8 mg of Bis-Tris base (90 mM; 3 equivalents) are added to a 1.5 mL Eppendorf microcentrifuge tube.
2. Next, 62.5 μL of the 2 M $CaCl_2$ stock is added to 937.5 μL of the protein in alkylation buffer.
3. The protein sample, containing calcium, is added to the microcentrifuge tube containing PMT and base. The alkylation mixture is then mixed by inversion several times (*see* **Note 5**).
4. The alkylation is permitted to occur for 45 min before termination by addition of 20.6 μL of the 250 mM DTT stock and 10.3 μL of the 500 mM EDTA stock.
5. After DTT incubation for 5 min, the alkylation sample is centrifuged at 5000 RCF for 5 min and the supernatant is extracted and buffer exchanged, using a PD-10 column, into cation-exchange mobile phase A.
6. After the buffer exchange, another A_{280} protein assay is performed to quantify the amount of total protein recovered from the phosphonomethylation reaction.
7. Another DTNB assay is carried-out to determine the amount of free thiol to assess the completeness of the phosphonomethylation reaction (*see* **Note 6**).

3.3 Purification via Cation-Exchange HPLC

1. Cation-exchange High Performance Liquid Chromatography (CEX-HPLC) is implemented to separate different forms of CheY, ultimately for the purification of phosphono-CheY (*see* **Note 7**).
2. The method is designed to elute protein using a gradient of 30.0–52.5% mobile phase B over 60 min at 3.0 mL/min. The separation is performed at room temperature.
3. A sample load of 5 mg is typically employed. Phosphono-CheY elutes at 9.3 min and unmodified CheY elutes at 36.9 min.
4. All peaks are collected, concentrated using Amicon™ Ultra-2 centrifugal filters, and analyzed for purity by RP-HPLC and mass spectrometry (*see* **Note 8**).

3.4 Characterization via Reversed-Phase HPLC

1. Reversed-Phase High Performance Liquid Chromatography (RP-HPLC) is utilized for relative quantitative and qualitative analysis of each phosphonomethylation reaction for CheY (*see* **Note 9**).
2. Initially, RP-HPLC is utilized to monitor the completeness of the phosphonomethylation reaction.
3. RP-HPLC is also utilized to characterize the purified phosphono-CheY analogue. The method is designed to elute varying forms of protein by implementing a gradient of 39–45% mobile phase B over 55 min at a flow rate of 200 μL/min. The

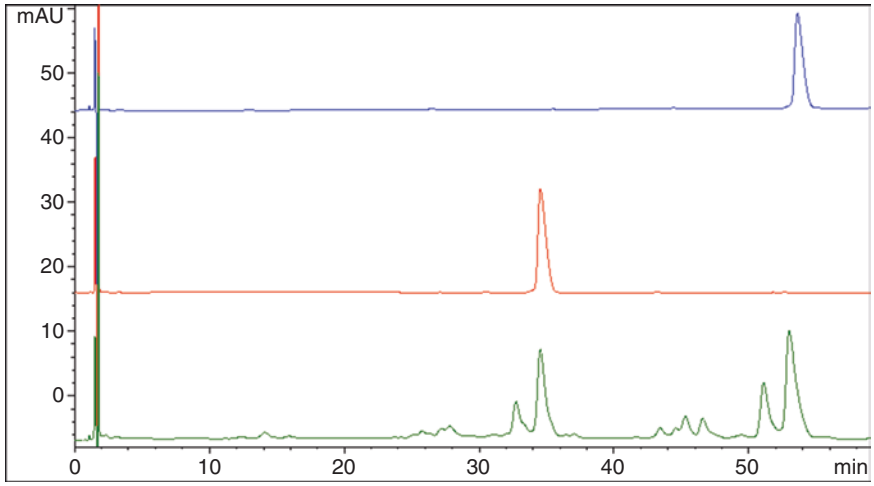

Fig. 2 Reversed-Phase High Performance Liquid Chromatography (RP-HPLC) chromatograms of (top) unmodified CheY, (middle) cation-exchange purified phosphono-CheY, and (bottom) a phosphonomethylation reaction mixture

separation is performed using a thermostatted column compartment at 30 °C. A sample load of 3 μg is sufficient for an alkylation mixture, and only 1 μg is required for a purified sample.

4. Phosphono-CheY elutes at 34.5 min and unmodified CheY elutes at 53.0 min (Fig. 2).

4 Notes

1. There are several methods available in the literature for SDM [16].
2. Di-*tert*-butyl-trifluoromethanesulfonylhydroxymethyl phosphonate is purified using flash silica gel chromatography. This modification removes a dark brown colored impurity that appears in some syntheses of PMT. Di-*tert*-butyl-trifluoromethanesulfonylhydroxymethyl phosphonate is loaded onto a flash silica gel column (30 g, 3 cm diameter) and eluted with 1:1 ethyl acetate–hexanes (2 cv), 2:1 ethyl acetate–hexanes (3 cv), and ethyl acetate (1 cv). The fractions containing the product are combined, and after removal of the solvent yield di-*tert*-butyl-hydroxymethylene phosphonate as a clear-ecru oil. ^{31}P NMR (162 MHz, Chloroform-*d*) δ ppm 4.11 (s, 1P); ^{31}P NMR (162 MHz, Chloroform-*d*, coupled) δ ppm 4.11 (t, 2H); ^{1}H NMR (400 MHz, Chloroform-*d*) δ ppm 1.55 (s, 18H) 4.46 (d, J = 8.44 Hz, 2H); ^{13}C NMR (101 MHz, Chloroform-*d*) δ ppm 85.21 (d, J = 8.04 Hz), 69.50 (d, J = 71.44 Hz), 30.30 (d, J = 4.02 Hz).

3. Other alkylation buffers have been successfully used, suggesting that the phosphonomethylation reaction tolerates a wide variety of conditions. A desirable buffer should have sufficient buffering capacity to hold the phosphonomethylation reaction at an optimal pH. Also, the buffer should have little affinity for the metal ion or PMT.
4. A successful prealkylation DTNB is >75% free thiol.
5. The previously described procedural series should be performed as quickly as possible to overcome the fast hydrolysis rate of PMT, but in a precise and controlled manner.
6. A successful postalkylation DTNB shows >50% decrease in free thiol, relative to the prealkylation DTNB assay.
7. Additional methods have been successfully developed to purify phosphono-CheY from CheY including through labeling of unreacted CheY with biotin for separation with avidin affinity chromatography.
8. Iron buildup in the HPLC system reduces phosphono-CheY yields. To combat this, the HPLC system and PolyCAT A™ column should be routinely passivated according to the manufacturer's instructions to minimize product loss.
9. DTNB assays are also routinely used to measure the completeness of phosphonomethylation reactions. Additional confirmation can be obtained from mass spectrometry, ^{31}P NMR, and total inorganic phosphate assay [17].

Acknowledgments

The authors acknowledge support from National Institutes of Health Grant R15 GM 063514-02A2 (C.J.H.) and R01 GM066775 (R.S. and B.C.). Instrumentation for the mass spectrometry facility in the Department of Chemistry and Biochemistry at UNCW was provided by a grant from the National Science Foundation Division of Chemistry (CHE-1039784). Special thanks to Dr. Brian Crane, Cory Bottone, R. Matthew Haas, Lindsey Boroughs, and Michael Harrington.

References

1. Bren A, Eisenbach M (1998) The N terminus of the flagellar switch protein, FliM, is the binding domain for the chemotactic response regulator, CheY. J Mol Biol 278: 507–514
2. Sarkar MK, Paul K, Blair D (2010) Chemotaxis signaling protein CheY binds to the rotor protein FliN to control the direction of flagellar rotation in *Escherichia coli*. Proc Natl Acad Sci U S A 107:9370–9375
3. Zhou J, Lloyd SA, Blair DF (1998) Electrostatic interactions between rotor and stator in the bacterial flagellar motor. Proc Natl Acad Sci U S A 95:6436–6441
4. Vartanian AS, Paz A, Fortgang EA, Abramson J, Dahlquist FW (2012) Structure of flagellar

motor proteins in complex allows for insights into motor structure and switching. J Biol Chem 287:35779–35783

5. Lowry DF, Roth AF, Rupert PB, Dahlquist FW, Moy FJ et al (1994) Signal transduction in chemotaxis. J Biol Chem 269:26358–26362
6. Shannon DA, Weerapana E (2015) Covalent protein modification: the current landscape of residue-specific electrophiles. Curr Opin Chem Biol 24:18–26
7. Boutureira O, Bernardes GJ (2015) Advances in chemical protein modification. Chem Rev 115:2174–2195
8. Halkides CJ, Zhu X, Phillion DP, Matsumura P, Dahlquist FW (1998) Synthesis and biochemical characterization of an analogue of CheY-phosphate, a signal transduction protein in bacterial chemotaxis. Biochemistry 37:13674–13680
9. Silversmith R, Bourret RB (1998) Synthesis and characterization of a stable analog of the phosphorylated form of the chemotaxis protein CheY. Protein Eng 11:205–212
10. Sircar R, Borbat PP, Lynch MJ, Bhatnagar J, Beyersdorf MS et al (2015) Assembly states of FliM and FliG within the flagellar switch complex. J Mol Biol 427:867–886
11. Halkides CJ, McEvoy MM, Casper E, Matsumura P, Volz K (2000) The 1.9 A resolution crystal structure of phosphono-CheY, an analogue of the active form of the response regulator, CheY. Biochemistry 39:5280–5286
12. McAdams K, Casper ES, Haas RM, Santarsiero BD, Eggler AL et al (2008) The structures of T87I phosphono-CheY and T87I/Y106W phosphono-CheY help to explain their binding affinities to the FliM and CheZ peptides. Arch Biochem Biophys 479:105–113
13. Halkides CJ, Bottone CJ, Casper ES, Haas RM, McAdams K (2007) Synthesis of a stable analog of the phosphorylated form of CheY: phosphono-CheY. Methods Enzymol 422:338–351
14. Penefsky HS (1979) A centrifuged-column procedure for the measurement of ligand binding by beef heart F_1. Methods Enzymol 56:527–530
15. Riddles PW, Blakeley RL, Zerner B (1983) Reassessment of Ellman's reagent. Methods Enzymol 91:49–60
16. Bachman J (2013) Site-directed mutagenesis. Methods Enzymol 529:241–248
17. Beyersdorf MS, Sircar R, Lookadoo DB, Bottone CJ, Lynch MJ et al (2017) Production, characterization, and assessment of a stable analog of the response regulator CheY-phosphate from *Thermotoga maritima*. Protein Sci 26(8):1547–1554

Part VIII

Computer Simulation of Chemotaxis

Chapter 27

Quantitative Modeling of Flagellar Motor-Mediated Adaptation

Pushkar P. Lele

Abstract

The bacterial flagellar motor is capable of adapting to changes in the concentrations of extracellular chemical stimuli by changing the composition of the switch complex of the flagellar motor. Such remodeling-based adaptation complements the receptor-mediated adaptation in the chemotaxis network to help maintain high sensitivity in the response of the motor to phospho-CheY concentrations, despite cell-to-cell variability in the abundances of chemotaxis proteins. In this chapter, a modeling approach is described that explains the mechanisms of switch-remodeling and motor-mediated adaptation. The approach is based on observations of structural differences, associated with the direction of motor rotation, that modulate the strength of FliM/FliN binding within the switch. By modulating the number of CheY-P-binding sites within the motor, remodeling maximizes sensitivity over a range of signal levels.

Key words Bacterial motility, Chemotaxis, Flagellar motors, Switch complex, Motor remodeling, Ultrasensitivity, Stochastic simulation

1 Introduction

Binding of the intracellular response regulator (CheY-P) to the flagellar switch proteins FliM and FliN modulates the probability of clockwise motor rotation (CW_{bias}). Modulation of motor reversals enables the cell to bias its random walk up or down a chemical gradient [1]. The switch remodels during fluctuations in [CheY-P], providing high sensitivities over a wide dynamic range [2]. Motor remodeling, along with the robust adaptability of the chemotaxis receptor array, helps the cell overcome variations in Che protein abundance [2] and allows cell migration during chemotaxis [3].

Switch remodeling was first observed by Yuan and coworkers, who found that single motors incorporate additional subunits of FliM when cells are stimulated by attractants [2]. A similar observation was made later with FliN [4, 5], implying that remodeling restructures the assembly of both FliM and FliN. Addition or removal of FliM/FliN protomers changes the number of CheY-P

Michael D. Manson (ed.), *Bacterial Chemosensing: Methods and Protocols*, Methods in Molecular Biology, vol. 1729, https://doi.org/10.1007/978-1-4939-7577-8_27,

binding sites, thereby effecting changes in CW_{bias} despite invariant levels of CheY-P. The mechanism by which motors remodel remained unclear until it was determined that remodeling occurs independently of CheY-P concentration [6]. Instead, the direction of flagellar rotation controls remodeling; CCW (counterclockwise) motors contain more FliM subunits than CW (clockwise) motors.

Here, we provide a description of theoretical models that explain how differences in the strength of binding of FliM and FliN facilitate motor-mediated adaptation to long-time variations in [CheY-P]. Simulation steps are discussed that accurately predict the stochastic nature of the structural and functional adaptations that occur in the switch complexes of single motors during chemical stimulation. These models are consistent with a variety of experimental measurements of the structure and function of switch complexes [7].

2 Methods

Detailed descriptions of the mechanisms discussed here are available elsewhere [7]. Briefly, switch remodeling is predicted to occur because of differences in the number of strong binding sites available within the motor for FliM/FliN protomers in the CW and CCW conformations. These differential affinities create an imbalance in the rates of unbinding/binding of FliM and FliN protomers when the motor switches the direction of rotation. Consequently, FliM and FliN remodel each time the direction of rotation changes. The end result is a modulation of the number of CheY-P-binding sites, which effects a change in motor sensitivity.

2.1 Assumptions Implicit in the Model for Motor Remodeling

1. The total number of binding sites ($M = 56$) within the motor for FliM/FliN protomers remains constant irrespective of rotor conformation.
2. Each protomer consists of 1 FliM and 4 FliN subunits, which binds or unbind from the motor as a single unit.
3. There are of two kinds of protomer-binding sites, strong and weak. Protomers bind to the weak sites reversibly, and only a few of these sites are occupied at any given time. Protomers bind to the strong sites irreversibly, and these sites remain fully occupied with little or no exchange of FliM/FliN (*see* **Note 1**).

2.2 Modeling Approach

1. The total protomers in a motor with a steady CW_{bias} are given by:

$$N = N_{NE}{}^{i} + C_S \tag{1}$$

Irreversibly bound protomers are represented by $N_{NE}{}^{i}$ ($i \in$ CCW, CW), and reversibly bound protomers are represented

by *C*. The subscripts NE and *S* refer to the nonexchanging fraction and the steady state, respectively.

2. The relation between the vacant weak sites *B*, and *M*, *C* and N_{NE} is given by:

$$M = N_{NE}{}^{i} + C_S + B_S \tag{2}$$

3. Each switch in the direction of rotation changes the value of $N_{NE}{}^{i}$. This change is incorporated into the model by assigning one of the two values to $N_{NE}{}^{i}$, depending on the direction of rotation following the switch. A change in $N_{NE}{}^{i}$ modifies *C*, providing the initial condition for solving the dynamic-remodeling equation (Eq. 4):

$$C\left(t = t_s\right) = N\left(t = t_s\right) - N_{NE}{}^{j} \tag{3}$$

Here, t_s is the instant of switch, $N\left(t = t_s\right)$ refers to the total FliM/FliN protomers existing in the motor at that instant, and the superscript *j* in $N_{NE}{}^{j}$ indicates the new rotational direction adopted by the motor.

4. The evolution of the switch to a new steady state is governed by the dynamics of the weakly bound protomers and is limited by the amount of time the motor spends in its newly adopted conformation. The kinetics driving the relaxation are:

$$\frac{dC}{dt} = k_{on}B - k_{off}C \tag{4}$$

k_{on} and k_{off} are the pseudo first order on rate and the off rate for the weakly bound protomers, respectively. The expressions above can be utilized to simulate the stochastic fluctuations in the number of motor-bound protomers with a simple Monte-Carlo Scheme [8]. For an indefinite CCW (or CW) interval, the labile fraction attains dynamic equilibrium, resulting in N_S = 45 (or N_S = 34) protomers, consistent with previous observations [2]. At a steady CW_{bias} ($\neq$ 0 or 1), the total number of protomers, N_S, fluctuates around a mean value that varies linearly with CW_{bias}.

2.3 Assumptions of the Model for Adaptation During Remodeling

1. The switch can be described by a two-state model, in which the CW conformation represents the higher-energy, unfavorable state. Switching is probabilistic.
2. The number of CheY-P molecules bound to the motor modulates the differences in free energy (*E*) between the CW and CCW conformations. Each CheY-P that binds contributes a small but constant offset towards *E* (*see* **Note 2**).

2.4 Modeling Approach

1. The number of CheY-P molecules (Υ_B) bound to N protomers at a given intracellular concentration of CheY-P (c) is determined from the following expression [7]:

$$\Upsilon_B = N^{CW}{}_S \left[\left(1 - CW_{bias}\right) \frac{c}{c + K_{CCW}} + CW_{bias} \frac{c}{c + K_{CW}} \right] + \left(N - N^{CW}{}_S\right)\left(1 - CW_{bias}\right) \frac{c}{c + K_{CCW}} \quad (5)$$

$N^{CW}{}_S$ indicates the maximum number of protomers that the motor can hold in the CW conformation. Equation 5 incorporates a linear dependence of N_S (the steady-state numbers of protomers) on the CW_{bias} (*see* **Note 3**). Binding of CheY-P to the motor in the two conformations is characterized by two dissociation constants, K_{CW} and K_{CCW} (*see* **Note 4**).

2. Modulation of the CW_{bias} by the bound molecules of CheY-P is calculated from a two-state model following an earlier approach [9]:

$$CW_{bias} = \frac{1}{1 + \exp\left(E - \Psi \Upsilon_B\right)} \quad (6)$$

2.5 Stochastic Simulations

1. Chemical stimulation of the cell perturbs CheY-P levels instantaneously, and the transient change in CheY-P can be estimated from quantitative models of the chemotaxis network [10]. The resultant perturbation in CW_{bias} is determined from the motor response vs [CheY-P] curves available for a range of N_S values [7] (*see* **Note 5**).
2. The perturbation in CW_{bias} modifies the distributions of wait-time intervals for CCW and CW rotation. This effect is accounted for by sampling from exponential distributions with means that vary with CW_{bias} (*see* **Note 6**).
3. Over the duration of the subsequent switch interval, the FliM/FliN protomers are updated following the remodeling approach described in Subheading 2.1 (*see* **Note 7**).
4. At the end of the interval, the probabilities of CW rotation are updated via Eqs. 5 and 6 to account for protomers newly added or removed (*see* **Note 8**).
5. All prior steps are run in a loop to progressively calculate the changes in the switch-structure and function, over a desired duration of stimulation (*see* **Note 9**).

3 Notes

1. Single motors have been observed to carry two kinds of switch-protomers, a core made up of strongly bound protomers and a labile fraction consisting of weakly bound protomers. Weakly bound protomers continuously exchange with a pool of free protomers in the cell [11, 12]. Based on our measurements, $N_{NE}{}^{i} \sim 12$ when the motor is in the CW conformation and ~34 when it is in the CCW conformation [6].
2. All parameters needed for simulations, either experimentally measured or estimated, are available in ref. 7.
3. At steady state, the dependence of the steady-state numbers of protomers in the motor and CW_{bias} can be derived from the model, given by:

$$N_S / N^{CW}{}_S = CW_{bias} + \left(1 - CW_{bias}\right) N^{CCW}{}_S / N^{CW}{}_S$$

   This relation matches experimental measurements of FliM numbers versus CW_{bias} reasonably well [7].
4. CheY-P binds with a higher affinity to the motor in the CW conformation than in the CCW conformation, K_{CCW} is ~4 K_{CW} [13, 14].
5. Motor-remodeling shifts the motor-response versus [CheY-P] curves, similar to the shifts in kinase activity versus external ligand curves. The true sensitivity of the motor has been recently measured [15]. The steepness of our predicted motor response versus [CheY-P] curve (for a given N) is similar to experimentally measured values [15].
6. Traces of motor switching are simulated by sampling wait-times from exponential distributions of respective intervals. The means of these distributions have been experimentally determined to vary with CW_{bias} [14].
7. A Monte-Carlo code is executed in each interval to simulate the stochastic binding and unbinding of protomers. Remodeling progresses through the process of binding and dissociation to the available weak sites. The process continues until the imbalance between the rates of binding and dissociation disappears or until the time interval ends. In an alternate formulation, the time interval can be terminated as soon as N (the number of protomers) changes by 1.
8. Equation 5 determines the change in the number of CheY-P molecules bound to the motor as a result of remodeling. Equation 6 links remodeling to the ultrasensitive switch response.

9. The time scales over which remodeling occurs are relatively slow, with $1/k_{off}$ about 25–50 s [11]. The mean wait-time intervals are typically several hundred milliseconds. Thus, a time-step of ~1 ms is used for the Monte-Carlo simulations. The cumulative time is updated at the end of each interval by summing over the individual time intervals obtained from each run.

Acknowledgment

This work was supported by funds from Texas A&M Engineering Experiment Station. The PI acknowledges support from the National Institute Of General Medical Sciences of the National Institutes of Health under Award Number R01GM123085. The content is solely the responsibility of the author and does not necessarily represent the official views of the National Institutes of Health.

References

1. Berg HC, Brown DA (1972) Chemotaxis in *Escherichia coli* analyzed by 3-dimensional tracking. Nature 239:500–504
2. Yuan J, Branch RW, Hosu BG, Berg HC (2012) Adaptation at the output of the chemotaxis signalling pathway. Nature 484:233–236
3. Dufour YS, Fu X, Hernandez-Nunez L, Emonet T (2014) Limits of feedback control in bacterial chemotaxis. PLoS Comput Biol 10:e1003694
4. Branch RW, Sayegh MN, Shen C, Nathan VS, Berg HC (2014) Adaptive remodelling by FliN in the bacterial rotary motor. J Mol Biol 426:3314–3324
5. Delalez NJ, Berry RM, Armitage JP (2014) Stoichiometry and turnover of the bacterial flagellar switch protein FliN. mBio 5:e01216–14
6. Lele PP, Branch RW, Nathan VS, Berg HC (2012) Mechanism for adaptive remodeling of the bacterial flagellar switch. Proc Natl Acad Sci U S A 109:20018–20022
7. Lele PP, Shrivastava A, Roland T, Berg HC (2015) Response thresholds in bacterial chemotaxis. Sci Adv 1:e1500299
8. Cai X (2007) Exact stochastic simulation of coupled chemical reactions with delays. J Chem Phys 126:124108
9. Turner L, Samuel ADT, Stern AS, Berg HC (1999) Temperature dependence of switching of the bacterial flagellar motor by the protein CheY(13DK106YW). Biophys J 77:597–603
10. Tu Y (2013) Quantitative modeling of bacterial chemotaxis: signal amplification and accurate adaptation. Annu Rev Biophys 42: 337–359
11. Delalez NJ, Wadhams GH, Rosser G, Xue Q, Brown MT et al (2010) Signal-dependent turnover of the bacterial flagellar switch protein FliM. Proc Natl Acad Sci U S A 107: 11347–11351
12. Fukuoka H, Inoue Y, Terasawa S, Takahashi H, Ishijima A (2010) Exchange of rotor components in functioning bacterial flagellar motor. Biochem Biophys Res Commun 394:130–135
13. Duke TA, Le Novère N, Bray D (2001) Conformational spread in a ring of proteins: a stochastic approach to allostery. J Mol Biol 308:541–553
14. Bai F, Branch RW, Nicolau DV Jr, Pilizota T, Steel BC et al (2010) Conformational spread as a mechanism for cooperativity in the bacterial flagellar switch. Science 327:685–689
15. Yuan J, Berg HC (2013) Ultrasensitivity of an adaptive bacterial motor. J Mol Biol 425: 1760–1764

Chapter 28

Molecular Modeling of Chemoreceptor:Ligand Interactions

Asuka A. Orr, Arul Jayaraman, and Phanourios Tamamis

Abstract

Docking algorithms have been widely used to elucidate ligand:receptor interactions that are important in biological function. Here, we introduce an in-house developed docking-refinement protocol that combines the following innovative features. (1) The use of multiple short molecular dynamics (MD) docking simulations, with residues within the binding pocket of the receptor unconstrained, so that the binding modes of the ligand in the binding pocket may be exhaustively examined. (2) The initial positioning of the ligand within the binding pocket based on complementary shape, and the use of both harmonic and quartic spherical potentials to constrain the ligand in the binding pocket during multiple short docking simulations. (3) The selection of the most probable binding modes generated by the short docking simulations using interaction energy calculations, as well as the subsequent application of all-atom MD simulations and physical-chemistry based free energy calculations to elucidate the most favorable binding mode of the ligand in complex with the receptor. In this chapter, we provide step-by-step instructions on how to computationally investigate the binding of small-molecule ligands to protein receptors by examining as control and test cases, respectively, the binding of L-serine and *R*-3,4-dihydroxymandelic acid (*R*-DHMA) to the *Escherichia coli* chemoreceptor Tsr. Similar computational strategies can be used for the molecular modeling of a series of ligand:protein receptor interactions.

Key words Chemoattractants, 3,4-Dihydroxymandelic acid (DHMA), Chemoreceptor Tsr, Molecular docking, Molecular dynamics simulations

1 Introduction

Molecular interactions, including protein:protein and small-molecule ligand (hereinafter referred to as ligand):protein interactions, govern the biological processes that are vital for life. Understanding the relationship between the structure and function of interactions at an atomic level is central both to understand the basic biochemistry of signal transduction and to discover novel chemical compounds that can be used in drug development [1]. Interactions between a protein and another protein or a ligand play a key role in chemotaxis, the mechanism by which bacteria control their motility to exploit the chemical composition of their surroundings. Through chemotaxis, bacteria approach chemically favorable environments

Michael D. Manson (ed.), *Bacterial Chemosensing: Methods and Protocols*, Methods in Molecular Biology, vol. 1729, https://doi.org/10.1007/978-1-4939-7577-8_28,

and avoid unfavorable ones [2]. Chemoreceptors are sensory protein receptors that rely on ligands to mediate bacterial chemotaxis. Signaling in bacteria such as *Escherichia coli,* transduced via ligand:chemoreceptor interactions, is relatively well understood at a molecular level [3]. Most of the known chemoattractants are nutrients [3]. Tsr senses L-serine and related amino acids [4, 5]; Tar senses L-aspartate and maltose [5, 6]; Trg senses ribose and galactose [7]; and Tap senses dipeptides and pyrimidines [8, 9]. Recent studies indicate that 3,4-dihydroxymandelic acid (DHMA) also induces chemotaxis in *E. coli* by binding to the chemoreceptor Tsr [10]. Chemotaxis to DHMA, a metabolite of the neurotransmitter and hormone norepinephrine, may contribute to virulence in *E. coli* and other Tsr containing enteric bacteria [10].

The atomic structure of amino acid ligand L-serine in complex with the periplasmic sensory domain of Tsr was resolved using X-ray crystallography [11]. According to the X-ray studies, the Tsr chemoreceptor is a dimer with two nearly identical ligand binding pockets. Each ligand binding pocket is formed by Arg64, Leu67, Asn68, Leu136, Leu139, and residues within the residue moiety 151–157 belonging to the majority half as well as residues Arg69′ and Ile72′ belonging to the minority half binding site [11]. (The symbol′ indicates residues from the minority half binding site [10].) Unlike the aspartate binding sites of Tar, of which only one is occupied at a time, both of the serine binding pockets of Tsr are bound by single L-serine molecules in the crystal structure [11]. It is possible that the serine molecule at the second site is an artifact of the high serine concentration used to soak the crystal, or it may represent an intermediate state in serine binding or dissociation [11]. It could also be related to the proposed high and low affinity serine-sensing systems of Tsr [12].

Computational methods are increasingly becoming powerful tools in the fields of protein structure prediction and design [13–15]. They can be used to produce accurate models of ligand:receptor complexes to offer important insights into how chemoeffector ligands interact with chemoreceptors. For example, in a recent study by Yu et al. [16], the binding conformations of the small ligand molecules aspartate, CHDCA, and cic-PDA in complex with Tar, as well as the corresponding Tar receptor motions, were investigated using a combination of molecular dynamics (MD) simulations and principal component analysis tools.

Computational docking methods aim to predict how ligands bind to receptors, relying on the combination of a search algorithm to generate possible binding conformations and a scoring function to evaluate the conformations [17]. Pioneered in the 1980s [18], advances in the power of computational resources and efficiency have allowed docking algorithms to evolve to include a wide array of search algorithms and scoring methods. Interestingly,

according to a comprehensive evaluation, the docking program with the greatest sampling power is 59.8% accurate in predicting the best ligand:receptor binding pose within a root mean square deviation of 2 Å from the experimentally resolved binding conformation [19]. The improvement of existing computational tools or the development of new ones that can accurately predict the structure of ligand:receptor complex is of great importance.

The computational procedure of docking a small ligand molecule in a complex with a receptor can potentially be categorized into two stages: (1) identify potential ligand-binding pockets of the receptor, (2) identify the most energetically favorable binding conformation in the identified binding pockets, which is the most probable conformation to occur in reality. In a scenario where experimental information (e.g., from site-directed mutagenesis studies) is available to reveal a ligand binding site, **stage 1** can be circumvented. In this case, the search space can be limited to a specific region of the receptor, which will be referred to as a binding pocket, and a docking protocol, which hereinafter will be referred to as docking-refinement protocol, can be introduced to refine the orientation and position of a ligand in the receptor's binding pocket, and thus elucidate the ligand:receptor structure.

In this chapter, we describe a newly developed in-house docking-refinement protocol that can be used to predict a highly accurate model of the conformation of a ligand in complex with a receptor. The protocol relies primarily on the use of MD simulations and energy calculations in CHARMM [20]. For studies in which the general location of a binding site is known, yet the orientation of the ligand in the binding pocket is unknown, this protocol can be implemented to produce a highly accurate model of the complex. For example, the same protocol has recently been applied by us to investigate the structure of 2,3,7,8-tetrachloridib enzo-p-dioxin (TCDD) in complex with the mouse aryl hydrocarbon receptor (AhR) [21]. The computational modeling of TCDD in complex with AhR was significantly facilitated by experimental data that mapped the binding site of TCDD within the receptor. In the same study, the protocol was also used to investigate the binding of 1,4-DHNA in complex with mouse AhR [21].

In the test case of the present study, which involves the investigation of binding of *R*-DHMA in complex with Tsr, experimental data suggest an overlap between the *R*-DHMA and serine binding sites in Tsr [10]. Thus, we introduced the protocol to computationally elucidate how *R*-DHMA binds to the *E. coli* Tsr receptor in the X-ray resolved binding pocket of serine in complex with Tsr [11]. It is worth noting that, in this chapter, the same protocol was used to successfully predict the binding of L-serine to the *E. coli* Tsr receptor, which serves as a validation of the specific system used in this study.

2 Materials

In the described protocol we primarily use CHARMM [20] and modules available in CHARMM [20]. Visit http://charmm.chemistry.harvard.edu for instructions on how to obtain a license and download the latest version. The instructions listed in this chapter apply to CHARMM version c39b1 [20].

3 Methods

In the following steps, we introduce our in-house developed docking-refinement protocol to computationally elucidate *R*-DHMA and serine binding to *E. coli* Tsr. The protocol was introduced first to elucidate the binding of L-serine to Tsr for validation purposes (control case), and subsequently it was introduced to elucidate the binding of *R*-DHMA to Tsr (test case). In docking studies involving other ligands and receptors, the docking-refinement protocol is recommended to be applied in a control case in which the binding conformation of the ligand has been experimentally resolved or heavily investigated for validation purposes.

3.1 Preparation of the Receptor and Ligand

1. If the structure of the receptor has been experimentally resolved, then the receptor structure is obtained from the Protein Data Bank (PDB). If there are PDB structures of both the receptor unbound by a ligand and a receptor bound by a ligand, and if the binding site of the ligand under investigation is known to overlap with the binding site of the resolved ligand, then the use of the bound structure of the receptor may be advantageous. Considerations include: (1) The binding pocket of the bound receptor can be more spacious, enabling an easier initial placement of the ligand under investigation, (2) If both the resolved ligand and the ligand under investigation elicit signals from the receptor, then starting from the structural conformation appropriate for active signaling state of the receptor may be beneficial. For our test case, the PDB structure of *E. coli* Tsr bound to L-serine (PDB ID: 3ATP [11]) corresponds to the receptor structure used to examine the binding of *R*-DHMA to Tsr. Residues 39 through 185 of Tsr were investigated in a complex with L-serine and with *R*-DHMA, independently.

   In cases where the receptor's structure has not been experimentally resolved, protein structure prediction methods can be implemented to model the receptor. Some possible protein structure prediction servers or programs include, but are not limited to, I-TASSER [22], HHpred [23], and SWISS-MODEL [24] (*see* **Note 1**).

2. A mol2 file of the ligand under investigation is obtained. The ligand is parametrized with an appropriate parametrization server or program compatible with CHARMM [20] and the corresponding CHARMM force field (e.g., CHARMM22 [25] or CHARMM36 [26]) that will be used in the subsequent simulations. Examples of parametrization servers or programs include CGENFF [27], MATCH [28], and SwissParam [29] (*see* **Note 2**). For our test case, *R*-DHMA (ZINC ID: 388311) is obtained from the ZINC Database [30] (http://zinc.docking.org) and is parametrized using the CGENFF [26] server (https://cgenff.paramchem.org). For our control case, the parameters for serine were obtained from the CHARMM36 [26] force field.
3. If a bound structure of the receptor is available, and if the ligand under investigation is known to bind to or interact with residues of the same binding pocket, then the initial placement of the ligand under investigation can be guided by the location of the resolved ligand in complex with the receptor. If a bound structure is unavailable, then experimental data can guide the initial placement of the ligand under investigation. ShaEP [31] is a computational tool that can be used to superimpose two rigid ligand-sized molecules based on the shape of the two structures and their electrostatic potential. In the former case, where a ligand-bound structure of the receptor is available, ShaEP [31] can be introduced to superimpose the ligand to be docked onto the resolved ligand. For our test case, we use the ShaEP [31] algorithm to superimpose *R*-DHMA onto the serine ligand bound in Chain A of Tsr to initially place *R*-DHMA inside the binding pocket. The initial placement of L-serine is in line with the X-ray structure [11].

   If a bound structure of an existing (preferably structurally analogous) compound in complex with the receptor is not available, then the ligand can be initially placed inside the binding pocket using a docking program such as AutoDock Vina [32], as in reference [21]. In these cases, the search space could optimally be guided by experimental data and mutagenesis studies determining receptor residues involved in ligand binding. The ideal search space in the receptor's structure is sufficiently large to permit the ligand's initial placement in the binding pocket.

   A recent study suggested that 3D similarity-based ranking in docking consistently improves the enrichment of active compounds compared to ranking obtained using scoring functions, even if only a single crystallographic ligand is used as a reference [33]. In the docking-refinement protocol, the initial placement of a ligand of interest inside the receptor's binding pocket is guided by 3D similarity to another ligand in complex

with the receptor if an experimental structure exists for the latter. Despite the fact that in the docking-refinement protocol the initial placement is not explicitly considered in the analysis and does not directly contribute to the conformations generated in the later steps, the initial placement is important as it determines the initial position of the center of mass of the ligand, and thus influences the generated binding poses.

4. After the initial placement of the ligand under investigation inside the binding pocket, the experimentally resolved ligand(s) are removed from the binding pocket. For our test case, the serine ligands within both binding pockets of Tsr (chain A [11] and chain B [11]) are removed after the initial placement of *R*-DHMA. For the initial placement of L-serine, the X-ray structure was used, and the serine ligand within chain B [11] was removed.
5. For the purposes of CHARMM syntax, *segnames* are assigned as needed to the PDB file of the ligand:receptor complex.
6. The terminal ends of the receptor and ligand are appropriately defined. If the structure under investigation is not entirely resolved, then the truncated N- and C-terminal ends may be acetylated and amidated, respectively, to alleviate the placement of artificial charges at the truncated termini. For the problem under investigation, the N-terminal and C-terminal ends of the Tsr chemoreceptor are respectively acetylated and amidated. For organic molecule ligands, no terminal end patch is assigned. Terminal end patches were not assigned for *R*-DHMA. For the control case, the N-terminal and C-terminal ends of serine are appropriately positively and negatively charged, respectively.

3.2 Generation and Selection of the Most Promising Docked Poses

In what follows, we describe how the docking poses of the ligand in complex with the receptor are generated through the docking-refinement protocol developed in-house, which is aimed at a near-infinite search of the binding poses that may occur within the ligand:receptor complex. In the last step of this section, the most promising ligand:receptor docked poses are selected for further investigation. The steps of this section are summarized in Fig. 1.

1. Appropriate molecular representations and force fields for the receptor and ligand are selected. The use of an implicit solvent model can be advantageous for the generation of the docked ligand:receptor poses, as the absence of explicitly modeled solvent molecules can facilitate the docking procedure by increasing the flexibility of the binding pocket and decreasing the amount of time needed for the simulation to complete. For our test case, the aqueous environment is taken into account implicitly using Generalized Born with a Simple Switching

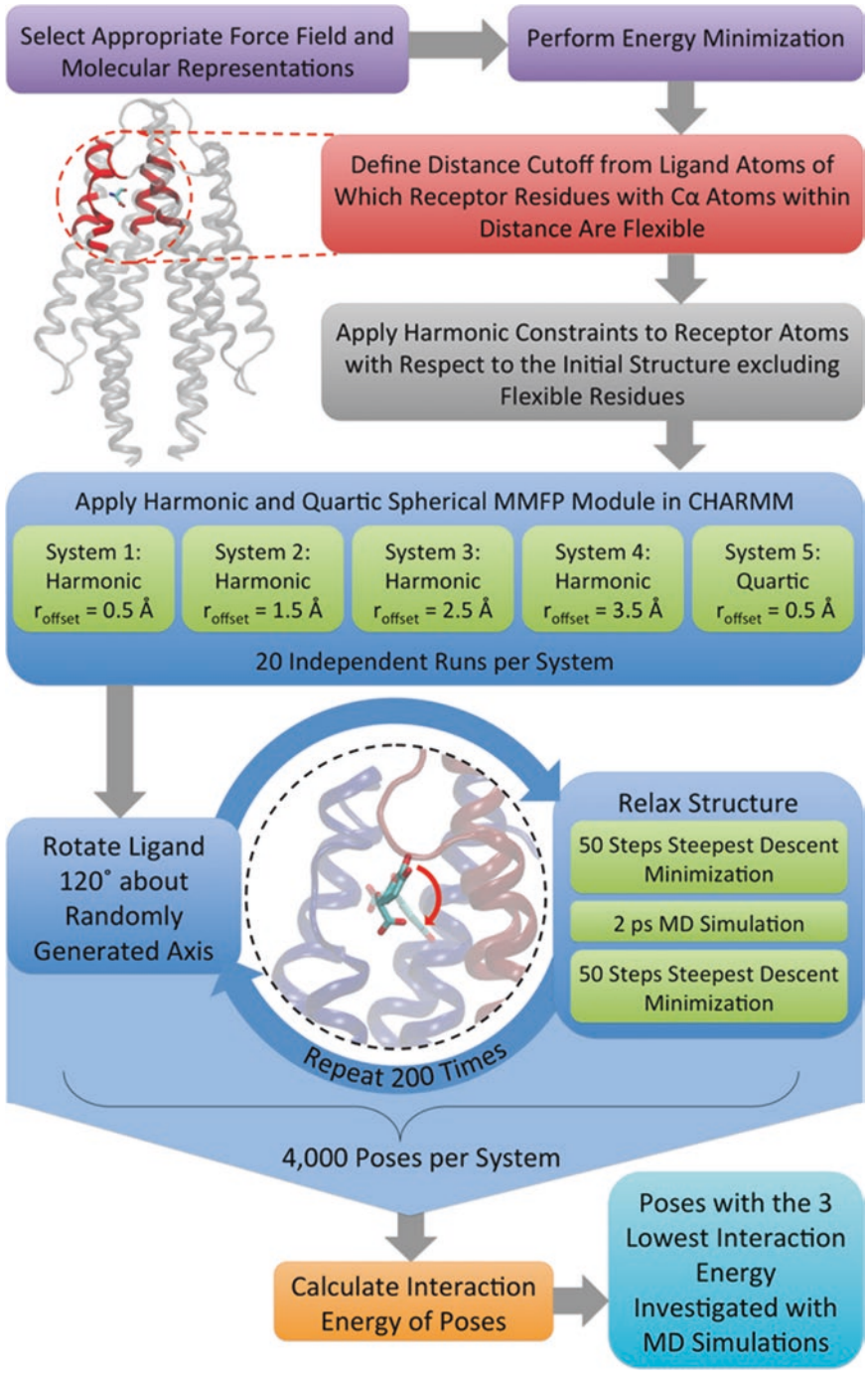

Fig. 1 Workflow for the generation and selection of ligand:receptor docked poses

(GBSW) [34], with the surface tension coefficient set to 0.03 kcal/(mol·Å^2). All simulations are performed using CHARMM [20]. The CHARMM36 force field [26] is used for the topology and parameters of the complex, and CGENFF [27] is used to parametrize *R*-DHMA. In these and all subsequent MD simulations, bond lengths to hydrogen atoms are constrained using the SHAKE algorithm [35].

2. A short energy minimization with all heavy atoms constrained is recommended to prepare the system for the subsequent steps and to alleviate any possible steric clashes in the structure. At this stage, a visual inspection can be beneficial to ensure that the ligand is properly placed.
3. The binding pocket of the receptor is defined using a specified distance cutoff, as follows. Both side-chain atoms and backbone atoms of receptor residues with Cα atoms within the defined distance cutoff are considered the binding pocket. The binding pocket is unconstrained and remains flexible during the subsequent docking simulations. The cut-off distance should maintain a balance between maximizing the flexibility of the binding pocket and minimizing any structural changes in the surrounding receptor residues (*see* **Note 3**). Flexibility within the binding pocket facilitates the docking procedure and allows both the ligand and receptor to explore more conformations. For our test and control cases, the distance cutoff is set to 9 Å from any atom of the experimentally resolved serine ligand to define our flexible binding pocket residues.
4. A harmonic constraint is applied to the atoms of the receptor with respect to the initial structure excluding the atoms of the residues defined as flexible in the step above. This constraint will be present throughout the docking simulation runs. The introduction of this constraint guarantees the preservation of the structural integrity of the receptor atoms outside the binding pocket, and also ensures that the docking simulations will not introduce any bias associated with potential allosteric effects due to ligand binding to the receptor. A harmonic force constant of 1.0 kcal/(mol·Å^2) proved to be sufficient to maintain the structure of the receptor during the docking simulations for both our test and control cases.
5. During the docking simulation runs, the ligand should remain within the expected binding pocket of the receptor. This can be achieved through the introduction of a spherical potential energetically "penalizing" the ligand from moving away from the binding pocket. The Miscellaneous Mean Field Potential (MMFP) module in CHARMM [20] provides the means to constrain the ligand within the binding pocket. The harmonic spherical MMFP energetically penalizes the ligand if its center of mass leaves a sphere of a set radius from the center of mass

of the ligand in its initial position. The potential enacted on the ligand by the harmonic spherical potential is defined by Eq. 1:

$$\left[E(r) = \frac{1}{2}a \cdot (r)^2\right] : \left[E(r) = 0 \forall r < r_{\text{offset}}\right] \quad (1)$$

where $E(r)$ is the potential, a is the amplitude of the potential, r is the difference between the initial and new center of mass of the ligand, and r_{offset} is a user-defined offset such that the potential is zero if r is less than r_{offset}.

The quartic spherical MMFP penalizes the ligand from moving away from the binding pocket, but it also simultaneously encourages the ligand to leave its initial position. With quartic spherical MMFP, the potential is defined by Eq. 2:

$$\left[E(r) = a \cdot (r - r_{\text{offset}})^2 \cdot \left((r - r_{\text{offset}})^2 - p\right)\right] : \left[E(r) = 0 \forall r < r_{\text{offset}}\right] \quad (2)$$

where $E(r)$ is the potential, a is the amplitude of the potential, r is the difference between the initial and new center of mass of the ligand, p is a parameter, and r_{offset} is a defined offset distance such that the potential is zero if r is less than r_{offset}. In addition to constraining the ligand to a sphere of a user-defined radius from the original center of mass of the ligand at the initial position within the binding pocket, the quartic spherical MMFP, as defined in Eq. 2, also allows the ligand to explore additional positions in which the center of mass will not coincide with the center of mass of its initial placement in the binding pocket; this can reduce the bias due to the initial positioning of the ligand. Both the harmonic spherical and quartic spherical harmonic potentials can be independently employed with user-defined parameters such as a, r_{offset}, and p.

For both serine:Tsr (the control case) and *R*-DHMA:Tsr (the test case) docking simulations, five systems of MMFP are used, of which four are harmonic spherical MMFPs and one is a quartic spherical MMFP. In Systems 1–4, the harmonic spherical MMFP is used with a set to 10.0 kcal/(mol-Å^2). In System 1, r_{offset} is set to 0.5 Å; in System 2, r_{offset} is set to 1.5 Å; in System 3, r_{offset} is set to 2.5 Å; in System 4, r_{offset} is set to 3.5 Å. In System 5, the quartic spherical MMFP is used with a set to 25.0 kcal/(mol-Å^2), r_{offset} is set to 0.5 Å, and p is set to 1.

6. For both the control and test cases, the five different systems are investigated. Per system, 20 independent runs of docking MD simulation runs are initiated. In summary, in each of the 20 independent runs, the ligand is rotated about a randomly generated axis (*see* below), an energy minimization is

performed, a 2 ps MD simulation is performed, and an energy minimization is performed again, and the produced docked structure is saved. This procedure is repeated 200 times for the 20 independent runs.

7. A random axis is generated, and the ligand is rotated by 120° around the axis. Note that an attempted rotation may fail, as the ligand may collide with a receptor residue, causing the docking simulation run to stop. In such an unlikely scenario, the docking run is repeated. For the control and test cases, serine and *R*-DHMA were independently rotated within the defined binding pocket of Tsr.
8. Upon rotation of the ligand, an energy minimization of the produced structure is performed, using 50 steps of steepest descent. The energy minimization is performed to alleviate any possible steric clashes due to the rotation performed in the previous step. Then, a 2 ps MD simulation is performed to allow the binding pocket and ligand to adjust to the rotation; the initial velocities are reassigned before the MD simulation begins. Upon completion of the short MD simulation, an additional energy minimization of the structure produced is performed using 50 steps of steepest descent. The constraints defined in **step 4** is present throughout this step.
9. **Steps 7** and **8** are repeated for 200 times in each of the 20 docking simulation runs for each system. A total of $20 \times 200 = 4000$ snapshots, or binding poses, are generated and extracted per system. As five systems are investigated for the test and control case, 20,000 snapshots total are independently saved for further investigation in both cases.
10. The interaction energy of the 4000 generated ligand:receptor docked poses per system is calculated. The binding poses with the three lowest interaction energies (accounting for van der Waals and electrostatic energies) per system are considered promising and are saved for subsequent use. This step acts as a fast initial screening in which the binding poses with the lowest interaction energies are selected for further investigation. Thus, for our test and control cases, a total of 15 candidate binding poses of both the *R*-DHMA:Tsr complex and the serine:Tsr complex are taken onto the next steps, independently (*see* **Note 4**).

3.3 Molecular Dynamics Simulations of Selected Complexes

All-atom explicit-solvent multi-ns MD simulations are performed using the selected promising candidate ligand:receptor binding poses as starting conformations. The aim is to refine the receptor:ligand conformations, to improve intermolecular interactions, and ultimately to determine the structural stability of the binding conformations and to assess the most energetically favorable binding conformation.

1. The use of explicit water as a solvent can be introduced to achieve higher accuracy in conjunction with the CHARMM36 force field [36]. For our test and control cases, we account for aqueous environment explicitly and solvated each complex in a truncated octahedron of size 110 Å with pre-equilibrated water and a potassium chloride ion concentration of 0.15 M using files produced by the CHARMM-GUI user interface [37] (http://www.charmm-gui.org). The TIP3P model is used for water. Fast table lookup routines are used for non-bonded interactions [38], and periodic boundary conditions are applied.
2. An energy minimization is performed on the starting conformations with heavy atoms of both the ligand and receptor constrained to alleviate possible steric clashes (*see* **Note 5**). For the 15 selected conformations of the control and test cases, we perform 50 steps of steepest descent minimization followed by 50 steps of Adopted Basis Newton-Raphson minimization with all atoms except solvent molecules (water and ions) fixed in space, and an additional 50 steps of steepest descent minimization followed by 50 steps of Adopted Basis Newton-Raphson minimization for the entire system, with heavy atoms of the ligand and receptor backbone atoms constrained. The harmonic force constants imposed on the receptor backbone atoms and side-chain atoms are equal to 1.0 kcal/(mol·Å^2), 1.0 kcal/(mol·Å^2) and 0.1 kcal/(mol·Å^2), respectively.
3. The ligand:receptor complexes encompassing the candidate binding poses are subjected to a position-restrained equilibration, which aims to avoid any unnecessary structural distortion when initiating the MD simulations. In this step, all receptor and ligand heavy atoms are constrained to their starting positions, allowing the solvent molecules to relax around the complex. The equilibration step may be tailored to the ligand:receptor docking study being performed (*see* **Note 6**). For the 15 selected energetically minimized conformations of the control and test cases, we equilibrate each complex using 1 ns explicit solvent MD simulations with the heavy atoms of the ligand and Tsr backbone atoms constrained with a harmonic force constant equal to 1.0 kcal/(mol·Å^2), and the Tsr side chain atoms constrained with a harmonic force constant equal to 0.1 kcal/(mol·Å^2). The temperature is maintained at 300 K using the Hoover thermostat, and the pressure is held at 1 atm.
4. The constraints imposed on the complexes during the equilibration stage are removed, and the 15 selected conformations of the control and test cases are investigated through 10 ns explicit solvent MD simulations. If necessary, some light constraints may be introduced to truncated termini of the receptor to maintain the integrity of the complexes (*see* **Note 7**). In this step, coordi-

nates are saved throughout the duration of the simulation for the analysis in the following steps. A portion of the beginning of the production run may also be considered as part of the equilibration of the complex and may not be used for structural or energetic analysis. In the control and test case, the temperature is maintained at 300 K using the Hoover thermostat and the pressure is held at 1 atm. Coordinates are saved every 10,000 steps for analysis purposes.

5. While the MD simulations are running, it is recommended to visually check the simulation snapshots to ensure that the runs are progressing properly.

3.4 Final Evaluation/ Scoring of Binding Poses

1. The MM-GBSA approximation [39] is introduced, analogously to references [40–44], to evaluate the simulated complexes average association free energy and to assess the most energetically favored binding mode(s). For our control and test cases, we use MM-GBSA [39] association free energy calculations to determine which of the 15 simulated trajectories of the serine:Tsr (the control case) and *R*-DHMA:Tsr (the test case) complexes acquire the lowest average association free energy. In the control case, the binding mode acquiring the lowest average MM-GBSA association free energy is selected. In the test case, among the 15 *R*-DHMA:Tsr simulations, two binding modes were nearly identical with regard to the ligand:receptor binding structure as well as with regard to the intermolecular interactions formed between the ligand and the receptor. Both binding modes acquire the two equally lowest average association free energies. We postulate that the structural complex encompassed within the two binding modes is highly likely to correspond to the naturally occurring one (*see* **Note 8**). The *R*-DHMA:Tsr binding mode with the lowest average RMSD (as calculated in Subheading 3.2) throughout its respective 10 ns simulation is selected. The selected complex structures of serine and *R*-DHMA acquiring the lowest average association free energies are shown in Fig. 2a, b, respectively. Ideally, the selected function that is used to assess the energetic binding favorability of the simulated complexes can clearly differentiate the most stable pose from the other poses (*see* **Note 9**). Possible alternative empirical or semi-empirical functions could additionally be used as scoring tools to assess the energetic favorability of the ligand:receptor simulated conformations under investigation, and may include among others the AutoDock Vina scoring function [32], the DSX scoring function [45], and so forth.
2. The control case is used to validate the capacity of the protocol to predict the ligand:receptor complex structure under investigation in the test case. In the validation, the structural and

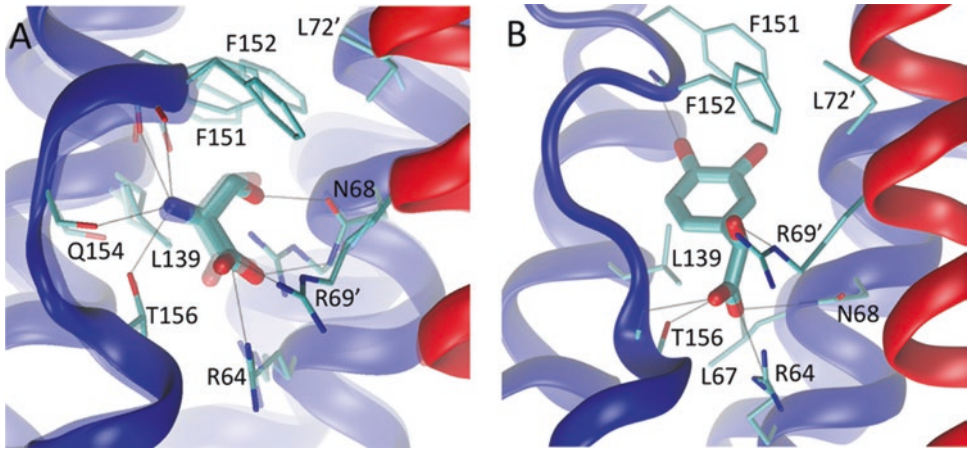

Fig. 2 Molecular graphics images of Tsr with ligands bound. (**a**) The lowest average association free energy binding mode of the L-serine:Tsr complex (opaque) in comparison with the X-ray structure (transparent; [11]). (**b**) the lowest average association free energy binding mode of the *R*-DHMA:Tsr complex. In both panels, the subunit providing the majority binding site is shown in blue, and the subunit providing the minority binding site is shown in red. Residues in the minority binding site as designed as, e.g., R69′, whereas residues in the majority binding site are unmarked. Key residues are shown in thin licorice representation

energetic properties of the X-ray resolved L-serine:Tsr structure [11] can be compared with the corresponding properties of the ensemble of simulated conformations within the selected-predicted serine:Tsr binding mode.

As for the structural validation, we used the backbone heavy atoms of the receptor binding pocket defined in Subheading 3.2 as a basis to perform a structural alignment of the simulation conformations of the selected serine:Tsr binding mode with respect to the experimentally resolved serine:Tsr X-ray structure [11] (*see* **Note 10**). Then, the average root mean square deviation (RMSD) between all heavy atoms of the ligand simulated conformations with respect to the experimentally resolved ligand structure is calculated. In the control case under investigation, the average RMSD was equal to 0.83 ± 0.16 Å. The apparent similarity between the predicted and experimentally resolved binding modes [11] is shown in Fig. 2a. The structural alignment and RMSD calculations can be performed using programs such as VMD [46] or Wordom [47]. Notably, when we repeated the procedure for the remaining 14 simulated serine:Tsr conformations, higher average RMSD values were observed. This suggests that, at least in the control case, the most energetically favored serine:Tsr simulated binding mode is also the one with the highest degree of similarity to the experimentally resolved serine:Tsr structure [11].

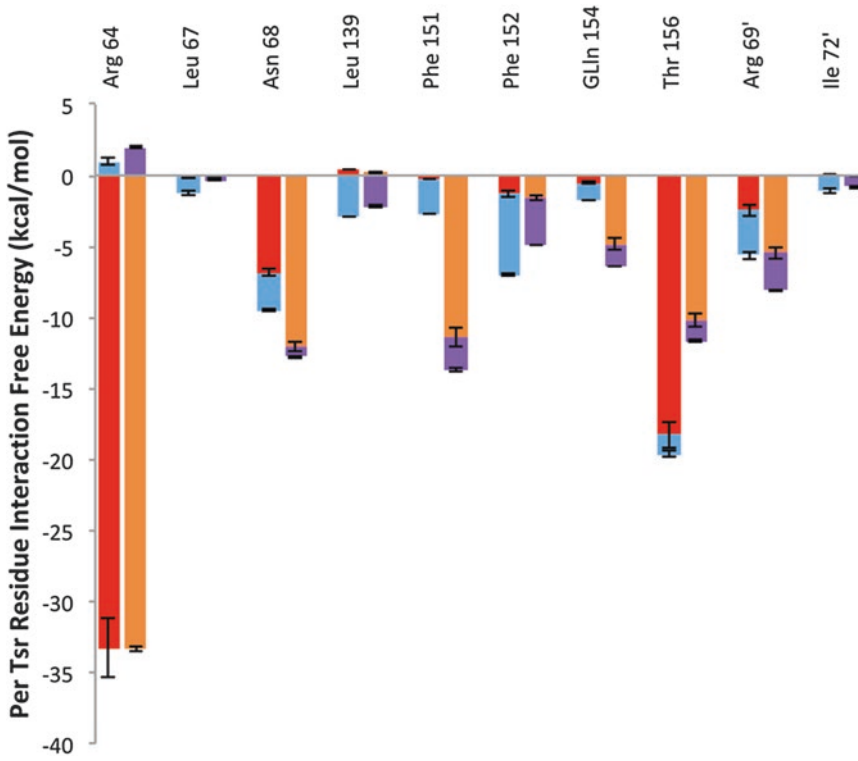

Fig. 3 Average interaction free energies (kcal/mol) decomposed into polar (red or orange) and nonpolar (blue or purple) components for Tsr interacting residues in complex with *R*-DHMA (first bar per residue) and in complex with serine (second bar per residue). The sum of the polar and nonpolar components corresponds to the total average per Tsr residue interaction free energy. Only per residue interactions with total interaction free energies less than −1.0 kcal/mol for either complex are considered in the plot. The average polar and nonpolar interaction free energy values and their standard deviations were calculated over four measurements, in which the first, second, third, and fourth measurements correspond to the individual average interaction free energy component of the first, second, third, and fourth 2.5 ns segments of the 10 ns MD simulation production run

As for the energetic validation, the average per receptor (Tsr) residue interaction free energies are calculated for the ensemble of simulated conformations within the selected serine:Tsr binding mode (Fig. 3; second bar per Tsr residue). These free energies are compared to the average per Tsr residue interaction free energies, which correspond to an additional 10 ns MD simulation we performed starting from the experimentally resolved serine:Tsr X-ray structure [11] (results not shown). In the control case, the comparison (e.g., through the calculation of ΔΔG per residue average interaction free energies, estimating the difference between the ΔG values of the two different simulations) showed that the energetic properties of the predicted binding mode were nearly identical to the energetic properties of the experimentally resolved serine:Tsr binding mode.

The methodology to calculate the average interaction free energies per receptor residue is analytically described in references [48–52] and is performed using CHARMM [20] and FORTRAN programs. The per residue average interaction free energy calculations take into account the: (1) van der Waals; (2) electrostatic; (3) GB solvation free energy; and (4) nonpolar solvation free energy of interaction between the entire ligand and the receptor residue under investigation. The sum of (1) and (4) corresponds to the total nonpolar average interaction free energy component, and the sum of (2) and (3) corresponds to the total polar average interaction free energy component.

3. For the control and test cases, the structural stability of the ligand in the receptor binding pocket within the selected lowest average MM-GBSA association free energy simulation(s) can be assessed using RMSD calculations. The simulation snapshots are structurally aligned based on the backbone heavy atoms of the receptor binding pocket defined in Subheading 3.2, and the average structure of the ligand is determined. Then, the average RMSD between all heavy atoms of the simulated conformations of the ligand with respect to its average structure are calculated. The corresponding RMSD values for the control and test cases are equal to 0.38 ± 0.14 Å and 0.51 ± 0.22 Å respectively, indicating a high structural stability of both serine and *R*-DHMA in the receptor binding pocket. Additionally, convergence of the running average of the MM-GBSA association free energy as a function of time could be checked.
4. A highly detailed trajectory analysis of the selected lowest average MM-GBSA association free energy simulation(s) can be performed to provide valuable insights into ligand:receptor binding. We calculated the average interaction free energy per Tsr residue interacting with *R*-DHMA and serine (first and second bar per Tsr residue, respectively, in Fig. 3). The resulting average per Tsr residue interaction free energy values are decomposed into polar and nonpolar components. This analysis can be combined with additional analyses, such as hydrogen bond analysis, and analysis of contacts between ligand groups and receptor residues, to provide a more thorough picture of how the ligand under investigation binds to the receptor. This approach identifies the key receptor interacting residues that are involved in binding and may also be associated with signaling. Hydrogen bond analysis and analysis of intermolecular contacts between ligand and receptor residues can be performed using Wordom [47].
5. An in-depth analysis of the simulation trajectory with the lowest average association free energy of *R*-DHMA in complex

with Tsr shows that *R*-DHMA primarily interacts with the same Tsr residues as serine. This is not a surprising result, as serine and *R*-DHMA share the same binding pocket, and both promote signaling-associated chemotaxis [10]. The key residues for serine binding to Tsr are Arg64, Asn68, Leu139, Phe151, Phe152, Gln154, Thr156, Arg69′, and Ile72′. Arg64 and Arg69′ form salt-bridges with the negatively charged carboxyl group of serine. The side chain amide group and oxygen of Asn68 form hydrogen bonds with the negatively charged carboxyl group of serine and the hydroxyl group of serine respectively. The backbone oxygens of Phe151, Phe152, and Gln154 all form hydrogen bonds with the positively charged amino group of serine. Additionally, the binding of serine to Tsr is facilitated by hydrophobic interactions with the side chain atoms of Leu139, Phe151, Phe152, and IIe72′. The key residues of *R*-DHMA binding to Tsr are largely the same as those listed for serine, with the addition of Leu67. Here, Arg64 forms a salt bridge with the negatively charged carboxyl group of *R*-DHMA. Arg69′ forms a hydrogen bond with the hydroxyl group of *R*-DHMA closest to the charged group. The polar side chain atoms of Asn68 and the hydroxyl group of *R*-DHMA closest to the charged group also form a hydrogen bond. Additionally, the hydroxyl side-chain group and backbone amide group of Thr156 both form hydrogen bonds with the negatively charged carboxyl group of *R*-DHMA. The inclusion of the hydrogen bond between the backbone amide group of Thr156 and *R*-DHMA may contribute to its lower average interaction free energy value with Thr156 as compared with serine. While serine forms hydrogen bonds with both Phe151 and Gln154 and simultaneously forms a hydrogen bond with Phe152, *R*-DHMA does not form hydrogen bonds with Phe151 or Gln154. *R*-DHMA also forms stronger interactions with Leu67 due to its larger size in comparison with serine, which brings it closer to Leu67.

3.5 Conclusions

In this chapter, we introduce a docking-refinement protocol and apply it to determining the binding conformation of *R*-DHMA in complex with Tsr. Similarly to references [40–44], in which MD simulations and energy calculations were introduced to investigate the binding conformations of protein:protein complexes, here we introduce a protocol developed in-house that consists of MD simulations and energy calculations to perform a nearly exhaustive search of the possible binding modes of a ligand in a receptor binding pocket. This protocol combines the following features. (1) The use of multiple, short docking simulations, with residues within the receptor binding pocket unconstrained, to examine nearly all possible binding modes of the ligand in the receptor binding pocket. (2) The initial positioning of the ligand within the receptor

binding pocket based on shape complementarity, and the use of both harmonic and quartic spherical potentials to constrain the ligand in the binding pocket during the multiple short MD docking simulations. (3) The selection of the most probable binding modes generated by the short docking simulations using interaction energy calculations, as well as the subsequent application of all-atom MD simulations and physical-chemistry based free energy calculations to elucidate the most favorable binding mode of the ligand in complex with the receptor.

The protocol was used to reproduce the binding conformation of L-serine in complex with Tsr (Fig. 2a), our control-validation case. The computationally predicted interactions of serine in complex with Tsr are nearly identical to the experimentally resolved X-ray structure of serine in a complex with Tsr [11]. Also, the same protocol was used to computationally elucidate the binding of *R*-DHMA to Tsr according to which *R*-DHMA, in general, interacts with the same residues of Tsr as serine does, with similar average interaction free energies. The interactions of Leu67, Leu139, Phe152, and Thr156 to *R*-DHMA are predicted to be stronger compared to serine. Longer-multiple MD simulations in conjunction with additional in-depth structural and energetic analyses could be used to understand whether and how these may contribute to sensing. Both serine and *R*-DHMA interact strongly with Tsr residues Arg64, Asn68, Phe151, Thr156, and Arg69′, which have been shown to be essential to serine sensing by Tsr [53, 11, 54].

4 Notes

1. Multiple modeling procedures may be introduced. The modeled structure with the highest agreement with existing experimental data may be selected for subsequent use.
2. In a specific study, it is preferable that all ligands are parametrized using the same method.
3. The size of the flexible receptor pocket may vary depending on the system under investigation. The docking simulation runs should be monitored to ensure that the interactions that do not include ligand:receptor interactions remain relatively stable.
4. The promising binding modes can be clustered, and the most energetically favorable can be selected at this stage, as in reference [44].
5. The duration of the energy minimization can be lengthened or shortened. Caution should be taken not to perform excessive energy minimization on the structures under investigation.

6. Gradual heating of the complex, and gradual release of constraints on the system, may be beneficial.
7. In some cases, light constraints may be needed to maintain the integrity of the receptor structure. These light constraints should not influence the binding pocket residues or the ligand itself. Nevertheless, the introduction of constraints may limit the investigation of potential allosteric effects.
8. In an unlikely scenario in which the most favorable binding mode according to MM-GBSA is not in complete agreement with experimental data (e.g., mutational studies), a thorough investigation of other potentially favorable binding modes or the use of other empirical or semiempirical scoring functions may be worthwhile.
9. The use of multiple scoring functions can be helpful in differentiating binding poses. Additionally, if multiple binding modes obtain similar scores, then a structural clustering analysis may reveal that the binding modes are nearly identical.
10. The heavy atoms of the ligand were not considered during the alignment.

Acknowledgments

We thank the Texas A&M High Performance Research Computing Facility for the use of the Ada supercomputing cluster, where all MD simulations and free energy calculations were performed. This study is supported by start-up funding from the Artie McFerrin Department of Chemical Engineering at Texas A&M University awarded to P.T. and the Texas A&M University Graduate Diversity Fellowship from the TAMU Office of Graduate and Professional Studies awarded to A.A.O.

References

1. McFedries A, Schwaid A, Saghatelian A (2013) Methods for the elucidation of protein-small molecule interactions. Chem Biol 20:667–673
2. Bren A, Eisenbach M (2000) How signals are heard during bacterial chemotaxis: protein-protein interactions in sensory signal propagation. J Bacteriol 182:6865–6873
3. Hazelbauer GL, Falke JJ, Parkinson JS (2008) Bacterial chemoreceptors: high-performance signaling in networked arrays. Trends Biochem Sci 33:9–19
4. Hegde M, Englert DL, Schrock S, Cohn WB, Vogt C et al (2011) Chemotaxis to the quorum-sensing signal AI-2 requires the Tsr chemoreceptor and the periplasmic LsrB AI-2-binding protein. J Bacteriol 193:768–773
5. Springer MS, Goy MF, Adler J (1977) Sensory transduction in *Escherichia coli*: two complementary pathways of information processing that involve methylated proteins. Proc Natl Acad Sci U S A 74:3312–3316
6. Hazelbauer GL (1975) Maltose chemoreceptor of *Escherichia coli*. J Bacteriol 122:206–214
7. Harayama S, Palva ET, Hazelbauer GL (1979) Transposon-insertion mutants of *Escherichia coli* K12 defective in a component common to galactose and ribose chemotaxis. Mol Gen Genet 171:193–203
8. Liu X, Parales RE (2008) Chemotaxis of *Escherichia coli* to pyrimidines: a new role for the signal transducer tap. J Bacteriol 190: 972–979

9. Manson MD, Blank V, Brade G, Higgins CF (1986) Peptide chemotaxis in *E. coli* involves the tap signal transducer and the dipeptide permease. Nature 321:253–256
10. Pasupuleti S, Sule N, Cohn WB, MacKenzie DS, Jayaraman A et al (2014) Chemotaxis of *Escherichia coli* to norepinephrine (NE) requires conversion of NE to 3,4-dihydroxymandelic acid. J Bacteriol 196:3992–4000
11. Tajima H, Imada K, Sakuma M, Hattori F, Nara T et al (2011) Ligand specificity determined by differentially arranged common ligand-binding residues in bacterial amino acid chemoreceptors Tsr and tar. J Biol Chem 286:42200–42210
12. Hedblom ML, Adler J (1980) Genetic and biochemical properties of *Escherichia coli* mutants with defects in serine chemotaxis. J Bacteriol 144:1048–1060
13. Calimet N, Simoes M, Changeux JP, Karplus M, Taly A et al (2013) A gating mechanism of pentameric ligand-gated ion channels. Proc Natl Acad Sci U S A 110:E3987–E3996
14. Taylor ND, Garruss AS, Moretti R, Chan S, Arbing MA et al (2016) Engineering an allosteric transcription factor to respond to new ligands. Nat Methods 13:177–183
15. Cassidy CK, Himes BA, Alvarez FJ, Ma J, Zhao G et al (2015) CryoEM and computer simulations reveal a novel kinase conformational switch in bacterial chemotaxis signaling. elife 4:e08419. [Epub ahead of print]
16. Yu D, Ma X, Tu Y, Lai L (2015) Both piston-like and rotational motions are present in bacterial chemoreceptor signaling. Sci Rep 5:8640
17. Yan Z, Wang J (2016) Methods and algorithms for molecular docking-based drug design and discovery. Ch 9. In: Scoring functions of protein-ligand interactions. IGI Global, Pennsylvania
18. Kuntz ID, Blaney JM, Oatley SJ, Langridge R, Ferrin TE (1982) A geometric approach to macromolecule-ligand interactions. J Mol Biol 161:269–288
19. Wang Z, Sun H, Yao X, Li D, Xu L (2016) Comprehensive evaluation of ten docking programs on a diverse set of protein-ligand complexes: the prediction accuracy of sampling power and scoring power. Phys Chem Chem Phys 18:12964–12975
20. Brooks BR, Brooks CL 3rd, Mackerell AD Jr, Nilsson L, Petrella RJ et al (2009) CHARMM: the biomolecular simulation program. J Comput Chem 30:1545–1614
21. Cheng Y, Jin UH, Davidson LA, Chapkin RS, Jayaraman A et al (2016) Microbial-derived 1,4-dihydroxy-2-naphthoic acid and related compounds as aryl hydrocarbon receptor agonists/antagonists: Structure-activity relationships and receptor modeling. Toxicol Sci 155(2):458–473. kfw230 [Epub ahead of print]
22. Yang J, Yan R, Roy A, Xu D, Poisson J et al (2015) The I-TASSER suite: protein structure and function prediction. Nat Methods 12:7–8
23. Söding J, Biegert A, Lupas AN (2005) The HHpred interactive server for protein homology detection and structure prediction. Nucleic Acids Res 33(W1):W244–2488
24. Biasini M, Bienert S, Waterhouse A, Arnold K, Studer G et al (2014) SWISS-MODEL: modelling protein tertiary and quaternary structure using evolutionary information. Nucl Acids Res 42(W1):W252–W258
25. MacKerell AD, Bashford D, Bellott M, Dunbrack RL, Evanseck JD et al (1998) All-atom empirical potential for molecular modeling and dynamics studies of proteins. J Phys Chem B 102:3586–3616
26. Best RB, Zhu X, Shim J, Lopes PE, Mittal J et al (2012) Optimization of the additive CHARMM all-atom protein force field targeting improved sampling of the backbone φ, ψ and side-chain χ(1) and χ(2) dihedral angles. J Chem Theory Comput 8:3257–3273
27. Vanommeslaeghe K, Hatcher E, Acharya C, Kundu S, Zhong S et al (2010) CHARMM general force field: a force field for drug-like molecules compatible with the CHARMM all-atom additive biological force fields. J Comput Chem 31:671–690
28. Yesselman JD, Price DJ, Knight JL, Brooks CL 3rd (2012) MATCH: an atom-typing toolset for molecular mechanics force fields. J Comput Chem 33:189–202
29. Zoete V, Cuendet MA, Grosdidier A, Michielin O (2011) SwissParam, a fast force field generation tool for small organic molecules. J Comput Chem 32:2359–2368
30. Irwin JJ, Shoichet BK (2005) ZINC–a free database of commercially available compounds for virtual screening. J Chem Inf Model 45:177–182
31. Vainio MJ, Puranen JS, Johnson MS (2009) ShaEP: molecular overlay based on shape and electrostatic potential. J Chem Inf Model 49:492–502
32. Trott O, Olson AJ (2010) AutoDock Vina: improving the speed and accuracy of docking with a new scoring function, efficient optimization and multithreading. J Comput Chem 31:455–461
33. Anighoro A, Bajorath J (2016) Three-dimensional similarity in molecular docking: prioritizing ligand poses on the basis of experi-

mental binding modes. J Chem Inf Model 56:580–587

34. Im W, Lee MS, Brooks CL 3rd (2003) Generalized born model with a simple smoothing function. J Comput Chem 24:1691–1702
35. Ryckaert JP, Ciccotti G, Berendsen HJC (1977) Numerical integration of the cartesian equations of motion of a system with constraints: molecular dynamics of n-alkanes. J Comput Phys 23:327–341
36. Godschalk F, Genheden S, Söderhjelm P, Ryde U (2013) Comparison of MM/GBSA calculations based on explicit and implicit solvent simulations. Phys Chem Chem Phys 15:7731–7739
37. Jo S, Kim T, Iyer VG, Im W (2008) CHARMM-GUI: a web-based graphical user interface for CHARMM. J Comput Chem 29:1859–1865
38. Nilsson L (2009) Efficient table lookup without inverse square roots for calculation of pair wise atomic interactions in classical simulations. J Comput Chem 30:1490–1498
39. Genheden S, Ryde U (2015) The MM/PBSA and MM/GBSA methods to estimate ligand-binding affinities. Expert Opin Drug Discov 10:449–461
40. Tamamis P, Floudas CA (2014) Molecular recognition of CCR5 by an HIV-1 gp120 V3 loop. PLoS One 9:e95767
41. Tamamis P, Floudas CA (2013) Molecular recognition of CXCR4 by a dual tropic HIV-1 gp120 V3 loop. Biophys J 105:1502–1514
42. Tamamis P, Floudas CA (2014) Elucidating a key component of cancer metastasis: CXCL12 (SDF-1α) binding to CXCR4. J Chem Inf Model 54:1174–1188
43. Tamamis P, Floudas CA (2014) Elucidating a key anti-HIV-1 and cancer-associated axis: the structure of CCL5 (Rantes) in complex with CCR5. Sci Rep 4:5447
44. Tamamis P, Kieslich CA, Nikiforovich GV, Woodruff TM, Morikis D et al (2014) Insights into the mechanism of C5aR inhibition by PMX53 via implicit solvent molecular dynamics simulations and docking. BMC Biophys 7:5
45. Neudert G, Klebe G (2011) DSX: a knowledge-based scoring function for the assessment of protein-ligand complexes. J Chem Inf Model 51:2731–2745
46. Humphrey W, Dalke A, Schulten K (1996) VMD: visual molecular dynamics. J Mol Graph 14:27–28–33–38
47. Seeber M, Cecchini M, Rao F, Settanni G, Caflisch A (2007) Wordom: a program for efficient analysis of molecular dynamics simulations. Bioinformatics 23:2625–2627
48. Tamamis P, López de Victoria A, Gorham RD Jr, Bellows-Peterson ML, Pierou P et al (2012) Molecular dynamics in drug design: new generations of compstatin analogs. Chem Biol Drug Des 79:703–718
49. Tamamis P, Pierou P, Mytidou C, Floudas CA, Morikis D et al (2011) Design of a modified mouse protein with ligand binding properties of its human analog by molecular dynamics simulations: the case of C3 inhibition by compstatin. Proteins 79:3166–3179
50. Tamamis P, Morikis D, Floudas CA, Archontis G (2010) Species specificity of the complement inhibitor compstatin investigated by all-atom molecular dynamics simulations. Proteins 78:2655–2667
51. Khoury GA, Smadbeck J, Tamamis P, Vandris AC, Kieslich CA et al (2014) Forcefield_NCAA: ab initio charge parameters to aid in the discovery and design of therapeutic proteins and peptides with unnatural amino acids and their application to complement inhibitors of the compstatin family. ACS Synth Biol 3:855–869
52. Kieslich CA, Tamamis P, Gorham RD, López de Victoria A, Sausman N (2012) Exploring protein-protein and protein-ligand interactions in the immune system using molecular dynamics and continuum electrostatics. Curr Phys Chem 2:324–343
53. Lee L, Mizuno T, Imae Y (1988) Thermosensing properties of *Escherichia coli tsr* mutants defective in serine chemoreception. J Bacteriol 170:4769–4774
54. Falke JJ, Hazelbauer GL (2001) Transmembrane signaling in bacterial chemoreceptors. Trends Biochem Sci 26:257–265

Chapter 29

Phylogenetic and Protein Sequence Analysis of Bacterial Chemoreceptors

Davi R. Ortega and Igor B. Zhulin

Abstract

Identifying chemoreceptors in sequenced bacterial genomes, revealing their domain architecture, inferring their evolutionary relationships, and comparing them to chemoreceptors of known function become important steps in genome annotation and chemotaxis research. Here, we describe bioinformatics procedures that enable such analyses, using two closely related bacterial genomes as examples.

Key words Chemotaxis, Chemoreceptors, Sequence analysis, Phylogenetic analysis, Protein domains, Rhizobia

1 Introduction

Chemoreceptors (also called methyl-accepting chemotaxis proteins or MCPs) are key components of bacterial chemosensory networks [1]. More than a half of sequenced bacterial and archaeal genomes contain chemoreceptor genes [2, 3]. Chemoreceptors are multidomain proteins that all share a conserved signaling domain, but they display a wide variety of sensory domains [4]. Moreover, even the conserved signaling domains consist of several classes that are distinguished by the number of helical heptads in their four-helix coiled-coil [5]. Chemoreceptors are also highly prone to horizontal gene transfer [6] and domain shuffling [7].

The Pfam domain model MCPsignal (accession PF00015) identifies chemoreceptor signaling domains with high sensitivity and specificity; however, it does not distinguish between different heptad classes. Many Pfam domain models detect chemoreceptor sensory domains, but their sensitivity varies from relatively high (e.g., models for newly redefined Cache domain families [8]) to fairly low, and many of these domains in various chemoreceptor sequences remain undetected. Consequently, phylogenetic and protein sequence analysis of chemoreceptors presents a challenge. Here, we demonstrate this analysis using two genomes

Michael D. Manson (ed.), *Bacterial Chemosensing: Methods and Protocols*, Methods in Molecular Biology, vol. 1729, https://doi.org/10.1007/978-1-4939-7577-8_29,

of two closely related bacterial species, *Rhizobium sp.* NT-26, which has never been studied with respect to chemotaxis, and *Sinorhizobium meliloti*, whose chemoreceptors have been studied in some detail [9–12].

2 Materials

Most of materials in computational sciences—both software and hardware—are under rapid development and the groundbreaking technologies of today might become obsolete within 5 years (*see* **Note1**). Here, we provide suggestions for software and hardware that are available in 2017.

2.1 Hardware

1. Processor: Multi-core Intel Xeon or AMD Opteron—2.3 GHz (*see* **Note 2**).
2. Random Access Memory (RAM): 16 GB RAM (*see* **Note 3**).
3. Storage: 1 TB.
4. Operational system: Linux (*see* **Note 4**).
5. Others: high-speed Internet connection.

2.2 Databases

1. RefSeq: The Reference Sequence database from the National Center for Biotechnology Information (NCBI) contains a comprehensive, nonredundant, and well-annotated set of DNA, RNA, and protein sequences [13]. Link: https://www.ncbi.nlm.nih.gov/refseq/
2. Pfam: The Pfam (Protein Families) database is one of the most comprehensive and commonly used databases of protein domains [14]. Link: http://pfam.xfam.org/
3. Chemoreceptor signaling domain models: Chemoreceptor signaling domain class-specific models, as developed by Alexander and Zhulin [5], are accessible from the following URL: http://genomics.utk.edu/hmms.html, or can be requested from the authors.

2.3 Bioinformatic Software

1. Multiple sequence alignment: MAFFT 7.304 [15].
2. Phylogeny: RAxML 8.2.9 [16].
3. Search engines: BLAST 2.5.0 [17], HMMER v3.1b2 [18].
4. Sequence visualization and analysis: Jalview 2.10.1 [19].
5. Sequence manipulation script: convert.sh. Link: http://sco.h-its.org/exelixis/resource/download/software/convert.sh
6. Tree visualization: Dendroscope 3.5.7 [20].

2.4 Other Software

1. Compression utility: gzip. Link: http://www.gzip.org/

3 Methods

3.1 Genome Download

1. As you open a terminal, the prompt is located at your home directory. Use the following commands to create a new directory:

   ```
   $ mkdir mcpBioinfo
   ```

   then enter the newly created directory by typing:

   ```
   $ cd mcpBioinfo
   ```

2. For the rest of this chapter, we will assume that all data files are in this directory. At any moment the list of files in this directory can be retrieved by typing:

   ```
   $ ls -lh
   ```

   (*see* **Note 5**).

   Here, the options "l" and "h" tell the computer to return a "l"ist of files and to show their size in "h"uman readable format.

3. Download the protein.faa.gz file of the *Rhizobium sp.* NT-26 from the RefSeq database using the link: ftp://ftp.ncbi.nlm.nih.gov/genomes/refseq/bacteria/Rhizobium_sp._NT-26/representative/GCF_000967425.1_ASM96742v1

4. Use gzip to decompress the FASTA formatted file contained the protein sequences encoded in the genome of *Rhizobium sp.* NT-26.

   ```
   $ gunzip GCF_000967425.1_ASM96742v1.protein.faa.gz
   ```

5. There should be a GCF_000967425.1_ASM96742v1.protein.faa file in the directory instead of the GCF_000967425.1_ASM96742v1.protein.faa.gz file.

3.2 Identification of Chemoreceptors

Chemoreceptors can be identified by matching a set of protein sequences against the Pfam protein domain model MCPsignal (*see* **Note 6**).

1. Download the Pfam model for MCPsignal from the Pfam webpage (http://pfam.xfam.org/). On the home page, click in JUMP TO under QUICK LINKS, type MCPsignal in the field, and click Go. You should be now in the main page of the MCPsignal domain model, which has the Pfam code PF00015. On the left menu, click in Curation & model, and in the session Download, click "download." After clicking on this link, a "MCPsignal.hmm" file should be downloaded automatically to your computer.

2. Use hmmsearch from HMMER software package to search matches to the Pfam MCPsignal domain in a FASTA formatted file (*see* **Note 7**). Assuming that the FASTA files containing the protein sequences, "GCF_000967425.1_ASM96742v1.

protein.faa," and the "MCPsignal.hmm" are in the same directory (or folder), type the following command line in the terminal prompt:

```
$ hmmsearch --noali --cut_tc MCPsignal.hmm
GCF_000967425.1_ASM96742v1.protein.faa > rhizo.mcps.hmmer.dat
```

(*see* **Note 8**)

Here, the option --noali will not display the alignment information in the output file and --cut-tc uses the trusted cutoff from the domain model itself to determine if the score received by the best match of the protein is in fact an MCPsignal protein domain or not. The results are saved in the rhizo.mcps.hmmer.dat. The file contains information about the hits and the main result is summarized in Fig. 1.

3. From this section of the output file, you can identify the sequences that match the MCPsignal domain model and thus isolate them from the original set of all protein sequences from a given genome (*see* **Note 9**).
4. Using any text editor, copy and paste the sequences (and headers) in the "GCF_000967425.1_ASM96742v1.protein.faa"

Query: MCPsignal [M=207]
Accession: PF00015.19
Description: Methyl-accepting chemotaxis protein (MCP) signaling domain
Scores for complete sequences (score includes all domains):

	--- full sequence ---			--- best 1 domain ---			-#dom-			
E-value	score	bias	E-value	score	bias	exp	N	Sequence	Description	
1.8e-60	202.2	39.3	2.8e-58	195.1	26.0	2.9	1	WP_052637176.1	chemotaxis protein [Rhizobium sp. NT-26]	
3.1e-59	198.2	26.2	3.1e-59	198.2	26.2	4.3	1	WP_052637427.1	chemotaxis protein [Rhizobium sp. NT-26]	
4e-59	197.9	38.3	6.8e-56	187.3	24.6	2.4	1	WP_052642117.1	chemotaxis protein [Rhizobium sp. NT-26]	
4.2e-59	197.8	47.3	3.7e-57	191.4	27.1	3.2	1	WP_052636691.1	chemotaxis protein [Rhizobium sp. NT-26]	
5.8e-59	197.3	51.4	2.4e-58	195.3	25.7	3.1	1	WP_052638282.1	chemotaxis protein [Rhizobium sp. NT-26]	
6e-59	197.3	39.3	2.9e-56	188.5	26.5	3.2	1	WP_052638756.1	chemotaxis protein [Rhizobium sp. NT-26]	
7.1e-59	197.0	36.1	4e-56	188.0	22.4	2.4	1	WP_052640661.1	chemotaxis protein [Rhizobium sp. NT-26]	
1.9e-57	192.4	25.0	1.9e-57	192.4	25.0	3.5	1	WP_052637180.1	chemotaxis protein [Rhizobium sp. NT-26]	
4.3e-57	191.2	23.4	4.3e-57	191.2	23.4	3.5	1	WP_052637732.1	hypothetical protein [Rhizobium sp. NT-26]	
9.8e-57	190.0	54.7	9.2e-56	186.9	25.4	3.3	1	WP_052638961.1	chemotaxis protein [Rhizobium sp. NT-26]	
5.5e-56	187.6	32.7	4.2e-55	184.7	19.8	4.8	1	WP_052638480.1	chemotaxis protein [Rhizobium sp. NT-26]	
1.6e-55	186.0	26.7	1.6e-55	186.0	26.7	3.7	1	WP_052637044.1	hypothetical protein [Rhizobium sp. NT-26]	
1.4e-54	183.0	25.3	1.4e-54	183.0	25.3	3.1	1	WP_052637800.1	hypothetical protein [Rhizobium sp. NT-26]	
9.3e-54	180.3	23.2	9.3e-54	180.3	23.2	3.3	1	WP_052638887.1	chemotaxis protein [Rhizobium sp. NT-26]	
1.7e-42	143.6	18.2	1.7e-42	143.6	18.2	2.7	1	WP_052636907.1	chemotaxis protein [Rhizobium sp. NT-26]	
1.7e-38	130.4	20.0	5.4e-31	106.0	7.0	2.0	1	WP_052639048.1	hypothetical protein [Rhizobium sp. NT-26]	
1.1e-26	91.9	30.8	2.2e-26	90.9	18.9	2.4	1	WP_052641496.1	MCP chemoreceptor protein [Rhizobium sp.	
9.4e-16	56.2	3.0	1.3e-15	55.7	3.0	1.2	1	WP_052640340.1	chemotaxis protein [Rhizobium sp. NT-26]	

Fig. 1 Result of a HMMER search against *Rhizobium sp.* NT-26 protein sequences using the MCP signal domain model

file that matches the sequence identifier (in the column Sequence) into a new file called "rhizo.mcps.fa" (*see* **Note 10**). The first lines of the file should look the image shown on Fig. 2.

3.3 Identification of Chemoreceptor Heptad Classes

1. To classify chemoreceptors into heptad classes, we assume that the mcp-class-library.3.hmm file is already in the mcpBioinfo directory. However, before using it to classify the selected MCP sequences, we must "press" the library using hmmpress from the HMMER package:

   ```
   $ hmmpress mcp-class-library.3.hmm
   ```

2. Use the hmmscan software from the HMMER package to classify the sequences of MCPs according to its heptad classes:

   ```
   $ hmmscan --noali --tblout rhizo.mcps.
   classes.tbl mcp-class-library.3.hmm
   rhizo.mcps.fa
   ```

   Here, the option --tblout ensures a table-like output format for hmmscan that makes it easier to identify the best matching class without extra information. The output file "rhizo.mcps.classes.tbl" format should be similar to the one shown on Fig. 2. The heptad class of each chemoreceptor is printed in the column target of the "rhizo.mcps.classes.tbl." The chemoreceptor is confidently assigned to the highest-scored class if the score is higher than 175 and the difference between the first and second highest scores is larger than 75 (*see* **Note 11**).

```
>WP_052637176.1 chemotaxis protein [Rhizobium sp. NT-26]
MAKRANLMTRILVAASVVVVVALAGFSFHINSIQHASVTKSVEDSISSAGRQASQALANWMNGRVVLTNM
VADAVSRNPDAVTAVLDNQVLTKEFSSTYFGDTAGTFTMWPNLPMPADYDPRQRPWYKDAVASGSVVLTE
PYVDASSGDLVVSAAVPVNREGALAGVVGSDFSLQSIVAMVKSIDLGVPATAFLVNKAGTVLIHPEASLV
MKTLADVFPQDTPATGATMVETTFGGRNVLVSFVPVAGLPSVQWYLGFAVDAEAAYASLTAFQTAAVIAT
VLAVALMIGAMAWMLSRLVVRPVTDMTHAMERLAAGDLTVAIPGEDRRDQIGAMAAAVSVFRTNALERER
LEGEAEEGRRLSDAERREREAQKAHDQAEAERAVKALAEALGALADGNLSHRIEVPFAAHIDRLRTDYNA
AVTQLKSALQAVGSNARTIDAGAEEIRVAADGLARRTEQQAASVEETAAALEEITTTVRDTAHRAEEVGT
LVSRARDGAEHSGAVVSKAVAAMTEIEDSSGKISNIIGVIDDIAFQTNLLALNAGVEAARAGEAGKGFAV
VAQEVRELAQRSAQAAKEIEALITASNTQVRSGVTLVAQTGEALQAIVSQVQEISRHVGAIVTATREQST
GLLEINNAVNAMDQGTQQNAAMVEEQTAASHSLAAEAAKLMELLARFNLGMAAQAGMSTQGGRRAA
>WP_052637427.1 chemotaxis protein [Rhizobium sp. NT-26]
MTRPKVKTALAGILILIGISFGLFATFALNRIGAINAHLEEIATDNMPTAITVKDMEVQLGSIRTAYRSH
ILRSDAEGKAAAAKAVETATAKLKEDITKFNTLNPSREESEIVVKLGQAVDEYNAVGATVFASSLAGHID
EANRILRDEMVKSANAATESAERLVAISNSDTTEAYANAQSAYSTTLTVAFVAIGVLAAVIAAAIWFAIT
GIARPIQTITGSMNTLARGDADTAIPYAGRTDEIGEMAAAVEVFRTNALENRRLEQEANAQRSQSEEQRR
RTAEQERIRAEAMAQATTGLADGLKQLSAGNLGVQLTQSFAEEFEGLREDFNRSVMQLRETMTAVAESTS
SIDSGSREISQSAEDLSKRTEQQAASLEETAAALDQITTNVANSSKRAEEARTVAIQANESARHSGAVVA
NAVDAMGKIEQSSSQISNIIGVIDDIAFQTNLLALNAGVEAARAGEAGKGFAVVAQEVRELAQRSATAAK
EIKDLIRNSSAEVGNGVKLVSDTGEALKTIESYIVTINQHMDAIATSAREQSVGLSEVNTAVNQMDQVTQ
QNAAMVEEANAAGATLANEASRLRGLIGQFQLGGAASYQPASHRAPAPVAKAGAKSAPVASPARSMMGKI
ANAFSAKGSAAVAVSNDSWEEF
…
```

Fig. 2 Image of a FASTA formatted file of *Rhizobium sp.* NT-26 chemoreceptor sequences (only two sequences are shown)

3. Add the classification information to the sequence header of each sequence by editing the "rhizo.mcps.fa." Save the new file as "rhizo.mcps.classified.fa."

3.4 Second Genome Download

1. In order to compare the chemoreceptors from *Rhizobium sp.* NT-26 and *S. meliloti*, execute the same steps for the *S. meliloti* protein sequence set, as described in Subheading 3.1, but using the following link: ftp://ftp.ncbi.nlm.nih.gov/genomes/refseq/bacteria/Sinorhizobium_meliloti/reference/GCF_000006965.1_ASM696v1.

```
$ gunzip GCF_000006965.1_ASM696v1_protein.faa.gz
$ hmmsearch --noali --cut_tc MCPsignal.hmm GCF_000006965.1_ASM696v1_protein.faa > meliloti.mcps.hmmer.dat
```

Based on "meliloti.mcps.hmmer.dat," make the "meliloti.mcps.fa" file with the MCP sequences from this genome.

```
$ hmmscan --noali --tblout meliloti.mcps.classes.tbl mcp-class-library.3.hmm meliloti.mcps.fa
```

Based on meliloti.mcps.classes.tbl, edit meliloti.mcps.fa with the classification information and save as meliloti.mcps.classified.fa.

Use the linux command 'cat' to put the classified mcp sequences of *Rhizobium sp.* NT-26 and *S. meliloti* in the same file:

```
$ cat rhizo.mcps.classified.fa meliloti.mcps.classified.fa > rhizo.n.meliloti.mcps.classified.fa
```

3.5 Identification of Chemoreceptor Sensory Domains

Use CDvist, a Comprehensive Domain Visualization Tool [21], available at http://cdvist.zhulinlab.org to search and visualize the domain architecture of all chemoreceptor sequences from both genomes at once. On the home page, click "choose," select "rhizo.n.meliloti.mcps.classified.fa" file and click submit (*see* **Note 12**). Using the default settings, CDvist will predict transmembrane regions and protein domains using the best search algorithms (first specific, and then more sensitive), and databases and results will be returned in a format shown in Fig. 3.

3.6 Multiple Sequence Alignment

1. Construct the multiple sequence alignment of the chemoreceptor sequences from both genomes using the accurate L-INS-I algorithm from the MAFFT package (*see* **Note 13**) as follows:

```
$ linsi rhizo.n.meliloti.mcps.classified.fa > rhizo.n.meliloti.mcps.classified.linsi.fa
```

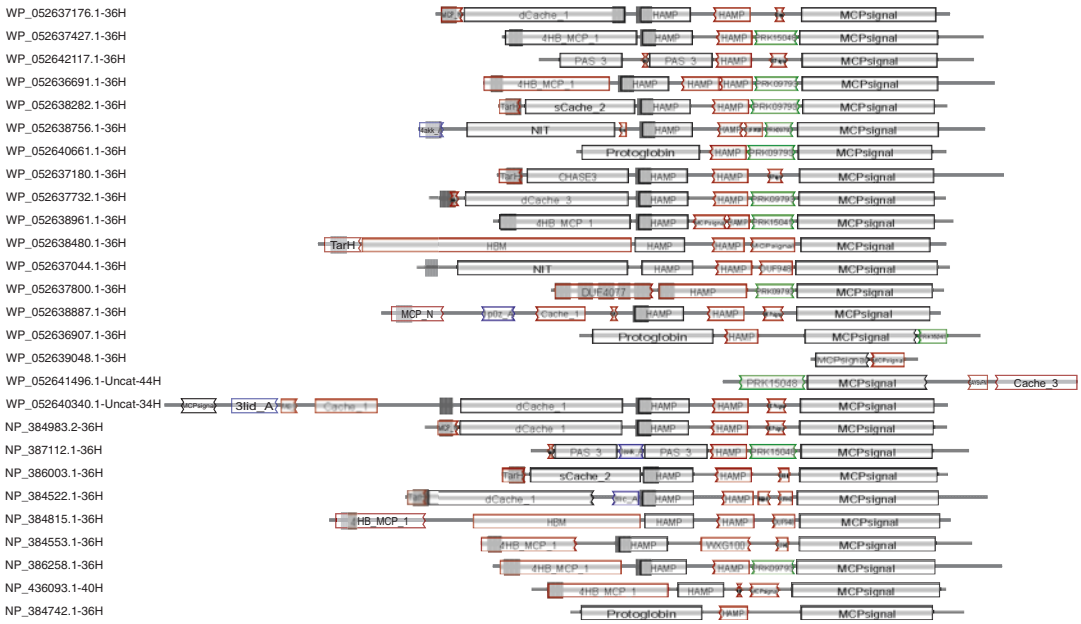

Fig. 3 Result of a CDvist search shows the diversity of domain architecture in the chemoreceptor sequences from the two rhizobial genomes. Protein domains are represented by boxes with colored borders and transmembrane regions by gray rectangles

The final alignment is stored in the file "rhizo.n.meliloti.mcps.classified.linsi.fa."

As often happens to alignments of MCPs, only the C-terminal half of the sequences will be aligned because all of them contain the same MCPsignal domain. The large number of gaps in the N-terminal half of alignment indicates that different chemoreceptor sequences contain different sensory domains, as seen by the domain architecture visualization shown in Fig. 3. Thus, for constructing a proper MSA, it is necessary to select only those parts of chemoreceptor sequences that are common to all of them.

2. Load the "rhizo.n.meliloti.mcps.classified.linsi.fa" file to Jalview (File > Input Alignment > From file) and in the window of the alignment, click Colour > Clustalx to color amino acid residues using clustalX color code. It is easy to notice the borders of the well-aligned region, which corresponds to the MCPsignal domain (Fig. 4). Use Jalview to select only the columns that are part of the well-aligned region. To do that, hold shift and click at the alignment coordinate grid on the top of the alignment in both columns that determine the region of interest. The selected region will be highlighted in red. Invert column selection by clicking Select > Invert column selection. In each side

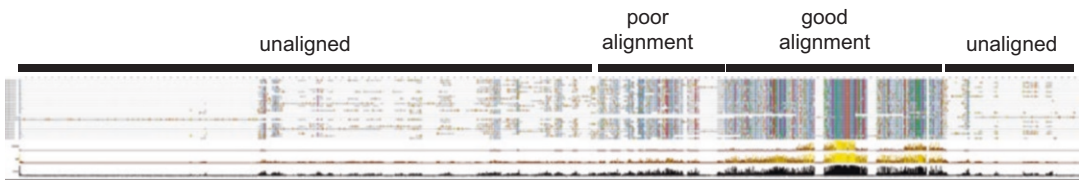

Fig. 4 Output file of a multiple-sequence alignment of chemoreceptor sequences. Good alignment region corresponds to the MCP signaling domain

of the alignment there will be regions selected. In each of them, right click on the region of the alignment coordinate bar (now highlighted above in red) and click Hide column. Only the region of interest should be displayed. Save the alignment as "rhizo.n.meliloti.mcps.classified.linsi.manualTrim.fa."

3. Convert the file from FASTA format to phylip format (*see* **Note 14**) to prepare multiple sequence alignment for phylogenetic analysis:

```
$ sh convert.sh rhizo.n.meliloti.
mcps.classified.linsi.manualTrim.fa >
rhizo.n.meliloti.mcps.classified.linsi.
manualTrim.phy
```

3.7 Phylogenetic Tree

1. Use RAxML software (*see* **Note 15**) to infer the phylogeny of chemoreceptors:

```
$ raxml -m PROTGAMMAIAUTO -p 12345 -f a
-d -x 123 -N 250 -s rhizo.n.meliloti.
mcps.classified.linsi.manualTrim.phy -n
rhizo.n.meliloti.mcps.newick
```

   Here, the option "–m" selects which model of evolution the maximum likelihood (ML) search will use. In this case, we let the program automatically pick the evolutionary model using a gamma distribution with four categories (default parameters) and allowing for Invariant sites. The option "-f a" performs a ML search for the best tree of the 250 bootstrap runs (determined by the flag "-N 250"). The flags "-x" and "-p" set the seed for the ML-search and the rapid bootstrap strategy. Finally, the sequence file in PHYLIP format is passed after the flag "-s" and the output sulfix of all output files is passed after "-n" (see **Note 16**).

2. Use Dendroscope to visualize trees generated by RAxML. The file "RAxML_bipartitionsBranchLabels.rhizo.n.meliloti.mcps.newick" contains the best tree found by RAxML with the bootstrap support score mapped to the branches (Fig. 5; *see* **Note 17**). The tree reveals five sets of chemoreceptors that can be identified as orthologs present in both genomes (shaded).

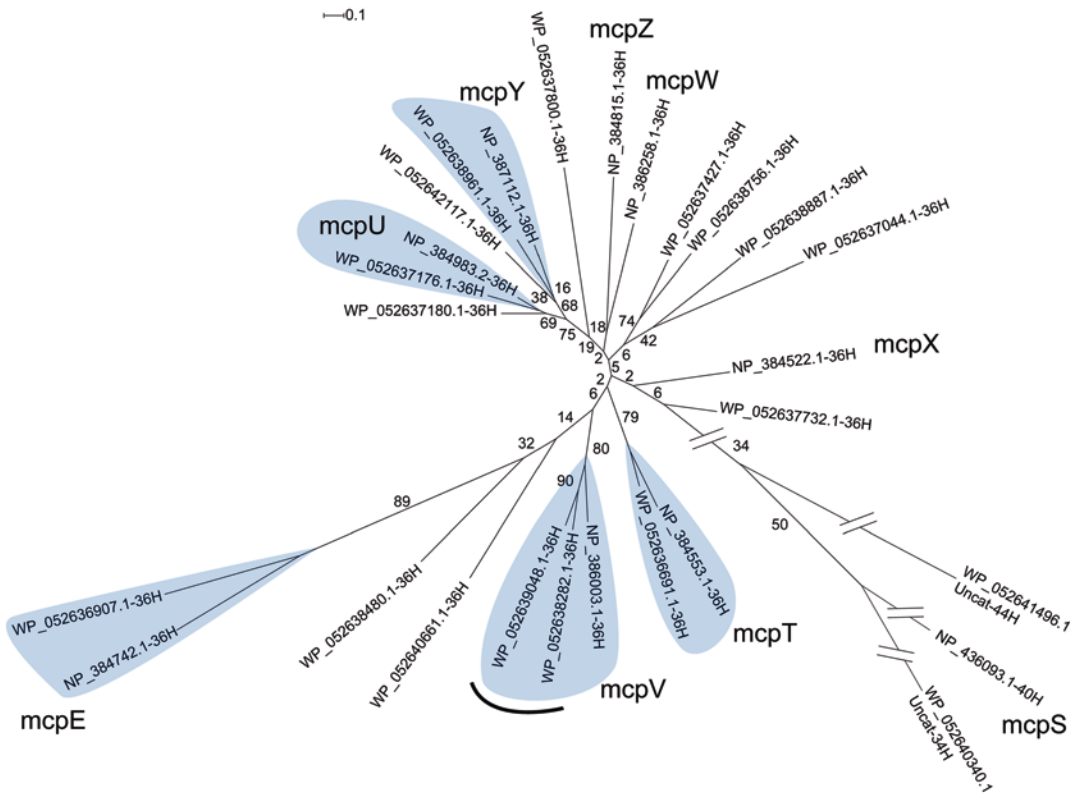

Fig. 5 Maximum likelihood phylogenetic tree of chemoreceptor sequences from two rhizobial genomes. Orthologous groups of sequences are highlighted

These chemoreceptors, common to both species, were likely present in their common ancestor. There is also at least one gene duplication event in *Rhizobium sp*. NT-26 that led to two copies of McpV (black arch). This duplication occurred after the separation of lineages that gave rise to these two genomes.

3. Another conspicuous feature is the lack of bootstrap support in the deepest branches of the tree. In practice, it is a rule of thumb not to consider branches with low bootstrap support (typically less than 75%) to infer evolutionary relationships. A larger set of sequences from distantly related species is needed to resolve these.

4. *S. meliloti* is an emerging model to study chemotaxis plant-associated bacteria. The phylogenetic analysis presented here helps to transfer knowledge obtained for chemoreceptors in *S. meliloti* (identified by gene names) to an organism for which no such information is available. Chemoreceptors in *Rhizobium sp*. NT-26 are likely to have the same function as their *S. meliloti* orthologs (shaded branches), except for McpV, because gene duplication often results in a change of function (*e.g.*, ligand binding specificity) in one or both paralogs.

4 Notes

1. The software used here work with most modern computers. The hardware specification suggested is the result of a compromise between performance and cost. The better the computer, the less computing time required. Most of computational bottlenecks in bioinformatics are due to limited RAM. Therefore, as a general recommendation, investment in memory is a good choice.
2. To choose a balanced combination between RAM and processor, compare specifications from leading computer manufacturers and search for suggested products.
3. To date, most of the bioinformatics programs do not take advantage of the Graphic Processor Units (GPU). However, in the near future, more bioinformatics software will be compatible with this powerful device. It is likely that these new programs will be built using CUDA programming language, which is designed specifically to NVIDIA graphic cards, thus limiting the choices for a GPU that can enhance the performance of bioinformatics applications.
4. We limit the scope of this chapter to the use of command-line in Unix-based operational systems: Max OS X or Linux. If you must run your machine in Windows environment, there are options to emulate Linux environments from within, such as Cygwin or even an entire independent Linux machine using Virtual Box from Oracle.
5. This is a command line instruction. It should be typed without the "$."
6. Chemoreceptors can also be recognized as protein sequences containing the MA domain model (accession number SM00283) from the SMART database [22], which largely overlaps with the MCPsignal domain model from Pfam. If needed, download the MA raw HMM from SMART (http://smart.embl-heidelberg.de/) and perform the same steps as described for the Pfam model.
7. There are many formats for files that contains protein sequence data. The most frequently used is the FASTA format. The FASTA format requires the file to start with a sequence header of one line, defined by the character ">" in the beginning of the line, and a second line with the amino acid sequence. It is acceptable for the amino acid sequence to be divided into multiple lines, and it is considered part of the same sequence until a line starting with ">" appears in the file. An example of FASTA file looks as follows:

```
>Sequence 1
AAAAAAAAAAAAA
>Sequence 2
KKKKKKKKKKKKKK
```

8. This is a command line instruction and should be typed in a single line without enter.
9. Sequences with matches to the MCPsignal domain model can be selected manually using copy and paste. However, it is very advantageous to learn a scripting language, such as Perl or Python, to avoid repetitive manual tasks. For example, it only requires an introductory level knowledge in one of these languages to be able to write a script that tells the computer how to find the selected sequences in the hmmsearch output file and copy them from the original "GCF_000967425.1_ASM96742v1.protein.faa" to a new "rhizo.mcps.fa" FASTA file.
10. Useful tip: leave an empty line at the end of each FASTA file. This is useful in case you concatenate files using "cat" command.
11. In the original models developed for HMMER2, the minimum score and minimum difference between the scores of the first and second best hits were determined empirically. The new HMMER3 models, created by conversion from models built for HMMER2, perform slightly differently, and the new thresholds reported here are designed to capture the outcome closest to the HMMER2 performance. However, it is always important to verify the scores and multiple sequence alignments in order to classify chemoreceptors that have borderline scores with confidence.
12. CDvist has access to many databases and, if needed, the default settings can be changed to obtain more information about each sequence.
13. MAFFT can be downloaded at http://mafft.cbrc.jp/alignment/software/ under the menu tab "Download version." Click the version that suits your system and follow the instructions to install.
14. Sequence files come in different formats. Phylip is a well-known format that is traditionally used by several types of phylogenetic software. The specifications of the format can be found at: http://evolution.genetics.washington.edu/phylip/doc/sequence.html. It is a good introductory programming exercise to write your own script to convert FASTA files into phylip and other formats.
15. RAxML can be downloaded from https://github.com/stamatak/standard-RAxML. Follow the instructions in the README to install the most suitable version to your hardware as instructed.
16. RAxML is a powerful software for phylogenetic inference using maximum likelihood. It allows parallelization to take advantage of multi-core computers using the flag "-T N," where

"N" is the number of cores available. Check out the manual for many other capabilities.

17. After visualizing and manipulating the tree in Dendroscope, click in File > Export image to export the tree in pdf. Use a vector graphics editor, such as Adobe Illustrator, to further edit the figure (e.g., to highlight relevant parts and to label relevant features).

Acknowledgment

This work was supported by NIH grant R35 GM122588 to D.R.O and R01 GM072285 to I.B.Z.

References

1. Hazelbauer GL, Falke JJ, Parkinson JS (2008) Bacterial chemoreceptors: high-performance signaling in networked arrays. Trends Biochem Sci 33:9–19
2. Wuichet K, Zhulin IB (2010) Origins and diversification of a complex signal transduction system in prokaryotes. Sci Signal 3:ra50
3. Adebali O, Zhulin IB (2017) Aquerium: a web application for comparative exploration of domain-based protein occurrences on the taxonomically clustered genome tree. Proteins 85:72–77
4. Wuichet K, Alexander RP, Zhulin IB (2007) Comparative genomic and protein sequence analyses of a complex system controlling bacterial chemotaxis. Methods Enzymol 422:1–31
5. Alexander RP, Zhulin IB (2007) Evolutionary genomics reveals conserved structural determinants of signaling and adaptation in microbial chemoreceptors. Proc Natl Acad Sci U S A 104:2885–2890
6. Borziak K, Fleetwood AD, Zhulin IB (2013) Chemoreceptor gene loss and acquisition via horizontal gene transfer in *Escherichia coli*. J Bacteriol 195:3596–3602
7. Day CJ, King RM, Shewell LK, Tram G, Najnin T et al (2016) A direct-sensing galactose chemoreceptor recently evolved in invasive strains of *Campylobacter jejuni*. Nat Commun 7:13206
8. Upadhyay AA, Fleetwood AD, Adebali O, Finn RD, Zhulin IB (2016) Cache domains that are homologous to, but different from PAS domains comprise the largest superfamily of extracellular sensors in prokaryotes. PLoS Comput Biol 12:e1004862
9. Meier VM, Scharf BE (2009) Cellular localization of predicted transmembrane and soluble chemoreceptors in *Sinorhizobium meliloti*. J Bacteriol 191:5724–5733
10. Webb BA, Hildreth S, Helm RF, Scharf BE (2014) *Sinorhizobium meliloti* chemoreceptor McpU mediates chemotaxis toward host plant exudates through direct proline sensing. Appl Environ Microbiol 80:3404–3415
11. Webb BA, Helm RF, Scharf BE (2016) Contribution of individual chemoreceptors to *Sinorhizobium meliloti* chemotaxis towards amino acids of host and nonhost seed exudates. Mol Plant-Microbe Interact 29:231–239
12. Webb BA, Karl Compton K, Castañeda Saldaña R, Arapov TD, Keith Ray W et al (2017) *Sinorhizobium meliloti* chemotaxis to quaternary ammonium compounds is mediated by the chemoreceptor McpX. Mol Microbiol 103:333–346
13. O'Leary NA, Wright MW, Brister JR, Ciufo S, Haddad D et al (2016) Reference sequence (RefSeq) database at NCBI: current status, taxonomic expansion, and functional annotation. Nucleic Acids Res 44:D733–D745
14. Finn RD, Coggill P, Eberhardt RY, Eddy SR, Mistry J et al (2016) The Pfam protein families database: towards a more sustainable future. Nucleic Acids Res 44:D279–D285
15. Katoh K, Standley DM (2013) MAFFT multiple sequence alignment software version 7: improvements in performance and usability. Mol Biol Evol 30:772–780
16. Stamatakis A (2014) RAxML version 8: a tool for phylogenetic analysis and post-analysis of large phylogenies. Bioinformatics 30:1312–1313

17. Altschul SF, Madden TL, Schäffer AA, Zhang J, Zhang Z et al (1997) Gapped BLAST and PSI-BLAST: a new generation of protein database search programs. Nucleic Acids Res 25:3389–3402
18. Eddy SR (2011) Accelerated profile HMM searches. PLoS Comput Biol 7(10):e1002195
19. Waterhouse AM, Procter JB, Martin DM, Clamp M, Barton GJ (2009) Jalview version 2--a multiple sequence alignment editor and analysis workbench. Bioinformatics 25:1189–1191
20. Huson DH, Scornavacca C (2012) Dendroscope 3: an interactive tool for rooted phylogenetic trees and networks. Syst Biol 61:1061–1067
21. Adebali O, Ortega DR, Zhulin IB (2015) CDvist: a webserver for identification and visualization of conserved domains in protein sequences. Bioinformatics 31:1475–1477
22. Letunic I, Doerks T, Bork P (2015) SMART: recent updates, new developments and status in 2015. Nucleic Acids Res 43:D257–D260

INDEX

Michael D. Manson (ed.), *Bacterial Chemosensing: Methods and Protocols*, Methods in Molecular Biology, vol. 1729, https://doi.org/10.1007/978-1-4939-7577-8, © Springer Science+Business Media, LLC 2018

T

U